

ENGINEERING PHYSICOCHEMICAL AND ELECTROCHEMICAL PROPERTIES OF  
PYRIDINIUM ANOLYTES FOR NONAQUEOUS REDOX FLOW BATTERIES

By

Sharmila Samaroo

A DISSERTATION

Submitted to  
Michigan State University  
in partial fulfillment of the requirements  
for the degree of

Chemical Engineering – Doctor of Philosophy

2024

## ABSTRACT

Redox flow batteries (RFBs) are an energy storage technology that can provide convenient, versatile energy distribution. They can fulfill growing energy consumption needs while reducing harmful emissions by enabling the use of intermittent renewable energy generation. RFBs can deliver grid-scale energy capacities and feature the unique ability to scale power and capacity independently. These systems store electrical energy as chemical energy in the form of two charged redox-active species in solution. The electrochemical and physicochemical properties of individual redox-active species influence all RFB system performance metrics (e.g., energy densities, power densities, lifespan) and dictate system costs. Although RFBs have entered the commercial market as vanadium RFBs, their affordability remains a major limitation.

The pursuit of cost-effective redox-active species with competitive performance characteristics remains a tedious process of individual synthesis, measurement, and evaluation. To expand the material design space, we explored organic species paired with non-aqueous solvents. Careful selection and analysis of redox-active electrolyte libraries can help discern meaningful correlations that will help advance the molecular design of optimal compounds for use in these systems. It should be acknowledged that high-performance redox-active species do not guarantee economic or environmental feasibility, as we show using a hypothetical nitrate-recovery and ammonia-generation system. Using pyridinium salts as model anolytes, we have identified an insightful solubility correlation to dispersion forces (i.e., C-H $\cdots$  $\pi$  interactions). Furthermore, we discuss that pyridinium solutions demonstrate properties uncommon among other redox-active electrolytes, including low viscosities and high conductivities. Future work in pyridinium development should include exploring physicochemical and electrochemical structure-property relationships to improve molecular design strategies and assess tangential effects of their scaled application.

Copyright by  
SHARMILA SAMAROO  
2024

Dedicated to Roopnarine, Omila, Shardha, Priya, and Ollie Samaroo.



## ACKNOWLEDGEMENTS

I would like to take the opportunity to thank everyone who has supported me through various projects and endeavors at Michigan State University. It was difficult entering a doctoral program during Fall 2020, but the friendships I have grown and community I have surrounded myself with have made all the difference in my successful completion of this challenging adventure.

First, I would like to thank my advisor, Professor David Hickey, for his guidance and support throughout this program, especially in promoting my growth as a scientist, writer, and researcher. Second, I would like to thank my doctoral advising committee Professor Scott Barton, Professor Chengcheng Fang, and Professor Thomas Hamann, for their advice, critiques, and questions throughout the completion of program milestones. Third, I would like to thank the Chemical Engineering and Material Science Department for the resources they supply and their support of the ChEMS Graduate Student Association. Involvement in the ChEMS GSA provided an excellent launching point for engagement with the department and other organizations within MSU.

I would like to thank those at Jolt Energy Storage Technologies for their support through my internship experience, specifically Professor Tom Guarr, Jack Johnson, Charley Hengesbach, and Will Kruper. Tom and Jack kindly created this internship opportunity allowing me to experience and conduct research within a startup environment. Additionally, I appreciate the equipment and facilities provided by Jolt to support experiments for my doctoral research.

I would like to express my appreciation to Professor Christopher Saffron, for his assistance in understanding and applying Life Cycle Assessment methods to evaluate a new system. Dr. Saffron was extremely accommodating over the course of numerous meetings and clarification emails and provided the mentorship necessary to complete evaluations and construct an interesting discussion.

I would like to express my appreciation to Professor Richard Staples for his timely assistance in data collection and pleasant nature. Through periods of urgency, during final preparation of a manuscript Dr. Staples provided exceptional data, documentation, and support. It was always an enjoyable experience to drop off new samples and introduce new lab mates to Dr. Staples.

I would like to thank the MSU Graduate School for the professional development groups they organize and fund. I would like to express my appreciation to Dr. Julie Rojewski for facilitating the Broadening Experiences in Scientific Training (BEST) Program. The BEST program has provided numerous career development trainings, mentorship for professional document preparation, and a community of like-minded graduate students to network with. I would like to thank the Leadership Fellowship Program including Dr. Meg Moore, Lizzy King, and Philip Montgomery for providing leadership, mentorship, and funding. The Leadership Fellowship provided the necessary guidance and funding to build and pilot the ChEMS Mentorship program and has supported my growth as a leader offering the opportunity to serve as a Co-Coordinator in my final year. These roles have allowed me to develop diverse and dynamic skills employable within research, professional roles, and beyond.

Finally, I would also like to thank Professor Melanie Sanford for connecting me with David and the opportunity to pursue a doctoral degree. I would like to express a great thank you to previous Sanford Lab members and friends, Dr. James, Suttill, Dr. Danielle Samblanet, Dr. Nicole Camasso, and Dr. Christo Sevov for their training as a young researcher as well as their advice and support throughout undergrad, graduate school, and life.

Thank you all!

Sharmila Samaroo

## TABLE OF CONTENTS

<b>LIST OF SYMBOLS AND ABBREVIATIONS .....</b>	<b>viii</b>
<b>Chapter 1. Introduction.....</b>	<b>1</b>
1.1 Energy, Environmental, and Economic Targets Drive Energy Storage .....	1
1.2 RFB Function and Key Performance Parameters .....	4
1.3 Status and Challenges of RFB Development .....	11
1.4 Technoeconomic Analysis and Life Cycle Assessment .....	17
1.5 Overview of Included Works .....	21
<b>Chapter 2. C-H<math>\cdots\pi</math> Interactions Disrupt Electrostatic Interactions Between Non-Aqueous Electrolytes to Increase Solubility .....</b>	<b>24</b>
2.1 Introduction .....	25
2.2 Methods.....	28
2.3 Results and Discussion .....	34
2.4 Conclusions.....	51
<b>Chapter 3. Low Viscosity, High Concentration Pyridinium Anolytes for Organic Non-Aqueous Redox Flow Batteries .....</b>	<b>52</b>
3.1 Introduction .....	53
3.2 Methods.....	57
3.3 Results and Discussion .....	64
3.4 Conclusions.....	78
<b>Chapter 4 Electrochemical Ammonia Production from Nitrates in Agricultural Tile Drainage: Technoeconomic and Global Warming Analysis.....</b>	<b>80</b>
4.1 Introduction.....	81
4.2 Methods.....	87
4.3 Results and Discussion .....	94
4.4 Conclusions.....	105
<b>Chapter 5. Conclusions and Future Work .....</b>	<b>107</b>
5.1 Summary .....	107
5.2 Future Work .....	114
5.3 Conclusions.....	118
<b>BIBLIOGRAPHY .....</b>	<b>121</b>
<b>APPENDIX A: CHAPTER 2 SUPPLEMENTAL INFORMATION .....</b>	<b>142</b>
<b>APPENDIX B: CHAPTER 3 SUPPLEMENTAL INFORMATION.....</b>	<b>276</b>
<b>APPENDIX C: CHAPTER 4 SUPPLEMENTAL INFORMATION .....</b>	<b>313</b>

## LIST OF SYMBOLS AND ABBREVIATIONS

APV	Agrophotovoltaics
AU	Absorbance unit
CV	Cyclic Voltammograms
DFT	Density functional theory
ED	Electrodialysis
GCE	Glassy carbon electrode
GHG	Greenhouse gas
GWP	Global warming potential
HPLC	High performance liquid chromatography
KOH	Potassium hydroxide
LCA	Life cycle assessment
LCOE	Levelized cost of energy
Me <sub>2</sub> Py <sup>+</sup>	2,6-Dimethylpyridinium
NC	Nitrate capture
NCC	Nitrate capture and conversion
NMR	Nuclear Magnetic Resonance
NRC	Natural Resources Conservation Services
NRFB	Non-aqueous redox flow batteries
PEG	Polyethylene glycol
RFB	Redox flow batteries
ROM	Redox-active organic molecules
SE	Stokes-Einstein

SOC	State of charge
TCI	Total capital investments
TEA	Technoeconomic analysis
TEMPO	2,2,6,6-tetramethylpiperidine-1-oxyl
TFI	Total farmer investment
THF	Tetrahydrofuran
TMNR	Theoretical Maximum %N Recovery
UV-Vis	Ultraviolet-Visible
VRFB	Vanadium redox flow batteries

## Chapter 1. Introduction

### 1.1 Energy, Environmental, and Economic Targets Drive Energy Storage

Society faces the challenge of meeting growing consumer demands and reducing concurrent emissions while being limited to technologies that guarantee economic feasibility. Finding optimal outcomes at the intersection of these challenges is desirable for both energy producing and consuming industries. Energy storage technologies that would promote this energy transition currently encounter performance and price limitations that hinder their widespread adoption.<sup>1-3</sup> Emerging energy storage technologies must be scalable to meet the projected increasing energy demands, pair with renewable energy technologies that reduce the production of greenhouse gas emissions, and redistribute stored energy at competitive prices, as shown in Figure 1.1. The goal of decoupling emissions from economic growth has initiated a transition to clean energy and will require fundamental innovations that are economically competitive to sustain the growing demands in energy.<sup>4,5</sup>

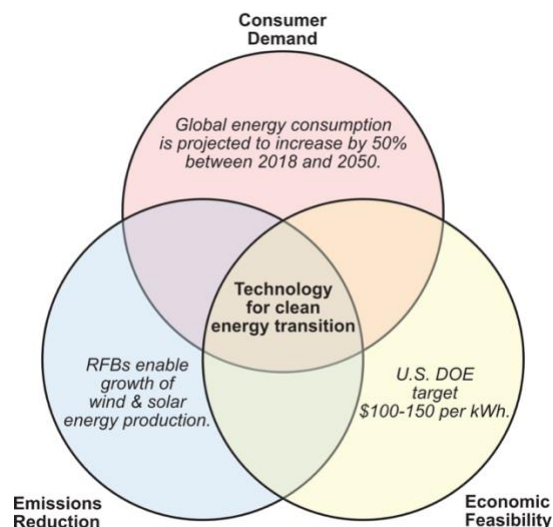


**Figure 1.1. Venn diagram of factors that drive energy storage research.** Energy storage technologies must be designed to scale to meet the projected increasing energy demands, effectively interface with renewable sources, and redistribute stored energy at competitive prices.<sup>6,7</sup>

Energy consumption is projected to increase by nearly 50% between 2018 and 2050, and of this increase, renewable energy is projected to grow from a share of 15% to 28% of primary energy consumption worldwide.<sup>8</sup> The expected growth in renewables is enabled by technological advancements in solar production<sup>9</sup> and wind turbine design.<sup>10</sup> Paired with advancements in technology for energy conversion to electricity are new challenges in interim energy storage. Energy storage is necessary due to the intermittent and uncontrollable nature of renewable sources. Services provided by the electrical grid must continue to be extremely responsive and be prepared to supply anticipated consumer demand. Energy storage technologies provide the necessary buffer between renewable supply and variable demand. Increased control of energy distribution must match grid-scale application needs from fast-discharge and high-power settings (e.g., critical power systems, transportation, and power grids) to extended-discharge and high-energy scenarios (e.g., energy management, back-up power, and load leveling).<sup>11,12</sup>

Established energy storage technologies meet diverse needs by providing variable energy capacity and power densities, however the emerging energy storage systems necessary to meet growing energy demands remain expensive. For grid-scale applications, high energy capacity and minimized costs are favored. Pumped hydroelectric energy storage contributes >99% of the global large-scale energy storage. Both pumped hydro and compressed air energy storage require the use of vast reservoirs (i.e., rivers, lakes, underground caverns).<sup>13</sup> Although these established technologies demonstrate high performance and low cost, their ability to meet growing energy needs is hindered by the need for specific geographical factors, and therefore make these options unavailable in many locations. To improve accessibility and overcome these geographical limitations, numerous alternative energy storage technologies are of interest including mechanical (e.g., flywheels), electrical (e.g., capacitors), chemical (e.g., fuels) or electrochemical (e.g.,

batteries).<sup>1-3</sup> In addition to meeting grid-scale timescale and capacity performance targets for energy storage, economic feasibility must be demonstrated.

Emerging energy storage technologies are complex and will be entering an ever-changing energy infrastructure. It can be challenging to accurately anticipate their economic potential and feasibility in the market. Technoeconomic analyses (TEAs) provide useful estimations from which the decisions to support, reject, or modify future energy storage research can be made. A detailed assessment of economic projections based on the current and anticipated state of the technology can be conducted with a realistic acknowledgment of uncertainty. These intermediate evaluations can provide a sense of the most optimal directions to commit resources for further development as well as describe adjacent challenges that may support or limit the future success of a new technology. An economic parameter that offers a basis of comparison is the levelized cost of energy (LCOE), which is the cost of a system during its lifetime over the total electrical energy generated over its lifetime ( $\$ \text{kWh}^{-1}$ ).<sup>14</sup> The U.S. Department of Energy defines target values of \$100-\$150 per kWh in technoeconomic analyses that must be demonstrated before an energy storage technology is considered cost-competitive.<sup>15</sup> Additionally, in an increasingly environmentally conscious world, the role of life-cycle assessments (LCAs) has grown and proven to be a useful intermediary tool to direct research goals.

Life-cycle assessments can support and expand the understanding of developing technologies and the consequences of their overall impacts on the environment (e.g., global warming potential, eutrophication potential), sustainability (e.g., land availability, water shortage potential), and human health (i.e., toxicity or  $\text{LC}_{50}$ ). LCAs follow a standard method of evaluating processes and technologies.<sup>16</sup> These assessments of major stages over the course of a product's lifespan can reveal subtle challenges or complications that may otherwise be overlooked during preliminary



conceptualization and proposal phases. Importantly, results generated by these additional evaluation methods (i.e., TEA and LCA) that consider broader financial and ethical measures emphasize critical areas to consider prior to commercialization but demonstrating the functional performance requirements of the technology must be prioritized.

Electrochemical styles of energy storage (i.e. batteries) can be designed for various power and capacity needs, but not all styles are sufficient for target grid-scale capacities (i.e. kWh to MWh) and time-scales (i.e. hours to days).<sup>17,18</sup> Lithium-ion technologies for example, are an excellent match for small mobile applications (e.g., phone or vehicle batteries) but are not designed to serve the large capacities necessitated by grid-scale applications. Redox flow batteries (RFBs) have been introduced as an electrochemical energy storage technology that can meet grid-scale energy needs. Additionally, RFBs feature the unique capability of scaling power and capacity independently, enabling flexibility in desired applications. Various efforts have been made to accelerate the design of more affordable RFBs including identifying predictive cost parameters (e.g., concentration, molecular weight, cell voltage),<sup>1,19</sup> TEAs showing synergistic effects with renewable energy technologies,<sup>20</sup> and studies determining optimal sizing and operating parameters that extend system lifespans.<sup>21</sup> The advancement of RFB technologies will require the combined efforts of fundamental research to improve practical operation, TEAs to clarify parameters that enable RFBs affordability within the grid-scale energy storage market, and LCAs to ensure that all phases of RFBs production and implementation are designed with a sustainable outlook.

## **1.2 RFB Function and Key Performance Parameters**

Redox flow batteries are uniquely designed for grid-scale (kWh to MWh capacity) energy storage applications.<sup>17,18</sup> As shown in Figure 1.2, RFBs consist of three components: an electrochemical conversion cell, liquid electrolyte storage tanks, and the ion-selective membrane.

RFBs store electrical energy as chemical energy in redox-active electrolytes (anolyte or catholyte).

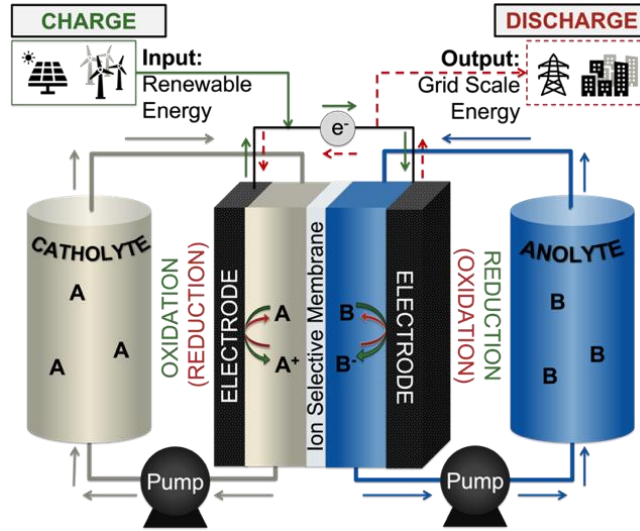


**Figure 1.2. Standard scheme of RFB.** Consists of an electrochemical conversion cell (center block), electrolyte storage tanks (catholyte, A, and anolyte, B), and ion-exchange membrane (center).

At the electrode surface, the catholyte (dissolved in solution, “A” in Figure 1.2) undergoes a non-spontaneous (i.e., electrolytic) oxidation during charging and a subsequent spontaneous (i.e., galvanostatic) reduction to produce the original uncharged species. A parallel reduction, and then oxidation occurs for the anolyte (“B” in Figure 1.2) in the opposite half of the electrochemical conversion cell, similarly electrolytic during charging and galvanostatic during discharging. The total cell voltage ( $E_{cell}$ , V) of the system describes the cell potential during charging, given by (Eq. 1.1), is dependent on the oxidation potential of the catholyte ( $E_{ox}$ , V) and the reduction potential of the catholyte ( $E_{red}$ , V). Charge neutrality of the system is preserved by free movement of an inert supporting electrolyte through an ion selective membrane that separates the anodic and cathodic halves of the electrochemical cell. The primary advantage of RFBs is their ability to decouple system power and energy capacity, unlike their solid-state battery counterparts, for which energy storage capacity is directly related to the amount of electrode material.<sup>22</sup> This arrangement is advantageous as it allows the scaling and design of multiple system components (i.e., tank

volumes, electrode surface areas, multiple electrochemical conversion cell stacks) such that it may meet a wide array of performance criteria (i.e., fast-discharge and high-power settings, extended-discharge and high-energy scenarios).<sup>11,12</sup>

$$E_{cell} = E_{ox} - E_{red} \quad \text{(Eq. 1.1)}$$

The common performance characteristics used to evaluate and compare RFBs are energy density ( $ED$ ),<sup>18</sup> power density ( $PD$ ),<sup>18</sup> and capacity fade ( $CF$ ).<sup>23</sup> Each of these is highly dependent on the electrochemical nature of the redox-active species, and these parameters are described quantitatively by the following equations:

$$ED = n \cdot C_{redox} \cdot F \cdot E_{cell} = \frac{n \cdot N_{redox} \cdot F \cdot E_{cell}}{V} \quad \text{(Eq. 1.2)}$$

$$PD = \frac{i \cdot E_{cell}}{A} \quad \text{(Eq. 1.3)}$$

$$CF = \frac{\Delta Q\%}{\Delta t} = \frac{\Delta(n \cdot N_{redox} \cdot F \cdot E_{cell})}{\Delta t} \quad \text{(Eq. 1.4)}$$

where the system energy density ( $ED$ , Wh L<sup>-1</sup>) is dependent on the number of electrons transferred ( $n$ ), concentration or moles of redox-active species ( $C_{redox}$ , mol m<sup>-3</sup> or  $N_{redox}$ , mol), Faraday's constant (96,485 C mol<sup>-1</sup>), total cell voltage ( $E_{cell}$ , V), and system volume ( $V$ , L); the system power density ( $PD$ , W m<sup>-2</sup>) is dependent on discharge current ( $i$ , A), total cell voltage ( $E_{cell}$ , V), and the surface area of the electrode ( $A$ , m<sup>2</sup>); and the capacity fade is a measure of percent capacity ( $\Delta Q$ , %) loss over time ( $\Delta t$ , day). Here the capacity ( $Q$ , Wh) is related to the number of electrons transferred ( $n$ ), redox-active species concentration ( $C_{redox}$ , mol m<sup>-3</sup>), Faraday's constant (96,485 C mol<sup>-1</sup>), and cell voltage ( $E_{cell}$ , V). These three variables (i.e.,  $ED$ ,  $PD$ , and  $CF$ ) are interrelated, as they are all dependent on reactions within the electrolyte solutions employed. Additionally, they are subject to secondary properties or behaviors resulting from the selected redox active species, solvents, and supporting electrolytes that influence variables directly impacting each performance characteristic.

For example, the selection of a solvent that the redox active species demonstrates high solubility in, that also forms degradation products with the charged species and results in high solution viscosities; would be advantageous for *ED*, but deleterious for *CF* and *PD*. Elevated redox species concentrations would directly increase *ED*, but the rapid formation of degradation products would lead to high *CF* rates and high viscosities could limit operating currents and lower *PD*. Overall, careful material selection and compatibility evaluations are necessary to generate the full array of desirable RFB performance targets including high energy densities, high power densities, and extremely low rates of capacity fade.

### **1.2.1 RFB Categorization, Advantages, and Limitations**

Vanadium redox flow batteries (VRFBs) are the primary commercialized standard for RFBs. Since RFBs conceptualization in the 1970s and commercialization of the popularized all vanadium system (discovered in 1984), RFBs have been marketed for large scale application but have yet to be adopted as a mainstream energy management system.<sup>24,25</sup> VRFBs have energy densities of 10 to 30 Wh L<sup>-1</sup>, power ratings of 30 kW to 3 MW, lifespans of 5 to 10 years, and LCOEs of \$150 to \$1000 per kWh.<sup>13,26</sup> The main advantage of VRFBs is the symmetry of the system, operating with the same redox species in both halves of the electrochemical cell in different charge states. This is possible because vanadium in these systems can reversibly access four different charge states (i.e., V<sup>2+</sup>, V<sup>3+</sup>, V<sup>4+</sup> and V<sup>5+</sup>). When redox active materials in an asymmetrical system pass through the membrane the loss of charged molecules to the opposite half of the cell result in energy inefficiencies and introduces the risk of irreversible reactions to form degradation products. Fortunately, the symmetry of the VRFBs means that redox species crossover only results in loss of efficiency but does not introduce the risk of degradation product formation.<sup>27,28</sup> Current research is focused on improving variables that influence VRFB cost, which is its primary limitation. Any emerging RFB technology must outcompete the standards set by VRFBs in performance and cost.

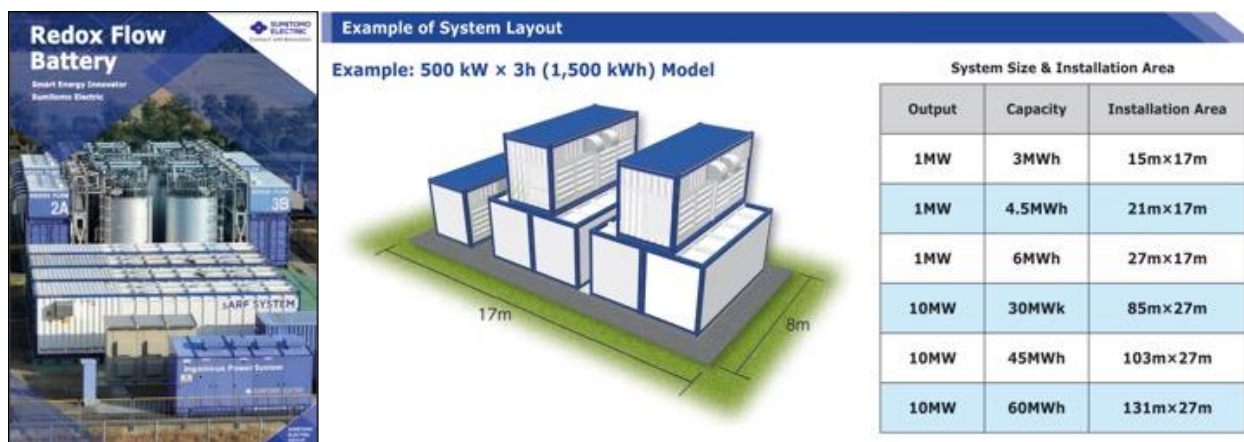


**Figure 1.3. State-of the art vanadium RFBs.** Cover depicting commercial RFB system and design excerpt adapted from Sumitomo Electric Brochure.<sup>29</sup>

The four broad classes of RFBs are defined by the solvent and redox-species. These choices result in tradeoffs in cost and performance as summarized in Table 1.1. The first choice is between aqueous and non-aqueous solvents and the second is between metal-based and organic redox species.<sup>17,30–32</sup> For cost, an aqueous solvent system is cheaper due to the wide availability of water. However, the desire to increase cell potential (i.e.,  $E_{cell}$ ) has led to the use of non-aqueous solvents. The total aqueous electrochemical window is limited to around 1.5 to 2 V, while utilizing other solvents such as acetonitrile or propylene carbonate allows voltage ranges exceeding 4 to 5 V.<sup>33</sup> Selecting non-aqueous solvents introduces a tradeoff impacting theoretical power density, because the current density ( $i/A$ ,  $A\ m^{-2}$ ) achievable in aqueous systems is  $>100\ mA\ cm^{-2}$  which exceeds current densities  $<0.5\ mA\ cm^{-2}$  common in non-aqueous solvents.<sup>34</sup> There is an additional tradeoff between solvent options, with conductivity, aqueous-based electrolytes offer higher conductivities (e.g., 60 to 740  $mS\ cm^{-1}$ ) often a magnitude higher than commonly achieved in non-aqueous electrolyte solutions (e.g., 2 to 35  $mS\ cm^{-1}$ ).<sup>35,36</sup>

**Table 1.1. Four main RFB design classes and pros and cons.** RFB electrolyte solutions can consist of (first row) metal-based redox species paired with aqueous solvent, (second row) organic redox species paired with aqueous solvent, (third row) metal-based redox species paired with non-aqueous solvent, and (fourth row) organic redox species paired with non-aqueous solvent. These pairings can have advantageous properties (green), disadvantageous properties (red), or unknown properties (yellow) with respect to cost and performance targets.

Solvent	Redox Species	Solvent Cost	Solvent Conductivity	Solvent Voltage Window	Electrolyte Voltage Window	Electrolyte Cost
Aqueous	Metal based	cheap	high	narrow	narrow	?
Aqueous	Organic	cheap	high	narrow	narrow	?
Non-aq.	Metal based	?	limited	wide	?	?
Non-aq.	Organic	?	limited	wide	?	?

Considering anolyte and catholyte material, the options are broadly split between metal based and organic, where predictions of cost are less reliable. However, it is known that costs will be high for materials involving precious metals or complex and unscalable synthetic methods for organic species. Regardless of the individual species, redox characteristics of the materials will be restricted to the solvent in which they operate; electrolytes operating in aqueous solvents will have both a limited electrochemical stability window and elevated solution conductivity, and those in non-aqueous solvents could have wider stability windows but may require higher concentrations of inert supporting electrolytes to achieve equivalent conductivities. A general comparison of aqueous and nonaqueous redox-active organic molecules (ROMs) and their respective advantages in RFB systems is detailed in Figure 1.4. Non-aqueous organic electrolytes systems remain a promising RFB class for development, as they offer wider voltage windows afforded by non-aqueous solvents and versatility made available by the tunable nature of organic molecules.<sup>18</sup>

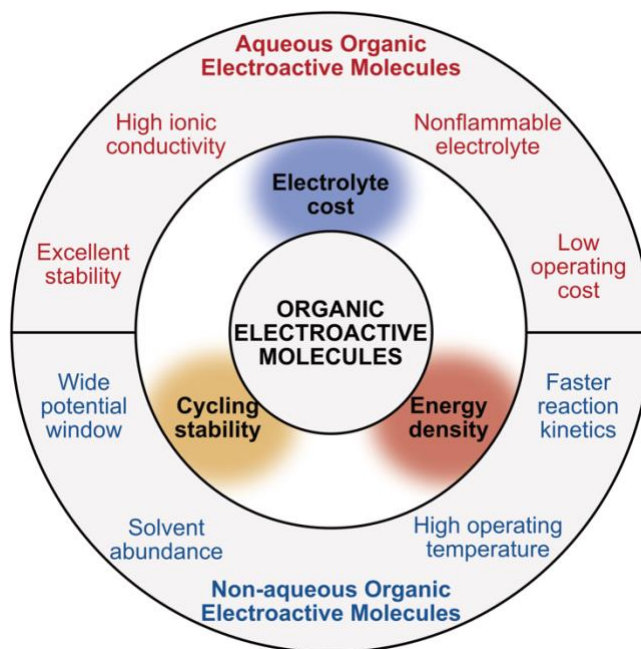


**Figure 1.4. Summary of ROM properties based on their solvent systems.** Comparison of aqueous and non-aqueous ROMs (or electroactive molecules). Adapted from Zhong et al. 2020.<sup>37</sup>

### 1.2.2 Ideal ROM Properties for NRFBs

Within ROM development for nonaqueous redox flow batteries (NRFBs) the most significant properties that must be improved to generate a high-performing and cost competitive energy storage solution are stability, solubility, multielectron transfer, redox potentials, and costs.<sup>38,39</sup> Low reduction potentials (for anolytes) or high oxidation potentials (for catholytes) are desirable as they improve maximum cell voltage and subsequently increase theoretical energy density. ROMs that are electrochemically stable enough to donate or accept more than one electron, or undergo multi-electron transfer, can greatly increase energy densities with each additional electron transferred. Importantly, a ROM material that is abundant and cheaply produced will contribute to the overall affordability of the electrolyte solutions. ROMs that can produce desirable solution properties (i.e. low viscosity, high conductivity) without the addition of supplemental solution components (i.e., supporting electrolyte, secondary solvents) could be advantageous, by reducing cost and solution complexity.

The most desirable ROM property is electrochemical stability, such that if achieved, high stability can justify less ideal secondary properties is electrochemical stability. Two forms of electrochemical stability are important for NRFBs (1) shelf stability and (2) charge-discharge stability, these provide information on the routes of degradation occurring in the flow system storage tanks and electrochemical conversion cell stacks, respectively. Quantitative assessment of these stabilities is reflected in the operating efficiencies (e.g., Coulombic, voltage, energy efficiencies) and capacity fade of the system. Shelf stability provides a reflection of the materials resistance to decomposition stored as a concentrated solution with the ROM in its charged states. This reflects losses and inefficiencies that may arise from the solution in the external storage tanks of the system. Charge-discharge stability would reflect ROM decomposition primarily occurring as a result of the charging and discharging of the solution including interactions at the electrodes, with the solvent, and crossover through the membrane. Decomposition of the ROM species (anolytes or catholytes) can be expensive, resulting in a loss of functional capacity and requiring the replacement of ROM material or other system components. Not only does ROM stability present an economic advantage, avoiding the regular replacement of system components and waste disposal would be environmentally beneficial as well.

### **1.3 Status and Challenges of RFB Development**

Current research directions for the advancement of RFBs focus on optimizing performance of operational parameters, membrane design, and redox-active species. Improvements in various operation parameters can be guided by technoeconomic analysis<sup>1,23</sup> and assessment of system scales.<sup>21</sup> RFB membrane advancements focus on optimizing between permeability, conductivity, chemical stability, and cost.<sup>40</sup> Strategies to both understand and control organic electrolyte material solubility, redox potential, reversibility, stability, reaction kinetics, and cost are significant



research areas.<sup>35,41,42</sup> Though all areas of development for RFBs are critical to enable broader adoption of this technology, the energy density, power density, and capacity fade are all fundamentally tied to physicochemical and electrochemical properties of the redox-active species. As shown in (Eq. 1.2, RFB energy density is dependent on number of electrons transferred, cell voltage, and redox-active species concentration. Targeting high, tunable solubility or multielectron transfer as methods to maximize energy density remains a prominent challenge that is often approached by molecular design through specific functionalization.<sup>43,44</sup> Optimization of energy density will allow grid-scale RFBs to be affordable while reducing necessary storage volumes and land footprint of the system.

### **1.3.1 Status and Challenges of ROM Physicochemical Properties in NRFBs**

RFB systems are designed to serve grid scale energy needs. Due to the large scales required, the resulting physicochemical properties of the liquid electrolyte become increasingly consequential to the overall installation and operating costs. The liquid electrolyte solutions consist of ROMs and an inert supporting electrolyte, both of which are dissolved in the desired solvent. The final solution properties are the cumulative product of various intermolecular interactions among the solute and solvent molecules.

Because system energy densities are dependent on the concentration of each ROM, a popular strategy involves manipulation of molecular structure to increase maximum solubility of the ROM in the solution.<sup>45</sup> Ideal solubilities for ROMs in NRFBs must achieve ranges of 4 to 5 M to be cost effective.<sup>46</sup> Maximum solubility of the electroactive species is understood to be a result of solvent properties (e.g., viscosity, polarity, dielectric constant)<sup>47</sup> in addition to the molecular structure of the electroactive species.<sup>37</sup> Common strategies employed to promote solubility of organic electroactive molecules include addition of alkyl, carbonyl, and ester substituents.<sup>37</sup> Although

these strategies exist, it remains necessary to experimentally synthesize and evaluate solubilities; these methods do not reliably or predictably affect ROM solubility, and may influence other solution properties negatively. For example, the introduction of polyether chains, may improve the solubility of a ROM but has been shown to lead to high solution viscosities.<sup>48-50</sup>

Solution viscosity is an important system property that shares a complex and interrelated relationship with maximum ROM solubility. Unfortunately, highly soluble ROMs commonly produce solutions with high dynamic viscosity ( $> 10$  cP) and low conductivity ( $< 5$  mS cm<sup>-1</sup>) at operating concentrations ( $> 0.5$  M).<sup>51,52</sup> Highly viscous electrolyte solutions in RFBs can negatively affect system flow rates (i.e., increase pressure drop, reduce mass transport, and limit charge/discharge rates), and poorly conductive solutions can lead to high overpotentials and lower storage efficiencies.<sup>53,54</sup> Zhang and coworkers recently highlighted that electrolyte concentrations within NRFBs must redesign targets with respect to concentration-dependent conductivity and viscosity.<sup>55</sup> This reframing can help draw focus on additional, though secondary, properties that have significant effects on the operation of RFBs. In addition to solubility, electrochemical characteristics of individual ROMs are critical variables that influence energy density.

### **1.3.2 Status and Challenges of ROM Electrochemical Properties in NRFBs**

Cell voltage ( $E_{cell}$ ) is a critical variable that influences energy density, power density and capacity fade; multiple approaches are used to expand the voltage window including varying the redox-active species and the system solvent. As stated, our focus on non-aqueous solvents is motivated by the extended voltage windows available in certain non-aqueous solvents (e.g., acetonitrile range: -3.5 V to 2 V vs. SCE reference).<sup>33</sup> The wider windows of the solvent enable cell voltage optimization by designing a catholyte with a redox couple at a high (i.e., more positive oxidation) voltage and pairing it with an anolyte that has a redox couple at a low (i.e., more

negative reduction) voltage. Importantly, both redox events must occur within the stable window of the solvent, prior to the applied voltage leading to solvent decomposition.

Both redox events must be reversible and electrochemically stable in the system solvent, and they must be able to undergo charging and discharging electron transfer without reacting or decomposing. Tuning the redox potential of organic electrolytes often requires installing electron withdrawing or electron donating groups as the electronic nature of substituents can affect reduction potential of the overall molecule.<sup>38,56,57</sup> Assessment of redox potential and other electrochemical parameters (e.g., reversibility, diffusion coefficient, kinetic rate constant) provide critical preliminary information on the potential applicability of the material, however these parameters do not reflect material stability over longer time scales (i.e., over hours or days). In contrast, capacity fade describes longer time-scale stability and is the result of electrochemical decomposition, cross-over through the membrane, and system component compatibility.<sup>43,58</sup>

### **1.3.3 Status and Challenges of ROM Electrochemical Stability in NRFBs**

RFBs involve complex interactions among charged and uncharged ROMs and other solution constituents, and any degradation reactions will increase capacity fade and shorten total system lifespans. Ensuring that the ROMs selected are non-reactive in the charged state and uncharged state, with itself and other electrolyte solution components (i.e., solvent molecules, supporting electrolytes), is critical for stable charging and discharging of RFBs. Modifying the electrochemical stability of a redox active molecule can be achieved by adding substituents at specific positions that have a tendency to become reactive and lead to irreversible conversions to decomposition products. These decomposition byproducts are often electrochemically inactive or have a lower reduction potential<sup>23</sup>, and would result in loss of capacity over time as redox active molecules are continually consumed by degradation reactions.<sup>58</sup> Further, inadequate membrane

selectivity can add routes of decomposition by allowing anolytes and catholytes to leave their respective halves of the electrochemical cell and irreversibly react.<sup>23,59</sup> Material crossover can also foster unfavorable, decomposition reactions, further contaminating individual halves of the cell.<sup>59</sup>

Capacity fade (*CF*) reflects the electrochemical stability of the redox species; unstable ROMs will react to form inactive material by electrochemical decomposition. Decomposition products as well as loss of material by transport through the membrane both reduce the functional energy density and operational efficiencies of the systems.<sup>58,60</sup> It has also been demonstrated that careful operation of the system and selection of compatible materials (e.g., membrane, pumps, storage vessels, etc.) can mitigate this result and extend the system lifespan. The electrolyte lifespan is represented by the capacity fade (percent capacity loss per day) - or rate of loss of functional capacity.<sup>58</sup> Multiple factors such as temperature, concentration, state of charge (SOC, or percent of capacity accessed), and current rates can all affect capacity fade.<sup>21,61</sup> The electrochemical instability of the redox-active species and crossover are the major mechanisms resulting in capacity losses.<sup>23</sup> The capacity fade regimes are defined as “high” (>1%/day), “moderate” (0.1-1%/day), “low” (0.02-0.1%/day), and “extremely low” (<0.02%/day).<sup>58</sup> Extrapolated to a year, the “high” rates yield total capacity losses of 36.5% while “extremely low” rates would result in 7.3% total capacity loss. Given that target lifetimes for these systems are >20 years<sup>26</sup>, systems experiencing high rates of capacity fade face significant limitations.

The capacity fade directly affects RFB lifespans, in an effort to extend operational life, groups have investigated the mechanisms underlying capacity fade.<sup>58</sup> Kwabi *et al.* reviewed aqueous electrolytes and commonly associated decomposition mechanisms as well as detailed capacity fade evaluation, to provide strategies for capacity fade mitigation in future system designs. The specified common decomposition routes that specific electroactive species are subject to include:

(i) nucleophilic addition/substitution, (ii) disproportionation, (iii), dimerization or polymerization, and (iv) tautomerization.<sup>58</sup> They argue that a comprehensive understanding of the decomposition mechanisms each electrolyte is most inclined to undergo can inform the design of electrolyte structures with advanced electrochemical stability.

Another popular strategy to extend RFB lifespans beyond the chemistry of the system investigates the physical operation of the system. Variables such as temperature, depth of cycling (i.e., SOC), and cycling currents can all contribute to accelerating capacity fade.<sup>21</sup> Limited lifespans reduce the cost effectiveness of electrochemical energy storage systems; regular replacement of the battery in solar or wind power generation plants is a major cost that must be minimized.<sup>21</sup> Proper system scaling based on energy and power needs and maintain operation within defined limits (e.g., SOC, charging or discharging currents) can be used to mitigate avoidable capacity fade.<sup>21</sup> Goulet *et al.* identified a specific example demonstrating the significance of SOC on capacity fade rates. When cycling model anolyte and catholyte (2,6-dihydroxyanthraquinone vs. potassium ferrocyanide) and maintaining a current density of 100 mA cm<sup>-2</sup> (i.e., galvanostatic cycling) the capacity fade rates were shown to increase with increasing SOC. When utilizing 88% SOC, with a potential cutoff at 1.25 V, the capacity fade was 0.14% per day; conversely, during the case utilizing 99.9% capacity, with a potential cutoff at 1.6 V, the capacity fade was 5.6% per day. Additionally, they verified that similar losses occurred when the system was cycled at a constant potential (i.e., potentiostatic cycling).<sup>62</sup>

Other strategies employed to reduce capacity fade have focused on losses associated with crossover of redox active species through the membrane. This problem can be approached from both membrane advancements and electrolyte design. Membranes have been a challenging component of RFBs because they must carefully balance selectivity, conductivity, and stability all

while being chemically and mechanically stable within the greater system.<sup>59</sup> Electrolyte design to mitigate crossover primarily involves the synthesis of larger, polymerized versions of existing electrolytes. The combination of these concepts leads to the redox-active oligomers being paired with membrane polymers of intrinsic microporosity (pore size <1nm) using size exclusion to reduce crossover.<sup>59</sup> These research routes to slow capacity fade can inform improved RFB system design for extended lifespans through improved understanding of electrolyte decomposition, operational limits, and crossover mitigation.

#### **1.4 Technoeconomic Analysis and Life Cycle Assessment**

As economic feasibility and environmental responsibility are two focuses of emerging technologies, technoeconomic analyses (TEAs) and life-cycle assessments (LCAs) can help evaluate their current metrics and highlight areas for improvement, as depicted in Figure 1.5. Technoeconomic analyses are a method of evaluating industrial processes or technologies by comparing various economic parameters based on technical data, assumptions, and predictions. These may include variables such as fixed capital investment, net present value, operating cost, etc.<sup>63</sup> LCAs involve a standardized procedure for calculating and comparing the environmental impact of various life cycle stages of an industrial process or technology. Frequently of interest concerning emerging technology development, is the impact on variables effecting global warming, hazardous waste production, and effects on human health and safety.<sup>16,63</sup> Results generated by these evaluation methods that consider broader financial and environmental perspectives direct research goals that improve feasibilities for widespread adoption.

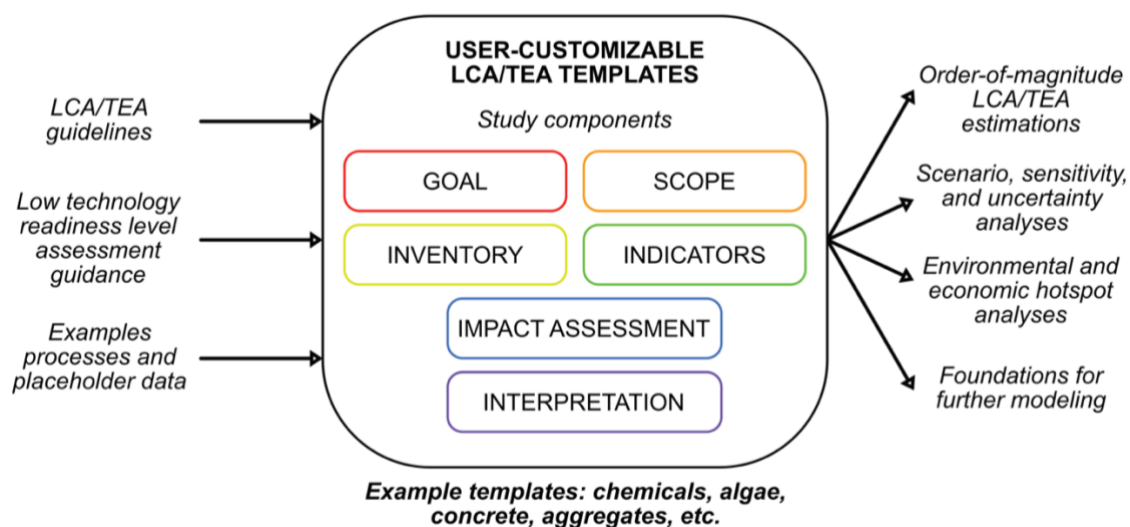


**Figure 1.5. Example of LCA and TEA inputs and outputs.** These analysis tools can provide useful insights by estimating comprehensive effects of economic and environmental variables. Adapted from Faber et al. 2021.<sup>63</sup>

#### 1.4.1 Technoeconomic Analyses and Life Cycle Assessments for RFBs

As technoeconomic feasibility is the primary challenge preventing the broader use of RFBs, more detailed analyses of system variables that dictate these costs can inform forward research progress. Schmidt *et al.* highlight both the utility and uncertainty of experience-curves (i.e., price projections per cumulative installed capacity) as a tool in estimating and understanding cost projections for various forms of energy storage.<sup>64</sup> State-of-the-art RFB systems ranged from \$500 to \$1500 per kWh over the last ten years, with projections estimating costs of \$300 per kWh by 2040; this projection currently exceeds the U.S. Department of Energy defined target values from \$100 to \$150 per kWh as a competitive energy storage cost range.<sup>7,64</sup> As there are myriad variables with their respective influences on system performance, as well as cost, detailed technoeconomic analyses can clarify preventative challenges and the optimal areas for improvement. In a recent summary, Darling acknowledges that projections for ROM containing systems are particularly speculative as synthesis and scaled production of these electrolytes could vary widely in terms of costs.<sup>65</sup> This nuanced and circumstantial form of analysis can reveal markets and opportunities

where specific technologies can be economical and verify scenarios where they would fail to compete. Currently established Li-ion systems demonstrate a great advantage in mobile energy storage applications, and Darling's work highlights the circumstances where RFB styles have the highest potential of being cost competitive (i.e., scenarios with >8 hr discharge time).<sup>65</sup> These evaluations also confirm the significance of properties of focus (e.g., energy density, power density, capacity fade) and bring attention to additional parameters that may influence system affordability (e.g., required solubility vs. active material cost).<sup>46,65-67</sup> A study of particular interest carried out by Kosswattaarachchi *et al.* shows that highly viscous flow battery electrolyte solutions can hinder flow rates and reduce solution conductivities, and thereby negatively impact operating costs.<sup>53,54</sup> When developing a new technology to address environmental challenges, it is equally critical to prevent the introduction of new sources of environmental concern.

LCAs that encompass various energy storage technologies provide an environmental vantage point for the cost and benefits of specific technologies, beyond the economic outlook. LCAs investigating RFBs have been completed to provide information on life cycle stages, operational configurations, and technological comparison points.<sup>68</sup> For RFBs, the World Energy Council recognizes that chemical stability of the electrolyte, membrane, and electrodes incur the greatest costs over the lifespan of these batteries.<sup>69</sup> These components are critical to system function and identifying inexpensive alternatives is not trivial. From a performance perspective, extended electrolyte lifespans would reduce capacity fade rates<sup>23</sup> and improve system efficiencies<sup>60</sup> associated with decomposition. When evaluating environmental impacts, an extended lifespan of RFB systems is desirable. Commercial RFBs require large volumes and the liquid electrolytes and solvents can be hazardous or toxic.<sup>70</sup> RFB redox chemistries in development involve a range of metal-based and organic materials,<sup>30</sup> and recycling practices could reduce extraction necessary for



metal-based species and reduce manufacturing costs of organic species.<sup>71</sup> In a broad appraisal of LCAs that investigated RFBs (predominantly VRFBs), expected lifetimes, cycle lives, and efficiencies were major variables of consideration.<sup>66</sup> The benefits of this study are two-fold, (1) they summarize commonalities in LCA findings and (2) highlight dangers and discrepancies that may arise from misplaced assumptions in estimations for systems that lack real-world operational data for LCAs.<sup>66</sup> In summary, results from LCAs paired with TEAs can provide a comprehensive approach to RFB research and directing new redox active molecule design.

#### **1.4.2 Evaluations of Systems Employing Electroactive Molecules**

From a broader scope, electrochemical technologies designed using renewable forms of electricity, such as electroactive molecules, are of increasing interest across numerous fields.<sup>63</sup> The concept of isolating nitrate from agricultural wastewater and generating ammonia is a recurring idea projected in the field of nitrate reduction catalysis.<sup>72</sup> This goal is motivated by the need to prevent nitrates from agricultural wastewater producing harmful human health outcomes and resulting in eutrophication in local aquatic environments. In the past, the necessary electro dialysis and electrocatalysis systems required high energy consumption. Fortunately, the latest developments in both redox-active species and conversion catalysts have reinvigorated interests in pursuing these systems while anticipating reduced energy requirements.<sup>73-75</sup> Several emerging electrochemical technologies have been developed independently to enable efficient recovery and recycling of nitrate waste; however, it remains unclear whether the implementation of such combined technologies can be economically viable. The energy efficient technologies incorporated include: electro dialysis for nitrate separation, electrocatalysis for ambient ammonia production, and agrophotovoltaics as a clean energy source.<sup>73-75</sup> TEAs and LCAs of technologies at this stage can project the magnitude of economic and environmental benefits of pursuing these innovations.

## 1.5 Overview of Included Works

This thesis discusses applications of electroactive molecules that have been experimentally and hypothetically evaluated. Primarily, a fundamental understanding of pyridinium behavior in solution is consequential to RFB development. Additionally, expanding the understanding of applications of electroactive materials informs future advances in sustainable technologies. A summary of the works detailed in this dissertation is illustrated in Figure 1.6.

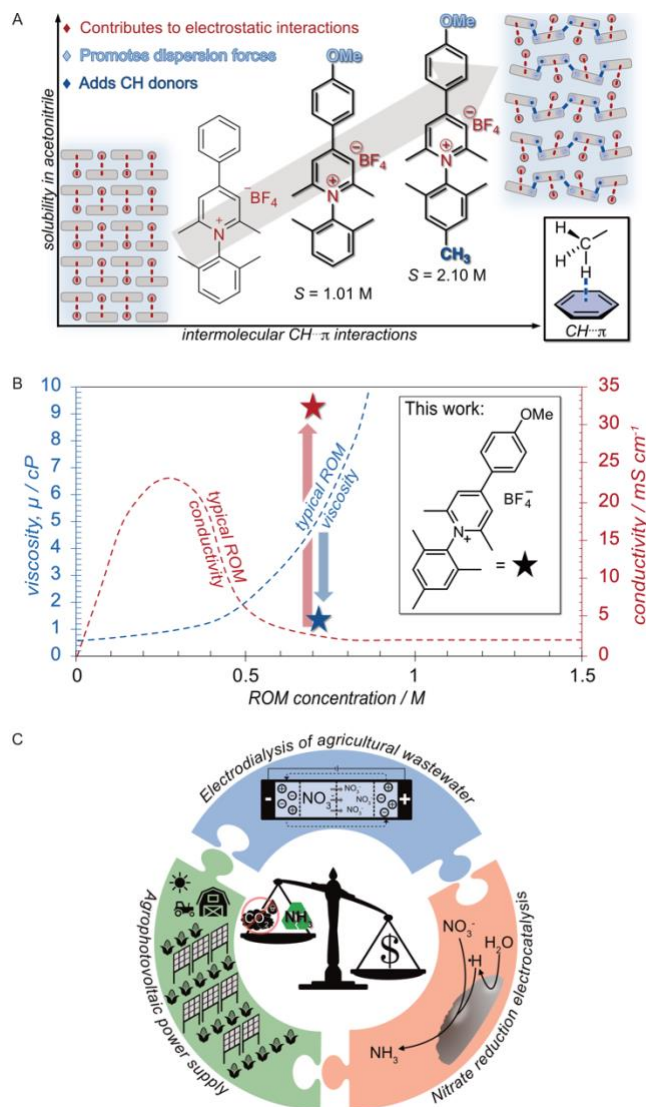


**Figure 1.6. Overview of included works.** (A) C–H... $\pi$  interactions disrupt electrostatic interactions between non-aqueous electrolytes to increase solubility, (B) Low viscosity, high concentration pyridinium anolytes for organic non-aqueous redox flow batteries,

**Figure 1.6.** (cont'd)

(C) Electrochemical ammonia production from nitrates in agricultural tile drainage: Technoeconomic and global warming analysis.

Chapter 2, titled “C–H··· $\pi$  interactions disrupt electrostatic interactions between non-aqueous electrolytes to increase solubility,” will introduce pyridiniums as a promising anolyte and detail the identification of a unique correlation between maximum ROM solubility and the extent of specific intermolecular interactions. We discuss the notable effect of dispersion interactions (between cationic molecules) on increasing solubility by competing with the stronger electrostatic interactions (between the cations and anions), as depicted in Figure 1.6A. Additionally, the solubility trends shown in the original solvent (i.e., acetonitrile) were duplicated in three more organic solvents (i.e., tetrahydrofuran, cyclohexanone, and propylene carbonate), suggesting the identified trends could be more generalizable. This chapter has been adapted from a previously published article in *Nature Chemistry*.<sup>76</sup>

Chapter 3, titled “Low viscosity, high concentration pyridinium anolytes for organic non-aqueous redox flow batteries,” will extend the discussion of pyridiniums and their solution properties in acetonitrile. For the same library of molecules discussed in Chapter 2, we evaluate basic electrochemical properties (i.e., reversibility and diffusion coefficients) and include a preliminary assessment of charged shelf-life stability. We discuss the advantageous properties of high concentration pyridinium solutions including low viscosities and high conductivities and highlight a particular pyridinium derivative capable of realizing this coveted pair of characteristics, depicted in Figure 1.6B. This chapter has been adapted from a previously published article in *ACS Applied Energy Materials*.<sup>77</sup>

Chapter 4, titled “Electrochemical ammonia production from nitrates in agricultural tile drainage: Technoeconomic and global warming analysis,” details an evaluation of a hypothetical arrangement of emerging technologies that employ state-of-the-art electrochemical processes. The

three technologies and their roles within this system are represented in Figure 1.6C. The discussion of these systems involves hypothetical functions under variable conditions and summarizes projections of their environmental benefits and economic feasibility. Notably, the challenges of introducing preventative and remediation style technologies arise and we discuss potential strategies to encourage sustainability driven systems. This chapter has been adapted from a previously published article in the *American Institute of Chemical Engineers (AIChE) Journal*.<sup>78</sup>

In summary, the cumulative works of this dissertation target strategies to improve the understanding of pyridiniums as a potential anolyte for RFBs by investigating variables that influence the physicochemical properties (i.e., solubility, viscosity), determining the electrochemical properties (i.e., reversibility, conductivity, etc.), evaluating preliminary electrochemical stabilities (i.e., charged species shelf life), and assessing the economic and environmental potential for electroactive molecules in emerging applications.

## Chapter 2. C-H $\cdots\pi$ Interactions Disrupt Electrostatic Interactions Between Non-Aqueous Electrolytes to Increase Solubility<sup>1</sup>

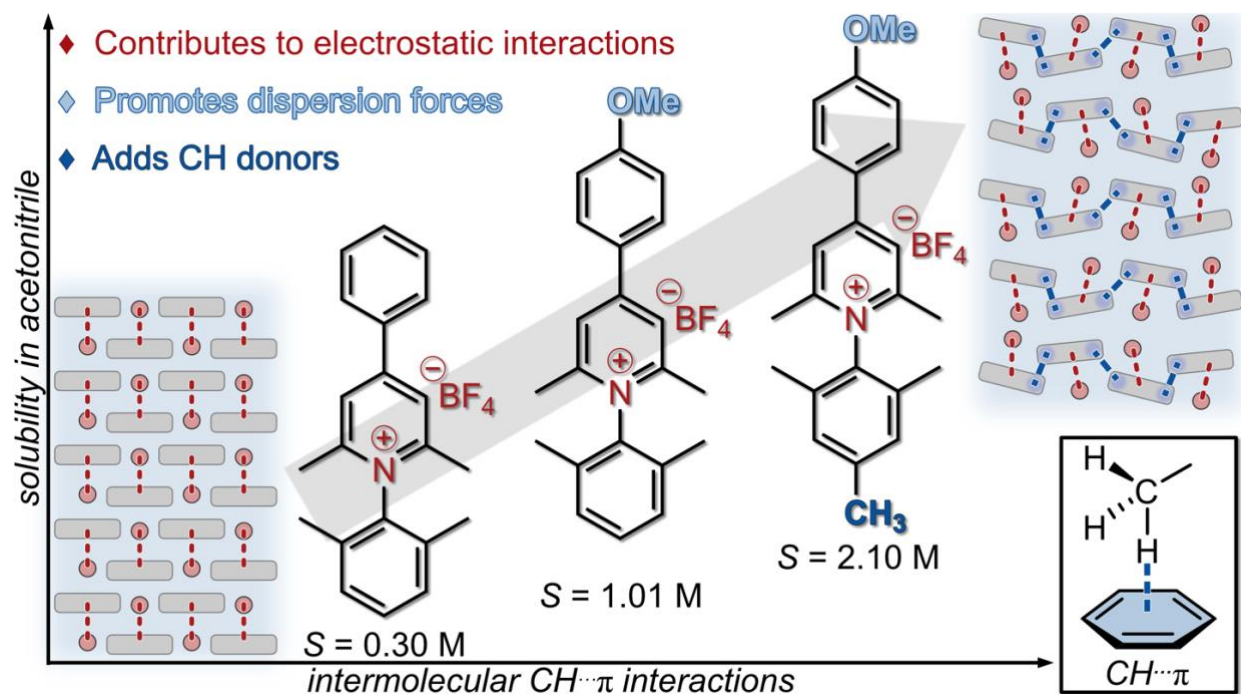


**Figure 2.1. Chapter 2: Graphical Abstract.** Discrete, attractive interactions between C–H groups and  $\pi$  electrons of an aromatic ring (C–H $\cdots\pi$  interactions) describe the solubility of N-substituted pyridinium salts in a non-aqueous solvent. A direct correlation exists between the number of C–H $\cdots\pi$  interactions for each pyridinium salt and its solubility in acetonitrile. This chapter highlights a consequence of disrupting strong electrostatic interactions with weak dispersion interactions, showing how minimal structural change can dramatically impact pyridinium solubility.

<sup>1</sup> This work is published as Samaroo, S.; Hengesbach, C.; Bruggeman, C.; Carducci, N. G. G.; Mtemeri, L.; Staples, R. J.; Guarr, T.; Hickey, D. P. C–H $\cdots\pi$  Interactions Disrupt Electrostatic Interactions between Non-Aqueous Electrolytes to Increase Solubility. *Nat Chem* **2023**. <https://doi.org/10.1038/s41557-023-01291-1>.

## 2.1 Introduction

Redox-active organic molecules (ROMs) have garnered significant interest for their use in non-aqueous redox flow batteries (NRFBs) to address the challenge of intermittent renewable energy production and distribution.<sup>30,59,79</sup> These devices provide a grid-scale energy storage solution by interconverting electrical and chemical energy using two electrolyte solutions, which consist of dissolved ROMs that can donate or accept electrons at either high (catholyte) or low (anolyte) redox potentials. ROMs are defined as any solvated organic molecule with a reversible redox couple.<sup>31,59</sup> Ideal ROMs for NRFBs, however, exhibit characteristics that maximize the battery's energy density. The energy density of a NRFB is the total energy stored per volume of the electrolyte solution and is dependent on the cell voltage and concentration of each ROM.<sup>45</sup> Consequently, desirable ROMs possess extreme redox potentials (either high oxidation potential or low reduction potential) and high solubility in the desired solvent system.

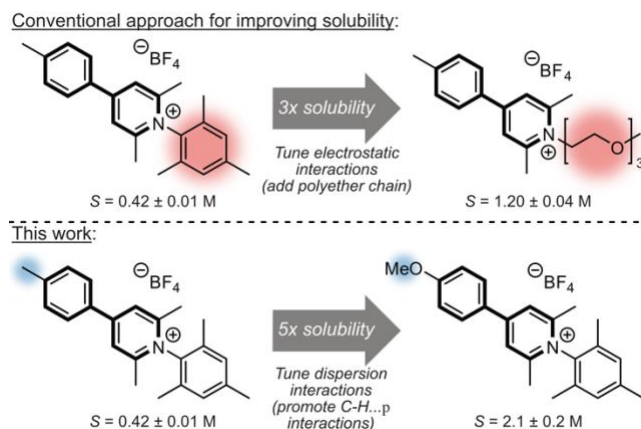


**Figure 2.2. Comparison of strategies for improving electrolyte solubility in nonaqueous solvent.** Conventional strategies (top) involve tuning electrostatic intermolecular interactions, while this work (bottom) highlights the significance of promoting dispersion forces as a strategy to improve solubility.

A primary benefit of ROMs is that their electrochemical and physicochemical properties can be tuned through judicious functionalization of a parent molecular structure. Significant progress has been made towards understanding the relationship between molecular structure and redox

potential, thereby enabling the careful design of ROMs with favorable redox potentials for use in NRFBs.<sup>80-82</sup> Unfortunately, equivalent correlations between molecular structure and solubility are comparatively limited, and there remains a need to develop strategies for improving ROM solubility.<sup>50</sup> Previously, an iterative design approach was used in combination with parameterized modelling to develop a series of pyridinium-based ROMs that exhibit low standard reduction potentials with exceptionally high persistence in multiple redox states.<sup>83</sup> Based on this, we considered the possibility of employing a similar strategy for designing pyridinium ROMs with improved solubility. We hypothesize that the use of parameterized modelling with a systematically functionalized library of pyridinium ROMs will reveal correlations between their molecular structure and solubility.

Solubility is defined by a dynamic equilibrium between a given compound as a solid precipitate and the same compound surrounded by solvent molecules.<sup>84</sup> This equilibrium depends on a complex combination of electrostatic, ionic, and London dispersion interactions of a molecule with itself (solute-solute) and with the bulk solvent (solvent-solute). Within the scope of NRFB ROMs, strategies for improving the solubility of a parent species in non-aqueous media are based on the rule that “like dissolves like”.<sup>85,86</sup> Consequently, previous efforts to improve ROM solubilities have focused on promoting solvent-solute interactions by introducing either hydrophilic (e.g., oligoether chains, small ionic groups) or hydrophobic (e.g., long paraffinic chains, large ionic groups) substituents to match the desired solvent (Figure 2.2),<sup>44,50,87</sup> as demonstrated in phenothiazine-,<sup>44,88</sup> 1,4-dimethoxybenzene-,<sup>89</sup> and quinone-<sup>80</sup> based ROMs. This approach affords considerable increases in solubilities over the parent ROMs by as much as 0.5 M; however, the introduction of common solubilizing substituents often results in adverse electrochemical or physicochemical properties. For example, the incorporation of large functional groups, such as

polyether chains, may improve the solubility of a parent compound but may also produce undesired physicochemical properties, such as high viscosity, that are detrimental to NRFB operation.<sup>48-50</sup> Thus, there remains a need to identify more nuanced structural features that may be tuned to improve ROM solubility.

In the pursuit of effective ROMs for NRFB use, pyridinium derivatives have been explored as anolytes.<sup>82,90</sup> Specifically, *N*-substituted 2,6-dimethyl-pyridinium derivatives exhibit particularly high persistence in the charged state with low standard reduction potentials.<sup>83</sup> Although rigorous optimization resulted in the exceptional combination of electrochemical potential and cyclability, similar strategies to manipulate physicochemical properties, such as solubility, of *N*-substituted 2,6-dimethyl-pyridiniums has not been performed, and the corresponding solubilities remain generally below 1 M. Additionally, further synthetic derivatization of this class of anolytes was limited by poor reactivity of the 2,6-dimethyl pyridine progenitor, thereby hindering further tuning to improve solubility.

Herein, we describe the preparation of a class of pyridinium salts, *N*- and 4-substituted 2,6-dimethyl-pyridiniums, and their use as a model system to investigate the relationship between molecular structure and solubility in polar aprotic solvents. Solubilities and electrochemical properties are defined for each derivative in acetonitrile, and subsequent crystal structure analysis reveals a series of discrete intermolecular dispersion interactions (between hydrogen atoms and aromatic  $\pi$ -electrons from neighboring pyridiniums, C-H $\cdots\pi$ ) that provide a univariate correlation to solubility. A linear correlation between solubility and intermolecular C-H $\cdots\pi$  interactions highlights the non-negligible contribution of weak dispersion forces on solvation behavior and suggests that molecular structure plays a critical role in promoting solute-solute interactions to improve pyridinium solubility.



## 2.2 Methods

### 2.2.1 Materials

All starting materials, including 2,6-dimethyl- $\gamma$ -pyrone (Ambeed), Grignard reagents (Alfa Aesar or Sigma-Aldrich), and all amines (various sources) were of the highest purity available and used as received. Solubility measurements were performed using HPLC grade acetonitrile, 99.93+%, from Millipore Sigma. Solubilities were measured by UV-vis spectrophotometry on an OLIS RSM 1000 UV/Vis Rapid Scanning Spectrophotometer. Crystallography experiments were performed on a XtaLAB Synergy, Dualflex, HyPix diffractometer.

### 2.2.2 General Synthesis of 2,6-Dimethylpyridinium (Me<sub>2</sub>Py<sup>+</sup>) ROMs

All pyryliums were synthesized following a modified procedure reported by DiMauro and Kozłowski.<sup>91,92</sup> In an oven-dried 250 mL round bottom flask, 2,6-dimethyl- $\gamma$ -pyrone was dissolved in THF under nitrogen. The stirring solution was cooled to 5 °C via ice bath, then one equivalent of arylmagnesium bromide (in a 1 M solution with THF) was added dropwise. The reaction mixture was subsequently allowed to warm to room temperature while stirring over an hour. The crude mixture was poured over a boron trifluoride diethyl etherate solution to yield a precipitate which was filtered and washed with diethyl ether. The product was purified by recrystallization in a 1:1 water/methanol mixture.

The resulting pyrylium intermediates were then reacted with a primary amine to afford the desired pyridinium derivatives. In a 50 mL round bottom flask equipped with a magnetic stir bar and condenser, 4-substituted 2,6-dimethyl-pyrylium tetrafluoroborate was suspended in ethanol (~30 mL). Approximately 1.2 equivalents of the corresponding primary amine was added and the mixture was refluxed for 4 hours while under nitrogen. The solution was cooled to room

temperature overnight and diluted with diethyl ether. The precipitate was isolated by filtration and dried under vacuum to afford a solid product.

### **2.2.3 Solubility of Me<sub>2</sub>Py<sup>+</sup> Derivatives**

Solubility measurements and calibration curve measurements for each pyridinium salt were completed in triplicate. Stock solutions (stock concentration = 0.25 mM) of each pyridinium were prepared using a 50 mL volumetric flask. A precision scale was used to obtain the target mass of pyridinium salt for the stock solution. To ensure accuracy, measurements were repeated for each mass until value settled within +/- 0.02 mg of the target mass for two successive measurements without any removal/addition of material to the vial. The material weighed into the vial was transferred by dissolving the sample in a small amount of solvent (acetonitrile, THF, propylene carbonate) and transferring to a 50 mL volumetric flask by pipette. To ensure that all material was moved from the vial to the flask, pure acetonitrile was added to the vial and then transferred by pipette to the flask and repeated five to seven times. The flask was subsequently filled to a total volume of 50 mL with acetonitrile.

Unless otherwise noted, calibration curves for each pyridinium sample included the UV-vis measurements at five different concentrations. The stock solution was diluted four times to yield calibration solution 1, serial dilutions by half were repeated for calibration solutions 2, 3, 4, and 5 to generate the full calibration series.

Saturated solutions of each pyridinium species were made by incrementally adding pyridinium salt to a small vial and stirring in solvent (acetonitrile, THF, propylene carbonate) at 22 °C for 30 minutes. The final unfiltered saturated solution was cloudy and contained undissolved solids. This mixture was filtered through Whatman Quantitative filter paper (Grade 1, Particle retention: 11 μm), to yield final saturated solution. Small circles of filter paper were placed into the “pocket” of

a syringe needle, creating two to three layers of filter paper. Then the unfiltered saturated solution was drawn into the “needle-less” syringe barrel. The filled barrel was connected to the needle-tip containing filter paper. The depression of the plunger forced the cloudy solution through the filter paper and removed the undissolved particles. The saturated solution was measured with Eppendorf pipettes (10  $\mu$ L, 20  $\mu$ L, 1 mL) and diluted in a 10 mL volumetric flask consecutively, until the solution generated had an absorbance measurement that fell within the range of the calibration curve. The degree of dilution here determined the dilution factor.

Absorbance measurements were collected for all 15 calibration curve solutions, and the three diluted-saturated solutions using a UV-vis spectrophotometer at the selected wavelength giving the maximum absorbance. To generate the calibration curve, the absorbance (AU) was plotted vs. concentration (mM), which gave a linear relationship. Calibration curves were considered acceptable once a linearity of  $R^2 > 0.99$  was achieved. The slope of this line is the molar absorptivity constant ( $\epsilon$  [ $\text{L cm}^{-1} \text{mol}^{-1}$ ]), found from the Beer-Lambert law. Absorbances of dilution solutions were all within the calibration curve range. A rearrangement of this equation was used to calculate concentration of the diluted solutions from the absorbance measurements. The dilution factor was used to solve for the concentration of the saturated solutions. The error reported included error propagation of the calibration data and the deviation of diluted saturated solutions.

### **2.2.3.1 Solubility of Me<sub>2</sub>Py<sup>+</sup> Derivatives in Cyclohexanone**

The procedure used for the determination of maximum concentration of pyridinium salt, deviated from the standard procedure due to an overlap in absorbance ranges of the solvent and pyridiniums (peak absorbance wavelengths range 300-340 nm). The saturated solutions were made in cyclohexanone (as described above), then 5 mL was transferred to a small vial and the cyclohexanone was removed by roto-evaporation. The residual pyridinium material was then

dissolved in acetonitrile and further diluted. The maximum concentration of pyridinium in cyclohexanone was determined using the existing calibration curves in acetonitrile. It should be noted that the absorbance peak of cyclohexanone, after two degrees of dilution (5 mL:3 mL and then 1 mL:3 mL) would fall in the baseline of acetonitrile while the absorbance of the pyridiniums would fall within the calibration curve absorbance.

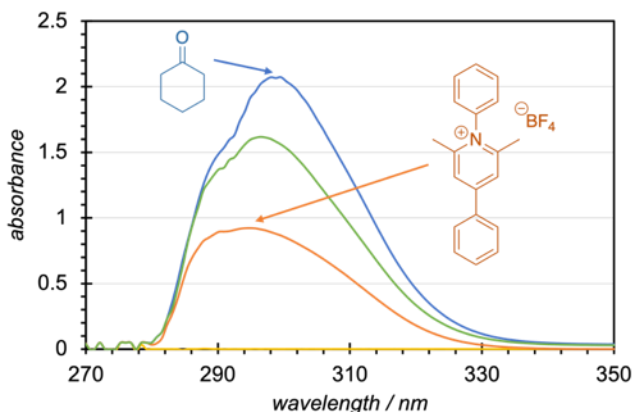


**Figure 2.3. Absorbance of cyclohexanone overlaps with representative pyridinium (compound 1).** There is a baseline solution of acetonitrile (yellow), compound 1 in acetonitrile (orange), cyclohexanone in acetonitrile (blue) and a mixture of cyclohexanone and compound 1 in acetonitrile (green).

#### 2.2.4 Electrochemical Analysis of Me<sub>2</sub>Py<sup>+</sup> Derivatives

The measured redox potentials ( $E_{1/2}$ ) of all 24 pyridinium derivatives were determined by cyclic voltammetry in acetonitrile with ferrocene as an internal redox standard, and all redox couples were found to be completely reversible. Experiments were performed using 3 mm GCE working electrode and Ag/Ag<sup>+</sup> reference electrode with 100 mM tetrabutylammonium hexafluorophosphate in acetonitrile as the supporting electrolyte at 25 °C and 200 mV s<sup>-1</sup> under a N<sub>2</sub> atmosphere.

#### 2.2.5 Crystallographic Analysis of Me<sub>2</sub>Py<sup>+</sup>

Crystals used in analysis of C-H... $\pi$  interactions were grown from acetonitrile to ensure similarity of the packing structures to assemblies forming in solubility studies. A saturated

solution made by adding the pyridinium salt to acetonitrile and stirring at 22-23 °C, for 30 minutes. Undissolved pyridinium salt was removed by filtering through Whatman Grade 1 Qualitative Filter Paper to yield the final saturated solution. The saturated solution was stored in a capped 4 mL vial at 22-23 °C, and acetonitrile was allowed to evaporate from the vial slowly over a time ranging from 1-2 days to 1-2 months.

A suitable crystal with dimensions  $0.21 \times 0.07 \times 0.06 \text{ mm}^3$  was selected and mounted on a nylon loop with paratone oil on a XtaLAB Synergy, Dualflex, HyPix diffractometer. The crystal was kept at a steady  $T = 100.00(10) \text{ K}$  during data collection. The structure was solved with the ShelXT solution program using dual methods and by using Olex2 1.5 as the graphical interface.<sup>93-95</sup> The model was refined with ShelXL 2018/3 using full matrix least squares minimization on  $F^2$ .

### 2.2.6 Identification of C-H $\cdots\pi$ Interactions from Crystallographic Analysis

X-Ray crystallography data was used to identify potentially significant  $\pi$  interactions for pyridinium salts. C-H $\cdots\pi$  interactions were defined based on criteria previously defined by Nishio and coworkers;<sup>96</sup> an H-centroid distance cutoff of 3.6 Å was used and only H atoms within the cylindrical region normal to an aromatic ring were considered. While the majority of intermolecular interactions observed were C-H $\cdots\pi$  interactions, all  $\pi$  interactions were incorporated in the final parameter calculation (this included one  $\pi$ - $\pi$  interaction, one cation- $\pi$  interaction, and one C-F $\cdots\pi$  interaction). Nevertheless, all interactions in calculation of the C-H $\cdots\pi$  parameter ( $\sum d^{-6}$ ) are dominated by dispersion forces.<sup>97-99</sup>

The polyaromatic ionic nature of the compounds studied herein may result in incidental C-H $\cdots\pi$  interactions that are not likely to strongly associate in solution. To minimize the possibility of including coincidental (or potentially irrelevant) C-H $\cdots\pi$  interactions, we employed an additional exclusion criterion based on the number of electrostatic interactions that the aromatic

CH acceptor is engaged in. The number of predominately electrostatic  $\text{H}\cdots\text{BF}_4^-$  interactions less than the sum of the corresponding Van der Waals radii was compared to the number of  $\text{C-H}\cdots\pi$  interactions for a given acceptor. For a given CH acceptor, if the number of  $\text{H}\cdots\text{BF}_4^-$  interactions exceeded the number of  $\text{C-H}\cdots\pi$  interactions (typically one), then the  $\text{C-H}\cdots\pi$  interaction excluded. This criterion resulted in removing a total of three interactions from the entire set of compounds studied that would have otherwise met the criteria for a  $\text{C-H}\cdots\pi$  interaction. An example of one such interaction that was excluded, and a representative example of a  $\text{C-H}\cdots\pi$  interaction that was included are detailed in Figure 2.4.

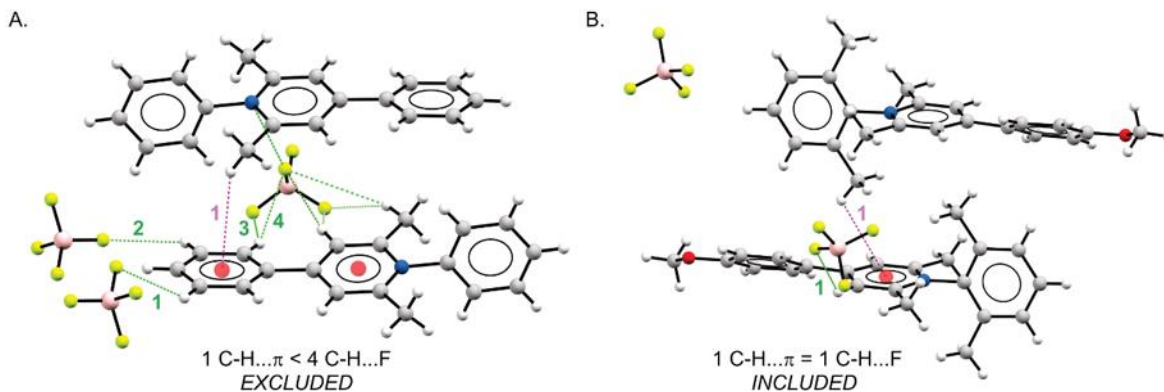


**Figure 2.4. Representative examples of interactions found in the crystal structures of pyridinium salts studied in this work.** (A) The structure of N-phenyl-4-phenyl-2,6-dimethylpyridinium tetrafluoroborate, **1**, exhibits one interaction that meets the criteria as a  $\text{C-H}\cdots\pi$  interaction (pink number and dashed line); however, the lattice is dominated by a network of strong electrostatic  $\text{H}\cdots\text{F}$  interactions. The interatomic distances of highlighted  $\text{H}\cdots\text{F}$  interactions (green numbers and dashed lines) are all shorter than the corresponding sum of Van der Waals radii; therefore, the  $\text{C-H}\cdots\pi$  interaction was excluded from consideration. (B) The structure of N-(2,6-xylyl)-4-(p-methoxyphenyl)-2,6-dimethylpyridinium tetrafluoroborate, **17**, revealed one interaction that meets the criteria as a  $\text{C-H}\cdots\pi$  interaction (pink number and dashed line), and the CH acceptor is simultaneously participating in one strong electrostatic interaction (green number and dashed line). Therefore, the  $\text{C-H}\cdots\pi$  interaction was included in the final solubility correlations.

### 2.2.7 $^1\text{H-NMR}$ Analysis of $\text{C-H}\cdots\pi$ Interactions between Solvated $\text{Me}_2\text{Py}^+$ ROMs

$^1\text{H-NMR}$  experiments of pyridiniums were performed using  $\text{CD}_3\text{CN}$ , and spectra were collected using an Agilent 500 MHz NMR Spectrometer, at 20 °C.

## 2.3 Results and Discussion

### 2.3.1 Synthesis and Solubility of 2,6-Dimethylpyridinium ROMs

Previous strategies to synthesize *N*-alkyl- and *N*-arylpyridinium anolytes relied on either the Zincke reaction or nucleophilic substitution for the final *N*-functionalization step from a parent pyridine molecule.<sup>83,100</sup> Unfortunately, these approaches are not possible for 2,6-dimethyl pyridine derivatives due to the steric hinderance of the methyl substituents. As a result, existing reactions to produce 2,6-dimethylpyridiniums (Me<sub>2</sub>Py<sup>+</sup>) require high temperatures and are limited to *N*-methyl and *N*-ethyl derivatives.<sup>83</sup> Alternatively, use of a pyrylium intermediate enables the facile production of structurally and electronically diverse *N*-substituents. Pyridinium salts of the current work were prepared via a modular, two-step synthesis from a commercially available  $\gamma$ -pyrone. This synthetic approach (Figure 2.5A) leverages a Grignard reaction with 2,6-dimethyl- $\gamma$ -pyrone to afford a stable pyrylium intermediate, which subsequently forms **1** upon reaction with aniline (Figure 2.3B).<sup>91,92</sup> Four base pyryliums were generated with varying 4-aryl substituents (i.e., phenyl, *p*-tolyl, 2,6-dimethylphenyl, or *p*-methoxyphenyl), with the latter two pyryliums demonstrating the successful use of sterically hindered aryl Grignard reagents on the multigram scale. Subsequent reactions of pyrylium intermediates were similarly modular, working effectively with electron poor (*p*-trifluoromethyl-), electron rich (4-methyl-, 2,6-dimethoxy-), and sterically hindered (2,6-dimethyl-2,4-dimethyl-) aniline derivatives as well as several aliphatic chains (*n*-butylamine and 2-(2-(2-methoxyethoxy)ethoxy)ethylamine). This simple, two-step synthesis was employed to introduce steric and electronic diversity to a parent *N*-aryl-4-aryl-2,6-dimethylpyridinium structure and generate pyridinium salt **24** (Figure 2.5B) on the gram scale.<sup>91,92</sup> The breadth of 4- and *N*-substituents afforded by this synthetic procedure enabled the systematic investigation of relationships between molecular structure and pyridinium solubility.

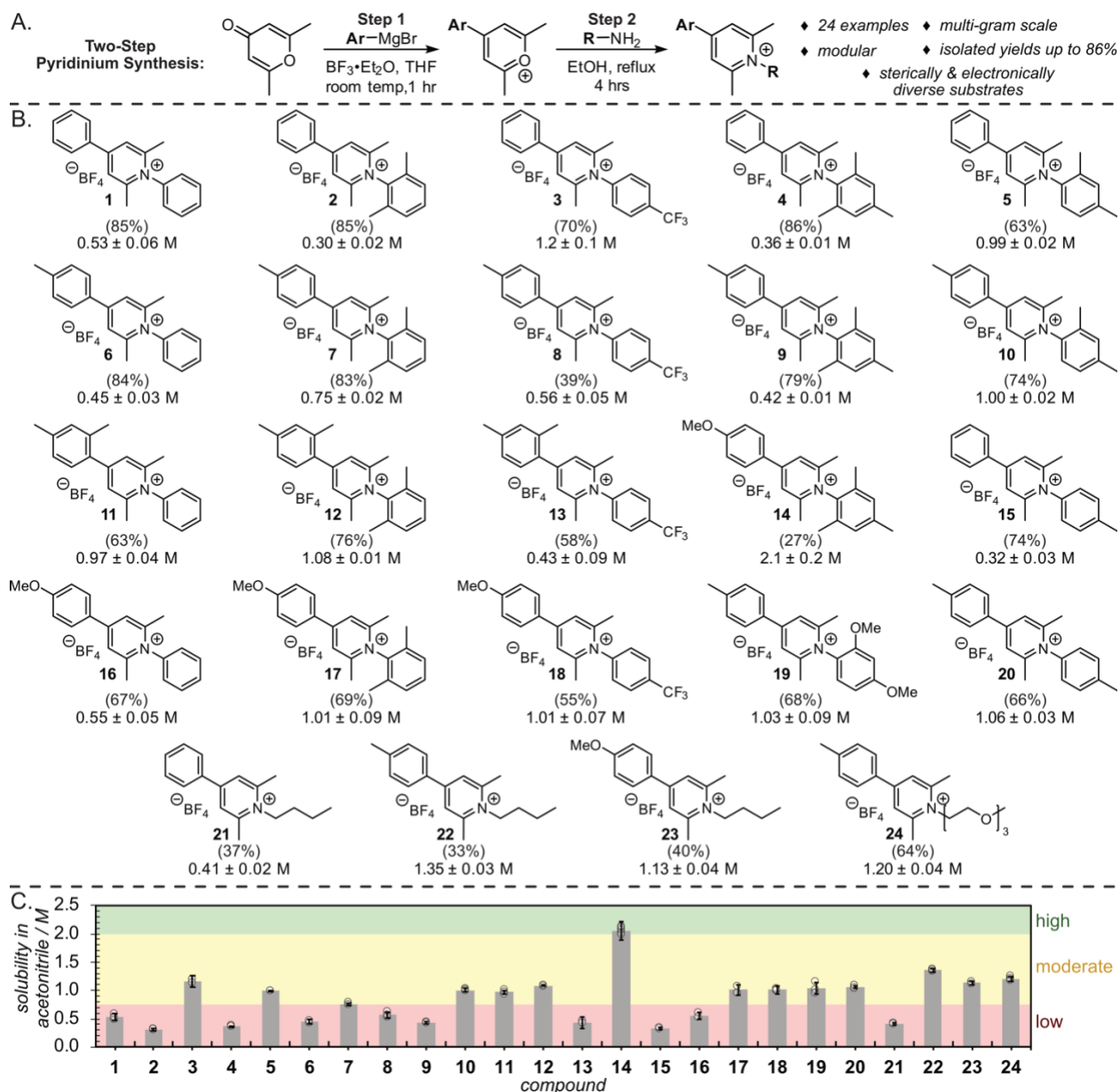


**Figure 2.5. Synthesis and nonaqueous solubility of pyridinium ROMs.** (A) Synthesis of pyrylium intermediates and pyridinium species corresponding to 24 derivatives of  $N$ - and 4-substituted  $\text{Me}_2\text{Py}^+$  tetrafluoroborate salts. (B) Structures, isolated yields, and solubilities of pyridinium salts in the current study; a streamlined version of this figure is included in Appendix A Table A.1. (C) Plot comparing solubilities of all 24 pyridinium derivatives; solubilities fit into clusters defined as low ( $< 0.75$  M), moderate ( $0.75$  M –  $2.0$  M), and high ( $> 2.0$  M). Pyrylium syntheses were completed at the multigram scale and pyridinium syntheses were completed at the gram scale. Isolated yields for each step are reported below each structure. Solubility measurements were performed using pure acetonitrile at  $22$  °C. Solubility reported mean values  $\pm$  SD where  $n = 3$  for all compounds except for compound **17** ( $n = 5$ ), compound **24** ( $n = 5$ ), and compound **14** ( $n = 9$ ), and individual data points are shown in grey circles in-line with corresponding compound label.



Using this library of electronically and sterically diverse pyridinium salts, we sought to identify substituent effects that correlate to solubility in a polar, aprotic solvent. Pyridinium solubilities were measured by UV-vis spectrophotometry in pure acetonitrile (Figure 2.5B). Despite maintaining a consistent molecular architecture and ion pair, pyridinium solubilities were found to vary widely from 0.3 M to 2.1 M. Additionally, pyridinium solubilities fit into three regions (Figure 2.5C) defined as low (<0.75 M), moderate (0.75 M – 2.0 M), and high (>2.0 M) solubility. Upon initial examination, the data revealed dramatic increases in solubility resulting from minimal variations in molecular structure.

Comparing 4-phenyl and 4-(*p*-tolyl) derivatives of *N*-(*p*-tolyl)-Me<sub>2</sub>Py<sup>+</sup> (**15** and **20**, respectively), the structural variation is sufficiently distal to the ionic center that we would not expect it to significantly alter intermolecular electrostatic interactions, yet the solubility of **20** is more than three times that of **15** (1.06 ± 0.03 M vs. 0.32 ± 0.03 M). Similar juxtapositions can be made between 4-phenyl- and 4-(*p*-tolyl)-*N*-(2,6-xylyl)-Me<sub>2</sub>Py<sup>+</sup> (**2** and **7**, respectively) (0.30 ± 0.02 M vs. 0.75 ± 0.02 M) and 4-(*p*-tolyl)- and 4-(2,4-xylyl)-*N*-phenyl-Me<sub>2</sub>Py<sup>+</sup> (**6** and **11**, respectively) (0.45 ± 0.03 M vs. 0.97 ± 0.04 M); each comparison demonstrates significant increased solubility with minimal structural change (i.e., the addition of a single methyl substituent). Interestingly, the *N*-mesityl subclass shows only a subtle increase between 4-phenyl- and 4-(*p*-tolyl)-*N*-(mesityl)-Me<sub>2</sub>Py<sup>+</sup> (**4** and **9**, respectively) (0.36 ± 0.01 M vs. 0.42 ± 0.01 M), while the solubility of *N*-(mesityl)-4-(*p*-methoxyphenyl)-Me<sub>2</sub>Py<sup>+</sup> (**14**) is at least five times that of **4** or **9**. These apparent patterns of increasing solubility with 4-(*p*-tolyl) or 4-(*p*-methoxyphenyl) additions, however, lack consistency as shown between 4-phenyl- and 4-(*p*-tolyl)-*N*-(phenyl)-Me<sub>2</sub>Py<sup>+</sup> (**1** and **6**, respectively) (0.53 ± 0.06 M vs. 0.45 ± 0.03 M) and 4-phenyl- and 4-(*p*-methoxyphenyl)-*N*-(phenyl)-Me<sub>2</sub>Py<sup>+</sup> (**1** and **16**, respectively) (0.53 ± 0.06 M vs. 0.55 ± 0.05 M). As substituent

changes did not reliably correlate to solubility, we turned to computationally modelled parameters (e.g., electronic descriptors and Sterimol parameters) to probe the factors driving these large solubility variations between structurally similar pyridinium derivatives.

### 2.3.2 Electrochemistry and Computational Analysis of Me<sub>2</sub>Py<sup>+</sup> ROMs

Density functional theory (DFT) computations were used to generate molecular descriptors with the potential to correlate to measured solubilities. To ensure that all computed pyridinium structures accurately reflect their experimental counterparts, we compared experimentally measured one-electron reduction potentials with those calculated from DFT outputs (Figure 2.6B). Notably, the fully reversible redox couples for many derivatives are among the lowest reported for known ROMs (-1.54 to -1.77 V vs. Fc/Fc<sup>+</sup>). The linear correlation between measured and modelled redox potentials (Figure 2.6C,  $R^2 = 0.86$ ) confirms the validity of individual geometry-optimized structures from which modelled parameters were determined.

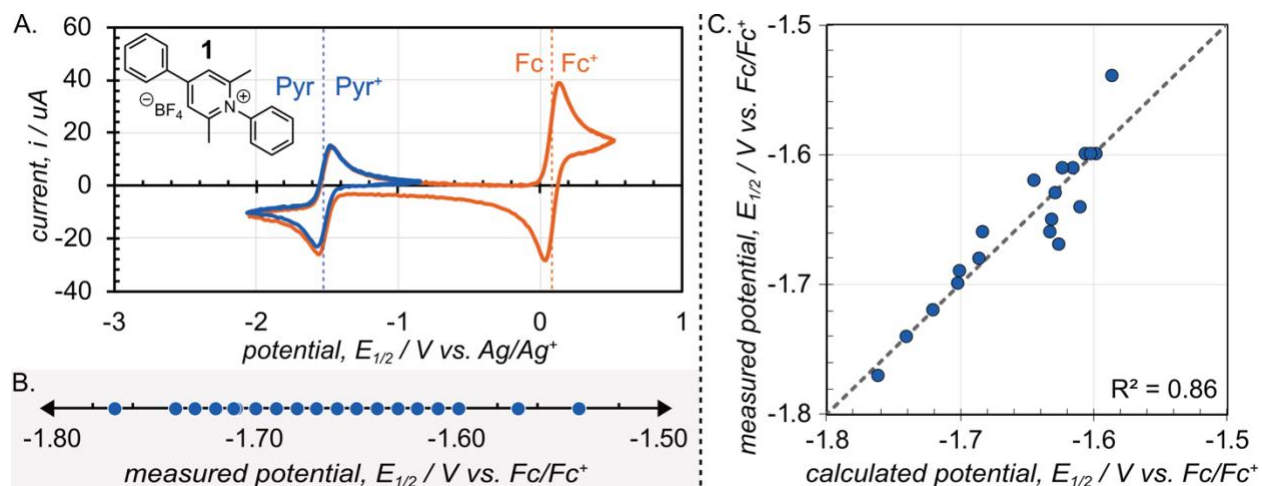


**Figure 2.6. Experimental pyridinium redox potentials enable validation of DFT-optimized structures.** (A) A representative cyclic voltammogram of 1 mM *N*-phenyl-4-phenyl-Me<sub>2</sub>Py<sup>+</sup> tetrafluoroborate (1) using 1 mM ferrocene as an internal reference. (B) A 1-dimensional plot containing the redox potentials ( $E_{1/2}$ ) of all synthesized pyridinium derivatives. (C) A plot of experimentally measured redox potentials versus the corresponding computed potentials for all pyridiniums. Experiments were performed using 3 mm GCE working electrode and Ag/Ag<sup>+</sup> reference electrode with 100 mM tetrabutylammonium hexafluorophosphate in acetonitrile as the supporting electrolyte at 25 °C and 200 mV s<sup>-1</sup> under a N<sub>2</sub> atmosphere. pyridinium solubility.

For each pyridinium salt, density functional theory (DFT) was used to compute the geometry-optimized ground state energy with a B3LYP functional in combination with 6-31+G(d,p) basis set and CPCM polarizable conductor solvation model in acetonitrile. This functional and basis set were previously found to provide an optimal balance between accuracy and computational time for DFT computations of structurally similar pyridinium salts.<sup>101</sup> In order to validate the geometry-optimized structures determined computationally, the standard reduction potential was computed by DFT from the ground state energies of each pyridinium species the oxidized (pyridinium cation) and reduced (neutral radical) form in the gas phase and solvated (shown in Figure 2.7) according to the following free energy equations;

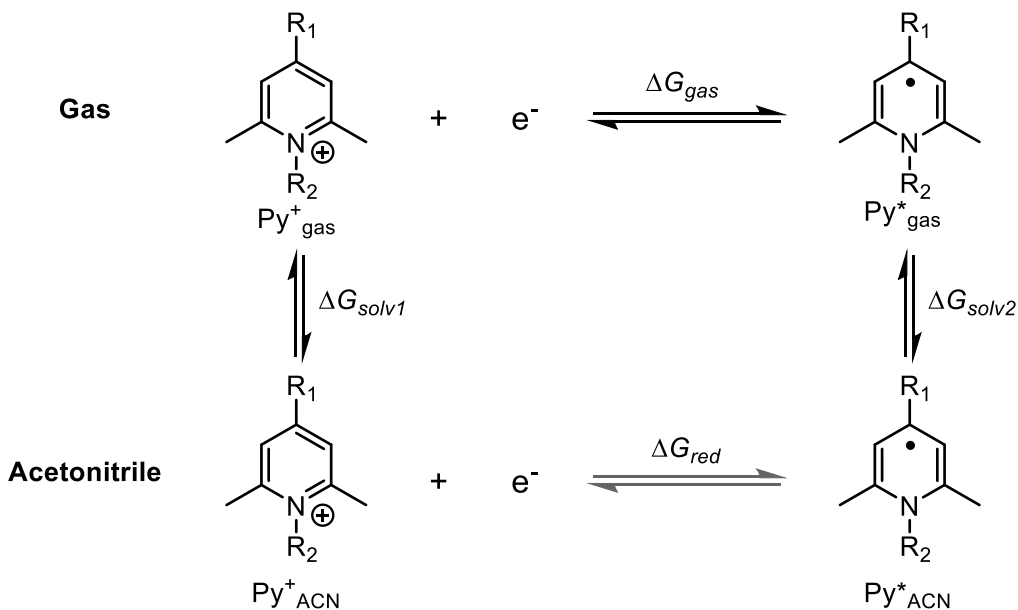


**Figure 2.7. Gas phase and solvated pyridinium species.** Ground state energies of each pyridinium species the oxidized (pyridinium cation) and reduced (neutral radical) forms.

$$\Delta G_{\text{red}} = \Delta G_{\text{gas}} + \Delta G_{\text{sol}2} - \Delta G_{\text{sol}1} \quad (\text{Eq. 2.1})$$

$$E_{\text{red}}^o = -\left(\frac{\Delta G_{\text{red}}}{nF}\right) \quad (\text{Eq. 2.2})$$

$$E_{\text{red}} = E_{\text{red}}^o - 4.86 \quad (\text{Eq. 2.3})$$

where  $\Delta G_{gas}$  is the gas phase ionization free energy,  $\Delta G_{solv}$  are the solvation of the oxidized and reduced pyridinium,  $n$  is the number of electrons transferred in the reaction (here assumed to be one),  $F$  is the Faraday constant (96,485 C mol<sup>-1</sup> of electrons),  $E^o_{red}$  is the pyridinium standard reduction potential, and  $E_{red}$  is the formal pyridinium reduction potential. The value of -4.86 V is the computed standard reduction potential for ferrocene/ferrocenium in acetonitrile; this value was computed previously by DFT ground state energies using a SMD solvation model.<sup>102</sup> Consequently, all redox potentials computed herein are reported versus the standard ferrocene/ferrocenium reduction potential.

An array of molecular descriptors was extracted from computed geometry-optimized pyridinium structures in the oxidized state, to identify correlations between molecular structure and solubility. Descriptors were selected to test the applicability of previously reported structure/solubility relationships observed with small organic molecules. Two parameters frequently used to describe the impact of solute-solvent interactions on solubility are solute polarizability and molecular dipole moment (which in turn describe electronic deformability and charge distribution, respectively).<sup>103,104</sup> Plots of pyridinium polarizability or dipole moment versus solubility (Figure 2.8A and Figure 2.8B), however, do not yield univariate correlations. Moreover, several additional commonly used electronic parameters were investigated (e.g., natural bonding orbital (NBO) charges for each atom of the core pyridinium structure), but none revealed any meaningful correlation to solubility (additional parameters described in Appendix A in Figure A.1, Figure A.2, and Figure A.3).

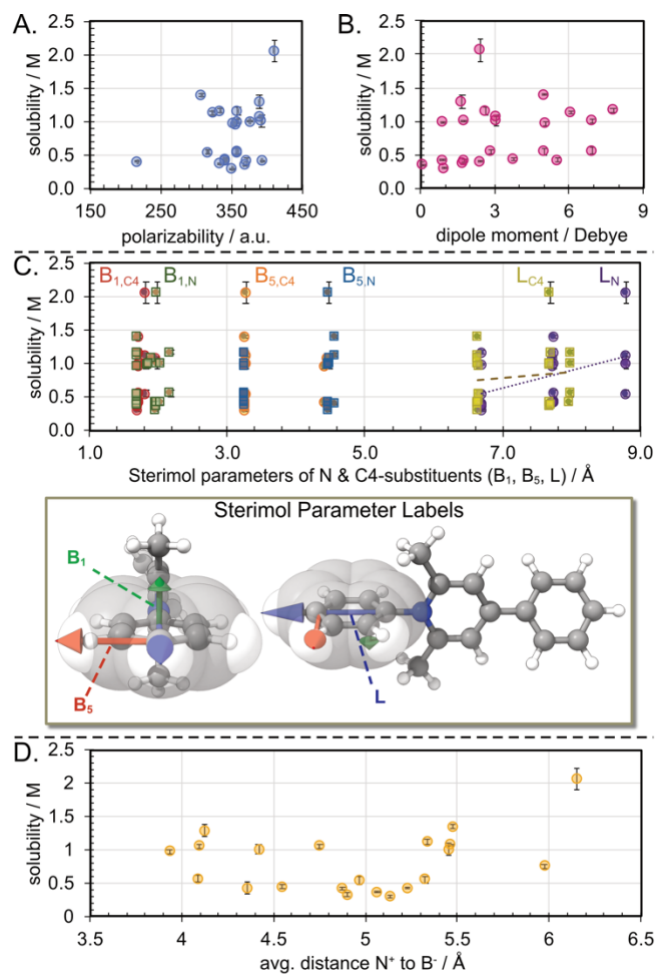


**Figure 2.8. Conventional physical organic molecular descriptors do not correlate with pyridinium solubility.** Plots of solubility versus several computationally derived molecular descriptors. Pyridinium solubility is plotted against (A) polarizability, (B) dipole moment, (C) Sterimol parameters<sup>105,106</sup>, top, illustration of corresponding B<sub>1</sub>, B<sub>5</sub>, and L parameters, bottom, and (D) and the average distance between anion, B<sup>-</sup>, and cation, N<sup>+</sup>. Solubility is plotted for panels A, B, C, and D as mean values  $\pm$  SD with  $n = 3$  for all compounds except for compound **17** ( $n = 5$ ), compound **24** ( $n = 5$ ), and compound **14** ( $n = 9$ ). It should be noted that Sterimol parameters fall within a comparatively narrow distribution, even after normalization (despite the wide variation in solubilities), which suggests that steric hindrance of individual substituents is insufficient to account for the differences in solubility.

In addition to investigating parameters describing solute-solvent interactions, we examined parameters that describe solute-solute interactions. Specifically, we considered two distinct but interrelated instances of solute-solute interactions, (1) between neighboring pyridinium molecules or (2) between pyridinium cations and tetrafluoroborate anions. Multivariate structure-activity modelling has previously identified Sterimol parameters as effective descriptors of steric influence

by molecular substituents on their corresponding reactivity.<sup>107</sup> Similar to other reversible chemical reactions, dynamic solubility is dependent on both the forward and reverse rate constant for precipitate formation. Therefore, we considered using Sterimol parameters to describe the influence of sterics of the *N*- and 4-substituents on pyridinium solubility. Sterimol parameters ( $B_1$ ,  $B_5$ , and  $L$ ) define steric variation where  $B_1$  is the minimum substituent width from a defined atom,  $B_5$  is the maximum substituent width from a defined atom, and  $L$  is the substituent length, as shown in Figure 2.8C.<sup>108,109</sup> Unfortunately, no univariate correlations were found using Sterimol parameters. Finally, it should be noted that several attempts were made to identify linear combinations of steric and electronic molecular descriptors that correlate to solubility; however, no multivariate model was found.

Having exhausted traditional computationally derived molecular descriptors, we turned to X-ray crystallography to experimentally probe intermolecular interactions that may provide insights into pyridinium solubility behavior. Pyridinium crystals were grown by slow evaporation from pure acetonitrile, ensuring that molecular orientations within crystals were representative of assemblies occurring in acetonitrile only. A qualitative crystallographic analysis indicates that molecular packing is predominantly controlled by strong ( $\text{BF}_4^- \cdots \text{pyridinium}^+$ ) and weak ( $\text{CH} \cdots \text{BF}_4^-$ ) electrostatic interactions. From this, we would expect to find a correlation between solubility and the energy of electrostatic  $\text{BF}_4^- \cdots \text{pyridinium}^+$  interactions (which is inversely proportional to the distance between counterions); however, a plot of the average  $\text{BF}_4^- \cdots \text{pyridinium}^+$  distance versus solubility (Figure 2.8D) reveals no apparent correlation. The average ionic distance provides a preliminary approximation of the total electrostatic energy in each crystal lattice; however, the absence of any apparent trend suggests that electrostatic interactions cannot singly describe pyridinium solubility.

### 2.3.3 Correlating Me<sub>2</sub>Py<sup>+</sup> Solubility and C-H··· $\pi$ Interactions

A direct comparison of the crystal structures for two pyridinium derivatives, representing low and moderate solubility species, emphasizes dispersion forces as the notable difference between structurally similar derivatives. *N*-(*p*-tolyl)-4-phenyl-Me<sub>2</sub>Py<sup>+</sup>, **15**, exhibits poor solubility and *N*-(*p*-tolyl)-4-(*p*-tolyl)-Me<sub>2</sub>Py<sup>+</sup>, **20**, exhibits moderate solubility; their corresponding crystal structures both contain electrostatic interactions, but, unlike the lattice of **15**, that of **20** contains C-H··· $\pi$  interactions (between the Me<sub>2</sub>Py<sup>+</sup> methyl CHs and the  $\pi$ -electrons of the 4-aryl ring, Figure 2.9A/B). This comparison reveals a subtle but key difference between the otherwise structurally similar pyridinium derivatives and suggests that weak dispersion forces, specifically C-H··· $\pi$  interactions, may play a role in dictating solubility behavior.

C-H··· $\pi$  interactions are composed primarily of attractive London dispersion forces and are defined as occurring between a C-H donor and  $\pi$ -electrons of an aromatic ring (Figure 2.9D).<sup>110</sup> Recently, non-covalent C-H··· $\pi$  interactions have garnered significant interest for their role in molecular recognition, protein binding, and molecular catalysis.<sup>111–113</sup> Despite being significantly weaker than their electrostatic and hydrogen bonding counterparts, they can dictate transition state geometry in (e.g.) molecular catalysis, where intermolecular distances approach the Van der Waals radii.<sup>114,115</sup> Based on this, we considered the possibility that C-H··· $\pi$  interactions may disrupt electrostatic interactions during the assembly of pyridinium salts near their solubility limit (Figure 2.9E).

As highlighted in Figure 2.9A, **20** exists as a self-complementary dimer via two symmetrical C-H··· $\pi$  interactions. This motif represents a significant distinction from the crystal lattice of **15**, which is dominated by alternating ionic interactions (Figure 2.9B). Crystallographic analysis of all pyridiniums reveals several distinct C-H··· $\pi$  interactions as parts of either dimeric pairs containing

one C-H $\cdots\pi$ , self-complementary dimers containing two C-H $\cdots\pi$  (analogous to that of **20**), or dimers containing three asymmetric C-H $\cdots\pi$  (Appendix A from Figure A.4 to Figure A.19). Furthermore, crystal lattices of several pyridinium species revealed repeating clusters of pyridiniums (as many as four) linked through combinations of C-H $\cdots\pi$  interactions. Individual dispersion forces within self-complementary dimers are weaker than electrostatic forces arising from pairs of pyridinium and BF<sub>4</sub><sup>-</sup> counterions but may be kinetically favored when solvated. Thus, the formation of C-H $\cdots\pi$  dimers (or higher order aggregates) could restrict the total number of electrostatic interactions possible near the solubility limit, thereby destabilizing the precipitate and promoting pyridinium solubility.



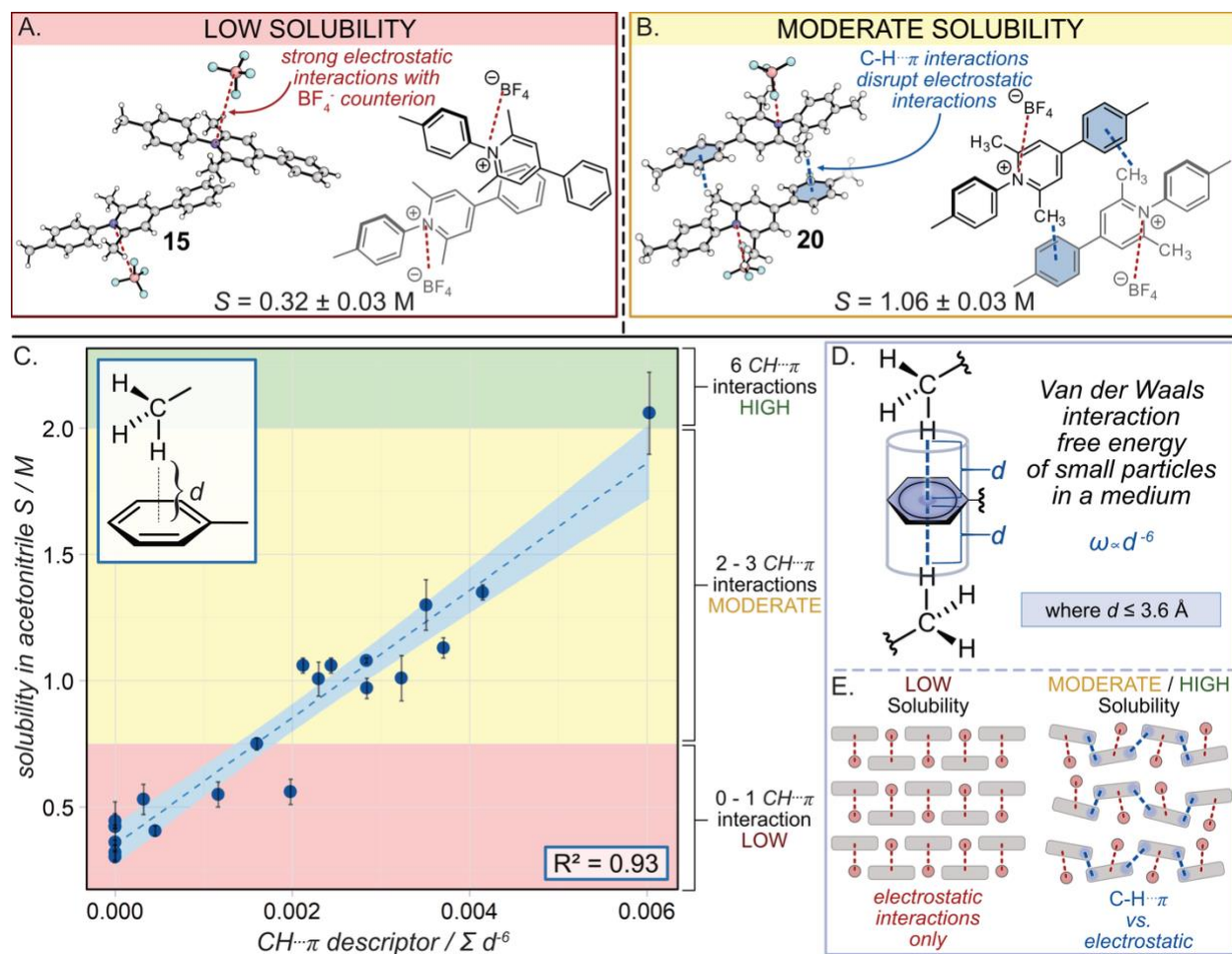


**Figure 2.9. C-H $\cdots\pi$  interactions increase pyridinium solubility by disrupting ionic crystal lattice.** The chemical structure and crystal lattice of (A) *N*-(*p*-tolyl)-4-phenyl-Me<sub>2</sub>Py<sup>+</sup> (**15**) and (B) *N*-(*p*-tolyl)-4-(*p*-tolyl)-Me<sub>2</sub>Py<sup>+</sup> (**20**). The herringbone assembly exhibited in the lattice of **15** is dominated by electrostatic interactions between pyridinium cations and BF<sub>4</sub><sup>-</sup> counterions whereas electrostatic interactions in the lattice of **20** are disrupted by C-H $\cdots\pi$  interactions. (C) A plot comparing pyridinium solubility in pure acetonitrile to a descriptor of C-H $\cdots\pi$  interactions (defined here as  $\sum d^{-6}$ , for C-H $\cdots\pi$  interactions identified via crystallographic analysis, where  $d = \text{H} - \text{centroid}$  distance); solubility plotted as mean values  $\pm$  SD where  $n = 3$  for all compounds except for compound **17** ( $n = 5$ ), compound **24** ( $n = 5$ ), and compound **14** ( $n = 9$ ); a light blue region around the curve represents the 95% confidence interval. (D) Illustration of the criteria used to identify C-H $\cdots\pi$  interactions (previously defined by Nishio and coworkers (Umezawa et al., 1998)); an H-centroid distance cutoff  $d \leq 3.6 \text{ \AA}$  was used and only H atoms within the cylindrical region normal to an aromatic ring were considered. (E) Illustration depicting electrostatic interactions in representative crystal packing structures in the absence (left) and presence (right) of C-H $\cdots\pi$  interactions.

We next sought to define a parameter describing the extent that these C-H $\cdots\pi$  interactions correlate to solubility. The energy of each interaction can be calculated as the Van der Waals free

energy for small particles in a medium (at short distances), which is inversely proportional to the H $\cdots$  $\pi$  centroid distance ( $d^{-6}$ ),<sup>116,117</sup>

$$\omega(d) = \frac{-6k_B T}{(4\pi\epsilon_0)^2 d^6} \sum_{n=0,1,2\dots}^{\infty} \frac{(\alpha_{molecule})^2}{(\epsilon_{solvent})^2} \quad (\text{Eq. 2.4})$$

where  $d$  is intermolecular distance,  $k_b$  is the Boltzmann constant,  $T$  is temperature,  $\epsilon_0$  is vacuum permittivity,  $\alpha_{molecule}$  is solute polarizability, and  $\epsilon_{solvent}$  is the solvent dielectric permittivity. To approximate the relative contribution of C-H $\cdots$  $\pi$  interactions to the overall crystal lattice, we defined a molecular descriptor as the sum of C-H $\cdots$  $\pi$  interactions weighted by the inverse H $\cdots$  $\pi$  distance,  $d$ , to the sixth power ( $\sum d^{-6}$ ). A plot of  $\sum d^{-6}$  versus solubility for 23 pyridiniums (Figure 2.9C) results in a direct linear correlation ( $R^2 = 0.93$ ), thus highlighting the relationship between solubility and the number of C-H $\cdots$  $\pi$  interactions observed in each corresponding crystal lattice. This empirical relationship suggests that the full range of pyridinium solubilities observed (i.e., 0.3–2.1 M in acetonitrile) can be described exclusively as a function of C-H $\cdots$  $\pi$  interactions. Most pyridiniums in this study engage in zero to three unique C-H $\cdots$  $\pi$  interactions, as depicted in Figure 2.9C; however, six such interactions are observed in the extreme case of **14**, which is soluble up to  $2.1 \pm 0.2$  M in acetonitrile. The zones of low, moderate, and high solubility are accurately predicted by the number of C-H $\cdots$  $\pi$  interactions (i.e., 0-1 C-H $\cdots$  $\pi$ , 2-3 C-H $\cdots$  $\pi$ , and 6 C-H $\cdots$  $\pi$  interactions, respectively). Importantly, this implies that promoting a greater number of C-H $\cdots$  $\pi$  interactions is more influential than improving the corresponding interaction strength when tuning solubility.<sup>39</sup>

### 2.3.4 <sup>1</sup>HNMR Analysis of C-H $\cdots$ $\pi$ Interactions between Me<sub>2</sub>Py<sup>+</sup> ROMs

It should be noted that direct links between solid-state features and solvated-state properties are not commonplace,<sup>118</sup> and it is difficult to faithfully derive information about the nature of

solvated intermolecular solute-solute interactions from the crystalline state without complementary solution state studies.<sup>119,120</sup> (Davey et al., 2006; Hulme et al., 2007) To provide such analysis, we investigated the extent to which C-H... $\pi$  interactions could be observed in solvent at concentrations approaching the solubility limit. To this end, <sup>1</sup>H-NMR spectra of **14** were measured at variable concentrations in CD<sub>3</sub>CN (Figure 2.10A). At higher concentrations, signals for protons not implicated in C-H... $\pi$  interactions shift downfield (a common phenomenon caused by increased ionic strength of the NMR solution).<sup>121</sup> However, signals corresponding to mesityl Hs of **14** shift upfield at increased concentrations; this shielding effect is consistent with C-H... $\pi$  interactions occurring in solution. Similar shifts can be seen for all Hs implicated in C-H... $\pi$  interactions by crystallographic analysis, suggesting that these assemblies form at concentrations significantly lower than their solubility limit. Interestingly, at concentrations above 0.11 M, the peaks corresponding to methyl Hs on the 4-methoxy substituent of **14** shift upfield and are spin-coupled to an adjacent intramolecular aryl H. This suggests that rotation of the methoxy group becomes restricted at high concentrations, and again, is consistent with the crystal structure assembly. Taken together, the <sup>1</sup>H-NMR analysis is consistent with C-H... $\pi$  interactions occurring at modest concentrations (as low as 0.2 M) for high-solubility pyridinium salts.

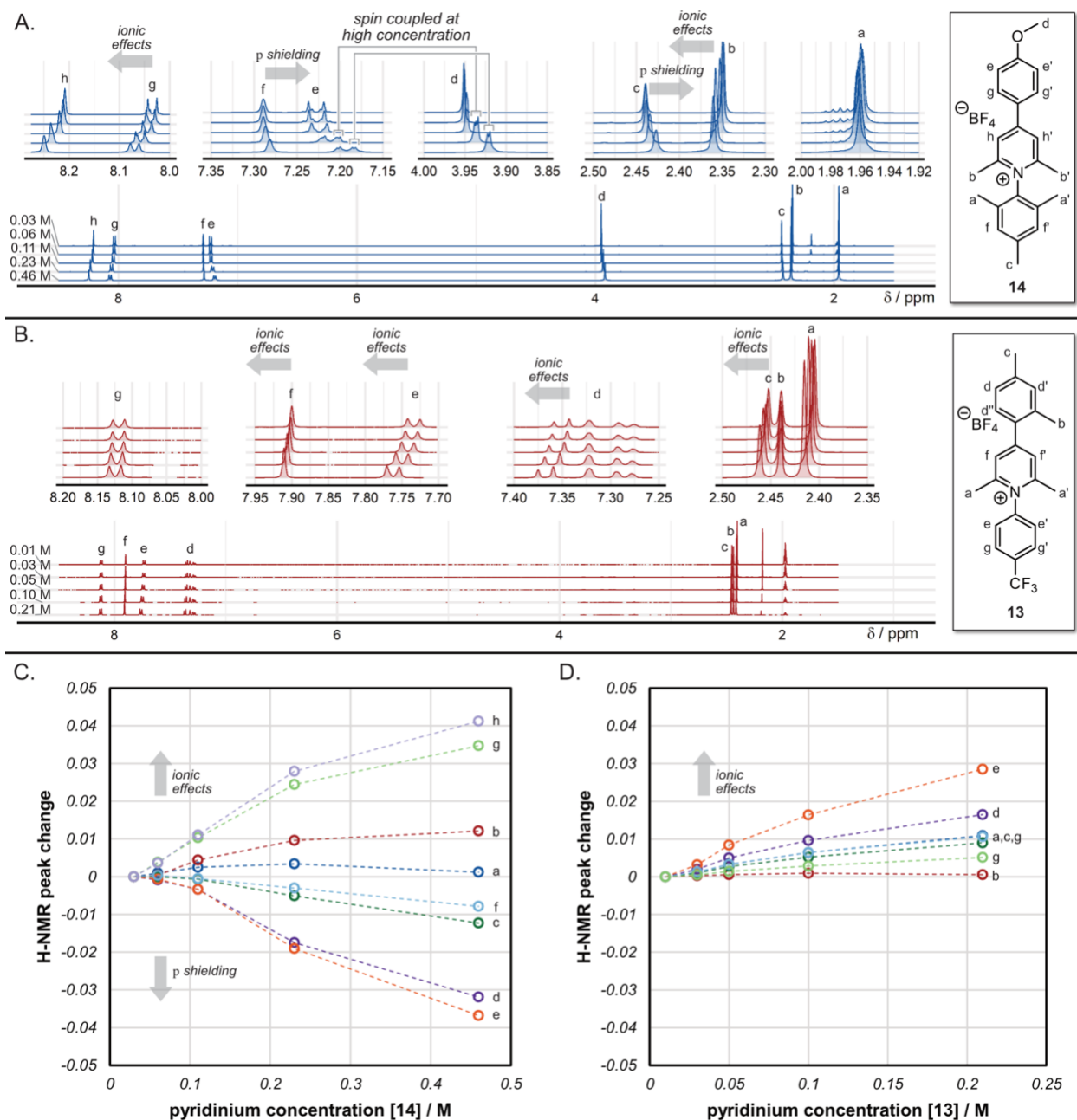


**Figure 2.10.**  $^1\text{H-NMR}$  confirms  $\text{C-H}\cdots\pi$  interactions are present between solvated pyridiniums. Variable concentration  $^1\text{H-NMR}$  spectra of (A) **14** and (B) **13** reveals upfield shifts of peaks corresponding to protons involved in  $\text{C-H}\cdots\pi$  interactions (due to  $\pi$  shielding effects upon  $\text{C-H}\cdots\pi$  association), while all other peaks shift downfield at higher concentrations, which is consistent with effects of increased ionic strength. (C) Plot of  $^1\text{H-NMR}$  peak change with concentration for **14**. (D) Plot of  $^1\text{H-NMR}$  peak change with concentration for **13**. Experiments were performed using variable concentrations of **14** or **13** in  $\text{CD}_3\text{CN}$  at  $20^\circ\text{C}$ .

A comparative  $^1\text{H-NMR}$  experiment of *N*-(*p*-trifluoromethylphenyl)-4-(2,4-xylyl)- $\text{Me}_2\text{Py}^+$  (**13**) demonstrated that only downfield shifting (reflecting ionic effects) is observed for poorly

soluble pyridinium salts, as shown in Figure 2.10B. The magnitude and direction for **14** and **13** proton shifts are summarized in Figure 2.10C and Figure 2.10D, respectively. These plots illustrate the complete absence of  $\pi$ -shielding effects in **13** at increasing concentrations, while H-NMR peaks of **14** exhibit both  $\pi$ -shielding and ionic interactions at increasing concentrations. These comparisons of in-solution behavior confirm that crystal packing structures directly reflect the intermolecular (solute-solute) interactions correlated to observed solubility.<sup>44</sup>

### 2.3.5 Correlating Solubility & C-H $\cdots\pi$ Interactions in Additional Solvents

To determine whether the prevalence of C-H $\cdots\pi$  interactions (as quantified by  $\sum d^{-6}$ ) provides an accurate indicator of solubility in solvents other than acetonitrile, we measured the solubility of nine representative pyridiniums in three additional solvents (tetrahydrofuran, cyclohexanone, and propylene carbonate). Pyridiniums were selected to represent a distribution of low (**1**, **2**, **6**, **16**), moderate (**5**, **10**, **12**, **20**) and high (**14**) propensities to participate in C-H $\cdots\pi$  interactions. Due to the importance of solvent dielectric in altering the strength of noncovalent interactions, polar aprotic solvents were selected with low (THF,  $\epsilon = 7.6$ ), moderate (cyclohexanone,  $\epsilon = 18$ ), and high (propylene carbonate,  $\epsilon = 66$ ) dielectric constants.<sup>122–125</sup> Plots of solubility vs  $\sum d^{-6}$  (Figure 2.11A) reveal linear correlations in cyclohexanone and propylene carbonate (PC) ( $R^2 = 0.75$  and  $R^2 = 0.72$  for cyclohexanone and PC, respectively), while the solubility of pyridiniums in THF was relatively invariant. It should be noted that the lack of linearity as measured by the coefficient of determination ( $R^2$ ) for pyridiniums in THF may be attributed to generally poor solubility (pyridinium solubilities all < 10 mM). Nevertheless, these combined data emphasize the importance of C-H $\cdots\pi$  interactions in describing Me<sub>2</sub>Py<sup>+</sup> solubility across several aprotic solvents.

Poor solubility of pyridiniums in low-dielectric solvents may be rationalized by the increased strength of both electrostatic (Me<sub>2</sub>Py<sup>+</sup> $\cdots$ BF<sub>4</sub><sup>-</sup>) and dispersion (i.e., C-H $\cdots\pi$ ) solute-solute

interactions, which are both inversely proportional to solvent dielectric.<sup>45-48</sup> However, a semi-log plot of pyridinium solubility and solvent dielectric (Figure 2.11B) does not result in a continuously increasing trend. This non-linear trend suggests that global solubility of pyridiniums in polar aprotic solvents depends on a more complex relationship between electrostatic and dispersion interactions, and increasing Me<sub>2</sub>Py<sup>+</sup> solubility for NRFB applications may be accomplished by carefully balancing these fundamental forces. Further corroboration of the identified relationship between the molecular descriptor ( $\sum d^6$ ) and solubility suggests that this correlation may directly inform molecular design strategies to improve solubility.

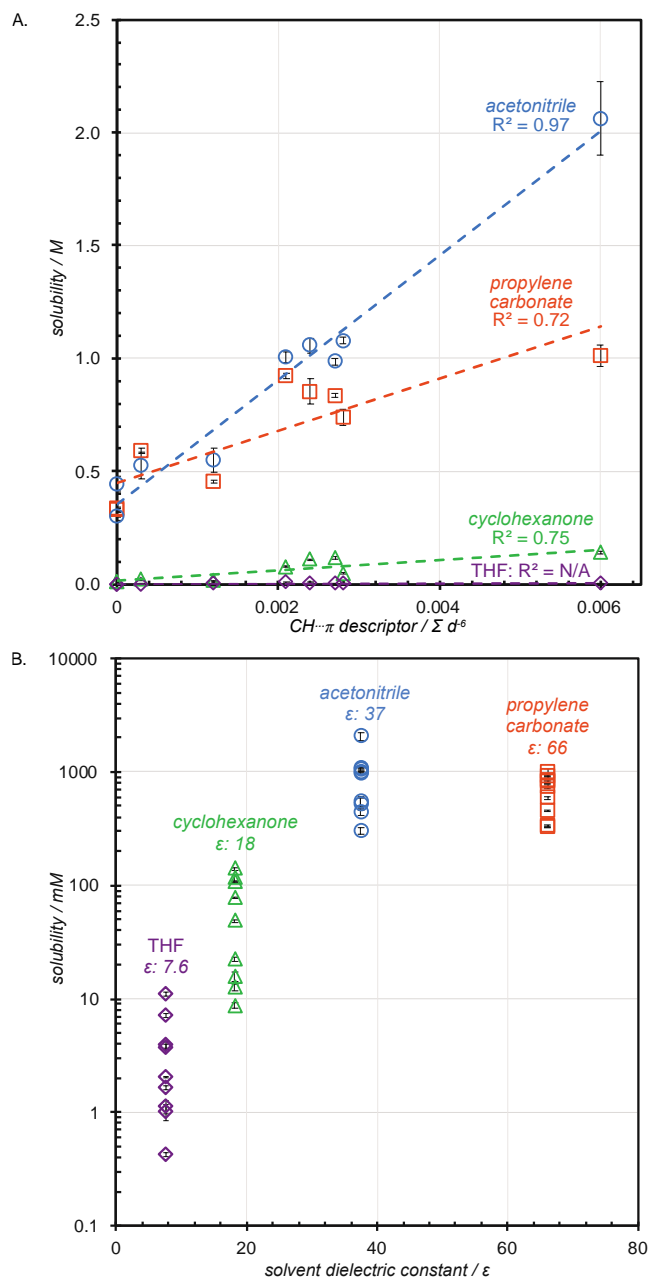


**Figure 2.11. C-H... $\pi$  interactions correlate with pyridinium solubility in several aprotic solvents.** Plots comparing solubilities of nine representative pyridinium derivatives from low (**1**, **2**, **6**, **16**), moderate (**5**, **10**, **12**, **20**) and high (**14**) solubility regimes (in acetonitrile). Solubilities were evaluated in acetonitrile (blue circles), THF (purple diamonds), cyclohexanone (green triangles), and propylene carbonate (orange squares). (A) A plot comparing pyridinium solubility in each solvent to a descriptor of C-H... $\pi$  interactions ( $\Sigma d^6$ ). (B) Semi-log plot of pyridinium solubility in each solvent vs. the dielectric constant of the respective solvent (i.e.,  $\epsilon_{\text{THF}} = 7.6$ ,  $\epsilon_{\text{cyclohexanone}} = 18$ ,  $\epsilon_{\text{acetonitrile}} = 37$ , and  $\epsilon_{\text{PC}} = 66$ ). Solubility measurements were performed at 22 °C. Data are presented as mean solubility +/- SD with  $n = 3$  for all compounds except for compound **17** ( $n = 5$ ), compound **24** ( $n = 5$ ), and compound **14** ( $n = 9$ ).

## 2.4 Conclusions

The primary results of this work provide a direct correlation between solubility and chemical structure, suggesting that C-H $\cdots$  $\pi$  interactions alone can have a dramatic impact on the physical properties of ROMs. A modular synthetic approach enabled the preparation of an electronically and sterically diverse pyridinium library. This molecular class provided a structurally rigid framework to probe structure-solubility trends. While molecular descriptors, traditionally used as indicators of solubility, did not result in any correlation with observed solubility trends, we identified a strong univariate correlation between pyridinium solubility and the number of C-H $\cdots$  $\pi$  interactions observed in the corresponding crystal lattice. Variable concentration  $^1\text{H-NMR}$  experiments indicate that these interactions occur between solvated pyridiniums at concentrations substantially below their solubility limit, thereby suggesting a causal relationship between the propensity of a pyridinium to form C-H $\cdots$  $\pi$  interactions and its solubility in polar aprotic solvents. This work highlights the need to expand such approaches to consider dispersion-based substituent effects to produce molecules with the desired physicochemical characteristics. Finally, several physical properties are correlated through known empirical relationships (e.g., between melting point and solubility).<sup>126</sup> In drawing connections between C-H $\cdots$  $\pi$  interactions and solubility, our findings may provide a bridge linking molecular structure to other consequential physical properties.



### Chapter 3. Low Viscosity, High Concentration Pyridinium Analytes for Organic Non-Aqueous Redox Flow Batteries<sup>2</sup>

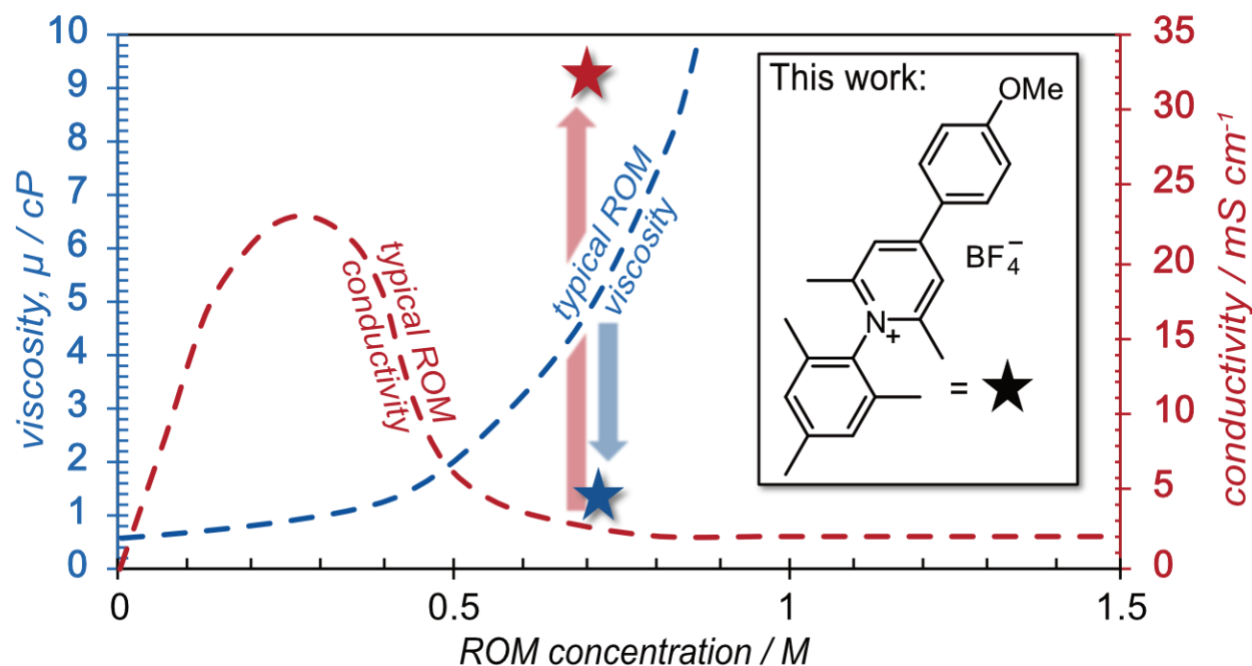


**Figure 3.1. Chapter 3: Graphical Abstract.** The use of ROMs at elevated concentrations in an RFB often causes solution properties – such as viscosity and conductivity – to vary in unpredictable and impactful ways. At elevated concentration, strong electrostatic interactions between ROMs, solvent, and supporting electrolyte often result in high viscosity and low solution conductivity, both of which are deleterious to practical RFB operation. The class of 2,6-dimethylpyridinium ROMs demonstrate low reduction potentials and rapid diffusion coefficients at low concentrations, and we find that representative pyridinium ROMs exhibit low dynamic viscosities ( $\sim 1$  mPa·s), and high conductivities (25.0 - 32.8  $mS\ cm^{-1}$ ) at elevated concentrations in acetonitrile.

<sup>2</sup> This work is published as Samaroo, S.; Pattillo, A. L.; Servinski, D.; Kruper, W. R.; Carter, D. D.; Guarr, T. F.; Hickey, D. P. Low Viscosity, High Concentration Pyridinium Analytes for Organic Nonaqueous Redox Flow Batteries. *ACS Applied Energy Materials*. American Chemical Society 2023. <https://doi.org/10.1021/acsaem.3c02370>.

### 3.1 Introduction

Redox flow batteries (RFBs) are an attractive form of large-scale energy storage that may aid in integrating the growing number of renewable energy resources into the existing electrical grid. RFBs store energy in the form of solvated redox-active molecules by interconverting electrical and chemical energy through electrochemical redox reactions.<sup>38,127–129</sup> One subset of RFBs, non-aqueous redox flow batteries (NRFBs), are particularly attractive because of their wide electrochemical stability window (up to 4 V) and because they enable the utilization of cost-effective and modular redox-active organic molecules (ROMs).<sup>65,130</sup> While many promising ROMs are sparingly soluble in water, they exhibit substantially higher solubility in polar aprotic solvents, such as acetonitrile and propylene carbonate. This improved solubility is important, because NRFB energy storage capacity is directly proportional to ROM concentration. Despite the recent advancements in identifying and developing numerous classes of ROMs that exhibit promising electrochemical stability and low reduction potentials (or high oxidation potentials), many suffer from high dynamic viscosity ( $> 10$  cP) and low conductivity ( $< 5$  mS cm<sup>-1</sup>) at concentrations that would be sufficiently high for practical operation ( $> 0.5$  M).<sup>51,52</sup> In the context of an NRFB, highly viscous ROM solutions limit flow rates and cause pressure drop across the flow field (both of which limit mass transport, and thus limit charge/discharge rates), while poorly conductive solutions result in high overpotentials and low storage efficiency.<sup>53,131</sup> Therefore, there remains a need to identify classes of ROMs demonstrating moderate viscosities and conductivities at elevated concentrations.

A unique correlation was recently reported between intermolecular solute-solute interactions and the maximum solubility for a class of 2,6-dimethyl-4-arylpyridinium ROMs in polar aprotic solvents.<sup>76</sup> Specifically, intermolecular interactions between CH groups and  $\pi$ -electrons of

neighboring pyridinium ROMs were shown to disrupt the formation of stable ionic lattices. As a result, the propensity for a particular pyridinium ROM to participate in CH- $\pi$  interactions is proportional to its solubility in acetonitrile, propylene carbonate, cyclohexanone, and THF.<sup>76</sup> Conventional molecular engineering-centered strategies to improve ROM solubility involve tuning a parent structure to either promote electrostatic solute-solvent interactions (i.e., adding a polyethylene glycol, PEG, chain or a charged functional group)<sup>132,133</sup> or increase solvent-accessible surface area (e.g., by adding a flexible alkyl pendant group).<sup>48,49,134</sup> Both of these strategies can increase the maximum solubility of a parent ROM but require the incorporation of a large molecular substituent. Unfortunately, substantial increases in molecular weight of the ROM solute are often accompanied by increased viscosity at high concentrations. By contrast, promotion of CH- $\pi$  interactions (and, thus, increased solubility) can be accomplished with minimal modification to the parent pyridinium ROM structure (as illustrated in Figure 3.2). Consequently, we considered the possibility that this unique method of enhancing pyridinium ROM solubility may break the conventional solubility/viscosity paradigm, which suggests RFB solutions with sufficiently high concentration of active material will suffer from high viscosity. Herein, we present a study on the impact of ROM concentration on viscosity and conductivity for a series of 4-aryl-2,6-dimethylpyridinium salts in acetonitrile.

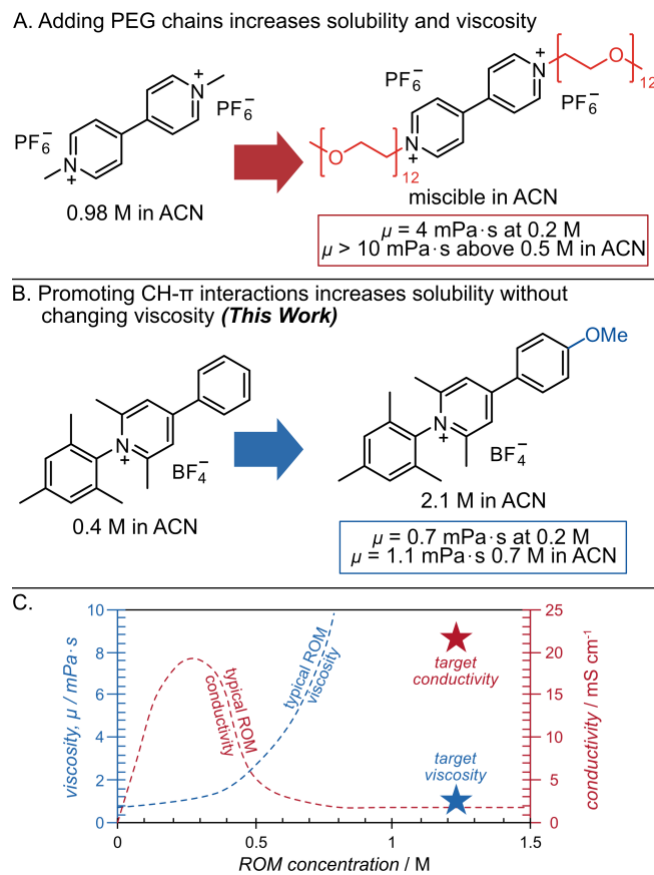


**Figure 3.2 Comparison of strategies used to increase ROM solubilities and the resulting viscosity and conductivity trends.** (A) An example of a conventional strategy (i.e., adding PEG chains) used to increase viologen<sup>12,13</sup> ROM solubility. (B) An alternative approach promoting CH- $\pi$  interactions in pyridinium<sup>76</sup> ROMs (bottom) with their respective viscosities and conductivities at increasing concentrations in acetonitrile. (C) Ideal ROMs have low dynamic viscosity ( $< 10 \text{ mPa}\cdot\text{s}$ ) and high conductivity ( $> 5 \text{ mS cm}^{-1}$ ) at elevated concentrations ( $> 0.5 \text{ M}$ ).<sup>51,52</sup>

Viscosity is a fundamental property of NRFB solutions that is complex and critical for dictating the economic viability of any proposed flow battery. Highly viscous electrolyte solutions require higher energy demand to pump the active NRFB fluid through a porous electrode during charging and discharging. Consequently, solution viscosity is a significant factor for determining performance and operating costs.<sup>67,135</sup> In addition to cost, highly viscous RFB solutions are intrinsically linked to performance limitations, as shown by the Stokes-Einstein equation,

$$D = \frac{k_B T}{\alpha \pi \mu d} \quad (\text{Eq. 3.1})$$

where  $D$  is solute diffusivity,  $k_B$  is the Boltzmann constant,  $T$  is absolute temperature,  $\alpha$  is a coefficient that arises from the boundary conditions of the solute-solvent interface (where  $\alpha$  ranges from 4 for no-slip to 6 for slip conditions),  $\mu$  is the dynamic viscosity, and  $d$  is the molecular diameter.<sup>136</sup> Viscosity of NRFB solutions is inversely proportional to ROM diffusivity as well as solution conductivity, both of which are critical for achieving high power densities.<sup>131,137</sup> Recent works have explored the effect of varying either ROM or supporting electrolyte salt concentrations in non-aqueous systems on the properties, such as ionic conductivity and viscosity, of the corresponding electrolyte solution.<sup>53,55,131,138</sup> While ionic conductivity gradually decreases with increasing concentration for non-ionic ROMs, for ionic ROMs and supporting electrolyte, the relationship between concentration and ionic conductivity is parabolic, increasing at low concentration but decreases after reaching a maximum value.<sup>137</sup> The dependence of viscosity on solute concentration is proportionally similar for both ionic and nonionic solutes; as concentration increases, viscosity increases asymptotically. Therefore, it is desirable to identify molecular design strategies to increase both the concentration of maximum conductivity and the onset of exponential increase in viscosity with concentration.

Identifying structure-property relationships in ROMs is complicated by the often-limited ability to systematically vary steric and electronic influence of a parent ROM's substituents. Recently, we reported a modular synthetic procedure to prepare a diverse library of N-substituted 4-aryl-2,6-dimethylpyridinium derivatives.<sup>76</sup> These ROMs provide a modular, rigid core structure that is ideal for probing structure-property relationships. Furthermore, they are promising anolyte candidates, exhibiting exceptionally low reduction potentials, persistence in the radical state, and high solubility in multiple polar aprotic solvents. Herein, we assess the electrochemical

characteristics of this uniquely modular class of pyridinium ROMs and evaluate the viscosity and ionic conductivity as a function of concentration for a representative selection of molecules. Diffusion coefficients are measured by cyclic voltammetry for each pyridinium derivative in acetonitrile to provide insight into solute-solvent interactions. Additionally, solution viscosities and conductivities of a representative selection of pyridiniums in acetonitrile are measured at variable concentrations to determine the impact of CH- $\pi$  interactions on these critical physicochemical properties as ROMs approach their solubility limits in acetonitrile.

## **3.2 Methods**

### **3.2.1 Materials**

All synthetic starting materials, including 2,6-dimethyl- $\gamma$ -pyrone (Ambeed), Grignard reagents (Alfa Aesar or Sigma-Aldrich), and all amines (various sources) were of the highest purity available and used as received. Arylmagnesium bromides were purchased as 1 M solutions in THF from Sigma-Aldrich or Thermo Scientific. Anhydrous tetrabutylammonium hexafluorophosphate (99.8%) was purchased from MilliporeSigma. The acetonitrile used during electrochemical evaluation was purchased from Acros Organics (99.9%, Extra Dry over Molecular Sieve, AcroSeal) and the acetonitrile used to make conductivity and viscosity solutions was purchased from Oakwood Chemical (HPLC grade).

### **3.2.2 General Synthesis of 2,6-Dimethylpyridiniums**

All pyrylium intermediates were synthesized following a modified procedure reported by DiMauro and Kozlowski and all pyridiniums were synthesized using procedure previously reported by the Hickey lab.<sup>76,139,140</sup> A complete analytical summary for all compounds used for electrochemical testing is available in the Supplementary Information of Hickey lab paper.<sup>76</sup> Method for synthesis and analysis for compounds used in viscosity and conductivity

determinations are described. The pyridinium compounds synthesized were analyzed by UPLC (Ultra Performance Liquid Chromatography) for purity.

### **3.2.2.1 Synthesis of 2,6-Dimethylpyrylium Intermediate**

In an oven-dried 250 mL round bottom flask, 2,6-dimethyl- $\gamma$ -pyrone (27 – 34 mmol) was dissolved in THF (120 – 140 mL) under nitrogen and cooled to 5 °C in an ice bath. One equivalent of aryl magnesium bromide (in a 1 M solution with THF) was added dropwise to the stirring solution. After the addition, the reaction mixture warmed to room temperature over an hour. Boron trifluoride diethyl etherate solution was added to the stirring reaction mixture, yielding a precipitate that was isolated by filtration and washed with diethyl ether. The intermediate pyrylium product was purified by recrystallization in a 1:1 water/methanol mixture (yields ranged from 40% to 48%).

### **3.2.2.2 Synthesis of 2,6-Dimethylpyridinium**

The desired pyridinium derivatives were generated by reacting the respective pyrylium intermediate with a primary amine. In a 50 mL round bottom flask equipped with a magnetic stir bar and condenser, 4-substituted 2,6-dimethyl-pyrylium tetrafluoroborate (9 – 18 mmol) was suspended in ethanol. Approximately 1.2 equivalents of the corresponding primary amine were added, and the mixture was refluxed for 4 hours under flowing nitrogen. The solution was cooled to room temperature overnight and diluted with diethyl ether. The precipitate was isolated by filtration and dried under vacuum to afford a solid product (yields ranged from 45% to 68%).

### **3.2.2.3 UPLC Method Details**

UPLC analysis was completed using a Waters Acquity UPLC© (H Class Plus) using a photodiode array (PDA) detector. The method used a gradient of two phases: phase A (Aqueous pH 4.5 buffer sodium acetate per acetic acid buffer at 10 mM capacity, ammonium acetate as ion

pairing agent at 9mM, yellow) and phase B (Acetonitrile, blue). The method was applied with an injection volume 3  $\mu\text{L}$  and a flow rate of  $0.5 \text{ mL min}^{-1}$  using a Waters Acquity UPLC<sup>®</sup> Column (BEH C18 1.7  $\mu\text{m}$  2.1x50 mm).

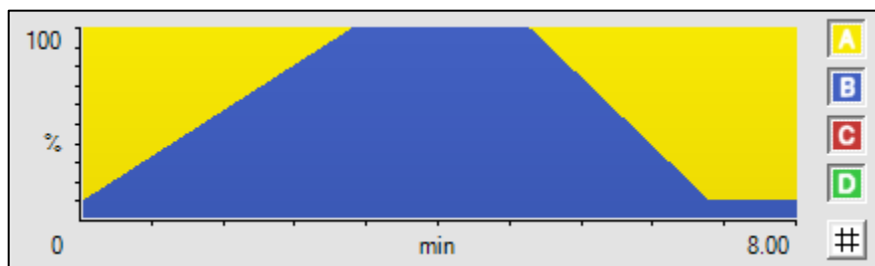


**Figure 3.3. UPLC method visualization of phase distribution vs. elution time.**

### 3.2.3 Cyclic Voltammetry

Cyclic voltammograms (CVs) of all pyridinium derivatives were measured in a nitrogen atmosphere glovebox using a Metrohm MultiAutolab M204 Potentiostat. Solutions used for electrochemical experiments contained 1 mM pyridinium, 1 mM ferrocene as an internal reference, and 100 mM tetrabutylammonium hexafluorophosphate in acetonitrile (99%, Extra Dry) as the supporting electrolyte. Experiments were performed using 3 mm glassy carbon working electrode and a non-aqueous  $\text{Ag}/\text{Ag}^+$  reference electrode (10 mM  $\text{AgNO}_3$  in acetonitrile) at  $22^\circ\text{C}$ . Please note that  $iR$  compensation was not used for any CV measurements.

For reversibility assessments, CVs were collected at a scan rate of  $200 \text{ mV s}^{-1}$ . The anodic peak current ( $i_{pa}$ ) was divided by the cathodic peak current ( $i_{pc}$ ) to yield the peak height ratio, and the potentials at peak anodic current ( $E_{ipa}$ ) and cathodic current ( $E_{ipc}$ ) were used to measure peak-to-peak separations.

For determination of diffusion coefficients, CVs were performed at scan rates of 20, 50, 100, 200, 400, 800, 1200, and  $1600 \text{ mV s}^{-1}$ . Peak currents (anodic and cathodic,  $i_{pa}$  and  $i_{pc}$  respectively) were plotted vs the square root of the corresponding scan rate ( $\text{mV s}^{-1}$ ) to give a linear trend



consistent with the Randles-Sevcik equation to determine diffusion coefficients of each derivative. A detailed description of diffusion coefficient calculation can be found in the Appendix B.<sup>33</sup>

### 3.2.3.1 Reversibility Determination: Peak Height Ratio & Peak-to-Peak Separation

Cyclic voltammograms (CVs) of all pyridinium derivatives were measured in acetonitrile with ferrocene as an internal redox standard, and all redox couples were found to be completely reversible. CVs were collected at a scan rate of 200 mV s<sup>-1</sup>. The anodic peak current ( $i_{pa}$ ) was divided by the cathodic peak current ( $i_{pc}$ ) to yield the peak height ratio. The difference in corresponding potential for anodic peak current ( $i_{pa}$ ) and cathodic peak current ( $i_{pc}$ ) gave the peak-to-peak separation value (V).

### 3.2.3.2 Diffusion Coefficient Calculation from Pyridinium Crystal Structures

Diffusion coefficients were estimated for the oxidized form of pyridinium ROMs from the Stokes-Einstein equation ((Eq. 3.1).<sup>141,76</sup> The diameter of pyridinium species was calculated as the average of the maximum diameter along the N-to-C4 axis of the pyridinium ring and the maximum diameter perpendicular to this axis. This was done to account for the non-spherical shape of pyridinium ROMs.

### 3.2.3.3 Electrochemical Diffusion Coefficient Determination, from CV

Cyclic voltammograms (CVs) of all pyridinium derivatives were measured in acetonitrile with ferrocene as an internal redox standard, and all redox couples were found to be completely reversible. CVs were collected at scan rates of 20, 50, 100, 200, 400, 800, 1200, and 1600 mV s<sup>-1</sup>. The peak currents (anodic and cathodic,  $i_{pa}$  and  $i_{pc}$  respectively) were related to square root of the corresponding scan rate (mV s<sup>-1</sup>) using the Randles-Sevcik equation:

$$i_p = 0.4463 A C^0 \left( \frac{n^3 F^3 v D_0}{RT} \right)^{1/2} \quad \text{(Eq. 3.2)}$$

where  $i_p$  is the peak current,  $A$  is the surface area of the electrode ( $0.071 \text{ cm}^2$ ),  $C^0$  is the bulk concentration of pyridinium ( $1 \times 10^{-6} \text{ mol cm}^{-3}$ ),  $n$  is the number of electrons transferred (1 electron),  $F$  is Faraday's constant ( $96485 \text{ C mol}^{-1}$ ),  $R$  is the ideal gas constant ( $8.314 \text{ J mol}^{-1}\text{K}^{-1}$ ), and  $T$  is the absolute temperature ( $295 \text{ K}$ ). Experiments were performed using 3 mm GCE working electrode and Ag/Ag<sup>+</sup> reference electrode with 100 mM tetrabutylammonium hexafluorophosphate in acetonitrile as the supporting electrolyte at 22 °C and 200 mV s<sup>-1</sup> under a N<sub>2</sub> atmosphere. Using a rearrangement, based on the linear relationship of peak height vs. square root of the scan rate ( $i_{pa}$  and  $i_{pc}$  (A) vs.  $v^{1/2}$  (V s<sup>-1</sup>)<sup>1/2</sup>), the diffusion coefficient ( $D_0$ , cm<sup>2</sup> s<sup>-1</sup>) can be determined using the theoretical value of the slope.<sup>142</sup>  $D_R$  is the diffusion coefficient based on the anodic (i.e., the reduced pyridinium) component of the CV scan, and  $D_O$  is the diffusion coefficient based on the cathodic (i.e., oxidized pyridinium) component of the CV scan.

$$D_0 = \left( \frac{\text{slope}}{0.4463nFAC^0} \right)^2 \frac{RT}{nF} \quad \text{(Eq. 3.3)}$$

### 3.2.3.4 Correlation Between Redox Potential and Hammett Parameters

Hammett substituent constants were taken directly from literature sources,<sup>143</sup> when available, or were calculated using open-source substituent property prediction software.<sup>144</sup> The sum of sigma-para substituent constants for the 4-aryl and N-substituents of the 2,6-dimethylpyridinium ring correlate strongly ( $R^2 = 0.9$ ) to the experimental reversible redox potential of the corresponding pyridinium ROM.

### 3.2.4 Charged Solution Shelf Stability

Cyclic voltammograms were used to assess decomposition in reduced pyridinium solutions in propylene carbonate. Solutions of 10 mM pyridinium and 500 mM tetraethylammonium tetrafluoroborate in propylene carbonate were prepared in a 25 mL volumetric flask. Prior to charging, pyridinium solutions were dried for 12 hours over 3 Å molecular sieves and purged with

N<sub>2</sub> for 30-40 minutes. All subsequent electrochemical charging and measurements were conducted in a glovebox under a N<sub>2</sub> atmosphere.

In a symmetrical H-Cell, solutions were charged (reduced) first at a constant current of 5 mA to a -1.65 V potential cutoff, then further charged (reduced) at a constant current of 2.5 mA to a -1.65 V potential cutoff. Each half of the H-Cell contained 10 mL of pyridinium solution. The working and counter electrodes were composed of carbon felt Sigracet 6EA attached to steel wire using wire glue. Solution charging was conducted with a 3-electrode arrangement using a Ag/Ag<sup>+</sup> reference electrode. After charging, the reduced pyridinium solution was promptly removed from the H-Cell and isolated in a vial.

The isolated charged solutions were evaluated daily by CV and visual inspection of color. Daily CVs were performed using 3 mm GCE working electrode, platinum plated titanium rod counter electrode, and a Ag/Ag<sup>+</sup> reference electrode at 25 °C under a N<sub>2</sub> atmosphere. CVs were collected at 100 mV/s between 0 to -1.65 V every day to assess change in concentration or loss of material. Additionally, CVs were measured at 100 mV/s between 1.1 to -1.65 V at the first and last day of the shelf stability study to assess changes in concentration, loss of material, and formation of decomposition products.

### 3.2.5 Viscosity

Kinematic viscosities for solutions of compounds **3**, **5**, and **17** were evaluated at variable concentrations in pure acetonitrile using a calibrated Ubbelohde viscometer (Cannon, Size 0). Concentration ranges were selected based on the maximum solubility in acetonitrile; 0.96, 0.48, 0.24, 0.12, and 0.06 mM for **1**, 0.29, 0.15, 0.07, 0.04, and 0.02 mM for **3**; 0.32, 0.16, 0.08, 0.04, and 0.02 mM for **5**; 0.68, 0.34, 0.17, 0.09, and 0.04 mM for **17**. Solutions were made by saturating acetonitrile (HPLC grade) with each compound at ambient temperatures in a graduated cylinder,

then adding 3-5 mL of pure acetonitrile (to avoid precipitation in the highest concentration solutions occurring with slight temperature fluctuations). The initial solution was diluted by half with pure acetonitrile, and subsequent serial dilutions were prepared for a total of five concentrations for viscosity measurements. The viscosity of pure deionized water and pure acetonitrile were measured in the same viscometer to confirm calibration ranges and establish viscosities at ambient temperature. Ambient temperature was recorded at the start of each measurement ( $19.3\text{ }^{\circ}\text{C} \pm 0.4\text{ }^{\circ}\text{C}$ ). Reported values include the average of five consecutive measurements and their standard deviations.

The density of each solution was measured to calculate dynamic viscosity from the corresponding kinematic viscosity. Densities were measured by weighing 100  $\mu\text{L}$  of each solution at ambient temperature. Dynamic viscosities were calculated by multiplying the measured kinematic viscosity by the corresponding density for each solution.

### 3.2.6 Viscosity Interpretation (Jones-Dole Equation)

Concentration-dependent viscosities for salt solutions in the high concentration regime have previously been described using the extended Jones-Dole equation:

$$\frac{\eta(c)}{\eta_s} = 1 + A\sqrt{c} + Bc + Dc^2 \quad \text{(Eq. 3.4)}$$

where  $\eta(c)$  and  $\eta_s$  are the viscosities of the pyridinium/acetonitrile solution and pure acetonitrile solvent, respectively.<sup>145</sup> The empirical coefficients A, B, and C have been interpreted – using a variety of theoretical treatments – as molecular descriptors of ion- ion or ion-solvent interactions. The  $Ac^{1/2}$  term can be interpreted using Falkenhagen Theory to describe direct ion-ion (Coulombic) interactions, the  $Bc$  term has been used to describe solvent-mediated ion-ion interactions (i.e., ions are “structure makers” if  $B > 0$  and “structure breakers” if  $B < 0$ ), and  $Dc^2$  has been used to describe long range Coulombic interactions between ions. Concentration-dependent viscosity

measurements for compounds **1**, **3**, **5**, and **17** were fitted using the extended Jones-Dole equation above. Based on the structure maker/breaker interpretation of the B-coefficient, data for all compounds was fit with positive B-coefficients and would be considered structure makers. This description is also appropriate if the data is fit to a modified Jones-Dole equation that does not include the A-coefficient term (which has a small influence on the expression in the high concentration regime).<sup>145146147</sup>

### 3.2.7 Conductivity

Solution conductivities of compounds **1**, **3**, **5**, and **17** were evaluated at variable concentrations in acetonitrile using an Orion Star A212 Conductivity Meter (ThermoScientific). Solutions of each representative pyridinium were prepared as described above for viscosity measurements. The conductivity of pure deionized water and pure acetonitrile (HPLC grade) were measured to establish conductivities at ambient temperature. Ambient temperature was recorded at the start of each measurement ( $17.6\text{ }^{\circ}\text{C} \pm 0.5\text{ }^{\circ}\text{C}$ ). Reported values include the average of three consecutive measurements and their standard deviations.

## 3.3 Results and Discussion

For this study, we prepared a library of 23 structural derivatives of N-substituted 4-aryl-2,6-dimethylpyridinium tetrafluoroborate salts using a modular synthetic approach as described previously. Pyridiniums were derivatized by either varying the N-substituent or modifying the 4-aryl ring, and the library was selected to contain sufficient steric and electronic variation at both positions to elucidate broader structure-property relationships for this class of pyridinium ROMs. Variation of the 4-aryl ring was limited to either all hydrogen (i.e., the parent unmodified phenyl ring) (**1**, **3**, **4**, **5**, **7**, **18**), 4-methyl (**2**, **8**, **9**, **10**, **11**, **13**, **15**, **21**, **22**), 2,4-dimethyl (**12**, **19**, **20**), or 4-methoxy (**6**, **14**, **16**, **17**, **23**) substituents; however, variation of the N-substituent represents a wider

range of functionality, including flexible butyl or oligoether chains, and sterically hindering aryl rings with either electron donating or withdrawing substituents. The breadth of substituent variations spanning across all 23 compounds is particularly valuable in revealing the less predictable, combined effects of electron density and sterics in the 4-position and N-position.

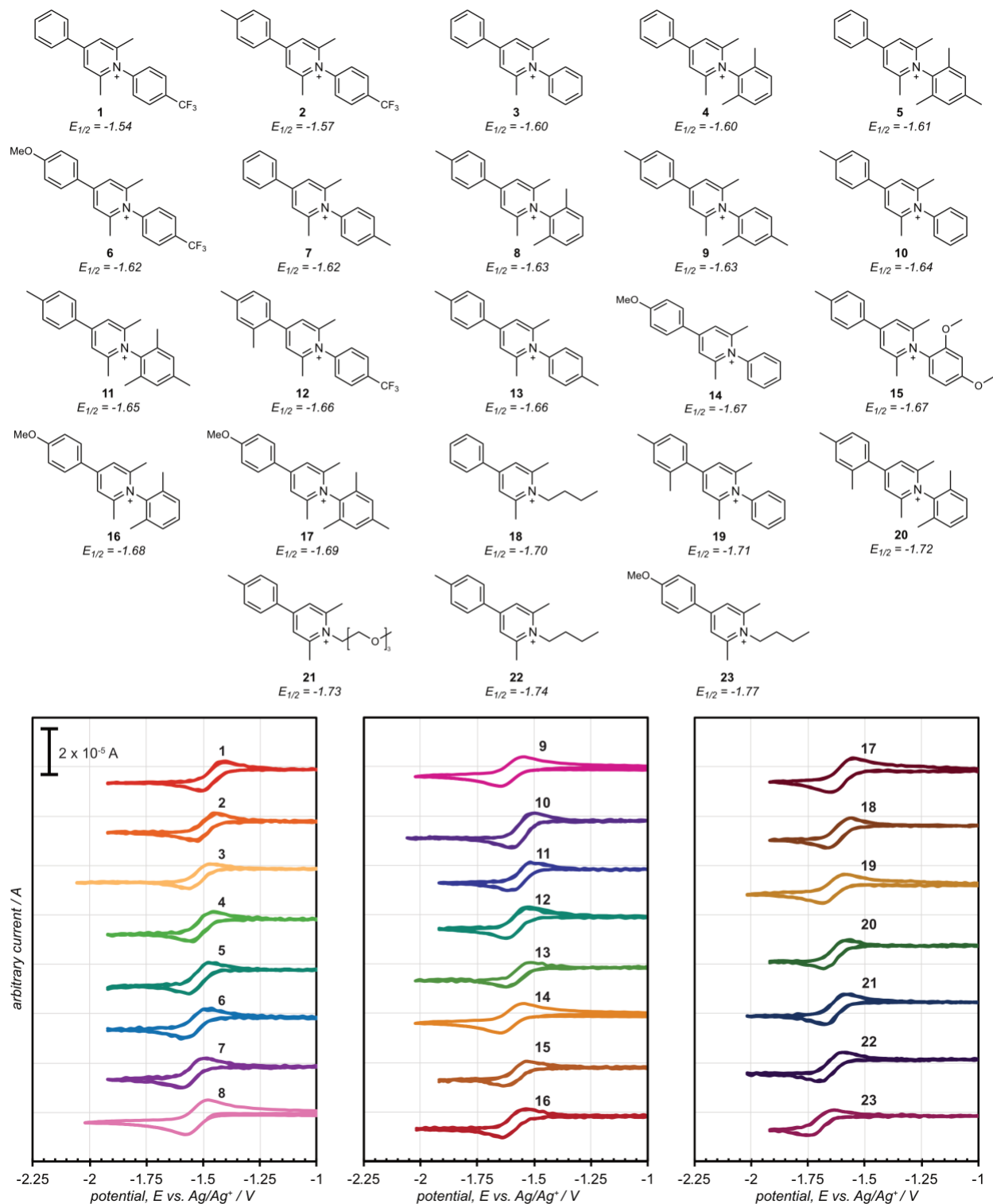


**Figure 3.4 Summary of molecular structures and representative cyclic voltammograms.** (Top) Structure and corresponding reversible redox potential (V vs.  $\text{Fc}/\text{Fc}^+$ ) for all 23 pyridinium ROMs studied. (Bottom) Representative cyclic voltammograms (CVs) for each pyridinium ROM (1 mM active species) in acetonitrile. Experiments were performed using 3 mm GCE working

**Figure 3.4.** (cont'd)

electrode and Ag/Ag<sup>+</sup> reference electrode with 100 mM tetrabutylammonium hexafluorophosphate in acetonitrile as the supporting electrolyte at 22 °C and 200 mV s<sup>-1</sup> under N<sub>2</sub> atmosphere.

**3.3.1 Electrochemistry**

To initiate our investigation, we first measured standard electrochemical properties of each pyridinium using cyclic voltammetry (CV) as shown in Figure 3.4. Redox potentials of the series of 23 compounds evaluated spans from -1.54 to -1.77 V vs. ferrocene, and CVs reveal that every derivative exhibit good electrochemical reversibility (*i.e.*, peak current ratio = 1 and peak-to-peak separation less than ~100 mV). It should be noted that compounds are numbered by decreasing redox potential, thus compound **1** has the most positive reduction potential and compound **23** has the most negative reduction potential. For anolyte ROMs, such as pyridiniums, more negative reduction potentials are desirable because both energy and power densities are dependent on the difference in catholyte oxidation potential and anolyte reduction potential. It is commonly understood that the electronic nature of substituents on a parent ROM influences the corresponding reduction potential.<sup>38,56,57</sup> Electron withdrawing groups pull electron density away from the core structure, making reduction easier (thus resulting in more positive redox potentials), while electron donating groups have the opposite effect, making reduction more difficult (thus resulting in lower redox potentials).

The influence of substituent electronics on redox potential can be observed across the library of pyridiniums. We can see these effects of certain substituents demonstrated across this library of molecules. Compounds **1** and **2** contain electron-withdrawing trifluoromethylphenyl N-substituents and exhibit the most positive redox potentials, while **22** and **23** contain electron-donating aliphatic chains as N-substituents and exhibit the most negative redox potentials in the library. Pyridinium redox potentials generally follow a Hammett relationship, in which redox potential is directly proportional to the sum of Hammett substituent constants ( $\sigma_p$ ) for groups on



the N- and 4-position of the parent 2,6-dimethylpyridinium ring.<sup>146</sup> This trend is illustrated in Figure 3.5; however, there are three notable (**12**, **19**, **20**) outliers that all contain 2,4-dimethylphenyl groups as the 4-substituent. The presence of a 2-methyl group on the 4-aryl substituent introduces enough steric hindrance to cause the 4-aryl ring to deviate from the pyridinium plane, thereby disrupting the overlap between the p-orbitals of the two rings. This disruption alters the inductive influence of the 4-aryl ring on the redox-active pyridinium ring and may account for the deviation from pure Hammett behavior. Taken together, these trends provide insights towards which functional groups may produce desirable properties in future iterations of pyridinium molecules. In addition to redox potentials, CV data was used to extract diffusivities for pyridinium ROMs in our library.

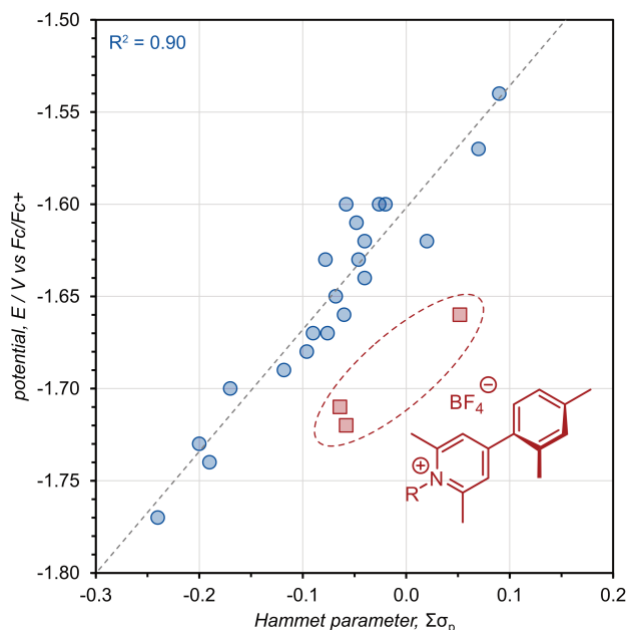


**Figure 3.5. Redox potential of pyridinium ROMs follows a Hammett relationship.** Reversible redox potential for all 23 pyridinium ROMs vs. the sum of Hammett  $\sigma_p$  parameters for the 4- and N-substituents.<sup>146</sup> Pyridiniums with 4-phenyl, 4-(*p*-methoxyphenyl), and 4-(*p*-methylphenyl) substituents (blue circles) correlate strongly to the sum of Hammett parameters, whereas pyridiniums with 4-(2,4-dimethylphenyl) (red squares) are notable outliers.

Diffusion coefficients (or diffusivities) are commonly measured as an initial assessment of electrode kinetics and provide critical information about how ROMs behave in solution. The

diffusion coefficients for the oxidized and reduced forms of all 23 compounds were determined by collecting cyclic voltammograms (CVs) at variable scan rates and applying the Randles-Sevcik relationship.<sup>33</sup> For the pyridiniums studied, most exhibited diffusion coefficients that range from  $3 \times 10^{-6} \text{ cm}^2 \text{ s}^{-1}$  and  $9 \times 10^{-6} \text{ cm}^2 \text{ s}^{-1}$ ; however, the most rapid diffusion coefficients of  $D = 1.9 \times 10^{-5} \text{ cm}^2 \text{ s}^{-1}$  and  $D = 1.4 \times 10^{-5} \text{ cm}^2 \text{ s}^{-1}$  for the oxidized forms of **3** and **10** respectively, were approximately twice as fast. For dilute solutions in which solution viscosity is the same for all pyridiniums, the Stokes-Einstein (SE) equation ((Eq. 3.1) suggests that diffusivity should change linearly with the Stokes radius. A plot of diffusion coefficients measured by CV for all 23 pyridiniums versus the diffusion coefficient calculated from the SE equation (using the molecular radii extracted from previously published crystal structures of each pyridinium, details provided in the Appendix B) is shown in Figure 3.6. The SE equation generally provides an accurate estimate of the measured diffusion coefficient based on the crystal lattice-derived molecular radius (where small deviations are within experimental error); however, it significantly underpredicts the diffusivities of **3** and **10** which are significantly faster despite having a similar molecular radius to the other measured pyridiniums.

One possible explanation for this faster than expected diffusivity may be related to the interaction between **3** or **10** with the surrounding solvent. The  $\alpha$  term in the SE equation describes the friction between the solute and surrounding solvent, where  $\alpha = 6$  is used for no-slip conditions (i.e., strong solvent-solute friction) and  $\alpha = 4$  is used for slip conditions (i.e., weak or no solvent-solute friction).<sup>147</sup> For most dilute electrolyte solutions, no-slip conditions ( $\alpha = 6$ ) provide an accurate estimate of diffusivity. If we assume that **3** and **10** interact more weakly with the solvent (i.e., allow  $\alpha = 4$ ), then their predicted diffusivities are more closely aligned with the measured values. While this interpretation is highly speculative and requires further experimental

investigation, the observation suggests that this class of pyridiniums exhibits physicochemical behavior which deviates from that predicted using simple molecular descriptors (e.g., Stokes radius).

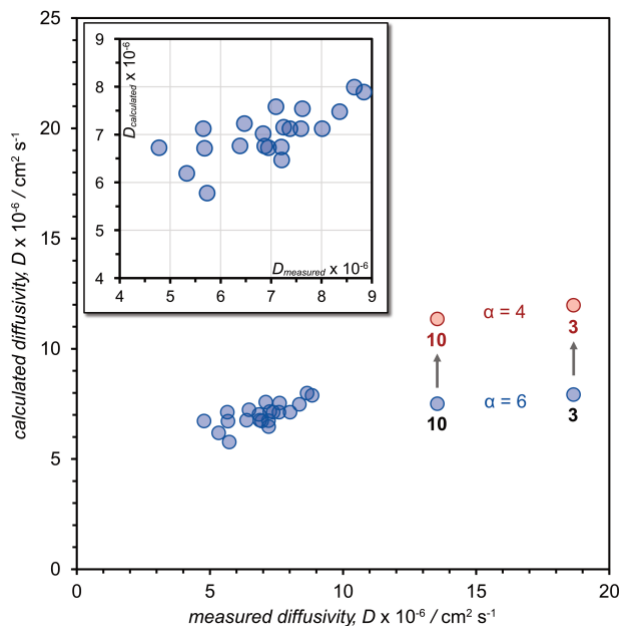


**Figure 3.6. Diffusion coefficients measured by CV vs calculated from Stoke-Einstein for pyridiniums in acetonitrile.** Calculated diffusion coefficients were determined from the Stokes-Einstein equation<sup>147</sup> based on the crystal structure-derived radius and using either the coefficient,  $\alpha = 6$  (blue circles) assuming the no-slip condition, or  $\alpha = 4$  (red circles) assuming slip conditions. Measured diffusion coefficients were determined from CVs at variable scan rates and applying the Randles-Sevcik relationship.<sup>33</sup> Experiments were performed using 3 mm GCE working electrode and Ag/Ag<sup>+</sup> reference electrode with 1 mM pyridinium and 100 mM tetrabutylammonium hexafluorophosphate in acetonitrile as the supporting electrolyte at 22 °C under a N<sub>2</sub> atmosphere.

### 3.3.2 Charged Solution Shelf Stability

Although derivatives of pyridiniums in previous works have shown improvements in charge-discharge cycling as a result of strategic molecular design choices, the current library of derivatives may demonstrate changes in electrochemical stability. To perform a preliminary study on the storage stability of the charged solution, independent of other system components (i.e., electrode material, flowing conditions, tubing, etc.), four selected pyridiniums were reduced in propylene carbonate and monitored by CV for degradation. As shown in Figure 3.7, for all derivatives, the

starting solutions (before reduction by bulk electrolysis) by CV show a single reversible peak around -1.2 V vs. Ag/Ag<sup>+</sup>; all CVs on day 9 show the same reversible peak as well as the development of new, irreversible peaks between 0.6 V to 0.8 V vs. Ag/Ag<sup>+</sup>. Evidence of charge loss by change in current response in daily CVs are shown in Appendix B from Figure B.1 to Figure B.5. These results suggest that the charged pyridinium species may be reacting to form the decomposition products that are reflected by the irreversible electrochemistry. The electrochemical storage stability is a result of numerous solution variables such as supporting electrolyte, solvent, charging process, electrode materials, and impurities; future assessment will expand on the testing conditions to determine if the degradation occurring in these experiments can be mitigated.

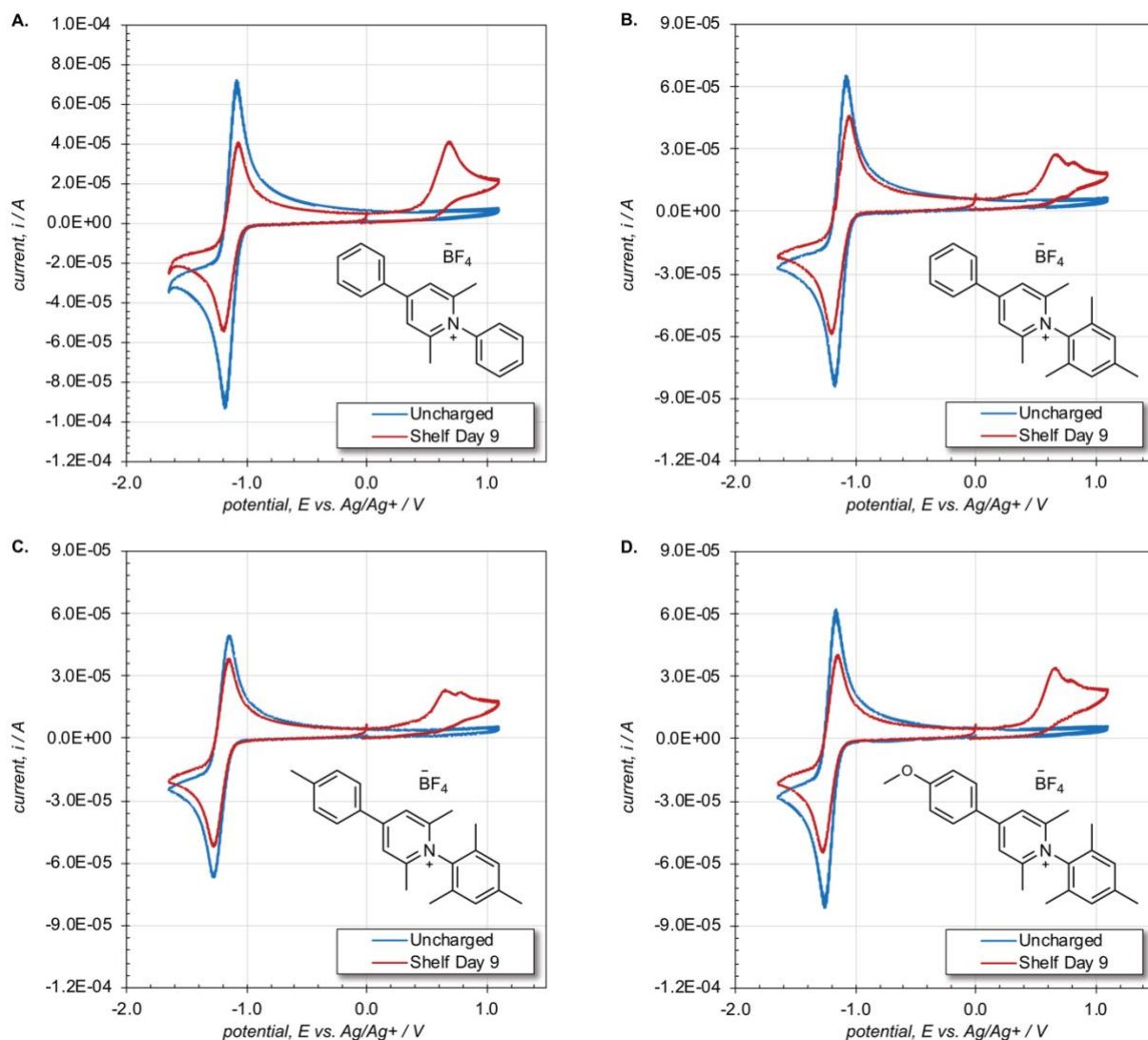


**Figure 3.7 Shelf storage stability studies in propylene carbonate.** Selected pyridiniums were charged by bulk electrolysis and electrochemical degradation was monitored daily for 9 days by cyclic voltammogram. Solutions contained 10 mM pyridinium and 500 mM tetraethylammonium tetrafluoroborate in propylene carbonate. Daily CVs were performed using 3 mm GCE working electrode, platinum plated titanium rod counter electrode, and a  $\text{Ag}/\text{Ag}^+$  reference electrode at 25 °C under a  $\text{N}_2$  atmosphere.

### 3.3.3 Viscosity

Pyridinium-based ionic liquids have been of previous interest for a variety of industrial applications, and some studies have explored how viscosity is influenced by varied substitution, aliphatic chain length, and counterions for simple pyridinium ionic liquids.<sup>148–150</sup> Changes in viscosity from these studies has been rationalized by effects of hydrogen bonding and Van der

Waals interactions; however, efforts to predict these behaviors is limited. Furthermore, many structure-viscosity correlations suggest that the incorporation of flexible aliphatic chains or oligoether chains (often used to improve ROM solubility) strongly correlates to substantially increased viscosity at concentrations approaching or exceeding 1 M in polar aprotic solvents.<sup>151</sup> Our recent work demonstrated the ability to achieve high ROM solubility without long, flexible substituents by exploiting intermolecular CH- $\pi$  interactions. Based on this, we hypothesized that pyridiniums known to exhibit CH- $\pi$  associations may not suffer from similar increases in viscosity at high concentrations.

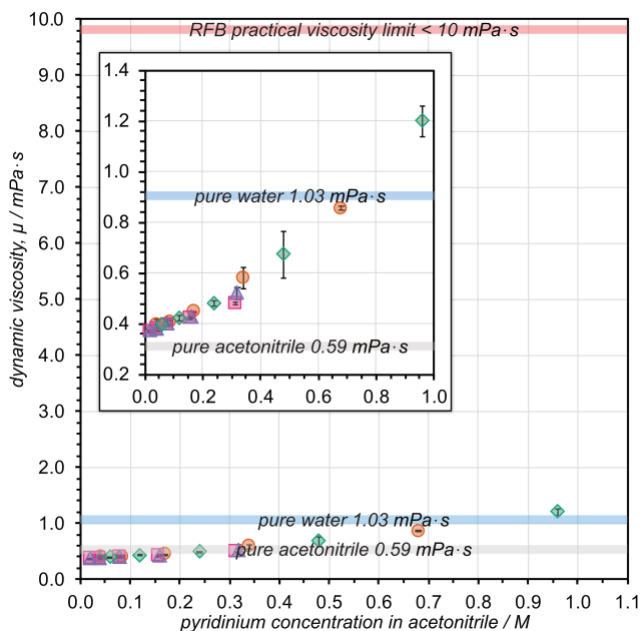


**Figure 3.8. Concentration dependent dynamic viscosities in acetonitrile.** Compound **1** (green diamonds), compound **3** (purple triangles), **5** (pink squares), and **17** (orange circles) pyridiniums. Reported viscosity values represent the average of  $n = 5$  replicates, and the error bars represent the respective standard deviations at  $(19.3 \text{ }^\circ\text{C} \pm 0.4 \text{ }^\circ\text{C})$ .

To test this hypothesis, we selected three pyridiniums previously determined to participate in varying amounts of CH- $\pi$  bonding and evaluated their kinetic viscosity at variable concentrations in acetonitrile. Compounds **1**, **3**, **5**, and **17** were selected for their incremental structural variation with 4- and N-substituents as 4-phenyl/N-phenyl, 4-phenyl/N-mesityl, or 4-*p*-methoxyphenyl/N-

mesityl, respectively. Additionally, **1**, **3**, **5**, and **17** were previously shown to exhibit either limited (**3**, **5**), moderate (**1**) or extensive (**17**) CH- $\pi$  solute-solute interactions.

A plot of dynamic viscosity vs pyridinium concentration is shown in Figure 3.8 and reveals a positive linear relationship between viscosity and concentration as each pyridinium nears their respective solubility limits in acetonitrile. This general trend is consistent with previously reported ROMs in polar aprotic solvents; however, the magnitude of their dynamic viscosities was found to be exceptionally low. The resulting dynamic viscosities for all three derivatives nearing their maximum solubility (in acetonitrile at  $19.3 \text{ }^\circ\text{C} \pm 0.4 \text{ }^\circ\text{C}$ ) were measured as  $1.19 \pm 0.05 \text{ mPa}\cdot\text{s}$  (at 1.0 M for **1**),  $0.521 \pm 0.016 \text{ mPa}\cdot\text{s}$  (at 0.3 M for **3**),  $0.482 \pm 0.003 \text{ mPa}\cdot\text{s}$  (at 0.3 M for **5**), and  $0.856 \pm 0.006 \text{ mPa}\cdot\text{s}$  (at 0.7 M for **17**). For comparison, many NRFB ROM solutions suffer from dynamic viscosities exceeding  $10 \text{ mPa}\cdot\text{s}$  at 0.5 M in comparable solvents.<sup>47,152</sup> Additionally, the dynamic viscosities of pyridinium solutions were all measured to be near or lower than that of pure water, which was measured to be  $1.00 \text{ mPa}\cdot\text{s}$  with the same experimental procedure and conditions. While there was no observed correlation between viscosity and CH- $\pi$  interactions for the set of compounds (and experimental conditions) tested, the low viscosities in acetonitrile highlight the promise of this class of pyridinium ROMs for NRFB applications.

### 3.3.4 Viscosity Interpretation (Jones-Dole Equation)

The concentration-dependent viscosity measurements for compounds **1**, **3**, **5**, and **17** were fitted using the extended Jones-Dole equation and results are summarized in Figure 3.9. It should be noted that the physical interpretation of the A-coefficient is based on the assumption that an ion has a higher probability of interacting with an ion of opposite charge rather than on of the same charge in solution.<sup>153</sup> While this is generally a reasonable assumption, several of the pyridinium ROMs studied here are known to form transient self-complimentary complexes in solution caused by

attractive CH- $\pi$  dispersion interactions (in both the concentrated regime and approaching the dilute regime). This type of cation-cation association has been experimentally observed and is in direct contradiction with the premise described by Falkenhagen in 1931. This may account for the negative values of the A-coefficient measured for compounds **1** and **17**, as shown in Figure 3.9, a value that should be exclusively positive according to theory and extensive experimental studies. Furthermore, there has been a significant amount of recent skepticism regarding the ability of the B-coefficient to act as a unique and reliable molecular descriptor for small sample sizes of electrolytes.<sup>154</sup> Any interpretation of these coefficients should be done with caution as the solute interactions associated with the designation of “structure-maker” have not been independently established for these compounds at high concentrations.



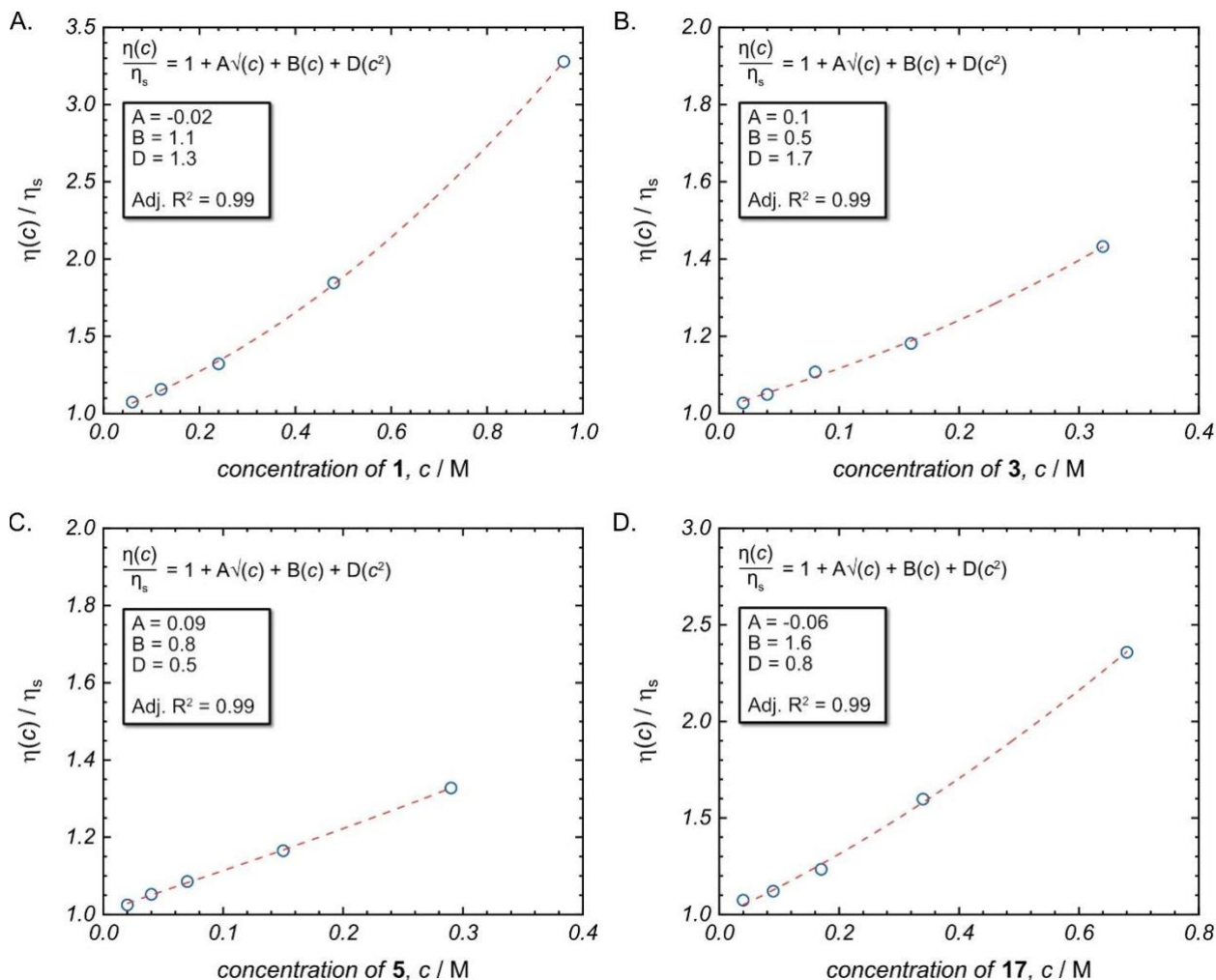


**Figure 3.9. Concentration-dependent viscosities of (A) 1, (B) 3, (C) 5, and (D) 17 fitted to the extended Jones-Dole equation in acetonitrile at  $19.3 \text{ }^\circ\text{C} \pm 0.4 \text{ }^\circ\text{C}$ . Fitted coefficients ( $A$ ,  $B$ , and  $D$ ) are presented in the inset of each plot. Mean viscosities are reported for each concentration with  $n = 5$ .**

### 3.3.5 Conductivities

Another critical property for NRGB ROMs, ionic conductivity, is inversely impacted by increasing viscosity; so that with incremental increases in viscosity in acetonitrile, one would expect reduced diffusivities and subsequently diminishing conductivities (consistent with the Stokes-Einstein equation and the Nernst-Stokes relationship).<sup>67,131,137</sup> At low concentrations of ionic ROMs in pure acetonitrile, increased viscosity is generally negligible and conductivity increases; however, as ROM concentrations generally approach  $\sim 0.4 \text{ M}$ , increasing viscosity (and

thus, decreasing ROM diffusivity) is sufficient to diminish the solutions ionic conductivity.<sup>137</sup> Consequently, large amounts of supporting electrolyte are necessary to maintain sufficiently high conductivity for practical operation of NRFBs.

To determine whether similar trends would be observed for 2,6-dimethyl pyridinium salts, ionic conductivities were measured for solutions of **1**, **3**, **5**, and **17** in pure acetonitrile at varying concentrations. The resulting plots of pyridinium concentration versus ionic conductivity (shown in Figure 3.10) reveal expected increases in conductivity with ROM concentration; however, in contrast to previous studies, the relationship between elevated pyridinium compound concentrations (and subsequent increases in solution viscosities) and conductivities of all solutions showed an approximately linear relationship up to the solubility limits of each species. The elevated concentrations that compound **17** could be assessed at, due to higher solubility, begins to show a plateau in conductivity, possibly corresponding to the influence of elevated viscosity having a dominant effect compared to the increased concentration of ions. Additionally, the maximum conductivities observed are 28.7 mS cm<sup>-1</sup>, 30.0 mS cm<sup>-1</sup>, 25.0 mS cm<sup>-1</sup>, and 32.8 mS cm<sup>-1</sup> for compounds **1**, **3**, **5**, and **17** respectively. Notably, the conductivities observed for compounds **1**, **3**, **5**, and **17** in pure acetonitrile are surprisingly comparable to that of conductivities reported for solutions of acetonitrile with catholyte (i.e., TEMPO) and 0.1 to 1.5 M TBAPF<sub>6</sub>, where reported conductivities range from 7.1 to a maximum of 26.8 mS cm<sup>-1</sup>.<sup>138</sup> These results suggest that to achieve similar solution conductivities, the pyridiniums solutions near their solubility limit may not require nearly as much supporting electrolyte, as an inert salt typically introduced to solution as a mechanism to increase solution conductivities. The paired result of increasing conductivities with elevated viscosities, as these compounds approach their solubility limits in

acetonitrile, is remarkably encouraging and further promotes 2,6-dimethylpyridiniums as a promising class of analytes.

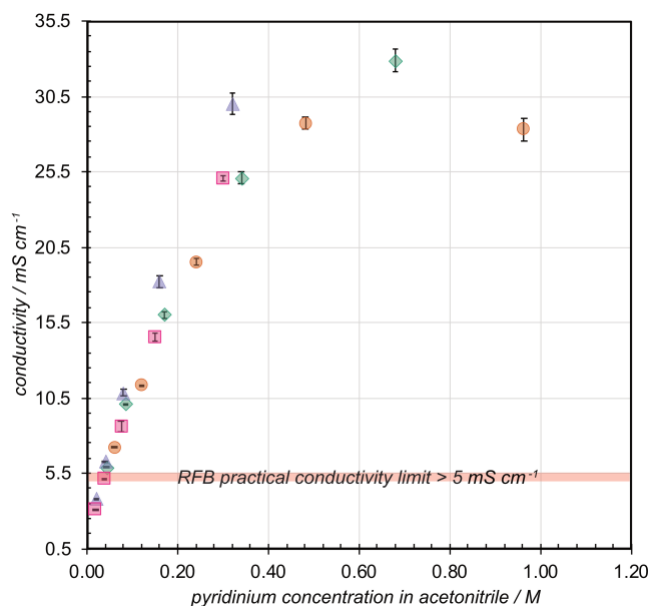


**Figure 3.10. Concentration dependent conductivities in acetonitrile.** Compound **1** (green diamonds), compound **3** (purple triangles), **5** (pink squares), and **17** (orange circles) pyridiniums. Reported conductivity values represent the average of  $n = 3$  replicates, and the error bars represent the respective standard deviations at ( $17.6\text{ }^{\circ}\text{C} \pm 0.5\text{ }^{\circ}\text{C}$ ).

### 3.4 Conclusions

In conclusion we have assessed primary electrochemical properties and subsequent physicochemical properties critical in the development of 2,6-dimethylpyridiniums as a potential analyte for application in organic non-aqueous redox flow batteries. We assessed 23 derivatives of 2,6-dimethylpyridiniums featuring structural variations in the 4-position and N-position. Redox potential was found to be predictably influenced by the electronic nature of the substituents at the 4-position and N-position combined; however, some deviation was observed when sterics at the 4-position cause divergence between the planes of the pyridinium ring and 4-aryl ring. Diffusivities in the low concentration regime were adequately predicted by the Stokes-Einstein equation with a few notable exceptions, which may indicate that there is significantly less friction

between solvent and solute than would be expected for organic salts in acetonitrile. Notably, we observe a limited effect on solution viscosities for three selected pyridiniums (compounds **1**, **3**, **5**, and **17**), which will minimize the energy requirements pumping RFB solutions as well as improve the mass-transfer mechanisms occurring in solution. Additionally, the corresponding conductivities of compound **1**, **3**, **5**, and **17** in pure acetonitrile near their solubility limits are comparable to solutions containing high concentrations of common non-aqueous supporting electrolyte, which may have implications in the formulation of pyridinium based RFB solutions. Overall, this library of 2,6-dimethylpyridiniums demonstrates robust electrochemistry, practical viscosities, and high conductivities in acetonitrile that further promote their candidacy as an anolyte for organic non-aqueous energy storage applications.

Chapter 4 Electrochemical Ammonia Production from Nitrates in Agricultural Tile Drainage: Technoeconomic and Global Warming Analysis<sup>3</sup>

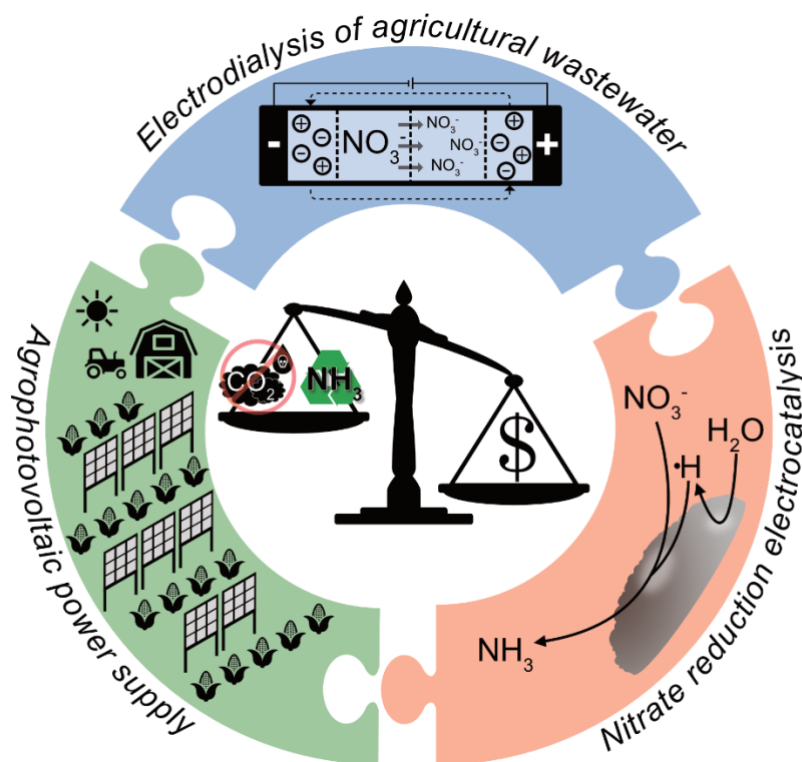


**Figure 4.1. Chapter 4: Graphical Abstract.** Nitrates from agricultural wastewater are harmful to human health and result in eutrophication. Technoeconomic and global warming potential analyses on several hypothetical nitrate capture and conversion systems for the recovery of nitrates from agricultural wastewater and conversion of nitrate to ammonia. The electrochemical technologies incorporated include: electro dialysis for nitrate separation, electrocatalysis for ambient ammonia production, and agrophotovoltaics. Despite advancements in nitrate separation and conversion, capital investments for system installation cannot be recovered by the financial benefit of on-site fertilizer production. Our analysis highlights the necessity of government intervention to promote nitrate abatement technologies to ensure environmental compliance and protect public health.

<sup>3</sup> This work is published as Samaroo, S.; Hickey, D. P. Electrochemical Ammonia Production from Nitrates in Agricultural Tile Drainage: Technoeconomic and Global Warming Analysis. *AIChE Journal* **2022**, No. July 2022, 1–12. <https://doi.org/10.1002/aic.17969>.

## 4.1 Introduction

Ammonia-based fertilizers are a critical component of commercial-scale farming around the world; however, the industrial-scale production and application of such fertilizers results in excessive nitrate concentrations in shared water resources that are correlated with algal blooms and negative human health impacts.<sup>155</sup> The primary method for producing ammonia is the Haber-Bosch process. As a result of global ammonia demand paired with the high energy consumption of this process, ammonia production is responsible for 1-2% of global energy use and 1.4% of global CO<sub>2</sub> emissions.<sup>156,157</sup> Although agricultural nutrient management has improved in the U.S. between 1970 and 1999, progress has plateaued and further improvements in efficiency are not anticipated.<sup>158</sup> Commercial-scale agriculture is notorious for nonpoint source pollution, and a major share is attributed to fertilization practices.<sup>159</sup> Nearly 80% of applied N escapes into the environment through several mechanisms, including leaching into the soil, dissolving into waterways, and escaping into the atmosphere.<sup>160,161</sup> When ammonia is applied as fertilizer it enters the nitrogen cycle and is partially converted to nitrate in the soil. After rainfall or irrigation, nitrate and unutilized ammonia migrates into communal water supplies. Employing point source pollution mitigation strategies to address these emissions on-site could circumvent the immense challenge of remediation after pollutants diffuse into the environment. In addition to the effects of excess nitrate pollution, reduction of global warming potential (GWP) is of immediate interest. As a result, several emerging electrified technologies, such as nitrate reduction electrocatalysis and electrodialysis, are targeted at decoupling ammonia production from the exorbitant rates of greenhouse gas (GHG) emissions concurrent with the Haber-Bosch process.<sup>74,75</sup> Despite substantial improvements in these independent technologies, it remains unclear whether their combination in this application will result in the desired environmental outcomes. Consequently,

broad scope analyses are needed to provide adequate context for this ongoing technological expansion. Accordingly, we considered the potential utility of performing a GWP analysis and technoeconomic analysis (TEA) for a hypothetical system that combines several emerging technologies aimed at capturing and recycling nitrates from agricultural wastewater; this analysis is meant to provide a snapshot of the current progress and remaining challenges in minimizing the environmental impact of agricultural nitrate waste. The hypothetical nitrate capture and conversion system evaluated herein, is designed to remove nitrates and produce ammonia on-site, with deliberate intention to reduce nitrate pollution while offsetting concurrent GHG emissions of traditional ammonia production.

There is interest and optimism surrounding the environmental value of removing nitrate and converting it to ammonia using nitrate reduction catalysts; however, there is reasonable skepticism surrounding the capital investment, process volumes, product separation, and maintenance necessary to execute these processes at scale.<sup>72</sup> Multiple individual technologies are currently in development that could be incorporated in a unified system which has the potential to recover nitrates and produce ammonia; specifically, electrodialysis for ion separation, electrocatalysis to produce ammonia, and agrophotovoltaics as a clean energy supply.<sup>73–75</sup> A summary of each technology and its independent function is detailed in Figure 4.2. These theoretical, combined systems can be designed to remove nitrate only (nitrate capture, NC) or remove nitrate and convert it to ammonia (nitrate capture and conversion, NCC). Their energy demand can be supplied by the state electric grid or by an on-site solar array.

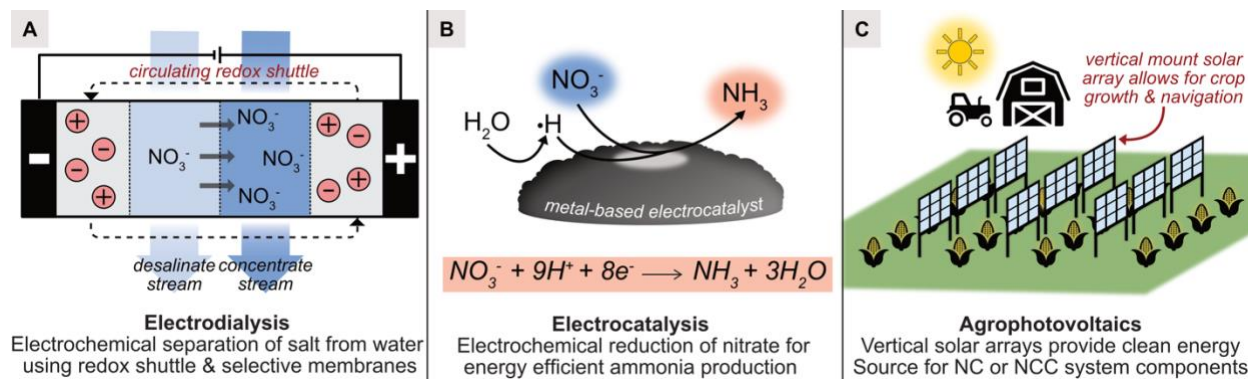


**Figure 4.2. Three individual technologies that can be combined in a system that recovers nitrates by electrodialysis (A), converts the nitrates to ammonia through electrocatalysis (B), and that can be sustainably powered by agrophotovoltaics (C).**

It should be noted that several approaches to manage nitrate waste are established and currently practiced, including controlled drainage, variable N application rates, and crop rotations.<sup>162</sup> Ongoing research efforts to advance nitrate removal technologies include membrane separation, ion exchange, adsorption, tailwater recovery systems, and field denitrification beds (e.g. woodchip bioreactors).<sup>162–167</sup> Furthermore, some emerging research efforts have demonstrated the ability to either produce or recycle unused ammonia. To this end recent systems designed to treat leachates or wastewater have employed electrical reactors such as biofiltration paired with electrocoagulation.<sup>168,169</sup> These applications employing microbial communities for denitrification show electric stimulation of bacteria can increase nitrate reduction (by enhancing enzyme activity) and will generate ammonia as a byproduct (through dissimilatory nitrate reduction to ammonium).<sup>166,170</sup> Unfortunately, many existing and emerging nitrogen management strategies either manage nitrate waste without generating usable ammonia or they are aimed at recycling unused ammonia (in the form of ammonium salts) from animal waste and do not treat tile drainage for nitrates.<sup>170–173</sup> Therefore, this work primarily focuses on emerging electrochemical technologies that can be combined to convert nitrogenous-waste to value added products, such as



ammonia and other fertilizers, thereby partially offsetting the GWP and financial cost associated with ammonia produced by the Haber-Bosch process.<sup>174,175</sup>

Our study examines a hypothetical three-part NCC system based on the three technologies listed above that have been demonstrated individually on the lab-scale. A schematic of this hypothetical system is presented in Figure 4.3, where the Haber-Bosch system boundaries are shown independently as well as supplemented by an NCC system. In the first unit, nitrate is removed from agricultural wastewater and concentrated by electro dialysis. In the second unit, nitrate is electrocatalytically reduced to ammonia under ambient conditions. Finally, the third unit consists of ammonia separation and storage stages to yield liquid ammonia fertilizer that can be stored on-site for future use. When applied in consecutive fertilization cycles, the ammonia fertilizer produced is a value-added product that reduces fertilizer purchasing costs. However, the ability of revenue streams from ammonia generation to compensate for the cost of operation and installation of this technology remains unstudied. To inform the prospective outlook of NCC systems, we compared them to NC systems at high or low nitrate recovery ranges and using electrical grid or solar energy sources. For each combination, we quantified the corresponding energy-use emissions and assessed technoeconomic feasibility.

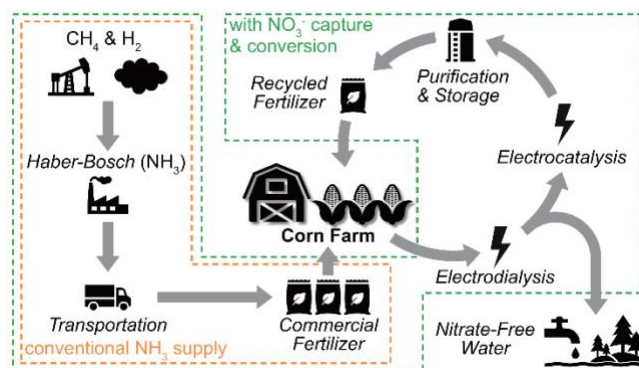


**Figure 4.3. System boundaries for commercial Haber-Bosch produced ammonia compared to fertilizer produced by NCC systems that are supplemented by purchased commercial ammonia.**

Independent electrochemical technologies, targeted at energy efficient nitrate separation and ambient ammonia production can be employed in tandem in NCC systems. The electro dialysis unit extracts nitrate ions from polluted water by applying a potential across a divided electrochemical cell. The polarized electrodes create an electrostatic driving force to pull anionic nitrate across an ion-selective membrane from the parent water stream into a concentrate stream.<sup>176,177</sup> Traditional electro dialysis systems use high voltages (4 - 6 V) to achieve efficient ion separation and exhibit substantial loss in separation efficiency at low ion concentrations. Electro dialysis systems utilizing a soluble redox-shuttling species (in contrast to a solid metal electrode) have been investigated as an alternative for water desalination.<sup>178-182</sup> Redox shuttling electro dialysis systems can achieve ion separation at reduced voltages (0.2 - 0.5 V) resulting in lower energy consumption than present systems.<sup>74</sup> Enhanced performance and low energy use are imperative qualities for technologies integrated in this remediation system.

In stark contrast to the Haber-Bosch process, an electrocatalytic nitrate conversion cell can generate ammonia with high energy efficiency and under ambient temperature and pressure. Several electrocatalysts have been developed and can be employed to achieve fast nitrate reduction to ammonia at ambient conditions.<sup>75,183-185</sup> Transition metals are of particular interest for nitrate reduction based on their electronic structure and are often designed as single metal, bimetallic or metal oxide style catalysts. These emerging catalysts for aqueous nitrate reduction feature promising faradic efficiencies (between 55-99%) and high selectivity (between 62-100%).<sup>186</sup> As an example, ruthenium nanocluster catalysts are particularly high-performing and capable of converting nitrate to ammonia at higher rates ( $5.56 \text{ mol g}_{\text{cat}}^{-1} \text{ h}^{-1}$ ) than the Haber-Bosch process. Additionally, this catalyst suppresses the competing hydrogen-hydrogen reduction reaction and is

nearly 100% selective for ammonia formation, which is favorable when optimizing efficiencies of energy consumption.<sup>75,184</sup>

To assess the maximum reduction in GHG emissions from energy consumption, we account for circumstances of NCC operation using on-site solar energy. Agrophotovoltaics (APVs) are a specific subset of solar arrays designed for agricultural applications. The primary challenge of applying standard solar panels to cropland is a conflict of land utilization. Standard solar arrays installed close to the ground can reduce sunlight to crops, hinder crop accessibility, and complicate navigation of crop equipment. APVs have been designed to address the sunlight and accessibility challenges through elevated solar array design and placement.<sup>187,188</sup> Because solar power paired with energy storage can have significant influence on both global warming potential and system affordability, we evaluated NC and NCC system operations with dependence both on the local electrical grid as well as on-site solar. Using the electrical grid these NC and NCC systems would incur the cost of electricity use, thereby representing a more affordable and near-term use of the technology. In contrast, pairing the NCC system with APV technology would guarantee minimized emissions during operation. This configuration requires a significantly higher initial cost and may demonstrate an optimistic future application. Overall, employing a NC system can mitigate these environmental penalties, and the incorporation of energy efficient nitrate-to-ammonia conversion technologies can enable the generation of a valuable fertilizer product stream.

When evaluating the economic viability of NC and NCC systems, it is important to precisely define the tradeoffs between total system costs and the value of regenerated ammonia combined with the environmental value of reduced nitrate emissions. In locations with lower crop yields, excessive application of fertilizer results in loss of nitrogen to the surrounding environment, and thus the loss of millions of dollars in fertilizer cost.<sup>189</sup> The development of new nitrogen

management practices could minimize such losses while reducing the consequent environmental damage. Despite the environmental and health benefits associated with the treatment and reuse of agricultural drainage, systems for such recycling efforts face prohibitively high capital investments and nontrivial modification of cropland.<sup>190</sup> As the U.S. advances towards reducing GHG emissions, environmentally driven systems are becoming increasingly economically beneficial.<sup>4</sup> Unfortunately, farming operations face economic challenges associated with variability in agricultural practices, crop types, and rainfall; all of which can appreciably influence the practical application of NC and NCC systems. Therefore, comprehensive environmental and economic analysis of hypothetical NC and NCC systems is needed to inform the direction of ongoing research into the corresponding nitrate recovery and recycling technologies.

Herein, we investigate the costs associated with reducing nitrate pollution, the financial benefit of converting nitrate to ammonia, and the economic impact of minimizing CO<sub>2</sub> equivalents. To illustrate extremes in system costs, nitrate emissions reduction, and CO<sub>2</sub> equivalents minimization, we compare eight theoretical cases of NC and NCC systems to a baseline Haber-Bosch process case. The eight cases include an NC or NCC system, assuming high or low nitrate recovery conditions, with energy supplied by the local electrical grid or by an on-site solar array. Additionally, we explore conditions that have the greatest opportunity to employ NC and NCC systems and introduce conceptual strategies to promote their implementation.

## **4.2 Methods**

### **4.2.1 System Boundaries and Cases**

For the basis of this evaluation, we used data from an existing study assessing a nitrogen mass balance in a tile drained watershed (Big Ditch watershed in Champaign, Illinois – referred to as the “reference study” herein) between 2001-2002.<sup>191</sup> This analysis assumes the use of tile

drainage, as it is widely used in the Midwest Corn Belt states (Illinois, Indiana, Iowa, Minnesota, and Ohio), and provides a distinct inlet source for a recovery system.<sup>192</sup> Corn fertilization rates and schedules used throughout this work reflect the crops of the reference study, however this system may be applied to any crop requiring N based fertilizers. Corn fertilization primarily occurs over three months from April through June.<sup>193</sup> Anhydrous ammonia was selected as the purchased form of fertilizer because it is widely used for corn crop fertilization for the average US farm.<sup>194,195</sup> After fertilizer is applied to fields, N is lost to the atmosphere and fixed into the corn as biomass. Importantly, only the fraction of nitrate leached into the soil and water can be recovered from drainage and converted to fertilizer. The fraction of N needed to fulfill crop needs that is not supplied by the recycled fertilizer, will be supplemented by commercial ammonia fertilizer that is assumed to be produced using the Haber-Bosch process as shown in Table 4.1.

**Table 4.1. Summary of evaluated inputs and outputs of the individual system boundaries for the base case and NCC systems as well as details pertaining to the feed acquisition, production processes, and transportation stages evaluated.**

	Feed Acquisition	Production Process	Transportation	Inputs <i>entering system boundaries</i>	Outputs <i>leaving system boundaries</i>
<b>Haber-Bosch Process</b>	<ul style="list-style-type: none"> <li>◆ H<sub>2</sub> production</li> <li>◆ N<sub>2</sub> production</li> </ul>	Haber-Bosch	NH <sub>3</sub> (ground transport)	<ul style="list-style-type: none"> <li>◆ nitrogen gas</li> <li>◆ hydrogen gas</li> <li>◆ tile drain water (contaminated with NO<sub>3</sub><sup>-</sup>)</li> </ul>	<p><i>Products</i></p> <ul style="list-style-type: none"> <li>NH<sub>3</sub></li> <li>clean water</li> </ul> <p><i>Emissions</i></p> <ul style="list-style-type: none"> <li>NO<sub>3</sub><sup>-</sup></li> <li>NO</li> <li>N<sub>2</sub>O</li> <li>CO<sub>2</sub></li> </ul>
<b>NCC System</b>	pumped tile drainage	<ul style="list-style-type: none"> <li>◆ electro dialysis</li> <li>◆ electrocatalysis</li> <li>◆ NH<sub>3</sub> separation &amp; storage</li> </ul>	<p>none</p> <p><i>(local production of NH<sub>3</sub> does not require transportation)</i></p>	<ul style="list-style-type: none"> <li>◆ electricity</li> <li>◆ transportation fuel</li> </ul>	

Most recoverable nitrates concentrate in tile drainage throughout the fertilization months (April through June). The theoretical maximum %N recovery (TMNR) is calculated based on Equation 1, where  $m_{NH3}$  is the mass of yearly applied anhydrous ammonia (82 wt% N) fertilizer (kg NH<sub>3</sub>),  $C_{NO3}$  is the average concentration of nitrate (22.5 wt% N) in the tile drainage water (kg NO<sub>3</sub><sup>-</sup> L<sup>-1</sup>) from April through June,  $V_{Tile}$  is the total volume of water leaving the tile drainage (L) from April through June. Table C.3 in Appendix C shows the range of variation in TMNR. The values of

TMNR are influenced by fertilizer application, rainfall, agriculture practices, etc. TMNR provides a value estimating the proportion of recycled fertilizer (generated by the recovery system), that displaces the total required fertilizer for the following crop cycle. High TMNR values would indicate that high N concentrations escape through tile drainage and could be recovered to provide a substantial fertilizer supply to the farmer; this supply would offset considerable purchased fertilizer costs. In contrast, low TMNR values would indicate that agricultural practices are successfully mitigating environmental risks, but the amount of recovered N would not appreciably offset the annual amount of fertilizer that must be purchased.

$$\textit{Theoretical Maximum \%N Recovery (TMNR)} = \frac{(C_{NO_3})(V_{Tile})(0.225)}{0.82 * m_{NH_3}} * 100\% \quad \textbf{(Eq. 4.1)}$$

This assessment includes feed acquisition, processing, and fertilizer product transportation for three nitrate recovery conditions and identifies the variables that most strongly influence installation costs, operating costs, and energy use. The base case considers a farming business required to purchase anhydrous ammonia fertilizer produced by the Haber-Bosch process. Two alternative cases were evaluated at 1.6% TMNR and at 32% TMNR, studying a farm using a NCC system that produces recycled fertilizer and offsets the purchased fertilizer needs for the following year. Supplementary fertilizer was assumed to be purchased from the same source as the base case, varying only in the mass of fertilizer required. The basis unit was held constant between cases at 28,400 kg NH<sub>3</sub> in the form of anhydrous ammonia. The basis unit was established by the average Illinois farm size (154 hectares) and fertilization rate (184 kg per hectare) of the reference study. This would require that approximately 28,400 kg anhydrous ammonia be applied yearly.<sup>195,196</sup> Purchased and recovered ammonia fertilizer allocation for the base case, 1.6% TMNR case, and 32% TMNR case is detailed in Table 4.2.

**Table 4.2. Distribution of nitrogen form and source for evaluated cases: base case and NCC cases.** Case descriptions: (1) Base Case: 100% Haber-Bosch supplied anhydrous ammonia without nitrate removal, (2) 1.6% TMNR Case: TMNR = 1.6% (1,700 kg NO<sub>3</sub><sup>-</sup>) recovered and supplemented by purchased ammonia, and (3) 32% TMNR Case: TMNR = 32% (44,400 kg NO<sub>3</sub><sup>-</sup>) recovered and supplemented by purchased ammonia.

	Base Case (kg N)	1.6 % TMNR (kg N)	32% TMNR (kg N)
kg NO <sub>3</sub> <sup>-</sup> Recovered (23% N)	0 (0 kg N)	1,700 (500 kg N)	44,400 (10,000 kg N)
kg NH <sub>3</sub> Recovered (82% N)	0 (0 kg N)	610 (500 kg N)	12,200 (10,000 kg N)
kg NH <sub>3</sub> Purchased (82% N)	28,400 (23,300 kg N)	27,800 (22,800 kg N)	16,200 (13,300 kg N)

A total of eight scenarios and a baseline case were compared, and definitions for each case are summarized in Table 4.3. For each TMNR case, we considered several combinations of technology and energy sources. Comparing NC to NCC demonstrated the difference between pollution abatement alone and pollution abatement paired with ammonia production for local use. Additionally, we considered two different energy supplies to power the hypothetical NC/NCC systems: energy directly from the electrical grid, and locally collected solar energy. These options contrast near-term, accessible electricity linked to GHG emissions production with a longer-term, electricity source that is not associated with GHG emission during system operation but requires an initial investment cost. The comparison highlights the cost of avoided GHG emissions in all NC and NCC systems considered.

**Table 4.3. Various arrangements of NC (nitrate capture) and NCC (nitrate capture and conversion) where electricity is supplied by either the state electrical grid (grid) or an installed, on-site APV system (solar).** These configurations are evaluated for global warming potential, initial investment, and operational costs.

	Base Case	1.6% TMNR	32% TMNR
NC & state electricity grid	Haber-Bosch process-produced ammonia	NC <sub>grid</sub> (1.6%)	NC <sub>grid</sub> (32%)
NC & on-site solar array		NC <sub>solar</sub> (1.6%)	NC <sub>solar</sub> (32%)
NCC & state electricity grid		NCC <sub>grid</sub> (1.6%)	NCC <sub>grid</sub> (32%)
NCC & on-site solar array		NCC <sub>solar</sub> (1.6%)	NCC <sub>solar</sub> (32%)

The rate of rainfall and tile drainage rates during April through June determines feed flow rates and nitrate concentrations. These rates were extrapolated from the reference study. The average nitrate concentration in the tile drainage during that time was  $14.8 \text{ mg L}^{-1}$  (2001-2002), which exceeds the EPA limit for allowable nitrate content ( $10 \text{ mg L}^{-1}$ ).<sup>195</sup> The average rainfall was 97 cm (1971-2000); this rate was scaled by 25% to give the proportion of tile and riverine discharge from the Big Ditch watershed area, which was further scaled by 30% to give the proportion associated with rainfall from April through June – yielding 7.3 cm in tile drainage. Across 154 hectares, the total drained volume is 112 million liters. The theoretical maximum mass of recoverable ammonia based on average drainage is 457 kg ammonia, which is 1.6% of the average applied fertilizer N. Consequently, this represents a low-alternative TMNR case. The base case involved conversion of gaseous ammonia feeds produced using the Haber-Bosch process, which were further converted to the target fertilizer before being shipped to the farm location. The calculated value of 1.6% N recovery represents a low-alternative case, and a hypothetical 32% N recovery (assuming average nitrate concentration in the tile was  $297 \text{ mg L}^{-1}$ ) represents a high-alternative case.

#### **4.2.2 Nitrate System Design**

The proposed nitrate recovery system is composed of three primary operating units: first, nitrate recovery by electrodialysis; second, nitrate reduction to ammonia by electrocatalysis; and third, the ammonia purification and storage. As detailed in Figure 4.4, tile drainage will be pumped to an electrodialysis unit where the nitrate will be extracted and concentrated at  $1 \text{ M NO}_3^-$  into a potassium hydroxide (KOH, 1 M) stream. Once the nitrate is isolated in the basic, aqueous stream, it is passed to the electrocatalysis unit.



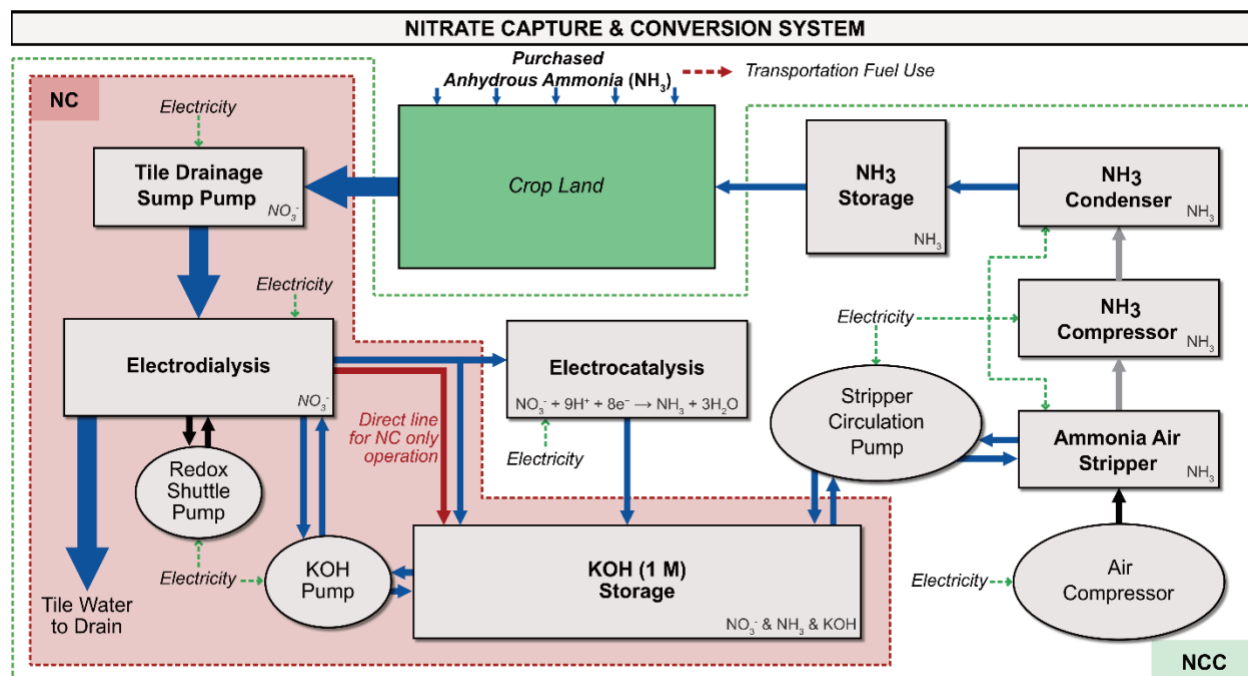


**Figure 4.4.** The process flow diagram for the proposed system for NCC as a method to generate anhydrous ammonia fertilizer from tile drainage water containing excessive nitrate concentrations. The NC system (red dashed line) demarks the equipment necessary to capture nitrate. The NCC system (green dashed line) shows all equipment necessary to both capture nitrate and generate, separate, and store ammonia.

Following the separation unit, the nitrates are reduced to ammonia using a recently reported ruthenium-based electrocatalyst (Ru-ST-12), which operates most efficiently under alkaline conditions (~1 M KOH) and at high nitrate concentrations (~1 M NO<sub>3</sub><sup>-</sup>).<sup>75</sup> Electrochemically generated ammonia is separated from the 1 M KOH solution by an air stripping column, and the ammonia gas is compressed, condensed, and stored. Once the 1 M KOH solution is fully stripped of ammonia, it can be recycled for further extraction of nitrate in the electro dialysis unit.<sup>197,198</sup> Potassium hydroxide storage tanks are paired with the electro dialysis unit to extract the nitrate ions during the three to four months of high nitrate loss to the environment. The operating time required for ammonia stripping was varied based on the total ammonia to be removed.

Sizing and energy use of the sump pump and electro dialysis (ED) unit are dictated by fluctuations in local rainfall (data for this study is from Champaign, Illinois). The sump pump,

electrodialysis unit, and the nitrate storage make up the NC system. Sizing and operation parameters of all remaining equipment associated with nitrate recycling is dictated by the anticipated TMNR. The NCC system is anticipated to operate roughly three months (April-June) of the year and have an extended period following the fertilization season to isolate and store the final product. This timeline indicates that the nitrate reduction and final conversion stages could reasonably run at low fertilizer production rates, and thus consume less energy by selecting efficient rates rather than executing rapid production targets. It should be noted that heterogeneity in field topography and relative placement of the system are expected to introduce variation in pumping requirements, but such variations were not considered for this study.

All equipment was scaled to account for the maximum expected rainfall; however, average rainfall was used to estimate energy consumption during operation. To represent a range of realistic fluctuations in operational energy use, 95% of the total energy requirements was taken as a baseline value and was calculated using average rain flow rates. The remaining 5% was calculated using the average rainfall plus three standard deviations to represent the highest rain flow rates and elevated energy demands. The fractions of statistical variation in rainfall were based on data from 2018-2021 but applied to the scale of rainfall data from 1971-2001. This was done to reflect the conditions of the original reference study and more accurately capture the intermittency of daily rainfall to define operating ranges and energy consumption of equipment.

Despite our best efforts to provide a comprehensive analysis, several variables are not reflected that may have nontrivial impacts on the results. These variables were not included due to lack of available data. The effect of variable drainage composition as well as the effect of residual ions crossing into the “clean” stream of the electrodialysis unit resulting in downstream system contamination was not evaluated. Additionally, much of the data associated with the nitrate

recovery system components are associated with lab-scale work and would require pilot scale studies to better reflect the system operations and determine component lifetimes. An estimate of converted cropland required to install the system, as well as pumping requirements dependent on field topography and system placement, will also affect initial costs and energy use. Detailed data on system performance and operational barriers of a pilot scale system would further inform these analyses. Finally, while our analysis considers the economic benefit provided by APV installation as it relates to the offset energy costs for hypothetical NC and NCC systems, we do not consider the ancillary benefits of offset energy costs that an APV system would provide for non-NC/NCC operations.<sup>199,200</sup>

### **4.3 Results and Discussion**

GWP is a measure of CO<sub>2</sub>, nitric oxide, and N<sub>2</sub>O emissions combined and compared as carbon dioxide equivalents. GWP is strongly influenced by energy consumption and fuel use in transportation for the eight compared NC and NCC arrangements. Figure 4.5 shows the GWP of all nine cases and shows the differences between the base case and all TMNR, operation, and energy source configurations. The reductions in GWP, though some negligible, suggest that the cumulative CO<sub>2</sub> equivalents associated with recycled fertilizer is lower per kg ammonia than the purchased fertilizer for all the NC and NCC operations. It follows that, as more purchased fertilizer is supplemented with recycled fertilizer, a greater fraction the CO<sub>2</sub> equivalents associated with the Haber-Bosch process can be displaced. The GWP comparison highlights optimal reductions can be achieved when applying the NC systems to crops that are significantly overfertilized.

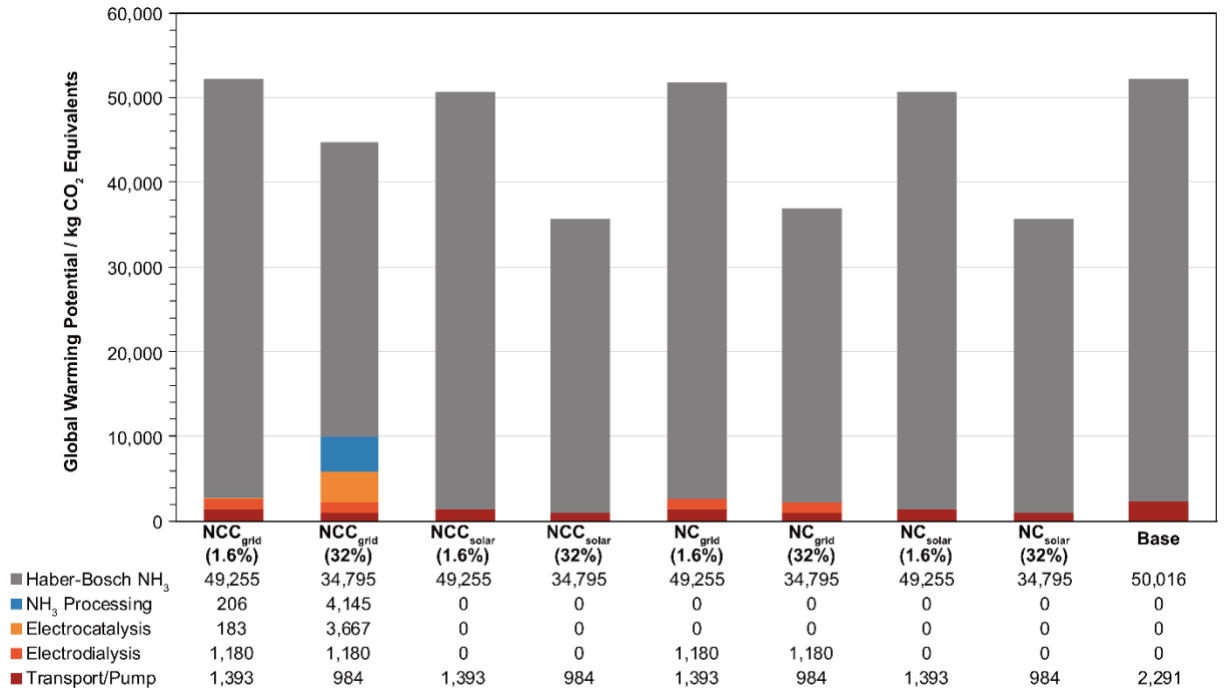


**Figure 4.5. The GWP (in kg CO<sub>2</sub> equivalents) for each of the eight nitrate abatement configurations, as well as the base case.** For the configurations supplied by on-site solar electricity, the GWP contributions are associated with the commercial ammonia production and transport. For the configurations supplied by local grid electricity, the CO<sub>2</sub> equivalents result from the Illinois electrical grid and commercial ammonia production and transport.

Figure 4.5 illustrates that the Haber-Bosch process, which is associated with purchased fertilizer, contributes the most to GWP for all cases studied. Comparing the NCC<sub>grid</sub> (1.6%) and NCC<sub>grid</sub> (32%) cases, the GWP contribution from the electrocatalysis unit and ammonia stripper increases. This result is expected, because operational stages in the NCC system after electrodialysis are dictated by anticipated TMNR. In the NCC<sub>grid</sub> (32%) case, these units must be larger and will consume more energy while separating and storing more ammonia. This consumption is linked to grid-based emissions, which yields larger fractions of GWP. Such variations in energy consumption are inconsequential when considering NC cases, because there is no grid electricity consumption, and the same volume of water is assumed to be processed for both TMNR conditions. Thus, all variation in GWP arises from Haber-Bosch processing and ammonia transport. For all 1.6% TMNR scenarios, 0.2% - 3.1% reduction in GWP is projected,

while for 32% TMNR scenarios, 14% - 32% reduction in GWP can be achieved. Because many of these technologies are still under development, the initial investments can be hindering even when advancements in performance make operational costs increasingly appealing.

The technoeconomic analysis presented here spans twenty years, and is based on annualizing the initial investment, operations, and maintenance costs at a discount rate of 1.5% to determine the net present values (NPV).<sup>201-203</sup> A summary of assumptions and calculated values for this analysis is shown in Table 4.4. A detailed example of cost distribution used to evaluate varied combinations of technology (NC vs. NCC), energy supply (grid vs. solar), TMNR (1.6% vs. 32%), maintenance frequency (every 5- or 10-year equipment replacement), and finally discount rates of 1.5% (federal and private/farmer), 1.5% (federal) and 7% (private/farmer), and 7% (federal and private/farmer) is included in Table C.15 of Appendix C. The single source of yearly cash in-flows are associated with the avoided cost of purchased anhydrous ammonia fertilizer, which is currently valued at \$1022 per metric ton. The yearly cash out-flows are associated with the electricity required to operate. Energy storage capacity for the solar array system was designed assuming five hours of sunshine, while using 20 kWh batteries and assuming \$0.71 W<sup>-1</sup> for solar array installation costs.<sup>188</sup> A sensitivity analysis of yearly operating costs for NCC grid 1.6% and NCC grid 32% arrangements with variation in TMNR, cost of electricity, electro dialysis electricity use, pumping, electrocatalysis electricity use, ammonia stripper electricity use, and cost of anhydrous ammonia is shown in Figure 4.6. While the use of solar panels and energy storage contributes further to the overall goal of reducing GHG emissions during operation of NCC, the installation of these system components contribute substantial costs.

**Table 4.4. The following assumptions and calculated values can be used to estimate the TMNR value needed to achieve a positive NPV over a 20-year lifespan of operation.**

System Lifespan (y)	20
Fertilization rate (N kg ha <sup>-1</sup> y <sup>-1</sup> )	200
Field Size (ha)	400
Federal Water Project Discount Rates (NCRS)	1.5%
NRCS Share of Capital Investment	75%
Farmer Discount Rate	1.5%
Farmer Share of Capital Investment	25%
Share of Equipment Cost	40%
Equipment Price Estimate (TMNR 1.6%)	\$14k
Equipment Price Estimate (TMNR 32%)	\$94k

Financially, operation of NC or NCC systems at elevated TMNR conditions benefits from both economies of scale for equipment costs, and the circumvented costs of purchased fertilizer. Nevertheless, for all eight cases the offset costs of generated ammonia (whether paying for grid electricity or using free solar electricity) fails to generate a positive NPV over the system lifespan. Overall the financial benefit of generating ammonia from the nitrates redirected from negatively impacting the environment remains too low, and alternative nitrate remediation (e.g., denitrification bioreactors) or prevention (e.g., fertilizer application rate reduction and timing) strategies remain more affordable and sometimes cost saving.<sup>162</sup> It should be noted that this economic analysis is an extremely lean, study-level assessment meant to provide a preliminary perspective on the scalability of the theoretical combination of technologies. As a result, additional factors that require more detailed analyses and capital (e.g., controllers, analyzers, operators etc.) were not explicitly evaluated or included. Extension of the study-level analysis to include additional equipment would incur higher capital costs and would not appreciably change the conclusion of the NC or NCC systems' economic outlook.

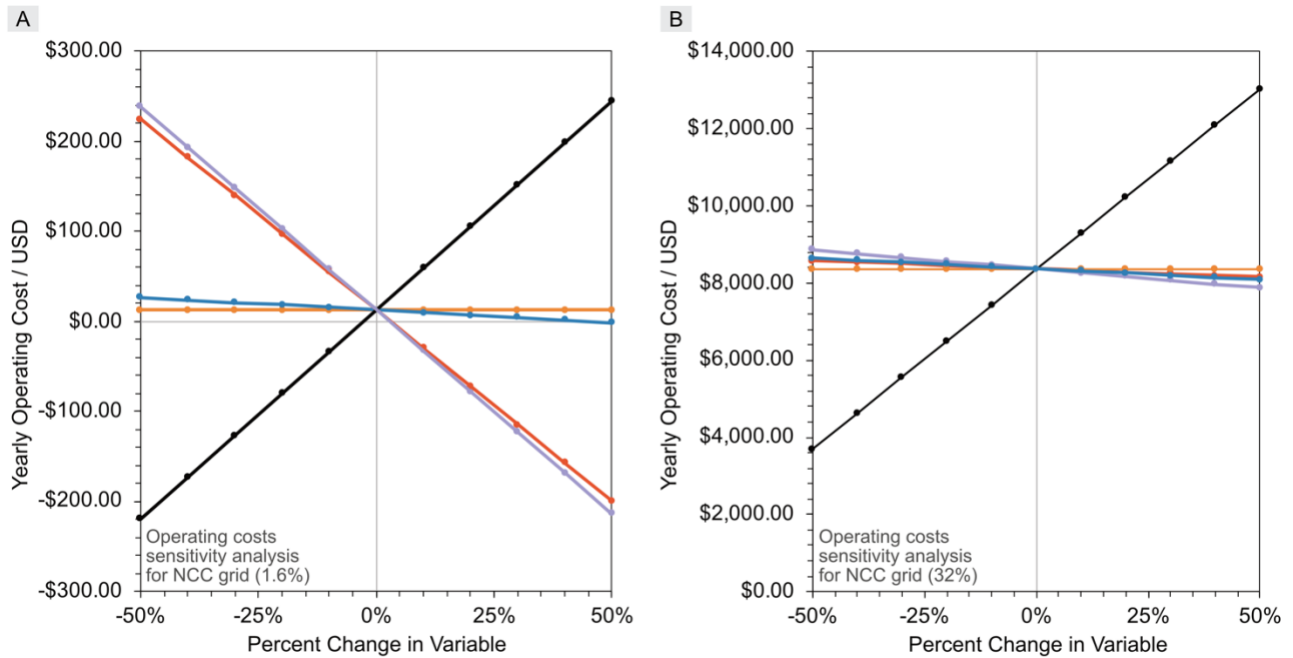


**Figure 4.6. Sensitivity analysis of yearly operating costs for NCC grid 1.6% and NCC grid 32% arrangements with variation in TMNR (grey), cost of electricity (lavender), electrodialysis electricity use (red), pumping (maroon), electrocatalysis electricity use (orange), ammonia stripper electricity use, and cost of anhydrous ammonia (black).** This analysis is based on assumptions from Table 4.4 in the main text. (A) The NCC grid 1.6% operation is most sensitive to the cost of electricity consumption, electricity needs for the electrodialysis unit, and the cost of ammonia. Small variation for NCC grid 1.6% operation can result net losses during operation, with high ammonia costs paired with low electricity cost and consumption promoting net gains. (B) The NCC grid 32% operation is most sensitive to the cost of ammonia. Even with operating variation, the NCC grid 32% operation will maintain net gains, with high ammonia costs optimal conditions.

Analogous water resource projects pursuing environmental benefits often face overwhelmingly high capital investments.<sup>192</sup> The NCC systems are not unique in that regard, but conditions exist where state or federal incentives (i.e. low discount rates from NRCS) can be used to improve economic returns.<sup>204</sup> Incorporation of this type of funding can reduce the initial fixed capital investment required by the farmer and reduce the operational time required before a positive NPV is achieved. Without additional economic drivers, these abatement technologies are likely to remain a poor financial decision. To accomplish critical pollution abatement of both nitrate and GHG emissions, federal financial assistance or emissions penalties may be necessary.

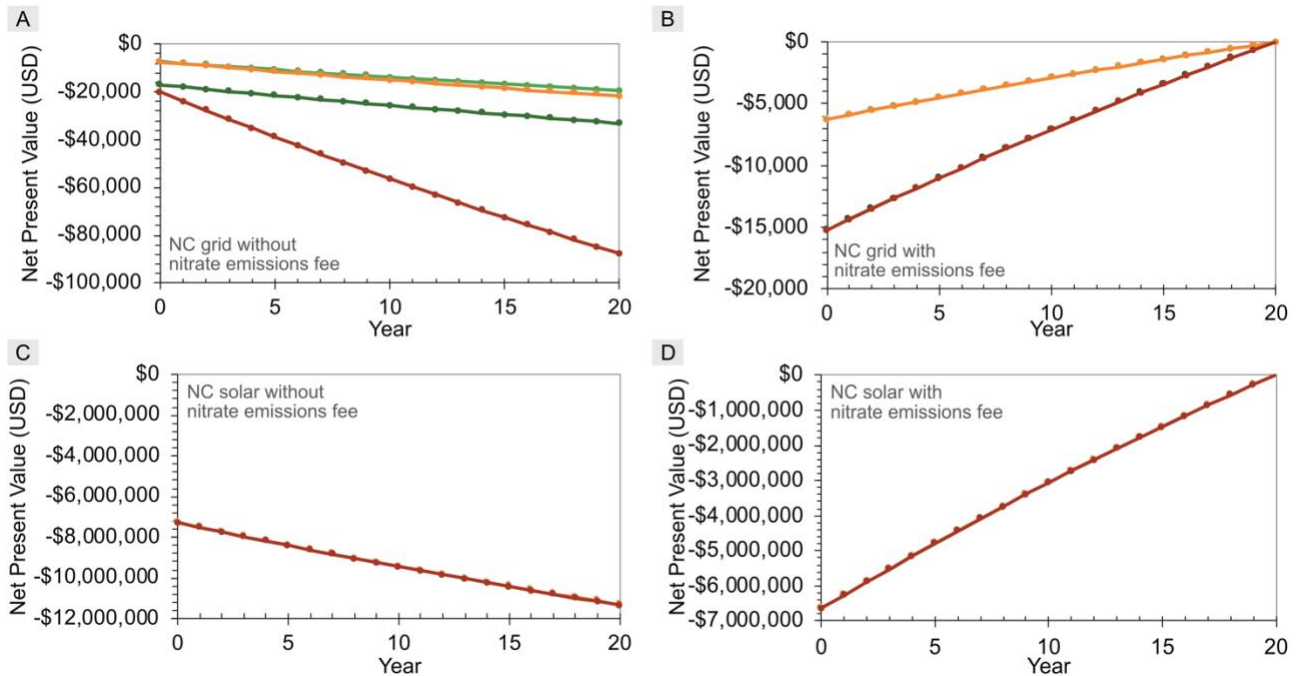


**Figure 4.7. Yearly net present values (NPV) of NC systems, providing pollution abatement-only, with and without nitrate emissions fees.** The fees were estimated to accomplish a positive NPV after 20 years of operation, by introducing another offset cost. The emissions fee per kg of nitrate is significantly lower to compensate for the initial investment of the NC grid systems, compared to the NC solar systems. Maintenance consists of replacing the anodes, cathodes and membranes of the systems, where high frequency corresponds to replacement every five years low frequency corresponds to replacement every ten years. The changes in NPVs are shown for high maintenance frequency of the NC grid 1.6% (light orange), low maintenance frequency of the NC grid 1.6% (light green), high maintenance frequency of the NC grid 32% (dark orange), low maintenance frequency of the NC grid 32% (dark green). (A) NPV of NC grid system with no nitrate emissions fees. (B) NPV of NC grid system with nitrate emissions fees. (C) NPV of NC solar system with no nitrate emissions fees. (D) NPV of NC solar system with nitrate emissions fees.

Previous models within agricultural economics have suggested multifaceted approaches to motivate the use of nonpoint source pollution mitigation systems, including: subsidies, threat of regulation, financial incentives, taxes, and policies applied separately or in combination.<sup>205,206</sup> Others suggest that conditional dependence on the success rate for pollution control by effluent fees, subsidies, marketable permits, and direct regulation.<sup>207</sup> The primary difficulty with nonpoint source pollution is quantifying the avoided harm associated with emissions. There would be losses indirectly linked to fish and wildlife professions, human health concerns, as well as operations



contributing to global warming potential. The financial benefits of the NCC systems are solely linked to avoided costs through on-site production of ammonia. The NC systems offers no avoided cost factor, but it is the arrangement that achieves the bare minimum function of pollution abatement. Working backwards from the NC<sub>grid</sub> arrangements initial investment and maintaining the same assumptions from Table 4.4 we can estimate the type of emissions fees that would need to be linked to nitrate emissions to promote the installation of such systems. Examples of yearly net present values (NPV) of NC systems, providing pollution abatement-only, with and without nitrate emissions fees are shown in Figure 4.7. These preliminary evaluations suggest a range of \$0.07 - \$0.08 per kg nitrate for 32% TMNR and \$0.69 - \$0.70 per kg nitrate lost to the environment. The fee range variability accommodates high or low frequency (5-year or 10-year) equipment maintenance costs. For comparison, in Table 4.5, the fee was estimated for the NC<sub>solar</sub> system. The necessary fee to support this solar powered arrangement shows much higher rates of about \$20 and \$416 per kg tile-drained nitrate. Given the extent of this assessment and the omissions of factors that would require higher initial or annual capital (e.g., controllers, analyzers, operators etc.), all reported emissions fees provide a low estimate of the magnitude of fees necessary.

**Table 4.5. Ranges of estimated nitrate emissions fees, that would push NC configurations into financial feasibility.** Recovery at different TMNR values and assuming varied energy sources can shift the estimated emissions fee rates. A comprehensive table of emissions fee estimates paired with varied combinations of technology (NC vs. NCC), energy supply (grid vs. solar), TMNR (1.6% vs. 32%), maintenance frequency (every 5- or 10-year equipment replacement), and finally discount rates of 1.5% (federal and farmer), 1.5% (federal) and 7% (farmer), and 7% (federal and farmer) is included in Table C.15 of Appendix C.

Nitrate Emissions Fee (\$/kg NO <sub>3</sub> )		
	1.6% TMNR	32% TMNR
NC grid	\$0.68 - \$0.70	\$0.07 - \$0.08
NC solar	~\$416	~\$20

Note: Cost ranges due to 10-year or 5-year maintenance frequency

The most affordable arrangement, NC<sub>grid</sub>, is also the most reasonable to consider for mandatory implementation in a case of more stringent environmental policy. If the only income generated in

the economic evaluation is the avoided costs of purchased ammonia (\$1.022 per kg ammonia), and the high (\$0.70 per kg tile drained nitrate) or low (\$0.07 per kg tile drained nitrate) emissions penalties, then the maximum affordable equipment cost (per hectare per year) to provide a possible return on investment can be estimated for a given TMNR. As shown in Figure 4.8, the NCC<sub>grid</sub> system scenarios are evaluated by considering several possible emissions policies with an extrapolation of the previously estimated equipment costs. For scenarios in which the estimated costs are below the maximum affordable equipment investment cost, the anticipated installation costs are low enough to yield a positive NPV over the course of 20 years. Scenarios with estimated costs exceeding the maximum affordable equipment investment cost offer no promise of return on investment. For all cases the higher TMNR scenarios are more promising than low TMNR scenarios. With zero emissions fee the estimated costs will never fall below the maximum affordable equipment cost target, however this condition is achieved at roughly 65% TMNR when applying the low emissions fee, and at 5% TMNR when applying the high emissions fee. The cost extrapolation of the total investment is shown in Figure 4.8, where the equipment makes up 40% of the initial capital investment. Of this 40%, the farmer is responsible for 25%, and 75% is covered by the Natural Resources Conservation Services (NRCS) or a similar government entity.<sup>167,208</sup>

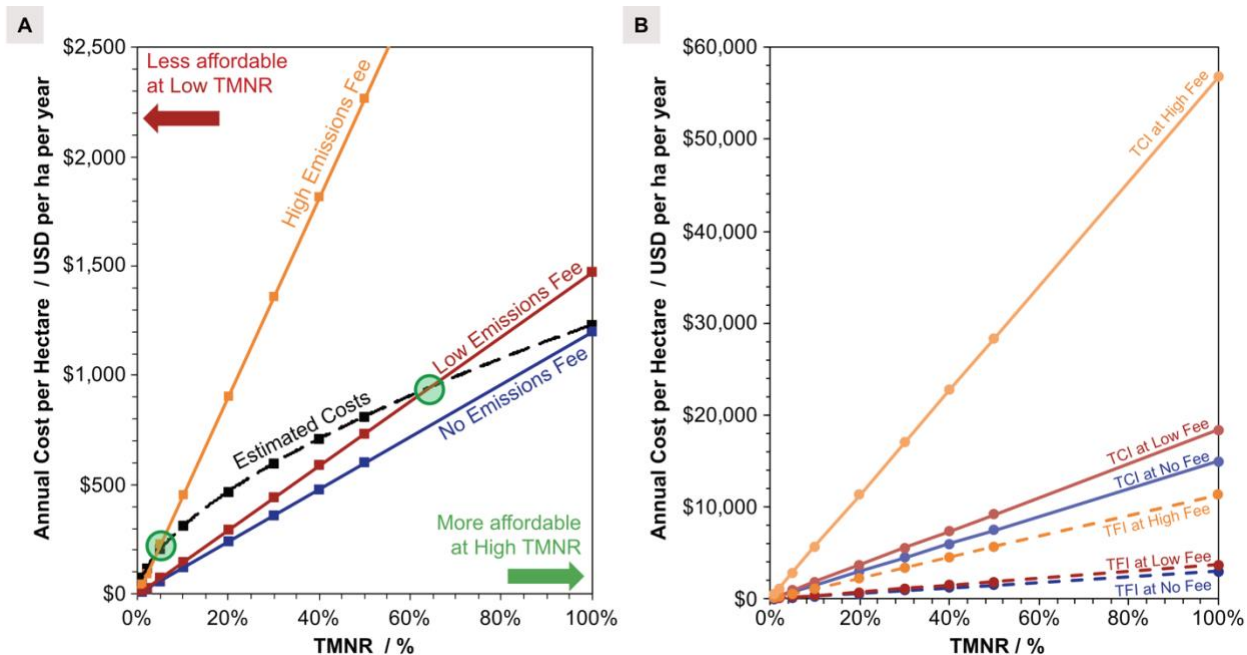


**Figure 4.8. (A) Comparison of the projected maximum affordable equipment cost per hectare per year using assumptions from Table 4, showing when the estimated costs become affordable enough to anticipate a return on investment in 20 years.** The estimated costs (black dashed line) are extrapolated using the six-tenths rule between the two price estimates for 1.6% and 32% TMNR configurations.<sup>209</sup> The linear estimate for maximum affordable total equipment cost is shown with zero avoided emissions fees (blue), the low emissions fee estimate (red), the high emissions fee estimate (orange). (B) The cost extrapolation of the total required investment at variable TMNR values where the equipment makes up 40% of the initial capital investment, of which the farmer is responsible for 25%, and 75% is supplemented by government assistance. The total capital investments (TCI) are shown with solid lines, and the total farmer investment (TFI) are shown by dashed lines and zero fees to supplement costs (blue), the low emissions fee estimate (red), the high emissions fee estimate (orange).

The cost distribution for all eight cases as well as the total cost associated with the distribution is detailed in Figure 4.9. Of the technologies involved in these nitrate abatement system arrangements, many of them are newer and have potential to become more affordable to purchase and install. The scenarios involving solar arrays are heavily encumbered by the cost of the APV system and the paired energy storage. The APV systems exemplify the current cost of the incremental reduction of GHG emissions during system operations. As APV systems become more widely available, this initial investment cost is expected to decrease substantially.<sup>210</sup> However, further inspection of the  $NC_{grid}$  and  $NCC_{grid}$  cases show that over half the initial investment is due

to aqueous chemical storage and pumps, both of which are more stable technologies whose components are not expected to become significantly cheaper. Therefore, cost reductions in electro dialysis and electrocatalysis installations may not have as significant an influence as reductions in APV systems, energy storage, liquid storage, and ammonia purification technologies in making these systems more cost-effective. These conclusions reflect and confirm the skepticism focused on capital investment, process volumes, product separation, and maintenance that are associated with system design for ammonia synthesis from waste nitrates.<sup>72</sup> These financial barriers again highlight the necessity of an external incentive, such as an emission fee, to incentivize the proposed concept toward economic viability.

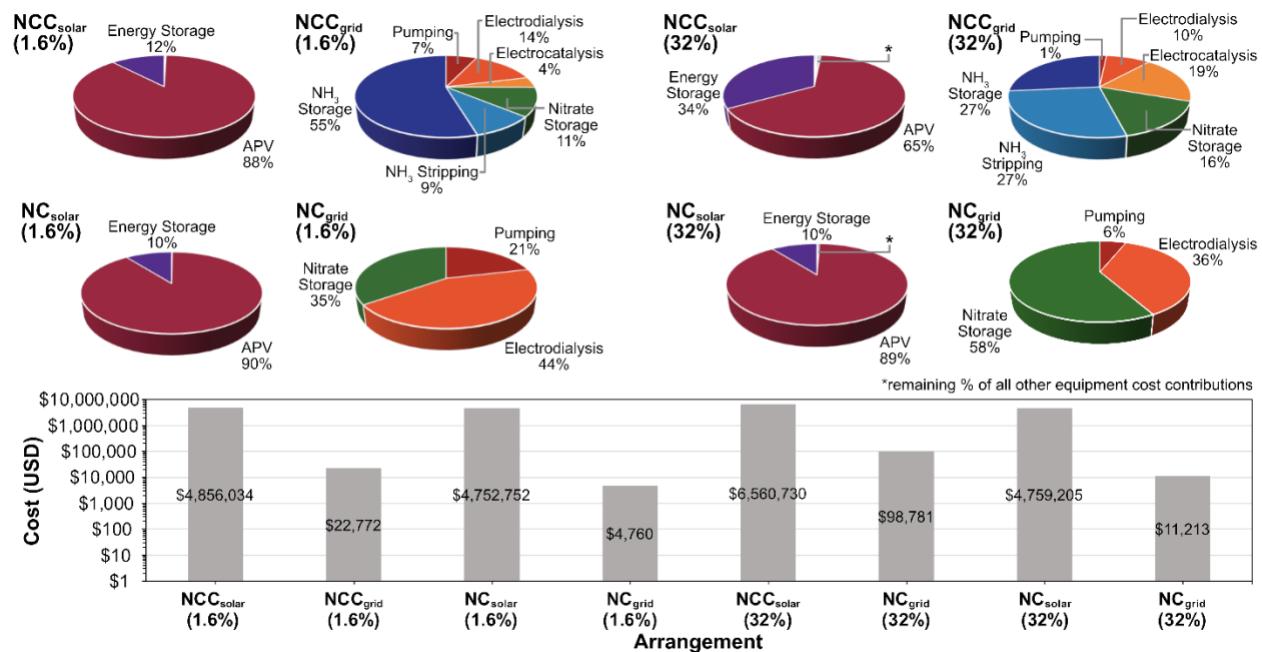


**Figure 4.9. The cost distribution for the initial equipment investment, for various TMNR, operation, and energy source configurations.** For each corresponding arrangement, the total equipment cost is shown in the bar graph below on a log scale. The cost distribution is shown for each case including tile drainage pumping (red), electro dialysis (orange), electrocatalysis (dark yellow), nitrate storage tank (green), ammonia stripping/compression/condensation (turquoise), and ammonia storage (dark blue), APV (dark pink), and energy storage (purple).

Although NC and NCC systems face economic limitations, it is interesting to consider the applicability of this technology with anticipated changes in climate, energy use, and federal

incentives. Environmental and economic drivers in the United States motivate the pursuit of low-emission energy sources (e.g. wind, solar) so the use of the electrical grid will have reduced GWP.<sup>211</sup> Solar power is becoming increasingly accessible and its direct integration into this system could guarantee reduced GHG emissions tied to ammonia production. Climate patterns are already changing, annual precipitation rates in the U.S. have been increasing since 1901 by approximately 0.2 inches per decade, and this growth would impact the recovery system in two ways.<sup>212</sup> Increasing total rainfall may result in increased nitrate concentration in tile drainage (potentially increasing TMNR), though high variability in rainfall may make optimal sizing of equipment challenging. A costly engineering solution to resolve this variability would be the installation of on-farm reservoirs, which would allow interim storage during heavy rains. The feed rate to the system from the reservoir could then be processed at intended rates. Previous studies concerning on-farm reservoirs, used for tail water recovery, have shown profitability in areas with limited water availability conditions.<sup>192,213,214</sup> Tail water recovery systems share a unified mission with the nitrate recovery system, in that they are designed to reduce the escape of nutrients, pesticides, and sediments off cropland.<sup>215,216</sup> Applying both systems in tandem could have compounding benefits.

Case studies investigating motivation in adoption of advancement nutrient management suggest that systems with increased profitability, better crop yields, existing financial government incentives are qualities of more favorably adopted conservation practices.<sup>217</sup> In addition to the persisting focus in remediation strategies, the USDA recently announced strong interest in funding fertilizer production that is domestic, innovative, and sustainable – as a means of reducing foreign fertilizer dependence.<sup>218</sup> If the initial capital investments for nitrate capture and conversion

systems are addressed by federal financial incentives that align with USDA goals, adoption of these systems will be made more attractive.

#### **4.4 Conclusions**

In summary, hypothesized NCC systems take harmful tile drainage waste and generate a value-added ammonia fertilizer; the GWP assessment emphasizes the environmental promise of this technology while the technoeconomic analysis reveals the necessity of government intervention. Moreover, these analyses reveal that optimal environmental and financial potential exists where the mass of recycled fertilizer generated considerably displaces the fertilizer needs of the following season (e.g. high TMNR). Greater quantities of offset fertilizer promote the reduction of emissions generated by standard Haber-Bosch fertilizer production methods. Further, if a nitrate emissions policy is introduced, this provides a financial incentive promoting these pollution abatement technologies. A major challenge in applying this technology will be estimating locations with adequate nitrate to recover, and this information is highly dependent on farming practices, climate, and location.

In conclusion, NCC systems can theoretically substantially reduce nitrate emissions, which reduces eutrophication potential and human health hazards, all while generating ammonia with lower emissions than traditionally produced ammonia. We have assessed the status of emerging electrochemical technologies extrapolated into NCC systems and determined that maximum reduction of emissions occur when applying the system to scenarios with high TMNR. Consequently, when more nitrate is recycled to fertilizer, the mass of purchased anhydrous ammonia is lower, and the corresponding Haber-Bosch related emissions will be reduced. NCC systems are similar to other nutrient management systems (e.g., TWR) with the mission of reduced agricultural emissions; and analogously they are not independently economically viable. NCC

systems currently, and for the foreseeable future, will require substantial support from NRCS (or similar government entities) to overcome high initial fixed capital investment challenges. Greater federal financial support, nitrate emissions penalties, and cost reductions in advanced technologies are all necessary to incentivize these NC and NCC systems as a realistic and cost-effective investment for nitrate pollution abatement.

## Chapter 5. Conclusions and Future Work

### 5.1 Summary

The work presented in this dissertation focuses on improving physicochemical and electrochemical properties of electrolytes and understanding the hypothetical implications of their economic and environmental evaluations. As with many disruptive technologies designed for the current energy transition, RFBs must demonstrate improvements in meeting energy demands, environmental impacts, and economic feasibility. The combination of experimental assessment and hypothetical evaluation have been employed to pursue these goals. A deeper fundamental understanding from experimental probing and rationalization will direct future molecular design while hypothetical assessment methods (i.e., LCA or TEA) can influence design goals for target markets and align research targets with desirable outcomes. Chapter 2 introduces pyridiniums as a promising anolyte, and details the identification of a unique correlation between maximum ROM solubility and the extent of C-H $\cdots\pi$  interactions.<sup>76</sup> Chapter 3 expands on the evaluation of pyridiniums and discusses solution properties (i.e., viscosity), electrochemical properties (i.e., reversibility, diffusion coefficients), and a preliminary study of charged shelf-life stability.<sup>77</sup> Chapter 4 details an evaluation of a hypothetical combination of emerging technologies that employ state-of-the-art electrochemical processes.<sup>78</sup>

The properties of redox active electrolytes are consequential in the performance and costs of systems that employ them, and one such performance metric is energy density. Energy per unit volume, in Wh L<sup>-1</sup>, is a critical parameter that impacts RFB size and cost, and the ability to elevate energy densities can improve technical and economic feasibilities. Established vanadium RFB systems demonstrate energy densities ranging between 10 to 30 Wh L<sup>-1</sup>. Exploration within the non-aqueous organic RFB design space is advantageous due to the stability of non-aqueous



solvents and the prevalence and tunability of organic molecules. Pyridiniums have been introduced as a potential anolyte, and in prior experimental investigations they demonstrate strong cycling stability and exceptionally low reduction potentials.

In previous works on pyridiniums, a class of anolytes, have been synthesized, characterized, and tested to assess their current candidacy as a ROM for use in RFBs. Despite these optimal characteristics, their synthesis was prohibitively difficult and energy intensive. These limitations necessitated the development of a new synthetic route before any further investigation of this class of molecules. The introduction of alternative synthetic methods, detailed in Chapter 2, enabled an easy and modular variation of the core structures. A library of pyridiniums with variation on the 4 and N positions, of 2,6-dimethylpyridinium derivatives were synthesized in two steps (1) the 4-position is fixed using a Grignard reagent (to form the pyrylium) and (2) a primary amine fixes the N position after reactions with the pyrylium intermediate. Through this synthesis 24 pyridiniums were generated and this method demonstrated synthetic modularity and promising yields.

As a result of this inventive synthetic procedure, the generated molecular library was evaluated to investigate properties of interest and their dependence on variations in molecular structure. Importantly, we established that the electrochemical properties of the core structure were not lost by the introduction of these various substituents, beginning by confirming that the low reduction potentials were maintained, described first in Chapter 2 and further evaluated in Chapter 3. The reduction potentials of the full library of pyridiniums were measured and their behaviors (based on variations in molecular structure) were consistent with that of ROMs in literature. This series follows well-studied trends in reduction potentials where substituents with more electron withdrawing natures decrease electron density and make it easier to reduce the molecule leading to a more positive redox potential. Oppositely, substituents with more electron donating tendencies

will increase electron density making it more difficult to reduce. These reduction potentials were determined by cyclic voltammetry of each derivative and range from -1.5 V to -1.7 V vs. ferrocene. All pyridinium derivatives undergo reversible reduction and oxidation at the short timescales of cyclic voltammograms. To quantitatively map and evaluate these results, the sum of the Hammett parameters for the corresponding substituents (in the 4- and N-positions) show a strong correlation with the reduction potential. Overall, we can use a relationship of these established parameters to anticipate the reduction potentials of derivatives like this parent molecule. Additionally, we have confirmed that derivatives within the new library of molecules demonstrate low reduction potentials and reversibility. Following the evaluation of preliminary electrochemical properties, we probed specific physicochemical properties of these molecules that are consequential to RFB energy density and operation.

As highlighted in Chapter 2, increasing maximum ROM solubility is a primary focus of those studying RFB electrolytes because it can enable increased energy densities. The resulting library of pyridiniums featured molecules with consistent  $\text{BF}_4^-$  counterions and core pyridinium structures. The maximum solubilities of these materials were measured in acetonitrile and from 0.3 M to 2.1 M in roughly three solubility regimes (1) low, (2), moderate, and (3) high. We identified dramatic solubility increases (doubling or tripling) from the simple introduction of a methyl substituent. However, this pattern lacked consistency across the full pyridinium library, and we concluded that molecular structure alone could not clearly rationalize these changes in maximum solubility. Parameters generated by density functional theory (DFT) modelling focused on variables that describe the charge distribution and shape of the molecule (i.e., polarizability, dipole moment or steric parameters) to understand solute-solvent interactions. Unfortunately, all DFT generated parameters failed to reveal any appreciable univariate or multivariate correlations.

Notably, DFT modelling does not generate information on multiple molecules or their interactions, thus x-ray crystallography was employed to provide more detail through an experimental understanding of intermolecular interactions.

We compared the crystal structures of low and moderately soluble derivatives and found that the lower solubility derivatives showed only strong electrostatic interactions with the  $\text{BF}_4^-$  ion, while in contrast the moderately soluble compounds showed  $\text{C-H}\cdots\pi$  interactions disrupting the strong electrostatic interactions.  $\text{C-H}\cdots\pi$  interactions are a weak dispersion interaction that can occur between a  $\pi$ -system and a hydrogen attached to a carbon. We rationalize this difference in solubility by considering that the strong interaction stabilizes the crystal lattice and decreases solubility, while the same strong interactions are disrupted by the weak  $\text{C-H}\cdots\pi$  interactions. This interference destabilizes the crystal lattice and encourages solvation. Discrepancies in the presence or absence of these interactions provided a strong indication that  $\text{C-H}\cdots\pi$  interactions may be a critical descriptor to quantify.

The criteria used to define a  $\text{C-H}\cdots\pi$  interaction was a maximum distance of 3.6 angstroms within the cylindrical extension orthogonal to the aromatic  $\pi$ -system. In addition to these position and distance criteria, we established criteria to exclude coincident  $\text{C-H}\cdots\pi$  interactions. To ensure that  $\text{C-H}\cdots\pi$  interactions were not a result of electrostatic forces, we compared the ratio of  $\text{C-H}\cdots\pi$  interactions to the interactions with  $\text{BF}_4^-$  to the  $\pi$ -system. From this selection criteria, we generated a linear correlation of  $\text{C-H}\cdots\pi$  descriptor and maximum pyridinium solubility in acetonitrile. The solubility descriptor is the sum of each interaction distance to the  $-6^{\text{th}}$ , where  $d$  is that distance between the hydrogen and centroid of the  $\pi$ -system (i.e. Figure 2.9). This descriptor correlated effectively with the solubility regions: the low solubility corresponds to species showing 0 or 1 total  $\text{C-H}\cdots\pi$  interaction, the moderate solubility corresponds to 2 or 3 total  $\text{C-H}\cdots\pi$  interactions,

and the high solubility derivative shows 6 distinct C-H $\cdots\pi$  interactions. As this relationship relies on the crystal structure, it is not predictive, but it begins to provide new design insights for solubility. It should be noted that the C-H $\cdots\pi$  interactions were evaluated from the solid state and have been extrapolated to describe a solvated state behavior, which is not commonly translatable.

To verify the existence of C-H $\cdots\pi$  interactions among pyridinium molecules in solution, we examined NMRs at increasing concentrations in acetonitrile. Importantly, the protons engaged in C-H $\cdots\pi$  interactions (as seen in the crystal structure) also shifted up-field at higher concentrations, while other protons shifted downfield. The trends in up-field shift align well with the C-H $\cdots\pi$  interaction hypothesis because the protons involved in a C-H $\cdots\pi$  interaction become increasingly shielded by the  $\pi$ -system at increasing concentrations. Conversely, pyridinium derivatives with zero determined C-H $\cdots\pi$  interactions, or zero protons involved in a C-H $\cdots\pi$  interaction, only shift downfield at increasing concentrations. The NMR studies confirm that the anticipated C-H $\cdots\pi$  interaction behavior indicated by crystal structure is reflected in the solvated state and can be used to conceptually rationalize the observed solubility trends in acetonitrile.

A further compelling series of results is the solubility trends of pyridinium in three additional organic solvents. These trends hold to varying degrees and suggest that the role of these intermolecular interactions (C-H $\cdots\pi$  interactions) may be similarly involved in solvation behavior in other solvents. When maximum solubility is graphed with the independent variable as the dielectric constant of the solvent, new correlations may be inferred pointing to a theoretical, solubility maxima. Overall, the number of C-H $\cdots\pi$  interactions (occurring in both the crystal structure and solvated state) indicates that the competition between these (strong electrostatic and weak dispersion) forces are important in understanding maximum solubility behaviors of ROMs

in non-aqueous solvents. Notably, at increased concentrations, properties such as viscosity and conductivities are impacted and must also be assessed.

As emphasized in Chapter 3, at elevated concentrations, some ROM solutions can become highly viscous. As a result of increased viscosity, higher pumping energies may be required and the conductivities of electrolyte solutions can be diminished as materials approach their solubility limit. We selected four derivatives to evaluate, two from the low solubility regime, one from the moderate regime, and the highly soluble derivative, and measured their kinematic viscosities at increasing concentrations. All derivatives at the maximum concentration evaluated demonstrate viscosities between that of acetonitrile and pure water and appear to follow analogous viscosity vs. concentration trends. Unlike the maximum solubilities of pyridiniums observed, the measured viscosities do not appear to vary widely, and thus we expect these general behaviors to be representative of the entire molecular library.

For the same solutions evaluated for viscosity, we measured the resulting solution conductivity and found that at elevated concentrations approaching their solubility limit, they demonstrate conductivities comparable to non-aqueous solutions of pure supporting electrolyte. This result is quite promising as it indicates that lower (or zero) quantities of inert supporting electrolyte may achieve operational solution conductivities. Overall, pyridiniums, as an anolyte class, demonstrate behaviors that deviate from common challenges encountered by flow battery electrolytes that achieve higher energy densities. However, it should be noted that success shown in redox-species development alone does not guarantee economic or environmental feasibility.

LCA and TEA style studies can help bolster arguments for applied technologies, costs, and environmental impacts that may not be immediately obvious when conducting more fundamental analyses on redox species. As discussed in Chapter 4, analyses on a hypothetical system for nitrate

pollution reduction and ammonia production were carried out. While redox-shuttles based on these systems have shown significant improvement in performance, the technologies employing them remain limited in their economic feasibility for certain applications.

High nitrate concentrations in ground water can lead to destructive algal bloom formations and negative human health impacts. The primary source of this nitrate is ammonia-based fertilizer application in the agricultural industry. Ammonia markets are projected to increase, and the production of ammonia is associated with 1.4% of global CO<sub>2</sub> emissions. Electrochemical catalysts in development for nitrate conversion to ammonia promote the value of energy efficient ammonia production from recycled nitrate. We recognized three individual technologies with potential to be combined for this purpose including: (1) electrodialysis systems that enable electrochemical separation of salts from water using redox shuttles and selective membranes, (2) electrocatalysts that enable energy efficient ammonia productions from waste nitrate, and (3) agrophotovoltaics that provide clean solar energy for the total system, without disturbing farm functions. We initially assessed the potential for nitrate pollution reduction (by recovering nitrate) and CO<sub>2</sub> emissions reduction (by electrocatalytic ammonia production).

To define the eight scenarios and base case, we first looked at standard Haber-Bosch-produced ammonia starting with methane and hydrogen, which was then converted to ammonia, and transported and delivered to the farm system. This defined the conventional ammonia base case. To add in the nitrate capture and conversion boundaries, we use electrodialysis to remove nitrate ions from tile-drainage producing a clean water stream and a nitrate concentrate stream that pass over the electrocatalyst and is converted to ammonia, from there the ammonia will be separated, purified, and stored for later use as fertilizer (offsetting the total fertilizer need from the Haber-Bosch process). The three varied functions or conditions include: (1) function of recovering nitrate

only (i.e., nitrate capture, NC) or both recovery and conversion (i.e., nitrate capture and conversion); (2) the theoretical maximum nitrate recovered (TMNR); and (3) the electrical source between grid electricity or on-site produced solar. All versions of these systems required exceptionally high fixed capital investments and the yearly revenue was not capable of recovering the initial spending over 20 years (the assumed lifespan of the project). The primary conclusion demonstrates that although great advancements in the electrochemical technologies have been made, these technologies make up around 15% of initial costs, and large fractions of costs remained associated with the cost of liquid storage and purification. Ultimately, despite the promise shown by this technology in emissions reductions, they are not economically feasible.

## **5.2 Future Work**

The scope of all intended future work involves the pursuit of a more comprehensive assessment of the pyridinium salts as organic electrolyte materials for RFB application. First, we can add breadth and depth to the fundamental understanding of solution properties such as solubility, viscosity, and conductivity and expand on the dispersion parameter correlation of recent analyses. Second, we must evaluate the existing materials for functional application in RFB systems and identify trends that will guide advancements in redox-species design. The overall objective is to conduct and evaluate experiments that enhance the understanding of molecular design and use these insights to strategically influence RFB performance characteristics of energy density, power density, and capacity fade.

### **5.2.1 Fundamental Investigation of Pyridinium Physicochemical Properties**

Understanding how structural moieties dictate intermolecular interactions and influence solvation behavior will accelerate redox species design. From the pyridinium library, the C-H $\cdots\pi$  interaction correlation describes a single interaction among many complex solvation interactions.

Experiments that can explore the fundamental directions include testing solubility with varying temperature, supporting electrolytes, varying the counterion (e.g.,  $\text{BF}_4^-$ ,  $\text{TFSI}^-$ ) paired with the pyridinium core, and comparing the solubility of the neutral radical pyridinium. Quantifying and correlating useful structure-property relationships between molecular design and solubility will be of particular interest, and additional correlations can be explored to explain other physicochemical properties pertinent to RFBs. Subsequent evaluation of trends in viscosity and conductivity will be necessary to provide a comprehensive assessment of the effect of variables of interest (i.e., temperature, supporting electrolytes, counterions, molecular structure). Furthermore, redox-active materials must stay in solution throughout all intended electron transfer processes. If the neutral radical species (that is generated by reduction during charging) is less soluble than the cationic species, the material could precipitate out of solution, and no longer be accessible for charge-discharge cycling. ROM precipitations would negatively impact capacity fade rates and system efficiencies. Inventive methods must be established to rigorously isolate and test the solubility of the neutral radical.<sup>219,220</sup> The expected instability of the radical species provides a challenge, and new methods of solubility assessment may be required.<sup>221</sup>

Understanding the radical solubility is not only theoretically interesting but will elucidate the effective concentration for each redox species accessible under RFB operating conditions. Similar methods to those described in Chapters 2 and 3, can be used to inform the underlying mechanisms causing resulting solution behaviors. To supplement these new investigations, crystal structures could enable visualization and isolation of specific intermolecular interactions, while proton shifts in NMR studies could clarify the anticipated intermolecular assembly behavior in solution. Beyond pyridinium ROMs, which was of primary focus in this dissertation, newly observed trends and the



associated rationalization of resulting solution behaviors, can be used to develop correlations that can guide molecular design and analogous electrolyte solution development.

### **5.2.2 Technological Feasibility by Electrochemical Assessment**

Further experiments to assess the technological feasibility of pyridinium style anolytes for RFB applications include evaluating performance characteristics such as: electrochemical parameters (e.g., electron transfer coefficients), charge-discharge cycling stability (under flowing conditions), and long-term storage stability of charged pyridiniums. The electrochemical parameters will provide insights about the reaction kinetics that influence the system currents and efficiencies.<sup>60</sup> The assessment of chemical stability under various conditions will inform the functional lifespan for each material, which directly impacts the levelized cost of energy and influences their economic and environmental viability.<sup>14</sup>

As the preliminary electrochemical assessment of pyridiniums has been shown in Chapter 3, understanding the effect of parameters of interest for manipulating solution behaviors will be important. It will be useful to understand the effect of supporting electrolytes, counterions, molecular structure, charge state, and concentration on the previously studied variables (diffusion coefficients) and variables that remain to be assessed (electron transfer coefficients).<sup>222,223</sup> The trends identified that increase understanding in redox potentials, diffusion coefficients, and electron transfer coefficients can be instrumental in improving energy densities and power densities.

Reversible redox species demonstrate the most basic form of electrochemical stability for charge-discharge cycling, and those candidates must be evaluated at variable timescales and conditions to demonstrate highly stable character. The operating conditions of an ideal RFB (e.g., high concentration, long charge/discharge cycles) contrast greatly with the conditions used in

typical cyclic voltammograms (e.g., low concentration, short charge/discharge cycles). Bulk electrolysis experiments more closely replicate operational conditions for materials to demonstrate long-term stability. Bulk electrolysis is a method where a defined fraction of the species in solution undergoes oxidation/reduction by applying a current or voltage and convection (e.g., stirring); after the expected fraction is “charged” the opposite current/voltage is applied to “discharge” the solution. These two charge-discharge steps can be repeated in succession for hours to days, and current/voltage data and various analysis of the resulting solution can quantify the cycling-stability of the species. Robust chemical and electrochemical stability are indicated by high coulombic efficiency, faradaic efficiency, and overall capacity. Each efficiency is a measure of electron accounting between cycles, and capacity fade indicated loss of the redox active species (by crossover or decomposition) over time. Many variables can be probed in bulk electrolysis experiments (e.g., current rate, cut-off voltage, concentration, supporting electrolyte, electrode material, membrane/separator, etc.) each variable indicating electrochemical stability, chemical compatibilities, or the lack thereof.

Beyond bulk electrolysis stability, the charged redox-active species must be stable on longer storage timescales necessary for commercial application and the electrolytes solutions must not undergo parasitic chemical reactions with other RFB system components to preserve the system lifespan. The charged species must be stored in solution for long periods without decomposition. The shelf-storage studies in Chapter 3 provide preliminary data on pyridinium shelf stability but more rigorous evaluation is necessary. Bulk electrolysis testing will indicate this type of stability, and it should be evaluated separately from electrochemical assessment (e.g., NMR, CV, UV-vis). Additionally, system compatibilities will be tested to ensure optimal conditions for scaled-up analysis. First, system components (e.g., seals, tubing, adapters) can be assessed independently

for swelling, fouling, and deterioration with system solutions. Then, compatible components can be assembled in a small-scale flow cell, where an electrochemical cell is paired with external chambers of anolyte and catholyte. Small-scale flow cycling will be an ultimate technical assessment for these pyridinium redox-species, and stability and compatibility data will guide the design of the next generation of pyridinium materials.

Finally, to add valuable perspective concerning the scaled use of pyridinium anolytes we will include technoeconomic and environmental assessments. As we pursue energy solutions that reduce harmful emissions, it is critical to ensure we are not introducing equally problematic waste streams. A proactive approach, evaluating broad-use costs and tangential emissions of pyridinium-based RFBs will supplement fundamental studies and bolster conclusions of anticipated feasibility, as well as provide parameters of comparison with other RFB electrolytes.

### **5.3 Conclusions**

Redox flow batteries are a commercialized, grid-scale energy storage solution that face cost limitations. The redox-active species selected as an RFB anolyte and catholyte influence all performance metrics including energy density, power density, lifespan, and costs. A design space being explored is organic non-aqueous RFBs, which offer the tunability of organic molecules and a wide voltage window of non-aqueous solvents. Within this growing subset of RFBs, there is a need to better understand how molecular structure affects physicochemical properties as well as functional properties. Using a distinct library of pyridinium tetrafluoroborate salts, we probed the relationship of intermolecular interactions in solution and its relationship to maximum solubility. We revealed a single descriptor of solubility, C-H $\cdots\pi$  interactions, from numerous non-correlating descriptors. C-H $\cdots\pi$  interactions provide a simple but powerful direct correlation to maximum solubility and suggest that increasing competition between dispersion forces and electrostatic

forces could be a structural modification targeted to increase solvation. Additionally, we have evaluated the subsequent effect of achieving these elevated concentrations on solution properties such as viscosity and conductivity. Fortunately, these solutions maintain low viscosities and high conductivities at maximum concentrations and demonstrate promise for additional investigation as anolyte materials for RFBs.

Redox-active species designed for RFBs or other applications will benefit from advanced understanding in how to tune their performance. Circumstances where progress in redox-active species performance delivers great improvements, such as electro dialysis, does not guarantee scalable or cost-effective application to all proposed technologies; the global warming and techno-economic analyses of the nitrate recovery and ammonia generation system provides an example of beneficial emissions reductions but infeasible technology costs. Similarly, after electrochemical and scaled technical assessment of pyridinium salts, a broad evaluation of costs or emissions associated with system life cycle stages (e.g., production, operation) when applying pyridiniums at large scales will provide critical information directing future research.

In summary, RFBs are an emerging energy storage technology that could supply the growing energy demand while promoting the use of renewable generation; to increase affordability and promote their widespread adoption, RFB performance and cost metrics must become more competitive. The redox-active species employed in these systems influence all critical parameters (e.g., energy density, power density, lifetime, cost, etc.). Careful development and analysis of redox-active electrolyte libraries can help discern meaningful relationships that will help advance molecular design of optimal compounds for use in these systems.

There are two directions this work can take, adding depth to the understanding of parameters that influence degree of solvation and evaluating the potential for these pyridinium salts to be

scaled for use in RFB technologies. Although these studies are focused on a specific class of organic salt for a distinct application, we must acknowledge that there is broad value in identifying relationships between structural variation and the resulting properties that can be employed for molecular design for a variety of applications.

## BIBLIOGRAPHY

- (1) Darling, R. M.; Gallagher, K. G.; Kowalski, J. A.; Ac, H.; Brushett, F. R. Pathways to Low-Cost Electrochemical Energy Storage: A Comparison of Aqueous and Nonaqueous Flow Batteries †. **2014**. <https://doi.org/10.1039/c4ee02158d>.
- (2) AL Shaqsi, A. Z.; Sopian, K.; Al-Hinai, A. Review of Energy Storage Services, Applications, Limitations, and Benefits. *Energy Reports* **2020**, *6*, 288–306. <https://doi.org/10.1016/j.egy.2020.07.028>.
- (3) Zakeri, B.; Syri, S. Electrical Energy Storage Systems: A Comparative Life Cycle Cost Analysis. *Renewable and Sustainable Energy Reviews* **2015**, *42*, 569–596. <https://doi.org/10.1016/j.rser.2014.10.011>.
- (4) Obama, B. The Irreversible Momentum of Clean Energy. *Science (1979)* **2017**, *355* (6321), 126–129. <https://doi.org/10.1126/science.aam6284>.
- (5) Kittner, N.; Lill, F.; Kammen, D. M. Energy Storage Deployment and Innovation for the Clean Energy Transition. *Nat Energy* **2017**, *2* (9), 1–6. <https://doi.org/10.1038/nenergy.2017.125>.
- (6) Kahan, A.; EIA. EIA Projects Nearly 50% Increase in World Energy Usage by 2050, Led by Growth in Asia - Today in Energy - U.S. Energy Information Administration (EIA). *24.09.2019* **2019**, *2019*, 2018–2021.
- (7) ARPA-E. GRIDS Program Overview. *GRIDS Program Overview* **2010**, 1–12.
- (8) Kahan, A.; EIA. EIA Projects Nearly 50% Increase in World Energy Usage by 2050, Led by Growth in Asia - Today in Energy - U.S. Energy Information Administration (EIA). *24.09.2019* **2019**, *2019*, 2018–2021.
- (9) Aqachmar, Z.; Ben Sassi, H.; Lahrech, K.; Barhdadi, A. Solar Technologies for Electricity Production: An Updated Review. *Int J Hydrogen Energy* **2021**, *46* (60), 30790–30817. <https://doi.org/10.1016/j.ijhydene.2021.06.190>.
- (10) Veers, P.; Dykes, K.; Lantz, E.; Barth, S.; Bottasso, C. L.; Carlson, O.; Clifton, A.; Green, J.; Green, P.; Holttinen, H.; Laird, D.; Lehtomäki, V.; Lundquist, J. K.; Manwell, J.; Marquis, M.; Meneveau, C.; Moriarty, P.; Munduate, X.; Muskulus, M.; Naughton, J.; Pao, L.; Paquette, J.; Peinke, J.; Robertson, A.; Rodrigo, J. S.; Sempreviva, A. M.; Smith, J. C.; Tuohy, A.; Wiser, R. Grand Challenges in the Science of Wind Energy. *Science (1979)* **2019**, *366* (6464). <https://doi.org/10.1126/science.aau2027>.
- (11) Farhadi, M.; Mohammed, O. Energy Storage Technologies for High-Power Applications. *IEEE Trans Ind Appl* **2016**, *52* (3), 1953–1962. <https://doi.org/10.1109/TIA.2015.2511096>.
- (12) Zablocki, A. Energy Storage: Fact Sheet (2019). *Environmental and Energy Study Institute* **2019**, *2040* (February), 1–8.

- (13) Aneke, M.; Wang, M. Energy Storage Technologies and Real Life Applications – A State of the Art Review. *Applied Energy*. Elsevier Ltd October 1, 2016, pp 350–377. <https://doi.org/10.1016/j.apenergy.2016.06.097>.
- (14) Lai, C. S.; Locatelli, G.; Pimm, A.; Tao, Y.; Li, X.; Lai, L. L. A Financial Model for Lithium-Ion Storage in a Photovoltaic and Biogas Energy System ☆. *Appl Energy* **2019**, *251* (January), 113179. <https://doi.org/10.1016/j.apenergy.2019.04.175>.
- (15) ARPA-E. GRIDS Program Overview. *GRIDS Program Overview* **2010**, 1–12.
- (16) Curran, M. A. Life Cycle Assessment: Principles and Practice (EPA/600/R-06/060). *U.S. Environmental Protection Agency* **2006**, *1* (January). <https://doi.org/10.1002/ejoc.201200111>.
- (17) Leung, P.; Li, X.; Ponce De León, C.; Berlouis, L.; Low, C. T. J.; Walsh, F. C. Progress in Redox Flow Batteries, Remaining Challenges and Their Applications in Energy Storage. *RSC Adv* **2012**, *2* (27), 10125–10156. <https://doi.org/10.1039/c2ra21342g>.
- (18) Li, M.; Rhodes, Z.; Cabrera-Pardo, J. R.; Minter, S. D. Recent Advancements in Rational Design of Non-Aqueous Organic Redox Flow Batteries. *Sustain Energy Fuels* **2020**, *4* (9), 4370–4389. <https://doi.org/10.1039/d0se00800a>.
- (19) Dmello, R.; Milshtein, J. D.; Brushett, F. R.; Smith, K. C. Cost-Driven Materials Selection Criteria for Redox Flow Battery Electrolytes. *J Power Sources* **2016**, *330*, 261–272. <https://doi.org/10.1016/j.jpowsour.2016.08.129>.
- (20) Denholm, P.; Jorgenson, J.; Hummon, M.; Palchak, D.; Kirby, B.; Ma, O.; O'malley, M. *The Impact of Wind and Solar on the Value of Energy Storage*; 2013.
- (21) Mehmood, K. K.; Khan, S. U.; Lee, S. J.; Haider, Z. M.; Rafique, M. K.; Kim, C. H. Optimal Sizing and Allocation of Battery Energy Storage Systems with Wind and Solar Power DGs in a Distribution Network for Voltage Regulation Considering the Lifespan of Batteries. *IET Renewable Power Generation* **2017**, *11* (10), 1305–1315. <https://doi.org/10.1049/iet-rpg.2016.0938>.
- (22) Mongird, K.; Viswanathan, V.; Alam, J.; Vartanian, C.; Sprenkle, V.; Baxter, R. 2020 Grid Energy Storage Technology Cost and Performance Assessment. *Energy Storage Grand Challenge Cost and Performance Assessment 2020* **2020**, No. December, 1–20.
- (23) Kwabi, D. G.; Ji, Y.; Aziz, M. J. Electrolyte Lifetime in Aqueous Organic Redox Flow Batteries: A Critical Review. *Chem Rev* **2020**, *120* (14), 6467–6489. <https://doi.org/10.1021/acs.chemrev.9b00599>.
- (24) Bartolozzi, M. Development of Redox Flow Batteries. A Historical Bibliography. *J Power Sources* **1989**, *27* (3), 219–234. [https://doi.org/10.1016/0378-7753\(89\)80037-0](https://doi.org/10.1016/0378-7753(89)80037-0).

- (25) Skyllas-Kazacos, M.; Chakrabarti, M. H.; Hajimolana, S. A.; Mjalli, F. S.; Saleem, M. Progress in Flow Battery Research and Development. *J Electrochem Soc* **2011**, *158* (8), R55. <https://doi.org/10.1149/1.3599565>.
- (26) Sumitomo Electric. Sumitomo Redox Flow Battery Brochure.
- (27) Rodby, K. E.; Carney, T. J.; Ashraf Gandomi, Y.; Barton, J. L.; Darling, R. M.; Brushett, F. R. Assessing the Levelized Cost of Vanadium Redox Flow Batteries with Capacity Fade and Rebalancing. *J Power Sources* **2020**, *460* (December 2019). <https://doi.org/10.1016/j.jpowsour.2020.227958>.
- (28) Li, X.; Zhang, H.; Mai, Z.; Zhang, H.; Vankelecom, I. Ion Exchange Membranes for Vanadium Redox Flow Battery (VRB) Applications. *Energy Environ Sci* **2011**, *4* (4), 1147–1160. <https://doi.org/10.1039/c0ee00770f>.
- (29) Sumitomo Electric. Sumitomo Redox Flow Battery Brochure.
- (30) Winsberg, J.; Hagemann, T.; Janoschka, T.; Hager, M. D.; Schubert, U. S. Redox-Flow Batteries: From Metals to Organic Redox-Active Materials. *Angewandte Chemie - International Edition* **2017**, *56* (3), 686–711. <https://doi.org/10.1002/anie.201604925>.
- (31) Kowalski, J. A.; Su, L.; Milshstein, J. D.; Brushett, F. R. Recent Advances in Molecular Engineering of Redox Active Organic Molecules for Nonaqueous Flow Batteries. *Curr Opin Chem Eng* **2016**, *13*, 45–52. <https://doi.org/10.1016/j.coche.2016.08.002>.
- (32) Wei, X.; Duan, W.; Huang, J.; Zhang, L.; Li, B.; Reed, D.; Xu, W.; Sprenkle, V.; Wang, W. A High-Current, Stable Nonaqueous Organic Redox Flow Battery. *ACS Energy Lett* **2016**, *1* (4), 705–711. <https://doi.org/10.1021/acseenergylett.6b00255>.
- (33) Elgrishi, N.; Rountree, K. J.; McCarthy, B. D.; Rountree, E. S.; Eisenhart, T. T.; Dempsey, J. L. A Practical Beginner's Guide to Cyclic Voltammetry. *J Chem Educ* **2018**, *95* (2), 197–206. <https://doi.org/10.1021/acs.jchemed.7b00361>.
- (34) Wei, X.; Duan, W.; Huang, J.; Zhang, L.; Li, B.; Reed, D.; Xu, W.; Sprenkle, V.; Wang, W. A High-Current, Stable Nonaqueous Organic Redox Flow Battery. *ACS Energy Lett* **2016**, *1* (4), 705–711. <https://doi.org/10.1021/acseenergylett.6b00255>.
- (35) Gong, K.; Fang, Q.; Gu, S.; Li, S. F. Y.; Yan, Y. Nonaqueous Redox-Flow Batteries: Organic Solvents, Supporting Electrolytes, and Redox Pairs. *Energy Environ Sci* **2015**, *8* (12), 3515–3530. <https://doi.org/10.1039/c5ee02341f>.
- (36) Yim, C.-H.; Tam, J.; Soboleski, H.; Abu-Lebdeh, Y. On the Correlation between Free Volume, Phase Diagram and Ionic Conductivity of Aqueous and Non-Aqueous Lithium Battery Electrolyte Solutions over a Wide Concentration Range. *J Electrochem Soc* **2017**, *164* (6), A1002–A1011. <https://doi.org/10.1149/2.1601704jes>.



- (37) Zhong, F.; Yang, M.; Ding, M.; Jia, C. Organic Electroactive Molecule-Based Electrolytes for Redox Flow Batteries: Status and Challenges of Molecular Design. *Front Chem* **2020**, *8* (June), 1–14. <https://doi.org/10.3389/fchem.2020.00451>.
- (38) Li, M.; Rhodes, Z.; Cabrera-Pardo, J. R.; Minter, S. D. Recent Advancements in Rational Design of Non-Aqueous Organic Redox Flow Batteries. *Sustain Energy Fuels* **2020**, *4* (9), 4370–4389. <https://doi.org/10.1039/d0se00800a>.
- (39) Kowalski, J. A.; Su, L.; Milshtein, J. D.; Brushett, F. R. Recent Advances in Molecular Engineering of Redox Active Organic Molecules for Nonaqueous Flow Batteries. *Curr Opin Chem Eng* **2016**, *13*, 45–52. <https://doi.org/10.1016/j.coche.2016.08.002>.
- (40) Prifti, H.; Parasuraman, A.; Winardi, S.; Lim, T. M.; Skyllas-Kazacos, M. Membranes for Redox Flow Battery Applications. *Membranes (Basel)* **2012**, *2* (2), 275–306. <https://doi.org/10.3390/membranes2020275>.
- (41) Li, M.; Rhodes, Z.; Cabrera-Pardo, J. R.; Minter, S. D. Recent Advancements in Rational Design of Non-Aqueous Organic Redox Flow Batteries. *Sustain Energy Fuels* **2020**, *4* (9), 4370–4389. <https://doi.org/10.1039/d0se00800a>.
- (42) Winsberg, J.; Hagemann, T.; Janoschka, T.; Hager, M. D.; Schubert, U. S. Redox-Flow Batteries: From Metals to Organic Redox-Active Materials. *Angewandte Chemie - International Edition* **2017**, *56* (3), 686–711. <https://doi.org/10.1002/anie.201604925>.
- (43) Milshtein, J. D.; Kaur, A. P.; Casselman, M. D.; Kowalski, J. A.; Modekrutti, S.; Zhang, P. L.; Harsha Attanayake, N.; Elliott, C. F.; Parkin, S. R.; Risko, C.; Brushett, F. R.; Odom, S. A. High Current Density, Long Duration Cycling of Soluble Organic Active Species for Non-Aqueous Redox Flow Batteries. *Energy Environ Sci* **2016**, *9* (11), 3531–3543. <https://doi.org/10.1039/c6ee02027e>.
- (44) Attanayake, N. H.; Kowalski, J. A.; Greco, K. V.; Casselman, M. D.; Milshtein, J. D.; Chapman, S. J.; Parkin, S. R.; Brushett, F. R.; Odom, S. A. Tailoring Two-Electron-Donating Phenothiazines to Enable High-Concentration Redox Electrolytes for Use in Nonaqueous Redox Flow Batteries. *Chemistry of Materials* **2019**, *31* (12), 4353–4363. <https://doi.org/10.1021/acs.chemmater.8b04770>.
- (45) Soloveichik, G. L. Flow Batteries: Current Status and Trends. *Chem Rev* **2015**, *115* (20), 11533–11558. <https://doi.org/10.1021/cr500720t>.
- (46) Darling, R. M.; Gallagher, K. G.; Kowalski, J. A.; Ac, H.; Brushett, F. R. Pathways to Low-Cost Electrochemical Energy Storage: A Comparison of Aqueous and Nonaqueous Flow Batteries †. **2014**. <https://doi.org/10.1039/c4ee02158d>.
- (47) Ding, Y.; Zhang, C.; Zhang, L.; Zhou, Y.; Yu, G. Molecular Engineering of Organic Electroactive Materials for Redox Flow Batteries. *Chem Soc Rev* **2018**, *47* (1), 69–103. <https://doi.org/10.1039/c7cs00569e>.

- (48) Lall-Ramnarine, S. I.; Zhao, M.; Rodriguez, C.; Fernandez, R.; Zmich, N.; Fernandez, E. D.; Dhiman, S. B.; Castner, E. W.; Wishart, J. F. Connecting Structural and Transport Properties of Ionic Liquids with Cationic Oligoether Chains. *J Electrochem Soc* **2017**, *164* (8), H5247–H5262. <https://doi.org/10.1149/2.0371708jes>.
- (49) Gong, K.; Fang, Q.; Gu, S.; Li, S. F. Y.; Yan, Y. Nonaqueous Redox-Flow Batteries: Organic Solvents, Supporting Electrolytes, and Redox Pairs. *Energy Environ Sci* **2015**, *8* (12), 3515–3530. <https://doi.org/10.1039/c5ee02341f>.
- (50) Robinson, S. G.; Yan, Y.; Hendriks, K. H.; Sanford, M. S.; Sigman, M. S. Developing a Predictive Solubility Model for Monomeric and Oligomeric Cyclopropenium-Based Flow Battery Catholytes. *J Am Chem Soc* **2019**, *141* (26), 10171–10176. <https://doi.org/10.1021/jacs.9b04270>.
- (51) Zhang, J.; Corman, R. E.; Schuh, J. K.; Ewoldt, R. H.; Shkrob, I. A.; Zhang, L. Solution Properties and Practical Limits of Concentrated Electrolytes for Nonaqueous Redox Flow Batteries. *The Journal of Physical Chemistry C* **2018**, *122* (15), 8159–8172. <https://doi.org/10.1021/acs.jpcc.8b02009>.
- (52) Li, M.; Case, J.; Minter, S. D. Bipolar Redox-Active Molecules in Non-Aqueous Organic Redox Flow Batteries: Status and Challenges. *ChemElectroChem* **2021**, *8* (7), 1215–1232. <https://doi.org/10.1002/CELC.202001584>.
- (53) Kosswattarachchi, A. M.; Cook, T. R. Concentration-Dependent Charge-Discharge Characteristics of Non-Aqueous Redox Flow Battery Electrolyte Combinations. *Electrochim Acta* **2018**, *261*, 296–306. <https://doi.org/10.1016/j.electacta.2017.12.131>.
- (54) Barton, J. L.; Milshtein, J. D.; Hinricher, J. J.; Brushett, F. R. Quantifying the Impact of Viscosity on Mass-Transfer Coefficients in Redox Flow Batteries. *J Power Sources* **2018**, *399*, 133–143. <https://doi.org/10.1016/J.JPOWSOUR.2018.07.046>.
- (55) Zhang, J.; Corman, R. E.; Schuh, J. K.; Ewoldt, R. H.; Shkrob, I. A.; Zhang, L. Solution Properties and Practical Limits of Concentrated Electrolytes for Nonaqueous Redox Flow Batteries. *Journal of Physical Chemistry C* **2018**, *122* (15), 8159–8172. <https://doi.org/10.1021/acs.jpcc.8b02009>.
- (56) Er, S.; Suh, C.; Marshak, M. P.; Aspuru-Guzik, A. Computational Design of Molecules for an All-Quinone Redox Flow Battery. *Chem Sci* **2015**, *6* (2), 885–893. <https://doi.org/10.1039/c4sc03030c>.
- (57) Wedege, K.; Drazevic, E.; Konya, D.; Bontien, A. Organic Redox Species in Aqueous Flow Batteries: Redox Potentials, Solubility and Chemical Stability Supplementary Information. *Nature Publishing Group* **2016**, No. December, 1–13.
- (58) Kwabi, D. G.; Ji, Y.; Aziz, M. J. Electrolyte Lifetime in Aqueous Organic Redox Flow Batteries: A Critical Review. *Chem Rev* **2020**, *120* (14), 6467–6489. <https://doi.org/10.1021/acs.chemrev.9b00599>.

- (59) Li, M.; Rhodes, Z.; Cabrera-Pardo, J. R.; Minter, S. D. Recent Advancements in Rational Design of Non-Aqueous Organic Redox Flow Batteries. *Sustain Energy Fuels* **2020**, *4* (9), 4370–4389. <https://doi.org/10.1039/d0se00800a>.
- (60) Arenas, L. F.; Ponce de León, C.; Walsh, F. C. Engineering Aspects of the Design, Construction and Performance of Modular Redox Flow Batteries for Energy Storage. *J Energy Storage* **2017**, *11*, 119–153. <https://doi.org/10.1016/j.est.2017.02.007>.
- (61) Brushett, F. R.; Aziz, M. J.; Rodby, K. E. On Lifetime and Cost of Redox-Active Organics for Aqueous Flow Batteries. *ACS Energy Lett* **2020**, *5* (3), 879–884. <https://doi.org/10.1021/acsenergylett.0c00140>.
- (62) Goulet, M. A.; Tong, L.; Pollack, D. A.; Tabor, D. P.; Odom, S. A.; Aspuru-Guzik, A.; Kwan, E. E.; Gordon, R. G.; Aziz, M. J. Extending the Lifetime of Organic Flow Batteries via Redox State Management. *J Am Chem Soc* **2020**, *141* (20), 8014–8019. <https://doi.org/10.1021/jacs.8b13295>.
- (63) Faber, G.; Mangin, C.; Sick, V. Life Cycle and Techno-Economic Assessment Templates for Emerging Carbon Management Technologies. *Frontiers in Sustainability* **2021**, *2* (November), 1–16. <https://doi.org/10.3389/frsus.2021.764057>.
- (64) Schmidt, O.; Hawkes, A.; Gambhir, A.; Staffell, I. The Future Cost of Electrical Energy Storage Based on Experience Rates. *Nat Energy* **2017**, *2* (8), 1–8. <https://doi.org/10.1038/NENERGY.2017.110>.
- (65) Darling, R. M. Techno-Economic Analyses of Several Redox Flow Batteries Using Levelized Cost of Energy Storage. *Curr Opin Chem Eng* **2022**, *37*, 100855. <https://doi.org/10.1016/j.coche.2022.100855>.
- (66) Dieterle, M.; Fischer, P.; Pons, M. N.; Blume, N.; Minke, C.; Bischi, A. Life Cycle Assessment (LCA) for Flow Batteries: A Review of Methodological Decisions. *Sustainable Energy Technologies and Assessments* **2022**, *53* (February). <https://doi.org/10.1016/j.seta.2022.102457>.
- (67) Iyer, V. A.; Schuh, J. K.; Montoto, E. C.; Pavan Nemani, V.; Qian, S.; Nagarjuna, G.; Rodríguez-López, J.; Ewoldt, R. H.; Smith, K. C. Assessing the Impact of Electrolyte Conductivity and Viscosity on the Reactor Cost and Pressure Drop of Redox-Active Polymer Flow Batteries. *J Power Sources* **2017**, *361*, 334–344. <https://doi.org/10.1016/j.jpowsour.2017.06.052>.
- (68) Weber, S.; Peters, J. F.; Baumann, M.; Weil, M. Life Cycle Assessment of a Vanadium Redox Flow Battery. *Environ Sci Technol* **2018**, *52* (18), 10864–10873. <https://doi.org/10.1021/acs.est.8b02073>.
- (69) World Energy Council. Five Steps to Energy Storage. Innovation Insights Brief 2020. **2020**, 62.

- (70) Few, S.; Schmidt, O.; Gambhir, A. Energy Access through Electricity Storage: Insights from Technology Providers and Market Enablers. *Energy for Sustainable Development* **2019**, *48*, 1–10. <https://doi.org/10.1016/j.esd.2018.09.008>.
- (71) Unterreiner, L.; Jülch, V.; Reith, S. Recycling of Battery Technologies - Ecological Impact Analysis Using Life Cycle Assessment (LCA). *Energy Procedia* **2016**, *99* (March), 229–234. <https://doi.org/10.1016/j.egypro.2016.10.113>.
- (72) van Langevelde, P. H.; Katsounaros, I.; Koper, M. T. M. Electrocatalytic Nitrate Reduction for Sustainable Ammonia Production. *Joule* **2021**, No. 2020, 1–5. <https://doi.org/10.1016/j.joule.2020.12.025>.
- (73) Horowitz, K.; Ramasamy, V.; Macknick, J.; Margolis, R. Capital Costs for Dual-Use Photovoltaic Installations: 2020 Benchmark for Ground-Mounted PV Systems with Pollinator-Friendly Vegetation, Grazing, and Crops. **2020**, No. December.
- (74) Beh, E. S.; Benedict, M. A.; Desai, D.; Rivest, J. B. A Redox-Shuttled Electrochemical Method for Energy-Efficient Separation of Salt from Water. *ACS Sustain Chem Eng* **2019**, *7* (15), 13411–13417. <https://doi.org/10.1021/acssuschemeng.9b02720>.
- (75) Li, J.; Zhan, G.; Yang, J.; Quan, F.; Mao, C.; Liu, Y.; Wang, B.; Lei, F.; Li, L.; Chan, A. W. M.; Xu, L.; Shi, Y.; Du, Y.; Hao, W.; Wong, P. K.; Wang, J.; Dou, S. X.; Zhang, L.; Yu, J. C. Efficient Ammonia Electrosynthesis from Nitrate on Strained Ruthenium Nanoclusters. *J Am Chem Soc* **2020**, *142* (15), 7036–7046. <https://doi.org/10.1021/jacs.0c00418>.
- (76) Samaroo, S.; Hengesbach, C.; Bruggeman, C.; Carducci, N. G. G.; Mtemeri, L.; Staples, R. J.; Guarr, T.; Hickey, D. P. C–H··· $\pi$  Interactions Disrupt Electrostatic Interactions between Non-Aqueous Electrolytes to Increase Solubility. *Nat Chem* **2023**. <https://doi.org/10.1038/s41557-023-01291-1>.
- (77) Samaroo, S.; Pattillo, A. L.; Servinski, D.; Kruper, W. R.; Carter, D. D.; Guarr, T. F.; Hickey, D. P. Low Viscosity, High Concentration Pyridinium Anolytes for Organic Nonaqueous Redox Flow Batteries. *ACS Applied Energy Materials*. American Chemical Society 2023. <https://doi.org/10.1021/acsaem.3c02370>.
- (78) Samaroo, S.; Hickey, D. P. Electrochemical Ammonia Production from Nitrates in Agricultural Tile Drainage: Technoeconomic and Global Warming Analysis. *AIChE Journal* **2022**, No. July 2022, 1–12. <https://doi.org/10.1002/aic.17969>.
- (79) Luo, J.; Hu, B.; Hu, M.; Zhao, Y.; Liu, T. L. Status and Prospects of Organic Redox Flow Batteries toward Sustainable Energy Storage. *ACS Energy Lett* **2019**, *4* (9), 2220–2240. <https://doi.org/10.1021/acsenerylett.9b01332>.
- (80) Wedege, K.; Dražević, E.; Konya, D.; Bontien, A. Organic Redox Species in Aqueous Flow Batteries: Redox Potentials, Chemical Stability and Solubility. *Sci Rep* **2016**, *6* (November), 1–13. <https://doi.org/10.1038/srep39101>.

- (81) Er, S.; Suh, C.; Marshak, M. P.; Aspuru-Guzik, A. Computational Design of Molecules for an All-Quinone Redox Flow Battery. *Chem Sci* **2015**, *6* (2), 885–893. <https://doi.org/10.1039/c4sc03030c>.
- (82) Sevov, C. S.; Brooner, R. E. M.; Chénard, E.; Assary, R. S.; Moore, J. S.; Rodríguez-López, J.; Sanford, M. S. Evolutionary Design of Low Molecular Weight Organic Anolyte Materials for Applications in Nonaqueous Redox Flow Batteries. *J Am Chem Soc* **2015**, *137* (45), 14465–14472. <https://doi.org/10.1021/jacs.5b09572>.
- (83) Sevov, C. S.; Hickey, D. P.; Cook, M. E.; Robinson, S. G.; Barnett, S.; Minter, S. D.; Sigman, M. S.; Sanford, M. S. Physical Organic Approach to Persistent, Cyclable, Low-Potential Electrolytes for Flow Battery Applications. *J Am Chem Soc* **2017**, *139* (8), 2924–2927. <https://doi.org/10.1021/jacs.7b00147>.
- (84) Reichardt, C.; Welton, T. *Solvents and Solvent Effects in Organic Chemistry*; 2011.
- (85) Hansen, C. M. *Hansen Solubility Parameters: A User's Handbook*; Library of Congress Cataloging-in-Publication Data © 2000 CRC Press LLC, 2000.
- (86) Barton, A. F. M. Solubility Parameters. *Chem Rev* **1975**, *75* (6), 731–753. <https://doi.org/10.1021/cr60298a003>.
- (87) Geysens, P.; Evers, J.; Dehaen, W.; Fransaeer, J.; Binnemans, K. Enhancing the Solubility of 1,4-Diaminoanthraquinones in Electrolytes for Organic Redox Flow Batteries through Molecular Modification. *RSC Adv* **2020**, *10* (65), 39601–39610. <https://doi.org/10.1039/D0RA06851A>.
- (88) Milshtein, J. D.; Kaur, A. P.; Casselman, M. D.; Kowalski, J. A.; Modekrutti, S.; Zhang, P. L.; Harsha Attanayake, N.; Elliott, C. F.; Parkin, S. R.; Risko, C.; Brushett, F. R.; Odom, S. A. High Current Density, Long Duration Cycling of Soluble Organic Active Species for Non-Aqueous Redox Flow Batteries. *Energy Environ Sci* **2016**, *9* (11), 3531–3543. <https://doi.org/10.1039/c6ee02027e>.
- (89) Huang, J.; Cheng, L.; Assary, R. S.; Wang, P.; Xue, Z.; Burrell, A. K.; Curtiss, L. A.; Zhang, L. Liquid Catholyte Molecules for Nonaqueous Redox Flow Batteries. *Adv Energy Mater* **2015**, *5* (6), 1–6. <https://doi.org/10.1002/aenm.201401782>.
- (90) Sevov, C. S.; Hendriks, K. H.; Sanford, M. S. Low-Potential Pyridinium Anolyte for Aqueous Redox Flow Batteries. *Journal of Physical Chemistry C* **2017**, *121* (39), 24376–24380. <https://doi.org/10.1021/acs.jpcc.7b06247>.
- (91) DiMauro, E. F.; Kozłowski, M. C. Phosphabenzene as Electron Withdrawing Phosphine Ligands in Catalysis. *J Chem Soc Perkin 1* **2002**, *2* (3), 439–444. <https://doi.org/10.1039/b101454o>.
- (92) Yue, H.; Zhu, C.; Shen, L.; Geng, Q.; Hock, K. J.; Yuan, T.; Cavallo, L.; Rueping, M. Nickel-Catalyzed C–N Bond Activation: Activated Primary Amines as Alkylating Reagents

- in Reductive Cross-Coupling. *Chem Sci* **2019**, *10* (16), 4430–4435. <https://doi.org/10.1039/C9SC00783K>.
- (93) Sheldrick, G. M. Crystal Structure Refinement with SHELXL. *Acta Crystallogr C Struct Chem* **2015**, *71* (1), 3–8. <https://doi.org/10.1107/S2053229614024218>.
- (94) Sheldrick, G. M. SHELXT – Integrated Space-Group and Crystal-Structure Determination. *Acta Crystallogr A Found Adv* **2015**, *71* (1), 3–8. <https://doi.org/10.1107/S2053273314026370>.
- (95) Dolomanov, O. V.; Bourhis, L. J.; Gildea, R. J.; Howard, J. A. K.; Puschmann, H. OLEX2 : A Complete Structure Solution, Refinement and Analysis Program. *J Appl Crystallogr* **2009**, *42* (2), 339–341. <https://doi.org/10.1107/S0021889808042726>.
- (96) Umezawa, Y.; Tsuboyama, S.; Honda, K.; Uzawa, J.; Nishio, M. CH/  $\pi$  Interaction in the Crystal Structure of Organic Compounds. A Database Study. *Bull Chem Soc Jpn* **1998**, *71* (5), 1207–1213. <https://doi.org/10.1246/bcsj.71.1207>.
- (97) Kawahara, S. I.; Tsuzuki, S.; Uchimaru, T. Theoretical Study of the C-F/ $\pi$  Interaction: Attractive Interaction between Fluorinated Alkane and an Electron-Deficient  $\pi$ -System. *Journal of Physical Chemistry A* **2004**, *108* (32), 6744–6749. <https://doi.org/10.1021/jp047646o>.
- (98) Wheeler, S. E.; Houk, K. N. Substituent Effects in Cation/ $\pi$  Interactions and Electrostatic Potentials above the Centers of Substituted Benzenes Are Due Primarily to Through-Space Effects of the Substituents. *J Am Chem Soc* **2009**, *131* (9), 3126–3127. <https://doi.org/10.1021/ja809097r>.
- (99) Sinnokrot, M. O.; Sherrill, C. D. Substituent Effects in  $\Pi$ - $\pi$  Interactions: Sandwich and T-Shaped Configurations. *J Am Chem Soc* **2004**, *126* (24), 7690–7697. <https://doi.org/10.1021/ja049434a>.
- (100) Cheng, W. C.; Kurth, M. J. The Zincke Reaction. A Review. *Org Prep Proced Int* **2002**, *34* (6), 585–608. <https://doi.org/10.1080/00304940209355784>.
- (101) Sevov, C. S.; Hickey, D. P.; Cook, M. E.; Robinson, S. G.; Barnett, S.; Minter, S. D.; Sigman, M. S.; Sanford, M. S. Physical Organic Approach to Persistent, Cyclable, Low-Potential Electrolytes for Flow Battery Applications. *J Am Chem Soc* **2017**, *139* (8), 2924–2927. <https://doi.org/10.1021/jacs.7b00147>.
- (102) Namazian, M.; Lin, C. Y.; Coote, M. L. Benchmark Calculations of Absolute Reduction Potential of Ferricinium/Ferrocene Couple in Nonaqueous Solutions. *J Chem Theory Comput* **2010**, *6* (9), 2721–2725. <https://doi.org/10.1021/ct1003252>.
- (103) Reichardt, C.; Welton, T. *Solvents and Solvent Effects in Organic Chemistry*; 2011.

- (104) Abraham, M. H.; Le, J. The Correlation and Prediction of the Solubility of Compounds in Water Using an Amended Solvation Energy Relationship. *J Pharm Sci* **1999**, *88* (9), 868–880. <https://doi.org/10.1021/js9901007>.
- (105) Verloop, A.; Hoogenstraaten, W.; Tipker, J. Development and Application of New Steric Substituent Parameters in Drug Design. In *Drug Design*; Academic Press, 1976; Vol. 1962, pp 165–207. <https://doi.org/10.1016/b978-0-12-060307-7.50010-9>.
- (106) Verloop, A. *The Sterimol Approach: Further Development of the Method and New Applications*; International Union of Pure and Applied Chemistry, 1983. <https://doi.org/10.1016/b978-0-08-029222-9.50051-2>.
- (107) Brethomé, A. V.; Fletcher, S. P.; Paton, R. S. Conformational Effects on Physical–Organic Descriptors: The Case of Sterimol Steric Parameters. *ACS Catal* **2019**, *9* (3), 2313–2323. <https://doi.org/10.1021/acscatal.8b04043>.
- (108) Verloop, A.; Hoogenstraaten, W.; Tipker, J. Development and Application of New Steric Substituent Parameters in Drug Design. In *Drug Design*; Academic Press, 1976; Vol. 1962, pp 165–207. <https://doi.org/10.1016/b978-0-12-060307-7.50010-9>.
- (109) Verloop, A. *The Sterimol Approach: Further Development of the Method and New Applications*; International Union of Pure and Applied Chemistry, 1983. <https://doi.org/10.1016/b978-0-08-029222-9.50051-2>.
- (110) Karthikeyan, S.; Ramanathan, V.; Mishra, B. K. Influence of the Substituents on the CH... $\pi$  Interaction: Benzene–Methane Complex. *J Phys Chem A* **2013**, *117* (30), 6687–6694. <https://doi.org/10.1021/jp404972f>.
- (111) Wheeler, S. E.; Seguin, T. J.; Guan, Y.; Doney, A. C. Noncovalent Interactions in Organocatalysis and the Prospect of Computational Catalyst Design. *Acc Chem Res* **2016**, *49* (5), 1061–1069. <https://doi.org/10.1021/acs.accounts.6b00096>.
- (112) Neel, A. J.; Hilton, M. J.; Sigman, M. S.; Toste, F. D. Exploiting Non-Covalent  $\pi$  Interactions for Catalyst Design. *Nature* **2017**, *543* (7647), 637–646. <https://doi.org/10.1038/nature21701>.
- (113) Houser, J.; Kozmon, S.; Mishra, D.; Hammerová, Z.; Wimmerová, M.; Koča, J. The CH– $\pi$  Interaction in Protein–Carbohydrate Binding: Bioinformatics and In Vitro Quantification. *Chemistry – A European Journal* **2020**, *26* (47), 10769–10780. <https://doi.org/10.1002/chem.202000593>.
- (114) Knowles, R. R.; Jacobsen, E. N. Attractive Noncovalent Interactions in Asymmetric Catalysis: Links between Enzymes and Small Molecule Catalysts. *Proc Natl Acad Sci U S A* **2010**, *107* (48), 20678–20685. <https://doi.org/10.1073/pnas.1006402107>.
- (115) Tsuzuki, S.; Honda, K.; Uchimaru, T.; Mikami, M.; Tanabe, K. The Magnitude of the CH/ $\pi$  Interaction between Benzene and Some Model Hydrocarbons. *J Am Chem Soc* **2000**, *122* (15), 3746–3753. <https://doi.org/10.1021/ja993972j>.

- (116) Israelachvili, J. N. Intermolecular and Surface Forces: Third Edition. *Intermolecular and Surface Forces: Third Edition* **2011**, 1–676. <https://doi.org/10.1016/C2011-0-05119-0>.
- (117) Mclachlan, A. D. Effect of the Medium on Dispersion Forces in Liquids. *Discuss Faraday Soc* **1965**, *40* (3218), 239–245. <https://doi.org/https://doi.org/10.1039/DF9654000239>.
- (118) Davey, R. J.; Schroeder, S. L. M.; Ter Horst, J. H. Nucleation of Organic Crystals - A Molecular Perspective. *Angewandte Chemie - International Edition* **2013**, *52* (8), 2166–2179. <https://doi.org/10.1002/anie.201204824>.
- (119) Davey, R. J.; Dent, G.; Mughal, R. K.; Parveen, S. Concerning the Relationship between Structural and Growth Synthons in Crystal Nucleation: Solution and Crystal Chemistry of Carboxylic Acids as Revealed through IR Spectroscopy. *Cryst Growth Des* **2006**, *6* (8), 1788–1796. <https://doi.org/10.1021/cg060058a>.
- (120) Hulme, A. T.; Johnston, A.; Florence, A. J.; Fernandes, P.; Shankland, K.; Bedford, C. T.; Welch, G. W. A.; Sadiq, G.; Haynes, D. A.; Motherwell, W. D. S.; Tocher, D. A.; Price, S. L. Search for a Predicted Hydrogen Bonding Motif - A Multidisciplinary Investigation into the Polymorphism of 3-Azabicyclo[3.3.1]Nonane-2,4-Dione. *J Am Chem Soc* **2007**, *129* (12), 3649–3657. <https://doi.org/10.1021/ja0687466>.
- (121) Tresca, B. W.; Hansen, R. J.; Chau, C. V.; Hay, B. P.; Zakharov, L. N.; Haley, M. M.; Johnson, D. W. Substituent Effects in CH Hydrogen Bond Interactions: Linear Free Energy Relationships and Influence of Anions. *J Am Chem Soc* **2015**, *137* (47), 14959–14967. <https://doi.org/10.1021/jacs.5b08767>.
- (122) Kolling, O. W. Dielectric Characterization of Cosolvent Systems Containing Tetrahydrofuran. **1991**, *94* (3), 107–115.
- (123) Maryott, A. A.; Smith, E. R. *Table of Dielectric Constants of Pure Liquids*; U.S. Government Printing Office.
- (124) Richards, T. W.; Shipley, J. W. THE DIELECTRIC CONSTANTS OF TYPICAL ALIPHATIC AND. **2002**, *622* (1894), 2002–2012.
- (125) Simeral, L.; Amey, R. L. Dielectric Properties of Liquid Propylene Carbonate. **1970**, *74* (7), 1968–1971.
- (126) Pinal, R. Effect of Molecular Symmetry on Melting Temperature and Solubility. *Org. Biomol. Chem.* **2004**, *2*, 2692–2699. <https://doi.org/10.1039/B407105K>.
- (127) Li, Z.; Jiang, T.; Ali, M.; Wu, C.; Chen, W. Recent Progress in Organic Species for Redox Flow Batteries. *Energy Storage Mater* **2022**, *50* (April), 105–138. <https://doi.org/10.1016/j.ensm.2022.04.038>.
- (128) Chen, H.; Cong, G.; Lu, Y. C. Recent Progress in Organic Redox Flow Batteries: Active Materials, Electrolytes and Membranes. *Journal of Energy Chemistry* **2018**, *27* (5), 1304–1325. <https://doi.org/10.1016/j.jechem.2018.02.009>.



- (129) Leung, P.; Li, X.; Ponce De León, C.; Berlouis, L.; Low, C. T. J.; Walsh, F. C. Progress in Redox Flow Batteries, Remaining Challenges and Their Applications in Energy Storage. *RSC Adv* **2012**, *2* (27), 10125–10156. <https://doi.org/10.1039/c2ra21342g>.
- (130) Darling, R. M.; Gallagher, K. G.; Kowalski, J. A.; Ha, S.; Brushett, F. R. Pathways to Low-Cost Electrochemical Energy Storage: A Comparison of Aqueous and Nonaqueous Flow Batteries. *Energy Environ Sci* **2014**, *7* (11), 3459–3477. <https://doi.org/10.1039/C4EE02158D>.
- (131) Barton, J. L.; Milshtein, J. D.; Hinricher, J. J.; Brushett, F. R. Quantifying the Impact of Viscosity on Mass-Transfer Coefficients in Redox Flow Batteries. *J Power Sources* **2018**, *399* (June), 133–143. <https://doi.org/10.1016/j.jpowsour.2018.07.046>.
- (132) Attanayake, N. H.; Kowalski, J. A.; Greco, K. V.; Casselman, M. D.; Milshtein, J. D.; Chapman, S. J.; Parkin, S. R.; Brushett, F. R.; Odom, S. A. Tailoring Two-Electron-Donating Phenothiazines to Enable High-Concentration Redox Electrolytes for Use in Nonaqueous Redox Flow Batteries. *Chemistry of Materials* **2019**, *31* (12), 4353–4363. <https://doi.org/10.1021/acs.chemmater.8b04770>.
- (133) Preet Kaur, A.; Neyhouse, B. J.; Shkrob, I. A.; Wang, Y.; Harsha Attanayake, N.; Kant Jha, R.; Wu, Q.; Zhang, L.; Ewoldt, R. H.; Brushett, F. R.; Odom, S. A. Concentration-Dependent Cycling of Phenothiazine-Based Electrolytes in Nonaqueous Redox Flow Cells. *Chem Asian J* **2023**, *18* (5). <https://doi.org/10.1002/asia.202201171>.
- (134) Robinson, S. G.; Yan, Y.; Hendriks, K. H.; Sanford, M. S.; Sigman, M. S. Developing a Predictive Solubility Model for Monomeric and Oligomeric Cyclopropenium-Based Flow Battery Catholytes. *J Am Chem Soc* **2019**, *141* (26), 10171–10176. <https://doi.org/10.1021/jacs.9b04270>.
- (135) Alotto, P.; Guarnieri, M.; Moro, F. Redox Flow Batteries for the Storage of Renewable Energy: A Review. *Renewable and Sustainable Energy Reviews* **2014**, *29*, 325–335. <https://doi.org/10.1016/j.rser.2013.08.001>.
- (136) Zmpitas, J.; Gross, J. Modified Stokes-Einstein Equation for Molecular Self-Diffusion Based on Entropy Scaling. *Ind Eng Chem Res* **2021**, *60* (11), 4453–4459. [https://doi.org/10.1021/ACS.IECR.0C06090/SUPPL\\_FILE/IE0C06090\\_SI\\_001.PDF](https://doi.org/10.1021/ACS.IECR.0C06090/SUPPL_FILE/IE0C06090_SI_001.PDF).
- (137) Gering, K. L. Prediction of Electrolyte Viscosity for Aqueous and Non-Aqueous Systems: Results from a Molecular Model Based on Ion Solvation and a Chemical Physics Framework. *Electrochim Acta* **2006**, *51* (15), 3125–3138. <https://doi.org/10.1016/j.electacta.2005.09.011>.
- (138) Stumme, N.; Perera, A. S.; Horvath, A.; Ruhunage, S.; Duffy, D. H.; Koltonowski, E. M.; Tupper, J.; Dzierba, C.; McEndaffer, A. D.; Teague, C. M.; Risko, C.; Shaw, S. K. Probing Redox Properties of Extreme Concentrations Relevant for Nonaqueous Redox-Flow Batteries. *ACS Appl Energy Mater* **2022**. <https://doi.org/10.1021/acsaem.2c03712>.

- (139) DiMauro, E. F.; Kozlowski, M. C. Phosphabenzene as Electron Withdrawing Phosphine Ligands in Catalysis. *J Chem Soc Perkin 1* **2002**, *2* (3), 439–444. <https://doi.org/10.1039/b101454o>.
- (140) Yue, H.; Zhu, C.; Shen, L.; Geng, Q.; Hock, K. J.; Yuan, T.; Cavallo, L.; Rueping, M. Nickel-Catalyzed C–N Bond Activation: Activated Primary Amines as Alkylating Reagents in Reductive Cross-Coupling. *Chem Sci* **2019**, *10* (16), 4430–4435. <https://doi.org/10.1039/C9SC00783K>.
- (141) Zmpitas, J.; Gross, J. Modified Stokes-Einstein Equation for Molecular Self-Diffusion Based on Entropy Scaling. *Ind Eng Chem Res* **2021**, *60* (11), 4453–4459. [https://doi.org/10.1021/ACS.IECR.0C06090/ASSET/IMAGES/LARGE/IE0C06090\\_0007.JPG](https://doi.org/10.1021/ACS.IECR.0C06090/ASSET/IMAGES/LARGE/IE0C06090_0007.JPG).
- (142) Elgrishi, N.; Rountree, K. J.; McCarthy, B. D.; Rountree, E. S.; Eisenhart, T. T.; Dempsey, J. L. A Practical Beginner's Guide to Cyclic Voltammetry. *J Chem Educ* **2018**, *95* (2), 197–206. <https://doi.org/10.1021/acs.jchemed.7b00361>.
- (143) Hansch, C.; Leo, A.; Taft, R. W. A Survey of Hammett Substituent Constants and Resonance and Field Parameters. *Chem Rev* **1991**, *91* (2), 165–195. <https://doi.org/10.1021/cr00002a004>.
- (144) Ertl, P. A Web Tool for Calculating Substituent Descriptors Compatible with Hammett Sigma Constants\*\*. *Chemistry–Methods* **2022**, *2* (12), e202200041. <https://doi.org/10.1002/cmtd.202200041>.
- (145) Wang, Y.; Kaur, A. P.; Harsha Attanayake, N.; Yu, Z.; Suduwella, T. M.; Cheng, L.; Odom, S. A.; Ewoldt, R. H. Viscous Flow Properties and Hydrodynamic Diameter of Phenothiazine-Based Redox-Active Molecules in Different Supporting Salt Environments. *Physics of Fluids* **2020**, *32* (8). <https://doi.org/10.1063/5.0010168>.
- (146) Hansch, C.; Leo, A.; Taft, R. W. A Survey of Hammett Substituent Constants and Resonance and Field Parameters. *Chem Rev* **1991**, *91* (2), 165–195. <https://doi.org/10.1021/cr00002a004>.
- (147) Zmpitas, J.; Gross, J. Modified Stokes-Einstein Equation for Molecular Self-Diffusion Based on Entropy Scaling. *Ind Eng Chem Res* **2021**, *60* (11), 4453–4459. <https://doi.org/10.1021/acs.iecr.0c06090>.
- (148) Bandrés, I.; Alcalde, R.; Lafuente, C.; Atilhan, M.; Aparicio, S. On the Viscosity of Pyridinium Based Ionic Liquids: An Experimental and Computational Study. *Journal of Physical Chemistry B* **2011**, *115* (43), 12499–12513. <https://doi.org/10.1021/jp203433u>.
- (149) Holbrey, J. D.; López-Martin, I.; Rothenberg, G.; Seddon, K. R.; Silvero, G.; Zheng, X. Desulfurisation of Oils Using Ionic Liquids: Selection of Cationic and Anionic Components to Enhance Extraction Efficiency. *Green Chemistry* **2008**, *10* (1), 87–92. <https://doi.org/10.1039/b710651c>.

- (150) Verdía, P.; Hernaiz, M.; González, E. J.; Macedo, E. A.; Salgado, J.; Tojo, E. Effect of the Number, Position and Length of Alkyl Chains on the Physical Properties of Polysubstituted Pyridinium Ionic Liquids. *Journal of Chemical Thermodynamics* **2014**, *69*, 19–26. <https://doi.org/10.1016/j.jct.2013.09.028>.
- (151) Robinson, S. G.; Yan, Y.; Hendriks, K. H.; Sanford, M. S.; Sigman, M. S. Developing a Predictive Solubility Model for Monomeric and Oligomeric Cyclopropenium-Based Flow Battery Catholytes. *J Am Chem Soc* **2019**, *141* (26), 10171–10176. <https://doi.org/10.1021/jacs.9b04270>.
- (152) Li, M.; Case, J.; Minter, S. D. Bipolar Redox-Active Molecules in Non-Aqueous Organic Redox Flow Batteries: Status and Challenges. *ChemElectroChem* **2021**, *8* (7), 1215–1232. <https://doi.org/10.1002/celec.202001584>.
- (153) Falkenhagen, H. Viscosity of Electrolytes. *Nature* **1931**, *127* (3203), 439–440.
- (154) Chialvo, A. A.; Crisalle, O. D. Can Jones-Dole's b-Coefficient Be a Consistent Structure-Making/Breaking Marker? Rigorous Molecular-Based Analysis and Critical Assessment of Its Marker Uniqueness. *Journal of Physical Chemistry B* **2021**, *125* (43), 12028–12041. <https://doi.org/10.1021/acs.jpcc.1c07650>.
- (155) Singh, S.; Anil, A. G.; Kumar, V.; Kapoor, D.; Subramanian, S.; Singh, J.; Ramamurthy, P. C. Nitrates in the Environment: A Critical Review of Their Distribution, Sensing Techniques, Ecological Effects and Remediation. *Chemosphere* **2022**, 287 (P1), 131996. <https://doi.org/10.1016/j.chemosphere.2021.131996>.
- (156) Kyriakou, V.; Garagounis, I.; Vourros, A.; Vasileiou, E.; Stoukides, M. An Electrochemical Haber-Bosch Process. *Joule* **2020**, *4* (1), 142–158. <https://doi.org/10.1016/j.joule.2019.10.006>.
- (157) Capdevila-Cortada, M. Electrifying the Haber–Bosch. *Nat Catal* **2019**, *2* (12), 1055. <https://doi.org/10.1038/s41929-019-0414-4>.
- (158) Lu, C.; Zhang, J.; Cao, P.; Hatfield, J. L. Are We Getting Better in Using Nitrogen?: Variations in Nitrogen Use Efficiency of Two Cereal Crops Across the United States. *Earths Future* **2019**, *7* (8), 939–952. <https://doi.org/10.1029/2019EF001155>.
- (159) EPA. *Protecting Water Quality from Agricultural Runoff*; 2003.
- (160) Fowler, D.; Coyle, M.; Skiba, U.; Sutton, M. A.; Cape, J. N.; Reis, S.; Sheppard, L. J.; Jenkins, A.; Grizzetti, B.; Galloway, J. N.; Vitousek, P.; Leach, A.; Bouwman, A. F.; Butterbach-Bahl, K.; Dentener, F.; Stevenson, D.; Amann, M.; Voss, M. The Global Nitrogen Cycle in the Twentyfirst Century. *Philosophical Transactions of the Royal Society B: Biological Sciences* **2013**, *368* (1621). <https://doi.org/10.1098/rstb.2013.0164>.
- (161) Harrison, R.; Webb, J. A Review of the Effect of N Fertilizer Type on Gaseous Emissions. *Advances in Agronomy* **2001**, *73*, 65–108. [https://doi.org/10.1016/s0065-2113\(01\)73005-2](https://doi.org/10.1016/s0065-2113(01)73005-2).

- (162) Christianson, L.; Tyndall, J.; Helmers, M. Financial Comparison of Seven Nitrate Reduction Strategies for Midwestern Agricultural Drainage. *Water Resour Econ* **2013**, 2–3, 30–56. <https://doi.org/10.1016/j.wre.2013.09.001>.
- (163) Alshameri, A.; Ibrahim, A.; Assabri, A. M.; Lei, X.; Wang, H.; Yan, C. The Investigation into the Ammonium Removal Performance of Yemeni Natural Zeolite: Modification, Ion Exchange Mechanism, and Thermodynamics. *Powder Technol* **2014**, 258, 20–31. <https://doi.org/10.1016/j.powtec.2014.02.063>.
- (164) Ma, Z.; Li, Q.; Yue, Q.; Gao, B.; Li, W.; Xu, X.; Zhong, Q. Adsorption Removal of Ammonium and Phosphate from Water by Fertilizer Controlled Release Agent Prepared from Wheat Straw. *Chemical Engineering Journal* **2011**, 171 (3), 1209–1217. <https://doi.org/10.1016/j.cej.2011.05.027>.
- (165) Hua, G.; Salo, M. W.; Schmit, C. G.; Hay, C. H. Nitrate and Phosphate Removal from Agricultural Subsurface Drainage Using Laboratory Woodchip Bioreactors and Recycled Steel Byproduct Filters. *Water Res* **2016**, 102, 180–189. <https://doi.org/10.1016/j.watres.2016.06.022>.
- (166) Griebmeier, V.; Gescher, J. Influence of the Potential Carbon Sources for Field Denitrification Beds on Their Microbial Diversity and the Fate of Carbon and Nitrate. *Front Microbiol* **2018**, 9 (JUN), 1–12. <https://doi.org/10.3389/fmicb.2018.01313>.
- (167) Omer, A. R.; Baker, B. H. Water Quality Improvements from Implementation of Tailwater Recovery Systems. *Sustain Water Resour Manag* **2019**, 5 (2), 703–713. <https://doi.org/10.1007/s40899-018-0249-1>.
- (168) Rodziewicz, J.; Mielcarek, A.; Janczukowicz, W.; Józwiak, T.; Struk – Sokołowska, J.; Bryszewski, K. The Share of Electrochemical Reduction, Hydrogenotrophic and Heterotrophic Denitrification in Nitrogen Removal in Rotating Electrobiological Contactor (REBC) Treating Wastewater from Soilless Cultivation Systems. *Science of the Total Environment* **2019**, 683, 21–28. <https://doi.org/10.1016/j.scitotenv.2019.05.239>.
- (169) Dia, O.; Drogui, P.; Buelna, G.; Dubé, R. Strategical Approach to Prevent Ammonia Formation during Electrocoagulation of Landfill Leachate Obtained from a Biofiltration Process. *Sep Purif Technol* **2017**, 189 (August), 253–259. <https://doi.org/10.1016/j.seppur.2017.08.023>.
- (170) Mielcarek, A.; Bryszewski, K. Ł.; Rodziewicz, J.; Janczukowicz, W. Single-Stage or Two-Stage Bio-Electrochemical Treatment Process of Drainage from Soilless Tomato Cultivation with Alternating Current. *Sep Purif Technol* **2022**, 299 (June). <https://doi.org/10.1016/j.seppur.2022.121762>.
- (171) Kraft, B.; Strous, M.; Tegetmeyer, H. E. Microbial Nitrate Respiration - Genes, Enzymes and Environmental Distribution. *J Biotechnol* **2011**, 155 (1), 104–117. <https://doi.org/10.1016/j.jbiotec.2010.12.025>.

- (172) Strohm, T. O.; Griffin, B.; Zumft, W. G.; Schink, B. Growth Yields in Bacterial Denitrification and Nitrate Ammonification. *Appl Environ Microbiol* **2007**, *73* (5), 1420–1424. <https://doi.org/10.1128/AEM.02508-06>.
- (173) Cole, J. A.; Brown, C. M. Nitrite Reduction to Ammonia by Fermentative Bacteria: A Short Circuit in the Biological Nitrogen Cycle. **2016**, *7*, 1–23.
- (174) Wang, H.; Palys, M.; Daoutidis, P.; Zhang, Q. Optimal Design of Sustainable Ammonia-Based Food-Energy-Water Systems with Nitrogen Management. *ACS Sustain Chem Eng* **2021**, *9* (7), 2816–2834. <https://doi.org/10.1021/acssuschemeng.0c08643>.
- (175) Gao, J.; Shi, N.; Li, Y.; Jiang, B.; Marhaba, T.; Zhang, W. Electrocatalytic Upcycling of Nitrate Wastewater into an Ammonia Fertilizer via an Electrified Membrane. **2022**. <https://doi.org/10.1021/acs.est.1c08442>.
- (176) Vineyard, D.; Hicks, A.; Karthikeyan, K. G.; Barak, P. Economic Analysis of Electrodialysis, Denitrification, and Anammox for Nitrogen Removal in Municipal Wastewater Treatment. *J Clean Prod* **2020**, *262*, 121145. <https://doi.org/10.1016/j.jclepro.2020.121145>.
- (177) Mohammadi, R.; Ramasamy, D. L.; Sillanpää, M. Enhancement of Nitrate Removal and Recovery from Municipal Wastewater through Single- and Multi-Batch Electrodialysis: Process Optimisation and Energy Consumption. *Desalination* **2021**, *498* (April 2020), 114726. <https://doi.org/10.1016/j.desal.2020.114726>.
- (178) Wang, J.; Dai, J.; Jiang, Z.; Chu, B.; Chen, F. Recent Progress and Prospect of Flow-Electrode Electrochemical Desalination System. *Desalination* **2021**, *504* (November 2020), 114964. <https://doi.org/10.1016/j.desal.2021.114964>.
- (179) Ramalingam, K.; Liang, M.; Pyae, N. L. W.; Aung, S. H.; Oo, T. Z.; Srimuk, P.; Ma, J.; Presser, V.; Chen, F.; Waite, T. D. Self-Sustained Visible-Light-Driven Electrochemical Redox Desalination. *ACS Appl Mater Interfaces* **2020**, *12* (29), 32788–32796. <https://doi.org/10.1021/acsaami.0c08286>.
- (180) Chen, F.; Wang, J.; Feng, C.; Ma, J.; David Waite, T. Low Energy Consumption and Mechanism Study of Redox Flow Desalination. *Chemical Engineering Journal* **2020**, *401* (March), 126111. <https://doi.org/10.1016/j.cej.2020.126111>.
- (181) Srimuk, P.; Su, X.; Yoon, J.; Aurbach, D.; Presser, V. Charge-Transfer Materials for Electrochemical Water Desalination, Ion Separation and the Recovery of Elements. *Nat Rev Mater* **2020**, *5* (7), 517–538. <https://doi.org/10.1038/s41578-020-0193-1>.
- (182) Kim, N.; Jeon, J.; Elbert, J.; Kim, C.; Su, X. Redox-Mediated Electrochemical Desalination for Waste Valorization in Dairy Production. *Chemical Engineering Journal* **2022**, *428* (June 2021), 131082. <https://doi.org/10.1016/j.cej.2021.131082>.

- (183) Zhang, X.; Wang, Y.; Liu, C.; Yu, Y.; Lu, S.; Zhang, B. Recent Advances in Non-Noble Metal Electrocatalysts for Nitrate Reduction. *Chemical Engineering Journal* **2021**, *403* (June 2020), 126269. <https://doi.org/10.1016/j.cej.2020.126269>.
- (184) Lu, X.; Song, H.; Cai, J.; Lu, S. Recent Development of Electrochemical Nitrate Reduction to Ammonia: A Mini Review. *Electrochem commun* **2021**, *129*, 107094. <https://doi.org/10.1016/j.elecom.2021.107094>.
- (185) Chen, G. F.; Yuan, Y.; Jiang, H.; Ren, S. Y.; Ding, L. X.; Ma, L.; Wu, T.; Lu, J.; Wang, H. Electrochemical Reduction of Nitrate to Ammonia via Direct Eight-Electron Transfer Using a Copper–Molecular Solid Catalyst. *Nat Energy* **2020**, *5* (8), 605–613. <https://doi.org/10.1038/s41560-020-0654-1>.
- (186) Lu, X.; Song, H.; Cai, J.; Lu, S. Recent Development of Electrochemical Nitrate Reduction to Ammonia: A Mini Review. *Electrochem commun* **2021**, *129*, 107094. <https://doi.org/10.1016/j.elecom.2021.107094>.
- (187) Weselek, A.; Ehmman, A.; Zikeli, S.; Lewandowski, I.; Schindele, S.; Högy, P. Agrophotovoltaic Systems: Applications, Challenges, and Opportunities. A Review. *Agron Sustain Dev* **2019**, *39* (4). <https://doi.org/10.1007/s13593-019-0581-3>.
- (188) Horowitz, K.; Ramasamy, V.; Macknick, J.; Margolis, R. Capital Costs for Dual-Use Photovoltaic Installations: 2020 Benchmark for Ground-Mounted PV Systems with Pollinator-Friendly Vegetation, Grazing, and Crops. **2020**, No. December.
- (189) Basso, B.; Shuai, G.; Zhang, J.; Robertson, G. P. Yield Stability Analysis Reveals Sources of Large-Scale Nitrogen Loss from the US Midwest. *Sci Rep* **2019**, *9* (1), 1–9. <https://doi.org/10.1038/s41598-019-42271-1>.
- (190) Hejase, C. A.; Weitzel, K. A.; Stokes, S. C.; Grauberger, B. M.; Young, R. B.; Arias-Paic, M. S.; Kong, M.; Chae, S.; Bandhauer, T. M.; Tong, T.; Herber, D. R.; Stout, S.; Miara, A.; Huang, Z.; Evans, A.; Kurup, P.; Talmadge, M.; Kandt, A.; Stokes-Draut, J. R.; Macknick, J.; Borch, T.; Dionysiou, D. D. Opportunities for Treatment and Reuse of Agricultural Drainage in the United States. *ACS ES&T Engineering* **2022**, *2* (3), 292–305. <https://doi.org/10.1021/acsestengg.1c00277>.
- (191) Gentry, L. E.; David, M. B.; Below, F. E.; Royer, T. V.; McIsaac, G. F. Nitrogen Mass Balance of a Tile-Drained Agricultural Watershed in East-Central Illinois. *J Environ Qual* **2009**, *38* (5), 1841–1847. <https://doi.org/10.2134/jeq2008.0406>.
- (192) Hejase, C. A.; Weitzel, K. A.; Stokes, S. C.; Grauberger, B. M.; Young, R. B.; Arias-Paic, M. S.; Kong, M.; Chae, S.; Bandhauer, T. M.; Tong, T.; Herber, D. R.; Stout, S.; Miara, A.; Huang, Z.; Evans, A.; Kurup, P.; Talmadge, M.; Kandt, A.; Stokes-Draut, J. R.; Macknick, J.; Borch, T.; Dionysiou, D. D. Opportunities for Treatment and Reuse of Agricultural Drainage in the United States. *ACS ES&T Engineering* **2022**, *2* (3), 292–305. <https://doi.org/10.1021/acsestengg.1c00277>.

- (193) Lee, C.; Herbek, J.; Murdock, L.; Schwab, G.; Green, J. D.; Martin, J.; Sciences, S. Corn and Soybean Production Calendar. *University of Kentucky Extension* **2007**, 12.
- (194) Gentry, L. E.; David, M. B.; Smith, K. M.; Kovacic, D. A. Nitrogen Cycling and Tile Drainage Nitrate Loss in a Corn/Soybean Watershed. *Agric Ecosyst Environ* **1998**, 68 (1–2), 85–97. [https://doi.org/10.1016/S0167-8809\(97\)00139-4](https://doi.org/10.1016/S0167-8809(97)00139-4).
- (195) Gentry, L. E.; David, M. B.; Below, F. E.; Royer, T. V.; McIsaac, G. F. Nitrogen Mass Balance of a Tile-Drained Agricultural Watershed in East-Central Illinois. *J Environ Qual* **2009**, 38 (5), 1841–1847. <https://doi.org/10.2134/jeq2008.0406>.
- (196) National Agricultural Statistics Service. Farms and Land in Farms 2020 Summary. *United States Department of Agriculture* **2020**, No. February, 2.
- (197) Ferraz, F. M.; Povinelli, J.; Vieira, E. M. Ammonia Removal from Landfill Leachate by Air Stripping and Absorption. *Environmental Technology (United Kingdom)* **2013**, 34 (15), 2317–2326. <https://doi.org/10.1080/09593330.2013.767283>.
- (198) Bonmatí, A.; Flotats, X. Air Stripping of Ammonia from Pig Slurry: Characterisation and Feasibility as a Pre- or Post-Treatment to Mesophilic Anaerobic Digestion. *Waste Management* **2003**, 23 (3), 261–272. [https://doi.org/10.1016/S0956-053X\(02\)00144-7](https://doi.org/10.1016/S0956-053X(02)00144-7).
- (199) (US), D. of E. *Guide to the Federal Investment Tax Credit for Commercial Solar Photovoltaics*; 2020.
- (200) Weselek, A.; Ehmann, A.; Zikeli, S.; Lewandowski, I.; Schindele, S.; Högy, P. Agrophotovoltaic Systems: Applications, Challenges, and Opportunities. A Review. *Agron Sustain Dev* **2019**, 39 (4). <https://doi.org/10.1007/s13593-019-0581-3>.
- (201) Vought, R. T. *2021 Discount Rates for OMB Circular No. A-94*; 2021.
- (202) Soil Survey Staff. *Natural Resources Conservation Service, United States Department of Agriculture*. Web Soil Survey. <http://websoilsurvey.nrcs.usda.gov/app/>.
- (203) Sullivan, W. G.; Wicks, E. M.; Luxhoj, J. T. *Engineering Economy*, 12th Editi.; 2003.
- (204) Bouldin, J. L.; Bickford, N. A.; Stroud, H. B.; Guha, G. S. Tailwater Recovery Systems for Irrigation: Benefit/Cost Analysis and Water Resource Conservation Technique in Northeast Arkansas. *J Ark Acad Sci* **2004**, 58, 23–31.
- (205) Bostian, M. B.; Barnhart, B. L.; Kurkalova, L. A.; Jha, M. K.; Whittaker, G. W. Bilevel Optimization of Conservation Practices for Agricultural Production. *J Clean Prod* **2021**, 300, 126874. <https://doi.org/10.1016/j.jclepro.2021.126874>.
- (206) Segerson, K.; Wu, J. J. Nonpoint Pollution Control: Inducing First-Best Outcomes through the Use of Threats. *J Environ Econ Manage* **2006**, 51 (2), 165–184. <https://doi.org/10.1016/j.jeem.2005.04.007>.

- (207) Downing, P. B.; White, L. J. Innovation in Pollution Control. *J Environ Econ Manage* **1986**, *13* (1), 18–29. [https://doi.org/10.1016/0095-0696\(86\)90014-8](https://doi.org/10.1016/0095-0696(86)90014-8).
- (208) Omer, A. R.; Henderson, J. E.; Falconer, L.; Kröger, R.; Allen, P. J. Economic Analyses of Implemented Tailwater Recovery Systems in the Lower Mississippi Alluvial Valley. *Sustain Water Resour Manag* **2019**, *5* (2), 901–919. <https://doi.org/10.1007/s40899-018-0266-0>.
- (209) Berthouex, P. M. Evaluating Economy of Scale. **1972**, *44* (11), 2111–2119.
- (210) Kettani, M.; Bandelier, P.; Technico-économique, I. De; Énergétiques, S.; Atomique, É.; Alternatives, É.; Des, C. E. A. Techno-Economic Assessment of Solar Energy Coupling with Large-Scale Desalination Plant : The Case of Morocco. *Desalination* **2020**, *494* (June), 114627. <https://doi.org/10.1016/j.desal.2020.114627>.
- (211) Obama, B. The Irreversible Momentum of Clean Energy. *Science (1979)* **2017**, *355* (6321), 126–129. <https://doi.org/10.1126/science.aam6284>.
- (212) EPA, E. P. A. Climate Change Indicators: U.S. and Global Precipitation. *Climate Change Indicators in the United States* **2016**, No. August 2016, 22.
- (213) Omer, A. R.; Henderson, J. E.; Falconer, L.; Kröger, R.; Allen, P. J. Economic Costs of Using Tailwater Recovery Systems for Maintaining Water Quality and Irrigation. *J Environ Manage* **2019**, *235* (June 2018), 186–193. <https://doi.org/10.1016/j.jenvman.2019.01.038>.
- (214) Bouldin, J. L.; Bickford, N. A.; Stroud, H. B.; Guha, G. S. Tailwater Recovery Systems for Irrigation: Benefit/Cost Analysis and Water Resource Conservation Technique in Northeast Arkansas. *J Ark Acad Sci* **2004**, *58*, 23–31.
- (215) Popp, J.; Wailes, E.; Young, K.; Smartt, J. Assessing the Benefits Of On-Farm Reservoirs and Tail-Water Recovery Systems. **2004**, 1–16.
- (216) Popp, J.; Wailes, E.; Young, K.; Smartt, J.; Intarapapong, W. Use of On-Farm Reservoirs in Rice Production: Results from the MARORA Model. *Journal of Agricultural and Applied Economics* **2003**, *35* (2), 371–379. <https://doi.org/10.1017/s1074070800021337>.
- (217) Osmond, D. L.; Hoag, D. L. K.; Luloff, A. E.; Meals, D. W.; Neas, K. Farmers' Use of Nutrient Management: Lessons from Watershed Case Studies. *J Environ Qual* **2015**, *44* (2), 382–390. <https://doi.org/10.2134/jeq2014.02.0091>.
- (218) USDA. *USDA Announces Plans for \$ 250 Million Investment to Support Innovative American-made Fertilizer to give US Farmers more choices in the Marketplace.* <https://www.usda.gov/media/press-releases/2022/03/11/usda-announces-plans-250-million-investment-support-innovative>.
- (219) Sevov, C. S.; Hickey, D. P.; Cook, M. E.; Robinson, S. G.; Barnett, S.; Minter, S. D.; Sigman, M. S.; Sanford, M. S. Physical Organic Approach to Persistent, Cyclable, Low-



- Potential Electrolytes for Flow Battery Applications. *J Am Chem Soc* **2017**, *139* (8), 2924–2927. <https://doi.org/10.1021/jacs.7b00147>.
- (220) Liao, F.; Huang, W.; Chen, B.; Ding, Z.; Li, X.; Su, H.; Wang, T.; Wang, Y.; Miao, H.; Zhang, X.; Luo, Y.; Yang, J.; Zhang, G. Are Pyridinium Ylides Radicals? *Chemical Communications* **2020**, *56* (76), 11287–11290. <https://doi.org/10.1039/d0cc04604c>.
- (221) Li, M.; Odom, S. A.; Pancoast, A. R.; Robertson, L. A.; Vaid, T. P.; Agarwal, G.; Doan, H. A.; Wang, Y.; Suduwella, T. M.; Bheemireddy, S. R.; Ewoldt, R. H.; Assary, R. S.; Zhang, L.; Sigman, M. S.; Minteer, S. D. Experimental Protocols for Studying Organic Non-Aqueous Redox Flow Batteries. *ACS Energy Lett* **2021**, *6* (11), 3932–3943. <https://doi.org/10.1021/acsenergylett.1c01675>.
- (222) Bard, A. J.; Faulkner, L. R. *Electrochemical Methods*, 2nd editio.; 2019; Vol. 2. <https://doi.org/10.1038/s41929-019-0277-8>.
- (223) Nicholson, R. S.; Shain, I. *Theory of Stationary Electrode Polarography Single Scan and Cyclic Methods Applied to Reversible, Irreversible, and Kinetic Systems*; UTC, 1964; Vol. 01.
- (224) Zaniwski, A. M.; Reinholz, D. Increasing STEM Success: A near-Peer Mentoring Program in the Physical Sciences. *Int J STEM Educ* **2016**, *3* (1). <https://doi.org/10.1186/s40594-016-0043-2>.
- (225) DiMauro, E. F.; Kozlowski, M. C. Phosphabenzene as Electron Withdrawing Phosphine Ligands in Catalysis. *J Chem Soc Perkin 1* **2002**, *2* (3), 439–444. <https://doi.org/10.1039/b101454o>.
- (226) Yue, H.; Zhu, C.; Shen, L.; Geng, Q.; Hock, K. J.; Yuan, T.; Cavallo, L.; Rueping, M. Nickel-Catalyzed C–N Bond Activation: Activated Primary Amines as Alkylating Reagents in Reductive Cross-Coupling. *Chem Sci* **2019**, *10* (16), 4430–4435. <https://doi.org/10.1039/C9SC00783K>.
- (227) Ertl, P. A Web Tool for Calculating Substituent Descriptors Compatible with Hammett Sigma Constants\*\*. *Chemistry-Methods* **2022**, *2* (12), 1–6. <https://doi.org/10.1002/cmt.202200041>.
- (228) Li, J.; Zhan, G.; Yang, J.; Quan, F.; Mao, C.; Liu, Y.; Wang, B.; Lei, F.; Li, L.; Chan, A. W. M.; Xu, L.; Shi, Y.; Du, Y.; Hao, W.; Wong, P. K.; Wang, J.; Dou, S. X.; Zhang, L.; Yu, J. C. Efficient Ammonia Electrosynthesis from Nitrate on Strained Ruthenium Nanoclusters. *J Am Chem Soc* **2020**, *142* (15), 7036–7046. <https://doi.org/10.1021/jacs.0c00418>.
- (229) Mayo, M.; Collier, Z. A.; Winton, C.; Chappell, M. A. Data-Driven Method to Estimate Nonlinear Chemical Equivalence. *PLoS One* **2015**, *10* (7), 1–24. <https://doi.org/10.1371/journal.pone.0130494>.

- (230) Drury, C. F.; McKenney, D. J.; Findlay, W. I.; Gaynor, J. D. Division S-6-Soil & Water Management & Conservation. *Soil Sci. Soc. Am.* **1993**, 797–802.
- (231) Sawyer, J.; Many, A.; City, G. Estimating Nitrogen Losses. *Integrated Crop Management News* **2011**, 482 (14), 100–103.
- (232) Kladvico, E.; of Agronomy, D.; University, P. Soil Drainage and Nitrate Losses to Surface Waters. 2–6.
- (233) Zhou, M.; Butterbach-Bahl, K. Assessment of Nitrate Leaching Loss on a Yield-Scaled Basis from Maize and Wheat Cropping Systems. *Plant Soil* **2014**, 374 (1–2), 977–991. <https://doi.org/10.1007/s11104-013-1876-9>.
- (234) Beh, E. S.; Benedict, M. A.; Desai, D.; Rivest, J. B. A Redox-Shuttled Electrochemical Method for Energy-Efficient Separation of Salt from Water. *ACS Sustain Chem Eng* **2019**, 7 (15), 13411–13417. <https://doi.org/10.1021/acssuschemeng.9b02720>.
- (235) Facanha, C.; Horvath, A. Environmental Assessment of Freight Transportation in the U.S. *International Journal of Life Cycle Assessment* **2006**, 11 (4), 229–239. <https://doi.org/10.1065/lca2006.02.244>.
- (236) Smith, C.; Hill, A. K.; Torrente-Murciano, L. Current and Future Role of Haber-Bosch Ammonia in a Carbon-Free Energy Landscape. *Energy Environ Sci* **2020**, 13 (2), 331–344. <https://doi.org/10.1039/c9ee02873k>.
- (237) Weidema, B. P. Multi-User Test of the Data Quality Matrix for Product Life Cycle Inventory Data. *International Journal of Life Cycle Assessment* **1998**, 3 (5), 259–265. <https://doi.org/10.1007/BF02979832>.

## **APPENDIX A: CHAPTER 2 SUPPLEMENTAL INFORMATION**

### **A.1. Other Supplementary Materials for Chapter 2 include the following:**

Metrical parameters for the structures are available free of charge from the Cambridge Crystallographic Data Centre under reference numbers CCDC-2162134, 2163981, 2165226, 2157789, 2155765, 2155982, 2162102, 2156178, 2163473, 2155992, 2155704, 2156211, 2156206, 2155715, 2167771, 2157809, 2166708, 2168227, 2157813, 2156563, 2156214, 2158012

## A.2. Solubility Measurement Walkthrough

### Description & Figures

**Weigh material into 4 mL vials.** The mass used was determined for a target concentration of 0.25 mM for the stock solution based on volumetric flask being used (50 mL).

*Note: For the precision scale the last digit fluctuated, to ensure accuracy measurements were repeated until the value settled within +/- 0.02 mg of the target mass. This step was done precisely due to the defined volume of the volumetric flask.*

*Note: All solutions in this procedure were made in triplicate, except for the saturated solution.*

**Make stock solutions.** Material in the vial was transferred to volumetric flask by diluting with solvent and transferring by pipette. The small vial was rinsed with solvent and transferred to volumetric flask. This was repeated at least five to seven times to ensure all material in vial was transferred. Then solvent was added to flask until the meniscus aligned with the 50 mL line on the flask. The flask was shaken to ensure a homogeneous solution.

**Make calibration solutions.** The stock solution was diluted to a needed concentration for the first set, and then diluted by half for four subsequent dilutions. Dilutions were completed using Eppendorf pipettes (10 mL, 5 mL, 1 mL).



Most calibration sets were made by diluting 5 mL of stock to 20 mL to make the most concentrated calibration sample (A1). Subsequently, 5 mL of A1 was taken and diluted to 10 mL to make A2, etc., until A5 is made. As shown below, the final volumes were: A1 (15 mL), A2 (5mL), A3 (5mL), A4 (5mL), A5 (10 mL).



*Note: Eppendorf pipettes and 20 mL syringes can be used for dilution with no significant difference in calculated results. For this procedure Eppendorf pipettes were selected to make most calibration solutions.*

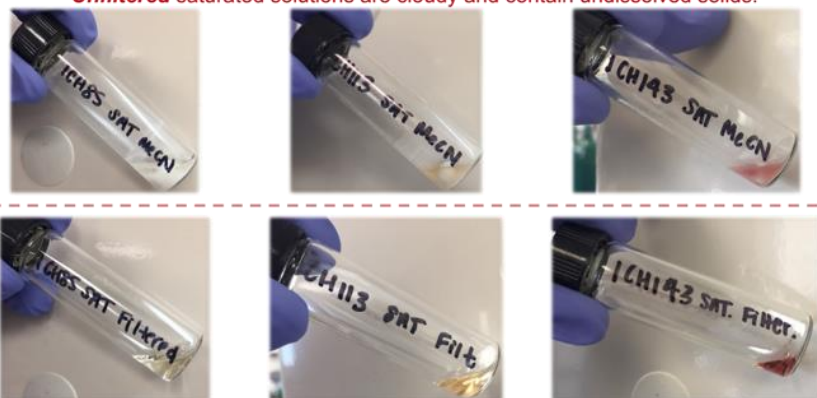
**Make the saturated solution.** Approximately 0.5 mL acetonitrile was added to a 4 mL vial with a stir bar, then slowly solid material was added until the solution became cloudy and further added material did not dissolve. The solution was stirred for 30 minutes after each addition of material, then the solution was re-evaluated.

*Note: This process took significantly longer for materials with very high solubility.*

*Note: The temperature of the room was recorded. The mixtures were NEVER heated to increase dissolution. The goal was to identify the solubility at the room temperature, NOT a super saturated solubility.*

**Filter saturated solution.** The connection of a syringe needle was packed with at least two small layers of Whatman 1 filter paper. The cloudy saturated solution was pulled into a 1 mL syringe (no needle). The Whatman packed syringe needle was connected to the filled syringe and then the solution was gently pressed through the filter paper into a clean 4 mL vial. This filtered solution was transparent, and free of any undissolved solids.

**Unfiltered** saturated solutions are cloudy and contain undissolved solids.



**Filtered** saturated solutions are clear, transparent, and contain no solids.

*Note: Compressing unfiltered saturated solution (with lots of sediments) too quickly can cause a significant pressure to build up and may cause the needle to be ejected from the end of the syringe. Gentle filtration is especially important for materials with high solubility.*

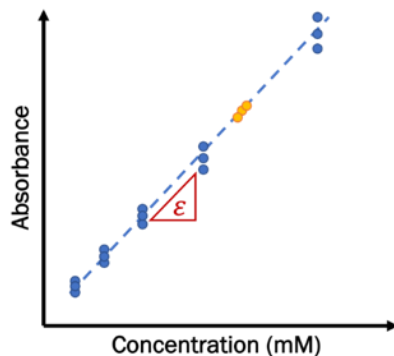
**Dilute the saturated solution.** The small volume of filtered saturated solution was diluted to a larger volume, targeting a concentration in the middle of the calibration curve. This often required two to three consecutive dilutions from the concentrated solution because the calibration solutions were very dilute.

**Identify the wavelength for solution absorbance measurements.**

The stock solution was diluted by approximately four times; this diluted solution was added to a cuvette, which was used to measure the solution's UV-vis absorbance spectrum. The maximum wavelength was identified for each pyridinium salt and was used for all subsequent measurements.

**Record solvent baseline.** A pure solvent baseline absorbance reading was collected. This baseline was set for all following solution measurements.

**Work-up absorbance data.** Maximum absorbance (absorbance units) was plotted versus pyridinium concentration (mM) at the selected wavelength for each of the 15 solutions in the calibration set. This resulted in a linear relationship. The slope of this line gave the molar absorptivity constant ( $\epsilon$  [L/(cm\*mol)]).



$$A = \epsilon l c$$

Known: Path Length (1cm) →  $\epsilon$   
Known: Concentration →  $c$   
Slope:  
Molar Absorptivity  
(L/cm\* $\text{mol}$ )

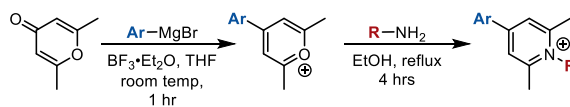
*\*Refer to Beer-Lambert's law for a further explanation of this relationship*

**Back-calculate saturated solution concentration.** Absorbances of the dilution set were related to a corresponding concentration using the linear calibration curve. Rearrangement of the linear equation was used to solve for concentration from the absorbance values. Concentration of the saturated solutions was then back calculated from this measurement.

**Report solubility and error.** The average and standard deviation for three measurements was calculated. Error propagation of the calibration curve and dilution solutions were calculated to report the solubility (mM) +/- one standard deviation (mM)).

*Note: Procedures to determine solubility using both glass (Hamilton Co.) and disposable plastic syringes were tested and compared (data not shown). It was determined that there were no notable differences between results among Eppendorf pipettes, glass syringes, and disposable plastic syringes.*

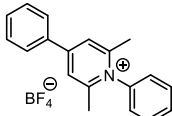
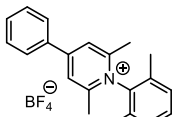
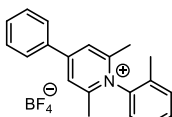
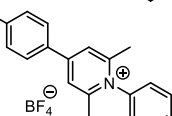
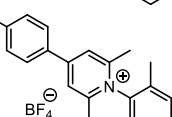
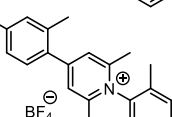
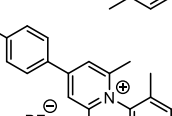
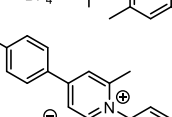
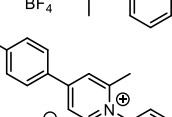
**Table A.1. Pyridinium Tetrafluoroborate Solubility in Pure Acetonitrile at 22 °C.**



Pyridinium Salt			synthetic yield	C-H... $\pi$ parameter ( $\Sigma d^6$ )	solubility / mol L <sup>-1</sup> in acetonitrile	Pyridinium Salt					
#	Ar	R				#	Ar	R	synthetic yield	C-H... $\pi$ parameter ( $\Sigma d^6$ )	solubility / mol L <sup>-1</sup> in acetonitrile
1			85%	0.0003	0.53 ± 0.06	13			58%	0	0.43 ± 0.09
2			85%	0	0.30 ± 0.02	14			27%	0.006	2.1 ± 0.2
3			70%	-	1.2 ± 0.1	15			74%	0	0.32 ± 0.03
4			86%	0	0.36 ± 0.01	16			67%	0.0012	0.55 ± 0.05
5			63%	0.0027	0.99 ± 0.02	17			69%	0.0032	1.01 ± 0.09
6			84%	0	0.45 ± 0.03	18			55%	0.0023	1.01 ± 0.07
7			83%	0.0016	0.75 ± 0.02	19			68%	0.0035	1.03 ± 0.09
8			39%	0.0020	0.56 ± 0.05	20			66%	0.0025	1.06 ± 0.03
9			79%	0	0.42 ± 0.01	21			37%	0.0005	0.41 ± 0.02
10			74%	0.0021	1.00 ± 0.02	22			33%	0.0041	1.35 ± 0.03
11			63%	0.0028	0.97 ± 0.04	23			40%	0.0037	1.13 ± 0.04
12			76%	0.0028	1.08 ± 0.01	24			64%	-	1.20 ± 0.04



**Table A.2. Representative pyridinium tetrafluoroborate solubilities in acetonitrile, tetrahydrofuran (THF), cyclohexanone, and propylene carbonate at 22 °C.**

#	Pyridinium Salt	C-H... $\pi$ parameter ( $\Sigma d^6$ )	solubility at 22 °C / mol L <sup>-1</sup>			
			acetonitrile	THF	cyclohexanone	propylene carbonate
1		0.0003	0.53 ± 0.06	0.0011 ± 0.0002	0.023 ± 0.001	0.59 ± 0.01
2		0	0.30 ± 0.02	0.00040 ± 0.00002	0.0087 ± 0.0005	0.33 ± 0.01
5		0.0027	0.99 ± 0.02	0.0039 ± 0.0002	0.12 ± 0.01	0.84 ± 0.01
6		0	0.45 ± 0.03	0.0010 ± 0.0002	0.013 ± 0.001	0.33 ± 0.01
10		0.0021	1.00 ± 0.02	0.0111 ± 0.0004	0.078 ± 0.001	0.92 ± 0.01
12		0.0028	1.10 ± 0.01	0.00210 ± 0.00004	0.049 ± 0.001	0.74 ± 0.03
14		0.006	2.1 ± 0.2	0.0037 ± 0.0002	0.140 ± 0.005	1.01 ± 0.05
16		0.0012	0.55 ± 0.05	0.0016 ± 0.0001	0.016 ± 0.001	0.45 ± 0.01
20		0.0024	1.10 ± 0.03	0.0071 ± 0.0002	0.108 ± 0.003	0.85 ± 0.06

**Table A.3. Table of pyridinium compounds and their respective experimentally measured and computationally determined redox potentials.** All calculated values were determined from DFT optimized structures [B3LYP/6-31+(d,p)] with CPCM in acetonitrile. In relating the measured and computed redox potentials, as plotted in the main text figure Fig. 3C, a value of -4.86 V is a correction constant used and all potentials are referenced versus the standard ferrocene/ferrocenium reduction potential in acetonitrile.

<b>Compound</b>	<b>E<sub>measured</sub></b> (V vs. Fc/Fc <sup>+</sup> )	<b>E<sub>calculated</sub></b> (V vs. Fc/Fc <sup>+</sup> )	<b>E<sub>calculated,correction</sub></b> (V vs. Fc/Fc <sup>+</sup> )
1	-1.60	-1.60	-1.60
2	-1.60	-1.61	-1.61
3	-1.54	-1.56	-1.59
4	-1.61	-1.63	-1.61
5	-1.60	-1.61	-1.60
6	-1.64	-1.62	-1.61
7	-1.63	-1.65	-1.63
9	-1.65	-1.65	-1.63
12	-1.72	-1.78	-1.72
13	-1.66	-1.72	-1.68
14	-1.69	-1.75	-1.70
15	-1.61	-1.64	-1.62
17	-1.68	-1.73	-1.69
18	-1.62	-1.67	-1.64
19	-1.67	-1.64	-1.63
20	-1.66	-1.65	-1.63
21	-1.70	-1.75	-1.70
22	-1.74	-1.80	-1.74
23	-1.77	-1.84	-1.76

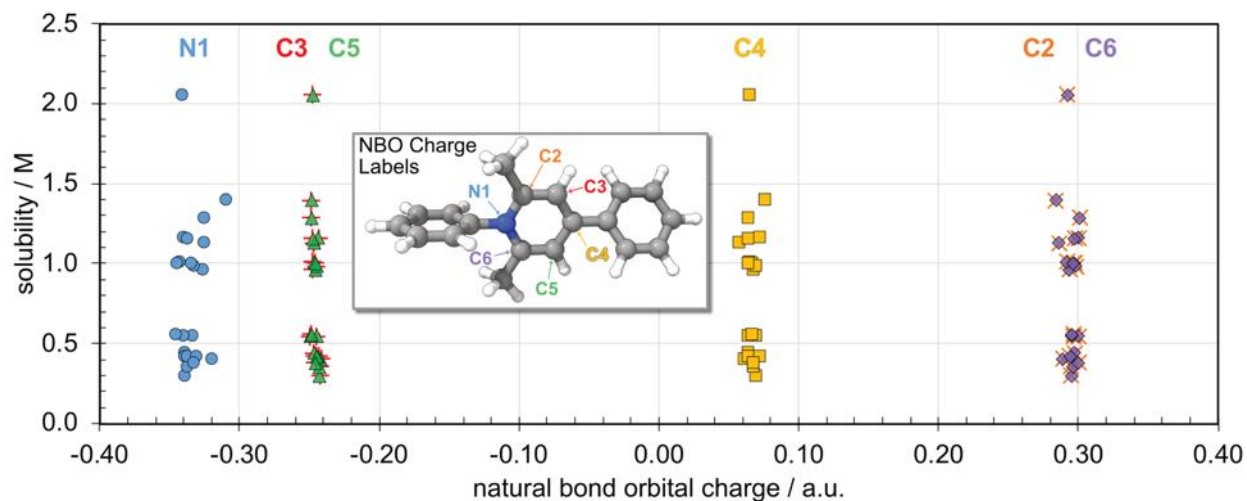


**Figure A.1.** Natural bond orbital (NBO) charge (corresponding labels shown in top middle panel) obtained using DFT modelling of the pyridinium molecules depict a complete absence of correlation with measured solubility. All values were determined from DFT optimized structures [B3LYP/6-31+(d,p)] with CPCM in acetonitrile. Solubility reported mean values +/- SD with  $n = 3$  for all compounds except for compound 17 ( $n = 5$ ), compound 24 ( $n = 5$ ), and compound 14 ( $n = 9$ ).

**Table A.4. Natural bond orbital (NBO) charge (plotted in Fig. S2) obtained using DFT modelling of the pyridinium molecules depict a complete absence of correlation with measured solubility. All values were determined from DFT optimized structures [B3LYP/6-31+(d,p)] with CPCM in acetonitrile.**

Compound	Pyridinium Solubility	NBO Charge – Pyridinium Ring						NBO Charge – 4-Phenyl Ring					
	M	N1	C2	C3	C4	C5	C6	C1	C2	C3	C4	C5	C6
1	0.6	-0.33	0.30	-0.25	0.07	-0.25	0.30	-0.09	-0.21	-0.24	-0.22	-0.24	-0.21
2	0.3	-0.34	0.30	-0.24	0.07	-0.24	0.30	-0.09	-0.21	-0.24	-0.22	-0.24	-0.21
3	1.2	-0.34	0.30	-0.24	0.07	-0.24	0.30	-0.09	-0.21	-0.24	-0.22	-0.24	-0.21
4	0.4	-0.34	0.30	-0.24	0.07	-0.24	0.30	-0.09	-0.21	-0.24	-0.22	-0.24	-0.21
5	1.0	-0.33	0.30	-0.25	0.07	-0.25	0.30	-0.09	-0.21	-0.24	-0.22	-0.24	-0.21
6	0.4	-0.34	0.30	-0.25	0.06	-0.25	0.30	-0.09	-0.20	-0.24	-0.01	-0.24	-0.21
7	0.4	-0.34	0.29	-0.24	0.07	-0.24	0.29	-0.09	-0.20	-0.24	-0.01	-0.24	-0.20
8	0.6	-0.35	0.30	-0.25	0.07	-0.25	0.30	-0.11	-0.20	-0.28	0.35	-0.32	-0.19
9	0.4	-0.34	0.29	-0.25	0.06	-0.25	0.29	-0.09	-0.21	-0.24	-0.01	-0.24	-0.21
10	1.0	-0.34	0.30	-0.25	0.06	-0.25	0.30	-0.09	-0.21	-0.24	-0.01	-0.24	-0.21
11	1.0	-0.33	0.29	-0.25	0.07	-0.25	0.29	-0.08	-0.01	-0.23	-0.01	-0.25	-0.21
13	0.4	-0.33	0.29	-0.25	0.07	-0.25	0.29	-0.08	0.00	-0.23	-0.01	-0.25	-0.21
14	2.1	-0.34	0.29	-0.25	0.07	-0.25	0.29	-0.11	-0.20	-0.28	0.35	-0.32	-0.19
15	0.4	-0.33	0.30	-0.25	0.07	-0.25	0.30	-0.09	-0.21	-0.24	-0.22	-0.24	-0.21
16	0.6	-0.34	0.30	-0.25	0.06	-0.25	0.30	-0.11	-0.20	-0.03	0.35	-0.32	-0.19
17	1.0	-0.34	0.29	-0.25	0.07	-0.25	0.29	-0.11	-0.20	-0.28	0.35	-0.32	-0.19
18	1.0	-0.35	0.30	-0.25	0.07	-0.25	0.30	-0.09	-0.20	-0.24	-0.01	-0.24	-0.20
19	1.3	-0.33	0.30	-0.25	0.06	-0.25	0.30	-0.09	-0.21	-0.24	-0.01	-0.24	-0.21
20	1.2	-0.34	0.30	-0.25	0.06	-0.25	0.30	-0.09	-0.20	-0.24	-0.01	-0.24	-0.21
21	0.4	-0.32	0.29	-0.24	0.06	-0.24	0.29	-0.10	-0.21	-0.24	-0.24	-0.24	-0.21
22	1.4	-0.31	0.28	-0.25	0.08	-0.25	0.28	-0.11	-0.20	-0.28	-0.01	-0.28	-0.20
23	1.1	-0.33	0.29	-0.25	0.06	-0.25	0.29	-0.11	-0.19	-0.32	0.34	-0.28	-0.20

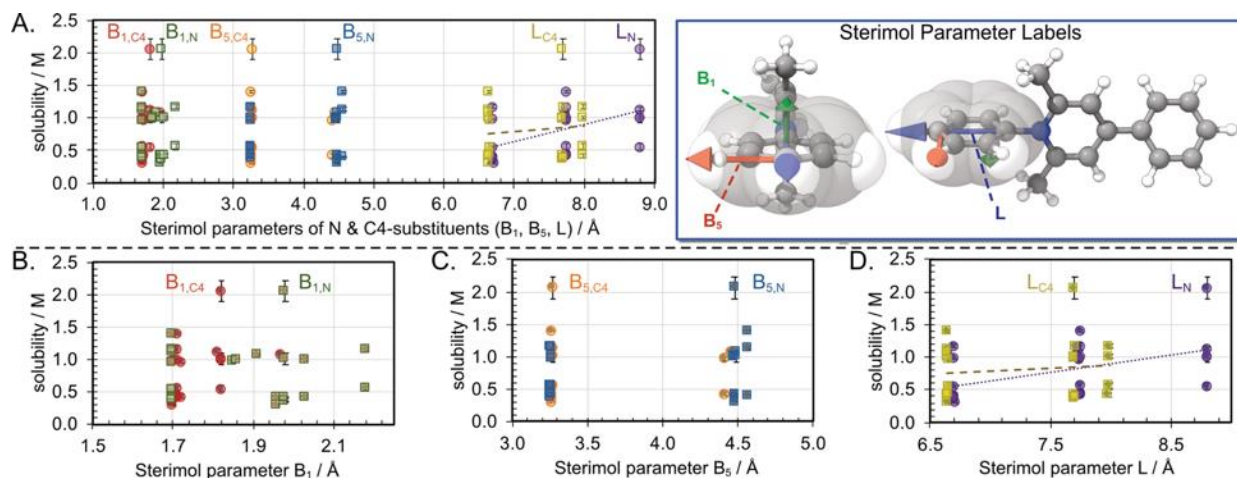


**Figure A.2. A series of Sterimol parameters (B<sub>1</sub>, B<sub>5</sub>, and L) that describe steric substituent properties shows no correlation with measured solubility (A).** The Sterimol parameter (B) B<sub>1</sub> is the minimum width of the molecule from a defined atom, (C) B<sub>5</sub> is the maximum width of the molecule from a defined atom, and (D) L is the bond length between the defined atom and the first atom in the substituent.<sup>108,109</sup> The corresponding molecular labels shown in top right panel. Sterimol parameter values were determined from DFT optimized pyridinium structures [B3LYP/6-31+(d,p)] with CPCM in acetonitrile. Solubility reported mean values +/- SD with n = 3 for all compounds except for compound **17** (n = 5), compound **24** (n = 5), and compound **14** (n = 9).

**Table A.5. Sterimol parameters (B1, B5, and L) that describe steric substituent properties (plotted in Figure A.1) obtained using DFT modelling of the pyridinium molecules depict a complete absence of correlation with measured solubility. All values were determined from DFT optimized structures [B3LYP/6-31+(d,p)] with CPCM in acetonitrile.**

Compound	Pyridinium	N-Position Substituent			4-Position Substituent		
	Solubility M	B <sub>1</sub> / Å	B <sub>5</sub> / Å	L / Å	B <sub>1</sub> / Å	B <sub>5</sub> / Å	L / Å
<b>1</b>	0.6	1.7	3	7	1.7	3	7
<b>2</b>	0.3	2.0	4	7	1.7	3	7
<b>3</b>	1.2	2.2	3	8	1.7	3	7
<b>4</b>	0.4	2.0	4	8	1.7	3	7
<b>5</b>	1.0	1.9	4	8	1.7	3	7
<b>6</b>	0.4	1.7	3	7	1.7	3	8
<b>7</b>	0.4	2.0	4	7	1.7	3	8
<b>8</b>	0.6	2.2	3	8	1.7	3	8
<b>9</b>	0.4	2.0	4	8	1.7	3	8
<b>10</b>	1.0	1.9	4	8	1.7	3	8
<b>11</b>	1.0	1.7	3	7	1.7	4	8
<b>13</b>	0.4	2.0	3	8	1.7	4	8
<b>14</b>	2.1	2.0	4	8	1.8	3	9
<b>15</b>	0.4	1.7	3	8	1.7	3	7
<b>16</b>	0.6	1.7	3	7	1.8	3	9
<b>17</b>	1.0	2.0	4	7	1.8	3	9
<b>18</b>	1.0	2.0	3	8	1.8	3	9
<b>20</b>	1.2	1.7	3	8	1.7	3	8
<b>21</b>	0.4	1.7	5	7	1.7	3	7
<b>22</b>	1.4	1.7	5	7	1.7	3	8
<b>23</b>	1.1	1.7	5	7	1.8	3	9

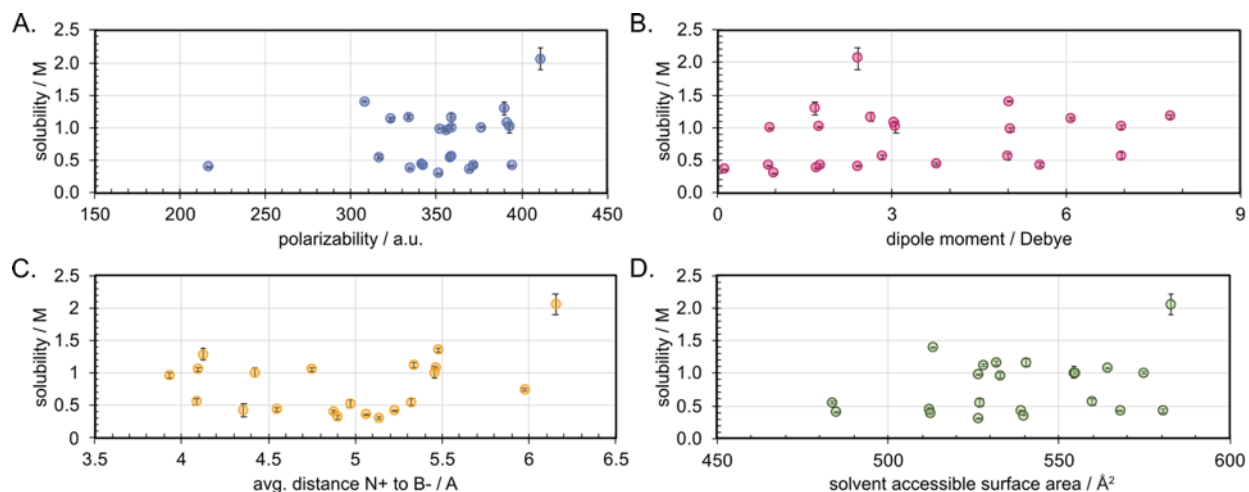


**Figure A.3. Additional computationally determined or crystal structure-derived parameters selected to represent electronic variations pyridinium derivatives.** (A) polarizability, (B) dipole moment, (C) avg. distance between pyridinium ( $N^+$ ) and tetrafluoroborate ( $B^-$ ), and (D) solvent accessible surface area are shown to have zero appreciable relationship with measured pyridinium solubility in acetonitrile. Solubility reported mean values  $\pm$  SD with  $n = 3$  for all compounds except for compound 17 ( $n = 5$ ), compound 24 ( $n = 5$ ), and compound 14 ( $n = 9$ ).

**Table A.6.** Additional computationally determined or crystal-structure derived parameters (plotted in Figure A.2) selected to represent electronic variations pyridinium derivatives.

Compound	Pyridinium Solubility	Solvent Accessible Surface Area	Dipole Moment Magnitude	Polarizability	Avg. Distance Between N <sup>+</sup> and B <sup>-</sup>
	M	Å <sup>2</sup>	Debye	(a.u.)	Å
1	0.6	484	3	317	4.97
2	0.3	527	1	351	5.13
3	1.2	532	8	334	-
4	0.4	540	0	370	5.06
5	1.0	527	1	352	-
6	0.4	512	4	341	4.55
7	0.4	539	2	342	5.97
8	0.6	560	7	358	4.08
9	0.4	568	1	394	5.23
10	1.0	555	2	376	4.75
11	1.0	533	5	356	3.93
13	0.4	581	6	372	4.36
14	2.1	583	2	411	6.15
15	0.4	512	2	335	4.90
16	0.6	527	5	358	5.33
17	1.0	554	3	393	5.46
18	1.0	575	7	358	4.42
19	1.3	-	2	390	4.12
20	1.2	541	3	359	4.10
21	0.4	485	2	217	4.88
22	1.4	513	5	308	5.48
23	1.1	528	6	323	5.34



#### A.4. Explicit C-H $\cdots\pi$ Interactions

Individual intermolecular  $\pi$  interactions used in the calculation of the C-H $\cdots\pi$  parameters ( $\Sigma d^6$ ) are provided from Figure A.4 to Figure A.19. Compounds in which no C-H $\cdots\pi$  interactions were identified are not included in this set of figures.

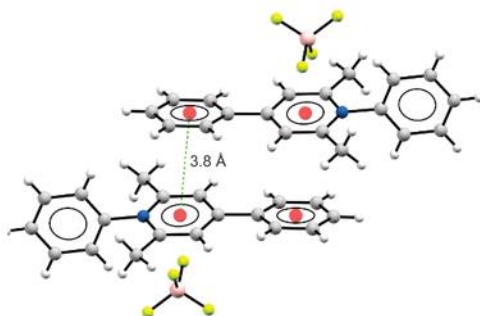


**Figure A.4.**  $\pi$ - $\pi$  interaction observed in the crystal structure of N-phenyl-4-phenyl-2,6-dimethylpyridinium tetrafluoroborate, **1**.

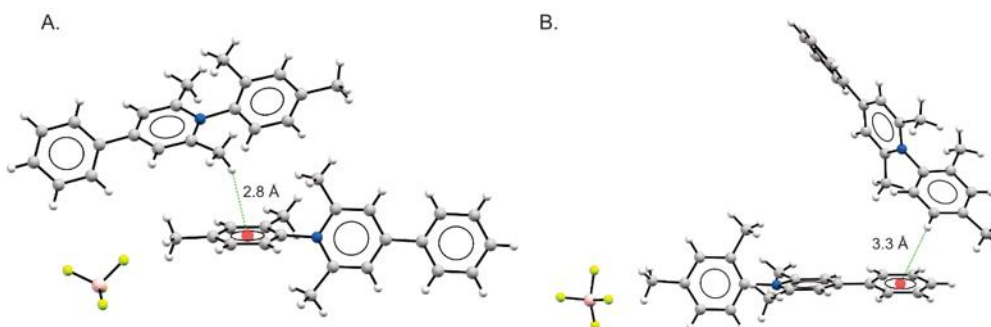


**Figure A.5.** (A)/(B) C-H $\cdots\pi$  interactions observed in the crystal structure of N-(2,4-xylyl)-4-phenyl-2,6-dimethylpyridinium tetrafluoroborate, **5**.

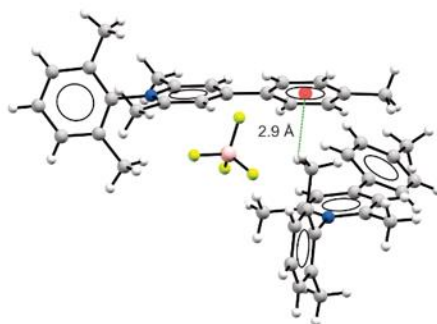


**Figure A.6.** C-H $\cdots\pi$  interaction observed in the crystal structure of N-(2,6-xylyl)-4-(p-tolyl)-2,6-dimethylpyridinium tetrafluoroborate, **7**.

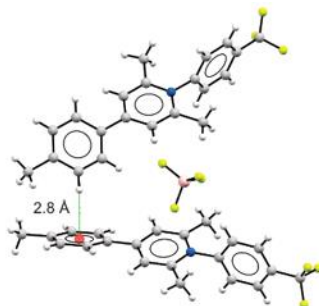


**Figure A.7.** C-H... $\pi$  interaction observed in the crystal structure of N-(p-trifluoromethylphenyl)-4-(p-tolyl)-2,6-dimethylpyridinium tetrafluoroborate, **8**.

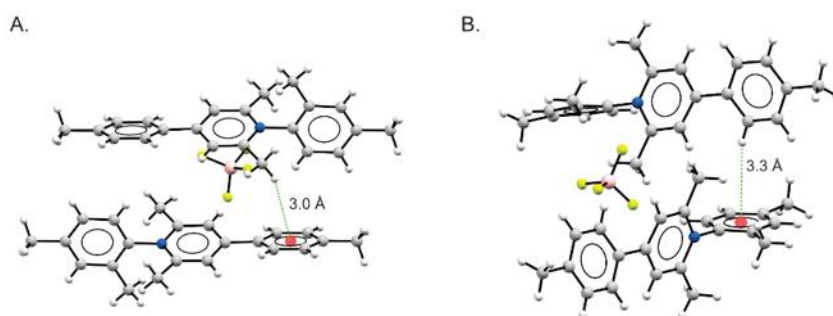


**Figure A.8.** (A)/(B) C-H...p interactions observed in the crystal structure of N-(2,4-xylyl)-4-(p-tolyl)-2,6-dimethylpyridinium tetrafluoroborate, **10**.

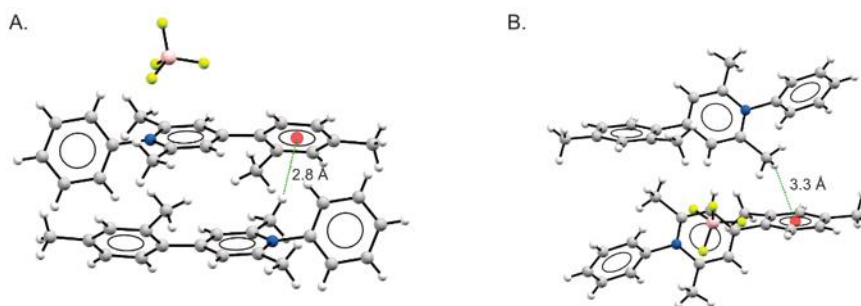


**Figure A.9.** (A)/(B) C-H...p interactions observed in the crystal structure of N-phenyl-4-(2,4-xylyl)-2,6-dimethylpyridinium tetrafluoroborate, **11**.



**Figure A.10.** (A)/(B)/(C) C-H...p interactions observed in the crystal structure of N-(2,6-xylyl)-4-(2,4-xylyl)-2,6-dimethylpyridinium tetrafluoroborate, **12**.

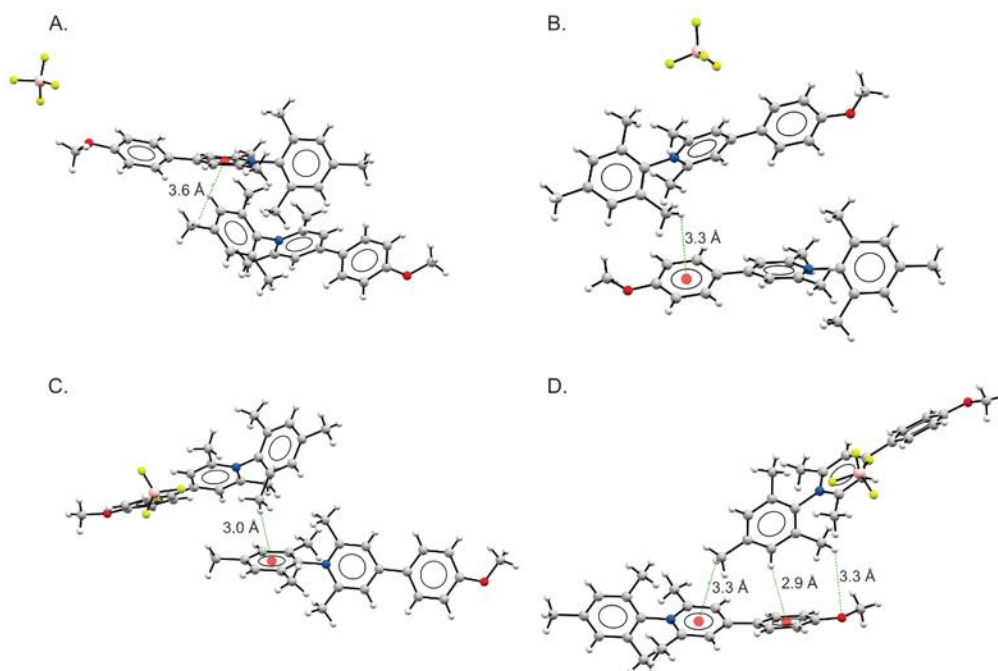


**Figure A.11.** (A)/(B)/(C)/(D) C-H...p interactions observed in the crystal structure of N-(mesityl)-4-(p-methoxyphenyl)-2,6-dimethylpyridinium tetrafluoroborate, **14**.

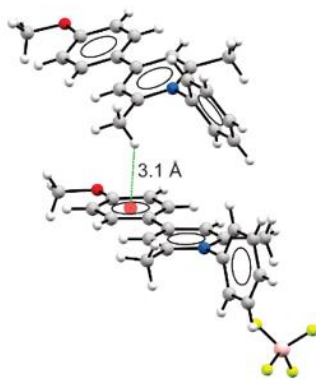


**Figure A.12.** C-H...p interaction observed in the crystal structure of N-phenyl-4-(p-methoxyphenyl)-2,6-dimethylpyridinium tetrafluoroborate, **16**.

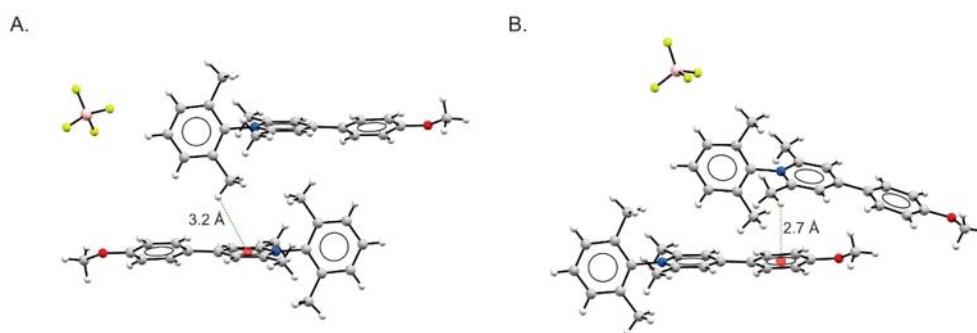


**Figure A.13.** (A)/(B) C-H...p interactions observed in the crystal structure of N-(2,6-xylyl)-4-(p-methoxyphenyl)-2,6-dimethylpyridinium tetrafluoroborate, **17**.

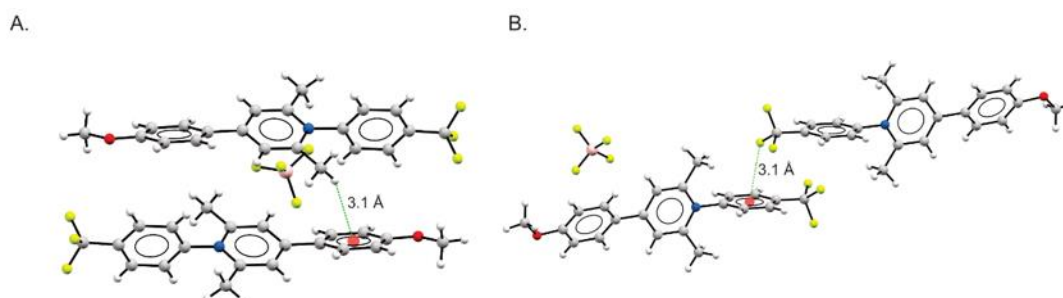


**Figure A.14.** (A) C-H... $\pi$  interaction and (B) C-F...p interaction observed in the crystal structure of N-(p-trifluoromethylphenyl)-4-(p-methoxyphenyl)-2,6-dimethylpyridinium tetrafluoroborate, **18**.

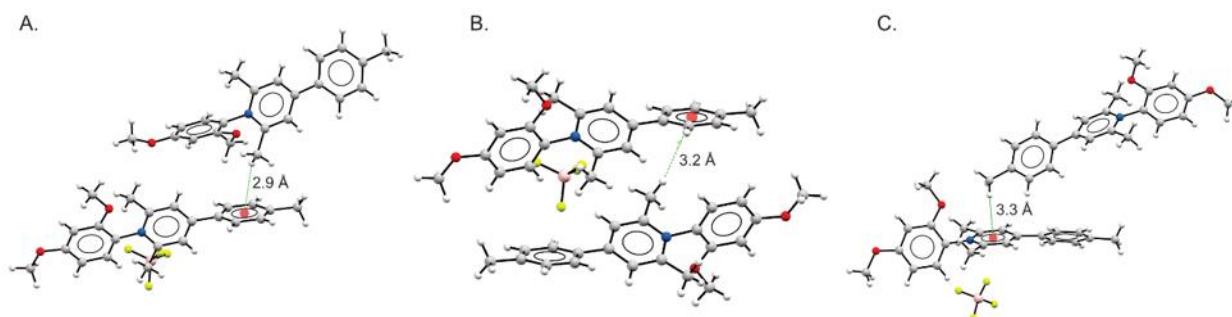


**Figure A.15.** (A)/(B)/(C) C-H... $\pi$  interactions observed in the crystal structure of N-(2,4-dimethoxybenzene)-4-(p-tolyl)-2,6-dimethylpyridinium tetrafluoroborate, **19**.

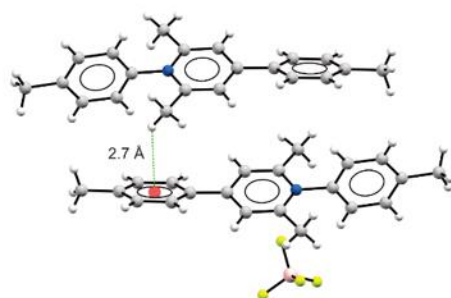


**Figure A.16.** C-H $\cdots$  $\pi$  interaction observed in the crystal structure of N-(p-tolyl)-4-(p-tolyl)-2,6-dimethylpyridinium tetrafluoroborate, **20**.

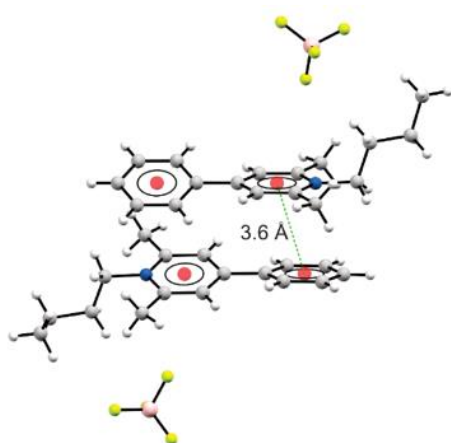


**Figure A.17.**  $\pi$ - $\pi$  interaction observed in the crystal structure of N-butyl-4-(p-phenyl)-2,6-dimethylpyridinium tetrafluoroborate, **21**.

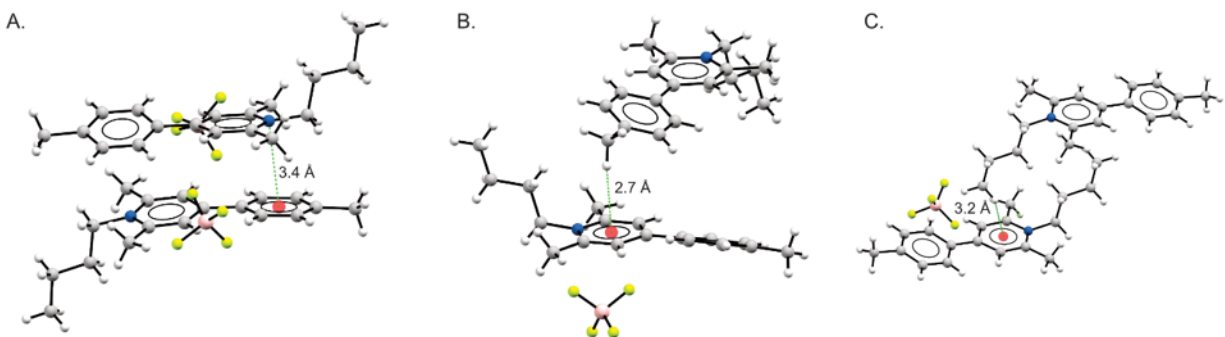


**Figure A.18.** (A) Cation- $\pi$ , and (B)/(C) C-H $\cdots$  $\pi$  interactions observed in the crystal structure of N-butyl-4-(p-tolyl)-2,6-dimethylpyridinium tetrafluoroborate, **22**.

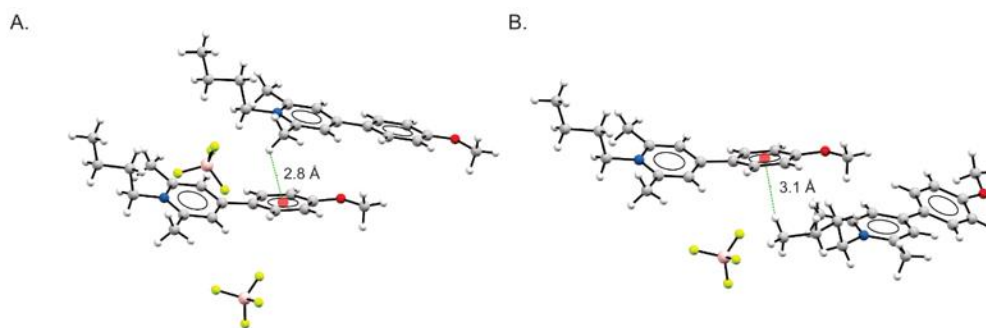


**Figure A.19.** (A)/(B) C-H... $\pi$  interactions observed in the crystal structure of N-butyl-4-(p-methoxyphenyl)-2,6-dimethylpyridinium tetrafluoroborate, **23**.

### A.5. General Procedure: Synthesis of Pyrylium Intermediates

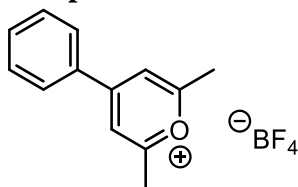
All pyryliums were synthesized following a modified procedure reported by DiMauro and Kozlowski.<sup>224</sup> In an oven-dried 250 mL round bottom flask, 2,6-dimethyl- $\gamma$ -pyrone was dissolved in THF under nitrogen. The stirring solution was cooled to 5 °C via ice bath, then one equivalent of phenylmagnesium bromide (in a 1 M solution with THF) was added dropwise. The reaction mixture was subsequently allowed to warm to room temperature while stirring over an hour. The crude mixture was poured over a boron trifluoride diethyl etherate solution to yield a yellow precipitate which was filtered and washed with diethyl ether. The product was purified by recrystallization in a 1:1 water/methanol mixture.

### A.6. General Procedure: Synthesis of Pyridinium Tetrafluoroborate Salts

All pyridiniums were synthesized following a modified procedure from Yue, *et al.*<sup>225</sup>

#### A.6.1. Pyrylium Synthesis

##### Compound SI-A



##### 2,6-dimethyl-4-phenylpyrylium tetrafluoroborate (SI-A)

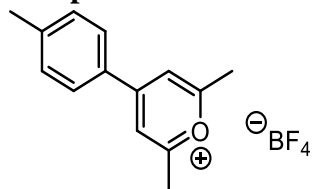
An oven dried 250 mL round bottom flask was charged with a magnetic stir bar before dissolving 2,6-dimethyl- $\gamma$ -pyrone (2.0 g, 0.016 mol) in THF (75 mL) while under nitrogen. After cooling the solution to 5 °C via ice bath, phenylmagnesium bromide as a 1 M solution in THF (16 mL, 0.016 mol) was added dropwise. The solution was allowed to warm to room temperature over an hour. The crude solution was then poured over boron trifluoride diethyl etherate (5.92 mL, 0.048 mol) to yield a yellow precipitate which was filtered and washed with diethyl ether. After recrystallizing in 1:1 water:methanol, the product was isolated as yellow crystals (3.0157 g, 0.011 mol) in 69% yield.

**Physical State:** yellow crystalline solid.

**<sup>1</sup>H NMR (500 MHz, Acetonitrile-*d*<sub>3</sub>):**  $\delta$  8.19 (s, 2H), 8.15 – 8.05 (m, 2H), 7.91 – 7.80 (m, 1H), 7.78 – 7.68 (m, 2H), 2.90 (s, 6H).

**<sup>13</sup>C NMR (126 MHz, Acetonitrile-*d*<sub>3</sub>):**  $\delta$  178.46, 166.25, 135.45, 130.25, 129.35, 118.55, 20.88

### Compound SI-B



#### 4-(*p*-tolyl)-2,6-dimethylpyrylium tetrafluoroborate (SI-B)

An oven dried 500 mL round bottom flask was charged with a magnetic stir bar before dissolving 2,6-dimethyl- $\gamma$ -pyrone (8.0 g, 0.065 mol) in THF (225 mL) while under nitrogen. After cooling the solution to 5 °C via ice bath, *p*-tolylmagnesium bromide as a 1 M solution in THF (65 mL, 0.065 mol) was added dropwise. The solution was allowed to warm to room temperature over an hour. The crude solution was then poured over boron trifluoride diethyl etherate (24 mL, 0.195 mol) to yield an orange precipitate which was filtered and washed with diethyl ether. After recrystallizing in 1:1 water:methanol, the product was isolated as orange crystals (11.45 g, 0.0415 mol) in 64% yield.

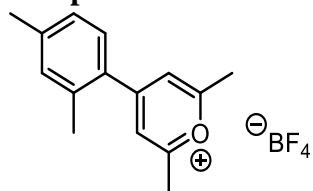
**Physical State:** orange crystalline solid.

**$^1\text{H}$  NMR (500 MHz, Acetonitrile- $d_3$ ):**  $\delta$  8.15 (s, 2H), 8.06 – 7.98 (m, 2H), 7.60 – 7.49 (m, 2H), 2.87 (s, 6H), 2.51 (s, 3H).

**$^{13}\text{C}$  NMR (126 MHz, Acetonitrile- $d_3$ ):**  $\delta$  177.87, 165.81, 147.88, 131.00, 129.50, 128.93, 117.74, 20.95, 20.78



### Compound SI-C



#### 4-(2,4-xylyl)-2,6-dimethylpyrylium tetrafluoroborate (SI-C)

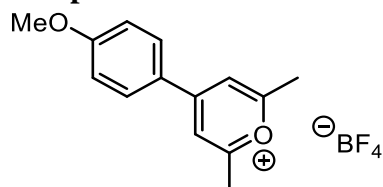
An oven dried 500 mL round bottom flask was charged with a magnetic stir bar before dissolving 2,6-dimethyl- $\gamma$ -pyrone (6.207 g, 0.05 mol) in THF (200 mL) while under nitrogen. After cooling the solution to 5 °C via ice bath, 2,4-dimethylphenylmagnesium bromide as a 0.5 M solution in THF (100 mL, 0.05 mol) was added dropwise. The solution was allowed to warm to room temperature over an hour. The crude solution was then poured over boron trifluoride diethyl etherate (18.5 mL, 0.15 mol) to yield a yellow precipitate which was filtered and washed with diethyl ether. After recrystallizing in 1:1 water:methanol, the product was isolated as orange crystals (6.0532 g, 0.02 mol) in 40% yield.

**Physical State:** orange crystalline solid.

**$^1\text{H}$  NMR (500 MHz, Acetonitrile- $d_3$ ):**  $\delta$  7.88 (s, 2H), 7.42 (d,  $J = 7.9$  Hz, 1H), 7.37 – 7.27 (m, 2H), 2.89 (s, 6H), 2.46 (s, 3H), 2.43 (s, 3H).

**$^{13}\text{C}$  NMR (126 MHz, Acetonitrile- $d_3$ ):**  $\delta$  177.88, 144.21, 132.94, 130.37, 127.93, 122.01, 20.82, 20.50, 19.61.

### Compound SI-D



#### 4-(*p*-methoxyphenyl)-2,6-dimethylpyrylium tetrafluoroborate (SI-D)

An oven dried 250 mL round bottom flask was charged with a magnetic stir bar before dissolving 2,6-dimethyl- $\gamma$ -pyrone (3.1 g, 0.025 mol) in THF (100 mL) while under nitrogen. After cooling the solution to 5 °C via ice bath, 4-methoxyphenylmagnesium bromide as a 0.5 M solution in THF (50 mL, 0.025 mol) was added dropwise. The solution was allowed to warm to room temperature over an hour. The crude solution was then poured over boron trifluoride diethyl etherate (9.25 mL, 0.075 mol) to yield a yellow precipitate which was filtered and washed with diethyl ether. After recrystallizing in 1:1 water:methanol, the product was isolated as reddish yellow crystals (5.0702 g, 0.017 mol) in 67% yield.

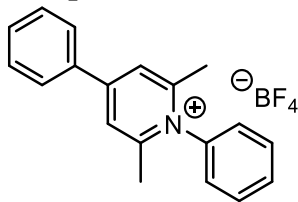
**Physical State:** red-yellow crystalline solid.

**$^1\text{H}$  NMR (500 MHz, Acetonitrile- $d_3$ ):**  $\delta$  8.21 – 8.10 (m, 2H), 8.07 (s, 2H), 7.28 – 7.19 (m, 2H), 3.98 (s, 3H), 2.82 (s, 6H).

**$^{13}\text{C}$  NMR (126 MHz, Acetonitrile- $d_3$ ):**  $\delta$  176.72, 166.58, 164.53, 132.24, 123.44, 116.37, 115.98, 56.04, 20.63

## A.6.2. Pyridinium Synthesis

### Compound 1



#### *N*-phenyl-4-phenyl-2,6-dimethylpyridinium tetrafluoroborate (**1**)

In a 50 mL round bottom flask equipped with a magnetic stir bar and condenser, 2,6-dimethyl-4-phenylpyrylium tetrafluoroborate (0.3 g, 1.1 mmol) was suspended in ethanol (20 mL). Aniline (0.12 mL, 1.3 mmol) was added and the mixture was refluxed for 4 hours while under nitrogen. The solution was cooled to room temperature overnight and diluted with diethyl ether. The precipitate was isolated by filtration and dried under vacuum to afford the white solid (0.325 g, 0.94 mmol) in 85% yield.

**IR** (KBr, Acetonitrile): 1375 (m), 1443 (m), 1561 (w), 1637 (m), 2252 (s), 2292 (w), 2943 (w), 3013 (m), 3034 (m), 3164 (w)

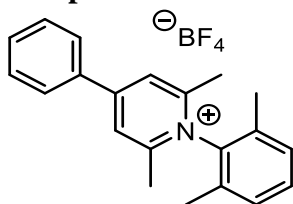
**MP:** 229 °C

**<sup>1</sup>H NMR (500 MHz, Acetonitrile-*d*<sub>3</sub>):** δ 8.19 (s, 2H), 8.06 – 7.96 (m, 2H), 7.83 – 7.76 (m, 3H), 7.75 – 7.65 (m, 3H), 7.54 – 7.46 (m, 2H), 2.44 (s, 6H).

**<sup>13</sup>C NMR (126 MHz, Acetonitrile-*d*<sub>3</sub>):** δ 156.29, 138.50, 134.07, 132.27, 131.36, 131.09, 129.85, 128.03, 125.59, 123.91, 21.65.

**HRMS:** Calc'd for C<sub>19</sub>H<sub>18</sub>N, [M-BF<sub>4</sub><sup>-</sup>]: 260.1439; found: 260.1433

## Compound 2



### *N*-(2,6-xylyl)-4-phenyl-2,6-dimethylpyridinium tetrafluoroborate (2)

In a 50 mL round bottom flask equipped with a magnetic stir bar and condenser, 2,6-dimethyl-4-phenylpyrylium tetrafluoroborate (0.5 g, 1.8 mmol) was suspended in ethanol (30 mL). 2,6-dimethylaniline (0.2 mL, 2.2 mmol) was added and the mixture was refluxed for 4 hours while under nitrogen. The solution was cooled to room temperature overnight and diluted with diethyl ether. The precipitate was isolated by filtration and dried under vacuum to afford the white solid (0.5784 g, 1.54 mmol) in 85% yield.

**Physical state:** white solid.

**IR** (KBr, Acetonitrile): 1338 (m), 1443 (m), 1473 (m), 1559 (m), 1636 (s), 2252 (s), 2925 (w), 3613 (w)

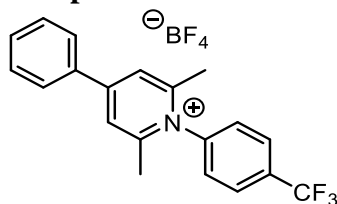
**MP:** 274 °C

**<sup>1</sup>H NMR (500 MHz, Acetonitrile-*d*<sub>3</sub>):** δ 8.27 (s, 2H), 8.05 – 7.99 (m, 2H), 7.77 – 7.68 (m, 3H), 7.62 – 7.55 (m, 1H), 7.48 (d, *J* = 7.6 Hz, 2H), 2.39 (s, 6H), 1.98 (s, 6H).

**<sup>13</sup>C NMR (126 MHz, Acetonitrile-*d*<sub>3</sub>):** δ 155.37, 132.69, 132.40, 131.34, 130.33, 129.86, 128.15, 125.15, 20.41, 16.32.

**HRMS:** Calc'd for C<sub>21</sub>H<sub>22</sub>N, [M-BF<sub>4</sub>]<sup>-</sup>: 288.1752; found: 288.1746

### Compound 3



#### ***N*-(*p*-trifluoromethyl)-4-phenyl-2,6-dimethylpyridinium tetrafluoroborate (3)**

In a 50 mL round bottom flask equipped with a magnetic stir bar and condenser, 2,6-dimethyl-4-phenylpyridinium tetrafluoroborate (0.5 g, 1.8 mmol) was suspended in ethanol (30 mL). 4-(trifluoromethyl)aniline (0.271 mL, 2.2 mmol) was added and the mixture was refluxed for 4 hours while under nitrogen. The solution was cooled to room temperature overnight and diluted with diethyl ether. The precipitate was isolated by filtration and dried under vacuum to afford the beige solid (0.5263 g, 1.27 mmol) in 70% yield.

**Physical State:** beige solid.

**IR** (KBr, Acetonitrile): 1326 (s), 1443 (m), 1566 (m), 1637 (s), 2252 (w), 2293 (w), 3003 (w), 3035 (w), 3618 (m)

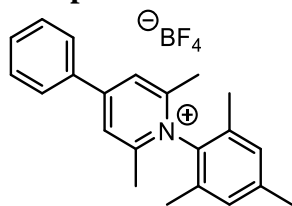
**MP:** 237 °C

**<sup>1</sup>H NMR (500 MHz, Acetonitrile-*d*<sub>3</sub>):** δ 8.21 (s, 2H), 8.11 (dd, *J* = 7.6, 1.4 Hz, 2H), 8.05 – 7.97 (m, 2H), 7.77 – 7.64 (m, 5H), 2.43 (s, 6H).

**<sup>13</sup>C NMR (126 MHz, Acetonitrile-*d*<sub>3</sub>):** δ 156.10, 133.90, 132.45, 129.89, 128.40, 128.08, 127.01, 124.02, 21.70.

**HRMS:** Calc'd for C<sub>20</sub>H<sub>17</sub>NF<sub>3</sub>, [M-BF<sub>4</sub><sup>-</sup>]: 328.1313; found: 328.1307

### Compound 4



#### ***N*-(mesityl)-4-phenyl-2,6-dimethylpyridinium tetrafluoroborate (4)**

In a 50 mL round bottom flask equipped with a magnetic stir bar and condenser, 2,6-dimethyl-4-phenylpyrylium tetrafluoroborate (0.5 g, 1.8 mmol) was suspended in ethanol (30 mL). 2,4,6-trimethylaniline (0.31 mL, 2.2 mmol) was added and the mixture was refluxed for 4 hours while under nitrogen. The solution was cooled to room temperature overnight and diluted with diethyl ether. The precipitate was isolated by filtration and dried under vacuum to afford the white solid (0.6013 g, 1.54 mmol) in 86% yield.

**Physical State:** white solid.

**IR** (KBr, Acetonitrile): 1375 (m), 1443 (m), 1635 (s), 2251 (s), 2292 (w), 2943 (w), 3001, 3626 (w)

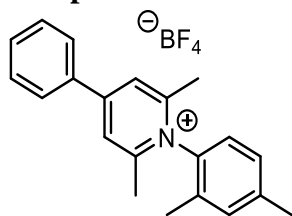
**MP:** 257 °C

**<sup>1</sup>H NMR (500 MHz, Acetonitrile-*d*<sub>3</sub>):** δ 8.26 (s, 2H), 8.06 – 7.97 (m, 2H), 7.78 – 7.64 (m, 3H), 7.34 – 7.24 (m, 2H), 2.45 (s, 3H), 2.39 (s, 6H), 1.83 (s, 6H).

**<sup>13</sup>C NMR (126 MHz, Acetonitrile-*d*<sub>3</sub>):** δ 156.58, 155.60, 141.76, 134.07, 132.36, 132.27, 130.81, 129.85, 128.14, 125.07, 20.43, 20.22, 16.23.

**HRMS:** Calc'd for C<sub>22</sub>H<sub>24</sub>N, [M-BF<sub>4</sub>]<sup>-</sup>: 302.1909; found: 302.1913

### Compound 5



#### *N*-(2,4-xylyl)-4-phenyl-2,6-dimethylpyridinium tetrafluoroborate (5)

In a 50 mL round bottom flask equipped with a magnetic stir bar and condenser, 2,6-dimethyl-4-phenylpyrylium tetrafluoroborate (0.5 g, 1.8 mmol) was suspended in ethanol (30 mL). 2,4-dimethylaniline (0.270 mL, 2.2 mmol) was added and the mixture was refluxed for 4 hours while under nitrogen. The solution was cooled to room temperature overnight and diluted with diethyl ether. The precipitate was isolated by filtration and dried under vacuum to afford the white solid (0.4263 g, 1.13 mmol) in 63% yield.

**Physical State:** white solid.

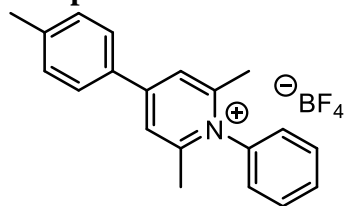
**MP:** 168 °C

**<sup>1</sup>H NMR (500 MHz, Acetonitrile-*d*<sub>3</sub>):** δ 8.22 (s, 2H), 8.05 – 7.98 (m, 2H), 7.75 – 7.63 (m, 3H), 7.48 – 7.38 (m, 2H), 7.28 (d, *J* = 8.0 Hz, 1H), 2.49 (s, 3H), 2.40 (s, 6H), 1.99 (s, 3H).

**<sup>13</sup>C NMR (126 MHz, Acetonitrile-*d*<sub>3</sub>):** δ 156.39, 156.07, 142.13, 134.09, 133.14, 132.41, 132.30, 129.84, 129.26, 128.07, 125.11, 124.41, 21.09, 20.29, 15.87.

**HRMS:** Calc'd for C<sub>21</sub>H<sub>22</sub>N, [M-BF<sub>4</sub><sup>-</sup>]: 288.1752; found: 288.1757

### Compound 6



#### ***N*-phenyl-4-(*p*-tolyl)-2,6-dimethylpyridinium tetrafluoroborate (6)**

In a 50 mL round bottom flask equipped with a magnetic stir bar and condenser, 4-(*p*-tolyl)-2,6-dimethylpyrylium tetrafluoroborate (0.4625 g, 1.6 mmol) was suspended in ethanol (25 mL). Aniline (0.177 mL, 1.9 mmol) was added and the mixture was refluxed for 4 hours while under nitrogen. The solution was cooled to room temperature overnight and diluted with diethyl ether. The precipitate was isolated by filtration and dried under vacuum to afford the white solid (0.4865 g, 1.35 mmol) in 84% yield.

**Physical State:** white solid.

**IR** (KBr, Acetonitrile): 1375 (m), 1443 (m), 1556 (w), 1594 (w), 1612 (m), 1637 (s), 2252 (s), 2293 (m), 2943 (m), 2997 (m), 3164 (w), 3620 (m)

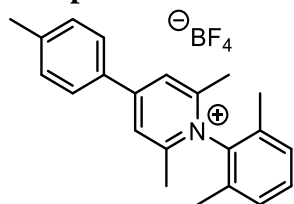
**MP:** 247 °C

**<sup>1</sup>H NMR (500 MHz, Acetonitrile-*d*<sub>3</sub>):** δ 8.17 (s, 2H), 7.96 – 7.88 (m, 2H), 7.82 – 7.72 (m, 3H), 7.55 – 7.40 (m, 4H), 2.50 (s, 3H), 2.42 (s, 6H).

**<sup>13</sup>C NMR (126 MHz, Acetonitrile-*d*<sub>3</sub>):** δ 156.14, 156.09, 143.51, 138.52, 131.33, 131.07, 131.06, 130.54, 128.00, 125.67, 123.37, 21.62, 20.56.

**HRMS:** Calc'd for C<sub>20</sub>H<sub>20</sub>N, [M-BF<sub>4</sub><sup>-</sup>]: 274.1596; found: 274.1588



**Compound 7*****N*-(2,6-xilyl)-4-(*p*-tolyl)-2,6-dimethylpyridinium tetrafluoroborate (7)**

In a 50 mL round bottom flask equipped with a magnetic stir bar and condenser, 4-(*p*-tolyl)-2,6-dimethylpyrylium tetrafluoroborate (0.5 g, 1.7 mmol) was suspended in ethanol (30 mL). 2,6-dimethylaniline (0.25 mL, 2.0 mmol) was added and the mixture was refluxed for 4 hours while under nitrogen. The solution was cooled to room temperature overnight and diluted with diethyl ether. The precipitate was isolated by filtration and dried under vacuum to afford the white solid (0.5464 g, 1.40 mmol) in 83% yield.

**Physical State:** white solid.

**IR** (KBr, Acetonitrile): 1325 (s), 1440 (w), 1557 (m), 1612 (s), 1637 (s), 2252 (m), 2925 (w), 3620 (w)

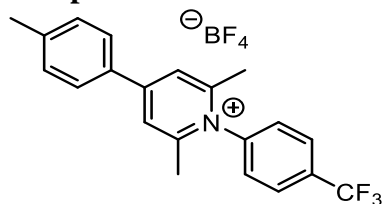
**MP:** 248 °C

**<sup>1</sup>H NMR (500 MHz, Acetonitrile-*d*<sub>3</sub>):** δ 8.25 (s, 2H), 7.96 – 7.91 (m, 2H), 7.61 – 7.44 (m, 5H), 2.51 (s, 3H), 2.37 (s, 6H), 2.00 (s, 6H).

**<sup>13</sup>C NMR (126 MHz, Acetonitrile-*d*<sub>3</sub>):** δ 156.54, 155.15, 143.70, 132.76, 131.31, 131.04, 130.55, 130.31, 128.11, 124.59, 20.59, 20.37, 16.32.

**HRMS:** Calc'd for C<sub>22</sub>H<sub>24</sub>N, [M-BF<sub>4</sub><sup>-</sup>]: 302.1909; found: 302.1902

### Compound 8



#### ***N*-(*p*-trifluoromethyl)-4-(*p*-tolyl)-2,6-dimethylpyridinium tetrafluoroborate (8)**

In a 50 mL round bottom flask equipped with a magnetic stir bar and condenser, 4-(*p*-tolyl)-2,6-dimethylpyridinium tetrafluoroborate (0.5 g, 1.7 mmol) was suspended in ethanol (30 mL). 4-(trifluoromethyl)aniline (0.263 mL, 2.1 mmol) was added and the mixture was refluxed for 4 hours while under nitrogen. The solution was cooled to room temperature overnight and diluted with diethyl ether. The precipitate was isolated by filtration and dried under vacuum to afford the pale yellow solid (0.2858 g, 0.66 mmol) in 39% yield.

**Physical State:** pale yellow solid.

**IR** (KBr, Acetonitrile): 1325 (s), 1375 (m), 1442 (m), 1612 (s), 1637 (s), 2252 (s), 2293 (m), 2943 (m), 3002 (m), 3164 (w), 3626 (m)

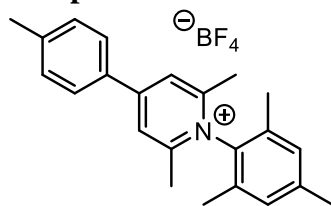
**MP:** 237 °C

**<sup>1</sup>H NMR (500 MHz, Acetonitrile-*d*<sub>3</sub>):** δ 8.18 (s, 2H), 8.14 – 8.06 (m, 2H), 7.96 – 7.87 (m, 2H), 7.75 – 7.67 (m, 2H), 7.56 – 7.45 (m, 2H), 2.49 (s, 3H), 2.41 (s, 6H).

**<sup>13</sup>C NMR (126 MHz, Acetonitrile-*d*<sub>3</sub>):** δ 156.60, 155.85, 143.73, 130.89, 130.55, 128.39, 128.36, 128.04, 127.08, 123.46, 21.66, 20.55.

**HRMS:** Calc'd for C<sub>21</sub>H<sub>19</sub>NF<sub>3</sub>, [M-BF<sub>4</sub><sup>-</sup>]: 342.1470; found: 342.1463

### Compound 9



#### ***N*-(mesityl)-4-(*p*-tolyl)-2,6-dimethylpyridinium tetrafluoroborate (9)**

In a 50 mL round bottom flask equipped with a magnetic stir bar and condenser, 4-(*p*-tolyl)-2,6-dimethylpyrylium tetrafluoroborate (0.3 g, 1.0 mmol) was suspended in ethanol (20 mL). 2,4,6-trimethylaniline (0.18 mL, 1.3 mmol) was added and the mixture was refluxed for 4 hours while under nitrogen. The solution was cooled to room temperature overnight and diluted with diethyl ether. The precipitate was isolated by filtration and dried under vacuum to afford the orange solid (0.3165 g, 0.78 mmol) in 78.5% yield.

**Physical State:** orange solid.

**IR** (KBr, Acetonitrile): 1375 (m), 1444 (m), 1612 (m), 1634 (s), 2252 (s), 2943 (w), 3544 (m), 3620 (w)

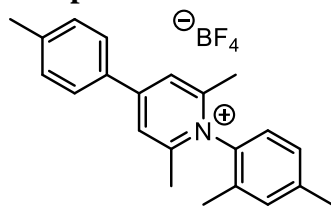
**MP:** 267 °C

**<sup>1</sup>H NMR (500 MHz, Acetonitrile-*d*<sub>3</sub>):** δ 8.23 (s, 2H), 7.97 – 7.87 (m, 2H), 7.57 – 7.47 (m, 2H), 7.29 (dd, *J* = 1.4, 0.7 Hz, 2H), 2.50 (s, 3H), 2.44 (s, 3H), 2.36 (s, 6H), 1.95 (d, *J* = 0.8 Hz, 6H).

**<sup>13</sup>C NMR (126 MHz, Acetonitrile-*d*<sub>3</sub>):** δ 155.35, 143.64, 132.32, 130.77, 130.52, 128.07, 124.49, 20.39, 16.23.

**HRMS:** Calc'd for C<sub>23</sub>H<sub>26</sub>N, [M-BF<sub>4</sub><sup>-</sup>]: 316.2065; found: 316.2069

### Compound 10



#### *N*-(2,4-xilyl)-4-(*p*-tolyl)-2,6-dimethylpyridinium tetrafluoroborate (10)

In a 50 mL round bottom flask equipped with a magnetic stir bar and condenser, 4-(*p*-tolyl)-2,6-dimethylpyrylium tetrafluoroborate (0.5 g, 1.7 mmol) was suspended in ethanol (30 mL). 2,4-dimethylaniline (0.26 mL, 2.1 mmol) was added and the mixture was refluxed for 4 hours while under nitrogen. The solution was cooled to room temperature overnight and diluted with diethyl ether. The precipitate was isolated by filtration and dried under vacuum to afford the white solid (0.4872 g, 1.35 mmol) in 74% yield.

**Physical State:** white solid.

**IR** (KBr, Acetonitrile): 1375 (s), 1444 (s), 1612 (m), 1636 (s), 2252 (s), 2292 (m), 2943 (m), 3002 (m), 3163 (m), 3617 (w)

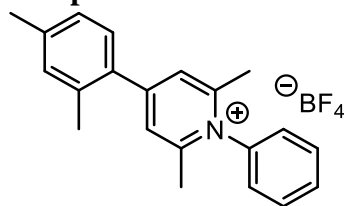
**MP:** 208 °C

**<sup>1</sup>H NMR (500 MHz, Acetonitrile-*d*<sub>3</sub>):** δ 8.19 (s, 2H), 7.96 – 7.86 (m, 2H), 7.56 – 7.49 (m, 2H), 7.47 – 7.44 (m, 1H), 7.44 – 7.40 (m, 1H), 7.28 (d, *J* = 8.1 Hz, 1H), 2.51 (s, 3H), 2.49 (s, 3H), 2.39 (s, 6H), 1.98 (s, 3H).

**<sup>13</sup>C NMR (126 MHz, Acetonitrile-*d*<sub>3</sub>):** δ 156.22, 155.84, 143.54, 142.07, 133.11, 132.46, 131.06, 130.51, 129.23, 128.02, 125.17, 123.85, 21.05, 20.56, 20.28, 15.88.

**HRMS:** Calc'd for C<sub>22</sub>H<sub>24</sub>N, [M-BF<sub>4</sub><sup>-</sup>]: 302.1909; found: 302.1905

## Compound 11



### *N*-phenyl-4-(2,4-dimethylphenyl)-2,6-dimethylpyridinium tetrafluoroborate (11)

In a 50 mL round bottom flask equipped with a magnetic stir bar and condenser, 4-(2,4-dimethylphenyl)-2,6-dimethylpyridinium tetrafluoroborate (0.5 g, 1.7 mmol) was suspended in ethanol (30 mL). Aniline (0.183 mL, 2.0 mmol) was added and the mixture was refluxed for 4 hours while under nitrogen. The solution was cooled to room temperature overnight and diluted with diethyl ether. The precipitate was isolated by filtration and dried under vacuum to afford the white solid (0.394 g, 1.05 mmol) in 63% yield.

**Physical State:** white solid.

**IR** (KBr, Acetonitrile): 1375 (s), 1444 (s), 1613 (w), 1636 (s), 2252 (s), 2292 (m), 2943 (m), 3001 (m), 3163 (w), 3619 (w)

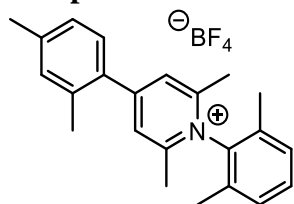
**MP:** 204-205 °C

**<sup>1</sup>H NMR (500 MHz, Acetonitrile-*d*<sub>3</sub>):** δ 7.87 (s, 2H), 7.83 – 7.73 (m, 3H), 7.54 – 7.46 (m, 2H), 7.38 – 7.19 (m, 3H), 2.44 (s, 3H), 2.43 (s, 3H), 2.40 (s, 6H).

**<sup>13</sup>C NMR (126 MHz, Acetonitrile-*d*<sub>3</sub>):** δ 158.96, 155.63, 138.57, 135.70, 133.02, 132.16, 131.35, 131.10, 129.50, 127.45, 127.02, 125.57, 21.53, 20.30, 19.32.

**HRMS:** Calc'd for C<sub>21</sub>H<sub>22</sub>N, [M-BF<sub>4</sub>]<sup>-</sup>: 288.1752; found: 288.1747

### Compound 12



#### *N*-(2,6-xylyl)-4-(2,4-xylyl)-2,6-dimethylpyridinium tetrafluoroborate (12)

In a 50 mL round bottom flask equipped with a magnetic stir bar and condenser, 4-(2,4-dimethylphenyl)-2,6-dimethylpyrylium tetrafluoroborate (0.5 g, 1.7 mmol) was suspended in ethanol (30 mL). 2,6-dimethylaniline (0.250 mL, 2.0 mmol) was added and the mixture was refluxed for 4 hours while under nitrogen. The solution was cooled to room temperature overnight and diluted with diethyl ether. The precipitate was isolated by filtration and dried under vacuum to afford the pale pink solid (0.5194 g, 1.29 mmol) in 76% yield.

**Physical State:** pale pink solid.

**IR** (KBr, Acetonitrile): 1336 (m), 1375 (m), 1446 (m), 1550 (m), 1633 (s), 2252 (s), 2292 (w), 2921 (w), 3397 (w)

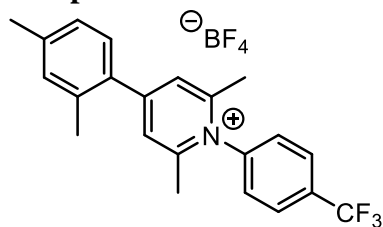
**MP:** 197 °C

**<sup>1</sup>H NMR (500 MHz, Acetonitrile-*d*<sub>3</sub>):** δ 7.97 (s, 2H), 7.58 (dd, *J* = 8.2, 7.1 Hz, 1H), 7.50 – 7.45 (m, 2H), 7.40 (d, *J* = 7.8 Hz, 1H), 7.33 – 7.24 (m, 2H), 2.46 (s, 3H), 2.43 (s, 3H), 2.35 (s, 6H), 2.01 (s, 6H).

**<sup>13</sup>C NMR (126 MHz, Acetonitrile-*d*<sub>3</sub>):** δ 159.27, 154.83, 141.40, 135.85, 132.80, 132.71, 132.23, 131.34, 130.34, 129.75, 128.16, 127.50, 20.33, 20.32, 19.44, 16.33

**HRMS:** Calc'd for C<sub>23</sub>H<sub>26</sub>N, [M-BF<sub>4</sub><sup>-</sup>]: 316.2065; found: 316.2068

### Compound 13



#### *N*-(*p*-trifluoromethylphenyl)-4-(2,4-xylyl)-2,6-dimethylpyridinium tetrafluoroborate (13)

In a 50 mL round bottom flask equipped with a magnetic stir bar and condenser, 4-(2,4-dimethylphenyl)-2,6-dimethylpyrylium tetrafluoroborate (0.5 g, 1.7 mmol) was suspended in ethanol (30 mL). 4-(trifluoromethyl)aniline (0.251 mL, 2.0 mmol) was added and the mixture was refluxed for 4 hours while under nitrogen. The solution was cooled to room temperature overnight and diluted with diethyl ether. The precipitate was isolated by filtration and dried under vacuum to afford the white solid (0.438 g, 0.9 mmol) in 58% yield.

**Physical State:** white solid.

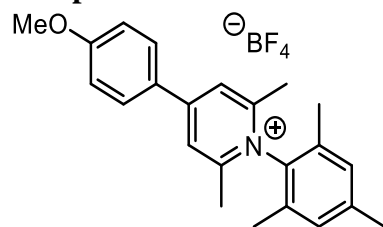
**IR** (KBr, Acetonitrile): 1325 (s), 1375 (s), 1443 (s), 1553 (m), 1614 (s), 1636 (s), 2252 (s), 2293 (m), 2943 (m), 3003 (m), 3621 (m)

**MP:** 200 °C

**<sup>1</sup>H NMR (500 MHz, Acetonitrile-*d*<sub>3</sub>):** δ 8.17 – 8.06 (m, 2H), 7.89 (s, 2H), 7.77 – 7.68 (m, 2H), 7.38 – 7.21 (m, 3H), 2.44 (s, 3H), 2.43 (s, 3H), 2.40 (s, 6H).

**<sup>13</sup>C NMR (126 MHz, Acetonitrile-*d*<sub>3</sub>):** δ 155.43, 135.75, 132.20, 129.52, 128.46, 128.43, 127.49, 127.16, 126.99, 21.59, 20.30, 19.32.

**HRMS:** Calc'd for C<sub>22</sub>H<sub>21</sub>NF<sub>3</sub>, [M-BF<sub>4</sub><sup>-</sup>]: 356.1626; found: 356.1619

**Compound 14*****N*-(mesityl)-4-(*p*-methoxyphenyl)-2,6-dimethylpyridinium tetrafluoroborate (14)**

In a 50 mL round bottom flask equipped with a magnetic stir bar and condenser, 4-(4-methoxyphenyl)-2,6-dimethylpyrylium tetrafluoroborate (0.0732 g, 0.205 mmol) was suspended in ethanol (10 mL). 2,4,6-trimethylaniline (0.043 mL, 0.307 mmol) was added and the mixture was refluxed for 4 hours while under nitrogen. The solution was cooled to room temperature overnight and diluted with diethyl ether. The precipitate was isolated by filtration and dried under vacuum to afford the yellow solid (0.023 g, 0.05 mmol) in 27% yield.

**Physical State:** yellow solid.

**IR** (KBr, Acetonitrile): 1375 (m), 1444 (m), 1612 (m), 1634 (s), 2252 (s), 2943 (w), 3544 (m), 3620 (w)

**MP:** 218 °C

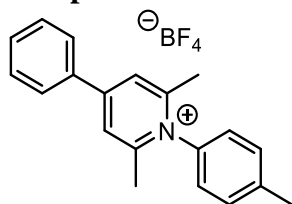
**<sup>1</sup>H NMR (500 MHz, Acetonitrile-*d*<sub>3</sub>):** δ 8.24 – 8.15 (m, 2H), 8.08 – 7.96 (m, 2H), 7.31 – 7.26 (m, 2H), 7.25 – 7.18 (m, 2H), 3.95 (s, 3H), 2.44 (s, 3H), 2.34 (s, 6H), 1.96 (s, 6H).

**<sup>13</sup>C NMR (126 MHz, Acetonitrile-*d*<sub>3</sub>):** δ 163.51, 155.80, 155.03, 141.66, 132.44, 130.75, 130.04, 125.72, 123.63, 115.34, 55.55, 20.35, 20.21, 16.24.

**HRMS:** Calc'd for C<sub>23</sub>H<sub>26</sub>NO, [M-BF<sub>4</sub>]: 332.2014; found: 332.2008



### Compound 15



#### ***N*-(*p*-tolyl)-4-phenyl-2,6-dimethylpyridinium tetrafluoroborate (15)**

In a 50 mL round bottom flask equipped with a magnetic stir bar and condenser, 2,6-dimethyl-4-phenylpyrylium tetrafluoroborate (0.5 g, 1.8 mmol) was suspended in ethanol (30 mL). *p*-toluidine (0.236 mL, 2.2 mmol) was added and the mixture was refluxed for 4 hours while under nitrogen. The solution was cooled to room temperature overnight and diluted with diethyl ether. The precipitate was isolated by filtration and dried under vacuum to afford the white solid (0.4831 g, 1.33 mmol) in 74% yield.

**Physical State:** white solid.

**IR** (KBr, Acetonitrile): 1375 (s), 1443 (s), 1509 (m), 1560 (m), 1637 (s), 2252 (s), 2292 (m), 2943 (m), 3005 (m), 3164 (m), 3617 (m)

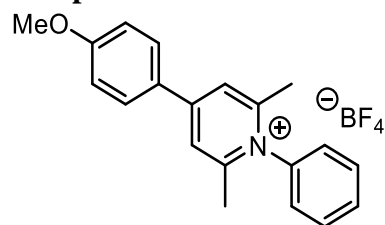
**MP:** 226 °C

**<sup>1</sup>H NMR (500 MHz, Acetonitrile-*d*<sub>3</sub>):** δ 8.18 (s, 2H), 8.03 – 7.98 (m, 2H), 7.75 – 7.66 (m, 3H), 7.62 – 7.56 (m, 2H), 7.40 – 7.32 (m, 2H), 2.53 (s, 3H), 2.44 (s, 6H).

**<sup>13</sup>C NMR (126 MHz, Acetonitrile-*d*<sub>3</sub>):** δ 156.49, 156.19, 142.01, 136.02, 134.10, 132.26, 131.46, 129.86, 128.03, 128.02, 125.28, 123.87, 21.66, 20.36.

**HRMS:** Calc'd for C<sub>20</sub>H<sub>20</sub>N, [M-BF<sub>4</sub><sup>-</sup>]: 274.1596; found: 274.1591

## Compound 16



### *N*-phenyl-4-(*p*-methoxyphenyl)-2,6-dimethylpyridinium tetrafluoroborate (16)

In a 50 mL round bottom flask equipped with a magnetic stir bar and condenser, 4-(4-methoxyphenyl)-2,6-dimethylpyrylium tetrafluoroborate (0.5 g, 1.65 mmol) was suspended in ethanol (30 mL). Aniline (0.182 mL, 2.0 mmol) was added and the mixture was refluxed for 4 hours while under nitrogen. The solution was cooled to room temperature overnight and diluted with diethyl ether. The precipitate was isolated by filtration and dried under vacuum to afford the white solid (0.4155 g, 1.10 mmol) in 67% yield.

**Physical State:** white solid.

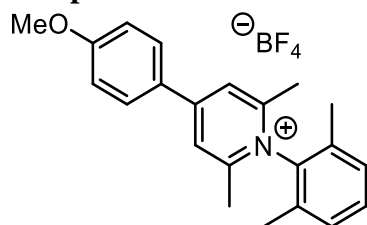
**IR** (KBr, Acetonitrile): 1375 (s), 1443 (s), 1603 (s), 1638 (s), 2252 (s), 2292 (s), 2943 (s), 3002 (s), 3164 (m), 3543 (m), 3620 (m)

**MP:** 219-222 °C

**<sup>1</sup>H NMR (500 MHz, Acetonitrile-*d*<sub>3</sub>):** δ 8.12 (s, 2H), 8.07 – 7.96 (m, 2H), 7.83 – 7.72 (m, 3H), 7.52 – 7.41 (m, 2H), 7.26 – 7.15 (m, 2H), 3.94 (s, 3H), 2.39 (s, 6H).

**<sup>13</sup>C NMR (126 MHz, Acetonitrile-*d*<sub>3</sub>):** δ 163.40, 155.72, 131.25, 131.01, 129.90, 125.73, 125.67, 122.50, 115.30, 55.53, 21.56.

**HRMS:** Calc'd for C<sub>20</sub>H<sub>20</sub>NO, [M-BF<sub>4</sub>]<sup>-</sup>: 290.1545; found: 290.1538

**Compound 17*****N*-(2,6-dimethyl-4-(*p*-methoxyphenyl)pyridin-2-yl)pyridinium tetrafluoroborate (17)**

In a 50 mL round bottom flask equipped with a magnetic stir bar and condenser, 4-(4-methoxyphenyl)-2,6-dimethylpyridinium tetrafluoroborate (0.5 g, 1.65 mmol) was suspended in ethanol (30 mL). 2,6-dimethylaniline (0.25 mL, 2.0 mmol) was added and the mixture was refluxed for 4 hours while under nitrogen. The solution was cooled to room temperature overnight and diluted with diethyl ether. The precipitate was isolated by filtration and dried under vacuum to afford the yellow solid (0.4596 g, 1.13 mmol) in 69% yield.

**Physical State:** yellow solid.

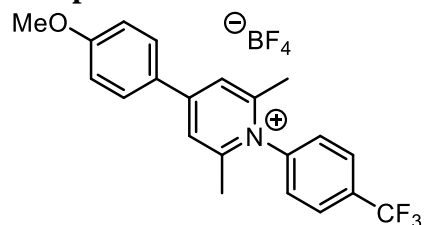
**IR** (KBr, Acetonitrile): 1375 (m), 1443 (m), 2253 (s), 2292 (m), 2409 (w), 2944 (m), 3003 (m), 3164 (m), 3618 (w)

**MP:** 224 °C

**<sup>1</sup>H NMR (500 MHz, Acetonitrile-*d*<sub>3</sub>):**  $\delta$  8.20 (s, 2H), 8.08 – 7.99 (m, 2H), 7.56 (dd,  $J$  = 8.2, 7.1 Hz, 1H), 7.46 (dq,  $J$  = 7.8, 0.7 Hz, 2H), 7.28 – 7.14 (m, 2H), 3.95 (s, 3H), 2.34 (s, 6H), 1.99 (d,  $J$  = 0.7 Hz, 6H).

**<sup>13</sup>C NMR (126 MHz, Acetonitrile-*d*<sub>3</sub>):**  $\delta$  163.51, 154.78, 132.84, 131.23, 130.24, 130.04, 125.67, 123.68, 115.33, 55.54, 20.30, 16.31.

**HRMS:** Calc'd for C<sub>22</sub>H<sub>24</sub>NO, [M-BF<sub>4</sub>]<sup>-</sup>: 318.1858; found: 318.1851

**Compound 18*****N*-(*p*-trifluoromethylphenyl)-4-(*p*-methoxyphenyl)-2,6-dimethylpyridinium tetrafluoroborate (18)**

In a 50 mL round bottom flask equipped with a magnetic stir bar and condenser, 4-(4-methoxyphenyl)-2,6-dimethylpyrylium tetrafluoroborate (0.5 g, 1.65 mmol) was suspended in ethanol (30 mL). 4-(trifluoromethyl)aniline (0.251 mL, 2.0 mmol) was added and the mixture was refluxed for 4 hours while under nitrogen. The solution was cooled to room temperature overnight and diluted with diethyl ether. The precipitate was isolated by filtration and dried under vacuum to afford the pale yellow solid (0.4046 g, 0.91 mmol) in 55% yield.

**Physical State:** pale yellow solid.

**IR** (KBr, Acetonitrile): 1326 (m), 1375 (s), 1444 (m), 1601 (m), 1637 (w), 2253 (s), 2292 (m), 2944 (w), 3003 (w), 3164 (w), 3619 (w)

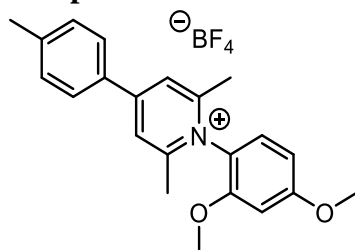
**MP:** 269 °C

**<sup>1</sup>H NMR (500 MHz, Acetonitrile-*d*<sub>3</sub>):** δ 8.15 (s, 2H), 8.11 – 8.07 (m, 2H), 8.05 – 8.00 (m, 2H), 7.73 – 7.67 (m, 2H), 7.25 – 7.17 (m, 2H), 3.94 (s, 3H), 2.39 (s, 6H).

**<sup>13</sup>C NMR (126 MHz, Acetonitrile-*d*<sub>3</sub>):** δ 163.57, 155.96, 155.48, 130.01, 128.35, 128.32, 127.17, 125.51, 122.58, 115.35, 55.56, 21.61.

**HRMS:** Calc'd for C<sub>21</sub>H<sub>19</sub>NF<sub>3</sub>O, [M-BF<sub>4</sub>]<sup>-</sup>: 358.1419; found: 358.1412

### Compound 19



#### ***N*-(2,4-dimethoxyphenyl)-4-(*p*-tolyl)-2,6-dimethylpyridinium tetrafluoroborate (19)**

In a 50 mL round bottom flask equipped with a magnetic stir bar and condenser, 4-(*p*-tolyl)-2,6-dimethylpyrylium tetrafluoroborate (0.5 g, 1.7 mmol) was suspended in ethanol (30 mL). 2,4-dimethoxyaniline (0.299 mL, 2.1 mmol) was added and the mixture was refluxed for 4 hours while under nitrogen. The solution was cooled to room temperature overnight and diluted with diethyl ether. The precipitate was isolated by filtration and dried under vacuum to afford the purple solid (0.4896 g, 1.16 mmol) in 68% yield.

**Physical State:** purple solid.

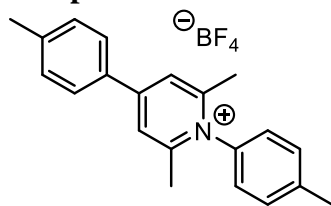
**IR** (KBr, Acetonitrile): 1375 (s), 1443 (s), 1511 (m), 1636 (s), 2252 (s), 2292 (s), 2943 (m), 3002 (m), 3164 (m), 3201 (w), 3618 (m)

**MP:** 183-185 °C

**<sup>1</sup>H NMR (500 MHz, Acetonitrile-*d*<sub>3</sub>):** δ 8.14 (s, 2H), 7.94 – 7.85 (m, 2H), 7.56 – 7.43 (m, 2H), 7.31 (d, *J* = 8.7 Hz, 1H), 6.88 (d, *J* = 2.5 Hz, 1H), 6.83 (dd, *J* = 8.8, 2.5 Hz, 1H), 3.94 (s, 3H), 3.84 (s, 3H), 2.49 (s, 3H), 2.41 (s, 6H).

**<sup>13</sup>C NMR (126 MHz, Acetonitrile-*d*<sub>3</sub>):** δ 157.15, 130.47, 128.01, 127.17, 123.24, 106.50, 100.17, 56.25, 55.83, 20.87, 20.53.

**HRMS:** Calc'd for C<sub>22</sub>H<sub>24</sub>NO<sub>2</sub>, [M-BF<sub>4</sub><sup>-</sup>]: 334.1807; found: 334.1811

**Compound 20*****N*-(*p*-tolyl)-4-(*p*-tolyl)-2,6-dimethylpyridinium tetrafluoroborate (20)**

In a 50 mL round bottom flask equipped with a magnetic stir bar and condenser, 4-(*p*-tolyl)-2,6-dimethylpyrylium tetrafluoroborate (0.5 g, 1.7 mmol) was suspended in ethanol (25 mL). *P*-toluidine (0.2143 g, 2.0 mmol) was added and the mixture was refluxed for 4 hours while under nitrogen. The solution was cooled to room temperature overnight and diluted with diethyl ether. The precipitate was isolated by filtration and dried under vacuum to afford the white solid (0.4209 g, 1.12 mmol) in 66% yield.

**Physical State:** white solid.

**IR** (KBr, Acetonitrile): 1375 (m), 1443 (m), 1509 (m), 1612 (m), 1637 (s), 2252 (s), 2292 (m), 2943 (m), 3002 (m), 3164 (w), 3617 (w)

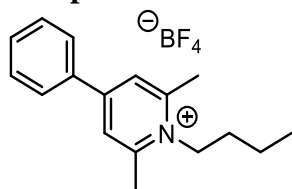
**MP:** 172 °C

**<sup>1</sup>H NMR (500 MHz, Acetonitrile-*d*<sub>3</sub>):** δ 8.14 (s, 2H), 7.97 – 7.85 (m, 2H), 7.62 – 7.55 (m, 2H), 7.53 – 7.45 (m, 2H), 7.39 – 7.30 (m, 2H), 2.52 (s, 3H), 2.49 (s, 3H), 2.41 (s, 6H).

**<sup>13</sup>C NMR (126 MHz, Acetonitrile-*d*<sub>3</sub>):** δ 161.53, 161.30, 148.75, 147.24, 136.70, 136.35, 135.80, 133.25, 130.61, 26.90, 25.83, 25.64.

**HRMS:** Calc'd for C<sub>21</sub>H<sub>22</sub>N, [M-BF<sub>4</sub><sup>-</sup>]: 288.1752; found: 288.1746

### Compound 21



#### ***N*-(*n*-butyl)-4-phenyl-2,6-dimethylpyridinium tetrafluoroborate (21)**

In a 50 mL round bottom flask equipped with a magnetic stir bar and condenser, 2,6-dimethyl-4-phenylpyrylium tetrafluoroborate (0.3 g, 1.1 mmol) was suspended in ethanol (20 mL). 1-butylamine (0.130 mL, 1.3 mmol) was added and the mixture was refluxed for 4 hours while under nitrogen. The solution was cooled to room temperature overnight and diluted with diethyl ether. The precipitate was isolated by filtration and dried under vacuum to afford the white solid (0.1324 g, 0.40 mmol) in 37% yield.

**Physical State:** pale yellow solid.

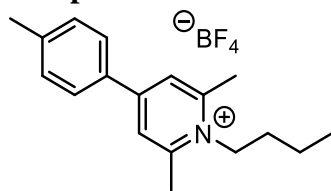
**IR** (KBr, Acetonitrile): 1331 (m), 1375 (s), 1447 (s), 1636 (s), 2250 (s), 2292 (s), 2943 (m), 3002 (m), 3164 (w), 3619 (w)

**MP:** 192 °C

**<sup>1</sup>H NMR (500 MHz, Acetonitrile-*d*<sub>3</sub>):** δ 8.02 (s, 2H), 7.96 – 7.86 (m, 2H), 7.71 – 7.60 (m, 3H), 4.48 – 4.36 (m, 2H), 2.88 (s, 6H), 1.92 – 1.79 (m, 2H), 1.64 – 1.49 (m, 2H), 1.06 (t, *J* = 7.4 Hz, 3H).

**<sup>13</sup>C NMR (126 MHz, Acetonitrile-*d*<sub>3</sub>):** δ 206.49, 155.25, 131.91, 129.72, 127.81, 124.98, 52.23, 29.90, 20.56, 19.61, 12.73.

**HRMS:** Calc'd for C<sub>17</sub>H<sub>22</sub>N, [M-BF<sub>4</sub><sup>-</sup>]: 240.1752; found: 240.1747

**Compound 22*****N*-(*n*-butyl)-4-(*p*-tolyl)-2,6-dimethylpyridinium tetrafluoroborate (22)**

In a 100 mL round bottom flask equipped with a magnetic stir bar and condenser, 4-(*p*-tolyl)-2,6-dimethylpyrylium tetrafluoroborate (0.9939 g, 3.47 mmol) was suspended in ethanol (50 mL). 1-butylamine (0.412 mL, 4.17 mmol) was added and the mixture was refluxed for 4 hours while under nitrogen. The solution was cooled to room temperature overnight and diluted with diethyl ether. The precipitate was isolated by filtration and dried under vacuum to afford the white solid (0.3945 g, 1.15 mmol) in 33.3% yield.

**Physical State:** white solid.

**IR** (KBr, Acetonitrile): 1375 (m), 1443 (m), 1561 (w), 1637 (m), 2252 (s), 2292 (w), 2943 (w), 3013 (m), 3034 (m), 3164 (w)

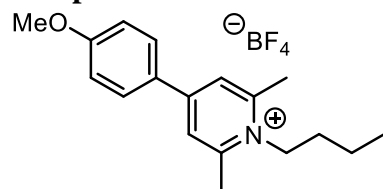
**MP:** 129 °C

**<sup>1</sup>H NMR (500 MHz, Acetonitrile-*d*<sub>3</sub>):** δ 7.99 (s, 2H), 7.87 – 7.78 (m, 2H), 7.52 – 7.41 (m, 2H), 4.44 – 4.33 (m, 2H), 2.86 (s, 6H), 2.47 (s, 3H), 1.91 – 1.76 (m, 2H), 1.57 (h, *J* = 7.4 Hz, 2H), 1.05 (t, *J* = 7.4 Hz, 3H).

**<sup>13</sup>C NMR (126 MHz, Acetonitrile-*d*<sub>3</sub>):** δ 143.03, 130.38, 127.73, 124.47, 52.11, 29.88, 20.53, 19.60, 12.73.

**HRMS:** Calc'd for C<sub>18</sub>H<sub>24</sub>N, [M-BF<sub>4</sub><sup>-</sup>]: 254.1909; found: 254.1900



**Compound 23*****N*-(*n*-butyl)-4-(*p*-methoxyphenyl)-2,6-dimethylpyridinium tetrafluoroborate (23)**

In a 50 mL round bottom flask equipped with a magnetic stir bar and condenser, 4-(4-methoxyphenyl)-2,6-dimethylpyrylium tetrafluoroborate (0.5 g, 1.65 mmol) was suspended in ethanol (30 mL). Aniline (0.247 mL, 2.5 mmol) was added and the mixture was refluxed for 4 hours while under nitrogen. The solution was cooled to room temperature overnight and diluted with diethyl ether. The precipitate was isolated by filtration and dried under vacuum to afford the pale-yellow solid (0.2289 g, 0.64 mmol) in 40% yield.

**Physical State:** pale yellow solid.

**IR** (KBr, Acetonitrile): 1375 (s), 1444 (s), 1525 (s), 1604 (s), 1636 (s), 2252 (s), 2292 (m), 2943 (m), 2969 (m), 3003 (m), 3163 (w), 3620 (w)

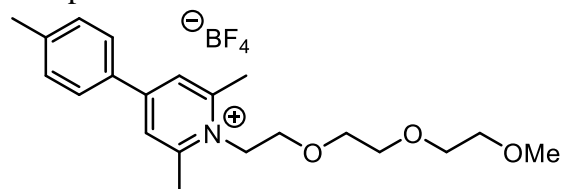
**MP:** 135-137 °C

**<sup>1</sup>H NMR (500 MHz, Acetonitrile-*d*<sub>3</sub>):** δ 7.95 (s, 2H), 7.94 – 7.89 (m, 2H), 7.19 – 7.13 (m, 2H), 4.42 – 4.28 (m, 2H), 3.91 (s, 3H), 2.83 (s, 6H), 1.90 – 1.75 (m, 2H), 1.55 (h, *J* = 7.4 Hz, 2H), 1.04 (t, *J* = 7.4 Hz, 3H).

**<sup>13</sup>C NMR (126 MHz, Acetonitrile-*d*<sub>3</sub>):** δ 154.76, 153.87, 129.60, 125.71, 123.71, 115.16, 55.46, 51.91, 29.93, 20.48, 19.59, 12.72.

**HRMS:** Calc'd for C<sub>18</sub>H<sub>24</sub>NO, [M-BF<sub>4</sub>]: 270.1858; found: 270.1852

Compound 24



***N*-(2-(2-(2-methoxyethoxy)ethoxy)ethyl)-4-(*p*-tolyl)-2,6-dimethylpyridinium tetrafluoroborate (24)**

In a 100 mL round bottom flask equipped with a magnetic stir bar and condenser, 4-(*p*-tolyl)-2,6-dimethylpyrylium tetrafluoroborate (1.0 g, 3.5 mmol) was suspended in ethanol (50 mL). 2-(2-(2-methoxyethoxy)ethoxy) ethanamine (0.694 mL, 4.2 mmol) was added and the mixture was refluxed for 4 hours while under nitrogen. The solution was cooled to room temperature overnight and diluted with diethyl ether. The precipitate was isolated by filtration and dried under vacuum to afford the white solid (0.969 g, 2.25 mmol) in 64% yield.

**Physical State:** white solid.

**IR (KBr, Acetonitrile):** 1375 (s), 1443 (s), 1511 (m), 1636 (s), 2252 (s), 2292 (s), 2943 (m), 3002 (m), 3164 (m), 3201 (w), 3618 (m)

**MP:** 192 °C

**<sup>1</sup>H NMR (500 MHz, Acetonitrile-*d*<sub>3</sub>):** δ 8.00 (s, 2H), 7.89 – 7.79 (m, 2H), 7.52 – 7.38 (m, 2H), 4.68 (t, *J* = 5.1 Hz, 2H), 3.96 (dd, *J* = 5.5, 4.7 Hz, 2H), 3.56 – 3.52 (m, 2H), 3.51 – 3.47 (m, 2H), 3.46 – 3.42 (m, 2H), 3.41 – 3.37 (m, 2H), 2.88 (s, 6H), 2.46 (s, 3H).

**<sup>13</sup>C NMR (126 MHz, Acetonitrile-*d*<sub>3</sub>):** δ 130.37, 127.80, 124.22, 71.54, 70.58, 69.93, 68.11, 57.85, 52.16, 21.34, 20.48.

**HRMS:** Calc'd for C<sub>21</sub>H<sub>30</sub>NO<sub>3</sub>, [M-BF<sub>4</sub>]<sup>-</sup>: 344.2226; found: 344.2222

## A.7. Pirylium & Pyridinium NMR Data

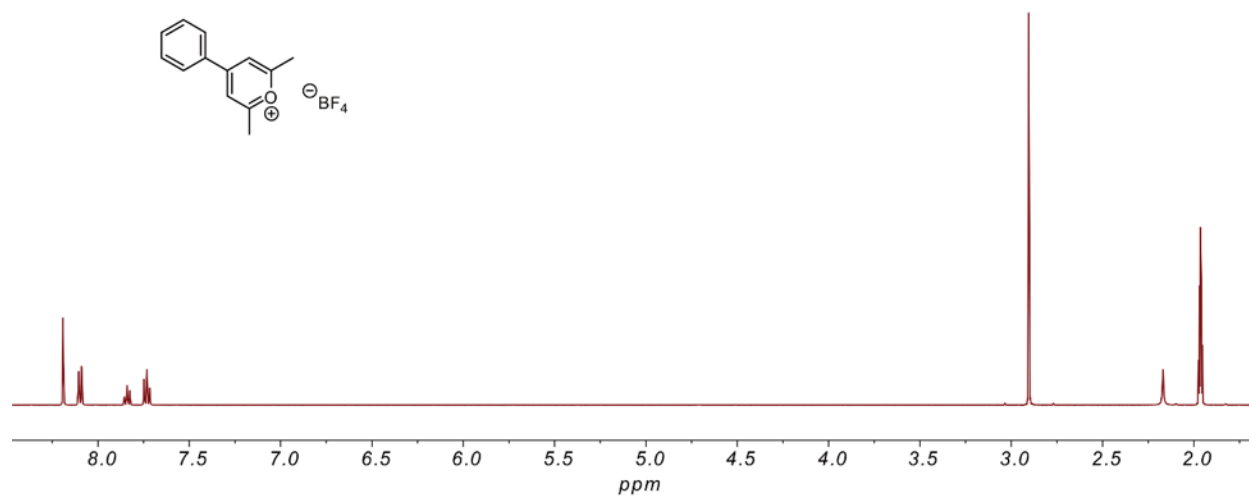


**Figure A.20.** <sup>1</sup>H-NMR spectrum of 2,6-dimethyl-4-phenylpyrylium tetrafluoroborate (SI-A) in CD<sub>3</sub>CN at 25 °C.

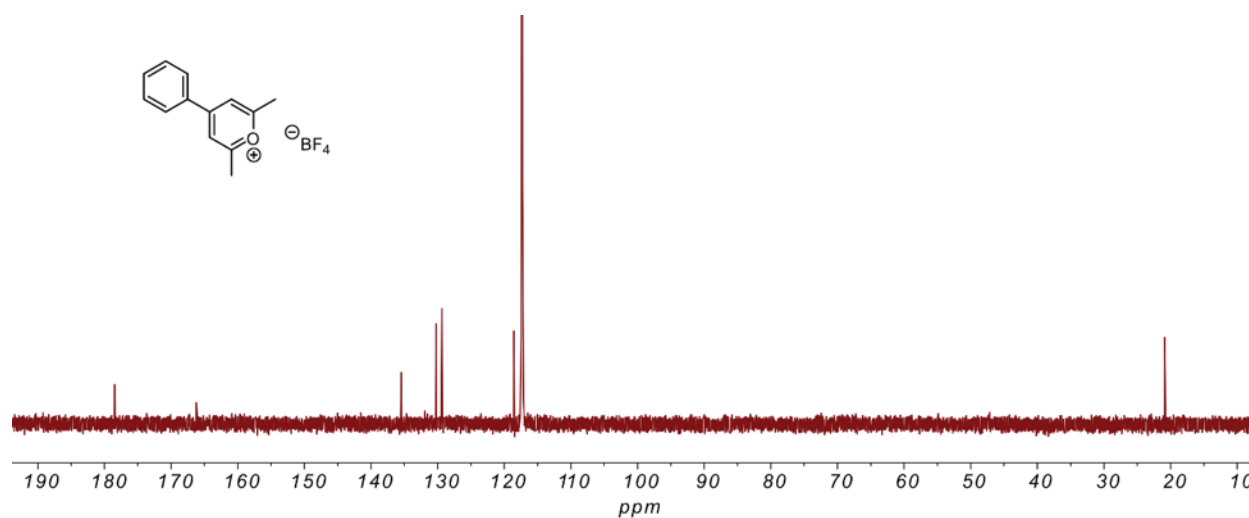


**Figure A.21.** <sup>13</sup>C-NMR spectrum of 2,6-dimethyl-4-phenylpyrylium tetrafluoroborate (SI-A) in CD<sub>3</sub>CN at 25 °C.

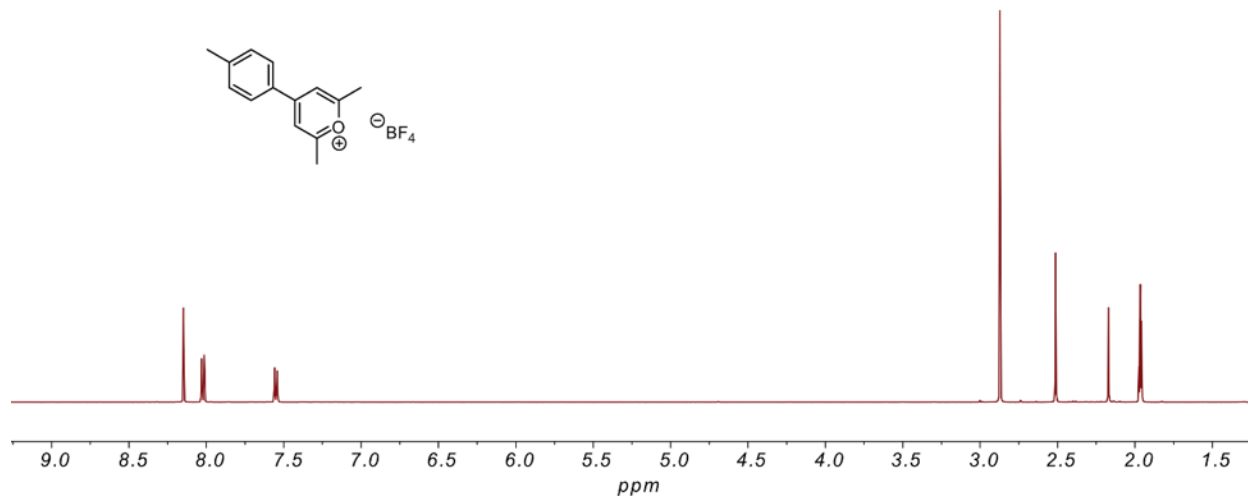


**Figure A.22.** <sup>1</sup>H-NMR spectrum of 4-(*p*-tolyl)-2,6-dimethyl-pyrylium tetrafluoroborate (SI-B) in CD<sub>3</sub>CN at 25 °C.

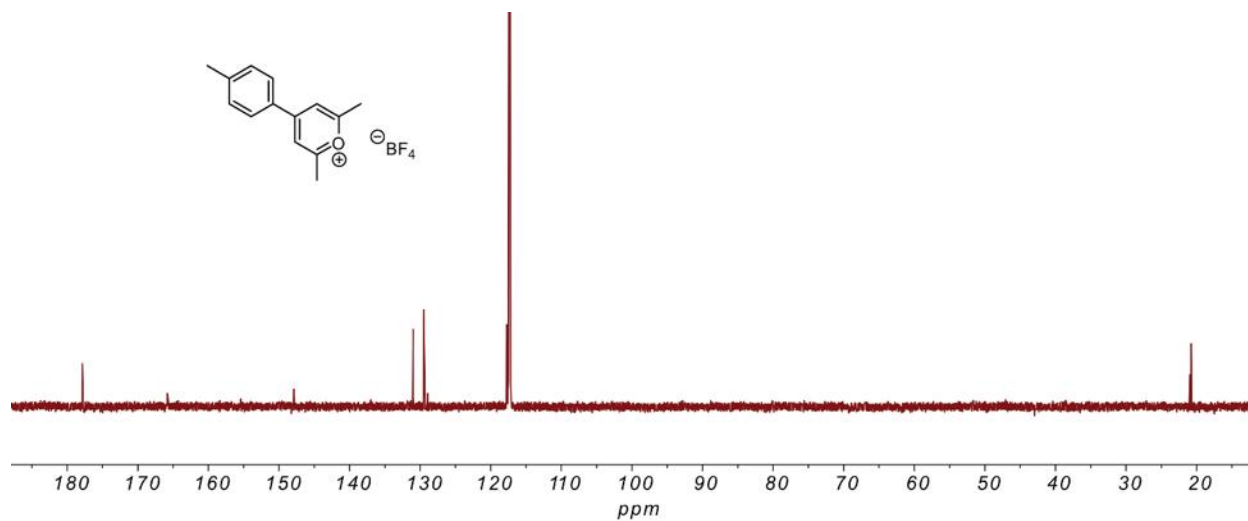


**Figure A.23.** <sup>13</sup>C-NMR spectrum of 4-(*p*-tolyl)-2,6-dimethyl-pyrylium tetrafluoroborate (SI-B) in CD<sub>3</sub>CN at 25 °C.

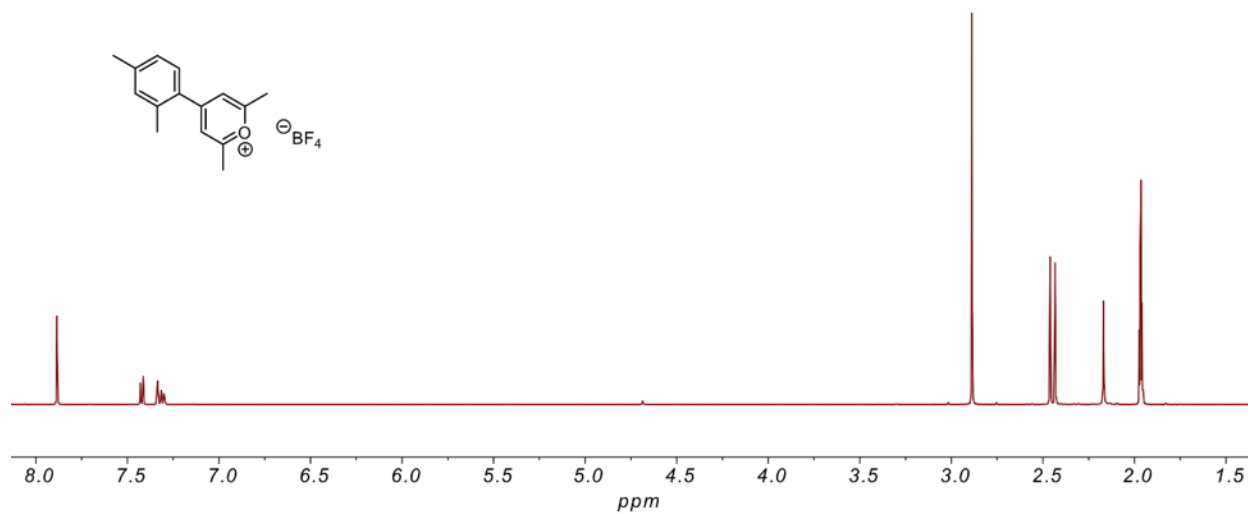


**Figure A.24.** <sup>1</sup>H-NMR spectrum of 4-(2,4-xylyl)-2,6-dimethylpyrylium tetrafluoroborate (SI-C) in CD<sub>3</sub>CN at 25 °C.

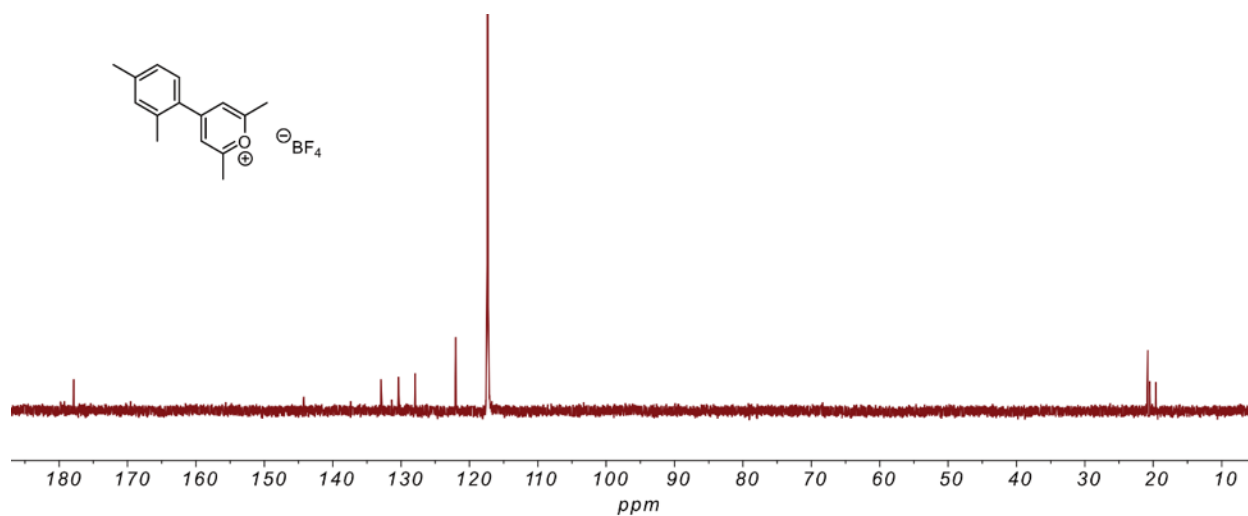


**Figure A.25.** <sup>13</sup>C-NMR spectrum of 4-(2,4-xylyl)-2,6-dimethylpyrylium tetrafluoroborate (SI-C) in CD<sub>3</sub>CN at 25 °C.

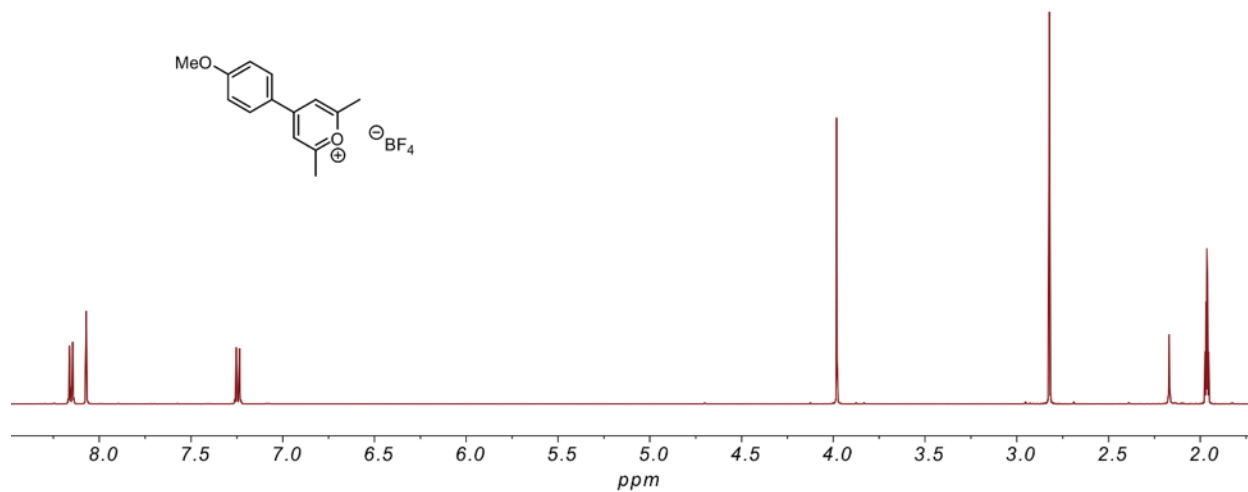


**Figure A.26.** <sup>1</sup>H-NMR spectrum of 4-(*p*-methoxyphenyl)-2,6-dimethylpyrylium tetrafluoroborate (SI-D) in CD<sub>3</sub>CN at 25 °C.

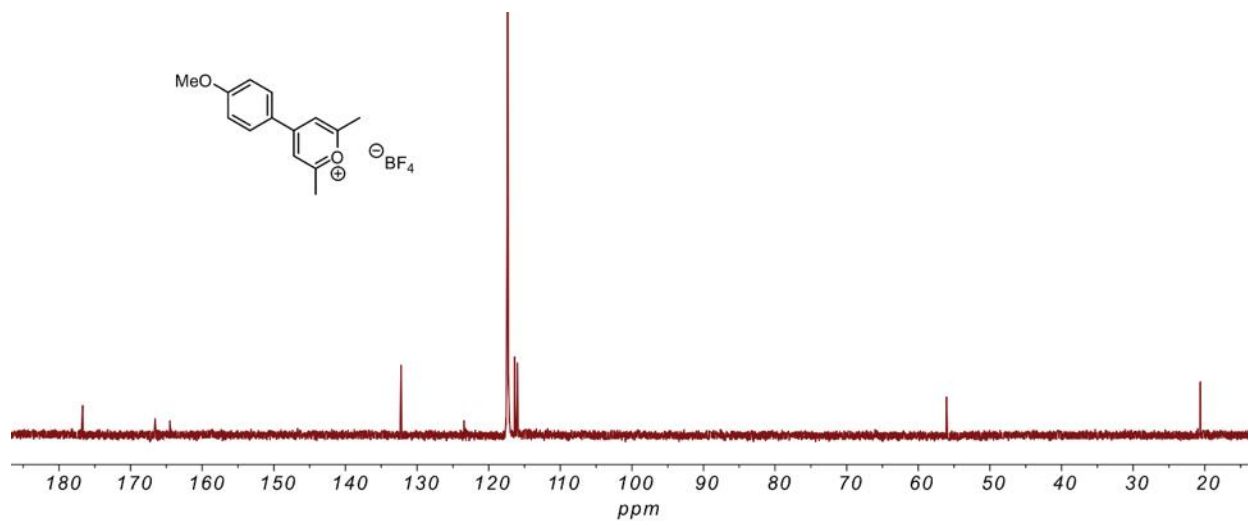


**Figure A.27.** <sup>13</sup>C-NMR spectrum of 4-(*p*-methoxyphenyl)-2,6-dimethylpyrylium tetrafluoroborate (SI-D) in CD<sub>3</sub>CN at 25 °C.

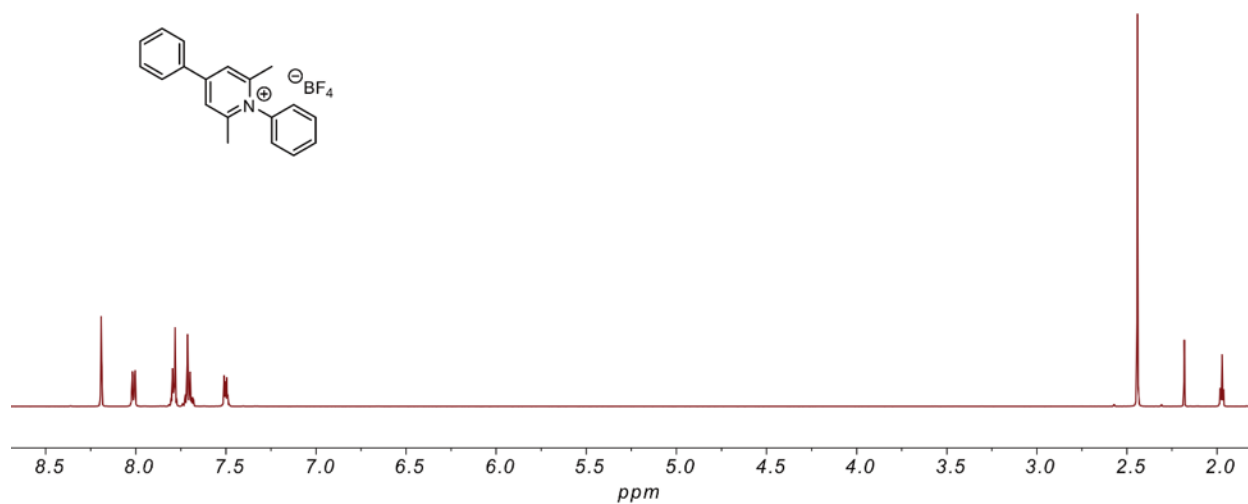


**Figure A.28.**  $^1\text{H-NMR}$  spectrum of *N*-phenyl-4-phenyl-2,6-dimethylpyridinium tetrafluoroborate (1) in  $\text{CD}_3\text{CN}$  at  $25\text{ }^\circ\text{C}$ .

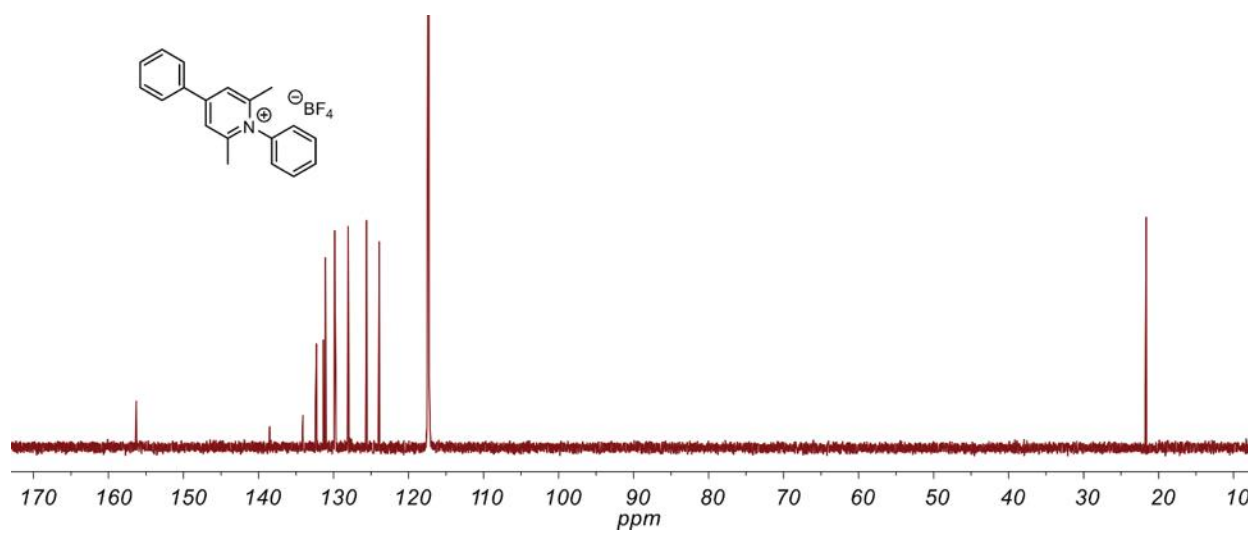


**Figure A.29.**  $^{13}\text{C-NMR}$  spectrum of *N*-phenyl-4-phenyl-2,6-dimethylpyridinium tetrafluoroborate (1) in  $\text{CD}_3\text{CN}$  at  $25\text{ }^\circ\text{C}$ .

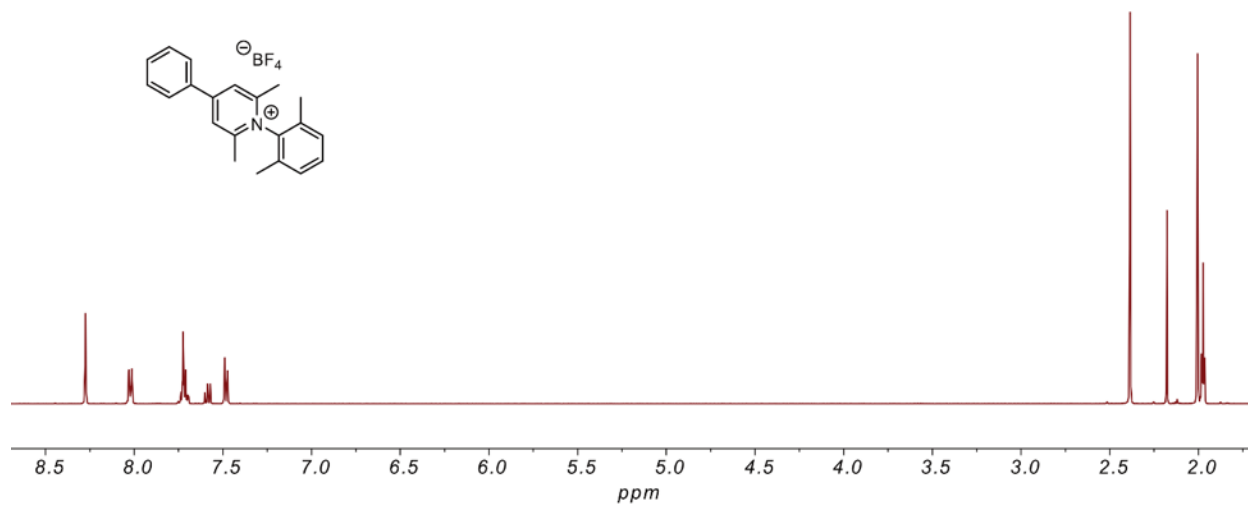


**Figure A.30.** <sup>1</sup>H-NMR spectrum of *N*-(2,6-xylyl)-4-phenyl-2,6-dimethylpyridinium tetrafluoroborate (2) in CD<sub>3</sub>CN at 25 °C.

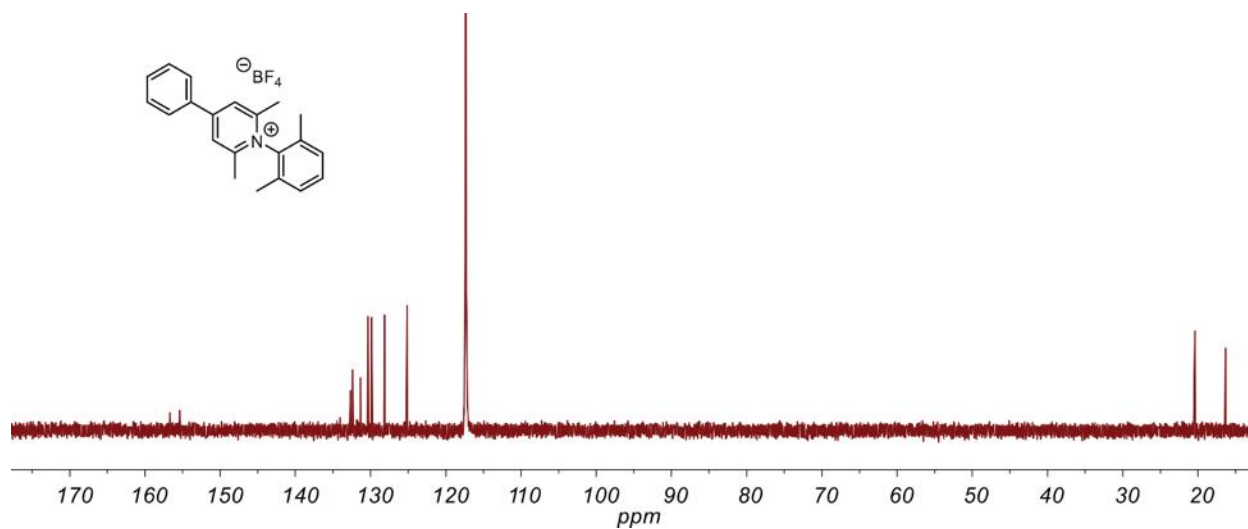


**Figure A.31.** <sup>13</sup>C-NMR spectrum of *N*-(2,6-xylyl)-4-phenyl-2,6-dimethylpyridinium tetrafluoroborate (2) in CD<sub>3</sub>CN at 25 °C.



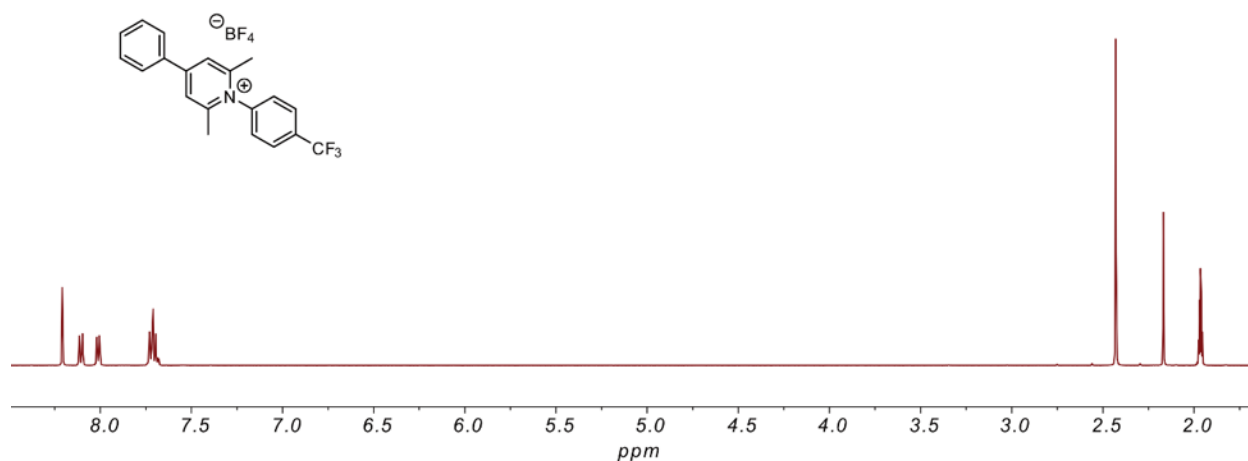


**Figure A.32.** <sup>1</sup>H-NMR spectrum of *N*-(*p*-trifluoromethylphenyl)-4-phenyl-2,6-dimethylpyridinium tetrafluoroborate (3) in CD<sub>3</sub>CN at 25 °C.

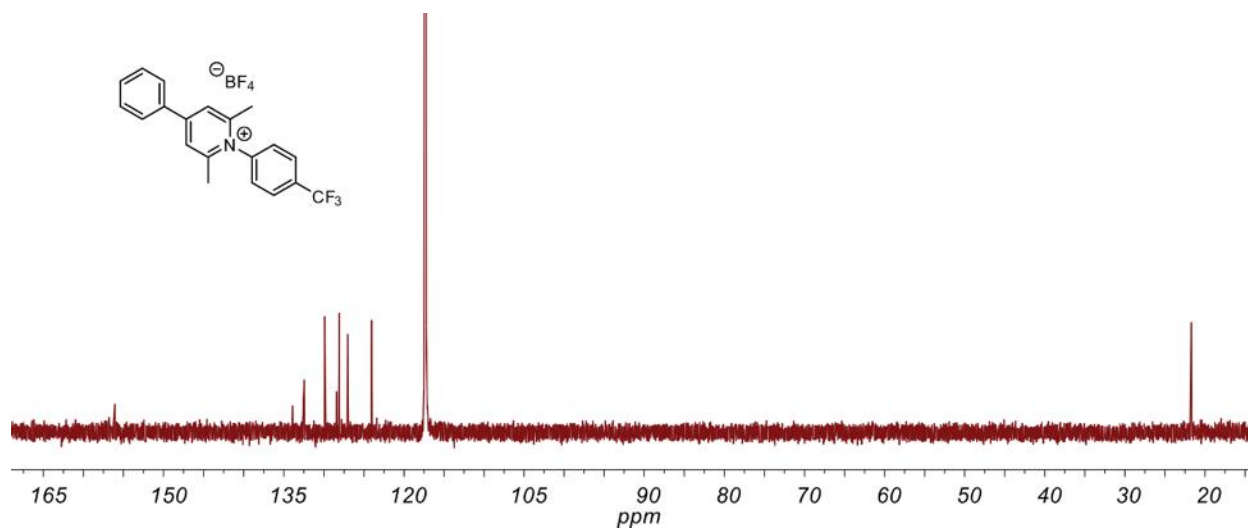


**Figure A.33.** <sup>13</sup>C-NMR spectrum of *N*-(*p*-trifluoromethylphenyl)-4-phenyl-2,6-dimethylpyridinium tetrafluoroborate (3) in CD<sub>3</sub>CN at 25 °C.

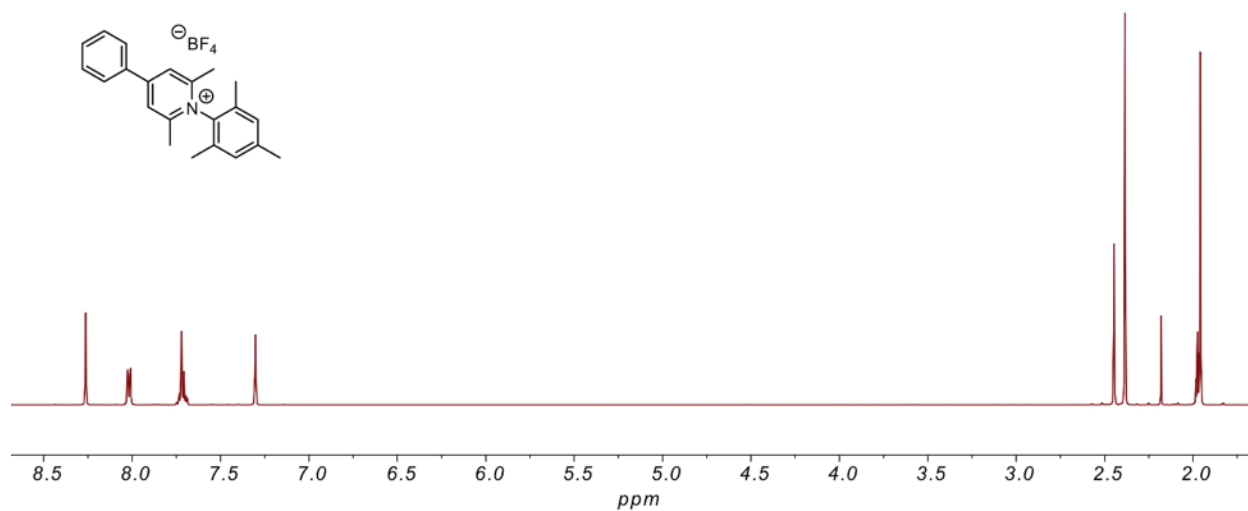


**Figure A.34.** <sup>1</sup>H-NMR spectrum of *N*-(mesityl)-4-phenyl-2,6-dimethylpyridinium tetrafluoroborate (**4**) in CD<sub>3</sub>CN at 25 °C.

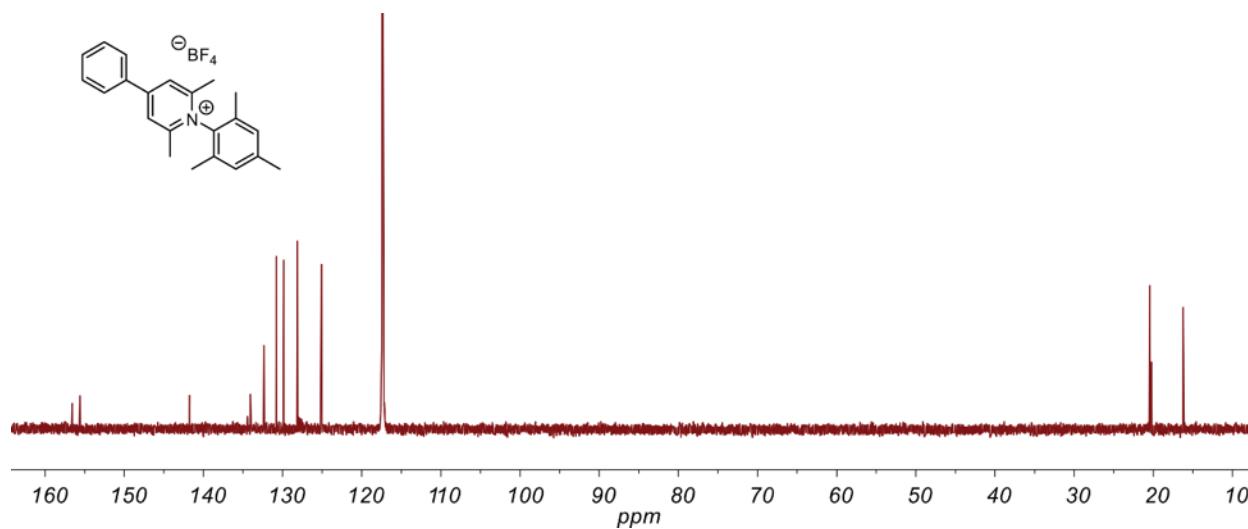


**Figure A.35.** <sup>13</sup>C-NMR spectrum of *N*-(mesityl)-4-phenyl-2,6-dimethylpyridinium tetrafluoroborate (**4**) in CD<sub>3</sub>CN at 25 °C.

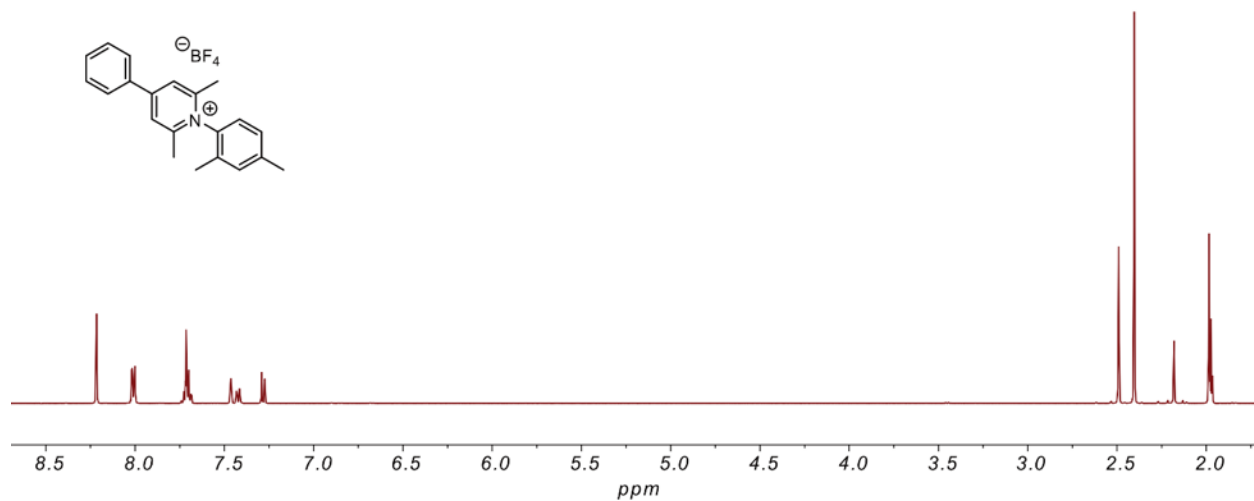


**Figure A.36.**  $^1\text{H-NMR}$  spectrum of  $N-(2,4\text{-xylyl})\text{-}4\text{-phenyl-}2,6\text{-dimethylpyridinium}$  tetrafluoroborate (5) in  $\text{CD}_3\text{CN}$  at  $25^\circ\text{C}$ .

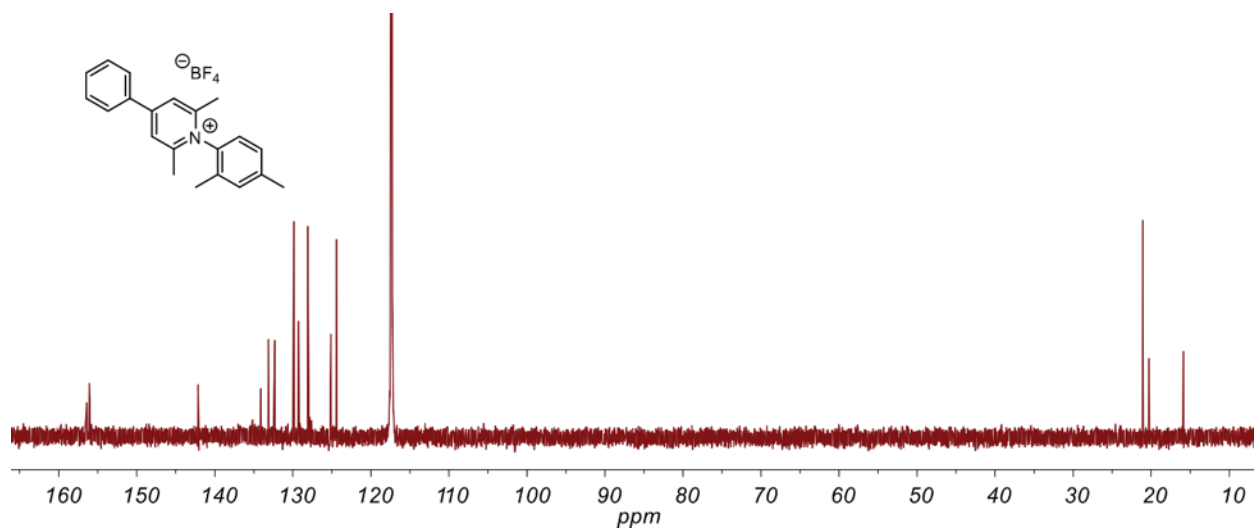


**Figure A.37.**  $^{13}\text{C-NMR}$  spectrum of  $N-(2,4\text{-xylyl})\text{-}4\text{-phenyl-}2,6\text{-dimethylpyridinium}$  tetrafluoroborate (5) in  $\text{CD}_3\text{CN}$  at  $25^\circ\text{C}$ .

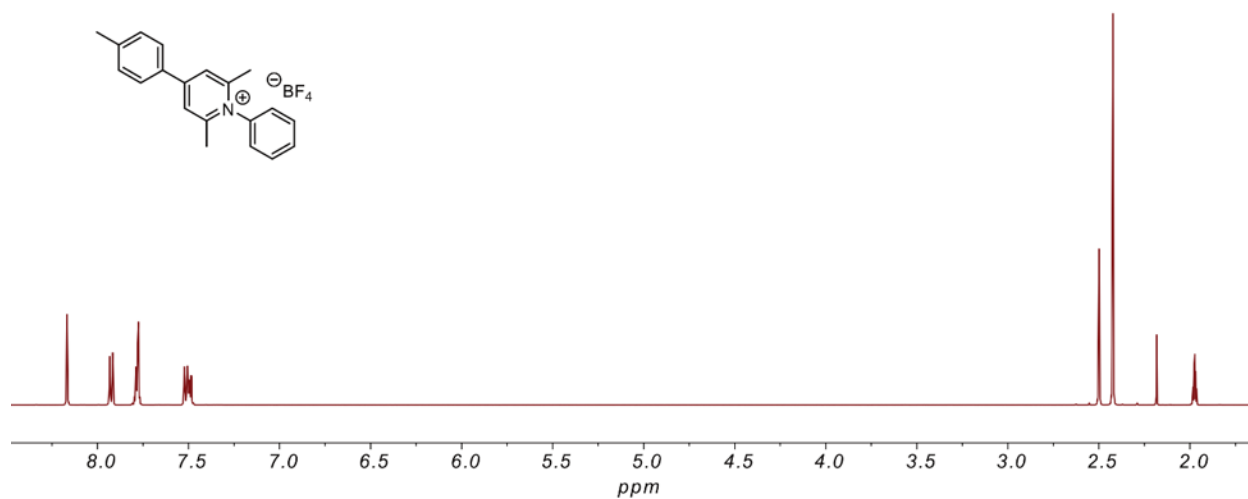


**Figure A.38.** <sup>1</sup>H-NMR spectrum of *N*-phenyl-4-(*p*-tolyl)-2,6-dimethylpyridinium tetrafluoroborate (6) in CD<sub>3</sub>CN at 25 °C.

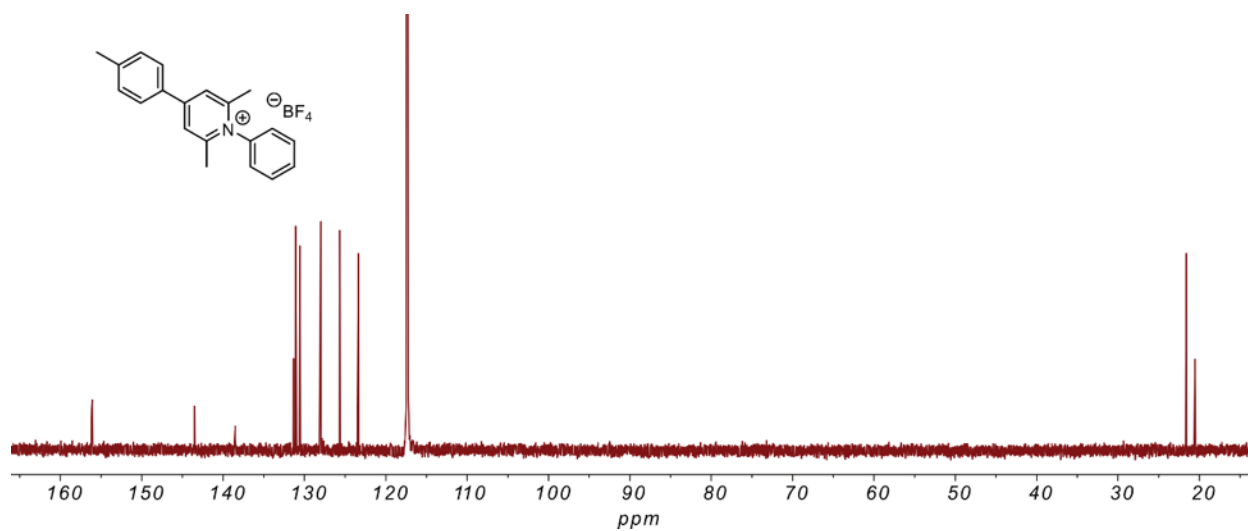


**Figure A.39.** <sup>13</sup>C-NMR spectrum of *N*-phenyl-4-(*p*-tolyl)-2,6-dimethylpyridinium tetrafluoroborate (6) in CD<sub>3</sub>CN at 25 °C.

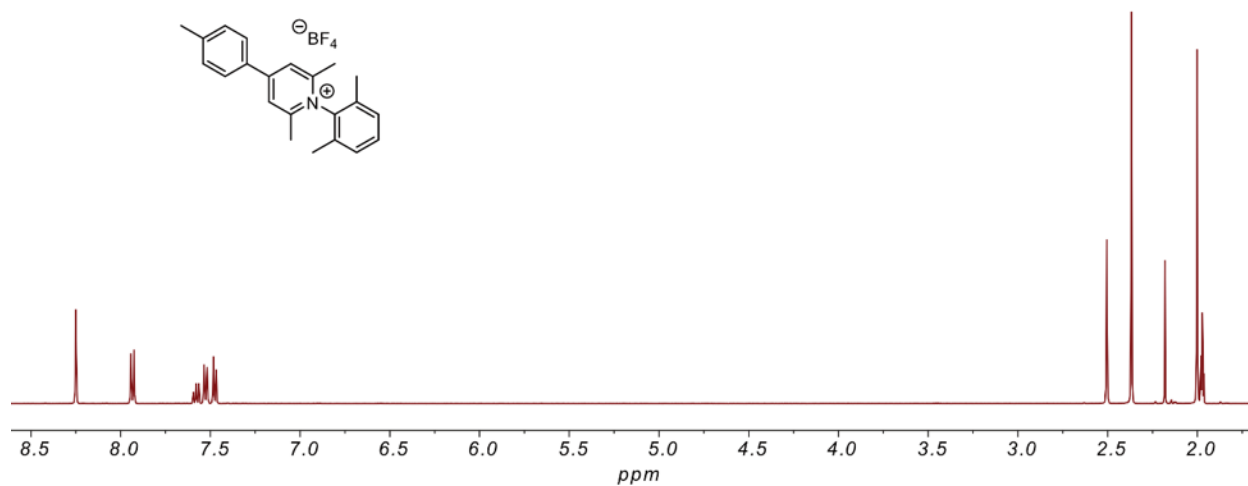


**Figure A.40.** <sup>1</sup>H-NMR spectrum of *N*-(2,6-xylyl)-4-(*p*-tolyl)-2,6-dimethylpyridinium tetrafluoroborate (7) in CD<sub>3</sub>CN at 25 °C.

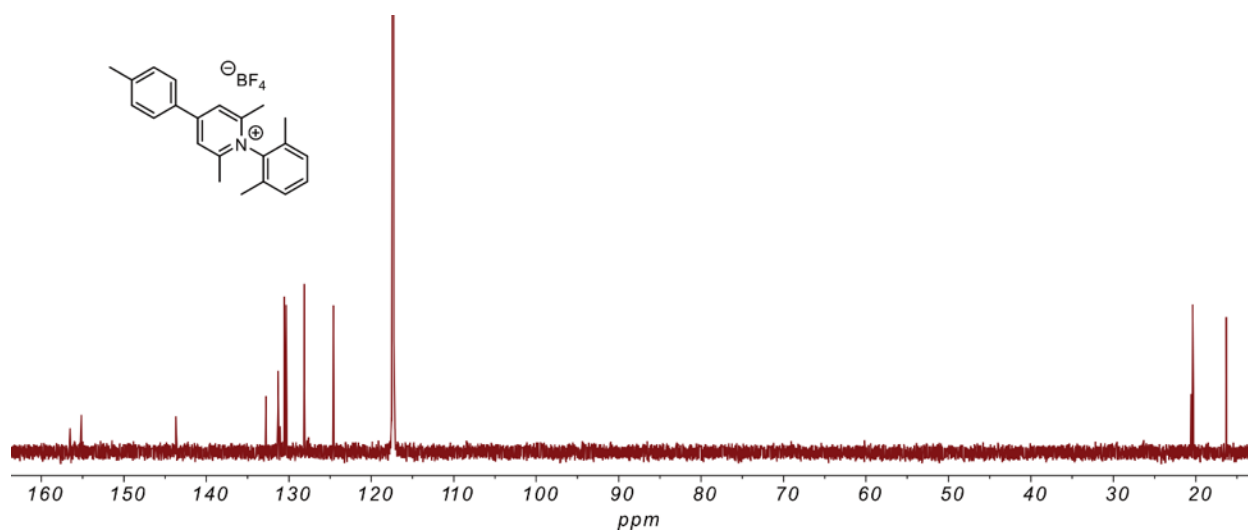


**Figure A.41.** <sup>13</sup>C-NMR spectrum of *N*-(2,6-xylyl)-4-(*p*-tolyl)-2,6-dimethylpyridinium tetrafluoroborate (7) in CD<sub>3</sub>CN at 25 °C.

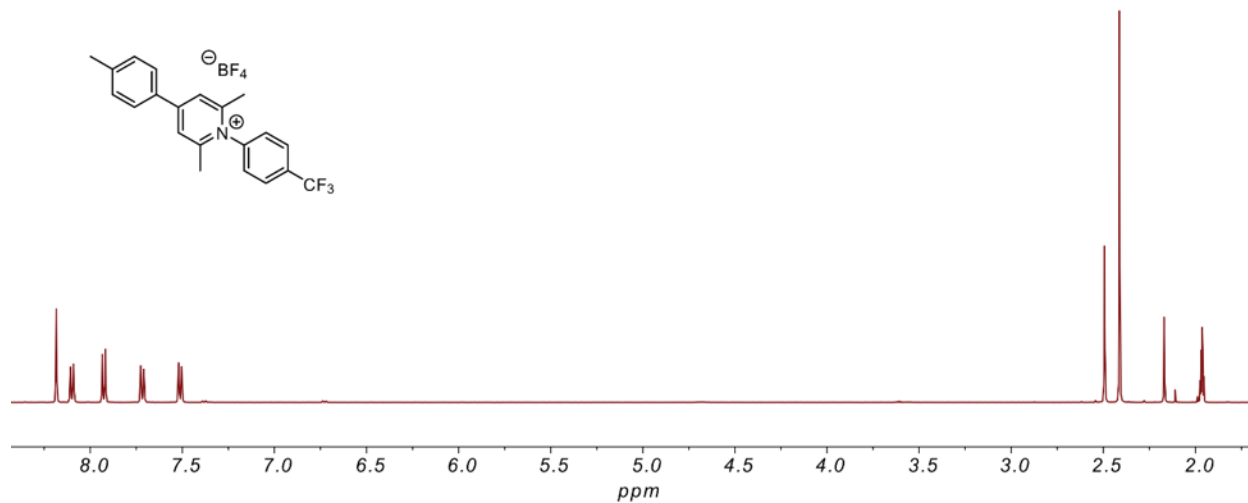


**Figure A.42.** <sup>1</sup>H-NMR spectrum of *N*-(*p*-trifluoromethylphenyl)-4-(*p*-tolyl)-2,6-dimethylpyridinium tetrafluoroborate (8) in CD<sub>3</sub>CN at 25 °C.

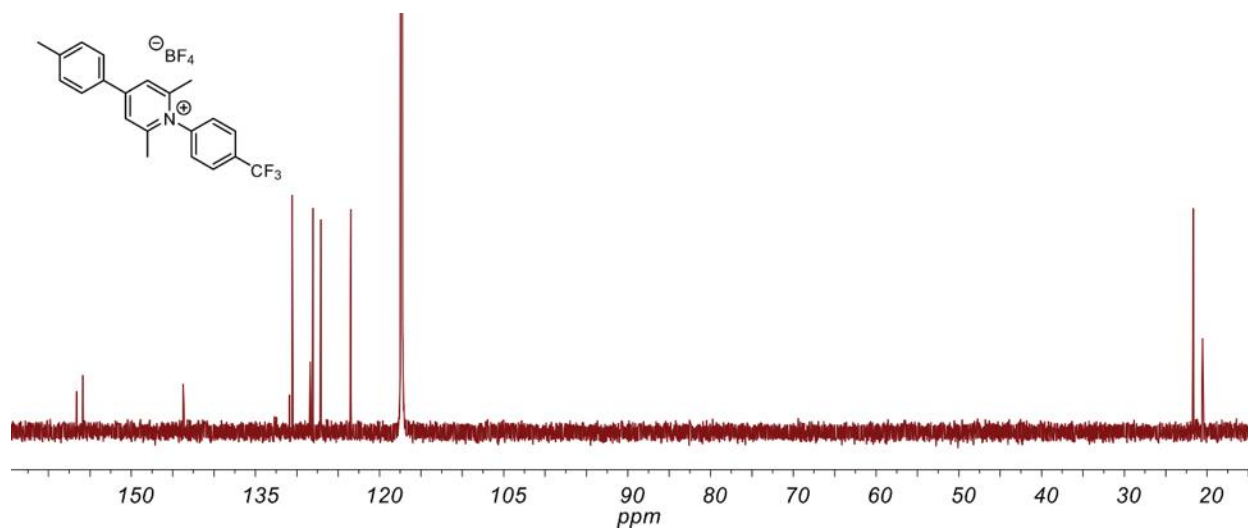


**Figure A.43.** <sup>13</sup>C-NMR spectrum of *N*-(*p*-trifluoromethylphenyl)-4-(*p*-tolyl)-2,6-dimethylpyridinium tetrafluoroborate (8) in CD<sub>3</sub>CN at 25 °C.

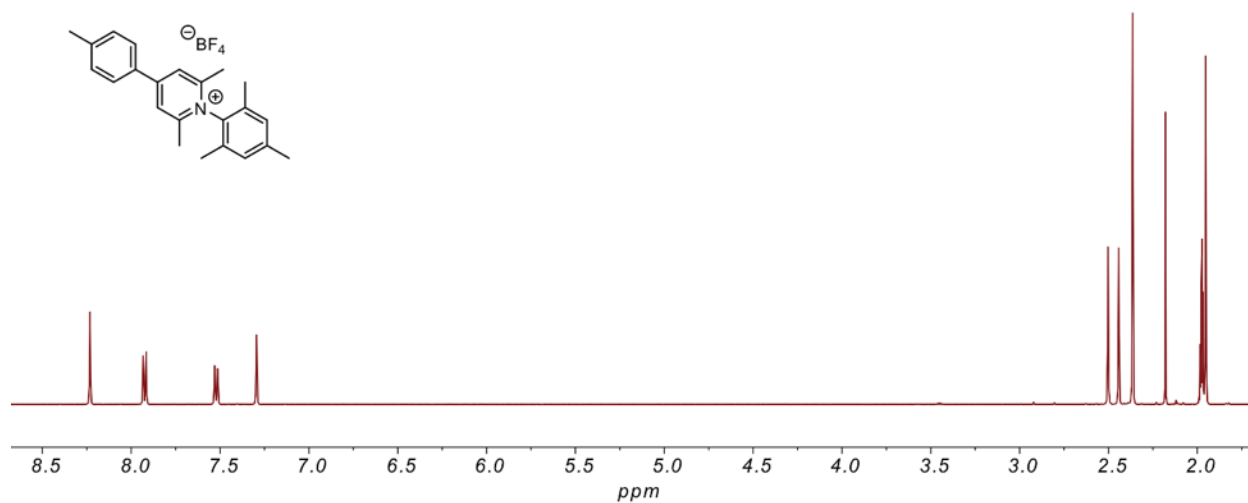


**Figure A.44.** <sup>1</sup>H-NMR spectrum of *N*-(mesityl)-4-(*p*-tolyl)-2,6-dimethylpyridinium tetrafluoroborate (**9**) in CD<sub>3</sub>CN at 25 °C.

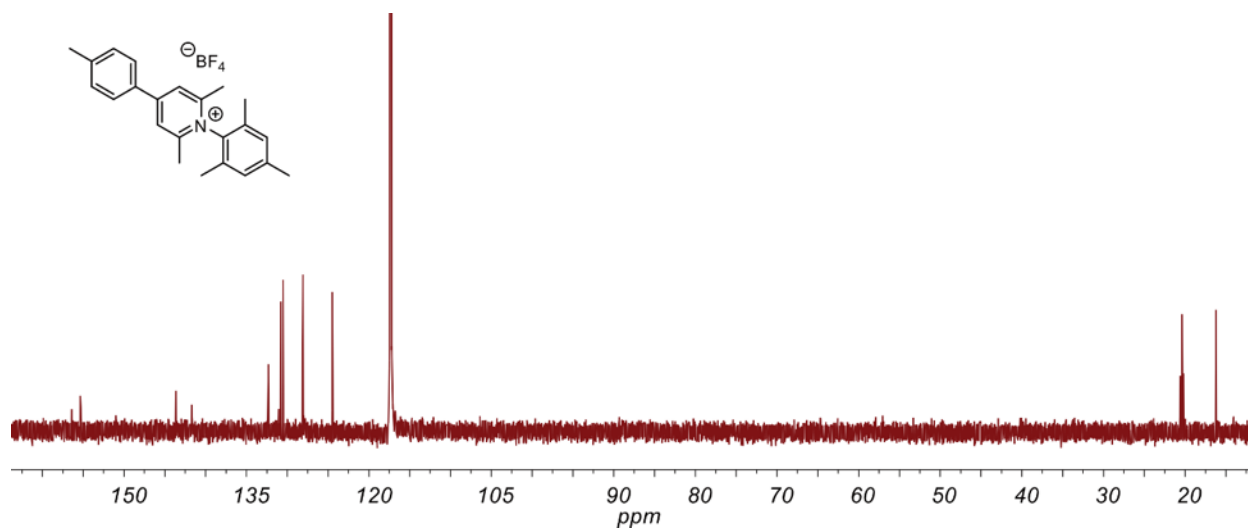


**Figure A.45.** <sup>13</sup>C-NMR spectrum of *N*-(mesityl)-4-(*p*-tolyl)-2,6-dimethylpyridinium tetrafluoroborate (**9**) in CD<sub>3</sub>CN at 25 °C.

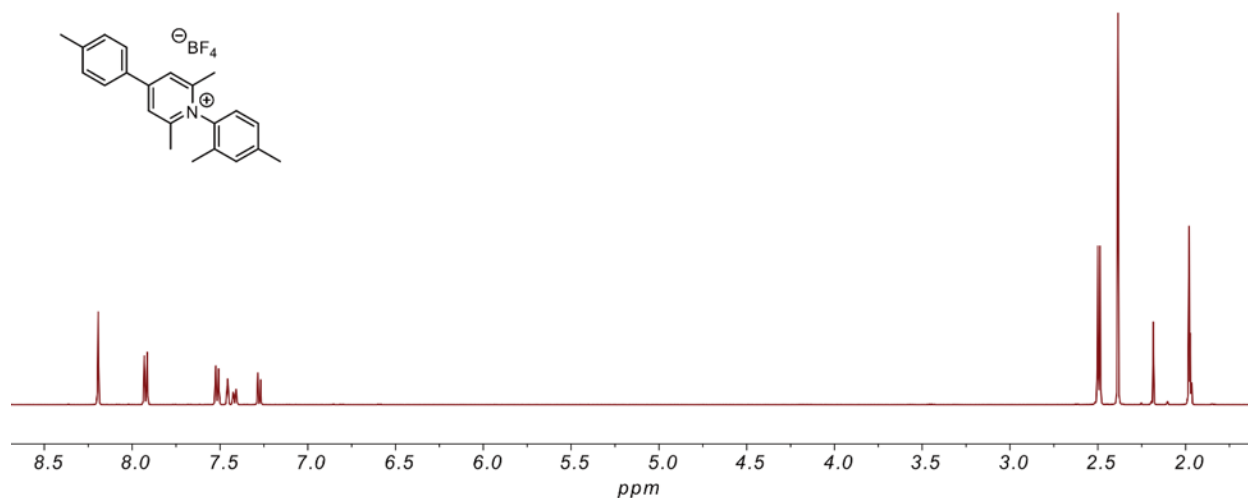


**Figure A.46.** <sup>1</sup>H-NMR spectrum of *N*-(2,4-xylyl)-4-(*p*-tolyl)-2,6-dimethylpyridinium tetrafluoroborate (10) in CD<sub>3</sub>CN at 25 °C.

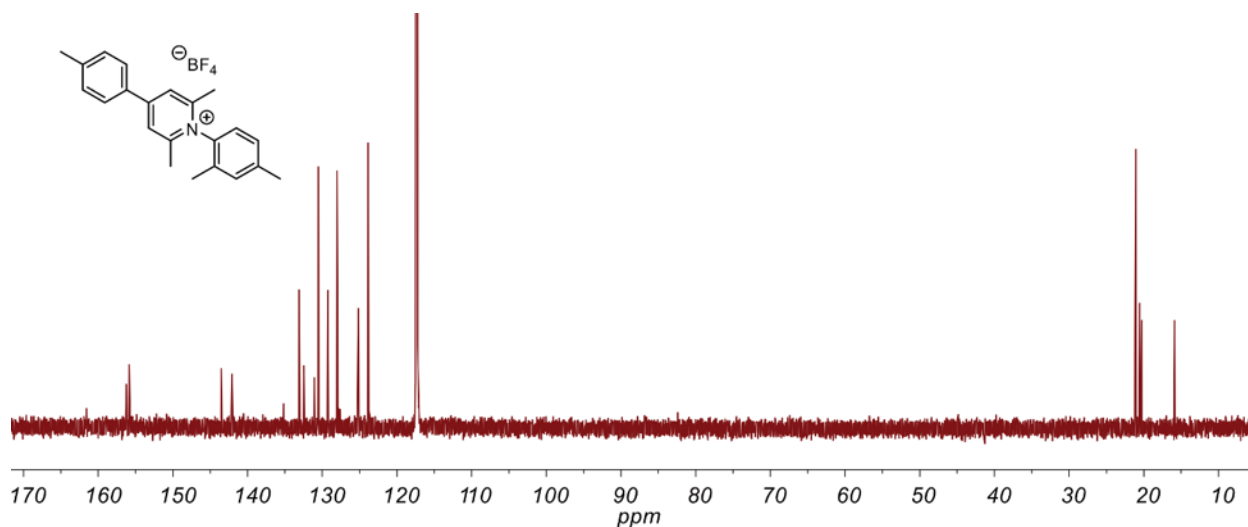


**Figure A.47.** <sup>13</sup>C-NMR spectrum of *N*-(2,4-xylyl)-4-(*p*-tolyl)-2,6-dimethylpyridinium tetrafluoroborate (10) in CD<sub>3</sub>CN at 25 °C.



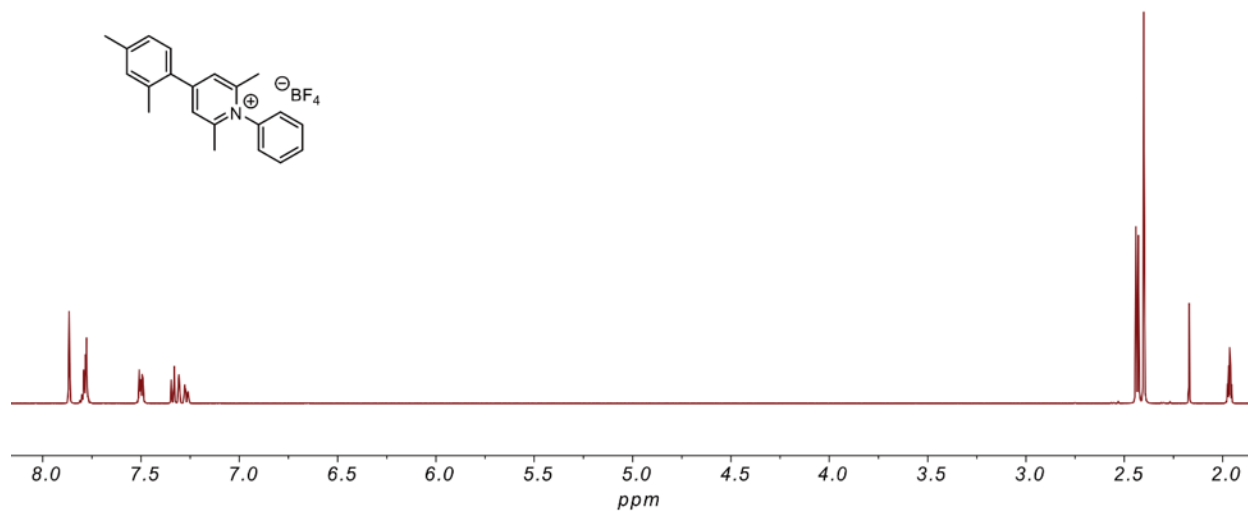


**Figure A.48.** <sup>1</sup>H-NMR spectrum of *N*-phenyl-4-(2,4-xylyl)-2,6-dimethylpyridinium tetrafluoroborate (11) in CD<sub>3</sub>CN at 25 °C.

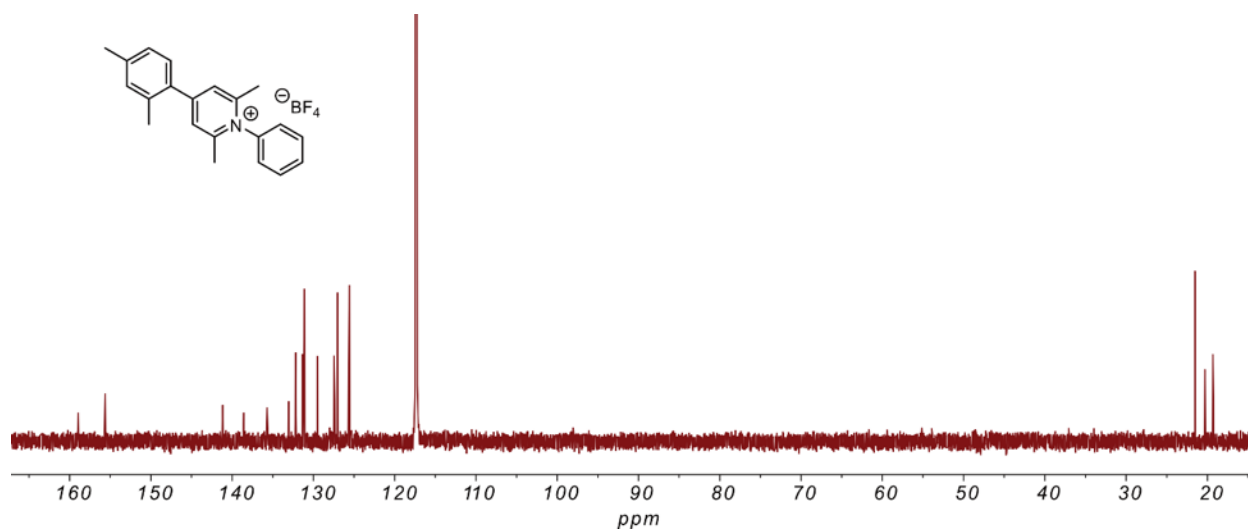


**Figure A.49.** <sup>13</sup>C-NMR spectrum of *N*-phenyl-4-(2,4-xylyl)-2,6-dimethylpyridinium tetrafluoroborate (11) in CD<sub>3</sub>CN at 25 °C.

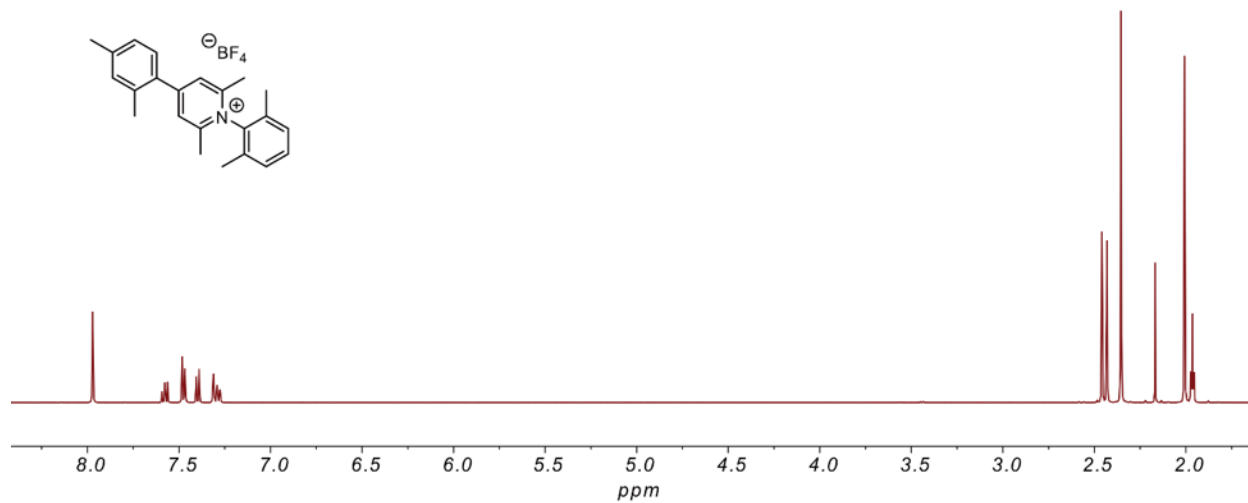


**Figure A.50.** <sup>1</sup>H-NMR spectrum of *N*-(2,6-xylyl)-4-(2,4-xylyl)-2,6-dimethylpyridinium tetrafluoroborate (12) in CD<sub>3</sub>CN at 25 °C.

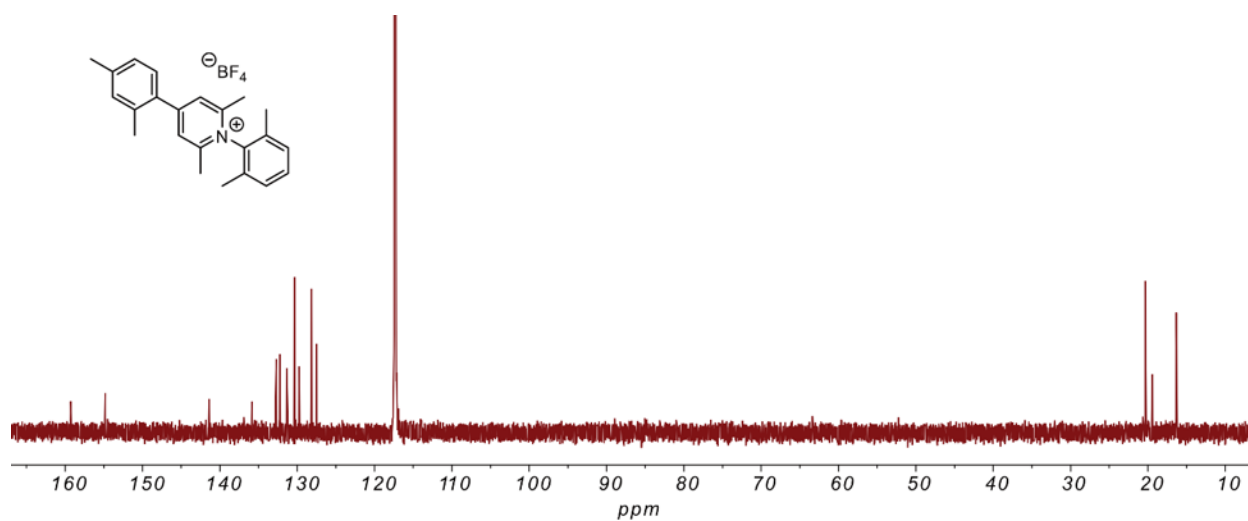


**Figure A.51.** <sup>13</sup>C-NMR spectrum of *N*-(2,6-xylyl)-4-(2,4-xylyl)-2,6-dimethylpyridinium tetrafluoroborate (12) in CD<sub>3</sub>CN at 25 °C.

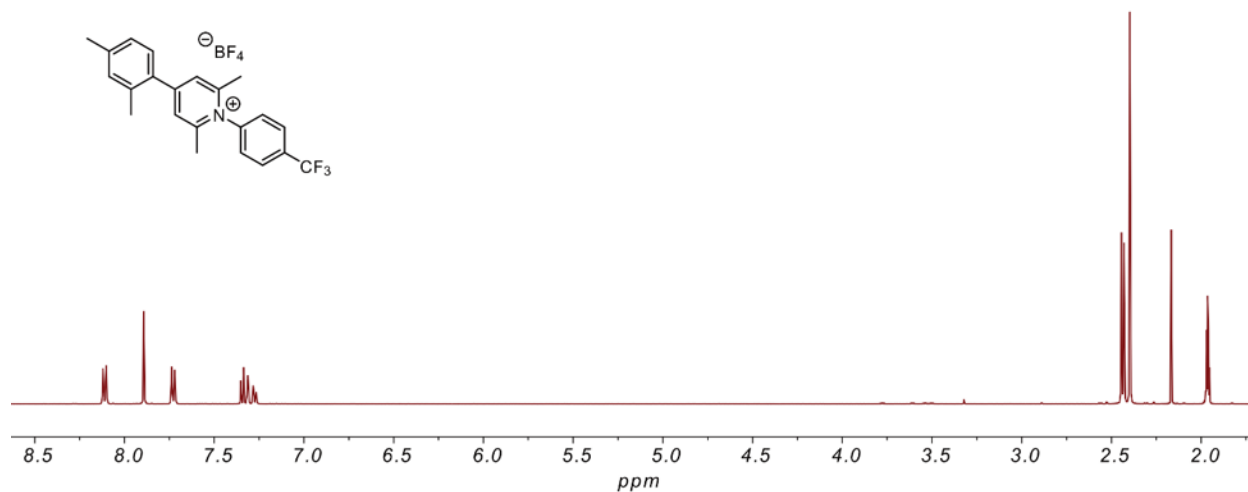


**Figure A.52.**  $^1\text{H}$ -NMR spectrum of *N*-(*p*-trifluoromethylphenyl)-4-(2,4-xylyl)-2,6-dimethylpyridinium tetrafluoroborate (13) in  $\text{CD}_3\text{CN}$  at 25 °C.

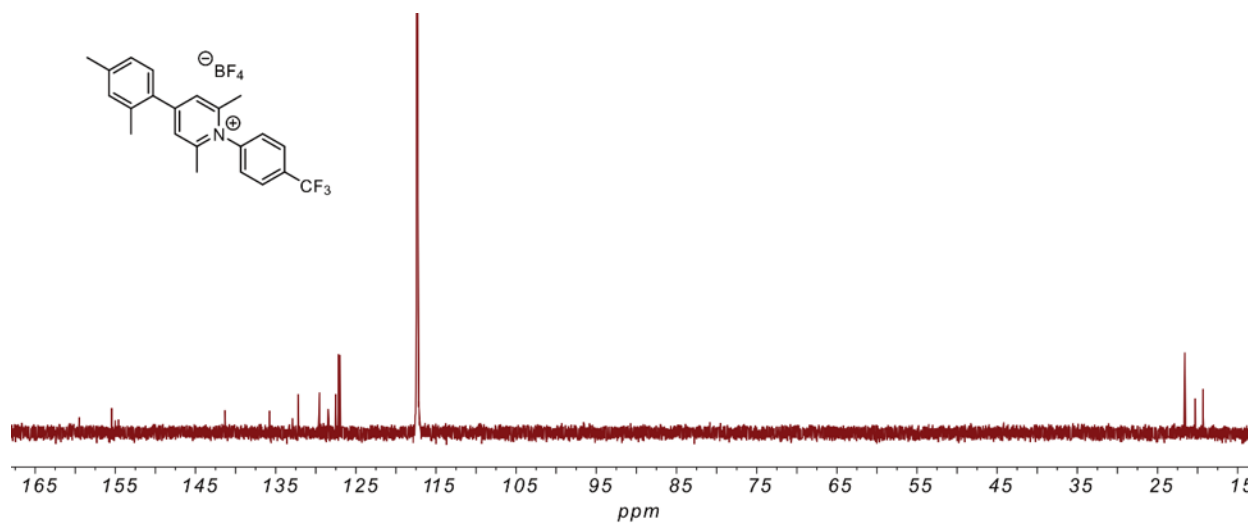


**Figure A.53.**  $^{13}\text{C}$ -NMR spectrum of *N*-(*p*-trifluoromethylphenyl)-4-(2,4-xylyl)-2,6-dimethylpyridinium tetrafluoroborate (13) in  $\text{CD}_3\text{CN}$  at 25 °C.

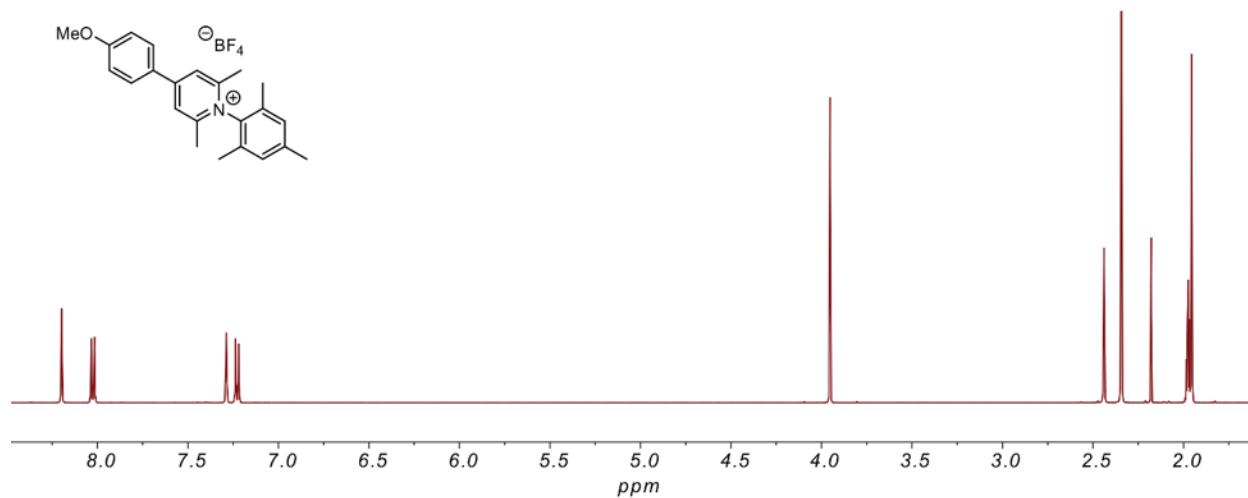


**Figure A.54.** <sup>1</sup>H-NMR spectrum of *N*-(mesityl)-4-(*p*-methoxyphenyl)-2,6-dimethylpyridinium tetrafluoroborate (14) in CD<sub>3</sub>CN at 25 °C.

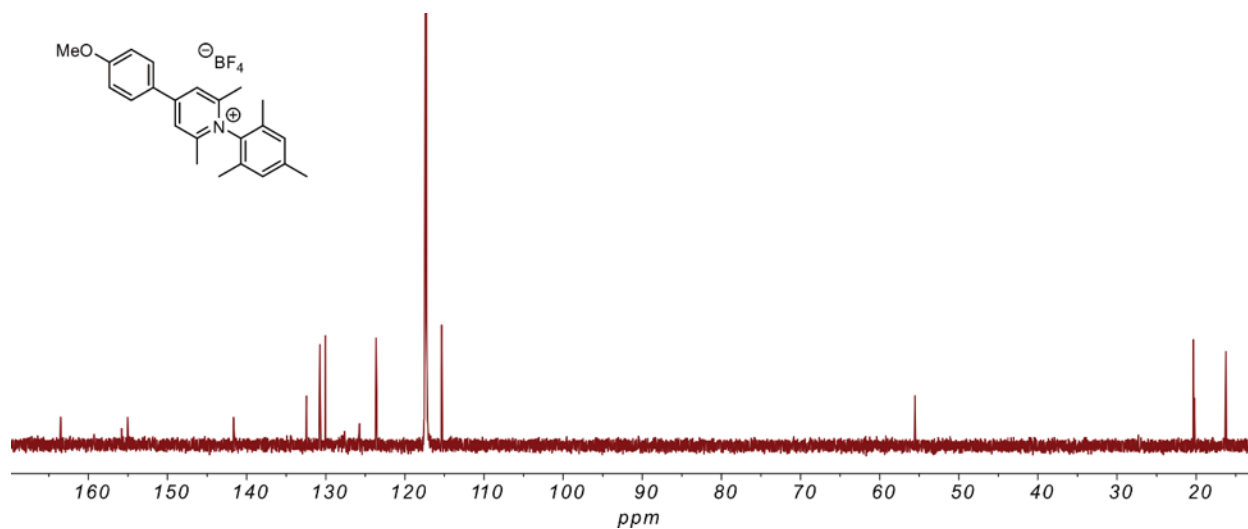


**Figure A.55.** <sup>13</sup>C-NMR spectrum of *N*-(mesityl)-4-(*p*-methoxyphenyl)-2,6-dimethylpyridinium tetrafluoroborate (14) in CD<sub>3</sub>CN at 25 °C.

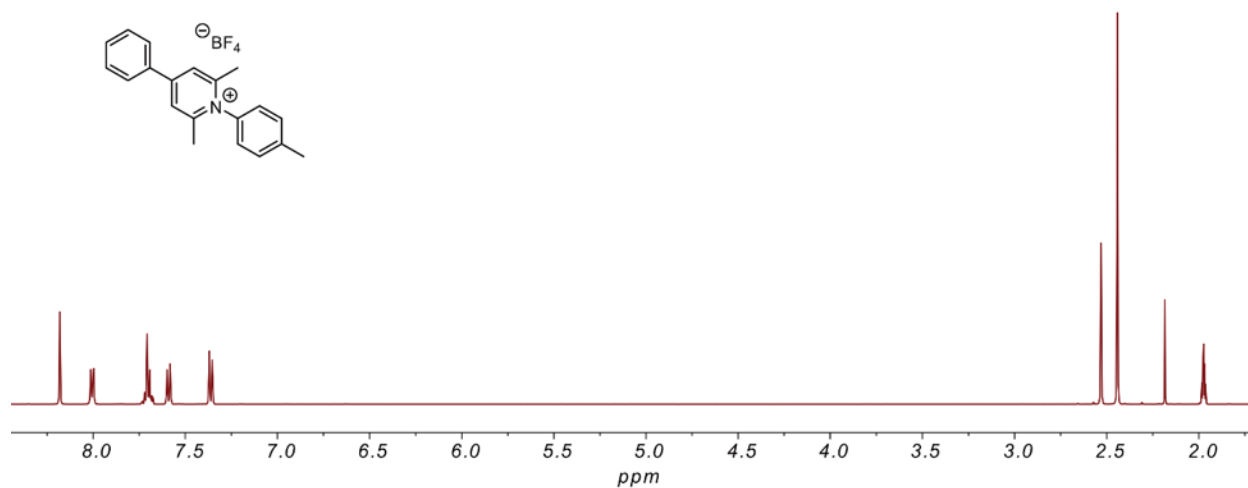


**Figure A.56.** <sup>1</sup>H-NMR spectrum of *N*-(*p*-tolyl)-4-phenyl-2,6-dimethylpyridinium tetrafluoroborate (15) in CD<sub>3</sub>CN at 25 °C.

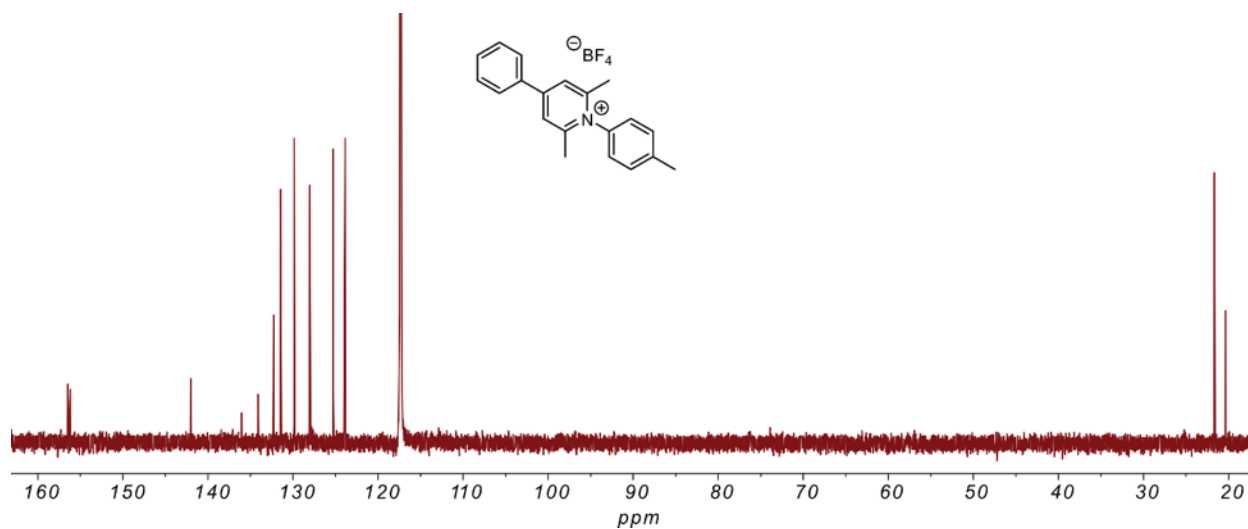


**Figure A.57.** <sup>13</sup>C-NMR spectrum of *N*-(*p*-tolyl)-4-phenyl-2,6-dimethylpyridinium tetrafluoroborate (15) in CD<sub>3</sub>CN at 25 °C.

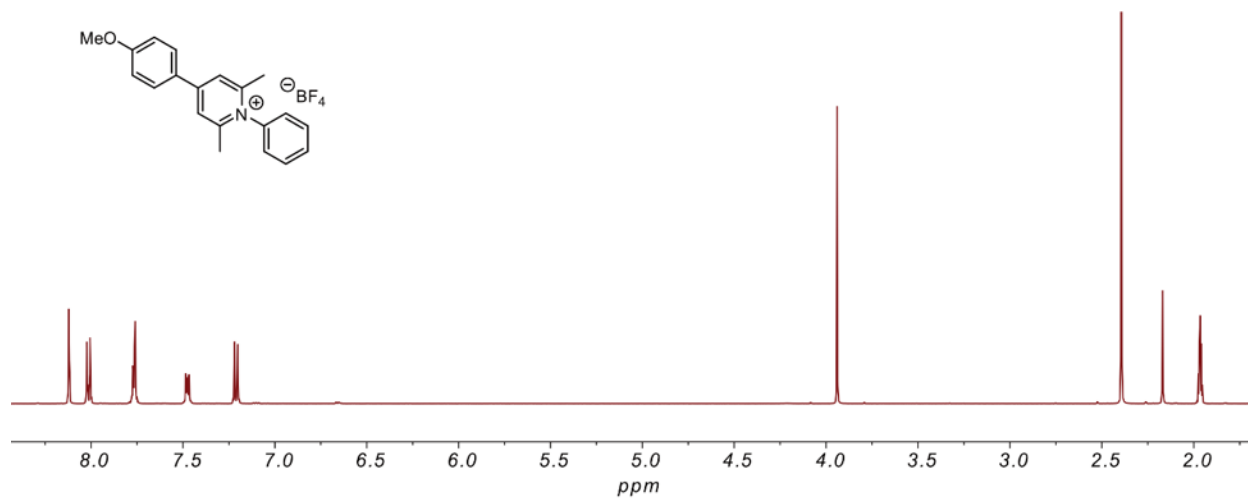


**Figure A.58.** <sup>1</sup>H-NMR spectrum of *N*-phenyl-4-(*p*-methoxyphenyl)-2,6-dimethylpyridinium tetrafluoroborate (16) in CD<sub>3</sub>CN at 25 °C.

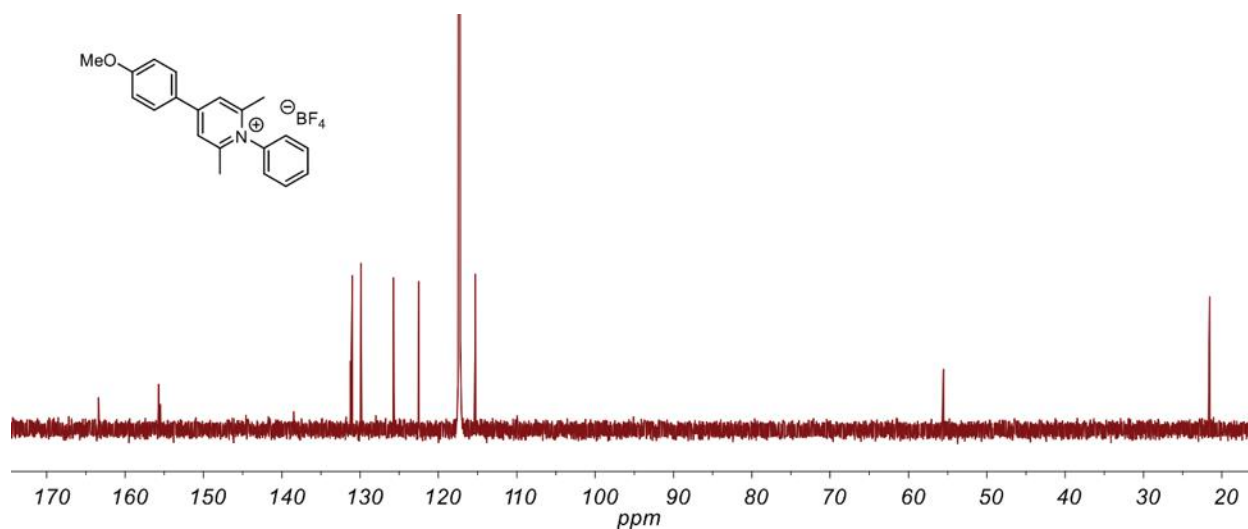


**Figure A.59.** <sup>13</sup>C-NMR spectrum of *N*-phenyl-4-(*p*-methoxyphenyl)-2,6-dimethylpyridinium tetrafluoroborate (16) in CD<sub>3</sub>CN at 25 °C.

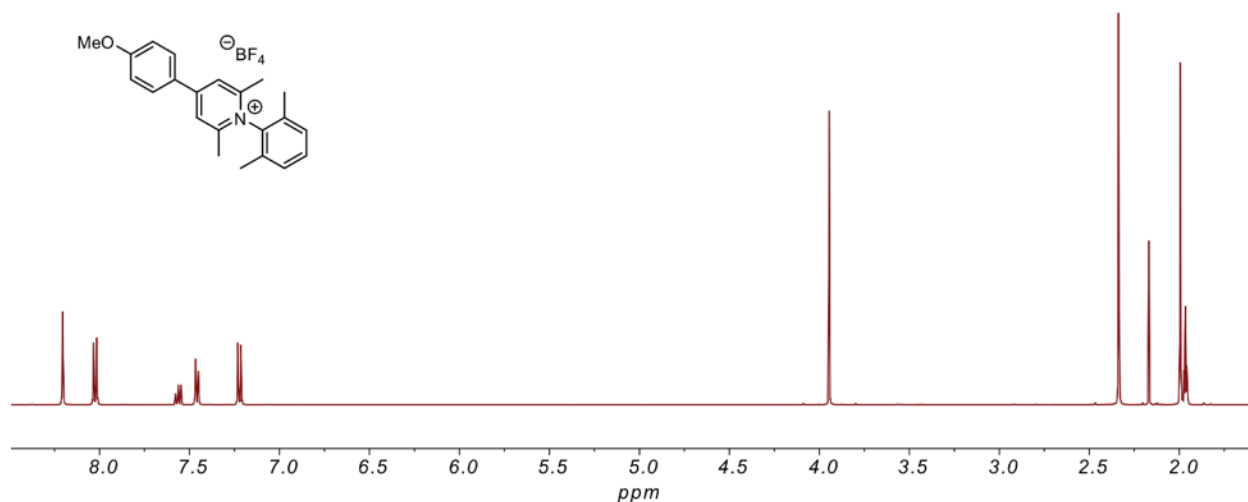


**Figure A.60.**  $^1\text{H-NMR}$  spectrum of *N*-(2,6-xylyl)-4-(*p*-methoxyphenyl)-2,6-dimethylpyridinium (17) tetrafluoroborate in  $\text{CD}_3\text{CN}$  at  $25\text{ }^\circ\text{C}$ .

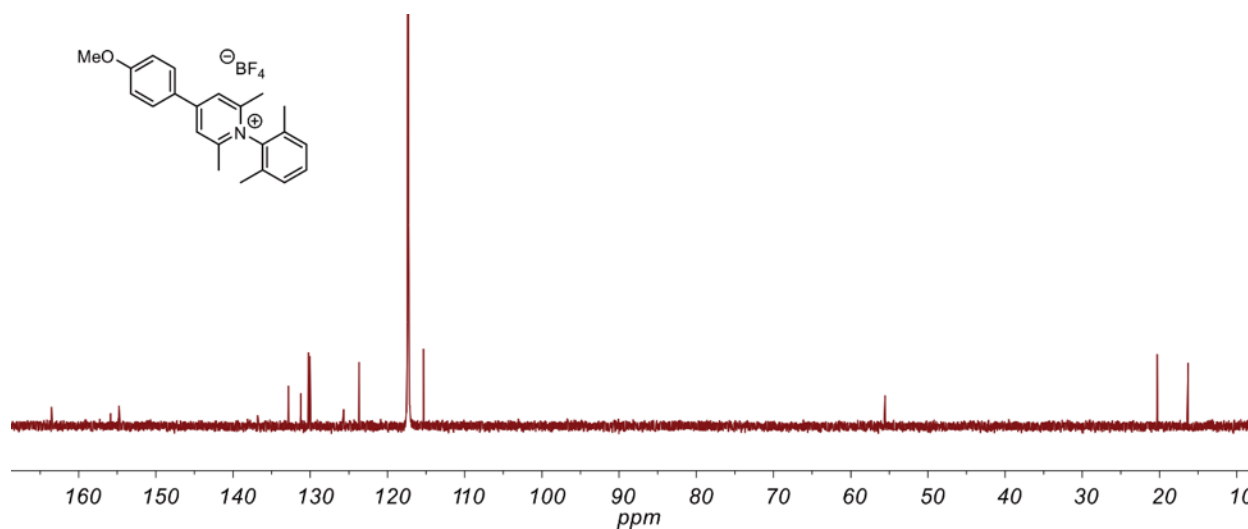


**Figure A.61.**  $^{13}\text{C-NMR}$  spectrum of *N*-(2,6-xylyl)-4-(*p*-methoxyphenyl)-2,6-dimethylpyridinium tetrafluoroborate (17) in  $\text{CD}_3\text{CN}$  at  $25\text{ }^\circ\text{C}$ .

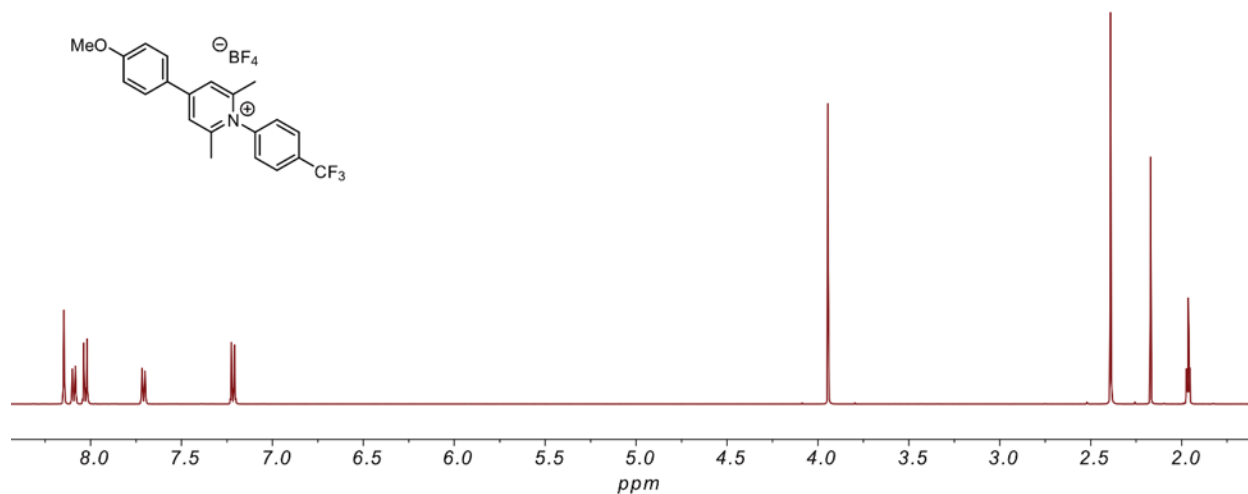


**Figure A.62.**  $^1\text{H}$ -NMR spectrum of *N*-(*p*-trifluoromethylphenyl)-4-(*p*-methoxyphenyl)-2,6-dimethylpyridinium tetrafluoroborate (18) in  $\text{CD}_3\text{CN}$  at 25 °C.

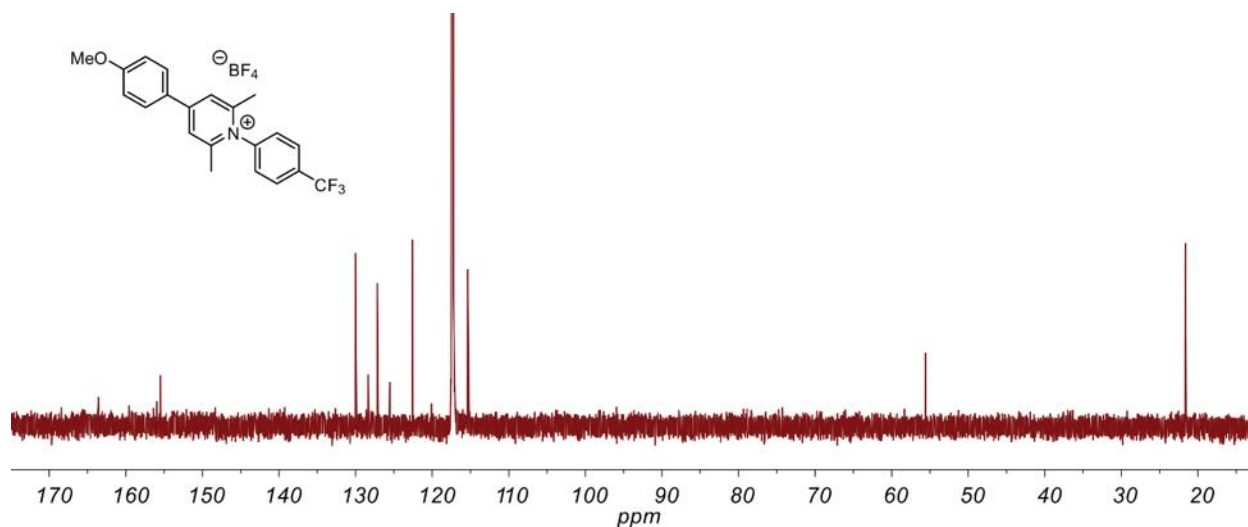


**Figure A.63.**  $^{13}\text{C}$ -NMR spectrum of *N*-(*p*-trifluoromethylphenyl)-4-(*p*-methoxyphenyl)-2,6-dimethylpyridinium tetrafluoroborate (18) in  $\text{CD}_3\text{CN}$  at 25 °C.



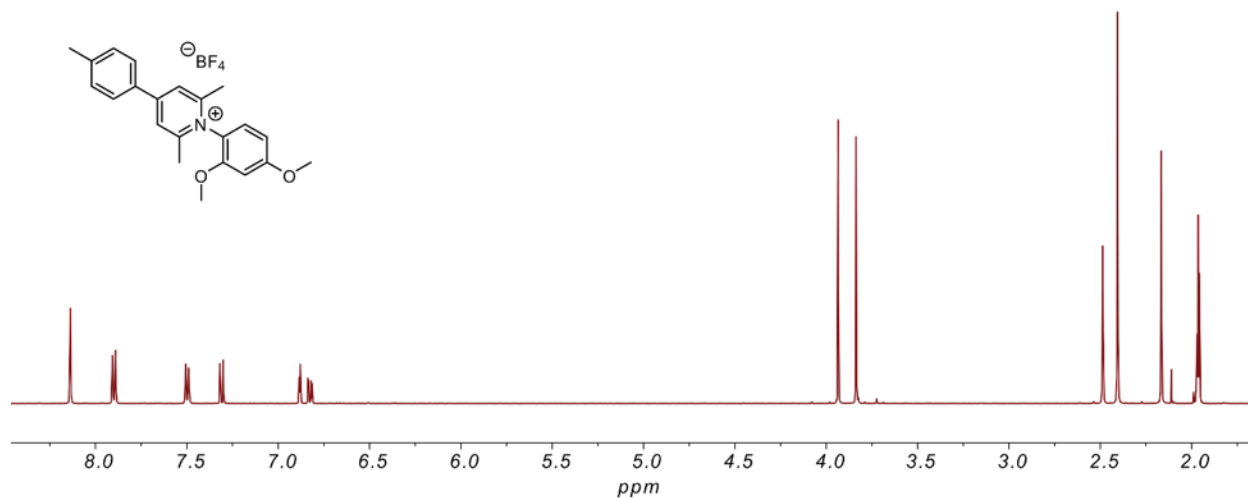


**Figure A.64.** <sup>1</sup>H-NMR spectrum of *N*-(2,4-dimethoxybenzene)-4-(*p*-tolyl)-2,6-dimethylpyridinium tetrafluoroborate (**19**) in CD<sub>3</sub>CN at 25 °C.

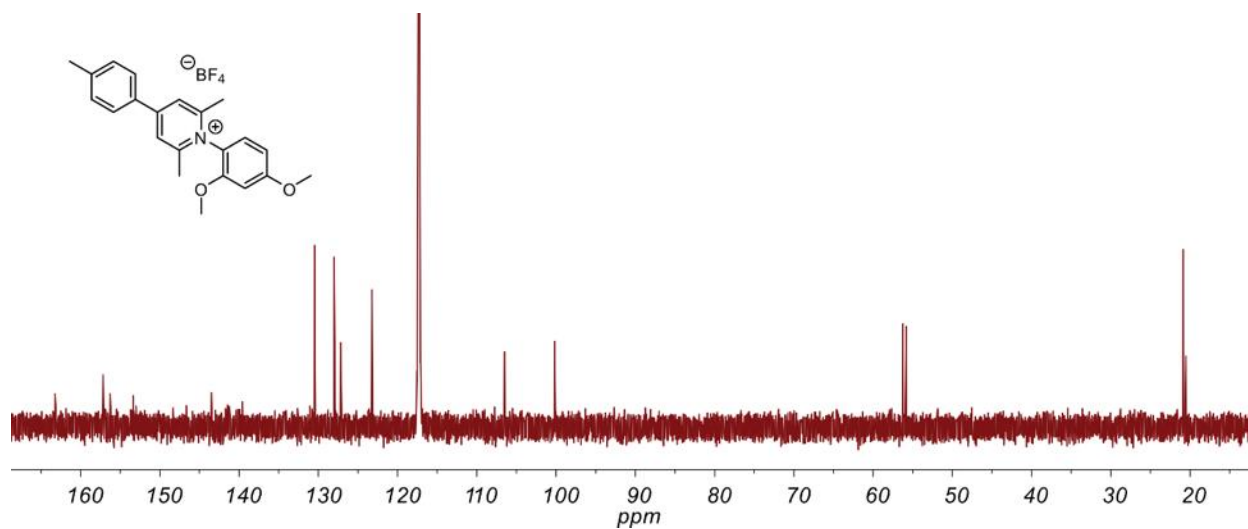


**Figure A.65.** <sup>13</sup>C-NMR spectrum of *N*-(2,4-dimethoxybenzene)-4-(*p*-tolyl)-2,6-dimethylpyridinium tetrafluoroborate (**19**) in CD<sub>3</sub>CN at 25 °C.

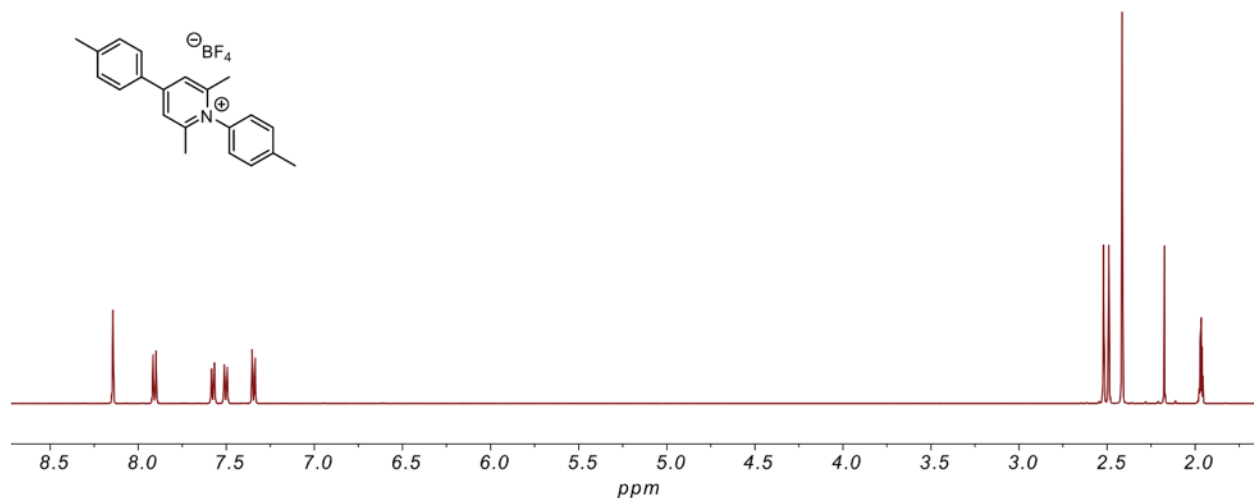


**Figure A.66.** <sup>1</sup>H-NMR spectrum of *N*-(*p*-tolyl)-4-(*p*-tolyl)-2,6-dimethylpyridinium tetrafluoroborate (20) in CD<sub>3</sub>CN at 25 °C.

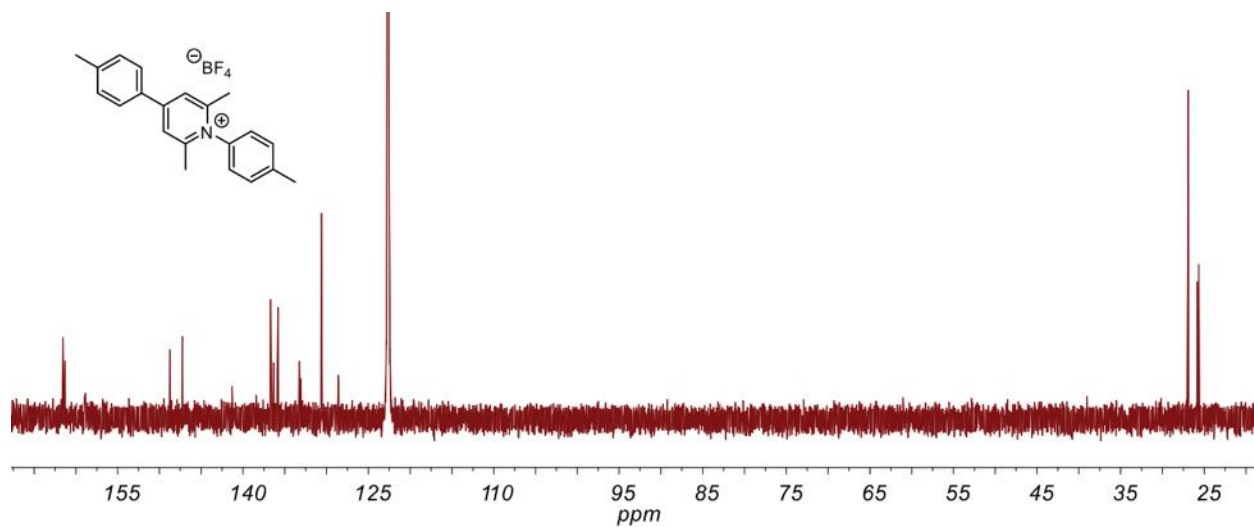


**Figure A.67.** <sup>13</sup>C-NMR spectrum of *N*-(*p*-tolyl)-4-(*p*-tolyl)-2,6-dimethylpyridinium tetrafluoroborate (20) in CD<sub>3</sub>CN at 25 °C.

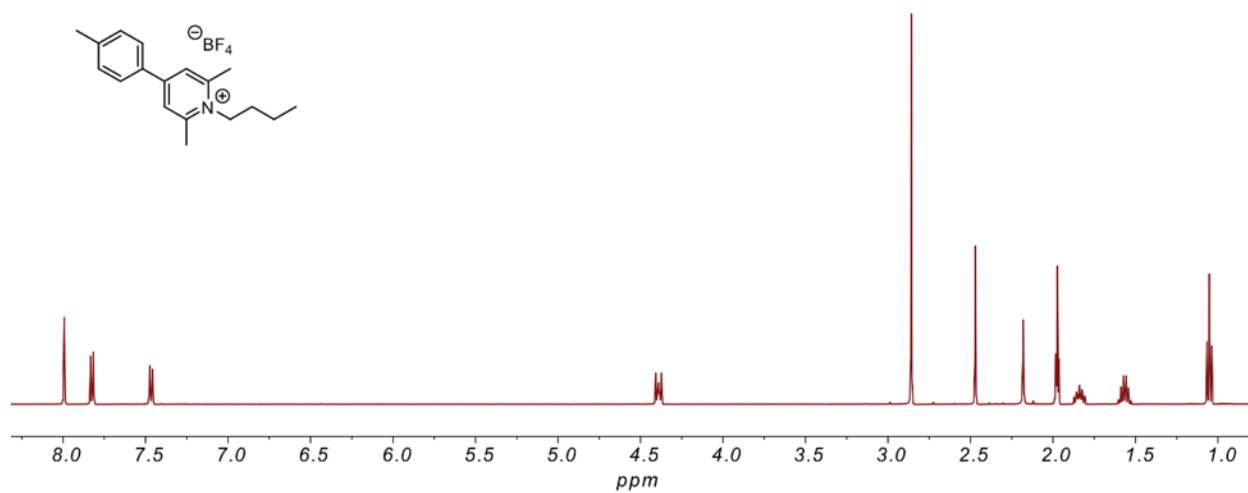


**Figure A.68.**  $^1\text{H-NMR}$  spectrum of  $N$ -(*n*-butyl)-4-(*p*-tolyl)-2,6-dimethylpyridinium tetrafluoroborate (22) in  $\text{CD}_3\text{CN}$  at 25 °C.

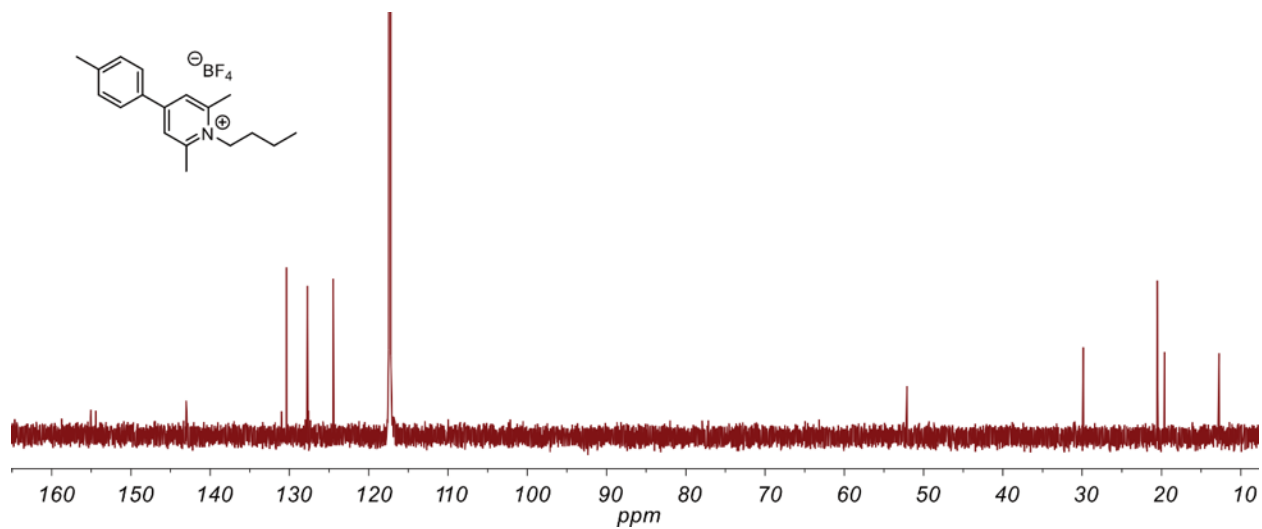


**Figure A.69.**  $^{13}\text{C-NMR}$  spectrum of  $N$ -(*n*-butyl)-4-(*p*-tolyl)-2,6-dimethylpyridinium tetrafluoroborate (22) in  $\text{CD}_3\text{CN}$  at 25 °C.

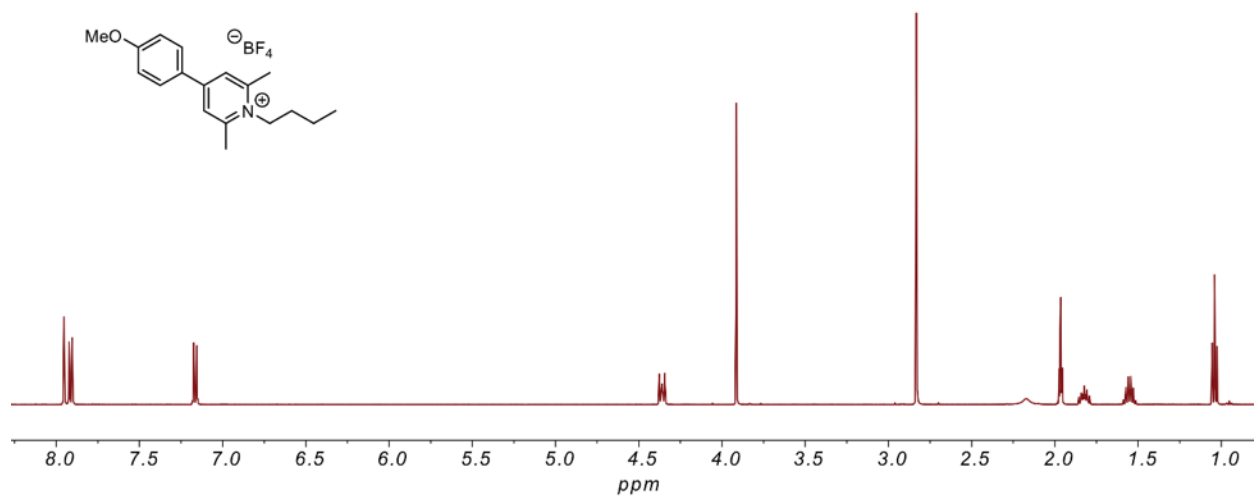


**Figure A.70.**  $^1\text{H}$ -NMR spectrum of *N*-(*n*-butyl)-4-(*p*-methoxyphenyl)-2,6-dimethylpyridinium tetrafluoroborate (23) in  $\text{CD}_3\text{CN}$  at  $25\text{ }^\circ\text{C}$ .

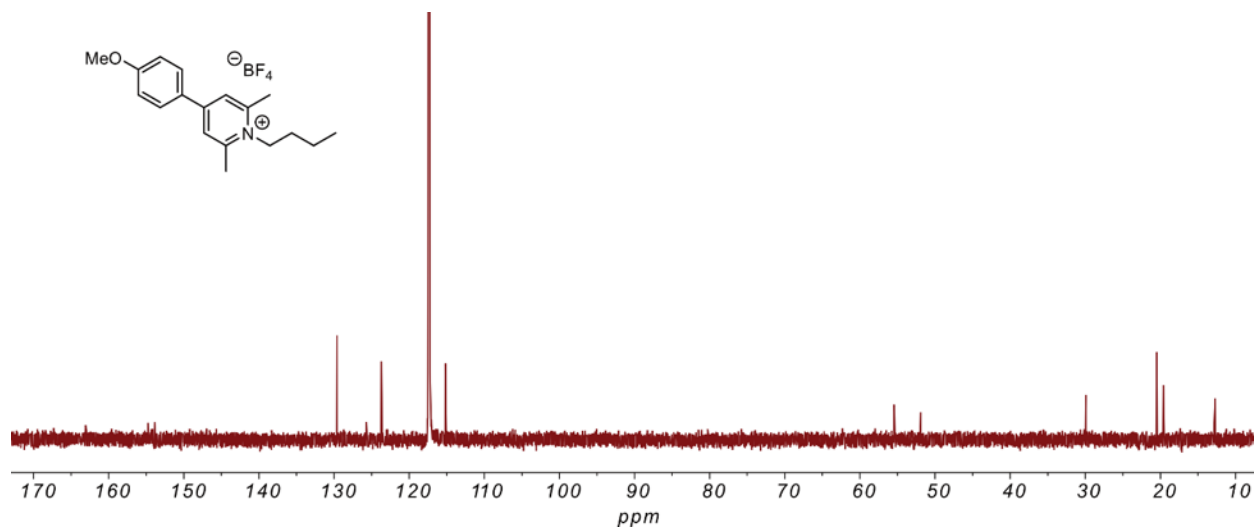


**Figure A.71.**  $^{13}\text{C}$ -NMR spectrum of *N*-(*n*-butyl)-4-(*p*-methoxyphenyl)-2,6-dimethylpyridinium tetrafluoroborate (23) in  $\text{CD}_3\text{CN}$  at  $25\text{ }^\circ\text{C}$ .

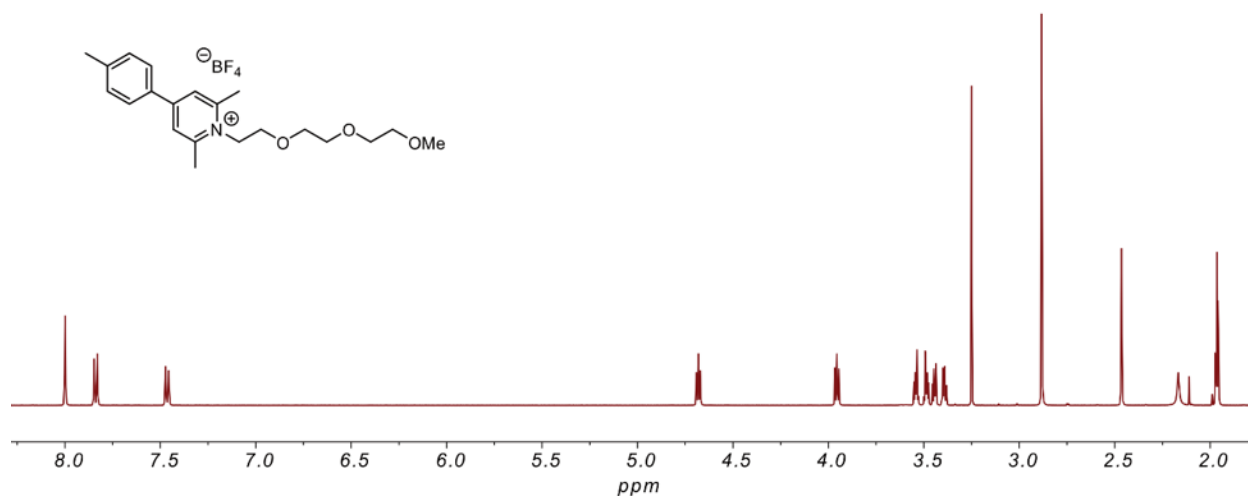


**Figure A.72.** <sup>1</sup>H-NMR spectrum of *N*-(2-(2-(2-methoxyethoxy)ethoxy)ethyl)-4-(*p*-tolyl)-2,6-dimethylpyridinium tetrafluoroborate (24) in CD<sub>3</sub>CN at 25 °C.

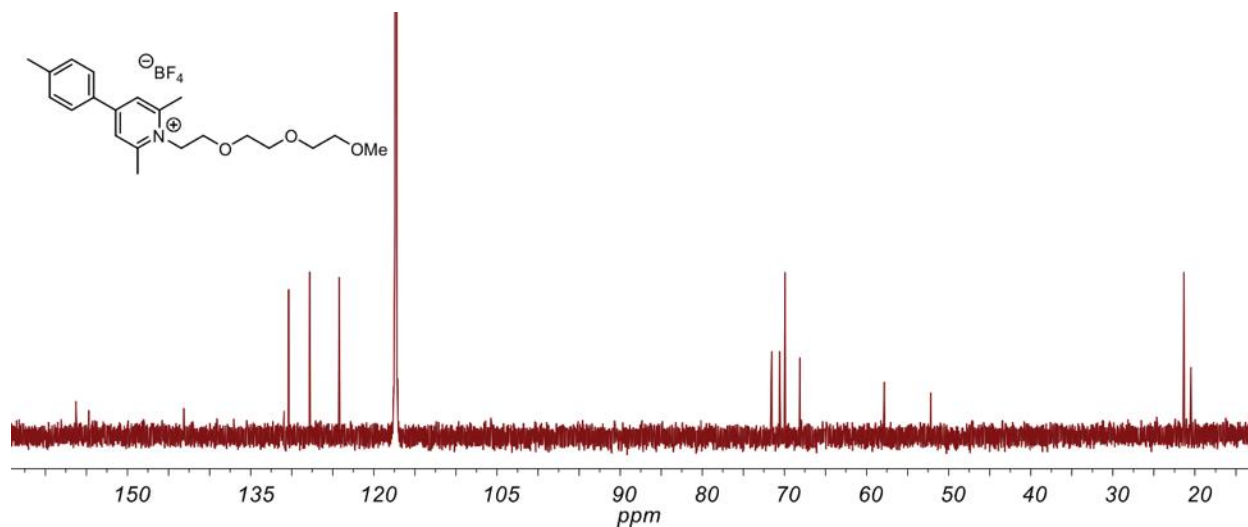


**Figure A.73.** <sup>13</sup>C-NMR spectrum of *N*-(2-(2-(2-methoxyethoxy)ethoxy)ethyl)-4-(*p*-tolyl)-2,6-dimethylpyridinium tetrafluoroborate (24) in CD<sub>3</sub>CN at 25 °C.

## A.8. X-ray Crystal Structures of Pyridinium Tetrafluoroborate Salts

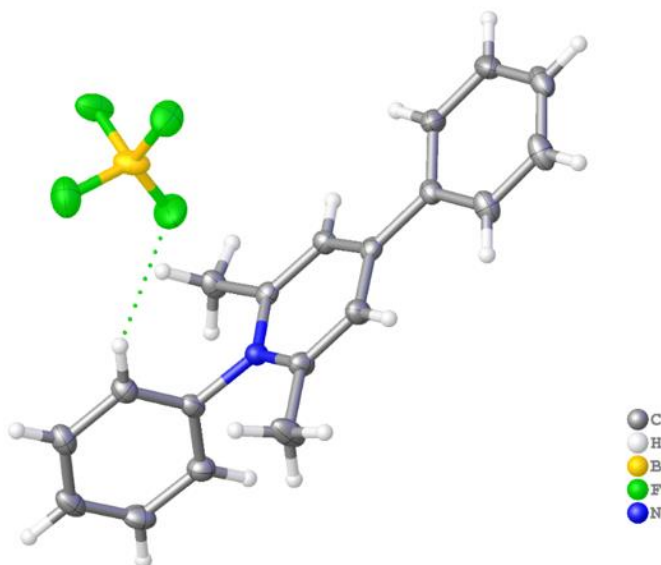


Figure A.74. X-Ray crystal structure of *N*-phenyl-4-phenyl-2,6-dimethylpyridinium tetrafluoroborate (1) [50% thermal ellipsoid]; CCDC-2157789.

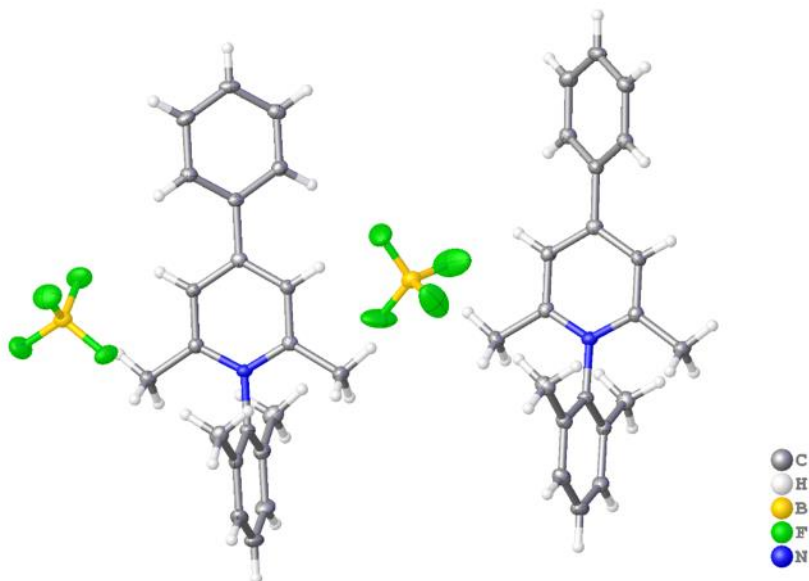


Figure A.75. X-Ray crystal structure of *N*-(2,6-xylyl)-4-phenyl-2,6-dimethylpyridinium tetrafluoroborate (2) [50% thermal ellipsoid]; CCDC-2156178

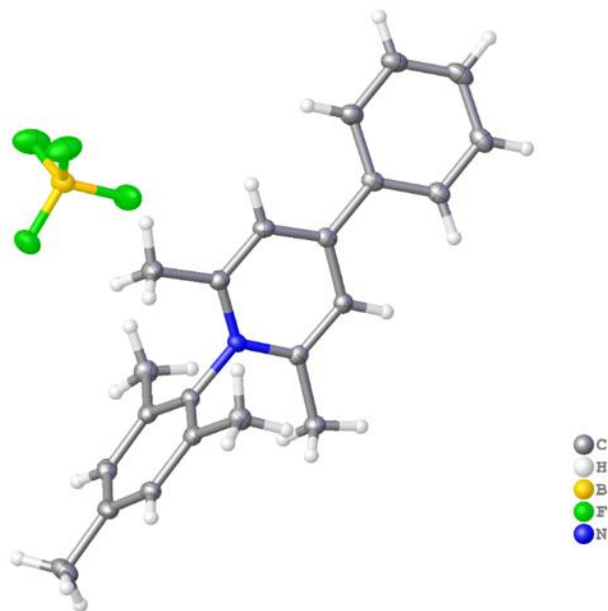


Figure A.76. X-Ray crystal structure of *N*-(mesityl)-4-phenyl-2,6-dimethylpyridinium tetrafluoroborate (4) [50% thermal ellipsoid]; CCDC-2156211.

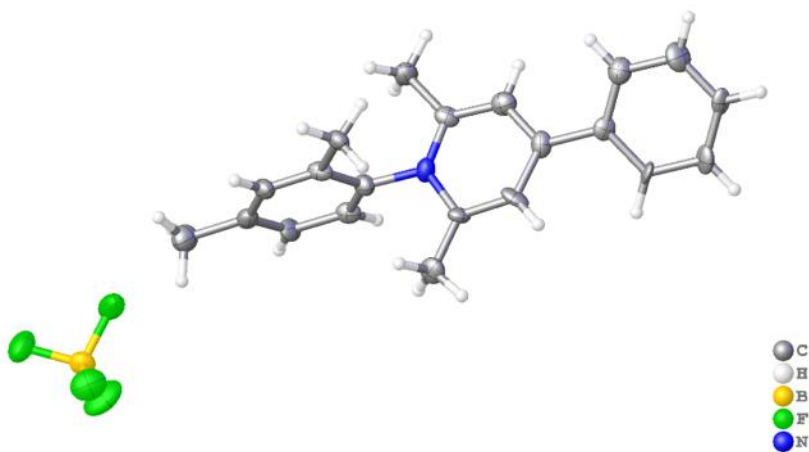
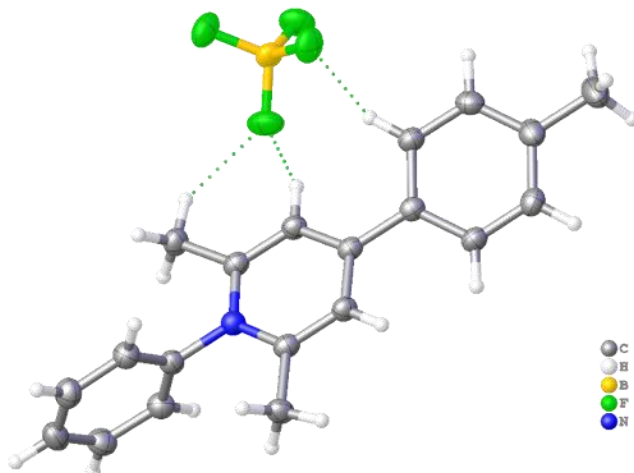
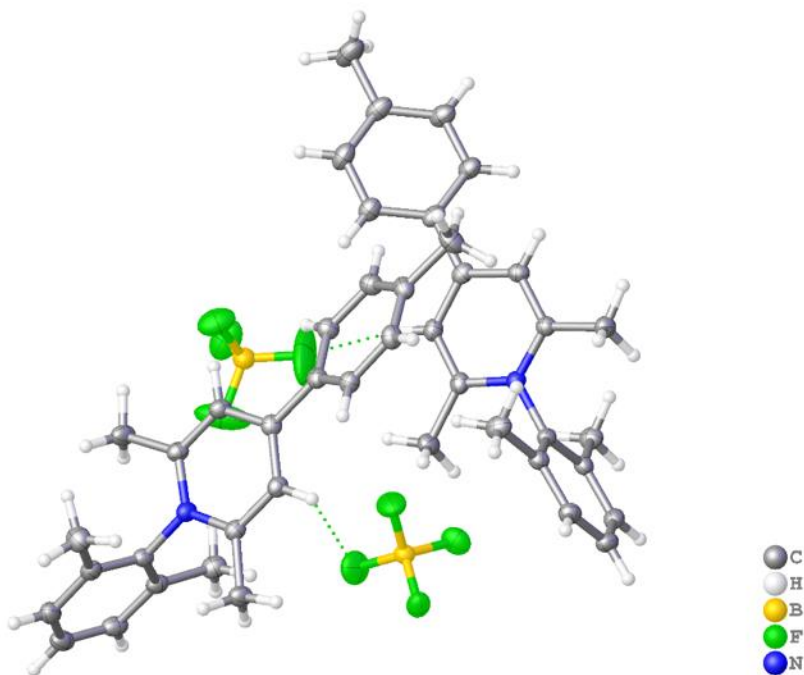


Figure A.77. X-Ray crystal structure of *N*-(2,4-xylyl)-4-phenyl-2,6-dimethylpyridinium tetrafluoroborate (5) [50% thermal ellipsoid]; CCDC-2167771. B-Level Alert Note: Parameter ratio,  $Z_{max} < 18$ , detected. The severe disorder results in many parameters which causes this value to be lower than desired, but no more data could be processed.



**Figure A.78.** X-Ray crystal structure of *N*-phenyl-4-(*p*-tolyl)-2,6-dimethylpyridinium tetrafluoroborate (6) [50% thermal ellipsoid]; CCDC-2155765.



**Figure A.79.** X-Ray crystal structure of *N*-(2,6-xylyl)-4-(*p*-tolyl)-2,6-dimethylpyridinium tetrafluoroborate (7) [50% thermal ellipsoid]; CCDC-2163473.



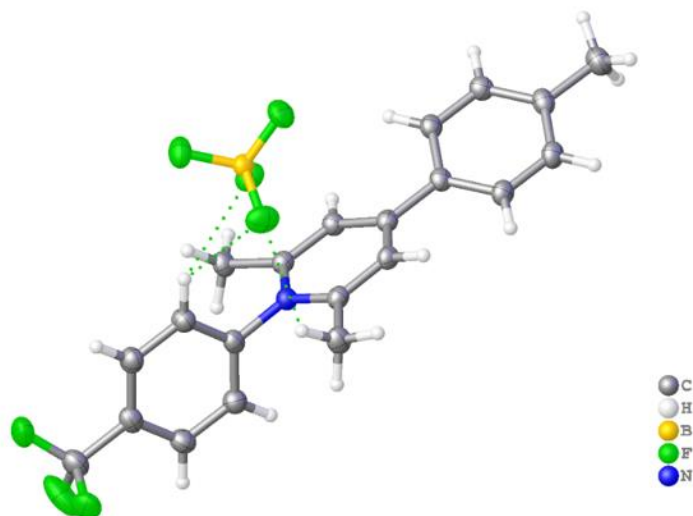


**Figure A.80.** X-Ray crystal structure of *N*-(*p*-trifluoromethylphenyl)-4-(*p*-tolyl)-2,6-dimethylpyridinium tetrafluoroborate (**8**) [50% thermal ellipsoid]; CCDC-2157813.

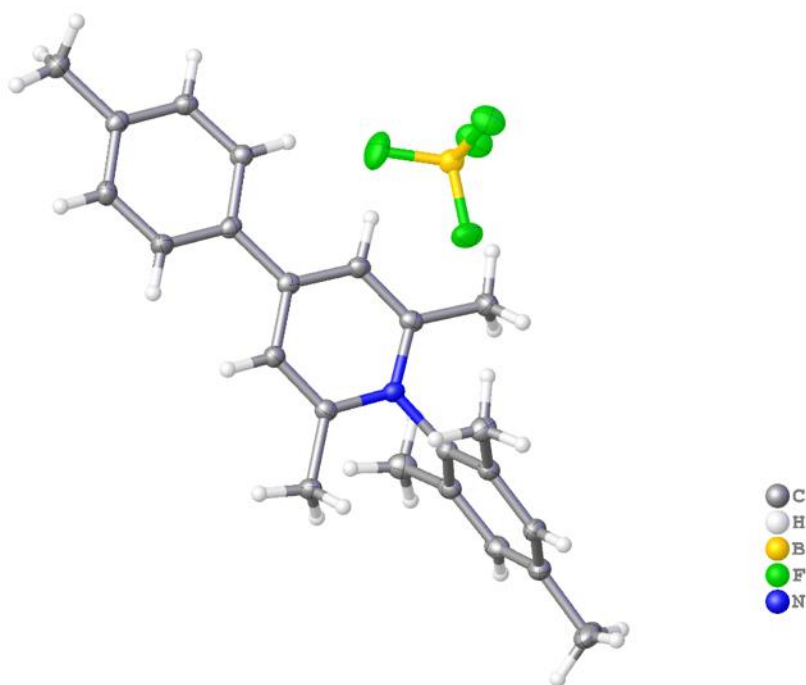


**Figure A.81.** X-Ray crystal structure of *N*-(mesityl)-4-(*p*-tolyl)-2,6-dimethylpyridinium tetrafluoroborate (**9**) [50% thermal ellipsoid]; CCDC-2156206.

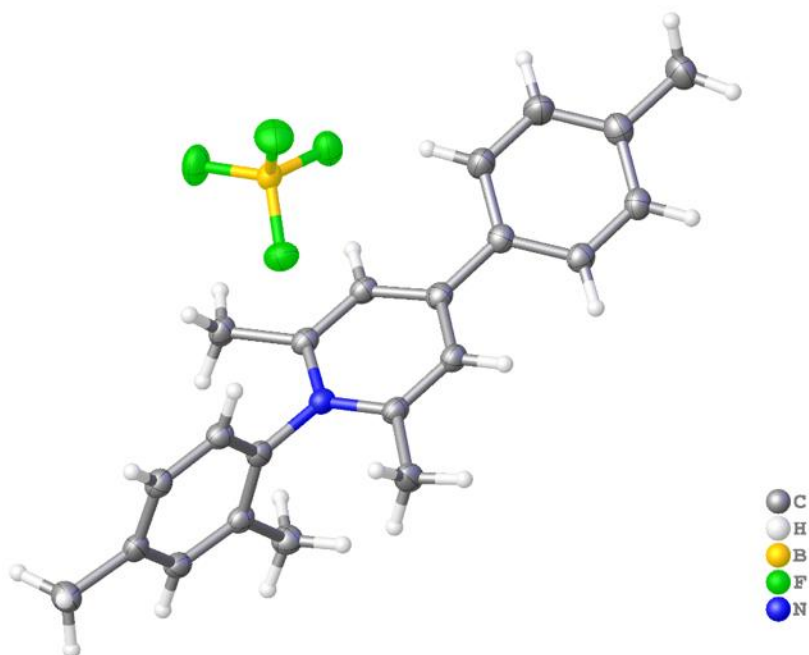


**Figure A.82.** X-Ray crystal structure of *N*-(2,4-xylyl)-4-(*p*-tolyl)-2,6-dimethylpyridinium tetrafluoroborate (10) [50% thermal ellipsoid]; CCDC-2157809.

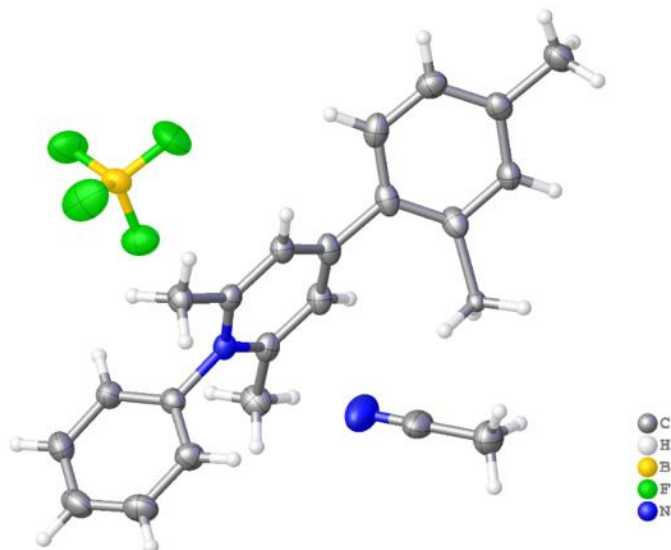


**Figure A.83.** X-Ray crystal structure of *N*-phenyl-4-(2,4-xylyl)-2,6-dimethylpyridinium tetrafluoroborate (11) [50% thermal ellipsoid]; CCDC-2155982. Note: Two protons ipso to methyl groups near the interannular linkage with pyridinium can be seen in the corresponding cif report; this observation is due to a disorder of the terminal xylyl such that there is half occupancy for C<sup>14</sup>(CH<sub>3</sub>)/H.

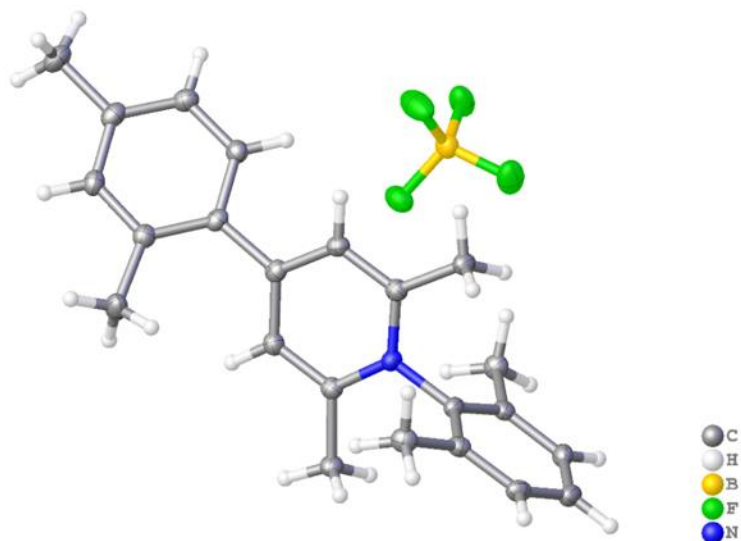


**Figure A.84.** X-Ray crystal structure of *N*-(2,6-xylyl)-4-(2,4-xylyl)-2,6-dimethylpyridinium tetrafluoroborate (12) [50% thermal ellipsoid]; CCDC-2155992.

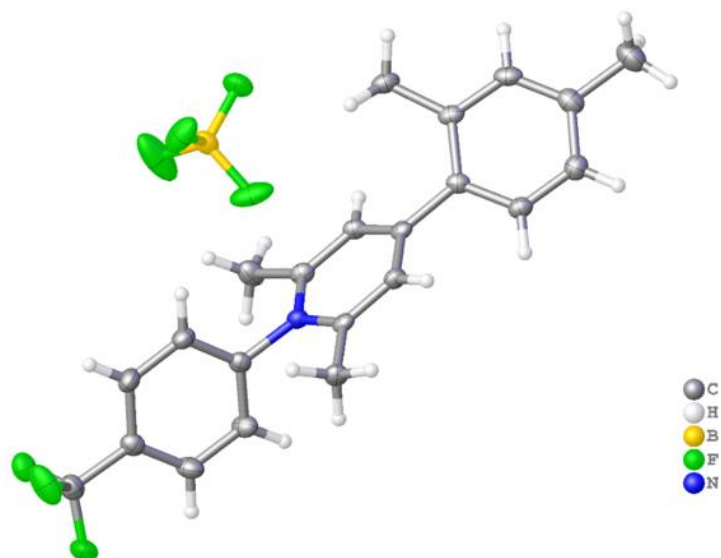


**Figure A.85.** X-Ray crystal structure of *N*-(*p*-trifluoromethylphenyl)-4-(2,4-xylyl)-2,6-dimethylpyridinium tetrafluoroborate (13) [50% thermal ellipsoid]; CCDC-2156563.

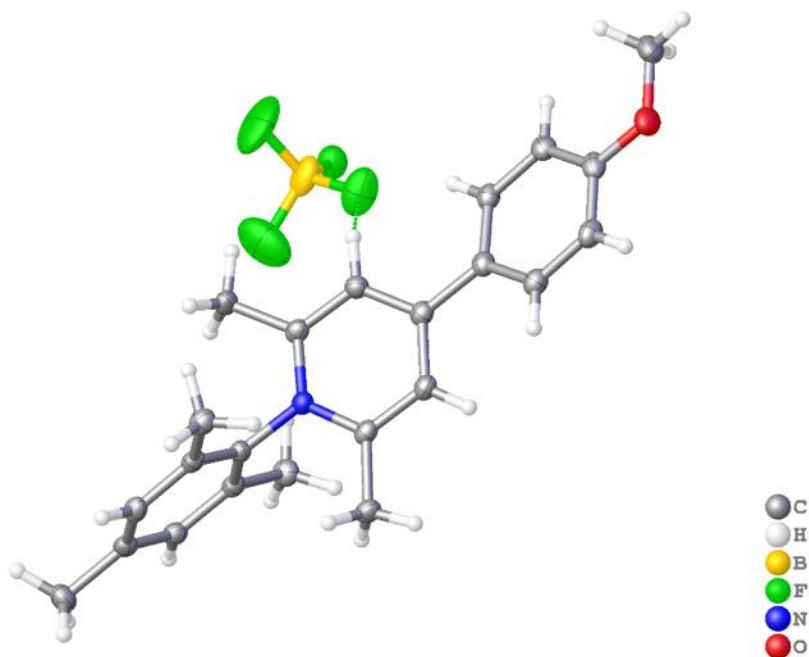


**Figure A.86.** X-Ray crystal structure of *N*-(mesityl)-4-(*p*-methoxyphenyl)-2,6-dimethylpyridinium tetrafluoroborate (14) [50% thermal ellipsoid]; CCDC-2155715. **B-Level Alert Note:** Positive residual density was detected (0.95 eÅ<sup>-3</sup>). This residual density resides in one of the BF<sub>4</sub><sup>-</sup> anions. Attempts to build disorder were not successful.

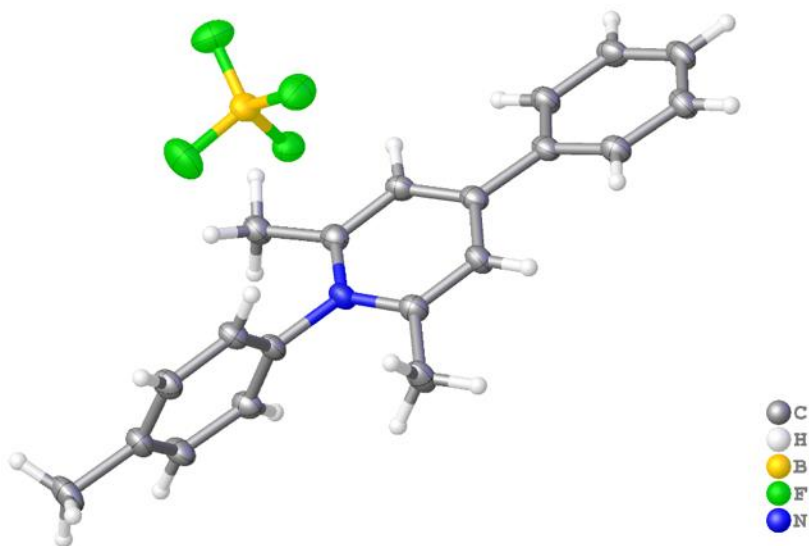


**Figure A.87.** X-Ray crystal structure of *N*-(*p*-tolyl)-4-phenyl-2,6-dimethylpyridinium tetrafluoroborate (15) [50% thermal ellipsoid]; CCDC-2166708.

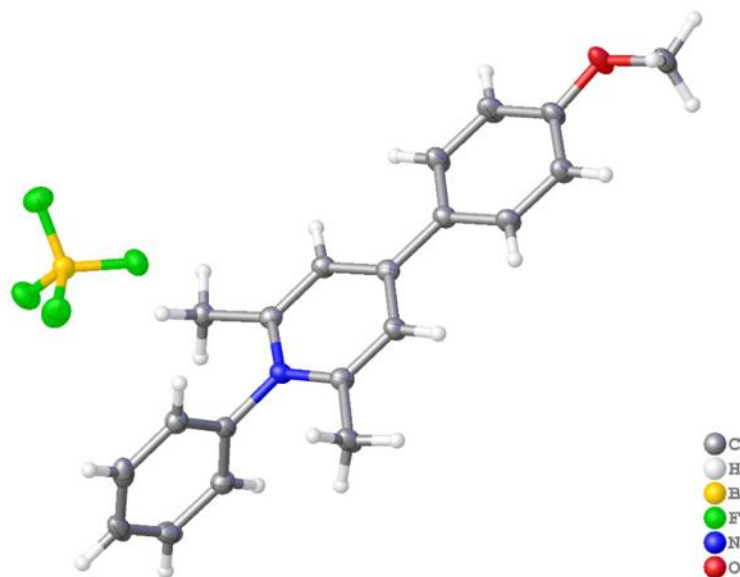


Figure A.88. X-Ray crystal structure of *N*-phenyl-4-(*p*-methoxyphenyl)-2,6-dimethylpyridinium tetrafluoroborate (16) [50% thermal ellipsoid]; CCDC-2162102.

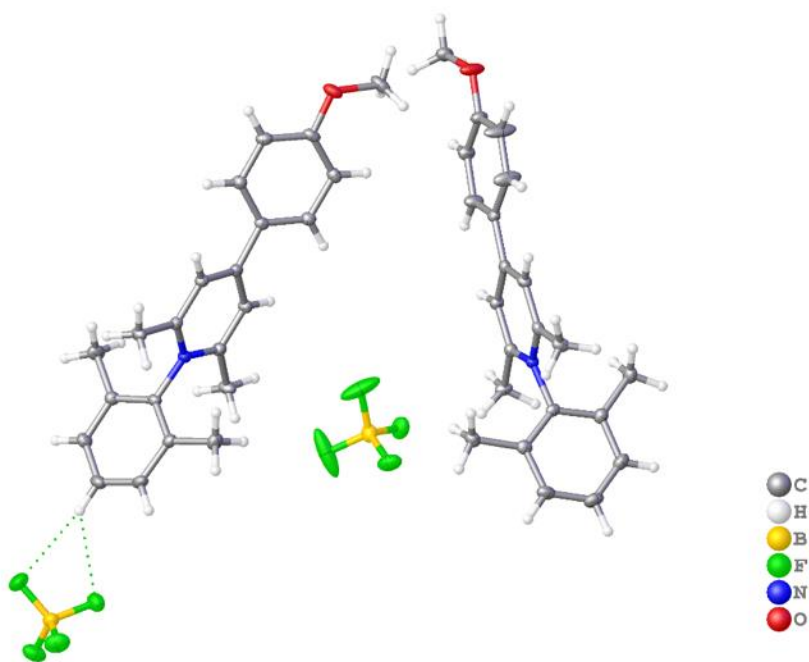


Figure A.89. X-Ray crystal structure of *N*-(2,6-xylyl)-4-(*p*-methoxyphenyl)-2,6-dimethylpyridinium tetrafluoroborate (17) [50% thermal ellipsoid]; CCDC-2155704.

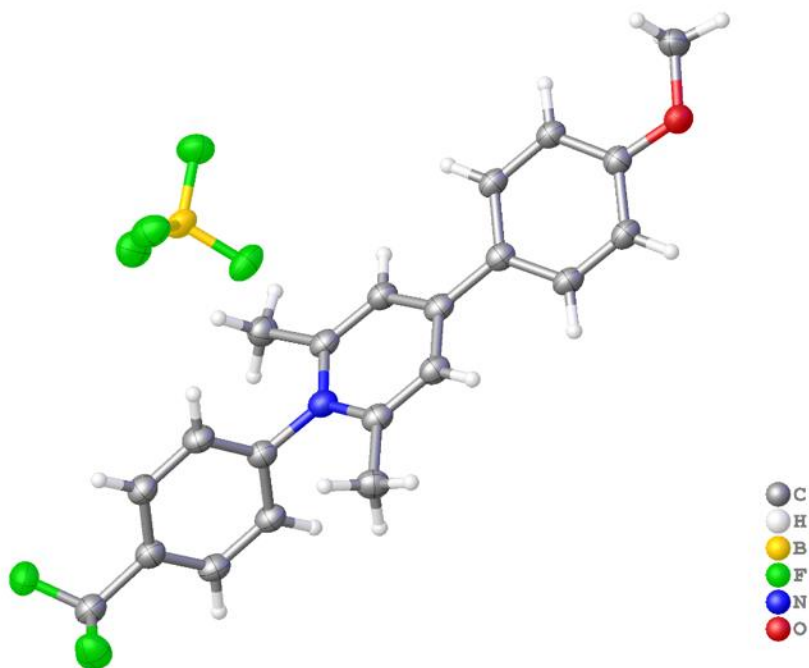


Figure A.90. X-Ray crystal structure of *N*-(*p*-trifluoromethylphenyl)-4-(*p*-methoxyphenyl)-2,6-dimethylpyridinium tetrafluoroborate (18) [50% thermal ellipsoid]; CCDC-2156214.

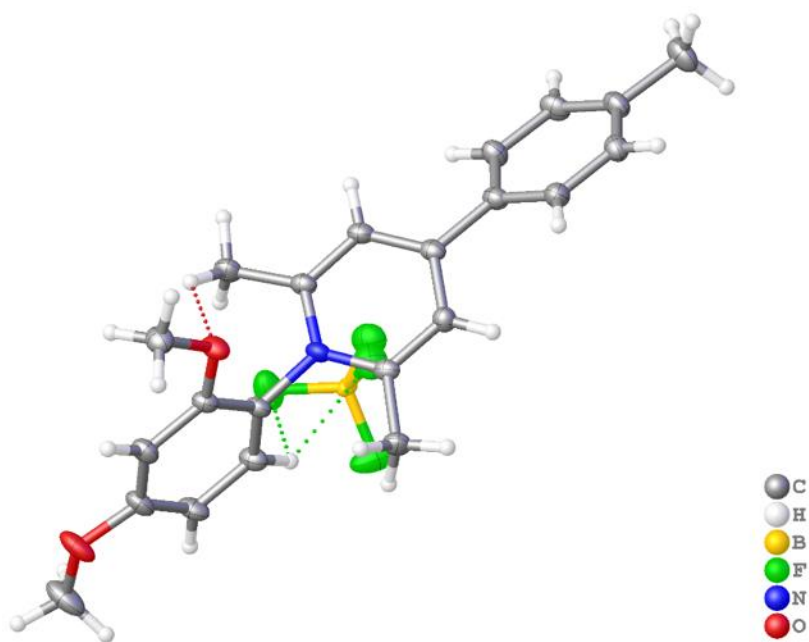
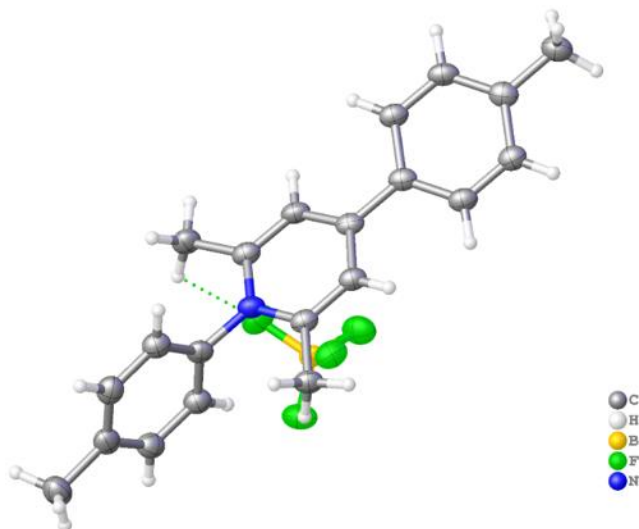
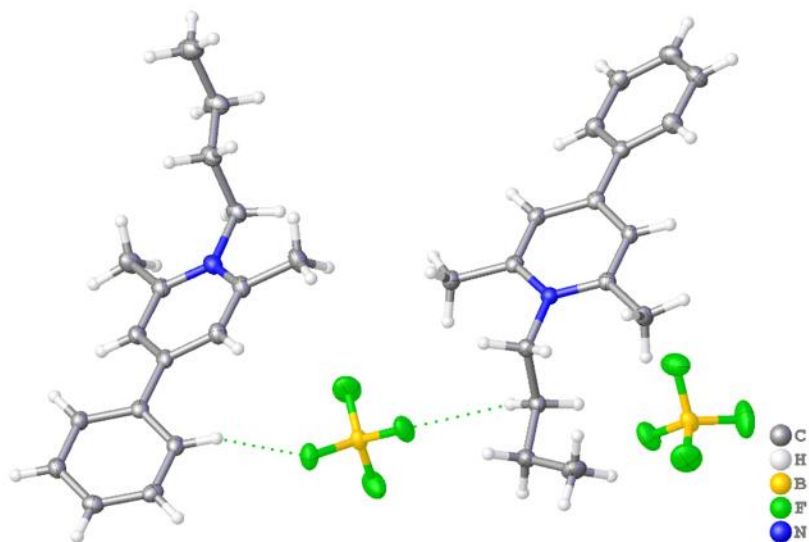


Figure A.91. X-Ray crystal structure of *N*-(2,4-dimethoxybenzene)-4-(*p*-tolyl)-2,6-dimethylpyridinium tetrafluoroborate (19) [50% thermal ellipsoid]; CCDC-2158012.



**Figure A.92.** X-Ray crystal structure of *N*-(*p*-tolyl)-4-(*p*-tolyl)-2,6-dimethylpyridinium tetrafluoroborate (20) [50% thermal ellipsoid]; CCDC-2168227. B-Level Alert Note: This crystal was refined as a 2-component twinned crystal; however, there appeared to be additional twin components. Due to difficulties associated with processing the additional components, a portion of the data was removed via an ‘omit’ statement to solve the structure as a two-component twin. This resulted in a deviation in theta(max) between the cif and fcf of 0.64 degrees.





**Figure A.93.** X-Ray crystal structure of *N*-(*n*-butyl)-4-(*p*-methoxyphenyl)-2,6-dimethylpyridinium tetrafluoroborate (21) [50% thermal ellipsoid]; CCDC-2162134. B-Level Alert Note: Positive residual density was detected (0.94 eÅ<sup>-3</sup>). This residual density resides in one of the BF<sub>4</sub><sup>-</sup> anions. Attempts to build disorder were not successful.

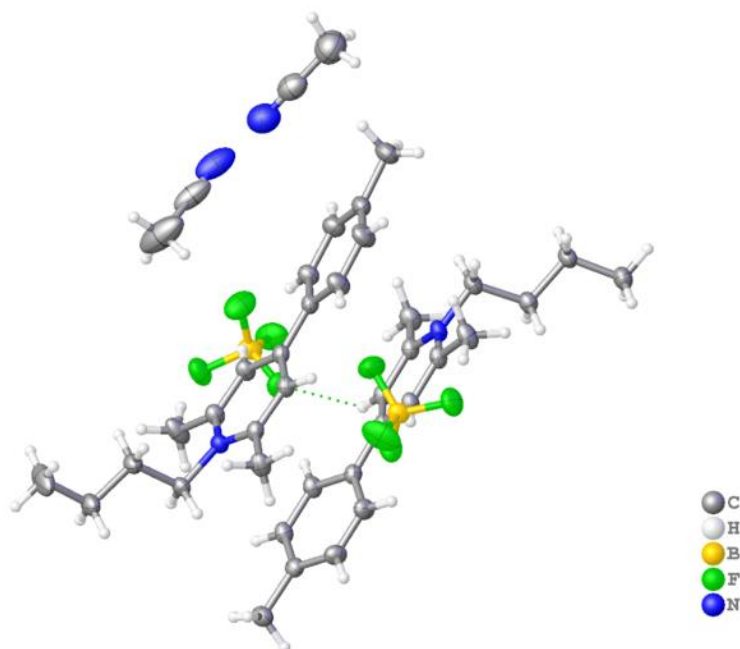


Figure A.94. X-Ray crystal structure of *N*-(*n*-butyl)-4-(*p*-tolyl)-2,6-dimethylpyridinium tetrafluoroborate (22) [50% thermal ellipsoid]; CCDC-2163981.

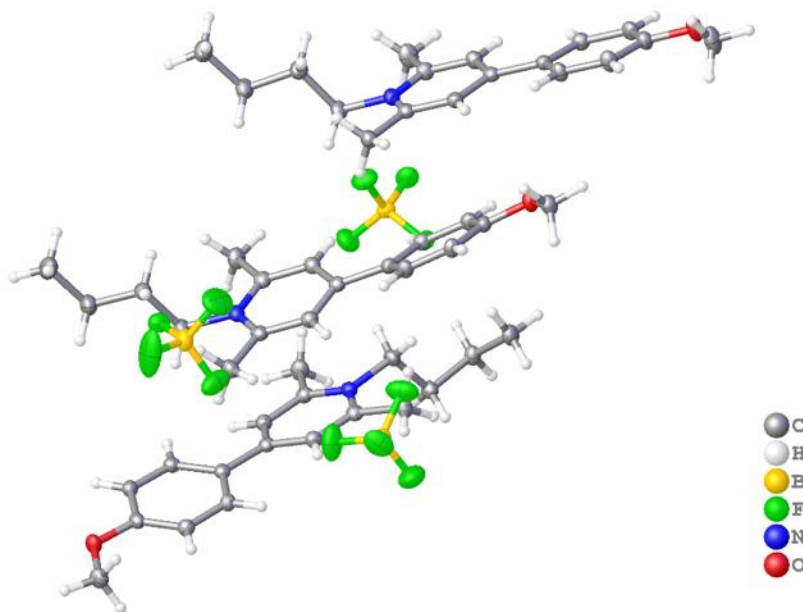


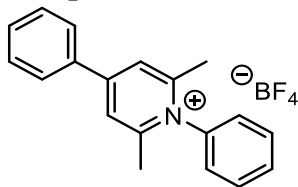
Figure A.95. X-Ray crystal structure of *N*-(*n*-butyl)-4-(*p*-methoxyphenyl)-2,6-dimethylpyridinium tetrafluoroborate (23) [50% thermal ellipsoid]; CCDC-2165226.

## A.9. DFT Coordinates of Geometry-Optimized Pyridinium Salts

Pyr\* = reduced state (neutral radical)

Pyr+ = oxidized state (cation)

### Compound 1

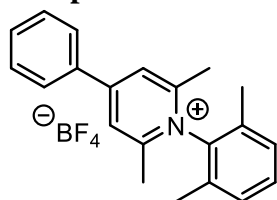


### *N*-phenyl-4-phenyl-2,6-dimethylpyridinium tetrafluoroborate

Pyr+				Pyr*			
Atom	X	Y	Z	Atom	X	Y	Z
C	-0.53268	-1.21426	-0.04372	C	-0.53677	-1.18153	-0.21388
C	0.83504	-1.20376	-0.04112	C	0.84845	-1.17845	-0.21332
C	1.61568	0	0	C	1.58137	0	0
C	0.83504	1.20376	0.04112	C	0.84844	1.17845	0.21331
C	-0.53268	1.21426	0.04372	C	-0.53677	1.18153	0.21387
H	1.31924	-2.17155	-0.08527	H	1.35416	-2.11535	-0.40873
H	1.31924	2.17155	0.08527	H	1.35416	2.11536	0.40872
C	3.06685	0	0	C	3.05964	0	0
C	3.82344	1.20722	-0.05845	C	3.77636	1.12224	-0.45724
C	3.82344	-1.20722	0.05845	C	3.77636	-1.12224	0.45724
C	5.21564	1.20303	-0.05814	C	5.17111	1.11838	-0.46188
H	3.3169	2.1645	-0.11427	H	3.24601	1.98888	-0.83844
C	5.21564	-1.20303	0.05814	C	5.17111	-1.11838	0.46188
H	3.3169	-2.1645	0.11428	H	3.246	-1.98888	0.83844
C	5.93458	0	0	C	5.87266	0	0
H	5.74688	2.15042	-0.10694	H	5.70904	1.98624	-0.83043
H	5.74688	-2.15042	0.10694	H	5.70904	-1.98624	0.83044
H	7.02033	0	0	H	6.95836	0	0
C	-1.32436	2.49092	0.09922	C	-1.32103	2.4375	0.45177
H	-0.6401	3.34019	0.14548	H	-0.63329	3.2667	0.61813
H	-1.96478	2.61484	-0.78131	H	-1.95571	2.67735	-0.4062
H	-1.97811	2.52864	0.97789	H	-1.97161	2.34136	1.32557
C	-1.32436	-2.49092	-0.09922	C	-1.32103	-2.4375	-0.45177
H	-0.6401	-3.34019	-0.14548	H	-0.63329	-3.26669	-0.61815
H	-1.96478	-2.61484	0.7813	H	-1.95569	-2.67736	0.40621
H	-1.97811	-2.52864	-0.97789	H	-1.97162	-2.34136	-1.32557
C	-2.68553	0	0	C	-2.66646	0	0
C	-3.38291	0.08479	-1.20977	C	-3.34524	0.23161	-1.19651
C	-3.38291	-0.08479	1.20977	C	-3.34523	-0.23161	1.19651
C	-4.78061	0.08543	-1.20772	C	-4.74233	0.23029	-1.19008

H	-2.83087	0.14888	-2.14255	H	-2.79201	0.40897	-2.11319
C	-4.78061	-0.08543	1.20773	C	-4.74232	-0.23029	1.19008
H	-2.83087	-0.14888	2.14255	H	-2.792	-0.40897	2.11319
C	-5.48083	0	0	C	-5.43951	0	0
H	-5.31974	0.1515	-2.14792	H	-5.28155	0.40908	-2.11464
H	-5.31974	-0.1515	2.14793	H	-5.28154	-0.40908	2.11465
H	-6.56666	0	0	H	-6.52491	0	0.00001
N	-1.24283	0	0	N	-1.20522	0	0

**Compound 2**

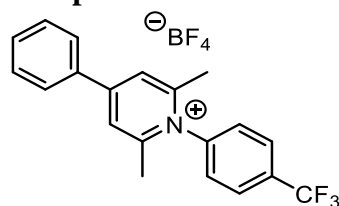


***N*-(2,6-xylyl)-4-phenyl-2,6-dimethylpyridinium tetrafluoroborate**

Pyr+				Pyr*			
Atom	X	Y	Z	Atom	X	Y	Z
C	-0.28047	0.949326	-0.73407	C	-0.2744	1.208548	-0.1139
C	1.104771	0.947874	-0.73212	C	1.093583	1.199279	-0.11069
C	1.837871	-1.9E-05	-0.00001	C	1.874357	-4E-06	-6.4E-05
C	1.104773	-0.9479	0.732124	C	1.093577	-1.19929	0.110524
C	-0.28047	-0.94936	0.734064	C	-0.2744	-1.20855	0.113691
C	-2.41544	-1.2E-05	-1E-06	C	-2.43053	0.000009	0
C	-3.0799	0.767145	0.972098	C	-3.11271	0.11946	1.226072
C	-4.48105	0.750192	0.949821	C	-4.51455	0.117495	1.203919
C	-5.17501	0.000018	0.000006	C	-5.21128	0.000015	0.000228
C	-4.48107	-0.75017	-0.94981	C	-4.51474	-0.11747	-1.20358
C	-3.07992	-0.76715	-0.9721	C	-3.11291	-0.11944	-1.22596
H	1.610943	1.689036	-1.33732	H	1.577625	2.163179	-0.20913
H	1.610947	-1.68903	1.337355	H	1.577614	-2.16319	0.208941
H	-5.02608	1.332351	1.686624	H	-5.05929	0.208673	2.139527
H	-6.26072	0.00003	0.000009	H	-6.29749	0.000017	0.000315
H	-5.02612	-1.33232	-1.68661	H	-5.05964	-0.20865	-2.1391
C	3.315877	-8E-06	-4E-06	C	3.325624	-4E-06	-1.9E-05
C	4.032471	1.207031	-0.10856	C	4.082173	1.208513	-0.01602
C	5.427186	1.205694	-0.10259	C	5.474386	1.204326	-0.01607
C	6.128654	0.000017	-5E-06	C	6.193292	-1E-06	0.000068
C	5.427208	-1.20567	0.102582	C	5.474387	-1.20433	0.016167
C	4.032493	-1.20704	0.108543	C	4.082174	-1.20852	0.016029
H	3.502264	2.152047	-0.16695	H	3.575667	2.167402	-0.01971
H	5.965131	2.145917	-0.17313	H	6.005614	2.152927	-0.02591
H	7.214353	0.000026	-5E-06	H	7.27904	-1E-06	0.0001
H	5.96517	-2.14589	0.173119	H	6.005616	-2.15293	0.026034
H	3.502304	-2.15206	0.166936	H	3.575669	-2.16741	0.019698
N	-0.95045	-0.00002	-7E-06	N	-0.98532	-2E-06	-0.00012
C	-2.33507	-1.57935	-2.00548	C	-2.36452	-0.2457	-2.53216
H	-3.03994	-2.11312	-2.64581	H	-3.06305	-0.33868	-3.3671
H	-1.67308	-2.3218	-1.54716	H	-1.70825	-1.12273	-2.54109
H	-1.71124	-0.95036	-2.64997	H	-1.72751	0.62555	-2.72028
C	-2.33502	1.579357	2.00545	C	-2.3641	0.245684	2.532148
H	-3.03988	2.112866	2.646002	H	-3.0625	0.338799	3.36719

H	-1.67331	2.322032	1.547082	H	-1.70771	1.122611	2.540936
H	-1.71089	0.950426	2.649707	H	-1.7272	-0.62565	2.720212
C	-1.0648	1.953703	-1.52623	C	-1.06577	2.480896	-0.24098
H	-1.70904	2.558117	-0.88153	H	-1.71456	2.651853	0.625371
H	-1.7073	1.468856	-2.26661	H	-1.71173	2.478048	-1.12612
C	-1.06479	-1.95369	1.526284	C	-1.06579	-2.4809	0.240743
H	-1.70902	-2.55816	0.881619	H	-1.71459	-2.65182	-0.6256
H	-1.70731	-1.4688	2.266626	H	-1.71173	-2.47807	1.125899
H	-0.37685	-2.61895	2.048139	H	-0.38081	-3.32681	0.323437
H	-0.37686	2.619007	-2.04802	H	-0.38079	3.326804	-0.3237

**Compound 3**

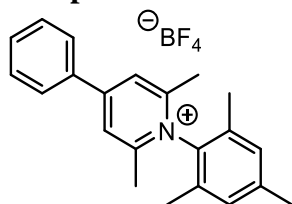


***N*-(4-trifluoromethyl)-4-phenyl-2,6-dimethylpyridinium tetrafluoroborate**

Pyr+				Pyr*			
Atom	X	Y	Z	Atom	X	Y	Z
C	-0.84363	1.18452	-0.20564	C	-0.8571	1.20881	-0.15886
C	-2.22819	1.17952	-0.20929	C	-2.22491	1.19396	-0.15317
C	-2.96118	0.00015	0.00117	C	-3.00095	-0.00048	-0.00182
C	-2.22822	-1.17837	0.21638	C	-2.22327	-1.19377	0.15009
C	-0.84366	-1.1819	0.2213	C	-0.85545	-1.20631	0.15876
C	1.28286	0.00242	0.01388	C	1.29079	0.00378	0.00833
C	1.96524	-0.23033	-1.1812	C	1.99937	-0.5096	-1.08774
C	3.35809	-0.22839	-1.17507	C	3.39134	-0.51047	-1.08047
C	4.04812	0.00508	0.02092	C	4.08344	0.0109	0.02137
C	3.35492	0.23659	1.21105	C	3.38177	0.52783	1.11442
C	1.95883	0.23569	1.20926	C	1.98666	0.51933	1.10799
H	-2.73376	2.11616	-0.40597	H	-2.71371	2.14771	-0.31112
H	-2.73402	-2.11553	0.40995	H	-2.71079	-2.14853	0.30584
H	1.41797	-0.40933	-2.10035	H	1.45935	-0.89356	-1.94659
H	3.89815	-0.40745	-2.09854	H	3.93345	-0.90506	-1.93376
H	3.89086	0.41705	2.13498	H	3.91432	0.92496	1.97068
H	1.40787	0.41431	2.12629	H	1.43807	0.90152	1.96218
C	-4.43883	-0.00076	-0.00367	C	-4.45492	-0.00146	-0.00222
C	-5.15772	1.12322	0.44629	C	-5.20803	1.20405	0.07608
C	-6.55234	1.1183	0.44647	C	-6.60073	1.19955	0.07476
C	-7.25151	-0.0026	-0.01298	C	-7.31696	-0.00329	-0.00259
C	-6.54785	-1.12257	-0.4678	C	-6.59917	-1.20521	-0.07978
C	-5.15326	-1.12566	-0.45838	C	-5.20646	-1.20793	-0.08073
H	-7.09211	1.98726	0.80961	H	-7.13332	2.14488	0.14192
H	-8.33719	-0.00331	-0.01657	H	-8.40273	-0.00398	-0.00269
H	-7.08407	-1.99224	-0.83451	H	-7.13054	-2.15122	-0.14701
H	-4.62132	-1.99357	-0.83436	H	-4.69587	-2.16141	-0.1628
N	-0.17611	0.00168	0.00996	N	-0.14389	0.00188	0.00107
C	5.55482	-0.00032	-0.00404	C	5.58543	0.0006	0.00243
F	6.10263	0.25497	1.206	F	6.13447	0.53688	1.11852
F	6.04948	0.92919	-0.86604	F	6.0912	0.69805	-1.0551
F	6.04955	-1.19937	-0.41631	F	6.08997	-1.26161	-0.11229
C	-0.0587	-2.43701	0.4608	C	-0.0715	-2.46885	0.38486
C	-0.0586	2.44053	-0.4402	C	-0.07489	2.47234	-0.38522

H	-0.74635	3.26873	-0.61065	H	-0.76506	3.2865	-0.61375
H	0.59594	2.34611	-1.31133	H	0.62554	2.36979	-1.22192
H	0.57049	2.68314	0.42123	H	0.51391	2.76551	0.49098
H	0.5888	-2.34235	1.33714	H	0.62644	-2.3668	1.22364
H	0.57757	-2.67799	-0.39582	H	0.52009	-2.75926	-0.49041
H	-0.74655	-3.26639	0.62496	H	-0.76075	-3.28479	0.60977
H	-4.62945	1.99182	0.82578	H	-4.69866	2.15815	0.15843

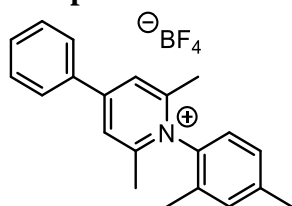


**Compound 4*****N*-(mesityl)-4-phenyl-2,6-dimethylpyridinium tetrafluoroborate**

Pyr <sup>+</sup>				Pyr <sup>*</sup>			
Atom	X	Y	Z	Atom	X	Y	Z
C	0.06269	0.9511	0.73237	C	0.062689	0.951098	0.732368
C	1.44806	0.94916	0.73001	C	1.448055	0.949159	0.730012
C	2.18034	-0.00057	-0.00037	C	2.18034	-0.00057	-0.00037
C	1.44649	-0.94955	-0.73013	C	1.446493	-0.94955	-0.73013
C	0.06111	-0.94999	-0.73142	C	0.061112	-0.94999	-0.73142
C	-2.07289	0.00138	0.00106	C	-2.07289	0.001383	0.001058
C	-2.74324	-0.75957	0.97259	C	-2.74324	-0.75957	0.972587
C	-4.14287	-0.73816	0.95025	C	-4.14287	-0.73816	0.950251
C	-4.8598	0.00507	0.00398	C	-4.8598	0.005073	0.003981
C	-4.14287	0.75034	-0.94071	C	-4.14287	0.750343	-0.94071
C	-2.74325	0.76613	-0.9675	C	-2.74325	0.766134	-0.9675
H	1.95489	1.69127	1.33353	H	1.954893	1.691266	1.333535
H	1.95207	-1.69222	-1.33402	H	1.952066	-1.69222	-1.33402
H	-4.6831	-1.31706	1.69461	H	-4.6831	-1.31706	1.694612
H	-4.68313	1.33814	-1.67805	H	-4.68313	1.338145	-1.67805
N	-0.60856	0.0009	0.00071	N	-0.60856	0.000905	0.000713
C	-0.72396	-1.95531	-1.52156	C	-0.72397	-1.95531	-1.52156
C	-0.72065	1.95731	1.52313	C	-0.72065	1.957305	1.523134
H	-0.03227	2.62338	2.04345	H	-0.03227	2.623385	2.043455
H	-1.36305	1.47368	2.26439	H	-1.36305	1.473676	2.264391
H	-1.36529	2.56038	0.87762	H	-1.36529	2.560376	0.877616
H	-1.36583	-1.47087	-2.26277	H	-1.36583	-1.47087	-2.26277
H	-1.36934	-2.55712	-0.8756	H	-1.36934	-2.55712	-0.8756
H	-0.03674	-2.6226	-2.04188	H	-0.03674	-2.6226	-2.04188
C	-6.36977	-0.01676	-0.01331	C	-6.36977	-0.01677	-0.01331
C	-2.00396	1.57987	-2.00407	C	-2.00396	1.579868	-2.00407
C	-2.00394	-1.57129	2.01073	C	-2.00394	-1.57129	2.010729
H	-2.71166	2.11196	-2.64273	H	-2.71167	2.111959	-2.64273
H	-1.38075	0.95166	-2.65006	H	-1.38075	0.951655	-2.65006
H	-1.34169	2.32387	-1.54847	H	-1.34169	2.323867	-1.54847
H	-2.71174	-2.09849	2.65334	H	-2.71174	-2.09849	2.653335
H	-1.34593	-2.31946	1.55576	H	-1.34593	-2.31946	1.555764
H	-1.37635	-0.94319	2.65255	H	-1.37636	-0.94319	2.652551
H	-6.77722	-0.1807	0.98828	H	-6.77722	-0.1807	0.988281

H	-6.77707	0.91981	-0.40448	H	-6.77707	0.91981	-0.40448
H	-6.7373	-0.82766	-0.65415	H	-6.7373	-0.82766	-0.65415
C	3.6585	-0.00133	-0.00099	C	3.658503	-0.00133	-0.00099
C	4.37448	-1.209	-0.10617	C	4.374478	-1.209	-0.10617
C	4.37582	1.20559	0.10357	C	4.375821	1.205592	0.103567
C	5.76923	-1.20838	-0.1009	C	5.769227	-1.20838	-0.1009
H	3.84372	-2.1539	-0.16153	H	3.84372	-2.1539	-0.16153
C	5.77056	1.20352	0.0971	C	5.770564	1.203525	0.097097
H	3.8461	2.15105	0.15939	H	3.846097	2.151049	0.159386
C	6.47139	-0.00279	-0.0022	C	6.471392	-0.00279	-0.0022
H	6.30664	-2.14911	-0.16891	H	6.306643	-2.14911	-0.16891
H	6.30902	2.14369	0.16464	H	6.309016	2.143687	0.16464
H	7.5571	-0.00336	-0.00267	H	7.557095	-0.00336	-0.00267

**Compound 5**

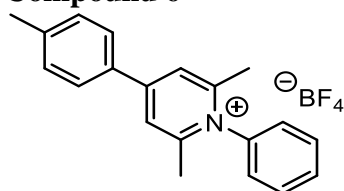


***N*-(2,4-xylyl)-4-phenyl-2,6-dimethylpyridinium tetrafluoroborate**

Pyr+				Pyr*			
Atom	X	Y	Z	Atom	X	Y	Z
C	0.032129	-1.10765	-0.47803	C	0.02938	-1.21249	-0.21825
C	-1.35289	-1.11377	-0.45201	C	-1.33768	-1.20409	-0.16905
C	-2.08646	0.02816	-0.09211	C	-2.11849	-0.00023	-0.12475
C	-1.35447	1.181395	0.232798	C	-1.33899	1.204652	-0.16372
C	0.030611	1.192594	0.206501	C	0.028052	1.214783	-0.21273
C	2.163508	0.049719	-0.15559	C	2.183083	0.002072	-0.19062
C	2.870486	-0.30242	1.003533	C	2.858745	-0.00067	1.043972
C	4.270897	-0.27489	0.922507	C	4.260711	0.003665	1.022031
C	4.955403	0.081506	-0.24709	C	4.99725	0.008433	-0.17155
C	4.202955	0.428443	-1.38018	C	4.292639	0.014841	-1.38386
C	2.810969	0.41269	-1.33708	C	2.897359	0.010369	-1.39123
H	-1.85901	-2.02432	-0.74607	H	-1.82091	-2.17333	-0.17314
H	-1.86036	2.089087	0.535918	H	-1.82326	2.173391	-0.16276
H	4.842126	-0.54122	1.807939	H	4.79392	0.005397	1.9701
H	4.70513	0.713317	-2.30012	H	4.834339	0.025255	-2.32585
H	2.227742	0.681433	-2.2125	H	2.35295	0.016919	-2.33104
N	0.70109	0.04405	-0.13945	N	0.739559	0.001544	-0.22619
C	6.464642	0.077949	-0.29629	C	6.507996	-0.01873	-0.14886
H	6.896872	0.004945	0.704922	H	6.902451	0.457449	0.753564
H	6.846672	0.98709	-0.77152	H	6.928448	0.492057	-1.02021
C	2.17695	-0.69487	2.286157	C	2.106827	-0.00425	2.353511
H	1.551032	-1.58468	2.155624	H	1.460365	-0.88425	2.445179
H	1.524626	0.102116	2.659696	H	1.458904	0.874225	2.449614
H	6.831833	-0.77261	-0.88281	H	6.880129	-1.05077	-0.16395
H	2.911125	-0.91601	3.063297	H	2.800773	-0.00588	3.197407
C	-3.56439	0.016911	-0.0602	C	-3.56798	-0.00114	-0.05614
C	-4.29789	1.176421	-0.37591	C	-4.32497	1.206975	-0.02007
C	-4.26395	-1.15438	0.287527	C	-4.32345	-1.21017	-0.01918
C	-5.69235	1.161562	-0.34967	C	-5.71564	1.201904	0.044694
H	-3.78185	2.08402	-0.67195	H	-3.82019	2.166467	-0.04209
C	-5.65825	-1.16261	0.323621	C	-5.71413	-1.2068	0.045547
H	-3.7199	-2.05297	0.560008	H	-3.81743	-2.16904	-0.03992
C	-6.37665	-0.00629	0.002628	C	-6.43326	-0.00289	0.07811
H	-6.2437	2.060015	-0.60893	H	-6.24672	2.150322	0.069921

H	-6.18256	-2.0699	0.607038	H	-6.24401	-2.15586	0.071639
H	-7.46205	-0.01518	0.026887	H	-7.51781	-0.00355	0.128899
C	0.814089	2.426604	0.543331	C	0.818309	2.492237	-0.274
H	1.398028	2.766941	-0.31694	H	1.412053	2.558619	-1.19278
H	1.514442	2.251259	1.364521	H	1.517634	2.586922	0.564301
C	0.816903	-2.31775	-0.89027	C	0.821101	-2.48869	-0.28622
H	1.528989	-2.62117	-0.11814	H	1.519377	-2.58782	0.552441
H	1.38793	-2.12288	-1.80305	H	1.416151	-2.54866	-1.2046
H	0.12838	3.222433	0.834465	H	0.135515	3.343511	-0.24539
H	0.133376	-3.14607	-1.07739	H	0.139203	-3.34088	-0.26381

**Compound 6**

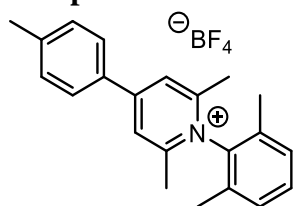


***N*-phenyl-4-(*p*-tolyl)-2,6-dimethylpyridinium tetrafluoroborate**

Pyr+				Pyr*			
Atom	X	Y	Z	Atom	X	Y	Z
C	-0.95361	1.18422	-0.20168	C	-0.95212	1.21447	-0.06453
C	0.4309	1.18194	-0.20272	C	0.41551	1.20367	-0.06298
C	1.16735	0.00192	-0.00269	C	1.19638	0.00081	-0.00324
C	0.43269	-1.17907	0.19829	C	0.41622	-1.20232	0.05876
C	-0.95181	-1.18305	0.19975	C	-0.95141	-1.2138	0.0634
H	0.93442	2.1217	-0.3895	H	0.90046	2.17026	-0.12603
H	0.93775	-2.11824	0.38392	H	0.90175	-2.16865	0.12143
C	2.64264	0.00254	-0.00308	C	2.64816	0.00119	-0.00428
C	3.36688	-1.12746	-0.43016	C	3.4084	-1.20208	-0.05972
C	3.36613	1.13303	0.42031	C	3.40845	1.20396	0.04541
C	4.75911	-1.12009	-0.43668	C	4.80011	-1.19522	-0.06142
C	4.75953	1.12742	0.42239	C	4.80098	1.1965	0.04267
H	2.84301	2.01409	0.77791	H	2.90677	2.16453	0.09306
C	5.48383	0.00355	-0.00519	C	5.53862	0.00083	-0.00747
H	5.29252	-1.99878	-0.78899	H	5.32816	-2.14563	-0.1117
H	5.29285	2.00972	0.76523	H	5.32957	2.14703	0.08213
C	-1.73509	-2.44227	0.42454	C	-1.74232	-2.4894	0.14738
H	-2.36892	-2.67425	-0.43626	H	-2.37359	-2.64139	-0.73546
H	-1.04665	-3.27248	0.58299	H	-1.05752	-3.33595	0.22584
H	-2.38643	-2.35582	1.2988	H	-2.40536	-2.50197	1.01992
C	-1.73882	2.44245	-0.42523	C	-1.74381	2.48975	-0.14614
H	-1.05167	3.27349	-0.58491	H	-2.37311	2.64105	0.73821
H	-2.39153	2.35514	-1.29838	H	-1.0596	3.33665	-0.22587
H	-2.37147	2.67372	0.43663	H	-2.40887	2.50232	-1.01715
C	-3.0832	-0.0007	0.00103	C	-3.105	-0.00018	0.00127
C	-3.76145	0.21813	1.20032	C	-3.80222	0.16006	1.20374
C	-3.76341	-0.22033	-1.197	C	-3.80408	-0.16085	-1.20008
C	-5.15855	0.21607	1.1953	C	-5.19991	0.16115	1.20274
H	-3.20757	0.38637	2.11834	H	-3.2498	0.28094	2.13067
C	-5.1605	-0.21994	-1.18939	C	-5.20176	-0.16276	-1.19681
H	-3.21103	-0.38785	-2.11605	H	-3.25309	-0.28143	-2.12789
C	-5.85679	-0.00235	0.0036	C	-5.90125	-0.00101	0.00353
H	-5.69698	0.38504	2.12219	H	-5.73828	0.28597	2.13743
H	-5.70045	-0.38954	-2.11528	H	-5.74158	-0.28792	-2.13063

H	-6.94221	-0.00299	0.0046	H	-6.98708	-0.00134	0.00441
N	-1.62237	0.00018	-0.00032	N	-1.66303	0.00019	0.00007
H	2.84336	-2.00632	-0.79258	H	2.90599	-2.16176	-0.11703
C	6.99218	-0.00906	0.01813	C	7.0488	-0.00295	0.02511
H	7.39874	-0.54826	-0.84286	H	7.4307	-0.13679	1.04648
H	7.40011	1.00534	0.01695	H	7.46078	-0.81772	-0.58014
H	7.36067	-0.51302	0.92037	H	7.45842	0.93963	-0.3522

**Compound 7**



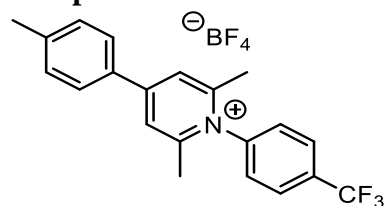
***N*-(2,6-xylyl)-4-(*p*-tyl)-2,6-dimethylpyridinium tetrafluoroborate**

Pyr+				Pyr*			
Atom	X	Y	Z	Atom	X	Y	Z
C	0.667427	0.977464	0.694808	C	0.664879	1.209484	0.108983
C	-0.71708	0.975708	0.692041	C	-0.70299	1.199548	0.104411
C	-1.45232	-0.00058	-0.00205	C	-1.4837	-0.00019	-0.00346
C	-0.71591	-0.97692	-0.69477	C	-0.70265	-1.19989	-0.10918
C	0.668635	-0.97851	-0.69531	C	0.665233	-1.2097	-0.11065
C	2.803728	-6.9E-05	0.000985	C	2.821622	0.000018	0.001299
C	3.468952	0.726506	-1.00145	C	3.505625	0.115413	-1.22427
C	4.87012	0.710796	-0.97794	C	4.907464	0.113567	-1.20078
C	5.563885	0.000826	0.002424	C	5.603012	0.000141	0.004007
C	4.869556	-0.70959	0.982059	C	4.905124	-0.11334	1.207438
C	3.468372	-0.72621	1.004108	C	3.503245	-0.11531	1.228197
H	-1.22231	1.740438	1.267838	H	-1.18792	2.163584	0.198977
H	-1.22002	-1.74166	-1.27151	H	-1.18721	-2.16406	-0.20426
H	5.415401	1.262016	-1.73799	H	5.453199	0.201651	-2.13614
H	6.649603	0.001177	0.00299	H	6.689229	0.000186	0.005068
H	5.4144	-1.26045	1.742686	H	5.44904	-0.20137	2.143856
C	-2.92739	-0.0002	-0.00301	C	-2.93549	-0.00011	-0.00457
C	-3.65072	1.203142	0.101938	C	-3.69581	1.204052	0.008088
C	-5.04354	1.199991	0.091705	C	-5.08793	1.197025	0.005882
C	-5.76846	0.001389	-0.00762	C	-5.82618	0.00025	-0.00802
C	-5.04447	-1.19773	-0.10985	C	-5.08816	-1.19667	-0.02582
C	-3.65177	-1.20263	-0.11285	C	-3.69608	-1.20403	-0.02314
H	-3.12727	2.152251	0.156364	H	-3.19396	2.165676	0.007024
H	-5.57639	2.144783	0.154732	H	-5.61619	2.148587	0.01009
H	-5.57829	-2.14116	-0.18477	H	-5.61656	-2.14803	-0.04123
N	1.339219	-0.00045	0.000209	N	1.376939	-5.7E-05	-0.00014
C	2.723678	-1.49638	2.069391	C	2.75339	-0.23726	2.533957
H	3.42893	-1.99596	2.736361	H	3.450864	-0.32641	3.370236
H	2.069352	-2.26356	1.64161	H	2.097863	-1.11482	2.545222
H	2.09192	-0.84393	2.68199	H	2.115244	0.634087	2.717706
C	2.72487	1.496229	-2.06749	C	2.758275	0.23733	-2.53146
H	3.430499	1.996127	-2.73382	H	3.457342	0.326539	-3.3664
H	2.069746	2.2631	-1.64038	H	2.102716	1.114853	-2.54396
H	2.09403	0.84341	-2.68064	H	2.120534	-0.63406	-2.71644

C	1.451215	2.012278	1.447685	C	1.456189	2.482202	0.23259
H	2.10204	2.585979	0.781946	H	2.106147	2.650505	-0.63353
H	2.087295	1.557102	2.212199	H	2.101321	2.482741	1.118473
C	1.453714	-2.01315	-1.44707	C	1.456948	-2.48236	-0.23219
H	2.103986	-2.58648	-0.78047	H	2.104967	-2.65044	0.63543
H	2.090513	-1.55786	-2.21092	H	2.104079	-2.483	-1.11662
H	0.766361	-2.70316	-1.93655	H	0.772145	-3.32871	-0.31263
H	0.763011	2.701931	1.936473	H	0.771118	3.328465	0.311627
H	-3.1292	-2.15189	-0.17254	H	-3.19448	-2.16574	-0.03205
C	-7.27672	-0.00087	0.019514	C	-7.33631	-6.3E-05	0.025812
H	-7.68465	-0.83453	-0.55924	H	-7.74778	-0.87668	-0.48553
H	-7.68406	0.93237	-0.37952	H	-7.74709	0.895189	-0.45272
H	-7.64407	-0.1058	1.048135	H	-7.71747	-0.01903	1.056055



**Compound 8**

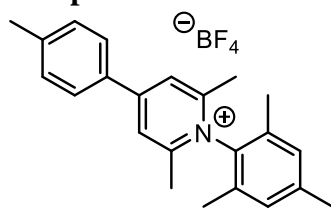


***N*-(*p*-trifluoromethyl)-4-(*p*-tolyl)-2,6-dimethylpyridinium tetrafluoroborate**

Pyr+				Pyr*			
Atom	X	Y	Z	Atom	X	Y	Z
C	-0.43868	1.17882	-0.18433	C	-0.44588	1.199767	-0.15719
C	-1.82129	1.179166	-0.18437	C	-1.81382	1.19005	-0.15295
C	-2.57023	-0.00117	-0.00166	C	-2.59486	-0.00038	0.000875
C	-1.8307	-1.18724	0.182607	C	-1.82293	-1.19592	0.160166
C	-0.44819	-1.1975	0.185271	C	-0.45509	-1.21518	0.17123
C	1.690518	-0.0172	0.00225	C	1.69656	-0.01556	0.007928
C	2.373138	-0.21724	-1.19783	C	2.397734	-0.56159	-1.07566
C	3.768415	-0.2227	-1.1938	C	3.791379	-0.57325	-1.07474
C	4.461701	-0.03095	0.005005	C	4.491082	-0.03167	0.009942
C	3.767833	0.168237	1.202435	C	3.795447	0.521355	1.092557
C	2.37269	0.175054	1.203984	C	2.402421	0.523356	1.092895
H	-2.32279	2.12179	-0.36334	H	-2.29933	2.144854	-0.31582
H	-2.3399	-2.12596	0.360423	H	-2.31588	-2.14706	0.322225
H	1.826378	-0.36828	-2.12355	H	1.852454	-0.96433	-1.92248
H	4.311932	-0.38176	-2.11848	H	4.326671	-0.99553	-1.91783
H	4.310952	0.311043	2.130056	H	4.334513	0.933144	1.938829
H	1.82553	0.325896	2.1295	H	1.860328	0.927213	1.941232
C	-4.03762	0.004106	-0.00278	C	-4.04965	0.004531	-0.00342
C	-4.76008	1.148337	0.393619	C	-4.80217	1.207564	0.075136
C	-6.15018	1.146747	0.395975	C	-6.19529	1.204853	0.06742
C	-6.87867	0.015004	-0.00816	C	-6.93439	0.012633	-0.01465
C	-6.15735	-1.12078	-0.41383	C	-6.20075	-1.18453	-0.0961
C	-4.76731	-1.13393	-0.40371	C	-4.80884	-1.19477	-0.09138
H	-6.68197	2.036411	0.72093	H	-6.72189	2.154847	0.132346
H	-6.69448	-2.00308	-0.7498	H	-6.73189	-2.13111	-0.17458
H	-4.24983	-2.02192	-0.75308	H	-4.3054	-2.15168	-0.18104
N	0.230637	-0.01193	0.001087	N	0.263209	-0.01026	0.008004
C	5.975471	0.010897	-0.00031	C	5.992196	0.007215	-0.00661
F	6.490009	-0.42614	1.169256	F	6.530799	-0.12289	1.234291
F	6.421658	1.276545	-0.18916	F	6.472948	1.187343	-0.50224
F	6.492217	-0.74943	-0.98929	F	6.5339	-0.97156	-0.77542
C	0.331668	-2.46329	0.397139	C	0.321614	-2.47936	0.412631
C	0.351242	2.43861	-0.39465	C	0.340723	2.458952	-0.39248
H	-0.33123	3.277587	-0.53361	H	-0.34673	3.273181	-0.62905

H	0.995736	2.368424	-1.276	H	1.042044	2.347137	-1.22734
H	0.996088	2.657044	0.461881	H	0.929533	2.758888	0.481508
H	0.974852	-2.39798	1.279827	H	1.020865	-2.3702	1.249591
H	0.976521	-2.68659	-0.45813	H	0.911275	-2.78605	-0.45843
H	-0.35745	-3.29705	0.534706	H	-0.37248	-3.28796	0.649107
H	-4.23716	2.034665	0.739007	H	-4.29458	2.162776	0.159031
C	-8.38477	0.011223	0.016338	C	-8.44472	0.011676	0.011043
H	-8.75081	-0.33542	0.991023	H	-8.82981	-0.18838	1.020032
H	-8.79113	1.012936	-0.14759	H	-8.84942	0.978215	-0.30528
H	-8.79635	-0.6582	-0.74382	H	-8.85631	-0.76063	-0.64777

**Compound 9**

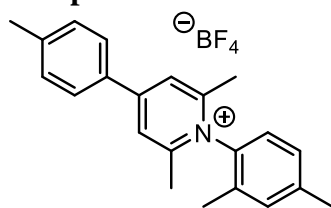


***N*-(mesityl)-4-(*p*-tolyl)-2,6-dimethylpyridinium tetrafluoroborate**

Pyr+				Pyr*			
Atom	X	Y	Z	Atom	X	Y	Z
C	-0.3234	0.980051	0.693972	C	-0.32437	1.210427	0.117316
C	1.061274	0.978095	0.692986	C	1.061915	1.20021	0.113215
C	1.796903	0.000191	0.001841	C	1.844487	-0.00144	-0.00199
C	1.060999	-0.977	-0.69004	C	1.059758	-1.20207	-0.11616
C	-0.32366	-0.97787	-0.69208	C	-0.32652	-1.20991	-0.11847
C	-2.45901	0.001367	0.00035	C	-2.48497	0.001712	0.000828
C	-3.13001	-0.7186	1.002213	C	-3.1731	-0.11879	1.222505
C	-4.52974	-0.6983	0.978648	C	-4.57451	-0.11248	1.198485
C	-5.24644	0.004468	0.00191	C	-5.29386	0.007143	0.002683
C	-4.52916	0.709682	-0.97287	C	-4.57549	0.12929	-1.19387
C	-3.12959	0.724925	-0.99943	C	-3.17447	0.127637	-1.21997
H	1.566025	1.743695	1.268066	H	1.548386	2.163093	0.214702
H	1.565693	-1.74304	-1.26461	H	1.544771	-2.16563	-0.2181
H	-5.07017	-1.2456	1.746408	H	-5.1146	-0.20132	2.138288
H	-5.06931	1.265831	-1.73448	H	-5.1165	0.230053	-2.132
N	-0.99516	0.00132	0.000749	N	-1.03969	0.000719	-3.4E-05
C	-1.10816	-2.01358	-1.44286	C	-1.12267	-2.48059	-0.24975
C	-1.10756	2.016336	1.444349	C	-1.11823	2.482437	0.249394
H	-0.41981	2.70755	1.931687	H	-0.43459	3.329223	0.333366
H	-1.74353	1.562207	2.209575	H	-1.7632	2.47636	1.135413
H	-1.75894	2.587706	0.777212	H	-1.76923	2.655065	-0.61512
H	-1.74327	-1.55895	-2.20851	H	-1.76765	-2.47362	-1.13576
H	-1.76043	-2.5843	-0.77602	H	-1.77389	-2.65139	0.614918
H	-0.42065	-2.7054	-1.9297	H	-0.44061	-3.32869	-0.33337
C	-6.75644	-0.0179	-0.01548	C	-6.80509	-0.02077	-0.00042
C	-2.39042	1.496128	-2.0682	C	-2.43245	0.259843	-2.52958
C	-2.39145	-1.4874	2.073138	C	-2.43016	-0.24905	2.531789
H	-3.09847	1.994461	-2.73322	H	-3.13418	0.365985	-3.36036
H	-1.75984	0.844061	-2.68256	H	-1.80389	-0.6153	-2.72858
H	-1.73525	2.264354	-1.64339	H	-1.76826	1.130962	-2.53423
H	-3.09991	-1.98055	2.741557	H	-3.13152	-0.33273	3.365441
H	-1.74025	-2.25981	1.649754	H	-1.78336	-1.13323	2.544475
H	-1.75692	-0.83548	2.68354	H	-1.78385	0.615461	2.719411
H	-7.16448	-0.15631	0.989676	H	-7.21276	0.343459	0.947146

H	-7.16348	0.90856	-0.43047	H	-7.21357	0.592037	-0.80965
H	-7.12378	-0.84447	-0.63608	H	-7.17686	-1.04282	-0.1458
C	3.272148	-0.00081	0.002168	C	3.296633	-0.00345	-0.00236
C	3.994921	-1.20469	-0.0989	C	4.056986	-1.20758	-0.01914
C	3.997117	1.20169	0.107585	C	4.059026	1.201723	0.01128
C	5.387869	-1.2021	-0.08921	C	5.450988	-1.20017	-0.0206
H	3.47101	-2.15374	-0.14993	H	3.555618	-2.16939	-0.02467
C	5.389781	1.196224	0.104169	C	5.450335	1.194395	0.010206
C	6.113304	-0.00356	0.005824	C	6.189138	-0.00447	-0.00418
H	5.920283	-2.14733	-0.1493	H	5.97935	-2.15156	-0.03281
H	5.924012	2.139711	0.1757	H	5.978801	2.146049	0.016221
H	3.474855	2.151325	0.164195	H	3.557192	2.163344	0.011577
C	7.62159	-0.00156	-0.02157	C	7.699719	0.001474	0.013494

**Compound 10**

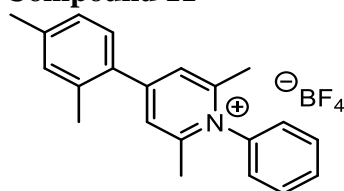


***N*-(2,4-xylyl)-4-(*p*-tolyl)-2,6-dimethylpyridinium tetrafluoroborate**

Pyr+				Pyr*			
Atom	X	Y	Z	Atom	X	Y	Z
C	0.431145	-1.11571	-0.45522	C	0.432848	-1.21287	-0.23027
C	-0.9532	-1.12044	-0.42934	C	-0.93414	-1.20382	-0.18262
C	-1.68863	0.028492	-0.09147	C	-1.71498	0.000205	-0.13901
C	-0.95328	1.186756	0.212405	C	-0.93537	1.205163	-0.17786
C	0.431148	1.196471	0.18618	C	0.431613	1.215823	-0.2254
C	2.56391	0.046258	-0.15575	C	2.58685	0.002208	-0.19192
C	3.272149	-0.28595	1.008431	C	3.254058	-0.00068	1.047508
C	4.672582	-0.2608	0.925628	C	4.656097	0.003359	1.036032
C	5.35611	0.074803	-0.25061	C	5.401461	0.007953	-0.15214
C	4.602654	0.402244	-1.3889	C	4.705726	0.014582	-1.36948
C	3.210758	0.388068	-1.34397	C	3.310425	0.010413	-1.387
H	-1.45843	-2.03646	-0.70721	H	-1.41828	-2.17282	-0.18778
H	-1.45707	2.100706	0.4995	H	-1.42045	2.1737	-0.17875
H	5.244559	-0.5122	1.814949	H	5.182331	0.005019	1.988028
H	5.104059	0.670438	-2.31428	H	5.254364	0.024928	-2.30747
H	2.626591	0.641722	-2.22329	H	2.772951	0.017109	-2.3308
N	1.101997	0.041552	-0.13843	N	1.144098	0.001833	-0.23791
C	6.86534	0.070923	-0.30129	C	6.912013	-0.01978	-0.11811
H	7.298476	-0.00736	0.699097	H	7.300201	0.465931	0.782005
H	7.247067	0.982801	-0.77173	H	7.339162	0.481347	-0.99178
C	2.579656	-0.65488	2.298597	C	2.492435	-0.00422	2.351424
H	1.946402	-1.54149	2.182773	H	1.846666	-0.88518	2.438889
H	1.934629	0.152539	2.662443	H	1.842291	0.873227	2.441675
H	7.231997	-0.77608	-0.89317	H	7.28371	-1.05209	-0.11908
H	3.314515	-0.87033	3.076712	H	3.179972	-0.00401	3.200582
C	-3.16366	0.019295	-0.06168	C	-3.16509	-0.00073	-0.07244
C	-3.90151	1.181937	-0.35416	C	-3.92582	1.202972	-0.03376
C	-3.87309	-1.1525	0.264451	C	-3.92437	-1.20524	-0.03529
C	-5.29422	1.167057	-0.32779	C	-5.31633	1.194947	0.030418
H	-3.39039	2.098152	-0.63191	H	-3.42536	2.165155	-0.04833
C	-5.26532	-1.15533	0.300671	C	-5.31507	-1.1988	0.028874
H	-3.33786	-2.05976	0.525859	H	-3.42285	-2.16686	-0.05085
C	-6.00412	0.000606	-0.00058	C	-6.05338	-0.00245	0.059958
H	-5.83892	2.075828	-0.56864	H	-5.84429	2.146209	0.061018

H	-5.78692	-2.06843	0.574261	H	-5.842	-2.15066	0.058307
C	1.215303	2.436055	0.501081	C	1.222136	2.493057	-0.28743
H	1.797564	2.76241	-0.36577	H	1.817405	2.558365	-1.20544
H	1.917361	2.274544	1.323628	H	1.920473	2.589296	0.551651
C	1.215266	-2.33371	-0.84546	C	1.224747	-2.48895	-0.2982
H	1.925207	-2.62524	-0.06675	H	1.922011	-2.58921	0.541295
H	1.788733	-2.15501	-1.76002	H	1.821342	-2.5484	-1.21575
H	0.53006	3.236561	0.780356	H	0.539385	3.344517	-0.26104
H	0.531035	-3.16417	-1.02023	H	0.542833	-3.34124	-0.27753
C	-7.51257	-0.01803	0.003274	C	-7.56351	-0.00291	0.093682
H	-7.9235	0.974127	0.209978	H	-7.95221	0.873612	0.62282
H	-7.9004	-0.71773	0.74928	H	-7.95194	-0.89826	0.590257
H	-7.89729	-0.33606	-0.9739	H	-7.99055	0.015993	-0.91843

**Compound 11**



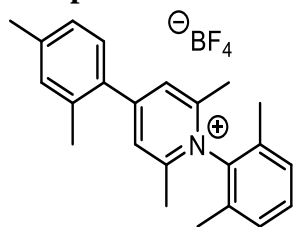
***N*-phenyl-4-(2,4-xylyl)-2,6-dimethylpyridinium tetrafluoroborate**

Pyr+				Pyr*			
Atom	X	Y	Z	Atom	X	Y	Z
C	1.092079	1.026448	-0.52256	C	1.101805	1.203593	0.408076
C	-0.29454	1.0217	-0.51313	C	-0.26744	1.187263	0.410964
C	-1.02376	-0.07124	-0.01744	C	-1.04659	0.047004	0.022349
C	-0.28316	-1.16299	0.466708	C	-0.27286	-1.07789	-0.40786
C	1.103049	-1.16118	0.466027	C	1.097566	-1.08187	-0.44135
N	1.766165	-0.06378	-0.02796	N	1.81373	0.060203	-0.01643
H	-0.80321	1.881459	-0.93144	H	-0.76608	2.081063	0.774963
H	-0.78991	-2.02943	0.876704	H	-0.76645	-1.96673	-0.78383
C	1.870513	2.187415	-1.06771	C	1.889772	2.390548	0.888195
C	1.892564	-2.3209	0.997519	C	1.881619	-2.2566	-0.95652
H	1.178294	2.949796	-1.42942	H	1.202372	3.153854	1.262225
H	2.517723	1.879028	-1.89568	H	2.496039	2.839559	0.091187
H	2.509873	2.632753	-0.29786	H	2.579278	2.12033	1.698596
H	2.527154	-2.7582	0.219175	H	2.557814	-1.96924	-1.77217
H	2.54569	-2.01408	1.82141	H	2.501588	-2.71989	-0.17799
H	1.207498	-3.08895	1.360921	H	1.190795	-3.01521	-1.33404
C	-2.50453	-0.11457	-0.03441	C	-2.51057	0.102971	-0.0122
C	-3.12089	-1.29531	-0.49783	C	-3.1411	1.333766	-0.33733
C	-3.31746	0.962133	0.398435	C	-3.36915	-1.00146	0.285609
C	-4.50513	-1.41208	-0.56899	C	-4.52438	1.476796	-0.39659
H	-2.50098	-2.1229	-0.83401	H	-2.52029	2.193187	-0.57938
C	-4.71045	0.805564	0.332934	C	-4.75873	-0.82606	0.211905
C	-5.32851	-0.35333	-0.15429	C	-5.37116	0.388272	-0.1324
H	-5.33644	1.622686	0.688196	H	-5.39445	-1.67652	0.460395
C	-6.83186	-0.45847	-0.24194	C	-6.87413	0.512605	-0.23098
H	-7.17939	-1.45249	0.062025	H	-7.22197	0.364614	-1.26373
H	-7.32357	0.288913	0.388977	H	-7.37934	-0.23507	0.391326
H	-7.17211	-0.29835	-1.27408	H	-7.21614	1.505681	0.084203
H	-4.94851	-2.33119	-0.9461	H	-4.95046	2.443594	-0.66231
C	-2.76561	2.250957	0.971047	C	-2.85351	-2.34762	0.752614
H	-3.50145	2.710131	1.63866	H	-3.63607	-2.88129	1.302991
H	-1.84388	2.095208	1.540394	H	-2.55002	-2.99563	-0.08081
H	-2.54707	2.983036	0.18258	H	-1.98331	-2.24338	1.41054
C	3.2279	-0.0557	-0.02706	C	3.252813	0.0586	-0.02193

C	3.90447	0.467953	1.076222	C	3.956734	-0.60581	0.991177
C	3.912507	-0.571	-1.12924	C	3.95294	0.719642	-1.03985
C	5.302235	0.473315	1.071608	C	5.354806	-0.61146	0.982773
H	3.349258	0.863826	1.922208	H	3.40768	-1.10962	1.782671
C	5.310247	-0.55963	-1.12229	C	5.351066	0.719601	-1.04018
H	3.363626	-0.97332	-1.97632	H	3.401285	1.224894	-1.82859
C	6.004014	-0.03897	-0.02477	C	6.054751	0.05279	-0.03084
H	5.838581	0.878081	1.925344	H	5.895352	-1.1286	1.771729
H	5.852822	-0.95785	-1.97516	H	5.888719	1.23431	-1.83269
H	7.090727	-0.03244	-0.02388	H	7.1419	0.050653	-0.03425



**Compound 12**

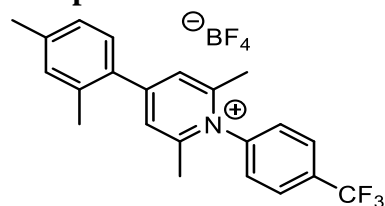


***N*-(2,6-xylyl)-4-(2,4-xylyl)-2,6-dimethylpyridinium tetrafluoroborate**

Pyr+				Pyr*			
Atom	X	Y	Z	Atom	X	Y	Z
C	-0.82055	-0.85368	0.907226	C	-0.81589	-0.99948	0.771583
C	0.565689	-0.85884	0.908911	C	0.553354	-0.98635	0.770579
C	0.58035	0.718307	-0.89275	C	1.334695	-0.0249	0.045187
C	-0.80635	0.722025	-0.90206	C	0.561594	0.914046	-0.7113
H	1.070959	-1.47638	1.643027	C	-0.80892	0.908345	-0.74298
H	1.090603	1.323664	-1.63168	N	-1.52594	-0.04574	0.012083
C	-1.61177	-1.68158	1.877433	H	1.05059	-1.72787	1.389421
C	-1.58291	1.552755	-1.88174	H	1.055367	1.649143	-1.33642
H	-0.92752	-2.24182	2.517055	C	-1.60983	-1.98842	1.579658
H	-2.26466	-2.39227	1.359979	C	-1.59634	1.883854	-1.57331
H	-2.24845	-1.05636	2.512409	H	-0.92557	-2.65214	2.114751
H	-2.22447	0.931614	-2.51565	H	-2.26351	-2.60758	0.952064
H	-2.22915	2.274856	-1.37157	H	-2.25452	-1.49555	2.31904
H	-0.88906	2.100796	-2.52157	H	-2.22973	1.38098	-2.31563
C	1.308332	-0.06992	0.01352	H	-2.26056	2.508414	-0.96171
N	-1.48332	-0.06109	0.001308	H	-0.9078	2.544694	-2.10659
C	2.788781	-0.11807	0.016734	C	2.798033	-0.0954	0.025382
C	3.603159	1.040121	-0.04601	C	3.423017	-1.36942	0.098679
C	3.404056	-1.38448	0.096419	C	3.662957	1.042255	-0.0397
C	4.995762	0.869023	-0.03879	C	4.805361	-1.53091	0.082067
C	4.788205	-1.52177	0.081771	H	2.798172	-2.25852	0.139177
H	2.783639	-2.27619	0.141342	C	5.051431	0.845375	-0.05962
C	5.612675	-0.38794	0.009896	C	5.657839	-0.41882	-0.00979
H	5.622757	1.759048	-0.06183	H	5.691527	1.727699	-0.0912
H	5.230457	-2.51456	0.12905	C	7.159821	-0.57545	-0.06969
C	-2.94839	-0.05119	-0.00128	H	7.503305	-0.76199	-1.09768
C	-3.60854	0.891211	0.806891	H	7.67082	0.327605	0.283764
C	-3.61906	-0.98474	-0.81107	H	7.499898	-1.42045	0.540992
C	-5.01037	0.879143	0.78764	H	5.226293	-2.53462	0.129773
C	-5.02065	-0.95361	-0.79548	C	3.155307	2.469743	-0.01493
C	-5.70987	-0.0325	-0.00488	H	3.942537	3.144175	0.339444
H	-5.55186	1.594034	1.402068	H	2.8516	2.827179	-1.0083
H	-5.57018	-1.66128	-1.41112	H	2.287424	2.580965	0.644883

H	-6.7969	-0.0252	-0.00626	C	-2.96965	-0.05396	-0.00492
C	-2.8575	1.883833	1.663375	C	-3.66925	0.72819	0.935717
H	-2.18044	1.389394	2.370301	C	-3.63986	-0.84288	-0.96131
H	-2.24575	2.565281	1.059154	C	-5.0714	0.707841	0.902673
H	-3.55806	2.491725	2.241709	C	-5.04252	-0.83666	-0.9599
C	-2.87949	-1.98748	-1.66576	C	-5.75427	-0.06796	-0.03646
H	-2.20093	-1.50167	-2.37722	H	-5.62787	1.305615	1.62138
H	-2.27117	-2.6716	-1.06118	H	-5.57657	-1.43972	-1.69108
H	-3.58725	-2.59166	-2.23918	H	-6.84177	-0.07341	-0.04879
C	3.053497	2.451095	-0.07146	C	-2.87617	-1.67389	-1.96594
H	2.83376	2.781849	-1.09502	C	-2.93661	1.56676	1.956973
H	2.13301	2.552526	0.511921	H	-2.22066	-1.05377	-2.58972
H	3.791237	3.148188	0.338095	H	-3.56495	-2.20863	-2.62663
C	7.115893	-0.52099	-0.02662	H	-2.23363	-2.41527	-1.47516
H	7.457867	-0.77169	-1.04007	H	-2.29339	0.952294	2.59895
H	7.608255	0.411663	0.267205	H	-2.28644	2.31063	1.480291
H	7.460955	-1.32083	0.63832	H	-3.64529	2.09878	2.598528

**Compound 13**

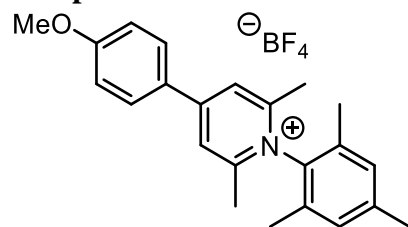


***N*-(*p*-trifluoromethyl)-4-(2,4-xylyl)-2,6-dimethylpyridinium tetrafluoroborate**

Pyr+				Pyr*			
Atom	X	Y	Z	Atom	X	Y	Z
C	-0.25921	1.169471	0.471996	C	-0.26945	1.208592	0.42125
C	-1.64475	1.167975	0.468678	C	-1.63958	1.187327	0.417701
C	-2.38244	0.07338	-0.0147	C	-2.41172	0.05373	0.011811
C	-1.6502	-1.01999	-0.50604	C	-1.63997	-1.06264	-0.43092
C	-0.26422	-1.02359	-0.5126	C	-0.26877	-1.06678	-0.46523
N	0.405956	0.070391	-0.01827	N	0.447098	0.071289	-0.02124
H	-2.15393	2.034262	0.87584	H	-2.14301	2.070423	0.800796
H	-2.15647	-1.88122	-0.92407	H	-2.13469	-1.94185	-0.82801
C	0.528124	2.331039	1.00242	C	0.504652	2.377193	0.964383
C	0.518222	-2.18395	-1.05304	C	0.506344	-2.21882	-1.04155
H	-0.15887	3.098134	1.363816	H	-0.19224	3.097056	1.40124
H	1.161838	2.769999	0.224102	H	1.088556	2.898136	0.19531
H	1.180366	2.028033	1.828562	H	1.211501	2.064683	1.744119
H	1.166827	-1.87743	-1.88074	H	1.202369	-1.88559	-1.82239
H	1.15503	-2.62864	-0.28053	H	1.102487	-2.75284	-0.29066
H	-0.17191	-2.94779	-1.4153	H	-0.19084	-2.93436	-1.48528
C	-3.86255	0.114078	-0.03521	C	-3.87913	0.104239	-0.02026
C	-4.4797	1.295135	-0.49704	C	-4.51134	1.326012	-0.36593
C	-4.67486	-0.96569	0.392293	C	-4.72768	-0.9985	0.299399
C	-5.86383	1.409402	-0.57217	C	-5.89558	1.462768	-0.42311
H	-3.86055	2.124821	-0.8293	H	-3.89254	2.182357	-0.62389
C	-6.06765	-0.8113	0.323034	C	-6.11872	-0.83058	0.228054
C	-6.68637	0.347763	-0.16335	C	-6.73555	0.375236	-0.13566
H	-6.69327	-1.63027	0.674629	H	-6.75036	-1.67895	0.49274
C	-8.18952	0.449195	-0.25649	C	-8.23927	0.492612	-0.23017
H	-8.52721	0.261653	-1.2849	H	-8.58765	0.337818	-1.26151
H	-8.68172	-0.28265	0.392066	H	-8.73923	-0.25406	0.397211
H	-8.53866	1.450227	0.020998	H	-8.58419	1.486036	0.080345
H	-6.30772	2.328702	-0.94808	H	-6.32716	2.422539	-0.70418
C	-4.12286	-2.25462	0.964487	C	-4.20114	-2.33501	0.781476
H	-4.85953	-2.71474	1.630501	H	-4.97408	-2.86209	1.351253
H	-3.90296	-2.98593	0.175682	H	-3.90832	-2.99434	-0.04669
H	-3.20228	-2.09896	1.535676	H	-3.32199	-2.21792	1.42485
C	1.86549	0.064488	-0.01425	C	1.876432	0.066242	-0.01384

C	2.541049	-0.45459	1.091203	C	2.575466	-0.78732	0.856566
C	2.55192	0.57898	-1.1146	C	2.593823	0.912619	-0.87451
C	3.936015	-0.45869	1.093632	C	3.968016	-0.79723	0.863375
C	3.947285	0.57225	-1.10851	C	3.987545	0.911338	-0.86252
C	4.633987	0.055914	-0.00465	C	4.677734	0.056842	0.00704
H	4.470478	-0.85678	1.950234	H	4.498039	-1.4534	1.547553
H	4.490084	0.97245	-1.9586	H	4.53205	1.566529	-1.53542
H	2.008587	0.981069	-1.96454	H	2.059903	1.558201	-1.56535
H	1.989068	-0.84886	1.939205	H	2.026058	-1.42634	1.541478
C	6.14102	0.005988	-0.01659	C	6.177605	0.00961	-0.00993
F	6.686262	0.975652	-0.7871	F	6.735795	1.147107	-0.49156
F	6.671663	0.139274	1.22216	F	6.708146	-0.19465	1.22386
F	6.604445	-1.17767	-0.50488	F	6.657984	-1.00423	-0.79114

**Compound 14**

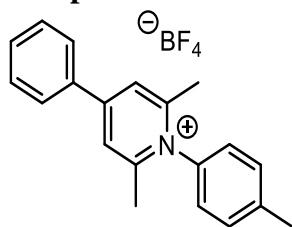


***N*-(mesityl)-4-(*p*-methoxyphenyl)-2,6-dimethylpyridinium tetrafluoroborate**

Pyr+				Pyr*			
Atom	X	Y	Z	Atom	X	Y	Z
C	-0.71215	-1.06388	-0.62212	C	-0.71385	-1.24567	-0.1241
C	0.671108	-1.09819	-0.62282	C	0.653995	-1.27075	-0.12162
C	1.437813	-0.09381	-0.00328	C	1.465645	-0.09309	-0.00251
C	0.725636	0.948764	0.6182	C	0.71578	1.125636	0.117373
C	-0.6574	0.987357	0.618721	C	-0.6513	1.170721	0.121599
C	-2.82066	0.018344	-9.1E-05	C	-2.83923	0.018713	0.000102
C	-3.47586	0.674707	-1.05492	C	-3.52539	0.163355	-1.21998
C	-4.87545	0.693644	-1.02901	C	-4.92576	0.193929	-1.19464
C	-5.60778	0.090447	0.001431	C	-5.64685	0.087221	0.001435
C	-4.90661	-0.55428	1.028275	C	-4.93078	-0.0596	1.196331
C	-3.50774	-0.60575	1.053915	C	-3.53054	-0.0949	1.220612
H	1.150849	-1.9165	-1.14392	H	1.113321	-2.24621	-0.22806
H	1.248333	1.739845	1.139991	H	1.225313	2.075943	0.223296
H	-5.40336	1.192363	-1.83754	H	-5.46422	0.301711	-2.13339
H	-5.45909	-1.03312	1.832389	H	-5.47317	-0.15063	2.134611
N	-1.35799	-0.02049	-0.00151	N	-1.39575	-0.01877	-0.00081
C	-1.41237	2.09661	1.290841	C	-1.40969	2.461846	0.259486
C	-1.52515	-2.13226	-1.29272	C	-1.53773	-2.49612	-0.26041
H	-0.85717	-2.87359	-1.73148	H	-0.87489	-3.35906	-0.3498
H	-2.15503	-1.71948	-2.0858	H	-2.18422	-2.47043	-1.14506
H	-2.18579	-2.638	-0.5829	H	-2.19109	-2.65728	0.604659
H	-2.06268	1.716946	2.083993	H	-2.05519	2.468631	1.145186
H	-2.0457	2.637113	0.58178	H	-2.05533	2.656174	-0.6045
H	-0.70578	2.8012	1.729716	H	-0.70338	3.289643	0.348047
C	-7.11658	0.155751	0.018245	C	-7.15679	0.15504	0.005585
C	-2.78587	-1.31274	2.177534	C	-2.79089	-0.25349	2.528578
C	-2.71979	1.338216	-2.18252	C	-2.78031	0.279302	-2.52934
H	-3.50365	-1.71106	2.897334	H	-3.49406	-0.33414	3.361023
H	-2.10936	-0.64176	2.718004	H	-2.13024	0.59804	2.72575
H	-2.18024	-2.15015	1.813743	H	-2.15889	-1.1483	2.531726
H	-3.41691	1.76689	-2.90517	H	-3.47944	0.394432	-3.36114
H	-2.07432	2.147224	-1.82294	H	-2.10281	1.140176	-2.53537
H	-2.07641	0.632016	-2.71848	H	-2.16497	-0.60579	-2.72524

H	-7.52491	0.197245	-0.99553	H	-7.57576	-0.22612	-0.93044
H	-7.5469	-0.70955	0.530238	H	-7.57967	-0.42262	0.832923
H	-7.45891	1.05392	0.546866	H	-7.50134	1.190447	0.120332
C	2.908154	-0.13265	-0.0054	C	2.918195	-0.12987	-0.00303
C	3.667384	1.04938	0.068483	C	3.710143	1.04921	0.011576
C	3.605933	-1.35881	-0.08436	C	3.646695	-1.35566	-0.01742
C	5.060688	1.026418	0.05892	C	5.106725	1.02005	0.012699
H	3.172965	2.014572	0.101311	H	3.235726	2.024327	0.013639
C	4.990925	-1.39778	-0.08149	C	5.033795	-1.39325	-0.01766
C	5.73296	-0.20405	-0.01325	C	5.785058	-0.20577	-0.00238
H	5.604728	1.961685	0.099723	H	5.648066	1.959264	0.021607
H	5.520598	-2.34369	-0.12442	H	5.556596	-2.34557	-0.02564
H	3.06183	-2.29686	-0.115	H	3.119877	-2.30351	-0.01972
C	7.902787	0.83016	0.05246	C	7.954339	0.830316	0.013391
H	8.930561	0.469515	0.035438	H	8.989975	0.489103	0.011222
H	7.728153	1.48538	-0.80702	H	7.772089	1.44759	-0.87429
H	7.719173	1.376536	0.983157	H	7.768318	1.425027	0.915582
O	7.081877	-0.34362	-0.02291	O	7.152743	-0.35031	-0.00317

**Compound 15**



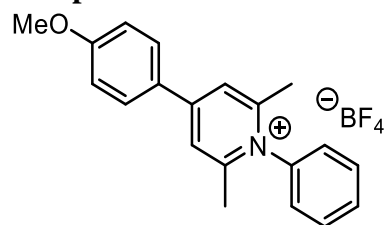
***N*-(*p*-tolyl)-4-phenyl-2,6-dimethylpyridinium tetrafluoroborate**

Pyr+				Pyr*			
Atom	X	Y	Z	Atom	X	Y	Z
C	0.14483	-1.17912	-0.21648	C	0.138301	-1.21298	-0.03613
C	-1.2405	-1.1775	-0.21601	C	-1.22955	-1.20386	-0.0336
C	-1.97441	0.000107	-0.00183	C	-2.01118	-0.00038	-0.00055
C	-1.24245	1.179099	0.211405	C	-1.23102	1.204059	0.031971
C	0.142882	1.183015	0.211816	C	0.136823	1.214862	0.034149
C	2.273517	0.002851	-0.00012	C	2.290744	0.001978	-0.00012
C	2.956547	-0.22706	1.193166	C	2.992984	-0.05213	1.207414
C	4.35249	-0.22221	1.186533	C	4.389653	-0.04803	1.203422
C	5.074386	0.006547	0.00468	C	5.112765	0.007441	0.001655
C	4.35567	0.238563	-1.17917	C	4.390864	0.065445	-1.20094
C	2.960253	0.237555	-1.19096	C	2.994377	0.060989	-1.20682
H	-1.74554	-2.1147	-0.41185	H	-1.71297	-2.17238	-0.06974
H	-1.74902	2.115532	0.407051	H	-1.71559	2.17201	0.067844
H	2.408191	-0.40362	2.113141	H	2.446338	-0.09277	2.144914
H	4.885168	-0.39733	2.116711	H	4.923676	-0.08632	2.149258
H	4.891225	0.424787	-2.10565	H	4.925873	0.11591	-2.14568
H	2.414373	0.419263	-2.11141	H	2.448696	0.106986	-2.14463
N	0.812945	0.002437	-0.00197	N	0.848035	0.001361	-0.00093
C	0.926064	2.439514	0.450216	C	0.927568	2.492593	0.077982
H	1.561429	2.679354	-0.40724	H	1.572039	2.605406	-0.80104
H	1.576343	2.343312	1.324242	H	1.577536	2.541076	0.958889
C	0.930073	-2.43428	-0.45515	C	0.930677	-2.48967	-0.08059
H	1.56446	-2.67424	0.402994	H	1.575426	-2.60197	0.798293
H	1.581572	-2.33617	-1.32806	H	1.5806	-2.53688	-0.96161
H	0.243181	-3.26391	-0.62311	H	0.247017	-3.34008	-0.11375
H	0.237816	3.268407	0.616198	H	0.242806	3.342127	0.110867
C	6.583847	-0.02091	-0.00008	C	6.623405	-0.019	0.000714
H	6.990092	0.233058	0.98276	H	7.030156	0.413407	0.919483
H	6.992085	0.678148	-0.73556	H	7.031101	0.533837	-0.85073
H	6.950836	-1.0213	-0.26033	H	6.995463	-1.04874	-0.06962
C	-3.45279	-0.00145	-0.00056	C	-3.46214	-0.00126	-1.1E-05
C	-4.17127	1.11935	-0.45855	C	-4.21978	1.205562	-0.05766
C	-4.16781	-1.1238	0.459057	C	-4.21826	-1.20899	0.05823

C	-5.56603	1.114024	-0.4615	C	-5.61194	1.200478	-0.05693
H	-3.64208	1.985962	-0.84147	H	-3.71397	2.163275	-0.11248
C	-5.56257	-1.12151	0.465175	C	-5.61043	-1.2056	0.058474
H	-3.63587	-1.98922	0.840847	H	-3.71124	-2.16608	0.112726
C	-6.26586	-0.0045	0.002646	C	-6.33026	-0.003	0.001021
H	-6.10538	1.980835	-0.83049	H	-6.14373	2.147624	-0.10493
H	-6.09919	-1.98947	0.835442	H	-6.14104	-2.15339	0.106882
H	-7.35157	-0.00566	0.003915	H	-7.41602	-0.00366	0.00141



**Compound 16**

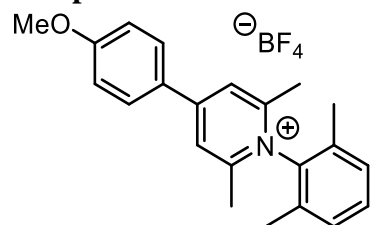


***N*-phenyl-4-(*p*-methoxyphenyl)-2,6-dimethylpyridinium tetrafluoroborate**

Pyr+				Pyr*			
Atom	X	Y	Z	Atom	X	Y	Z
C	-1.30491	-1.15995	0.21582	C	-1.30252	-1.18983	0.09845
C	0.07783	-1.11695	0.22875	C	0.06401	-1.1366	0.09578
C	0.78448	0.08332	0.02837	C	0.80729	0.08738	-0.00153
C	0.01321	1.2409	-0.18408	C	-0.00824	1.2633	-0.10277
C	-1.36976	1.20389	-0.19703	C	-1.37573	1.234	-0.10925
H	0.60449	-2.04142	0.42708	H	0.57922	-2.08449	0.19657
H	0.48903	2.19452	-0.3722	H	0.44853	2.24064	-0.20376
C	2.25463	0.12687	0.04081	C	2.26005	0.1308	0.00228
C	2.94701	1.3009	0.41334	C	2.98168	1.35786	0.07692
C	3.01878	-0.99782	-0.3198	C	3.05641	-1.04272	-0.06637
C	4.33187	1.34217	0.43104	C	4.36866	1.40187	0.08157
C	4.41195	-0.96686	-0.31955	C	4.45289	-1.00746	-0.06002
H	2.52818	-1.91089	-0.64031	H	2.58528	-2.01674	-0.14058
C	5.07889	0.20845	0.06112	C	5.12516	0.2196	0.01369
H	4.8576	2.24115	0.73536	H	4.88721	2.35443	0.14475
H	4.96053	-1.85023	-0.62113	H	4.99887	-1.94212	-0.11917
C	-2.18777	2.4386	-0.43527	C	-2.20387	2.48097	-0.24645
H	-1.5229	3.2897	-0.58358	H	-2.8307	2.6611	0.63438
H	-2.82205	2.332	-1.31989	H	-1.54429	3.34141	-0.37507
H	-2.84229	2.65153	0.41485	H	-2.876	2.43078	-1.11083
C	-2.05468	-2.43979	0.43993	C	-2.05394	-2.48506	0.23065
H	-2.673	-2.69426	-0.42582	H	-2.66547	-2.70075	-0.65291
H	-1.34493	-3.2495	0.60992	H	-1.34386	-3.30414	0.36015
H	-2.71723	-2.36732	1.30705	H	-2.73096	-2.47739	1.09257
C	-3.46799	-0.04026	-0.0112	C	-3.49175	-0.04276	-0.00137
C	-4.12913	-0.28251	-1.21564	C	-4.18642	-0.33318	-1.18118
C	-4.16581	0.16143	1.18	C	-4.19508	0.20602	1.18289
C	-5.52567	-0.32272	-1.22323	C	-5.58335	-0.37735	-1.17432
H	-3.56222	-0.43629	-2.12826	H	-3.63236	-0.51921	-2.09623
C	-5.56213	0.11858	1.16012	C	-5.59215	0.16686	1.18478
H	-3.62717	0.34776	2.10358	H	-3.64736	0.42517	2.09446
C	-6.24092	-0.12281	-0.03838	C	-6.28818	-0.12618	0.00743
H	-6.05039	-0.51011	-2.15445	H	-6.11871	-0.6032	-2.09166

H	-6.11524	0.27383	2.08076	H	-6.13429	0.36062	2.10549
H	-7.32581	-0.15507	-0.04901	H	-7.37354	-0.1585	0.01084
N	-2.00847	0.00252	0.00293	N	-2.05159	0.00027	-0.00581
H	2.39865	2.18342	0.72547	H	2.44904	2.29998	0.14709
O	6.4273	0.34725	0.10375	O	6.49194	0.37	0.02602
C	7.25263	-0.77174	-0.24874	C	7.29932	-0.80537	-0.03409
H	7.07972	-1.07387	-1.28667	H	7.12398	-1.36161	-0.96253
H	8.27904	-0.42532	-0.13404	H	8.33321	-0.45989	-0.00831
H	7.07178	-1.61754	0.42241	H	7.11232	-1.46086	0.82474

**Compound 17**

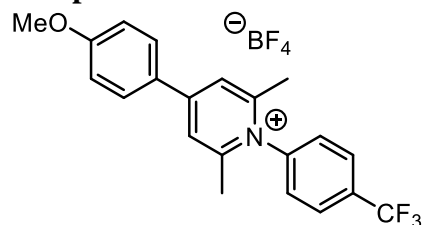


***N*-(2,6-xylyl)-4-(*p*-methoxyphenyl)-2,6-dimethylpyridinium tetrafluoroborate**

Pyr+				Pyr*			
Atom	X	Y	Z	Atom	X	Y	Z
C	0.795356	-1.36554	-0.31873	C	-0.84288	1.249241	-0.25086
C	-0.58827	-1.3988	-0.27829	C	0.525038	1.275828	-0.2035
C	-1.34876	-0.23018	-0.09399	C	1.337791	0.092604	-0.16391
C	-0.63381	0.976112	0.037276	C	0.589832	-1.13333	-0.20855
C	0.749044	1.015805	-0.00329	C	-0.77731	-1.17998	-0.25512
N	1.443852	-0.16281	-0.17038	N	-1.52305	0.01512	-0.26266
H	-1.07132	-2.35794	-0.42314	H	0.983062	2.259213	-0.20812
H	-1.16403	1.90483	0.200797	H	1.100341	-2.09057	-0.21383
C	5.019701	-0.27646	0.917484	C	-5.01683	-0.07968	1.063153
C	3.621829	-0.29924	1.006356	C	-3.61504	-0.03956	1.054028
C	2.905564	-0.14189	-0.19372	C	-2.96437	-0.0234	-0.1955
C	3.548797	0.027138	-1.41859	C	-3.70635	-0.04897	-1.37972
C	4.94402	0.044083	-1.46908	C	-5.10178	-0.08927	-1.34206
C	5.700669	-0.10784	-0.29917	C	-5.77987	-0.10205	-0.11463
H	5.5963	-0.39523	1.83319	H	-5.52938	-0.09641	2.024102
H	2.962329	0.144286	-2.32626	H	-3.18266	-0.04044	-2.33275
H	5.441941	0.176205	-2.42645	H	-5.6641	-0.11267	-2.27324
C	2.932463	-0.48203	2.337614	C	-2.83503	-0.01892	2.3472
C	7.210692	-0.09589	-0.33377	C	-7.29013	-0.11333	-0.05701
H	2.2825	-1.36573	2.34427	H	-2.20599	0.876753	2.424936
H	2.301974	0.379391	2.591451	H	-2.16392	-0.88334	2.42773
H	3.669415	-0.60296	3.135854	H	-3.51055	-0.03366	3.20756
H	7.618425	-1.05186	0.018199	H	-7.68592	0.909058	0.014309
H	7.585233	0.080579	-1.34667	H	-7.72009	-0.56912	-0.95534
H	7.613004	0.686841	0.321024	H	-7.65288	-0.66444	0.81764
C	-2.81891	-0.26657	-0.04439	C	2.789047	0.130864	-0.09453
C	-3.50475	-1.42167	0.395075	C	3.515065	1.357543	-0.03746
C	-3.58971	0.844345	-0.43385	C	3.582825	-1.04758	-0.0772
C	-4.88961	-1.45795	0.448088	C	4.901315	1.396289	0.027896
H	-2.94943	-2.29265	0.731142	H	2.986932	2.306206	-0.04155
C	-4.98344	0.817486	-0.39843	C	4.97867	-1.01707	-0.01129
H	-3.10494	1.742476	-0.80582	H	3.110749	-2.02454	-0.11613
C	-5.64421	-0.33873	0.048134	C	5.65518	0.20954	0.041635

H	-5.41024	-2.34267	0.803602	H	5.422304	2.350244	0.070832
H	-5.53768	1.690299	-0.72443	H	5.521248	-1.95719	-0.0023
C	1.538822	2.298215	0.124277	C	-1.53349	-2.47793	-0.3229
C	0.712359	3.561527	0.377617	C	-1.66788	2.504547	-0.31801
H	1.389898	4.417352	0.458561	H	-1.00783	3.37567	-0.29722
H	0.01517	3.767691	-0.44203	H	-2.36877	2.58646	0.522565
H	0.143233	3.497945	1.311919	H	-2.26724	2.548459	-1.23662
C	1.600803	-2.61141	-0.54716	H	-2.12939	-2.55374	-1.24161
H	0.929642	-3.47003	-0.6084	H	-2.22912	-2.59721	0.517513
H	2.317761	-2.78555	0.26177	C	7.820715	-0.82525	0.126391
H	2.170883	-2.54518	-1.48026	H	8.856748	-0.48478	0.181541
H	2.128367	2.423664	-0.79324	H	7.594424	-1.44778	1.002271
H	2.275996	2.176872	0.927418	H	7.679684	-1.41716	-0.78774
C	-7.81992	0.633401	-0.25407	O	7.020515	0.355816	0.108482
H	-8.84613	0.296375	-0.10115	H	-0.82757	-3.31227	-0.30215

**Compound 18**

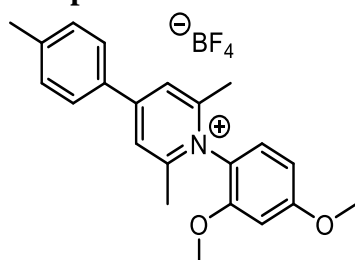


***N*-(*p*-trifluoromethyl)-4-(*p*-methoxyphenyl)-2,6-dimethylpyridinium tetrafluoroborate**

Pyr+				Pyr*			
Atom	X	Y	Z	Atom	X	Y	Z
C	0.083038	1.127985	0.194764	C	0.081125	1.122311	0.214712
C	1.463595	1.101373	0.201884	C	1.463499	1.094702	0.226408
C	2.195777	-0.094	0.025916	C	2.184596	-0.09738	0.025178
C	1.428236	-1.2656	-0.15872	C	1.42691	-1.26435	-0.18823
C	0.047442	-1.24829	-0.16904	C	0.044294	-1.24504	-0.20048
C	-2.07009	-0.02595	0.000219	C	-2.0654	-0.02485	-0.00891
C	-2.7634	-0.21102	1.196759	C	-2.75768	-0.24513	1.182242
C	-4.15844	-0.18891	1.186006	C	-4.15104	-0.22043	1.170598
C	-4.84195	0.015256	-0.01639	C	-4.83169	0.022466	-0.02789
C	-4.13825	0.199137	-1.21047	C	-4.12856	0.242726	-1.21554
C	-2.74326	0.17819	-1.20477	C	-2.73346	0.217719	-1.20788
H	1.977981	2.036185	0.383746	H	1.979108	2.025151	0.425385
H	1.914982	-2.21656	-0.33244	H	1.913924	-2.212	-0.3776
H	-2.22421	-0.37194	2.125243	H	-2.21789	-0.43404	2.103844
H	-4.70955	-0.33616	2.108159	H	-4.69836	-0.39329	2.090461
H	-4.67378	0.351496	-2.14097	H	-4.65725	0.428316	-2.14301
H	-2.18848	0.316816	-2.12765	H	-2.17554	0.383824	-2.1231
C	3.656316	-0.11925	0.035563	C	3.654211	-0.1232	0.037946
C	4.410281	1.028874	-0.28392	C	4.404893	1.01319	-0.3154
C	5.799822	1.014499	-0.2886	C	5.798028	0.999212	-0.31445
C	6.484434	-0.16803	0.048356	C	6.479078	-0.17025	0.05991
C	5.748985	-1.32538	0.378872	C	5.745731	-1.31543	0.42255
C	4.368286	-1.29973	0.363253	C	4.360747	-1.29113	0.403993
H	6.339546	1.912563	-0.56178	H	6.336003	1.890887	-0.6106
H	6.292166	-2.22376	0.650952	H	6.282365	-2.20953	0.722053
H	3.834407	-2.19963	0.650149	H	3.823285	-2.18212	0.710807
N	-0.61155	-0.04946	0.008567	N	-0.60781	-0.05003	0.001352
C	-6.35432	0.087385	-0.01818	C	-6.33706	0.087394	-0.01482
F	-6.87244	-0.33422	-1.19198	F	-6.87779	-0.07837	-1.24518
F	-6.77666	1.360922	0.174132	F	-6.78682	1.2879	0.44851
F	-6.89141	-0.66653	0.965089	F	-6.88349	-0.85909	0.790592
C	-0.75614	-2.49916	-0.38254	C	-0.75998	-2.48849	-0.43935
C	-0.68319	2.403593	0.399378	C	-0.68445	2.392446	0.440096

H	0.014692	3.229498	0.540346	H	0.015729	3.209395	0.614438
H	-1.33316	2.347727	1.277751	H	-1.34812	2.311707	1.305697
H	-1.31961	2.633408	-0.46049	H	-1.30199	2.64406	-0.42719
H	-1.39379	-2.42303	-1.2684	H	-1.40098	-2.38731	-1.31981
H	-1.40932	-2.70833	0.470006	H	-1.40506	-2.71565	0.414481
H	-0.08309	-3.34673	-0.5153	H	-0.08515	-3.33003	-0.59606
H	3.910672	1.94678	-0.57618	H	3.903601	1.922021	-0.63124
O	7.821269	-0.29614	0.084332	O	7.828487	-0.29281	0.102779
C	8.653879	0.829029	-0.22795	C	8.641107	0.837603	-0.24357
H	9.676443	0.470105	-0.12133	H	9.67131	0.50237	-0.12988
H	8.486382	1.163909	-1.257	H	8.465196	1.14266	-1.2801
H	8.476621	1.651338	0.473092	H	8.450007	1.677725	0.431763

**Compound 19**



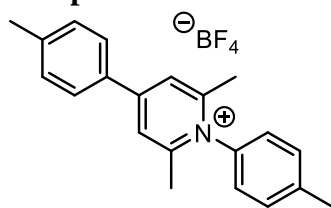
***N*-(2,4-xylyl)-4-(*p*-tolyl)-2,6-dimethylpyridinium tetrafluoroborate**

Pyr+				Pyr*			
Atom	X	Y	Z	Atom	X	Y	Z
C	-1.42701	0.414113	-1.13678	C	-1.41774	0.740642	-0.97177
C	-0.04282	0.389307	-1.1527	C	-0.05094	0.715665	-1.01328
C	-0.0433	-0.79539	0.933386	C	-0.05068	-1.07154	0.631002
C	-1.42759	-0.76868	0.946003	C	-1.41766	-1.03533	0.656436
C	-2.16231	-0.16477	-0.0885	C	-2.19832	-0.13384	-0.14287
H	-1.93209	0.875104	-1.97587	H	-1.9027	1.461622	-1.6187
H	-1.93183	-1.20581	1.798238	H	-1.90189	-1.72851	1.333601
C	2.080197	-0.24597	-0.13397	C	2.096079	-0.20095	-0.21627
C	2.787956	0.823678	0.455089	C	2.803183	0.63617	0.679869
C	2.761325	-1.30509	-0.71876	C	2.812655	-1.01505	-1.08661
C	4.181275	0.801903	0.441169	C	4.198278	0.633865	0.677599
C	4.157586	-1.33606	-0.73719	C	4.211929	-1.03054	-1.10227
H	2.197584	-2.11751	-1.1665	H	2.262147	-1.65393	-1.77068
C	4.863319	-0.27485	-0.15317	C	4.899807	-0.19815	-0.21208
H	4.764571	1.60074	0.880627	H	4.769472	1.261647	1.349682
H	4.66541	-2.17223	-1.19859	H	4.733024	-1.67837	-1.79498
C	-3.63748	-0.13749	-0.0742	C	-3.64919	-0.10635	-0.11303
C	-4.37484	-1.16936	0.53751	C	-4.4125	-1.04354	0.640453
C	-4.3473	0.922652	-0.66887	C	-4.40653	0.862262	-0.83219
C	-5.76723	-1.14186	0.544537	C	-5.80402	-1.01017	0.666062
H	-3.86255	-2.01409	0.986794	H	-3.91331	-1.81704	1.214177
C	-5.74006	0.948535	-0.64648	C	-5.798	0.884021	-0.79788
H	-3.81272	1.751323	-1.12206	H	-3.90193	1.622161	-1.4192
C	-6.47806	-0.08435	-0.04648	C	-6.53897	-0.0504	-0.05244
H	-6.31155	-1.95691	1.013727	H	-6.33454	-1.75183	1.26028
H	-6.26205	1.78851	-1.09649	H	-6.32362	1.651906	-1.36241
C	0.743976	1.002893	-2.27178	C	0.742722	1.637109	-1.89597
H	1.416884	1.781068	-1.89986	H	1.427903	2.26659	-1.31669
H	1.354641	0.255292	-2.78604	H	1.350378	1.085555	-2.62236
H	0.06006	1.450772	-2.99304	H	0.06212	2.290531	-2.44545
C	0.743661	-1.42201	2.045152	C	0.743618	-2.01844	1.485796
H	1.348531	-2.25765	1.681649	H	1.354538	-2.70003	0.883079

H	1.422437	-0.69838	2.50589	H	1.42595	-1.48592	2.158265
H	0.060175	-1.79373	2.808845	H	0.063234	-2.61722	2.094591
C	-7.98665	-0.07276	-0.05689	C	-8.04949	-0.0428	-0.04932
H	-8.37749	0.946274	-0.12528	H	-8.44468	0.969828	-0.18257
H	-8.37113	-0.63108	-0.91971	H	-8.45867	-0.65808	-0.86241
H	-8.39504	-0.54241	0.842784	H	-8.44958	-0.44181	0.888708
N	0.627174	-0.22325	-0.12098	N	0.660053	-0.20575	-0.22145
O	2.031859	1.809428	0.999918	O	2.044056	1.406395	1.505011
O	6.21884	-0.19021	-0.10821	O	6.259183	-0.11827	-0.12632
C	2.690855	2.927729	1.613884	C	2.702223	2.274525	2.434864
H	3.308731	2.600401	2.455786	H	3.320171	1.703321	3.135699
H	3.302891	3.46636	0.88387	H	3.318435	3.014402	1.913133
H	1.891175	3.574144	1.972944	H	1.904572	2.780286	2.978316
C	6.997078	-1.245	-0.68914	C	7.049084	-0.93453	-0.99757
H	8.037073	-0.95917	-0.53543	H	8.086593	-0.70679	-0.7539
H	6.799847	-2.19871	-0.18889	H	6.856167	-1.99849	-0.82283
H	6.795149	-1.33632	-1.76133	H	6.856779	-0.69043	-2.0479



**Compound 20**

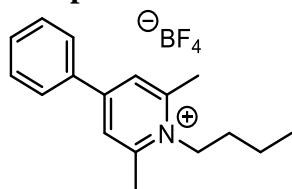


***N*-(*p*-tolyl)-4-(*p*-tolyl)-2,6-dimethylpyridinium tetrafluoroborate**

Pyr+				Pyr*			
Atom	X	Y	Z	Atom	X	Y	Z
C	0.560128	-1.18214	-0.20404	C	0.556272	-1.21376	-0.03974
C	-0.82453	-1.18095	-0.2051	C	-0.81147	-1.20413	-0.03898
C	-1.56158	-0.00149	-0.00463	C	-1.59325	-0.00068	-0.00312
C	-0.8276	1.179881	0.195951	C	-0.81319	1.203755	0.035511
C	0.557056	1.184342	0.19707	C	0.554532	1.215263	0.03984
C	2.68902	0.002829	0.000032	C	2.70905	0.002001	0.001272
C	3.371881	-0.21266	1.196441	C	3.412217	-0.06718	1.207667
C	4.767608	-0.20702	1.190848	C	4.808908	-0.06315	1.203466
C	5.490364	0.008244	0.006715	C	5.531793	0.007636	0.002373
C	4.772384	0.225814	-1.18003	C	4.809485	0.080926	-1.19914
C	3.376732	0.223762	-1.19269	C	3.412975	0.076235	-1.2046
H	-1.32758	-2.12097	-0.39192	H	-1.2956	-2.17234	-0.07931
H	-1.33319	2.118781	0.381616	H	-1.29875	2.171255	0.075608
H	2.822978	-0.37859	2.118067	H	2.865926	-0.11935	2.144818
H	5.299798	-0.37076	2.123421	H	5.343167	-0.11332	2.148642
H	5.30848	0.401512	-2.10822	H	5.344231	0.143385	-2.14335
H	2.831541	0.394284	-2.11568	H	2.867125	0.133701	-2.1417
N	1.228817	0.001823	-0.00267	N	1.266889	0.001218	0.000767
C	1.339561	2.44401	0.421823	C	1.345209	2.492719	0.091784
H	1.974077	2.675464	-0.4386	H	1.989329	2.612306	-0.78672
H	1.990646	2.357745	1.296281	H	1.995914	2.535468	0.972576
C	1.345961	-2.43992	-0.42775	C	1.348879	-2.49014	-0.08841
H	1.978696	-2.67066	0.434176	H	1.990881	-2.60786	0.791902
H	1.999188	-2.35151	-1.30039	H	2.001952	-2.5328	-0.96746
H	0.659428	-3.27141	-0.58797	H	0.665318	-3.34042	-0.12858
H	0.650812	3.274127	0.579587	H	0.660328	3.341971	0.130999
C	6.999871	-0.01876	0.004693	C	7.042452	-0.01879	0.000719
H	7.405114	0.29744	0.96991	H	7.44946	0.4019	0.924815
H	7.408559	0.632075	-0.77333	H	7.449976	0.54487	-0.8437
H	7.367499	-1.03381	-0.18963	H	7.414615	-1.04751	-0.08281
C	-3.03702	-0.00314	-0.00393	C	-3.04478	-0.00152	-0.00456
C	-3.76246	1.125589	-0.43209	C	-3.80589	1.200953	-0.06645
C	-3.7593	-1.13345	0.42189	C	-3.80502	-1.20456	0.051135
C	-5.15476	1.117253	-0.43724	C	-5.19781	1.193255	-0.06823

H	-3.23982	2.00424	-0.79632	H	-3.30431	2.16082	-0.12737
C	-5.15273	-1.12888	0.425293	C	-5.19726	-1.1978	0.048183
H	-3.2351	-2.01354	0.78031	H	-3.30305	-2.16479	0.10207
C	-5.87825	-0.00618	-0.00328	C	-5.93578	-0.00255	-0.00806
H	-5.68913	1.995032	-0.79038	H	-5.72638	2.143115	-0.12306
H	-5.68509	-2.01105	0.769996	H	-5.72538	-2.14845	0.0918
C	-7.38662	0.005376	0.021802	C	-7.44592	-0.00052	0.025713
H	-7.79388	-1.0093	0.018421	H	-7.85637	-0.92366	-0.39661
H	-7.7946	0.546574	-0.83725	H	-7.85777	0.842761	-0.53888
H	-7.75442	0.506562	0.925874	H	-7.8273	0.082638	1.052709

**Compound 21**

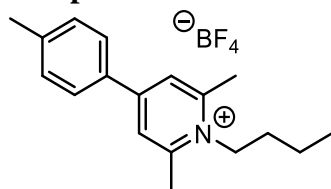


***N*-(*n*-butyl)-4-phenyl-2,6-dimethylpyridinium tetrafluoroborate**

Pyr+				Pyr*			
Atom	X	Y	Z	Atom	X	Y	Z
C	2.828477	0.023436	0.092796	C	2.7797	-0.000001	0.094621
C	3.420117	1.160169	0.675412	C	3.518224	1.20859	0.261225
C	4.794278	1.201174	0.911931	C	4.877198	1.20436	0.563515
C	5.600866	0.113574	0.561542	C	5.579419	-0.000004	0.71909
C	5.024438	-1.01911	-0.02237	C	4.877199	-1.204368	0.563498
C	3.649174	-1.06741	-0.25077	C	3.518225	-1.208594	0.261207
C	1.371298	-0.02347	-0.1543	C	1.363758	0.000001	-0.222538
C	0.644318	1.128964	-0.48589	C	0.601407	1.201024	-0.401997
C	-0.72256	1.087751	-0.71434	C	-0.740718	1.208119	-0.673406
C	-0.71757	-1.26685	-0.3031	C	-0.740721	-1.208112	-0.673408
C	0.649085	-1.2227	-0.07347	C	0.601404	-1.20102	-0.402
H	2.804004	2.002996	0.972048	H	3.023288	2.167609	0.154366
H	5.233439	2.079866	1.374021	H	5.395363	2.153102	0.680353
H	6.670874	0.148409	0.742269	H	6.639136	-0.000006	0.955472
H	5.645503	-1.86336	-0.30525	H	5.395366	-2.15311	0.680322
H	3.219307	-1.94432	-0.72414	H	3.023291	-2.167612	0.154333
H	1.144864	2.082199	-0.59791	H	1.081256	2.170035	-0.340183
H	1.144241	-2.14719	0.194944	H	1.08125	-2.170033	-0.340186
N	-1.38734	-0.10934	-0.61354	N	-1.446226	0.000005	-0.800807
C	-2.86699	-0.14704	-0.80621	C	-2.918591	0.000006	-0.815511
C	-3.63977	0.081517	0.500125	C	-3.549955	-0.000003	0.586952
H	-3.11756	-1.11162	-1.24333	H	-3.257449	-0.87173	-1.377013
H	-3.12265	0.608406	-1.54666	H	-3.25745	0.871748	-1.377003
C	-5.15647	0.024923	0.268109	C	-5.08324	-0.000001	0.531806
H	-3.35081	-0.67454	1.239255	H	-3.20029	-0.878986	1.143628
H	-3.36711	1.053695	0.926799	H	-3.200288	0.878971	1.143641
C	-5.95472	0.252302	1.556728	C	-5.730682	-0.00001	1.921489
H	-5.43841	0.780399	-0.47676	H	-5.425752	0.879026	-0.030925
H	-5.42166	-0.95011	-0.16088	H	-5.425754	-0.87902	-0.030937
H	-7.03134	0.205991	1.363511	H	-6.823609	-0.000008	1.849421
H	-5.7161	-0.50821	2.309043	H	-5.433232	-0.885292	2.495756
H	-5.73391	1.234217	1.990752	H	-5.43323	0.885264	2.495768
C	-1.45786	-2.57219	-0.23073	C	-1.481304	-2.499765	-0.898265
H	-1.83668	-2.86585	-1.21564	H	-1.900177	-2.55833	-1.91054

H	-2.30392	-2.53556	0.459479	H	-2.308462	-2.643854	-0.194454
C	-1.46526	2.333894	-1.10574	C	-1.481296	2.499775	-0.898264
H	-2.31995	2.532351	-0.45493	H	-2.308471	2.643855	-0.194469
H	-1.83149	2.267998	-2.13613	H	-1.900146	2.558354	-1.910547
H	-0.77544	-3.35048	0.110612	H	-0.790608	-3.335882	-0.774636
H	-0.78894	3.186531	-1.04477	H	-0.790603	3.335891	-0.774608

**Compound 22**

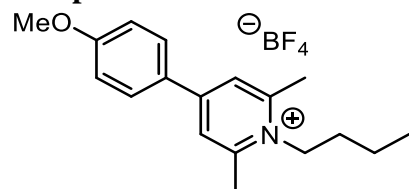


***N*-(*n*-butyl)-4-(*p*-tolyl)-2,6-dimethylpyridinium tetrafluoroborate**

Pyr+				Pyr*			
Atom	X	Y	Z	Atom	X	Y	Z
C	-2.40342	0.001393	-0.01669	C	-2.3532	0	-0.04183
C	-3.02438	-1.14332	0.51733	C	-3.0993	-1.20405	0.107131
C	-4.40132	-1.17401	0.727901	C	-4.46608	-1.19686	0.3717
C	-5.21258	-0.07526	0.402277	C	-5.19173	-1E-06	0.50808
C	-4.59044	1.064899	-0.13199	C	-4.46608	1.196855	0.371698
C	-3.21305	1.108202	-0.33489	C	-3.0993	1.204048	0.107129
C	-0.94379	0.040774	-0.23211	C	-0.92836	0.000001	-0.3201
C	-0.21361	-1.11626	-0.54506	C	-0.16165	-1.20115	-0.47971
C	1.158022	-1.08375	-0.74001	C	1.18731	-1.20876	-0.71408
C	1.156963	1.271609	-0.33523	C	1.18731	1.208758	-0.71408
C	-0.2145	1.236107	-0.13855	C	-0.16165	1.201151	-0.47971
H	-2.42851	-2.00438	0.803038	H	-2.60512	-2.1658	0.020799
H	-4.85229	-2.06367	1.158923	H	-4.98346	-2.14847	0.478432
H	-5.19295	1.929654	-0.39648	H	-4.98346	2.148473	0.478427
H	-0.71616	-2.06695	-0.66861	H	-0.64424	-2.16988	-0.43329
H	-0.70881	2.164899	0.115815	H	-0.64424	2.169884	-0.43329
N	1.828365	0.109396	-0.62522	N	1.897356	0.000001	-0.82229
C	3.312655	0.136782	-0.77557	C	3.368607	0.000001	-0.77165
C	4.045708	-0.09432	0.553068	C	3.937397	-1E-06	0.657395
H	3.582772	1.098705	-1.2069	H	3.732369	0.871755	-1.31752
H	3.584644	-0.62181	-1.50698	H	3.732369	-0.87175	-1.31752
C	5.568853	-0.04639	0.365982	C	5.47162	-1E-06	0.67125
H	3.738777	0.664103	1.282613	H	3.563025	0.879011	1.19787
H	3.755202	-1.06444	0.972677	H	3.563026	-0.87902	1.197867
C	6.327905	-0.27837	1.677252	C	6.056273	-3E-06	2.088489
H	5.868272	-0.80344	-0.37047	H	5.839127	-0.87901	0.124413
H	5.852074	0.927095	-0.05497	H	5.839127	0.879006	0.124416
H	7.40996	-0.23812	1.515507	H	7.151354	-3E-06	2.065511
H	6.0718	0.483399	2.422522	H	5.733383	0.885261	2.648885
H	6.089045	-1.25908	2.104398	H	5.733383	-0.88527	2.648882
C	1.903214	2.572888	-0.24823	C	1.933822	2.499794	-0.92212
H	2.309533	2.860647	-1.2239	H	2.384326	2.553443	-1.92115
H	2.730753	2.533674	0.46403	H	2.738794	2.648469	-0.19375
C	1.902933	-2.33507	-1.11085	C	1.933822	-2.49979	-0.92213

H	2.738883	-2.5385	-0.43757	H	2.73879	-2.64847	-0.19376
H	2.297151	-2.27242	-2.13107	H	2.384332	-2.55344	-1.92115
H	1.217053	3.35666	0.072546	H	1.239221	3.336187	-0.82435
H	1.219957	-3.18346	-1.06731	H	1.239219	-3.33619	-0.82436
H	-2.77256	2.000077	-0.76903	H	-2.60513	2.1658	0.020793
C	-6.70794	-0.12617	0.596168	C	-6.68118	-1E-06	0.759726
H	-7.20453	-0.47387	-0.31845	H	-7.25019	-3E-06	-0.18015
H	-7.11353	0.862135	0.831446	H	-6.99162	0.886053	1.323482
H	-6.98254	-0.81514	1.399852	H	-6.99162	-0.88606	1.323484

**Compound 23**



***N*-(*n*-butyl)-4-(*p*-methoxyphenyl)-2,6-dimethylpyridinium tetrafluoroborate**

Pyr+				Pyr*			
Atom	X	Y	Z	Atom	X	Y	Z
C	0.560128	-1.18214	-0.20404	C	-1.96198	0	0.012521
C	-0.82453	-1.18095	-0.2051	C	-2.70295	-1.20744	0.17092
C	-1.56158	-0.00149	-0.00463	C	-4.06604	-1.20736	0.453011
C	-0.8276	1.179881	0.195951	C	-4.76111	0.000002	0.595082
C	0.557056	1.184342	0.19707	C	-4.06603	1.207357	0.453015
C	2.68902	0.002829	0.000032	C	-2.70295	1.207443	0.170924
C	3.371881	-0.21266	1.196441	C	-0.54114	-1E-06	-0.28422
C	4.767608	-0.20702	1.190848	C	0.223554	-1.20117	-0.45272
C	5.490364	0.008244	0.006715	C	1.56978	-1.20846	-0.70255
C	4.772384	0.225814	-1.18003	C	1.56978	1.208457	-0.70255
C	3.376732	0.223762	-1.19269	C	0.223554	1.201166	-0.45273
H	-1.32758	-2.12097	-0.39192	H	-2.20757	-2.16746	0.0782
H	-1.33319	2.118781	0.381616	H	-4.59851	-2.14695	0.573921
H	2.822978	-0.37859	2.118067	H	-4.59851	2.146955	0.573928
H	5.299798	-0.37076	2.123421	H	-0.25764	-2.17021	-0.40068
H	5.30848	0.401512	-2.10822	H	-0.25764	2.170203	-0.40069
H	2.831541	0.394284	-2.11568	N	2.278067	-2E-06	-0.81815
N	1.228817	0.001823	-0.00267	C	3.750143	-2E-06	-0.7934
C	1.339561	2.44401	0.421823	C	4.343722	0.000002	0.625489
H	1.974077	2.675464	-0.4386	H	4.104102	0.87174	-1.34559
H	1.990646	2.357745	1.296281	H	4.104101	-0.87175	-1.34559
C	1.345961	-2.43992	-0.42775	C	5.877945	0.000001	0.612069
H	1.978696	-2.67066	0.434176	H	3.979	0.879006	1.172482
H	1.999188	-2.35151	-1.30039	H	3.979	-0.879	1.172488
H	0.659428	-3.27141	-0.58797	C	6.487565	0.000005	2.018753
H	0.650812	3.274127	0.579587	H	6.235658	-0.87901	0.058821
C	6.999871	-0.01876	0.004693	H	6.235659	0.879012	0.058816
H	7.405114	0.29744	0.96991	H	7.582054	0.000005	1.976335
H	7.408559	0.632075	-0.77333	H	6.174664	0.885279	2.584769
H	7.367499	-1.03381	-0.18963	H	6.174664	-0.88527	2.584774
C	-3.03702	-0.00314	-0.00393	C	2.313733	2.49967	-0.91838
C	-3.76246	1.125589	-0.43209	H	2.751312	2.554578	-1.923
C	-3.7593	-1.13345	0.42189	H	3.127865	2.646953	-0.20008
C	-5.15476	1.117253	-0.43724	C	2.313732	-2.49968	-0.91837

H	-3.23982	2.00424	-0.79632	H	3.12787	-2.64695	-0.20007
C	-5.15273	-1.12888	0.425293	H	2.751305	-2.55459	-1.92299
H	-3.2351	-2.01354	0.78031	H	1.620601	3.336006	-0.81056
C	-5.87825	-0.00618	-0.00328	H	1.620603	-3.33601	-0.81054
H	-5.68913	1.995032	-0.79038	H	-2.20757	2.167461	0.078208
H	-5.68509	-2.01105	0.769996	O	-6.10986	0.000002	0.929673
C	-7.38662	0.005376	0.021802	C	-7.00215	0.000001	-0.19509
H	-7.79388	-1.0093	0.018421	H	-8.01616	0.000001	0.209637
H	-7.7946	0.546574	-0.83725	H	-6.85374	-0.89475	-0.8118
H	-7.75442	0.506562	0.925874	H	-6.85374	0.89475	-0.81181



## APPENDIX B: CHAPTER 3 SUPPLEMENTAL INFORMATION

### B.1. Reversibility Determination: Peak Height Ratio & Peak-to-Peak Separation

Cyclic voltammograms (CVs) of all pyridinium derivatives were measured in acetonitrile with ferrocene as an internal redox standard, and all redox couples were found to be completely reversible. CVs were collected at a scan rate of 200 mV s<sup>-1</sup>. The anodic peak current ( $i_{pa}$ ) was divided by the cathodic peak current ( $i_{pc}$ ) to yield the peak height ratio. The difference in corresponding potential for anodic peak current ( $i_{pa}$ ) and cathodic peak current ( $i_{pc}$ ) gave the peak-to-peak separation value (V).

### B.2. Correlation Between Redox Potential and Hammett Parameters

Hammett substituent constants were taken directly from literature sources,<sup>146</sup> when available, or were calculated using open-source substituent property prediction software.<sup>226</sup> The sum of sigma-para substituent constants for the 4-aryl and N-substituents of the 2,6-dimethylpyridinium ring correlate strongly ( $R^2 = 0.9$ ) to the experimental reversible redox potential of the corresponding pyridinium ROM.

**Table B.1. Summary of the sum of Hammett  $\sigma_p$  substituent constants and pyridinium redox potential. Redox potentials were measured in acetonitrile vs Fc/Fc<sup>+</sup>.**

Entry	$E_{1/2}$ (V vs Fc/Fc <sup>+</sup> )	Hammett $\sigma_p$ parameter		
		4-aryl substituent	N-substituent	sum
1	-1.54	-0.010	0.100	0.090
2	-1.57	-0.030	0.100	0.070
3	-1.60	-0.010	-0.010	-0.020
4	-1.60	-0.010	-0.016	-0.026
5	-1.61	-0.010	-0.038	-0.048
6	-1.62	-0.080	0.100	0.020
7	-1.62	-0.010	-0.030	-0.040
8	-1.63	-0.030	-0.016	-0.046
9	-1.63	-0.030	-0.048	-0.078
10	-1.64	-0.030	-0.010	-0.040
11	-1.65	-0.030	-0.038	-0.068
12	-1.66	-0.048	0.100	0.052
13	-1.66	-0.030	-0.030	-0.060
14	-1.67	-0.080	-0.010	-0.090
15	-1.67	-0.030	-0.046	-0.076
16	-1.68	-0.080	-0.016	-0.096
17	-1.69	-0.080	-0.038	-0.118
18	-1.70	-0.010	-0.160	-0.170
19	-1.72	-0.048	-0.010	-0.058
20	-1.71	-0.048	-0.016	-0.064
21	-1.73	-0.030	-0.170	-0.200
22	-1.74	-0.030	-0.160	-0.190
23	-1.77	-0.080	-0.160	-0.240

### B.3. Diffusion Coefficient Calculation from Pyridinium Crystal Structures

Diffusion coefficients were estimated for the oxidized form of pyridinium ROMs from the Stokes-Einstein equation,

$$D_0 = \frac{k_B T}{\alpha \pi \mu d}$$

where  $D_0$  is pyridinium diffusion coefficient,  $k_B$  is the Boltzmann constant,  $T$  is absolute temperature,  $\alpha$  is a coefficient that arises from the boundary conditions of the solute-solvent interface (here,  $\alpha = 6$  for no-slip conditions is used as a preliminary assumption),  $\mu$  is the dynamic viscosity, and  $d$  is the molecular diameter as estimated from the x-ray crystal structures for all 23 pyridiniums.<sup>76,147</sup> The diameter of pyridinium species was calculated as the average of the maximum diameter along the N-to-C4 axis of the pyridinium ring and the maximum diameter perpendicular to this axis. This was done to account for the non-spherical shape of pyridinium ROMs.

**Table B.2. Diffusion coefficients of oxidized pyridinium species either calculated using the Stokes-Einstein (S.E.) equation with molecular diameters from the corresponding crystal structures or measured from CV experiments described below.**

Entry	$D_0 / \text{cm}^2 \text{s}^{-1}$		molecular radius / Å	
	from CV	from S.E.	from CV	from crystal structure
1	7.62E-06	7.52E-06	4.8	4.9
2	5.68E-06	6.69E-06	6.5	5.5
3	1.87E-05	7.98E-06	2.0	4.6
4	8.36E-06	7.48E-06	4.4	4.9
5	8.02E-06	7.12E-06	4.6	5.2
6	7.20E-06	6.74E-06	5.1	5.4
7	7.10E-06	7.58E-06	5.2	4.8
8	7.38E-06	7.12E-06	5.0	5.2
9	6.38E-06	6.76E-06	5.7	5.4
10	1.35E-05	7.57E-06	2.7	4.8
11	6.88E-06	6.76E-06	5.3	5.4
12	7.25E-06	7.15E-06	5.1	5.1
13	6.47E-06	7.23E-06	5.7	5.1
14	4.78E-06	6.72E-06	7.7	5.5
15	5.33E-06	6.19E-06	6.9	5.9
16	6.95E-06	6.72E-06	5.3	5.5
17	7.21E-06	6.46E-06	5.1	5.7
18	8.65E-06	7.94E-06	4.2	4.6
19	5.66E-06	7.12E-06	6.5	5.2
20	7.59E-06	7.12E-06	4.8	5.2
21	8.84E-06	7.88E-06	4.1	4.7
22	6.84E-06	6.98E-06	5.4	5.3
23	5.73E-06	6.45E-06	6.4	5.7

#### B.4. Electrochemical Diffusion Coefficient Determination, from CV

Cyclic voltammograms (CVs) of all pyridinium derivatives were measured in acetonitrile with ferrocene as an internal redox standard, and all redox couples were found to be completely reversible. CVs were collected at scan rates of 20, 50, 100, 200, 400, 800, 1200, and 1600 mV s<sup>-1</sup>. The peak currents (anodic and cathodic,  $i_{pa}$  and  $i_{pc}$  respectively) were related to square root of the corresponding scan rate (mV s<sup>-1</sup>) using the Randles-Sevcik equation:

$$i_p = 0.4463 A C^0 \left( \frac{n^3 F^3 v D_0}{RT} \right)^{1/2}$$

where  $i_p$  is the peak current,  $A$  is the surface area of the electrode (0.071 cm<sup>2</sup>),  $C^0$  is the bulk concentration of pyridinium (1x10<sup>-6</sup> mol cm<sup>-3</sup>),  $n$  is the number of electrons transferred (1 electron),  $F$  is Faraday's constant (96485 C mol<sup>-1</sup>),  $R$  is the ideal gas constant (8.314 J mol<sup>-1</sup> K<sup>-1</sup>), and  $T$  is the absolute temperature (295 K). Experiments were performed using 3 mm GCE working electrode and Ag/Ag<sup>+</sup> reference electrode with 100 mM tetrabutylammonium hexafluorophosphate in acetonitrile as the supporting electrolyte at 22 °C and 200 mV s<sup>-1</sup> under a N<sub>2</sub> atmosphere. Using a rearrangement, based on the linear relationship of peak height vs. square root of the scan rate ( $i_{pa}$  and  $i_{pc}$  (A) vs.  $u^{1/2}$  (V s<sup>-1</sup>)<sup>1/2</sup>), the diffusion coefficient ( $D_i$ , cm<sup>2</sup> s<sup>-1</sup>) can be determined using the theoretical value of the slope for either the oxidized or reduced pyridinium species.<sup>33</sup>  $D_a$  is the diffusion coefficient based on the anodic (i.e., the reduced pyridinium) component of the CV scan, and  $D_c$  is the diffusion coefficient based on the cathodic (i.e., oxidized pyridinium) component of the CV scan.

$$D_0 = \left( \frac{\text{slope}}{0.4463 n F A C^0} \right)^2 \frac{RT}{nF}$$

Note for following figures:

- anodic/oxidation data is shown in blue squares
- cathodic/reduction data is shown in orange circles
- CVs displayed at 20, 50, 100, 200, 400, and 800 mV s<sup>-1</sup>

### B.5. Shelf Stability Data for Compounds

Cyclic voltammograms were used to assess decomposition in reduced pyridinium solutions in propylene carbonate. Solutions of 10 mM pyridinium and 500 mM tetraethylammonium tetrafluoroborate in propylene carbonate were prepared in a 25 mL volumetric flask. Prior to charging, pyridinium solutions were dried for 12 hours over 3 Å molecular sieves and purged with N<sub>2</sub> for 30-40 minutes. All subsequent electrochemical charging and measurements were conducted in a glovebox under a N<sub>2</sub> atmosphere.

In a symmetrical H-Cell, solutions were charged (reduced) first at a constant current of 5 mA to a -1.65 V potential cutoff, then further charged (reduced) at a constant current of 2.5 mA to a -1.65 V potential cutoff. Each half of the H-Cell contained 10 mL of pyridinium solution. The working and counter electrodes were composed of carbon felt Sigracet 6EA attached to steel wire using wire glue. Solution charging was conducted with a 3-electrode arrangement using a Ag/Ag<sup>+</sup> reference electrode. After charging, the reduced pyridinium solution was promptly removed from the H-Cell and isolated in a vial.

The isolated charged solutions were evaluated daily by CV and visual inspection of color. Daily CVs were performed using 3 mm GCE working electrode, platinum plated titanium rod counter electrode, and a Ag/Ag<sup>+</sup> reference electrode at 25 °C under a N<sub>2</sub> atmosphere. CVs were collected at 100 mV/s between 0 to -1.65 V every day to assess change in concentration or loss of material. Additionally, CVs were measured at 100 mV/s between 1.1 to -1.65 V at the first and last day of the shelf stability study to assess changes in concentration, loss of material, and formation of decomposition products.

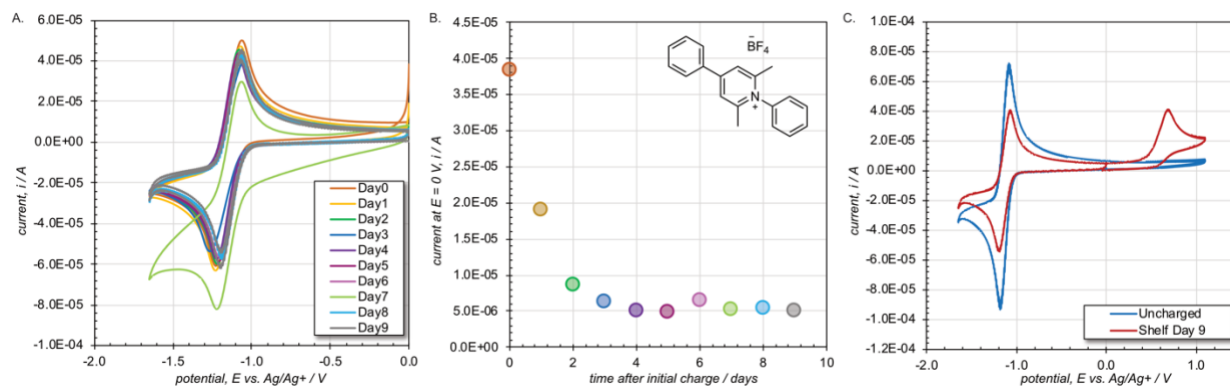


**Figure B.1. Charged solution shelf stability study for N-phenyl-4-phenyl-2,6-dimethylpyridinium tetrafluoroborate.** (A) Daily CVs of a charged pyridinium solution over nine days. (B) Plot of daily current response upon initiating CV measurements at  $E = 0$  V. (C) Comparative CVs of pyridinium solutions prior to charging (blue) and after nine days in the charged state (red).

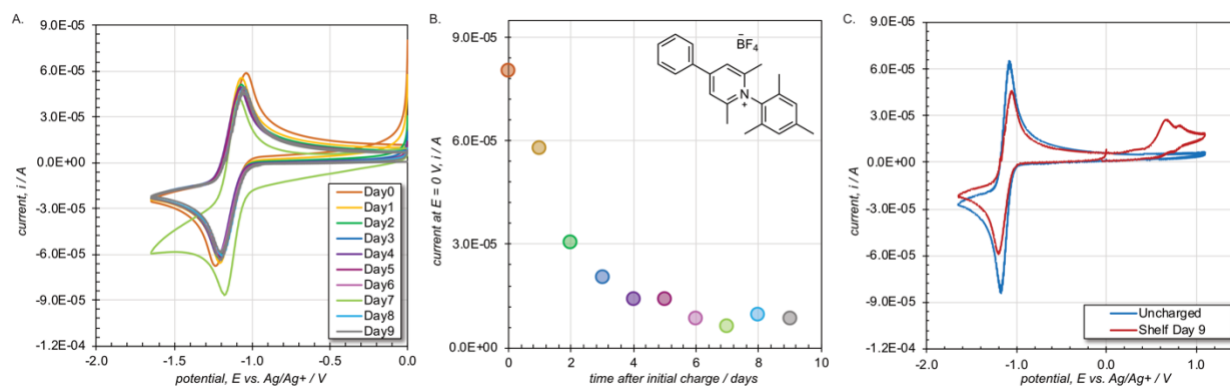


**Figure B.2. Charged solution shelf stability study for N-(mesityl)-4-phenyl-2,6-dimethylpyridinium tetrafluoroborate.** (A) Daily CVs of a charged pyridinium solution over nine days. (B) Plot of daily current response upon initiating CV measurements at  $E = 0$  V. (C) Comparative CVs of pyridinium solutions prior to charging (blue) and after nine days in the charged state (red).

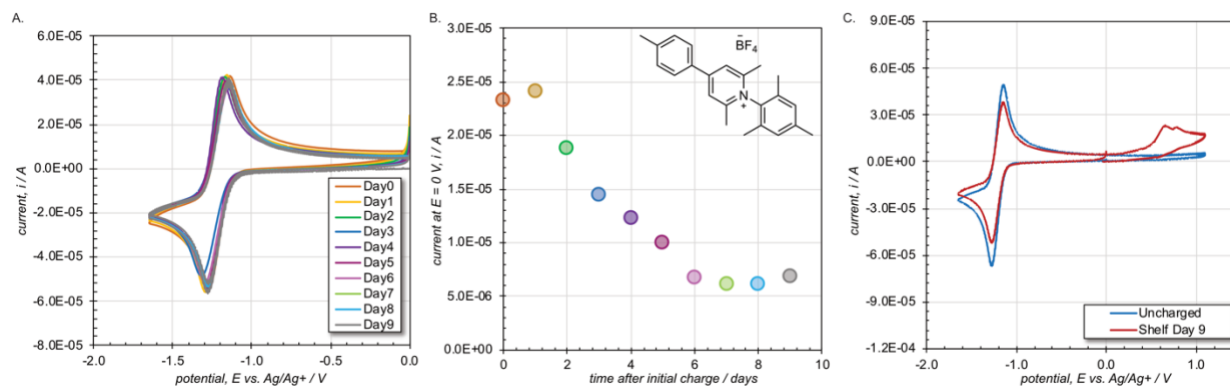


**Figure B.3. Charged solution shelf stability study for N-(mesityl)-4-(p-tolyl)-2,6-dimethylpyridinium tetrafluoroborate.** (A) Daily CVs of a charged pyridinium solution over nine days. (B) Plot of daily current response upon initiating CV measurements at  $E = 0$  V. (C) Comparative CVs of pyridinium solutions prior to charging (blue) and after nine days in the charged state (red).

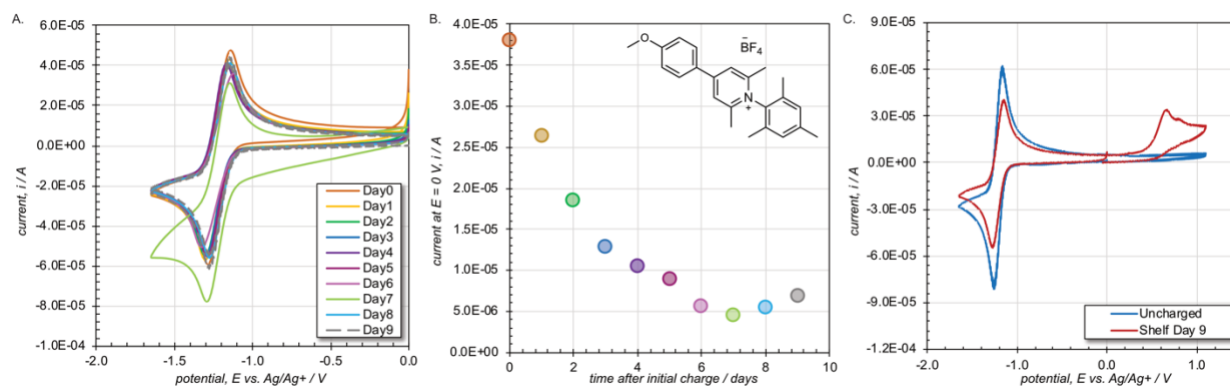


**Figure B.4. Charged solution shelf stability study for N-(mesityl)-4-(p-methoxyphenyl)-2,6-dimethylpyridinium tetrafluoroborate.** (A) Daily CVs of a charged pyridinium solution over nine days. (B) Plot of daily current response upon initiating CV measurements at  $E = 0$  V. (C) Comparative CVs of pyridinium solutions prior to charging (blue) and after nine days in the charged state (red).

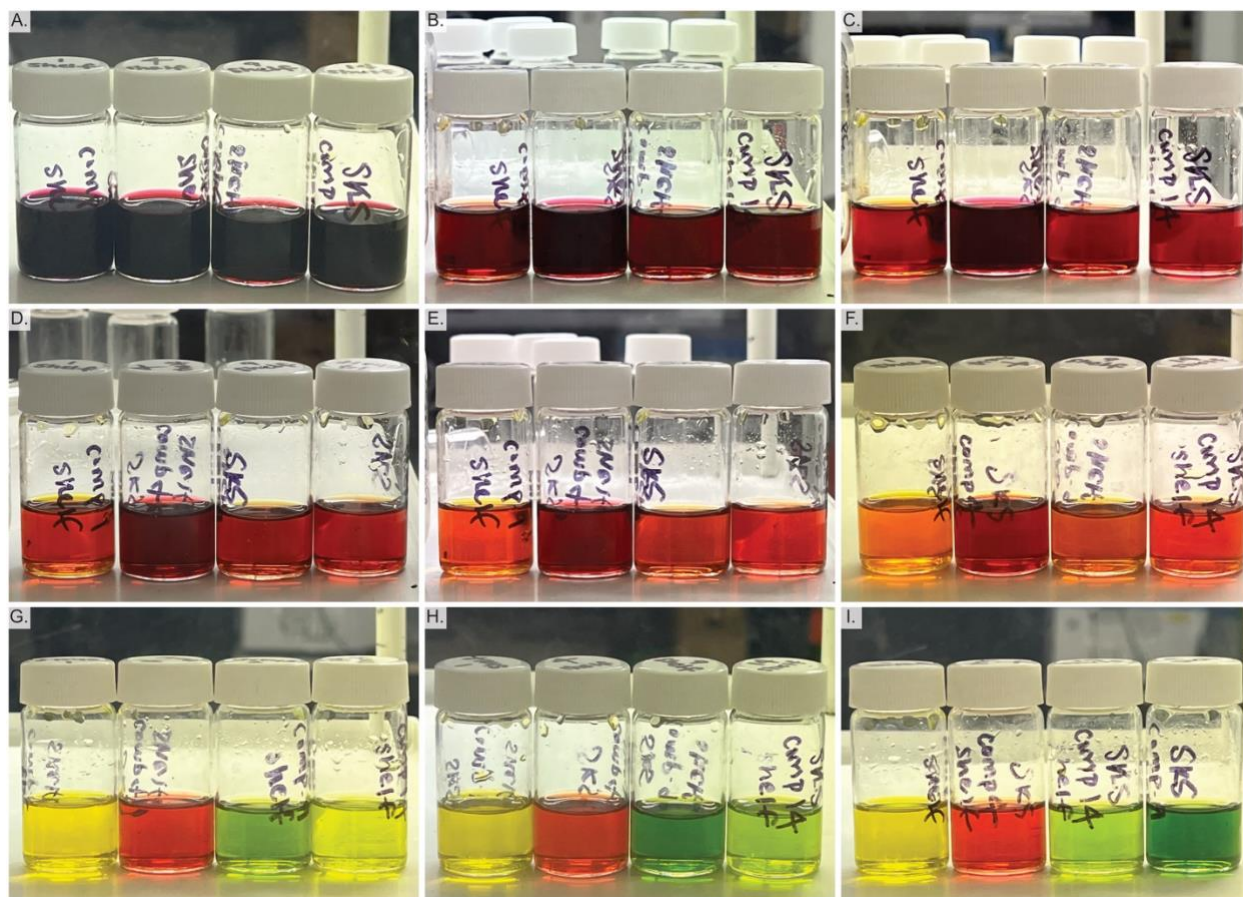


**Figure B.5. Daily visual assessment of color change of charged pyridinium solution shelf stability studies.** Compounds evaluated include: N-phenyl-4-phenyl-2,6-dimethylpyridinium tetrafluoroborate (leftmost vial), N-(mesityl)-4-phenyl-2,6-dimethylpyridinium tetrafluoroborate (left middle vial), N-(mesityl)-4-(p-tolyl)-2,6-dimethylpyridinium tetrafluoroborate (right middle vial), N-(mesityl)-4-(p-methoxyphenyl)-2,6-dimethylpyridinium tetrafluoroborate (rightmost vial) between day zero and day eight (A-I).

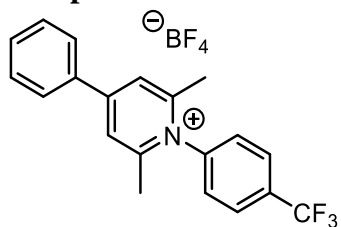
**B.6. Pyridinium Diffusion Coefficients, from CV (Anodic & Cathodic)**

**Table B.3. Summary of electrochemical data. Includes redox potential, anodic diffusion coefficients, cathodic diffusion coefficients, peak height ratios, and peak to peak separations.**

Compound	Reduction Potential $E_{1/2}$ vs Fc/Fc <sup>+</sup> (V)	Anodic diffusion coefficient $D_a$ (cm <sup>2</sup> s <sup>-1</sup> )	Cathodic diffusion coefficient $D_c$ (cm <sup>2</sup> s <sup>-1</sup> )	Peak Height Ratio $i_{pc}/i_{ac}$	Peak-to-Peak Separation (V)
1	-1.54	$8.50 \times 10^{-6}$	$7.62 \times 10^{-6}$	0.92	0.1
2	-1.57	$6.36 \times 10^{-6}$	$5.68 \times 10^{-6}$	1.1	0.1
3	-1.60	$1.55 \times 10^{-5}$	$1.87 \times 10^{-5}$	0.97	0.12
4	-1.60	$7.32 \times 10^{-6}$	$8.36 \times 10^{-6}$	0.89	0.1
5	-1.61	$7.64 \times 10^{-6}$	$8.02 \times 10^{-6}$	1.04	0.1
6	-1.62	$5.78 \times 10^{-6}$	$7.20 \times 10^{-6}$	0.94	0.1
7	-1.62	$5.63 \times 10^{-6}$	$7.10 \times 10^{-6}$	0.97	0.1
8	-1.63	$6.85 \times 10^{-6}$	$7.38 \times 10^{-6}$	1.1	0.1
9	-1.63	$5.27 \times 10^{-6}$	$6.38 \times 10^{-6}$	1	0.08
10	-1.64	$9.63 \times 10^{-6}$	$1.35 \times 10^{-5}$	0.95	0.1
11	-1.65	$7.65 \times 10^{-6}$	$6.88 \times 10^{-6}$	1	0.08
12	-1.66	$7.48 \times 10^{-6}$	$7.25 \times 10^{-6}$	0.98	0.1
13	-1.66	$5.90 \times 10^{-6}$	$6.47 \times 10^{-6}$	1.01	0.1
14	-1.67	$3.74 \times 10^{-6}$	$4.78 \times 10^{-6}$	0.96	0.1
15	-1.67	$4.72 \times 10^{-6}$	$5.33 \times 10^{-6}$	1	0.1
16	-1.68	$6.53 \times 10^{-6}$	$6.95 \times 10^{-6}$	0.96	0.1
17	-1.69	$7.78 \times 10^{-6}$	$7.21 \times 10^{-6}$	1	0.08
18	-1.70	$8.09 \times 10^{-6}$	$8.65 \times 10^{-6}$	0.82	0.12
19	-1.71	$5.71 \times 10^{-6}$	$5.66 \times 10^{-6}$	0.95	0.12
20	-1.72	$7.88 \times 10^{-6}$	$7.59 \times 10^{-6}$	0.93	0.12
21	-1.73	$9.43 \times 10^{-6}$	$8.84 \times 10^{-6}$	1.1	0.08
22	-1.74	$6.70 \times 10^{-6}$	$6.84 \times 10^{-6}$	1	0.1
23	-1.77	$5.08 \times 10^{-6}$	$5.73 \times 10^{-6}$	0.98	0.1



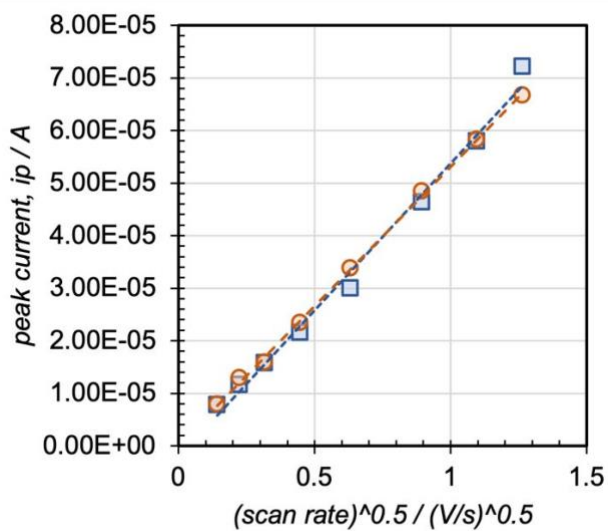
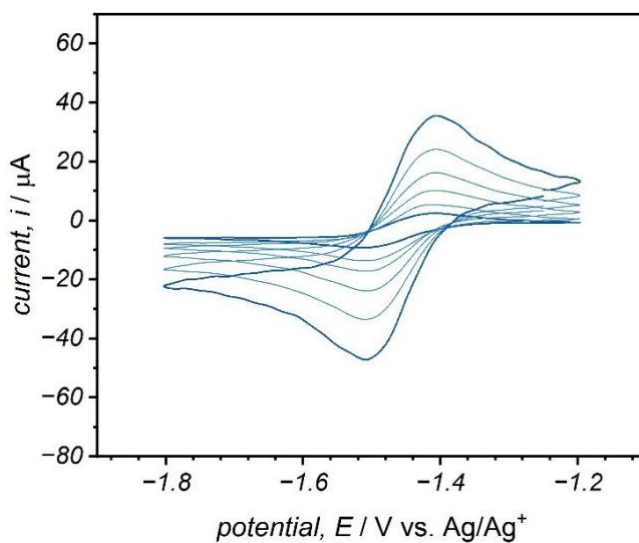
### Compound 1



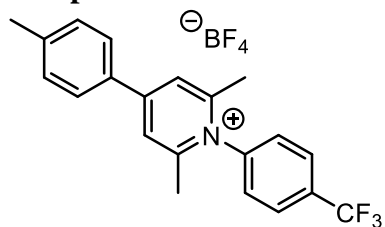
### N-(*p*-trifluoromethyl)-4-phenyl-2,6-dimethylpyridinium tetrafluoroborate (1)

$$D_a = 8.501\text{E-}06 \text{ cm}^2 \text{ s}^{-1}$$

$$D_c = 7.621\text{E-}06 \text{ cm}^2 \text{ s}^{-1}$$



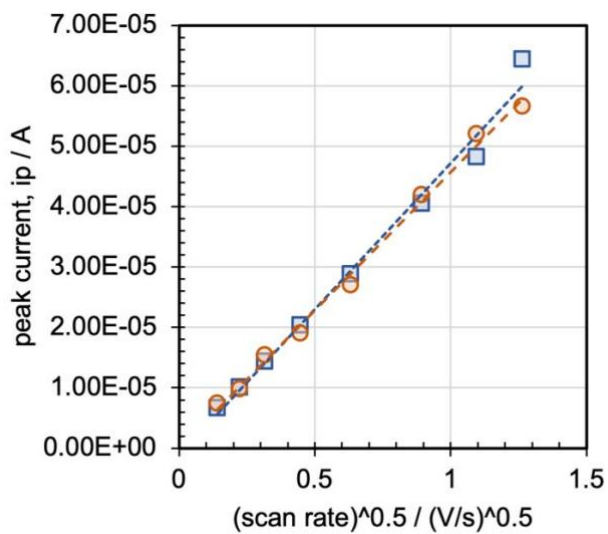
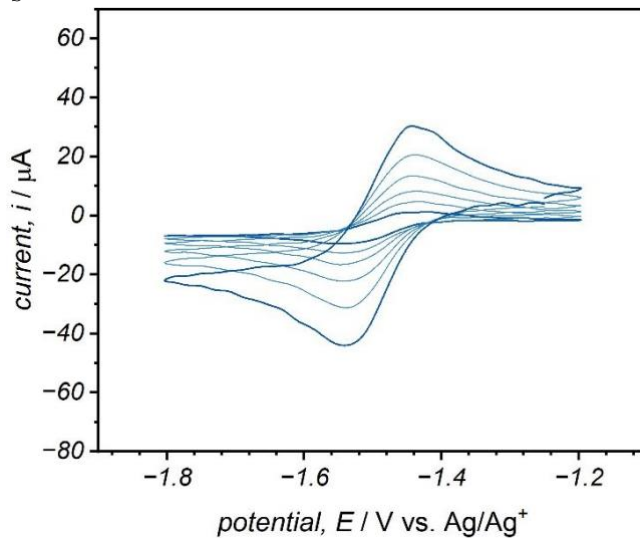
**Compound 2**



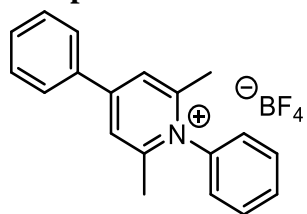
**N-(p-trifluoromethyl)-4-(p-tolyl)-2,6-dimethylpyridinium tetrafluoroborate (2)**

$$D_a = 6.360E-06 \text{ cm}^2 \text{ s}^{-1}$$

$$D_c = 5.683E-06 \text{ cm}^2 \text{ s}^{-1}$$



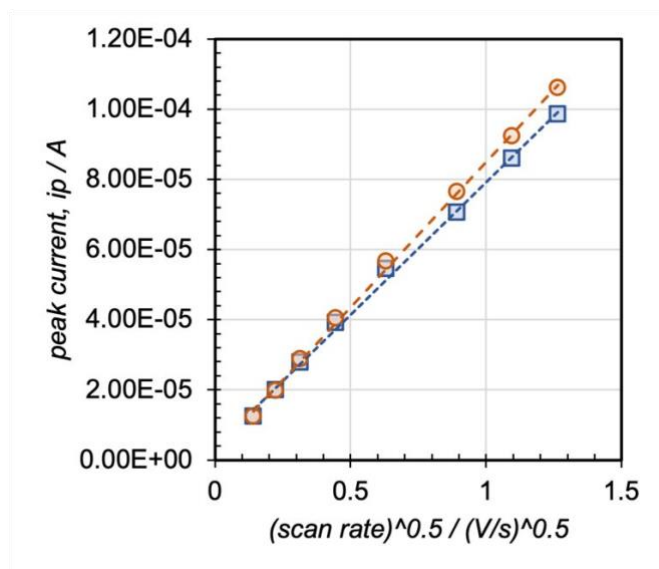
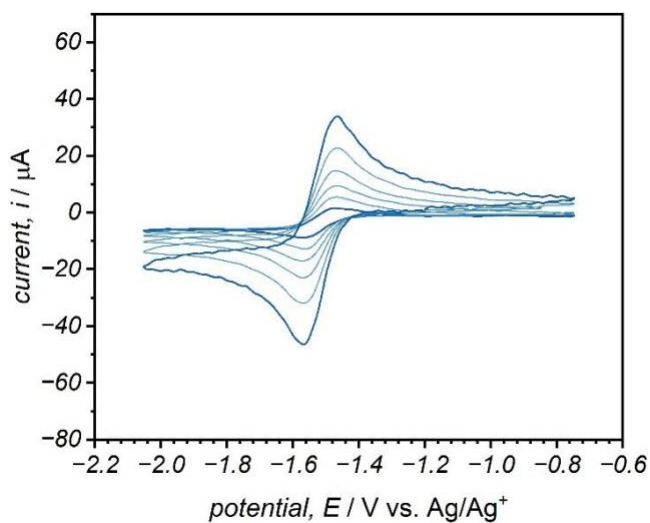
### Compound 3



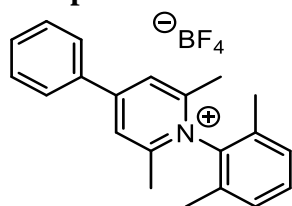
### N-phenyl-4-phenyl-2,6-dimethylpyridinium tetrafluoroborate (3)

$$D_a = 1.550E-05 \text{ cm}^2 \text{ s}^{-1}$$

$$D_c = 1.865E-05 \text{ cm}^2 \text{ s}^{-1}$$



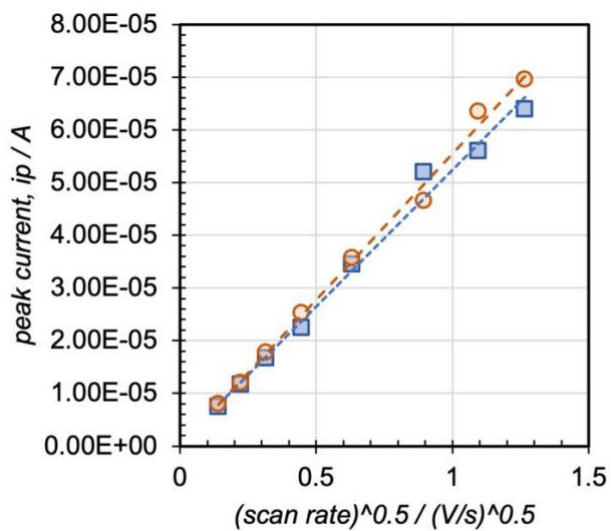
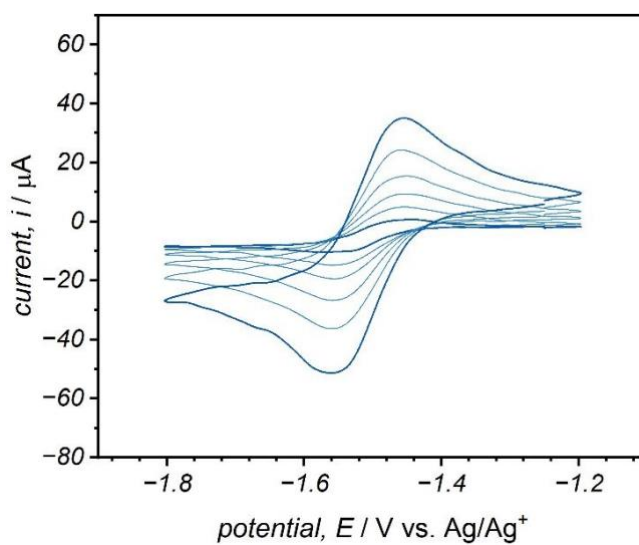
### Compound 4



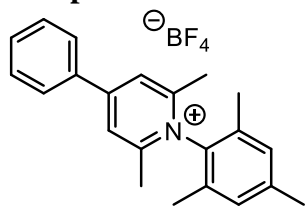
### N-(2,6-xylyl)-4-phenyl-2,6-dimethylpyridinium tetrafluoroborate (4)

$$D_a = 7.318E-06 \text{ cm}^2 \text{ s}^{-1}$$

$$D_c = 8.361E-06 \text{ cm}^2 \text{ s}^{-1}$$



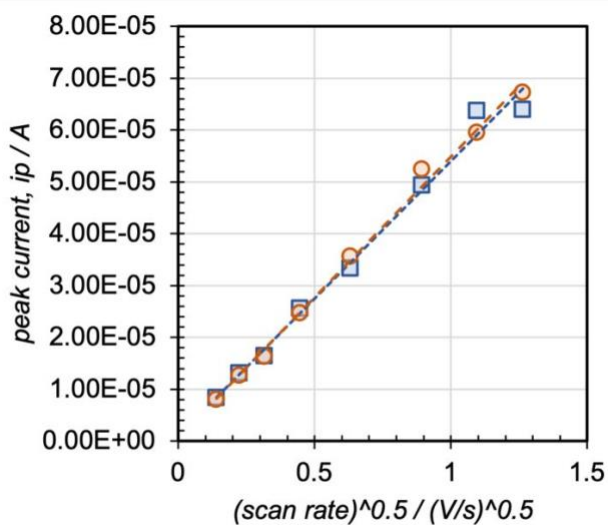
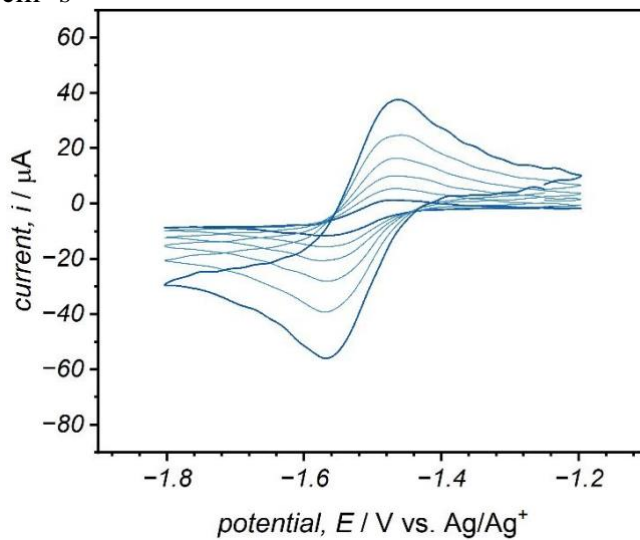
### Compound 5



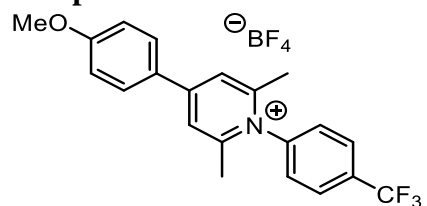
### N-(mesityl)-4-phenyl-2,6-dimethylpyridinium tetrafluoroborate (5)

$$D_a = 7.644\text{E-}06 \text{ cm}^2 \text{ s}^{-1}$$

$$D_c = 8.015\text{E-}06 \text{ cm}^2 \text{ s}^{-1}$$



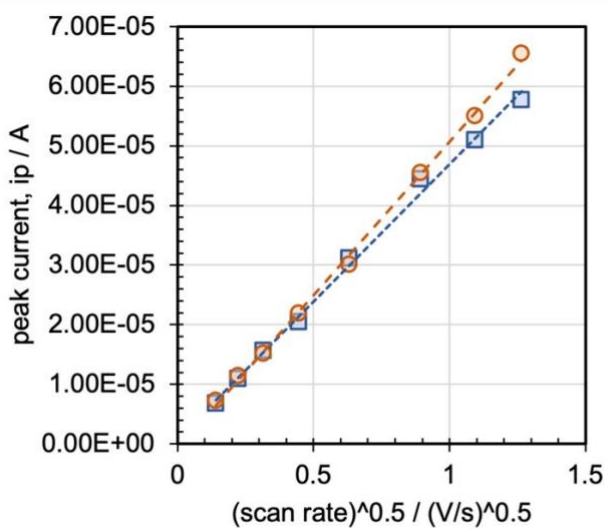
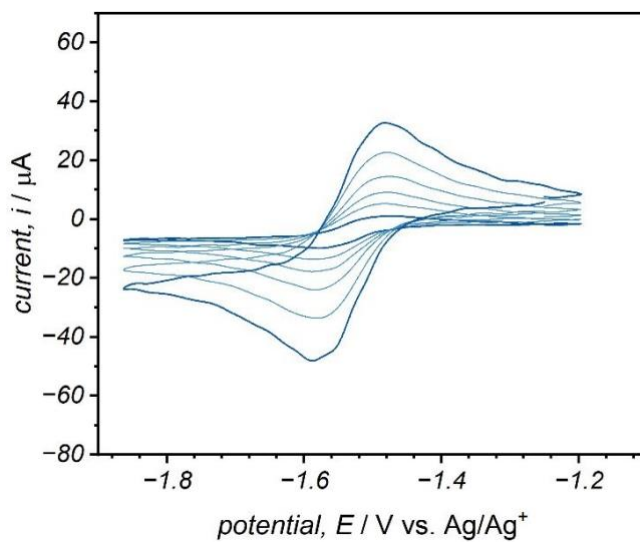
### Compound 6



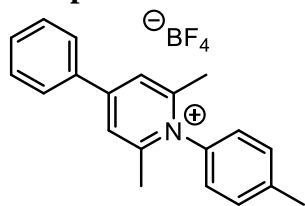
### N-(*p*-trifluoromethylphenyl)-4-(*p*-methoxyphenyl)-2,6-dimethylpyridinium tetrafluoroborate (**6**)

$$D_a = 5.780\text{E-}06 \text{ cm}^2 \text{ s}^{-1}$$

$$D_c = 7.204\text{E-}06 \text{ cm}^2 \text{ s}^{-1}$$



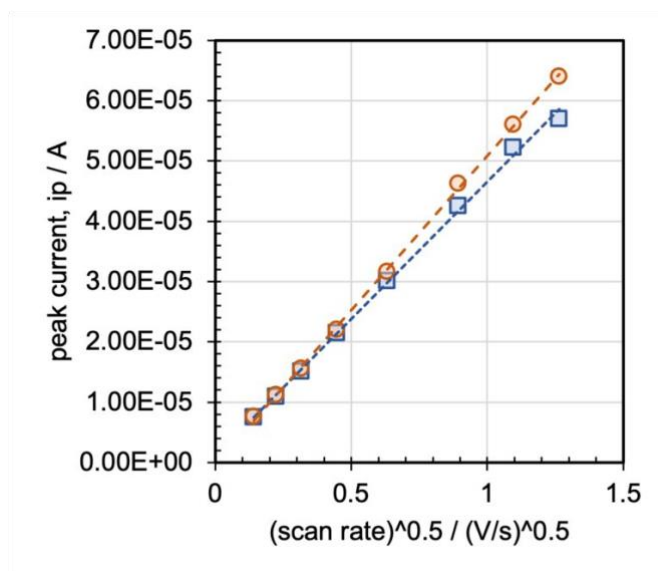
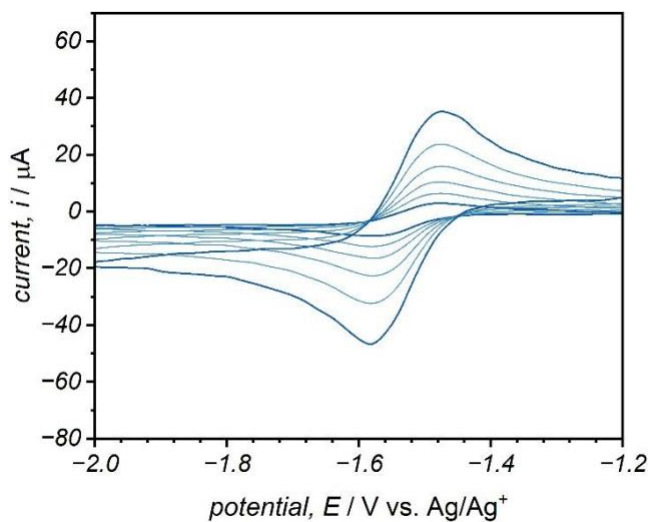
### Compound 7



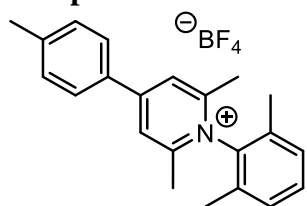
### N-(*p*-tolyl)-4-phenyl-2,6-dimethylpyridinium tetrafluoroborate (7)

$$D_a = 5.627\text{E-}06 \text{ cm}^2 \text{ s}^{-1}$$

$$D_c = 7.098\text{E-}06 \text{ cm}^2 \text{ s}^{-1}$$



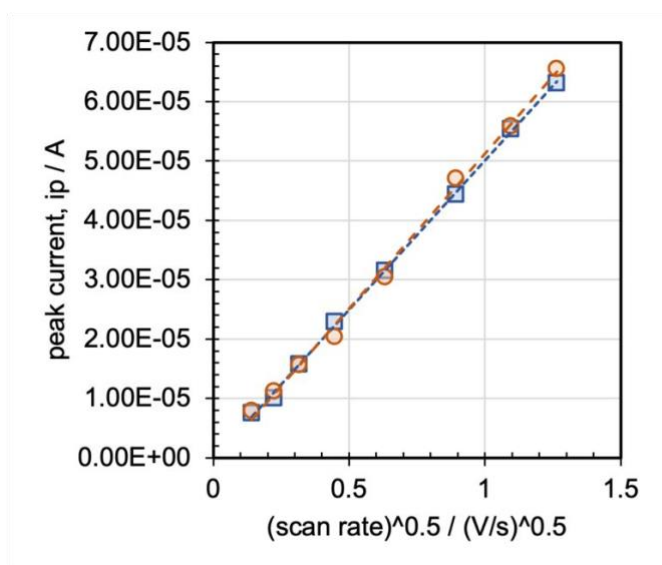
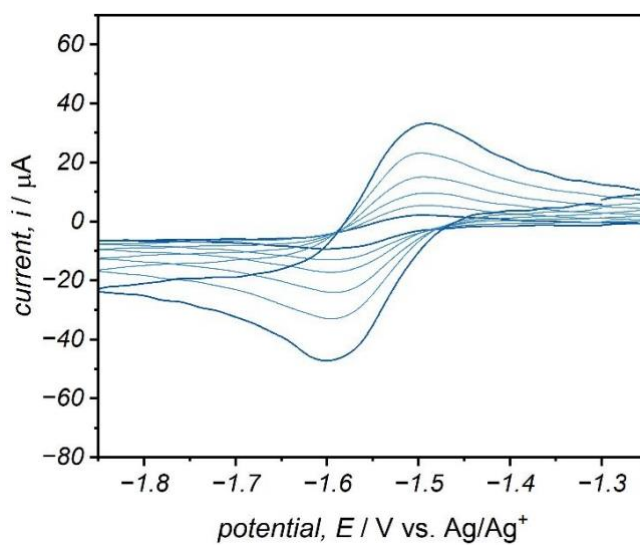
**Compound 8**



**N-(2,6-xylyl)-4-(p-tolyl)-2,6-dimethylpyridinium tetrafluoroborate (8)**

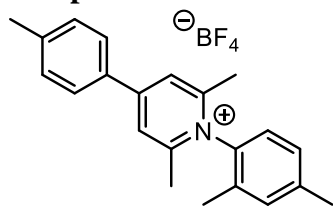
$$D_a = 6.854E-06 \text{ cm}^2 \text{ s}^{-1}$$

$$D_c = 7.376E-06 \text{ cm}^2 \text{ s}^{-1}$$





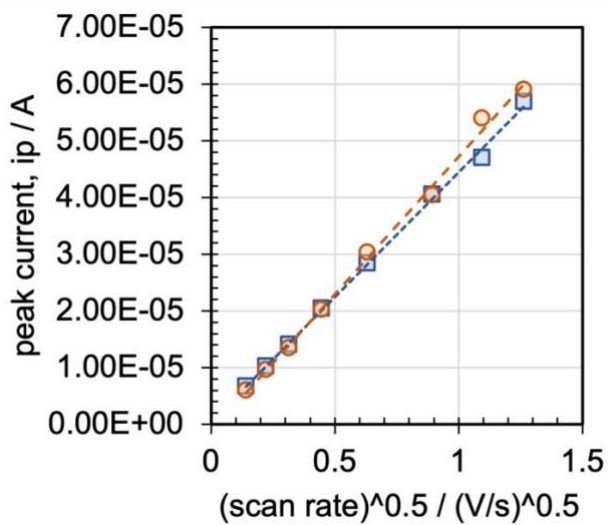
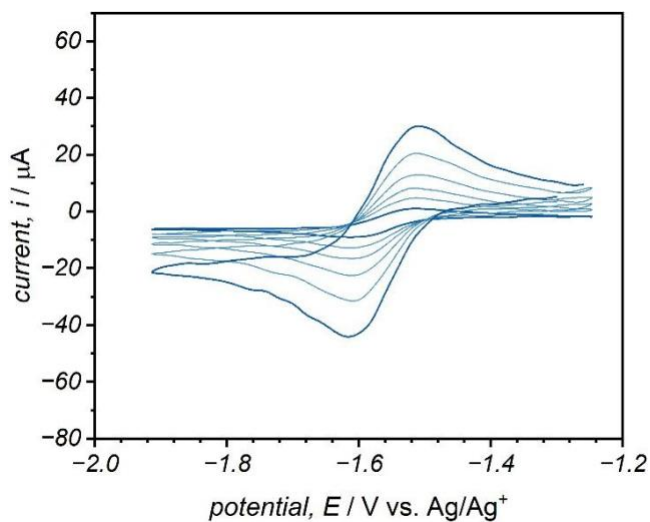
**Compound 9**



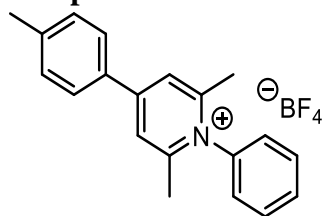
**N-(2,4-xylyl)-4-(p-tolyl)-2,6-dimethylpyridinium tetrafluoroborate (9)**

$$D_a = 5.265E-06 \text{ cm}^2 \text{ s}^{-1}$$

$$D_c = 6.384E-06 \text{ cm}^2 \text{ s}^{-1}$$



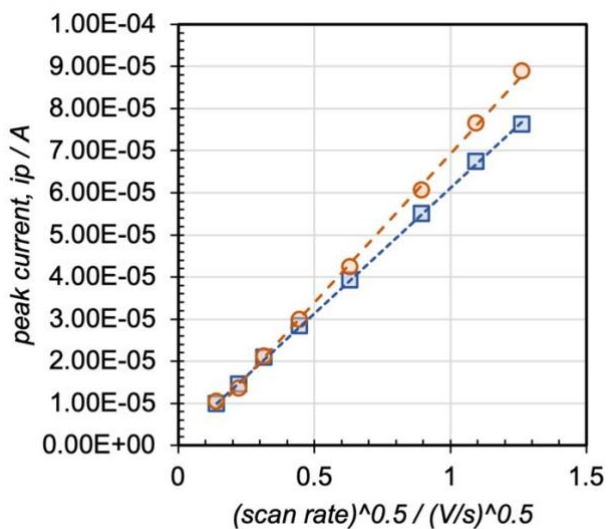
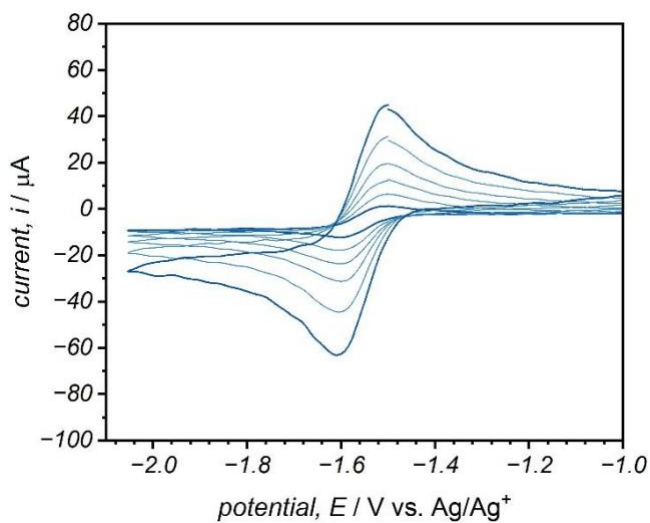
### Compound 10



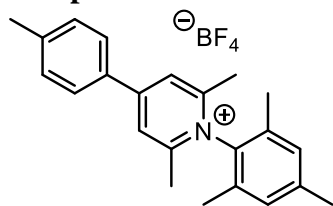
### N-phenyl-4-(p-tolyl)-2,6-dimethylpyridinium tetrafluoroborate (10)

$$D_a = 9.633\text{E-}06 \text{ cm}^2 \text{ s}^{-1}$$

$$D_c = 1.354\text{E-}05 \text{ cm}^2 \text{ s}^{-1}$$



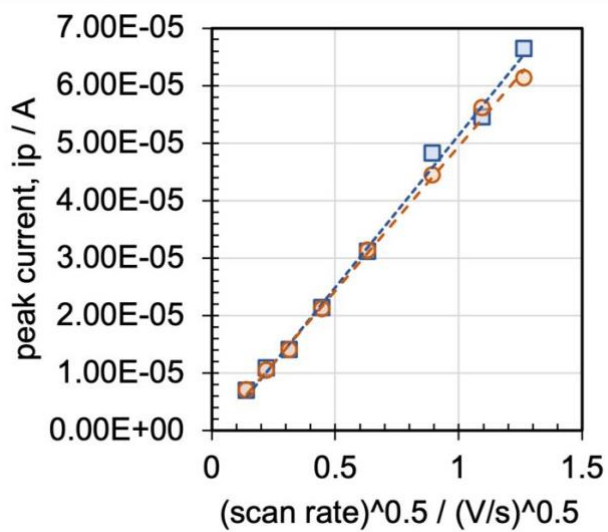
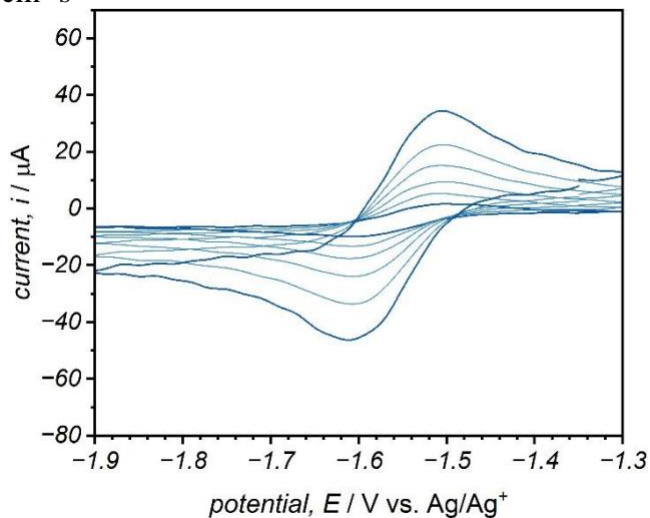
### Compound 11



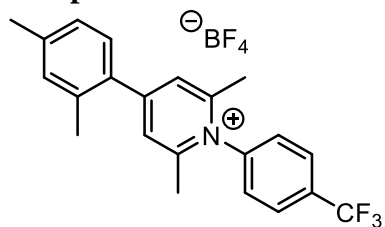
### N-(mesityl)-4-(p-tolyl)-2,6-dimethylpyridinium tetrafluoroborate (11)

$$D_a = 7.652E-06 \text{ cm}^2 \text{ s}^{-1}$$

$$D_c = 6.877E-06 \text{ cm}^2 \text{ s}^{-1}$$



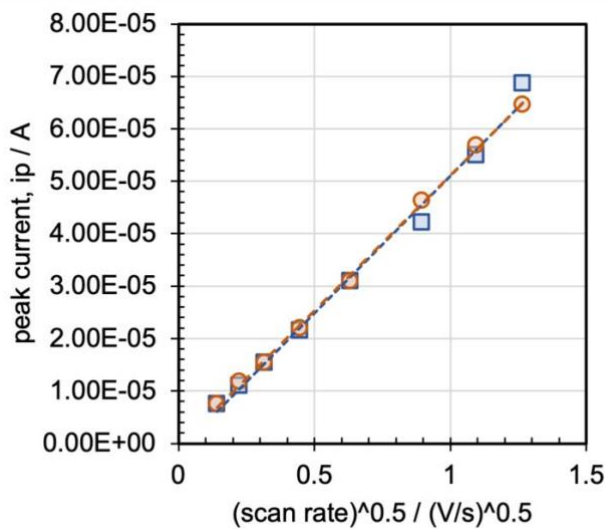
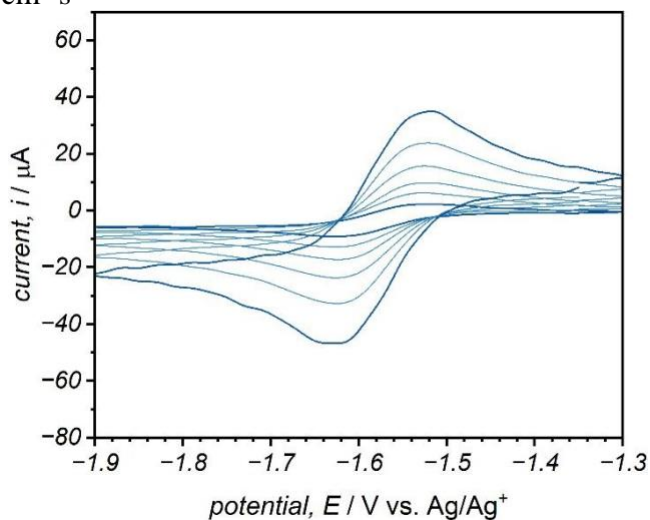
### Compound 12



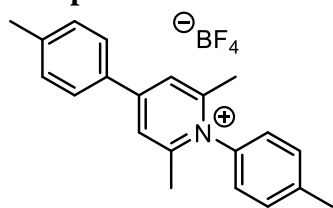
### N-(p-trifluoromethylphenyl)-4-(2,4-xylyl)-2,6-dimethylpyridinium tetrafluoroborate(12)

$$D_a = 7.478E-06 \text{ cm}^2 \text{ s}^{-1}$$

$$D_c = 7.249E-06 \text{ cm}^2 \text{ s}^{-1}$$



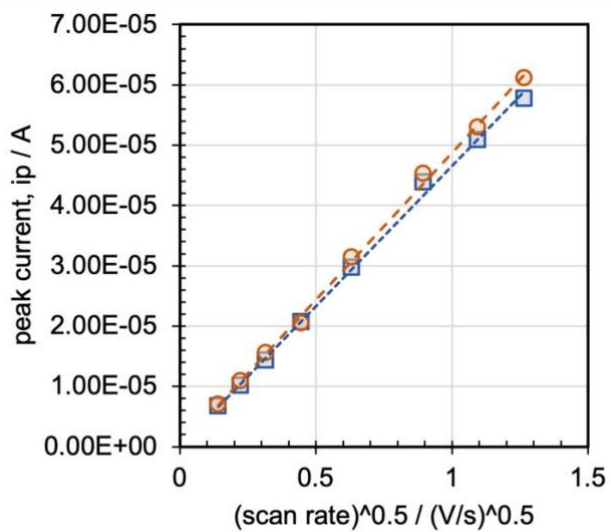
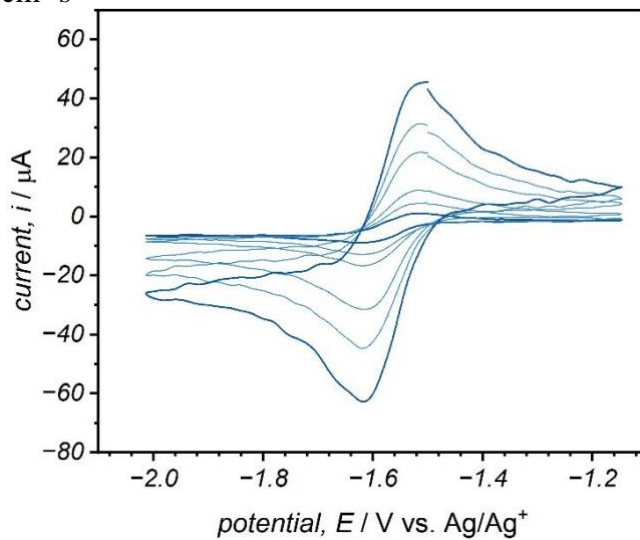
**Compound 13**



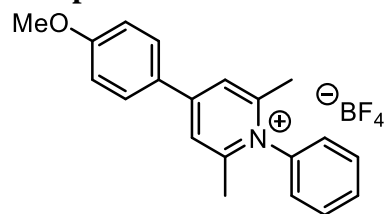
**N-(p-tolyl)-4-(p-tolyl)-2,6-dimethylpyridinium tetrafluoroborate (13)**

$$D_a = 5.899\text{E-}06 \text{ cm}^2 \text{ s}^{-1}$$

$$D_c = 6.473\text{E-}06 \text{ cm}^2 \text{ s}^{-1}$$



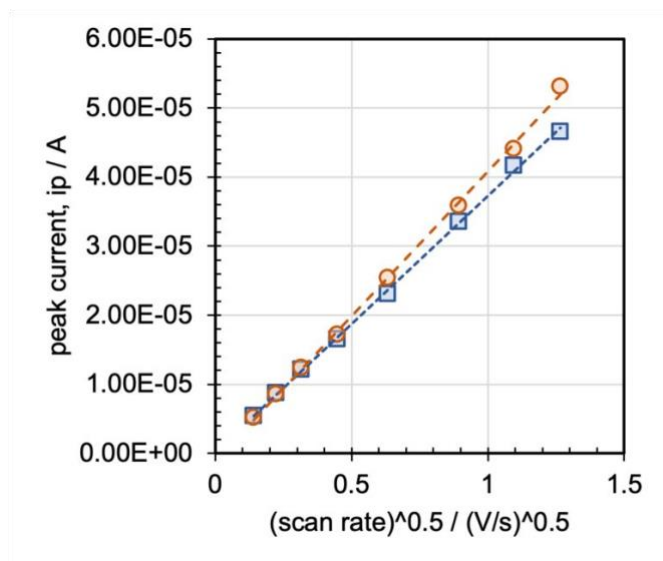
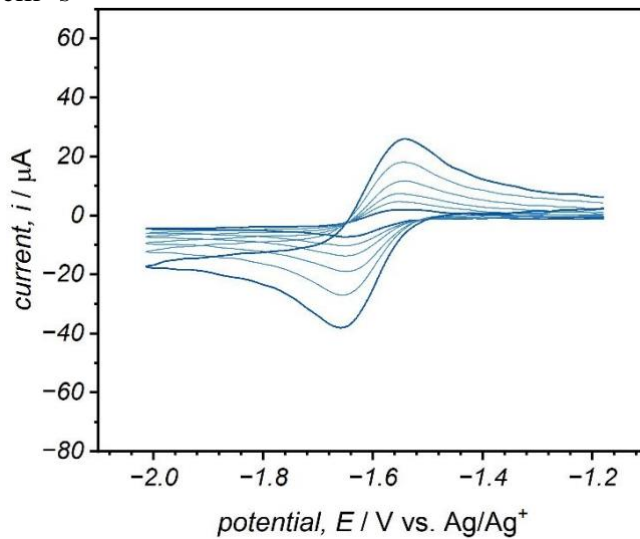
### Compound 14



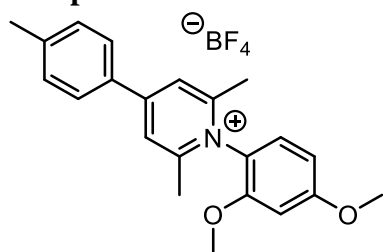
### N-phenyl-4-(p-methoxyphenyl)-2,6-dimethylpyridinium tetrafluoroborate (14)

$$D_a = 3.741\text{E-}06 \text{ cm}^2 \text{ s}^{-1}$$

$$D_c = 4.781\text{E-}06 \text{ cm}^2 \text{ s}^{-1}$$



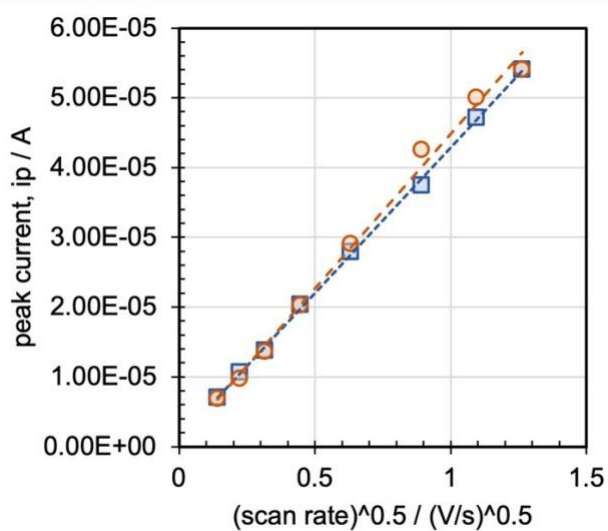
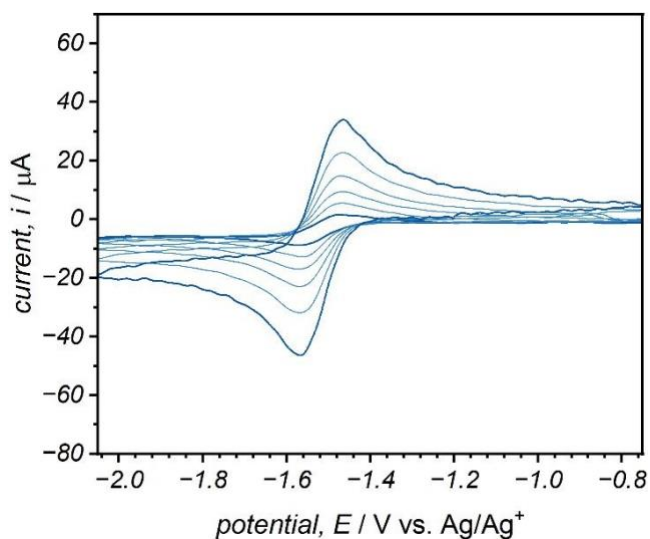
**Compound 15**



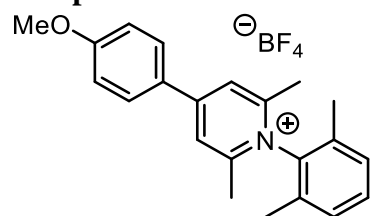
**N-(2,4-dimethoxy)-4-(p-tolyl)-2,6-dimethylpyridinium tetrafluoroborate (15)**

$$D_a = 4.720E-06 \text{ cm}^2 \text{ s}^{-1}$$

$$D_c = 5.331E-06 \text{ cm}^2 \text{ s}^{-1}$$



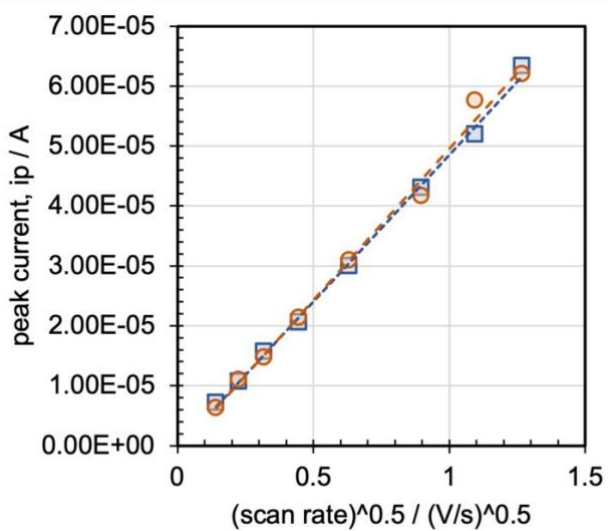
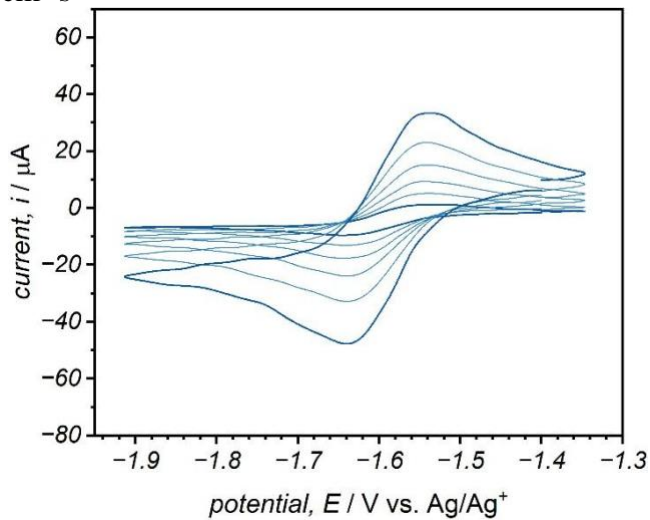
### Compound 16



### N-(2,6-xylyl)-4-(p-methoxyphenyl)-2,6-dimethylpyridinium tetrafluoroborate (16)

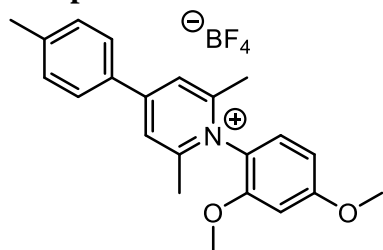
$$D_a = 6.525E-06 \text{ cm}^2 \text{ s}^{-1}$$

$$D_c = 6.950E-06 \text{ cm}^2 \text{ s}^{-1}$$





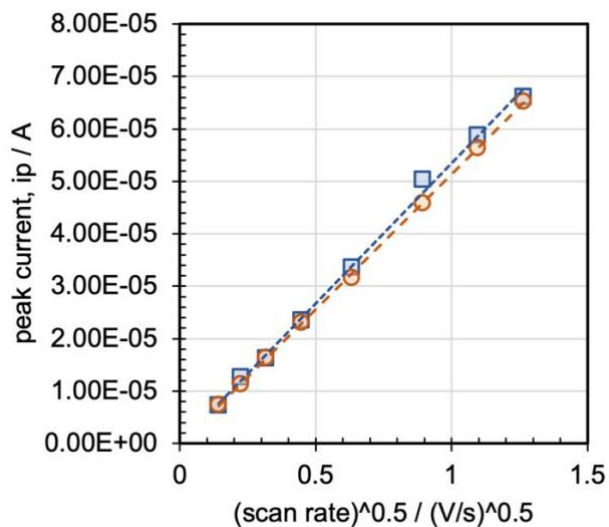
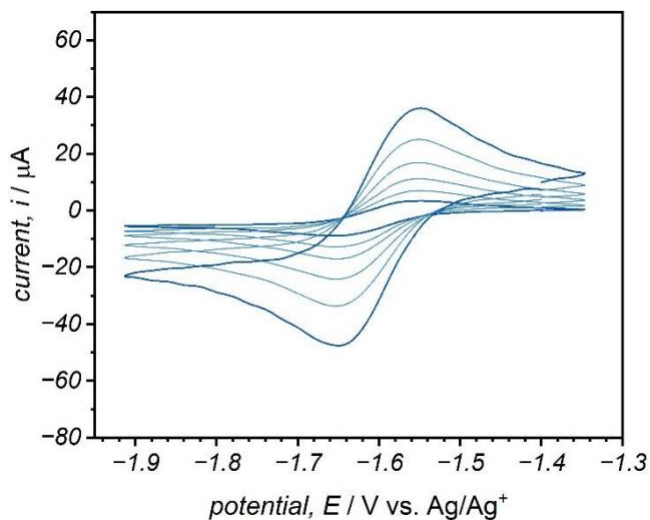
**Compound 17**



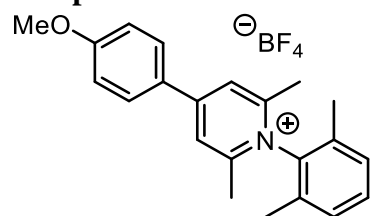
**N-(mesityl)-4-(p-methoxyphenyl)-2,6-dimethylpyridinium tetrafluoroborate (17)**

$$D_a = 7.778E-06 \text{ cm}^2 \text{ s}^{-1}$$

$$D_c = 7.212E-06 \text{ cm}^2 \text{ s}^{-1}$$



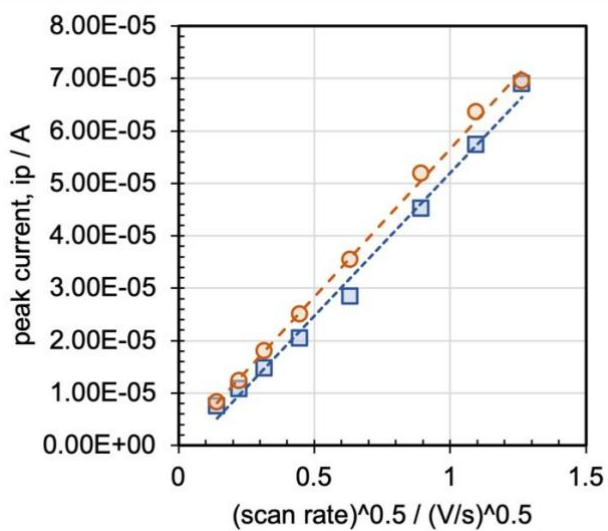
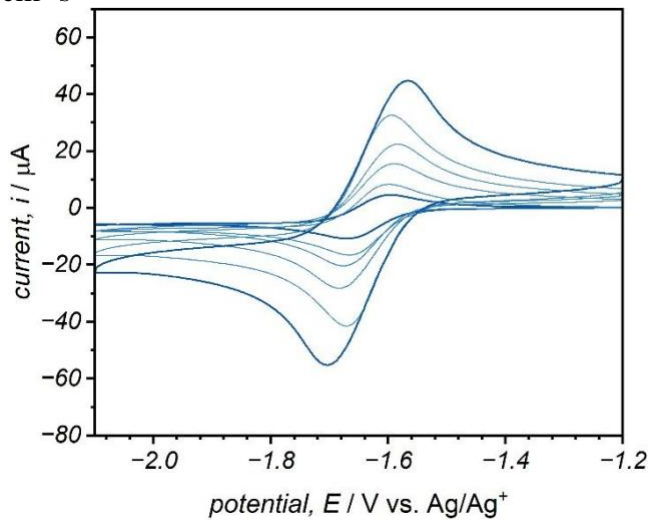
### Compound 18



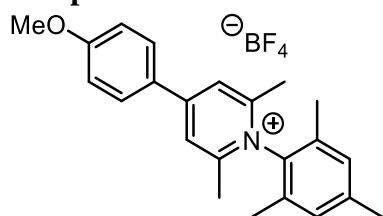
### N-(n-butyl)-4-phenyl-2,6-dimethylpyridinium tetrafluoroborate (18)

$$D_a = 8.094E-06 \text{ cm}^2 \text{ s}^{-1}$$

$$D_c = 8.653E-06 \text{ cm}^2 \text{ s}^{-1}$$



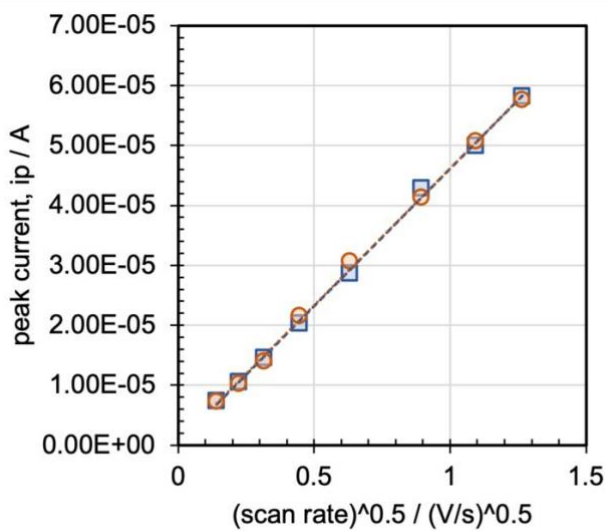
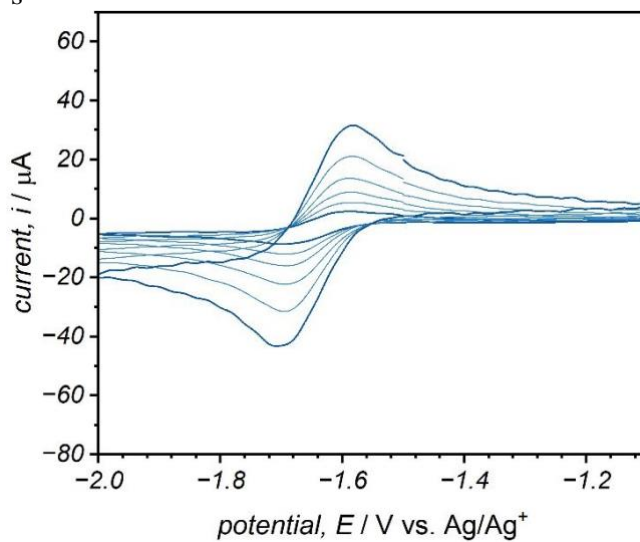
**Compound 19**



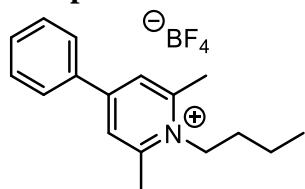
**N-phenyl-4-(2,4-xylyl)-2,6-dimethylpyridinium tetrafluoroborate (19)**

$D_a = 5.709E-06 \text{ cm}^2 \text{ s}^{-1}$

$D_c = 5.657E-06 \text{ cm}^2 \text{ s}^{-1}$



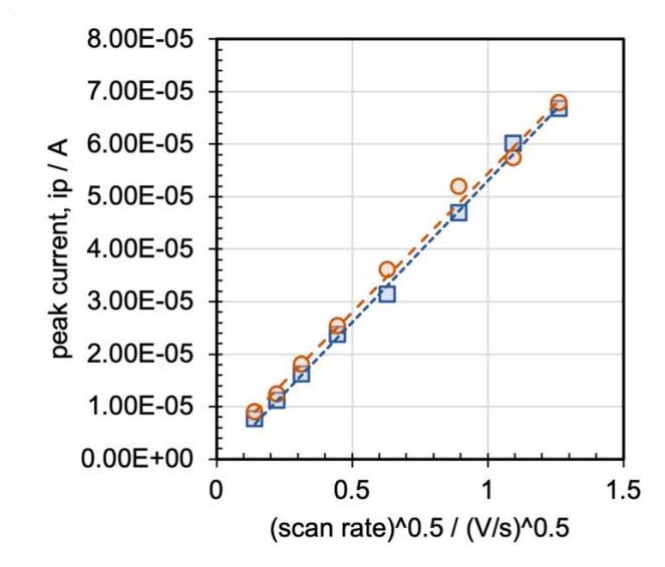
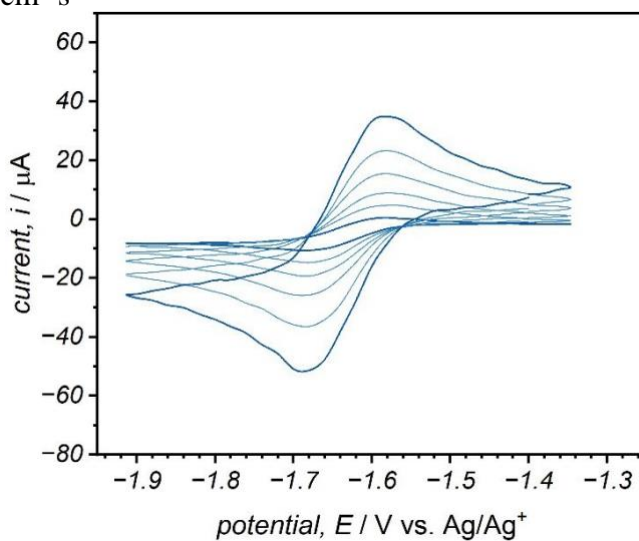
### Compound 20



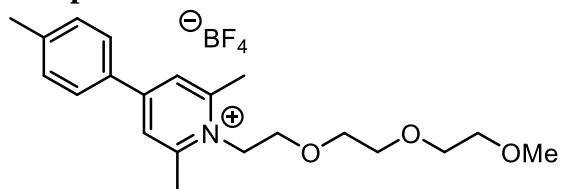
### N-(2,6-dimethyl-4-phenylpyridin-2-yl)butylpyridinium tetrafluoroborate (20)

$$D_a = 7.884 \times 10^{-6} \text{ cm}^2 \text{ s}^{-1}$$

$$D_c = 7.594 \times 10^{-6} \text{ cm}^2 \text{ s}^{-1}$$



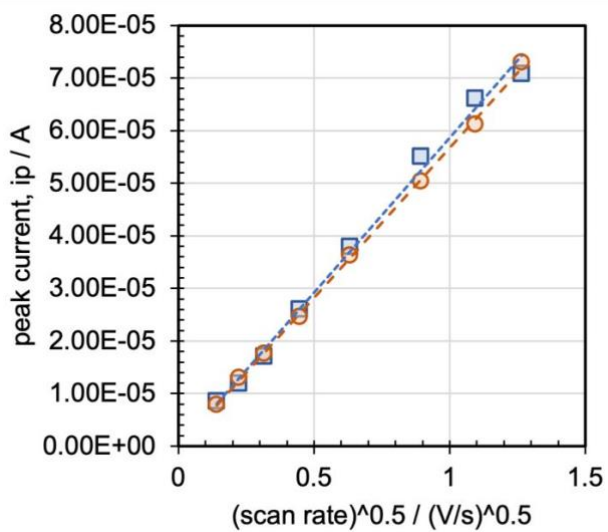
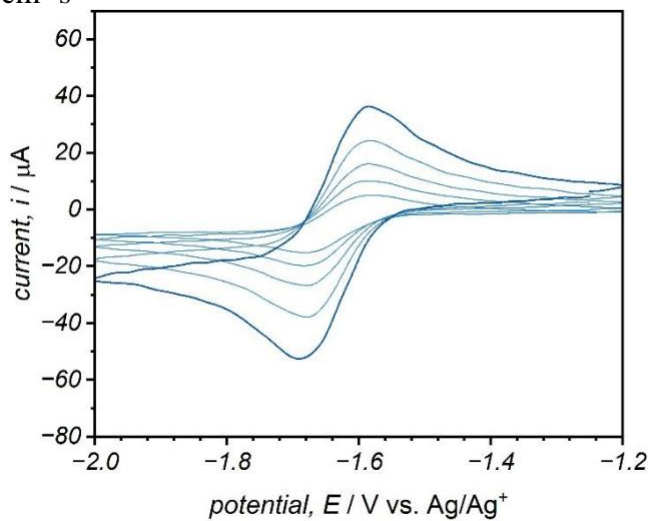
### Compound 21



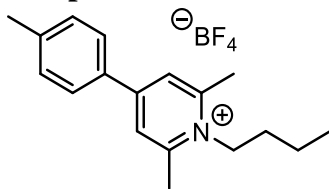
### N-(2-(2-(2-methoxyethoxy)ethoxy)ethyl)-4-(p-tolyl)-2,6-dimethylpyridinium tetrafluoroborate (21)

$$D_a = 9.432E-06 \text{ cm}^2 \text{ s}^{-1}$$

$$D_c = 8.842E-06 \text{ cm}^2 \text{ s}^{-1}$$



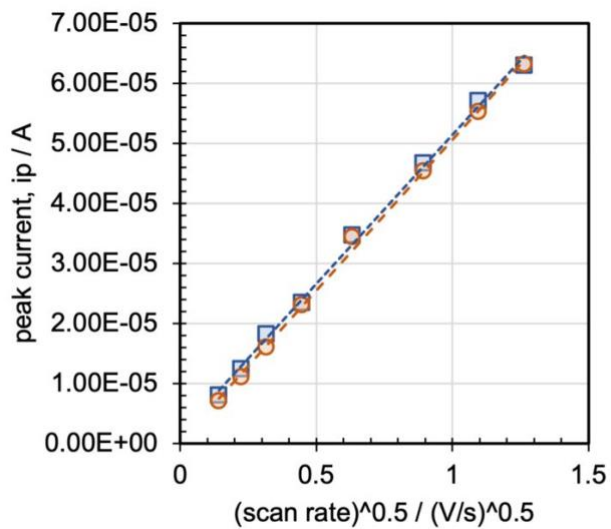
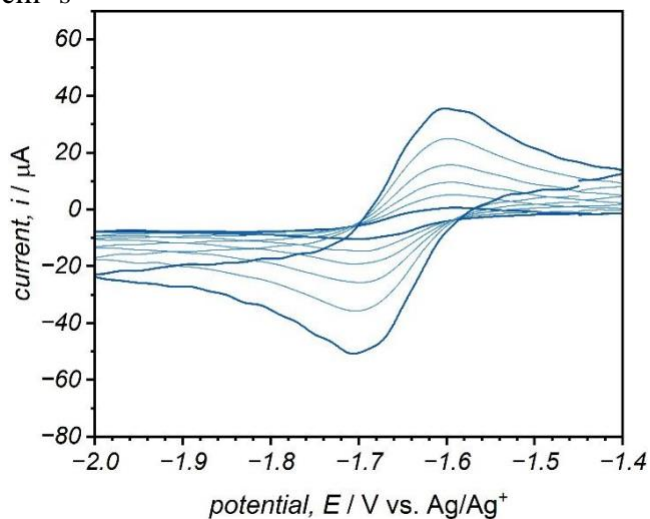
**Compound 22**



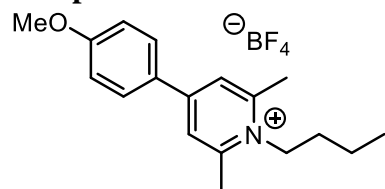
**N-(n-butyl)-4-(p-tolyl)-2,6-dimethylpyridinium tetrafluoroborate (22)**

$$D_a = 6.701E-06 \text{ cm}^2 \text{ s}^{-1}$$

$$D_c = 6.844E-06 \text{ cm}^2 \text{ s}^{-1}$$



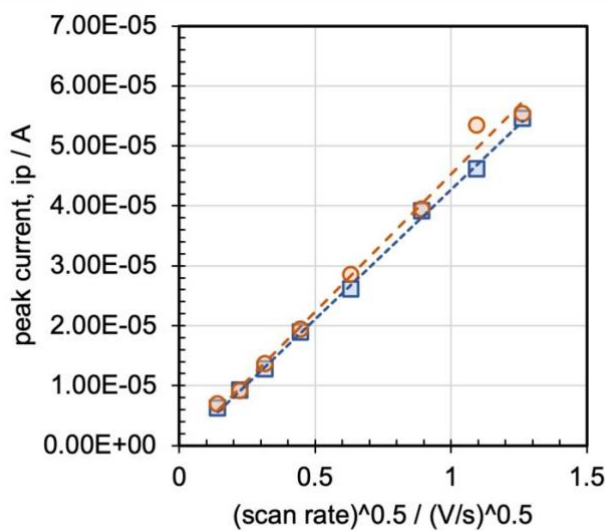
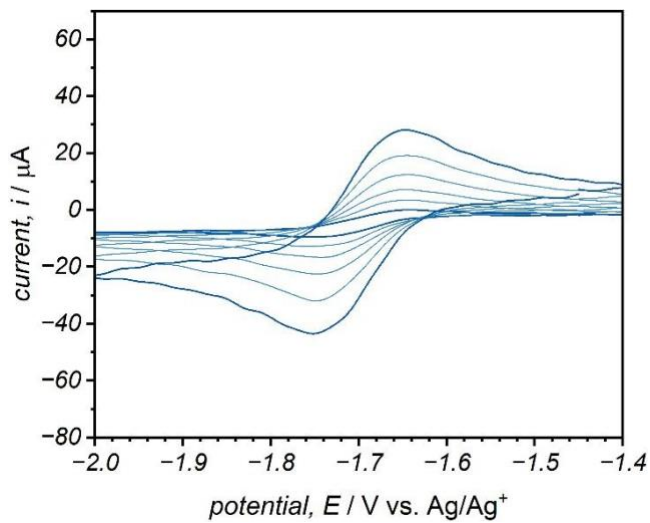
**Compound 23**



**N-(n-butyl)-4-(p-methoxyphenyl)-2,6-dimethylpyridinium tetrafluoroborate (23)**

$$D_a = 5.079E-06 \text{ cm}^2 \text{ s}^{-1}$$

$$D_c = 5.732E-06 \text{ cm}^2 \text{ s}^{-1}$$



## B.7. Kinematic Viscosity Data for Compounds 1, 3, 5, and 17

**Table B.4. Summary of concentration dependent viscosity data in acetonitrile of low (3 and 5), moderate (1), and high (17) solubility pyridiniums.** The kinematic viscosity of a pyridinium and supporting electrolyte mixture was evaluated, using 0.5 M TEABF<sub>4</sub> (tetraethylammonium tetrafluoroborate) and 0.5 M compound 17 in acetonitrile. Reported viscosity values represent the average of  $n = 5$  replicates, and the error bars represent the respective standard deviations at 19.3 °C  $\pm$  0.4 °C (for pure compound solutions) and 22.4 °C  $\pm$  0.5 °C (for solution mixture).

<b>Controls</b>	<b>Conc. (M)</b>	<b>Kinematic Viscosity (cSt)</b>	<b>Kinematic Viscosity Std. Dev. (cSt)</b>	<b>Temperature Avg. (°C)</b>	<b>Temperature Std. Dev. (°C)</b>
Water	N/A	1.038	0.005	20.0	0.23
Acetonitrile	N/A	0.462	0.001	19.8	0.27
<b>Compound 17</b>					
	0.68	0.949	0.007	18.9	0.29
	0.34	0.687	0.034	19.7	0.14
	0.17	0.551	0.002	19.3	0.59
	0.09	0.509	0.003	19.8	0.43
	0.04	0.498	0.020	20.3	0.58
<b>Compound 5</b>					
	0.29	0.577	0.004	19.5	0.52
	0.15	0.522	0.004	19.5	0.53
	0.07	0.494	0.004	19.2	0.17
	0.04	0.483	0.003	19.5	0.43
	0.02	0.472	0.004	19.8	0.23
<b>Compound 3</b>					
	0.32	0.620	0.019	19.0	0.51
	0.16	0.528	0.005	19.3	0.19
	0.08	0.504	0.011	19.2	0.35
	0.04	0.481	0.003	19.2	0.50
	0.02	0.473	0.002	19.1	0.46
<b>Compound 1</b>					
	0.96	1.26	0.057	20.2	1.0
	0.48	0.78	0.080	18.6	0.1
	0.24	0.58	0.009	18.4	0.1
	0.12	0.53	0.007	18.1	0.1
	0.06	0.50	0.005	18.3	1.0
<b>Compound 17 &amp; TEABF<sub>4</sub></b>					
(1:1 mixture)	0.5 M : 0.5 M	1.04	0.07	22.4	0.5



**Table B.5. Raw time data of individual Ubbelohde measurements for concentration dependent viscosities in acetonitrile of low (3 and 5), moderate (1), and high (17) pyridiniums.** The kinematic viscosity of a pyridinium and supporting electrolyte mixture was evaluated, using 0.5 M TEABF<sub>4</sub> (tetraethylammonium tetrafluoroborate) and 0.5 M compound 17 in acetonitrile. Reported viscosity values represent the average of n = 5 replicates, and the error bars represent the respective standard deviations at 19.3 °C ± 0.4 °C (for pure compound solutions) and 22.4 °C ± 0.5 °C (for solution mixture). Dynamic Viscosity Data for Compounds 1, 3, 5, and 17

	<b>Conc. (M)</b>	<b>Trial 1 (s)</b>	<b>Trial 2 (s)</b>	<b>Trial 3 (s)</b>	<b>Trial 4 (s)</b>	<b>Trial 5 (s)</b>
<b>Controls</b>						
Water	N/A	1013	1016	1027	1025	1022
Acetonitrile	N/A	454	453	454	456	454
<b>Compound 17</b>						
	0.68	931	930	930	947	928
	0.34	673	641	726	700	640
	0.17	539	545	543	542	539
	0.09	498	506	501	499	500
	0.04	527	474	487	486	473
<b>Compound 5</b>						
	0.29	567	563	573	572	563
	0.15	514	519	510	516	508
	0.07	492	483	486	483	483
	0.04	474	476	477	478	469
	0.02	470	468	461	460	462
<b>Compound 3</b>						
	0.32	594	620	640	600	592
	0.16	518	515	529	517	515
	0.08	513	495	488	503	481
	0.04	477	474	474	469	469
	0.02	468	467	463	462	464
<b>Compound 1</b>						
	0.96	1346	1206	1196	1207	1245
	0.48	707	727	770	913	703
	0.24	590	573	566	567	565
	0.12	506	527	521	513	517
	0.06	492	490	492	489	480
<b>Compound 17 &amp; TEABF<sub>4</sub></b>						
(1:1 mixture)	0.5 M : 0.5 M	959	981	964	1067	1122

**Table B.6. Summary of concentration dependent dynamic viscosity data in acetonitrile of low (3 and 5), moderate (1), and high (17) pyridiniums.** The dynamic viscosity of a pyridinium and supporting electrolyte mixture was evaluated, using 0.5 M TEABF<sub>4</sub>(tetraethylammonium tetrafluoroborate) and 0.5 M compound 17 in acetonitrile. Measured kinematic viscosity and measured density were used to determine the dynamic viscosities. Reported viscosity values represent the average of  $n = 5$  replicates, and the error bars represent the respective standard deviations at 19.3 °C ± 0.4 °C (for pure compound solutions) and 22.4 °C ± 0.5 °C (for solution mixture). Reported density values represent the average of  $n = 3$  replicates, and the error bars represent the respective standard deviations at (20 °C).

	<b>Avg. Conc. (M)</b>	<b>Avg. Density (mg mL<sup>-1</sup>)</b>	<b>Avg. Kinematic Viscosity (cSt)</b>	<b>Avg. Dynamic Viscosity (cP)</b>	<b>Std. Dev. Density (mg mL<sup>-1</sup>)</b>	<b>Std. Dev. Kinematic Viscosity (cSt)</b>	<b>Std. Dev. Dynamic Viscosity (cP)</b>
<b>Compound 17</b>							
	0.68	904	0.949	0.856	5	0.007	0.006
	0.34	844	0.690	0.580	8	0.030	0.030
	0.17	820	0.551	0.448	10	0.002	0.002
	0.09	795	0.509	0.407	6	0.003	0.002
	0.04	800	0.500	0.390	20	0.020	0.020
<b>Compound 5</b>							
	0.29	839	0.580	0.482	2	0.020	0.003
	0.15	811	0.522	0.423	6	0.005	0.003
	0.07	804	0.490	0.394	1	0.010	0.003
	0.04	789	0.483	0.382	3	0.003	0.002
	0.02	783	0.472	0.372	9	0.002	0.003
<b>Compound 3</b>							
	0.32	837	0.620	0.520	7	0.004	0.020
	0.16	812	0.528	0.429	5	0.004	0.004
	0.08	794	0.504	0.402	3	0.004	0.009
	0.04	796	0.481	0.381	4	0.003	0.002
	0.02	786	0.473	0.373	7	0.004	0.002
<b>Compound 1</b>							
	0.96	958	1.26	1.20	5	0.06	0.05
	0.48	880	0.78	0.67	10	0.08	0.07
	0.24	840	0.58	0.48	7	0.01	0.01
	0.12	793	0.53	0.42	4	0.01	0.01
	0.06	770	0.497	0.40	1	0.005	0.004
<b>Compound 17 &amp; TEABF<sub>4</sub> (1:1 mixture)</b>							
	0.5 M:0.5 M	880	1.04	0.90	20	0.07	0.06

**Table B.7. Raw data of individual measurements for concentration dependent densities in acetonitrile of low (3 and 5), moderate (1), and high (17) solubility pyridiniums.** The density of a pyridinium and supporting electrolyte mixture was evaluated, using 0.5 M TEABF<sub>4</sub> (tetraethylammonium tetrafluoroborate) and 0.5 M compound 17 in acetonitrile. Solution densities were determined by depositing 100  $\mu$ L of each concentration solution with an Eppendorf pipette, measuring the change in mass on a balance, and dividing the two values. This procedure was completed in triplicate to yield and average solution density at ambient temperature (20 °C).

	<b>Conc. (M)</b>	<b>Trial 1 (mg mL<sup>-1</sup>)</b>	<b>Trial 2 (mg mL<sup>-1</sup>)</b>	<b>Trial 3 (mg mL<sup>-1</sup>)</b>
<b>Compound 17</b>				
	0.68	899	910	902
	0.34	836	843	852
	0.17	808	811	827
	0.09	796	802	789
	0.04	811	776	812
<b>Compound 5</b>				
	0.29	834	845	833
	0.15	810	808	817
	0.07	792	795	797
	0.04	798	798	792
	0.02	778	792	788
<b>Compound 3</b>				
	0.32	834	845	833
	0.16	810	808	817
	0.08	792	795	797
	0.04	798	798	792
	0.02	778	792	788
<b>Compound 1</b>				
	0.96	955	964	955
	0.48	876	895	870
	0.24	832	845	844
	0.12	788	795	796
	0.06	770	769	771
<b>Compound 17 &amp; TEABF<sub>4</sub></b>				
(1:1 mixture)	0.5 M : 0.5 M	865	893	891

## B.8. Conductivity Data for Compounds 1, 3, 5, and 17

**Table B.8. Summary of concentration dependent conductivity data in acetonitrile of low (3 and 5), moderate (1), and high (17) solubility pyridiniums.** Reported viscosity values represent the average of  $n = 3$  replicates, and the error bars represent the respective standard deviations at ( $17.6\text{ }^{\circ}\text{C} \pm 0.5\text{ }^{\circ}\text{C}$ ).

<b>Controls</b>	<b>Conc. (M)</b>	<b>Conductivity (mS cm<sup>-1</sup>)</b>	<b>Conductivity Std. Dev (mS cm<sup>-1</sup>)</b>	<b>Temperature Avg. (°C)</b>	<b>Temperature Std. Dev. (°C)</b>
Water	N/A	0.012	0.000	N/A	N/A
Acetonitrile	N/A	0.001	0.000	17.7	0.1
<b>Compound 17</b>					
	0.68	32.8	0.2	17.7	0.8
	0.34	25.1	0.8	18.4	0.1
	0.17	16.0	0.2	18.6	0.3
	0.09	10.0	0.3	17.9	0.5
	0.04	5.80	0.03	19.5	0.9
<b>Compound 5</b>					
	0.29	25.0	0.2	17.7	0.2
	0.15	14.5	0.3	16.8	0.7
	0.07	8.5	0.3	17	1
	0.04	5.10	0.02	17.5	0.2
	0.02	3.00	0.03	18.4	0.3
<b>Compound 3</b>					
	0.32	30.0	0.7	16.9	0.7
	0.16	18.2	0.4	16.5	0.7
	0.08	10.8	0.2	16.2	0.6
	0.04	6.20	0.04	17.7	0.1
	0.02	3.80	0.04	18.1	0.3
<b>Compound 1</b>					
	0.96	28.3	0.4	18.2	0.4
	0.48	28.7	0.5	16.8	0.5
	0.24	19.5	0.2	17.3	0.3
	0.12	11.3	0.2	17.0	0.5
	0.06	7.2	0.1	17.6	0.2

**Table B.9. Raw conductivity data in acetonitrile of low (3 and 5), moderate (1), and high (17) pyridiniums collected at ambient temperature (17.6 °C ± 0.5 °C).**

	<b>Conc. (M)</b>	<b>Trial 1 (mS cm<sup>-1</sup>)</b>	<b>Trial 2 (mS cm<sup>-1</sup>)</b>	<b>Trial 3 (mS cm<sup>-1</sup>)</b>
<b>Controls</b>				
Water	N/A	0.011790	0.012400	0.012580
Acetonitrile	N/A	0.000544	0.000551	0.000549
<b>Compound 17</b>				
	0.68	33.00	32.80	32.70
	0.34	25.94	24.79	24.44
	0.17	16.21	15.92	15.78
	0.09	10.41	9.86	9.79
	0.04	5.83	5.88	5.83
<b>Compound 5</b>				
	0.29	25.20	24.97	24.82
	0.15	14.74	14.45	14.23
	0.07	8.93	8.37	8.33
	0.04	5.11	5.10	5.07
	0.02	3.08	3.03	3.02
<b>Compound 3</b>				
	0.32	30.80	29.67	29.46
	0.16	18.60	18.11	17.81
	0.08	11.02	10.75	10.60
	0.04	6.18	6.25	6.23
	0.02	3.80	3.75	3.73
<b>Compound 1</b>				
	0.96	28.69	28.06	28.01
	0.48	29.20	28.55	28.24
	0.24	19.65	19.43	19.33
	0.12	11.49	11.22	11.12
	0.06	7.22	7.15	7.12

## APPENDIX C: CHAPTER 4 SUPPLEMENTAL INFORMATION

### C.1. Equations, Summarize Results, and Raw Data

**Table C.1. Key equations used for global warming potential and technoeconomic analysis.**  
177,197,203,227,228

Description	Equation & Variables	Source
Pump hydraulic power	$P = \frac{Q \cdot H \cdot g \cdot \rho}{\text{pump efficiency} (0.85)}$ <p><i>P</i> [W] is the hydraulic power  <i>Q</i> [m<sup>3</sup> s<sup>-1</sup>] is the volumetric flow rate  <i>ρ</i> [kg m<sup>-3</sup>] is the fluid density  <i>g</i> [m s<sup>-1</sup>] is gravity  <i>H</i> [m] is differential head                      Pump efficiency [%] is assumed to be 85%</p>	(Mohammadi, 2021)
Electrocatalysis electricity consumption	$P = E_{app} \cdot J_{NITRR} \cdot SA_{cat}$ <p><i>P</i> [W] is the power required  <i>E<sub>app</sub></i> [V] is the applied potential  <i>J<sub>NITRR</sub></i> [A m<sup>-2</sup>] is the current density of the electrocatalytic nitrate reduction reaction (NITRR)  <i>SA<sub>cat</sub></i> [m<sup>2</sup>] is catalyst surface area</p>	(Li, 2020)
Ammonia stripper air/liquid ratio	$\text{air to liquid ratio} = \frac{Q_{air}}{Q_{leachate}}$ <p>Air to liquid ratio target is 50  <i>Q<sub>air</sub></i> [L h<sup>-1</sup>] is the air flow rate  <i>Q<sub>leachate</sub></i> [L h<sup>-1</sup>] is the liquid flow rate</p>	(Ferraz, 2013)
Global Warming Potential	$GWP = CO_{2,elec} + (310 \cdot NO_{X,elec}) + CO_{2,transport} + (310 \cdot NO_{X,transport})$ <p>GWP [CO<sub>2</sub> equivalents] is the total global warming potential  <i>CO<sub>2,elec</sub></i> [CO<sub>2</sub> equivalents] is the CO<sub>2</sub> equivalents attributed to electricity consumption by CO<sub>2</sub>  <i>NO<sub>X,elec</sub></i> [CO<sub>2</sub> equivalents] is the CO<sub>2</sub> equivalents attributed to electricity consumption by nitric oxide and N<sub>2</sub>O  <i>CO<sub>2,transport</sub></i> [CO<sub>2</sub> equivalents] is the CO<sub>2</sub> equivalents attributed to transportation by CO<sub>2</sub>  <i>NO<sub>X,transport</sub></i> [CO<sub>2</sub> equivalents] is the CO<sub>2</sub> equivalents attributed to transportation by nitric oxide and N<sub>2</sub>O</p>	(Mayo, 2015)
Net Present Value (Net Present Worth)	$NPV = \sum_{N=1}^n \frac{PV_N}{(1+i)^N}$ <p><i>NPV</i> [\$] is the net present value  <i>n</i> is the number of cash flows in the list of values  <i>N</i> [years] is the number of year from the present year  <i>i</i> [%] is the annual discount rate  <i>PV</i> [\$] are the value of cash flow in year <i>N</i></p> <p>NPV = 0 is the criterion used in setting annual nitrate emissions fee.</p>	(Sullivan, 2003)
Annualized Present Value (Annuity)	$A = PV \left( \frac{i(1+i)^N}{(1+i)^N - 1} \right)$ <p><i>A</i> [\$] is annuity equivalent to the present value  <i>N</i> [years] is the number of year from the present year  <i>i</i> [%] is the annual discount rate  <i>PV</i> [\$] are the value of cash flow in year <i>N</i></p>	(Sullivan, 2003)

**Table C.2. Results summary of Global Warming Potential (GWP) and capital investment costs for NC and NCC configurations.** Reference Table 2 in main text for breakdown of individual arrangement descriptions.

	NCC grid 1.6%	NCC grid 32%	NCC solar 1.6%	NCC solar 32%	NC grid 1.6%	NC grid 32%	NC solar 1.6%	NC solar 32%	Base
GWP kg CO2 equiv.	52,200	44,800	50,600	35,800	51,800	37,000	50,700	35,800	52,300
Feed Stage %	2.67%	2.20%	2.75%	2.75%	2.69%	2.66%	2.75%	2.75%	4.38%
ED Stage %	2.26%	2.64%	0.00%	0.00%	2.28%	3.19%	0.00%	0.00%	0.00%
EC Stage %	0.35%	8.19%	0.00%	0.00%	0.00%	0.00%	0.00%	0.00%	0.00%
NH3 Stage %	0.39%	9.26%	0.00%	0.00%	0.00%	0.00%	0.00%	0.00%	0.00%
HB Process %	94.3%	77.7%	97.2%	97.2%	95.0%	94.1%	97.2%	97.2%	95.6%
Initial Equipment Cost (USD)	\$22.8k	\$98.8k	\$4.86M	\$6.56M	\$7.34k	\$26.6k	\$4.76M	\$4.77M	N/A
Initial Investment Cost (USD)	\$56.9k	\$247k	\$12.1M	\$16.4M	\$18.3k	\$66.5k	\$11.9M	\$11.9M	N/A
Pumping %	6.80%	1.57%	0.03%	0.02%	21.1%	5.82%	0.03%	0.03%	N/A
ED %	14.1%	9.78%	0.07%	0.15%	43.8%	36.3%	0.07%	0.20%	N/A
EC %	4.19%	19.25%	0.02%	0.29%	0.00%	0.00%	0.00%	0.00%	N/A
NO3 <sup>-</sup> Storage %	11.3%	15.58%	0.05%	0.23%	35.1%	57.8%	0.05%	0.32%	N/A
NH3 Stripper %	9.19%	27.22%	0.04%	0.41%	0.00%	0.00%	0.00%	0.00%	N/A
NH3 Storage %	54.4%	26.6%	0.26%	0.40%	0.00%	0.00%	0.00%	0.00%	N/A
APV %	0.00%	0.00%	87.7%	64.9%	0.00%	0.00%	89.6%	89.2%	N/A
ES%	0.00%	0.00%	11.8%	33.6%	0.00%	0.00%	10.3%	10.2%	N/A

**Table C.3. Selection of examples of the variation in TMNR in different locations with variable application rates and types of ammonia fertilizer.** This table summarize data available in studies from Illinois, Ontario, Iowa, and Indiana; and Zhou and coworkers assessed nitrate leaching in a comprehensive nitrate leaching study.<sup>191,229–232</sup>

Location	Year	Conditions & Notes	Applied N (kg N ha <sup>-1</sup> ) [Fertilizer type]	NO <sub>3</sub> <sup>-</sup> Loss (kg N ha <sup>-1</sup> )	Theoretical Maximum %N Recovery (kg N ha <sup>-1</sup> )
Big Ditch Watershed (Champaign, IL)	2001	Flat tile drained area with row cropped agriculture	184	2.8	1.5%
	2002		[anhydrous NH <sub>3</sub> ]	3.1	1.7%
Eugene Whelan Experimental Station (Ontario, Canada)	1989	Conventional Tillage		1.87	0.6%
	1990	Conventional Tillage		2.51	0.8%
	1991	Conventional Tillage	132	0.29	0.1%
	1989	Ridge Tillage	[8-32-6 (N-P-K)]	2.62	0.9%
	1990	Ridge Tillage	&	5.48	1.9%
	1991	Ridge Tillage	168	1.70	0.6%
	1989	No Tillage	[NH <sub>4</sub> NO <sub>3</sub> ]	2.64	0.9%
	1990	No Tillage		4.10	1.4%
Iowa Ag-Drainage Research Site (Gilmore City, IW)	1990-1993	Tile drainage for combined corn-soybean sequence		58	32-34%
	1994-1999		168 – 179	10	5.6-6.0%
	2000-2004		[Not listed]	43	24-26%
	1997		Study Low: NO <sub>3</sub> <sup>-</sup> loss	1.1	0.6-0.7%
Southeast Purdue Agricultural Center (SEPAC) (Butler, IN)	1986-1988	3 m – tile drain spacing	280	49	18%
	1997-1999		[anhydrous NH <sub>3</sub> ] 252		
	2000-2015	10 m – tile drain spacing	[anhydrous NH <sub>3</sub> ] 196-224	34	15-17%
			[anhydrous NH <sub>3</sub> ] 280	36	
	1986-1988	20 m – tile drain spacing	[anhydrous NH <sub>3</sub> ] 252	16	13%
			[anhydrous NH <sub>3</sub> ] 196-224	26	
	1997-1999	20 m – tile drain spacing	[anhydrous NH <sub>3</sub> ] 280	27	9.6%
			[anhydrous NH <sub>3</sub> ] 252	12	
	2000-2015	20 m – tile drain spacing	[anhydrous NH <sub>3</sub> ] 196-224	24	4.8%
			[anhydrous NH <sub>3</sub> ]		



## C.2. Weidema Method: Data Quality Indicators

**Table C.4. Data quality indicators for each stage three scenarios: (1) Base Case, (2) 1.6% TMNR 3) 32% TMNR.** The data quality is evaluated based on the Weidema method. The Weidema method was used to evaluate the data quality using five categories: reliability of source, completeness, temporal correlation, geographical correlation, and further technological correlation. The data is assigned a value from 1 (higher quality) to 5 (lower quality) to indicate the independent data quality as well as how well the data reflects the system it is being used to represent.<sup>191,196,197,227,233–236</sup>

System Component	Value	Units	Source	DQI (Reliability)	DQI (Completeness)	DQI (Temporal)	DQI (Geographical)	DQI (Technological)
Nitrate Recycle Feedstock (Tile Drainage) – Alternative Cases								
Tile NO <sub>3</sub> <sup>-</sup> Concentration (1.6% TMNR)	14.8	NO <sub>3</sub> <sup>-</sup> mg L <sup>-1</sup>	Gentry et al. (2009)	1	1	5	1	4
Tile NO <sub>3</sub> <sup>-</sup> Concentration (32% TMNR)	297	NO <sub>3</sub> <sup>-</sup> mg L <sup>-1</sup>	Assumption	2	2	5	1	4
Fertilization Rate	184	kg ha <sup>-1</sup>	Gentry et al. (2009)	1	1	5	1	4
Average Illinois farm size	154	ha	USDA Farm Summary (2022)	1	1	1	1	4
Average Yearly Rainfall (1997-2001)	97	cm rain	Gentry et al. (2009)	1	1	5	1	4
Runoff Rainfall Proportion	25	%	Gentry et al. (2009)	1	1	5	1	4
April-June Rain Proportion	30	%	Illinois State Water Survey	1	1	1	1	4
Avg. Rainfall (April-June)	0.35	% Avg. Yearly Rainfall	(Gentry, 2009) Illinois State Water Survey (2018-2021)	1	1	1	1	4
Std. Dev. (April-June)	0.78	% Avg. Yearly Rainfall	(Gentry, 2009) Illinois State Water Survey (2018-2021)	1	1	1	1	4
Max Rainfall (April-June)	4.0	% Avg. Yearly Rainfall	(Gentry, 2009) Illinois State Water Survey (2018-2021)	1	1	1	1	4
Nitrate Recycle Electrodialysis – Alternative Cases								
Redox Shuttle Concentration	50	mM	Beh et al. (2019)	1	2	2	1	4
System Electrode Surface Area (1.6% TMNR)	1	m <sup>2</sup>	Beh et al. (2019)	1	2	2	1	4
System Electrode Surface Area (32% TMNR)	10	m <sup>2</sup>	Beh et al. (2019)	1	2	2	1	4
Current Density (1.6% TMNR)	37.4	mA cm <sup>-2</sup>	Beh et al. (2019)	1	2	2	1	4
Current Density (32% TMNR)	74.8	mA cm <sup>-2</sup>	Beh et al. (2019)	1	2	2	1	4
Nitrate Removal Rate	99.5	%	Beh et al. (2019)	1	2	2	1	4
Nitrate Recycle pH Adjustment – Alternative Cases								
Potassium Hydroxide (1.6% TMNR)	1,660	kg	Li et al. (2020) Calculated (1:1 M NO <sub>3</sub> <sup>-</sup> : KOH)	1	1	1	1	4
Potassium Hydroxide (32% TMNR)	33,100	kg	Li et al. (2020) Calculated (1:1 M NO <sub>3</sub> <sup>-</sup> : KOH)	1	1	1	1	4

**Table C.4. (cont'd)**

System Component	Value	Units	Source	DQI (Reliability)	DQI (Completeness)	DQI (Temporal)	DQI (Geographical)	DQI (Technological)
<b>Nitrate Recycle Electrocatalysis (Reduction of NO<sub>3</sub><sup>-</sup> to NH<sub>3</sub>) – Alternative Cases</b>								
Nitrate Reduction Rate	5.56	g <sub>NH<sub>3</sub></sub> mol <sub>cat</sub> <sup>-1</sup>	Li et al. (2020) Li et al. (2020)	1	1	1	1	4
Nitrate Conversion	~100%	%	(NITRRFE%)	1	1	1	1	4
Current density (Ru-ST-12)	125	mA cm <sup>-2</sup>	Li et al. (2020) Target (1:1 M NO <sub>3</sub> <sup>-</sup> :KOH)	1	1	1	1	4
Catalyst loading density	1.85	g m <sup>-2</sup>	Li et al. (2020)	1	1	1	1	4
Surface Area of Catalyst	2.12	m <sup>2</sup>	Li et al. (2020)	2	2	1	1	4
<b>Nitrate Recycle Ammonia Air Stripper – Alternative Cases</b>								
Liquid /air flow rate ratio	50		Ferraz et al. (2013)	1	2	3	1	4
Ammonia Stripper Recovery	95	%	Ferraz et al. (2013) Assumption (>88%)	1	2	3	1	4
Liquid flow rate (Low-Alt)	160	L h <sup>-1</sup>	Ferraz et al. (2013)	1	2	3	1	4
Liquid flow rate (High-Alt)	780	L h <sup>-1</sup>	Ferraz et al. (2013)	1	2	3	1	4
Air flow rate (Low-Alt)	7800	L h <sup>-1</sup>	Ferraz et al. (2013)	1	2	3	1	4
Air flow rate (High-Alt)	3900	L h <sup>-1</sup>	Ferraz et al. (2013)	1	2	3	1	4
<b>Supplementary Haber-Bosch Produced Ammonia – All Cases</b>								
Anhydrous Ammonia (Base Case)	28,400	kg	Gentry et al. (2009)	1	1	5	1	4
Supplementary Anhydrous Ammonia (Low-Alt)	27,500	kg	Gentry et al. (2009)	1	1	5	1	4
Supplementary Anhydrous Ammonia (High-Alt)	10,100	kg	Gentry et al. (2009)	1	1	5	1	4
Transportation Distance	200	mile	Rockford, IL to Champaign, IL	5	5	5	5	4
<b>General Information – All Cases</b>								
Fuel Emissions	0.8	g CO <sub>2</sub> ton-mile <sup>-1</sup>	Facanha et al. (2006)	1	1	5	5	4
CO <sub>2</sub> Grid Emissions	603	lb CO <sub>2</sub> MWh <sup>-1</sup>	EIA - Illinois Grid Emissions	1	1	1	1	1
SO <sub>2</sub> Grid Emissions	0.7	lb SO <sub>2</sub> MWh <sup>-1</sup>	EIA - Illinois Grid Emissions	1	1	1	1	1
NO <sub>x</sub> Grid Emissions	0.3	lb NO <sub>x</sub> MWh <sup>-1</sup>	EIA - Illinois Grid Emissions	1	1	1	1	1
Methane Extraction	0.073	ton <sub>CO<sub>2</sub></sub> ton <sub>NH<sub>3</sub></sub> <sup>-1</sup>	Smith et al. (2020)	1	1	2	4	1
HB Stoichiometry	1.22	ton <sub>CO<sub>2</sub></sub> ton <sub>NH<sub>3</sub></sub> <sup>-1</sup>	Smith et al. (2020)	1	1	2	4	1
Steam to Turbine	0.17	ton <sub>CO<sub>2</sub></sub> ton <sub>NH<sub>3</sub></sub> <sup>-1</sup>	Smith et al. (2020)	1	1	2	4	1
Steam to SMR	0.1	ton <sub>CO<sub>2</sub></sub> ton <sub>NH<sub>3</sub></sub> <sup>-1</sup>	Smith et al. (2020)	1	1	2	4	1
Other Steam	0.03	ton <sub>CO<sub>2</sub></sub> ton <sub>NH<sub>3</sub></sub> <sup>-1</sup>	Smith et al. (2020)	1	1	2	4	1
Heat loss/others	0.17	ton <sub>CO<sub>2</sub></sub> ton <sub>NH<sub>3</sub></sub> <sup>-1</sup>	Smith et al. (2020)	1	1	2	4	1

### C.3 Equipment costs, scaling, and supplier references

**Table C.5. Equipment costs, scaling, and references for NCC systems at 1.6% TMNR.**<sup>233</sup>

Description	Listed Price Cost	Listed Scale	1.6% TMNR Design Criteria	Scaled Cost	Notes/ Equipment Details	Reference/ Supplier
<b>Pump</b>						
Tile Sump Pump	\$1,549.00	25-15000 m <sup>3</sup> h <sup>-1</sup>	55-421 m <sup>3</sup> h <sup>-1</sup>	\$1,549.00	5 inch 1000 gpm 4500 gpm 500 m <sup>3</sup> /h horizontal centrifugal water pump 400 kw for irrigation	Hunan Zhongda Pump Industry Co., Ltd.
<b>Electrodialysis</b>						
Shuttle Pump	\$300.00	1-58 m <sup>3</sup> h <sup>-1</sup>	0.37-2.8 L h <sup>-1</sup>	\$300.00	KCB stainless steel cooking oil gear pump, Olive oil transfer pump, Soybean oil transfer pump	Botou Honghai Pump Co., Ltd.
1M KOH Storage Tank	\$3,500.00	50000 L	30,000 L	\$2,576.08	(>=10 Sets) Stainless Steel Elevated Water Tank Price Water Storage Tank 50000 Liter	Zaoqiang Longtime FRP Product Co., Ltd.
1M KOH Pump	\$300.00	1-58 m <sup>3</sup> h <sup>-1</sup>	13-100 mL h <sup>-1</sup>	\$300.00	KCB stainless steel cooking oil gear pump, Olive oil transfer pump, Soybean oil transfer pump	Botou Honghai Pump Co., Ltd.
Separators	\$284.00	N/A	1 m <sup>2</sup>	\$284.00	FuMA Tech GmbH	Beh et al. (2020) SI
Carbon felt	\$70.00	N/A	1 m <sup>2</sup>	\$70.00	PNNL	Beh et al. (2020) SI
Bipolar Plate	\$55.00	N/A	1 m <sup>2</sup>	\$55.00	PNNL	Beh et al. (2020) SI
		100,000 m <sup>2</sup>				
PVC Frame	\$16.84		0.29-2.2 MGD	\$382.80	PNNL	Beh et al. (2020) SI
Al end plate	\$193.00	N/A	1 m <sup>2</sup>	\$193.00	PNNL	Beh et al. (2020) SI
Tanks for Redox Shuttle	\$0.11	100,000	0.29-2.2 MGD	\$382.80	PNNL	Beh et al. (2020) SI
Cu current collector	\$115.00	N/A	1 m <sup>2</sup>	\$115.00	PNNL	Beh et al. (2020) SI
BTMAP-Fc shuttle	\$75.00	1	6.2 kg NO <sub>3</sub> <sup>-</sup> h <sup>-1</sup>	\$1,126.23	Harvard University	Beh et al. (2020) SI
Cables/Breakers/ Contactors/Transformer	\$0.08	100,000 W	0.29-2.2 MGD	\$1.91	PNNL: for 1 MW systems	Beh et al. (2020) SI
<b>Electrocatalysis</b>						
Separators	\$284.00	N/A	2.23 m <sup>2</sup>	\$633.32	FuMA Tech GmbH	Beh et al. (2020) SI
Carbon felt	\$70.00	N/A	2.23 m <sup>2</sup>	\$156.10	PNNL	Beh et al. (2020) SI
Bipolar Plate	\$55.00	N/A	2.23 m <sup>2</sup>	\$122.65	PNNL	Beh et al. (2020) SI
PVC Frame	\$16.84	N/A	13-100 mL/h	\$37.55	PNNL	Beh et al. (2020) SI
Starting Material (Ru-ST-12 Catalyst)	\$663.00	25 kg	4.12 g	\$3.56	Ruthenium(III) chloride hydrate	Sigma-Aldrich
Cables/Breakers/ Contactors/Transformer	\$0.08	100,000 W	13-100 mL h <sup>-1</sup>	\$0.03		Beh et al. (2020) SI
Cathode (Carbon Cloth)	\$50.00	1.00 m <sup>2</sup>	2.23 m <sup>2</sup>	\$78.48	(1-499 m <sup>2</sup> ) carbon fiber conductive cloth a electrical conductivity and mass transfer Flexible conductive carbon fiber cloth	Jiaxing Guohe Technology Co., Ltd.
Anode (Platinum)	\$150.00	15.00 m <sup>2</sup>	2.23 m <sup>3</sup>	\$46.37	{{(0.5-8m) by (30-50m) sheets} - Anode cathode platinum coated titanium mesh 50 60 80 100 Mesh Ti mesh for water electrolysis	Hebei Aegis Metal Materials Co., Ltd.

**Table C.5. (cont'd)**

<b>Description</b>	<b>Listed Price Cost</b>	<b>Listed Scale</b>	<b>1.6% TMNR Design Criteria</b>	<b>Scaled Cost</b>	<b>Notes/ Equipment Details</b>	<b>Reference/ Supplier</b>
<b>Ammonia Stripper, Compressor, Condenser</b>						
Stripper Feed Pump	\$300.00	1-58 m <sup>3</sup> h <sup>-1</sup>	155 L h <sup>-1</sup>	\$300.00	KCB stainless steel cooking oil gear pump, Olive oil transfer pump, Soybean oil transfer pump	Botou Honghai Pump Co., Ltd.
Ammonia Air stripper	\$1,499.00	8000 L h <sup>-1</sup>	7800 L h <sup>-1</sup> air flow	\$1,499.00	High Efficiency Absorption Column Wet Gas Scrubber Treatment Gas Scrubber System Industrial Water Filtration Mist Eliminator	XICHENG EP LTD
Air Compressor	\$629.00	5.3 CFM	4.8 CFM	\$592.69	California Air Tools SP Series Ultra Quiet & Oil-Free 2-HP 20-Gallon Steel Tank Air Compressor	California Air Tools
Ammonia Compressor	\$9,000.00	55 kg	500 kg NH <sub>3</sub> (2.2 kW)	\$1,304.60	Kaishan 330kw 55kw Industrial Open Type R717 Industrial Open Type Ammonia Refrigeration Screw Compressor, ASPEN MODEL	Shaanxi Kaishan Mechanical & Electrical Equipment Co., Ltd.
Ammonia Condenser	\$7,500.00	55 kg	500 kg NH <sub>3</sub> (0.28 kW)	\$1,087.17	JUAOTE Hacst Closed Cooling Tower Type Ammonia Evaporative Condenser, ASPEN MODEL	Foshan Juaote Hvac Technology Co., Ltd.
Ammonia Storage	\$10,000.00	5000 L	500 kg NH <sub>3</sub> (365 L)	\$10,000.00	Ammonia Storage Tank Liquid 5000 Liter	Huzhou Baihui Cryogenic Equipment Co., Ltd.
<b>Solar Arrays &amp; Energy Storage</b>						
Solar installation	\$0.71	per W	1,700-7,000 kWh per month	\$4,260,000	PNNL, Vertical Mount	Horowitz et a. (2020)
Energy Storage	\$6,785	per battery	1,700-7,000 kWh per month	\$573,261	High Quality Scalable Module All In One Solar Hybrid Inverter 6Kw 48 Volt Batterie Lithium 48V 10Kwh 20 Kwh Lithium Ion Battery	Shenzhen GSL Energy Co., Ltd.

**Table C.6. Equipment costs, scaling, and references for NCC systems at 32% TMNR.**<sup>233</sup>

Description	Listed Price Cost	Listed Scale	32% TMNR Design Criteria	Scaled Cost	Notes/ Equipment Details	Reference/ Supplier
<b>Pump</b>						
Tile Sump Pump	\$1,549.00	25-15000 m <sup>3</sup> h <sup>-1</sup>	55-421 m <sup>3</sup> h <sup>-1</sup>	\$1,549.00	5 inch 1000 gpm 4500 gpm 500 m3/h horizontal centrifugal water pump 400 kw for irrigation	Hunan Zhongda Pump Industry Co., Ltd.
<b>Electrodialysis</b>						
Shuttle Pump	\$300.00	1-58 m <sup>3</sup> h <sup>-1</sup>	0.37-2.8 L h <sup>-1</sup>	\$300.00	KCB stainless steel cooking oil gear pump, Olive oil transfer pump, Soybean oil transfer pump	Botou Honghai Pump Co., Ltd.
1M KOH Feed Storage Tank	\$3,500.00	50000 L	590,000 L	\$15,388.53	(>=10 Sets) Stainless Steel Elevated Water Tank Price Water Storage Tank 50000 Liter	Zaoqiang Longtime FRP Product Co., Ltd.
1M KOH Pump	\$300.00	1-58 m <sup>3</sup> h <sup>-1</sup>	13-100 mL h <sup>-1</sup>	\$300.00	KCB stainless steel cooking oil gear pump, Olive oil transfer pump, Soybean oil transfer pump	Botou Honghai Pump Co., Ltd.
Separators	\$284.00	N/A	10 m <sup>2</sup>	\$2,840.00	FuMA Tech GmbH	Beh et al. (2020) SI
Carbon felt	\$70.00	N/A	10 m <sup>2</sup>	\$700.00	PNNL	Beh et al. (2020) SI
Bipolar Plate	\$55.00	N/A	10 m <sup>2</sup>	\$550.00	PNNL	Beh et al. (2020) SI
PVC Frame	\$16.84	100,000 m <sup>2</sup>	0.29-2.2 MGD	\$382.80	PNNL	Beh et al. (2020) SI
Al end plate	\$193.00	N/A	10 m <sup>2</sup>	\$1,930.00	PNNL	Beh et al. (2020) SI
Tanks for Redox Shuttle	\$0.11	100,000	0.29-2.2 MGD	\$382.80	PNNL	Beh et al. (2020) SI
Cu current collector	\$115.00	N/A	10 m <sup>2</sup>	\$1,150.00	PNNL	Beh et al. (2020) SI
BTMAP-Fc shuttle	\$75.00	1	91.4 kg	\$1,126.23	Harvard University	Beh et al. (2020) SI
Cables/Breakers/Contactors/Transformer	\$0.08	100,000 W	0.29-2.2 MGD	\$1.91	PNNL: for 1 MW systems	Beh et al. (2020) SI
<b>Electrocatalysis</b>						
Separators	\$284.00	N/A	44.6 m <sup>2</sup>	\$12,666.40	FuMA Tech GmbH	Beh et al. (2020) SI
Carbon felt	\$70.00	N/A	44.6 m <sup>2</sup>	\$3,122.00	PNNL	Beh et al. (2020) SI
Bipolar Plate	\$55.00	N/A	44.6 m <sup>2</sup>	\$2,453.00	PNNL	Beh et al. (2020) SI
PVC Frame	\$16.84	N/A	13-100 mL h <sup>-1</sup>	\$751.06	PNNL	Beh et al. (2020) SI
Starting Material (Ru-ST-12 Catalyst)	\$663.00	25 kg	82.5 g	\$21.43	Ruthenium(III) chloride hydrate	Sigma-Aldrich
Cables/Breakers/Contactors/Transformer	\$0.08	100,000 W	13-100 mL h <sup>-1</sup>	\$0.03		Beh et al. (2020) SI
Cathode (Carbon Cloth)	\$50.00	1.00 m <sup>2</sup>	44.6 m <sup>2</sup>	\$488.17	(1-499 m2) carbon fiber conductive cloth a electrical conductivity and mass transfer Flexible conductive carbon fiber cloth	Jiaxing Guohe Technology Co., Ltd.
Anode (Platinum)	\$150.00	15.00 m <sup>2</sup>	44.6 m <sup>2</sup>	\$288.43	{{(0.5-8m) by (30-50m) sheets} - Anode cathode platinum coated titanium mesh 50 60 80 100 Mesh Ti mesh for water electrolysis	Hebei Aegis Metal Materials Co., Ltd.

**Table C.6. (cont'd)**

<b>Description</b>	<b>Listed Price Cost</b>	<b>Listed Scale</b>	<b>32% TMNR Design Criteria</b>	<b>Scaled Cost</b>	<b>Notes/ Equipment Details</b>	<b>Reference/ Supplier</b>
<b>Ammonia Stripper, Compressor, Condenser</b>						
Stripper Feed Pump	\$300.00	1-58 m <sup>3</sup> h <sup>-1</sup>	155 L h <sup>-1</sup>	\$1,500.00	KCB stainless steel cooking oil gear pump, Olive oil transfer pump, Soybean oil transfer pump	Botou Honghai Pump Co., Ltd.
Ammonia Air stripper	\$1,499.00	8000 L h <sup>-1</sup>	38800 L h <sup>-1</sup> air flow	\$19,335.90	High Efficiency Absorption Column Wet Gas Scrubber Treatment Gas Scrubber System Industrial Water Filtration Mist Eliminator	XICHENG EP LTD
Air Compressor	\$629.00	5.3 CFM	2500 L	\$7,547.72	California Air Tools SP Series Ultra Quiet & Oil-Free 2-HP 20-Gallon Steel Tank Air Compressor	California Air Tools
Ammonia Compressor	\$9,000.00	55 kg	22.8 CFM	\$592.69	Kaishan 330kw 55kw Industrial Open Type R717 Industrial Open Type Ammonia Refrigeration Screw Compressor, ASPEN MODEL	Shaanxi Kaishan Mechanical & Electrical Equipment Co., Ltd.
Ammonia Condenser	\$7,500.00	55 kg	4.8 CFM	\$3,426.58	JUAOTE Hacst Closed Cooling Tower Type Ammonia Evaporative Condenser, ASPEN MODEL	Foshan Juaote Hvac Technology Co., Ltd.
Ammonia Storage	\$10,000.00	5000 L	500 kg NH <sub>3</sub>	\$2,855.48	Ammonia Storage Tank Liquid 5000 Liter	Huzhou Baihui Cryogenic Equipment Co., Ltd.
<b>Solar Arrays &amp; Energy Storage</b>						
Solar installation	\$0.71	per W	500 kg NH <sub>3</sub>	\$4,260,000	PNNL, Vertical Mount	Horowitz et a. (2020)
Energy Storage	\$6,785	per battery	500 kg NH <sub>3</sub> (365 L)	\$2,201,949	High Quality Scalable Module All In One Solar Hybrid Inverter 6Kw 48 Volt Batterie Lithium 48V 10Kwh 20 Kwh Lithium Ion Battery	Shenzhen GSL Energy Co., Ltd.

#### C.4. Distribution of equipment/stage contributions to total GWP

**Table C.7. Distribution of equipment/stage contributions to total GWP for the NCC grid 1.6% arrangement.** The equipment sizing criteria and operating sizing are detailed, with the paired energy consumption associated with operation or transportation.

Description	Sizing Unit	Operation Unit	Electricity Consumption (kWh)	Electricity NOx Emissions (kg)	Electricity CO2 Emissions (kg)	Transportation Emissions NOx (kg)	Transportation Emissions CO2 (kg)
<b>Feed Acquisition</b>							
Tile drainage to sump pump	N/A N/A	0.29 MGD	0	0	0	4.47	7.26
Tile drainage to sump pump	2.22 MGD	2.22 MGD	0	0	0	0	0
<b>Electrodialysis (ED)</b>							
Sump Pump to ED	54.99 m <sup>3</sup> h <sup>-1</sup>	54.99 m <sup>3</sup> h <sup>-1</sup>	1,538	0.209	421	0	0
Sump Pump to ED	421.28 m <sup>3</sup> h <sup>-1</sup>	421.28 m <sup>3</sup> h <sup>-1</sup>	620	0.084	170	0	0
From ED to tile drain	2.22 MGD	0.29 MGD	0	0	0	0	0
	0.78 mL s <sup>-1</sup>	0.10 mL s <sup>-1</sup>	2,157	0.294	590	0	0
<b>Redox shuttle circulation pumps</b>							
<b>Electrocatalysis (EC)</b>							
From 1M KOH Feed Pump to ED	13.15 mL h <sup>-1</sup>	100.71 mL h <sup>-1</sup>	3.64E-04	4.95E-08	9.96E-05	0.59	0.96
<b>Ammonia Stripper/Condenser/Compressor</b>							
Liquid flow through stripper	155.29 L h <sup>-1</sup>	155.29 L h <sup>-1</sup>	2.83E-01	3.86E-05	7.75E-02	0	0
From Stripper storage to 1M KOH Storage	100.71 mL h <sup>-1</sup>	100.71 mL h <sup>-1</sup>	1.48E-04	2.02E-08	4.05E-05	0	0
Air flow through compressor	4.57 cfm	4.57 cfm	283	0.039	77	0	0
Ammonia Compress/Condense/Store	N/A N/A	N/A N/A	471	0	129	0	0
<b>Haber-Bosch Process</b>							
Methane extraction	27,938 kg	27,938 kg	0	2.37	2039.5	0	0
HB Reaction Stoichiometry	27,938 kg	27,938 kg	0	39.57	34084.9	0	0
Steam to turbine	27,938 kg	27,938 kg	0	5.51	4749.5	0	0
Steam to SMR	27,938 kg	27,938 kg	0	3.24	2793.8	0	0
Other Steam	27,938 kg	27,938 kg	0	0.97	838.2	0	0
Heat loss/others	27,938 kg	27,938 kg	0	5.51	4749.5	0	0

**Table C.8. Distribution of equipment/stage contributions to total GWP for the NCC grid 32% arrangement.** The equipment sizing criteria and operating sizing are detailed, with the paired energy consumption associated with operation or transportation.

Description	Sizing Unit	Operation Unit	Electricity Consumption (kWh)	Electricity NOx Emissions (kg)	Electricity CO2 Emissions (kg)	Transportation Emissions NOx (kg)	Transportation Emissions CO2 (kg)
Feed Acquisition							
Tile drainage to sump pump	N/A N/A	0.29 MGD	0	0	0	3.16	5.13
Tile drainage to sump pump	2.22 MGD	2.22 MGD	0	0	0	0	0
Electrodialysis (ED)							
Sump Pump to ED	54.99 m <sup>3</sup> h <sup>-1</sup>	54.99 m <sup>3</sup> h <sup>-1</sup>	1,538	0.209	421	0	0
Sump Pump to ED	421.28 m <sup>3</sup> h <sup>-1</sup>	421.28 m <sup>3</sup> h <sup>-1</sup>	620	0.084	170	0	0
From ED to tile drain	2.22 MGD	0.29 MGD	0	0	0	0	0
Redox shuttle circulation pumps	0.78 mL s <sup>-1</sup>	0.10 mL s <sup>-1</sup>	2,157	0.294	590	0	0
Electrocatalysis (EC)							
From 1M KOH Feed Pump to ED	26.29 mL h <sup>-1</sup>	201.42 mL h <sup>-1</sup>	7.28E-04	9.91E-08	1.99E-04	11.8	19.1
Ammonia Stripper/Condenser/Compressor							
Liquid flow through stripper	776.44 L h <sup>-1</sup>	776.44 L h <sup>-1</sup>	5.67E+00	7.71E-04	1.55E+00	0	0
From Stripper storage to 1M KOH Storage	201.42 mL h <sup>-1</sup>	201.42 mL h <sup>-1</sup>	2.96E-04	4.03E-08	8.11E-05	0	0
Air flow through compressor	22.85 cfm	22.85 cfm	5,661	0.770	1548	0	0
Ammonia Compress/Condense/Store	N/A N/A	N/A N/A	9,489	1	2,595	0	0
Haber-Bosch Process							
Methane extraction	19,736 kg	19,736 kg	0	1.67	1440.8	0	0
HB Reaction Stoichiometry	19,736 kg	19,736 kg	0	27.95	24078.4	0	0
Steam to turbine	19,736 kg	19,736 kg	0	3.89	3355.2	0	0
Steam to SMR	19,736 kg	19,736 kg	0	2.29	1973.6	0	0
Other Steam	19,736 kg	19,736 kg	0	0.69	592.1	0	0
Heat loss/others	19,736 kg	19,736 kg	0	3.89	3355.2	0	0



**Table C.9. Distribution of equipment/stage contributions to total GWP for the Haber-Bosch produced and purchased ammonia.** The energy consumption is associated with operation or transportation.

Description	Sizing Unit	Operation Unit	Electricity Consumption (kWh)	Electricity NOx Emissions (kg)	Electricity CO2 Emissions (kg)	Transportation Emissions NOx (kg)	Transportation Emissions CO2 (kg)
Feed Acquisition							
Tile drainage to sump pump	N/A N/A	N/A N/A	0	0	0	7.38	4.54
Tile drainage to sump pump	N/A N/A	N/A N/A	0	0	0	0	0
Electrodialysis (ED)							
Sump Pump to ED	N/A N/A	N/A N/A	0	0	0	0	0
Sump Pump to ED	N/A N/A	N/A N/A	0	0	0	0	0
From ED to tile drain	N/A N/A	N/A N/A	0	0	0	0	0
Redox shuttle circulation pumps	N/A N/A	N/A N/A	0	0	0	0	0
Electrocatalysis (EC)							
From 1M KOH Feed Pump to ED	N/A N/A	N/A N/A	0	0	0	0	0
Ammonia Stripper/Condenser/Compressor							
Liquid flow through stripper	N/A N/A	N/A N/A	0	0	0	0	0
From Stripper storage to 1M KOH Storage	N/A N/A	N/A N/A	0	0	0	0	0
Air flow through compressor	N/A N/A	N/A N/A	0	0	0	0	0
Ammonia Compress/Condense/Store	N/A N/A	N/A N/A	0	0	0	0	0
Haber-Bosch Process							
Methane extraction	28,370 kg	0.073 kg	0	2.40	2071.0	0	0
HB Reaction Stoichiometry	28,370 kg	1.22 kg	0	40.18	34611.5	0	0
Steam to turbine	28,370 kg	0.17 kg	0	5.60	4822.9	0	0
Steam to SMR	28,370 kg	0.1 kg	0	3.29	2837.0	0	0
Other Steam	28,370 kg	0.03 kg	0	0.99	851.1	0	0
Heat loss/others	28,370 kg	0.17 kg	0	5.60	4822.9	0	0

## C.5. Assumptions and Calculations

**Table C.10. Daily precipitation and monthly precipitation summary for April, May, and June rainfall between 2018-2021 from the Weather Observations for Champaign-Urbana, Illinois from the Illinois State Water Survey, Prairie Research Institute, University of Illinois.**

	2018	2019	2020	2021
Average Daily Rainfall (% of Annual Rainfall)	0.34%	0.36%	0.41%	0.31%
Standard Deviation Daily Rainfall (% of Annual Rainfall)	0.74%	0.68%	1.02%	0.70%
Maximum Daily Rainfall (% of Annual Rainfall)	4%	3%	6%	4%
Sum of Rainfall April through June (% of Annual Rainfall)	31%	33%	37%	28%
Annual Rain Fall (inches)	45.99	42.29	42.07	45.3

Day	April	May	June	April	May	June	April	May	June	April	May	June
	2018			2019			2020			2021		
	Precipitation (inches)											
1		0	0.71	0	0.79	0	0	0	0	0	0	0
2	0.24	0	0	0	0.07		0	0.01	0	0	0	0
3	0.4	0.63	0.28	0	0.32	0	0	0.3	0	0	0.15	0
4	0.2	0.01	0	0	0.03	0	0.05	0.01	2.51	0	0	0
5		0	0	0.12	0	0		0.14	0	0	0.17	0
6	0	0	0	0	0	0	0	0.14	0	0	0	0
7			0	0.05	0	0	0	0	0	0	0	0.23
8	0	0	0	1.18	0.04	0	0	0.05	0	0.26	0	0
9	0.14	0	0.19	0	1.48	0.01	0.39	0	0	0.29	1.05	0.22
10		1.23	1.15	0.27	0.01	0		0	0.16	0.01	0.15	0
11	0	0	1.62	0	0	0	0	0.03	0.02	0.24	0.04	0
12	0	0	1.47	0.5	0.2	0	0.14	0	0	0.21	0	0
13	0	0	0.18	0	0.03	0.62	0.01	0	0	0	0	0.61
14	0.85	0	0	0.61	0	0	0	0	0.02	0	0	0
15	0.27	0.06	0.02	0.37	0.03	0.28	0	0.21	0	0	0	0
16	0.02	0.03	0	0	0	0.73		0.01	0	0	0.01	0
17		0	0	0		0	0.23	1.57	0	0	0.35	0
18	0	0	0	0.57	0			0.6	0	0	0.46	0.02
19		0.04	0	0.32	0.06	0	0	0.01	0	0.02	0.14	0.74
20	0	0	0.87	0	0.22	0.56	0	0.09	0	0	0.01	0.01
21	0	0.02	0.63	0	0.04	0	0	0	1.09	0.32	0	0
22	0	0.02	0.68	0	1.02	0.45	0	0	0	0	0	0
23	0	0	0.07	0	0.4	0	0.15	0	1.31	0	0	0.01
24	0.2	0		0	0		0.33	0	0.06	0	0	0
25	0	0	0		0.01	0.08	0.8	0.64	0	0.03	0	1.5
26	0	0.35	0.37	0.53	0.79		1.24	0.17	0	0	0.26	1.64
27	0	0	0.02	0	0.05	0	0	0.01	0	0	0	0.65
28	0	0	0	0.18	0	0		0.07	0.67	0.01	0.38	1.29
29	0	0	0	0.17	0.37	0	1.79	0.03	0	0.71	0.34	0.03
30	0	0.11	0	0.02	0.05	0.09	0.46	0	0.04	0.01	0	0.29

**Table C.11. Assumptions and calculations for rainfall, land area, and equipment efficiencies.** <sup>191,197,227,233</sup>

	<b>1.6% TMNR</b>	<b>32% TMNR</b>	<b>Unit</b>	<b>Reference</b>
Theoretical Maximum Recovery (Recycled Ammonia / Needed Ammonia)	1.61%	32.20%	%	Calculated
Average nitrate concentration (April-June)	14.8	297	mg L <sup>-1</sup>	(Gentry, 2009)
Average precipitation 1971-2001	97	97	cm	(Gentry, 2009)
Average precipitation 1971-2001	0.97	0.97	m	Calculated
25% Average precipitation 1971-2001 April-June (30%)	0.07275	0.07275	m	(Gentry, 2009) Illinois State Water Survey
Average Farm Size (IL) 2021	381	381	acre	Farms and Land in Farms 2021 Summary
Average Farm Size (IL) 2021	154	154	ha	Calculated
Average Farm Size (IL) 2021	1,541,854	1,541,854	m <sup>2</sup>	Calculated
Tile runoff	112,170	112,170	m <sup>3</sup>	Calculated
Tile runoff	112,169,854	112,169,854	L	Calculated
Theoretical Max Recovered Nitrate	1,664	33,277	kg NO <sub>3</sub> <sup>-</sup>	Calculated
Theoretical Max Recovered Ammonia	457	9,134	kg NH <sub>3</sub>	Calculated
Fertilization rate Anhydrous Ammonia (82% N)	184	184	kg ha <sup>-1</sup>	(Gentry, 2009)
Total Fertilizer Needed Anhydrous Ammonia (82% N)	28,370	28,370	kg	Calculated
Max Percent Recovery	1.61%	32.20%		Calculated
Recovery from ED (99.5%)	454	9088	kg	(Beh, 2019)
Recovery from ED (99.5%)	1.60%	32.03%		Calculated
EC Conversion (100%)	454	9088	kg	(Li, 2020)
EC Conversion (100%)	1.60%	32.03%		Calculated
Ammonia Stripper Recovery (95%)	432	8634	kg	(Ferraz, 2013)
Ammonia Stripper Recovery (95%)	1.52%	30.43%		Calculated

**Table C.12. Assumptions and calculations for the NCC grid 1.6% and NCC grid 32% arrangements using the ruthenium nanocluster catalyst (Ru-ST-12) to convert nitrate to ammonia.<sup>227</sup>**

	NCC grid 1.6%	NCC grid 32%	Unit	Reference
Applied potential	0.2	0.2	V	(Li, 2020)
NITRR Current Density	125	125	mA/cm <sup>2</sup>	(Li, 2020)
NITRR Current Density	1250	1250	A/m <sup>2</sup>	(Li, 2020)
Catalyst Loading	0.185	0.185	mg/cm <sup>2</sup>	(Li, 2020)
Catalyst Loading	1.85	1.85	g/m <sup>2</sup>	(Li, 2020)
Total Ammonia Produced in EC (100% Conversion)	454	9,088	kg	Calculated
Time Running	2160	2160	hr	(Li, 2020)
Concentration	1	1	mol NO <sub>3</sub> /L	(Li, 2020)
Ammonia evolving rate	3	3	mol/h*g <sub>cat</sub>	(Li, 2020)
Mass catalyst needed	4.12	82.50	g Ru-ST-12	Calculated
Surface area of catalyst needed	2.23	44.59	m <sup>2</sup>	Calculated
Power	557	11149	W	Calculated
Energy Consumption	1,204	24,081	kWh	Calculated
Sulfur dioxide	0.382	7.646	kg SO <sub>2</sub>	Calculated
Nitrogen oxide	0.164	3.277	kg NO <sub>x</sub>	Calculated
Carbon dioxide	329	6586	kg CO <sub>2</sub>	Calculated

**Table C.13. Assumptions and calculations for the NCC grid 1.6% and NCC grid 32% arrangements using the ammonia air stripper, the primary design criteria was maintaining an air flow to liquid flow ratio of 50.<sup>197</sup>**

	NCC grid 1.6%	NCC grid 32%	Unit	Reference
Total height	2.5	2.5	m	(Ferraz, 2013)
Packed-bed height	2.0	2.0	m	(Ferraz, 2013)
Diameter	0.3	0.3	m	(Ferraz, 2013)
Cross-section Area	0.07065	0.07065	m <sup>2</sup>	Calculated
Packed-bed Volume	0.142	0.142	m <sup>3</sup>	(Ferraz, 2013)
Volume	0.177	0.177	m <sup>3</sup>	(Ferraz, 2013)
Number of Stripper Columns	1	5		(Ferraz, 2013)
Total Packed Bed Volume	25.1	125.3	m <sup>3</sup>	(Ferraz, 2013)
Total Lechate Volume	26,815	536,303	L	(Ferraz, 2013)
Liquid Flow Rate - TARGET	155	776	L h <sup>-1</sup>	(Ferraz, 2013)
Air Flow Rate - TARGET	7764	38822	L h <sup>-1</sup>	(Ferraz, 2013)
Air to Liquid Flow	50	50		(Ferraz, 2013)
Operation Time Needed	152	607	h	(Ferraz, 2013)
Operation Time Extra	190	759	h	Calculated
Operation Time	8	32	days	Calculated

## C.6. Economic Calculations: Net Present Values and Sensitivity Analysis

**Table C.14. Example calculation for annualized net present value (NPV) cash flow and nitrate emissions fee that yield NPV=0 after a 20-year lifespan under variable conditions.** To accommodate a range of low and high discount rates (if this project was to be pursued fully/partially with, or independent of government assistance) examples of the nitrate emission fee rate is estimated for 48 combinations of: technology (NC vs. NCC), energy supply (grid vs. solar), TMNR (1.6% vs. 32%), maintenance frequency (every 5- or 10-year equipment replacement), and finally discount rates of 1.5% (federal and private/farmer), 1.5% (federal) and 7% (private/farmer), and 7% (federal and private/farmer). Note maintenance consists of replacing the anodes, cathodes, and membranes of the systems, where high frequency replacement occurs every five years and low frequency replacement occurs every ten years. The NPV calculations were used for overall evaluation and to estimate effluent fee rates. The annual NPV is the sum of annual capital costs, annual operating costs, annual maintenance, and replacement fees, and proposed annual emissions fee; the NPV was set to equal zero to determine the value for the proposed annual emissions fee.

	Scaling Percent	NC <sub>grid</sub> (1.6%)	NC <sub>grid</sub> (32%)	NC <sub>solar</sub> (1.6%)	NC <sub>solar</sub> (32%)
<b>Fixed Capital Direct Costs</b>					
Purchased Equipment	40%	-\$4,759.74	-\$11,212.74	-\$4,752,752.23	-\$4,759,205.23
Equipment Installation	10%	-\$1,190	-\$2,803	-\$1,188,188	-\$1,189,801
Piping (includes insulation)	8%	-\$952	-\$2,243	-\$950,550	-\$951,841
Instruments and Control	5%	-\$595	-\$1,402	-\$594,094	-\$594,901
Electrical Equipment.	10%	-\$1,190	-\$2,803	-\$1,188,188	-\$1,189,801
Buildings	0%	\$0	\$0	\$0	\$0
Site Preparation	2%	-\$238	-\$561	-\$237,638	-\$237,960
Service Facilities	0%	\$0	\$0	\$0	\$0
Land	0%	\$0	\$0	\$0	\$0
<b>Fixed Capital Indirect Costs</b>					
Engineering and Supervision	5%	-\$595	-\$1,402	-\$594,094	-\$594,901
Construction Expenses	5%	-\$595	-\$1,402	-\$594,094	-\$594,901
Contractor's fee	5%	-\$595	-\$1,402	-\$594,094	-\$594,901
Contingency.	5%	-\$595	-\$1,402	-\$594,094	-\$594,901
Start up expenses	5%	-\$595	-\$1,402	-\$594,094	-\$594,901
<b>Total Fixed Capital Costs</b>	100%	-\$11,899	-\$28,032	-\$11,881,881	-\$11,898,013
<b>Federal Investment</b>					
NCRS Construction Cost	75%	-\$8,925	-\$21,024	-\$8,911,410	-\$8,923,510
NCRS Discount Rate (20 year project)		1.50%	1.50%	1.50%	1.50%
<b>Farmer Investment</b>					
Farmer Construction Cost	25%	-\$2,975	-\$7,008	-\$2,970,470	-\$2,974,503
Discount Rate		7.00%	7.00%	7.00%	7.00%
<b>Present Value Total Costs</b>		-\$23,532	-\$55,435	-\$23,497,160	-\$23,529,063
<b>Annualized Capital Costs</b>		-\$801	-\$1,886	-\$799,443	-\$800,528
<b>Annual Operating Costs</b>		-\$424	-\$424	\$0	\$0
<b>Annualized Maintenance &amp; Replacement Costs</b>		-\$53	-\$531	-\$53	-\$531
<b>Proposed Annual Emissions Fee</b>		\$1,277	\$2,841	\$799,496	\$801,059
<b>Net Present Value (Annualized)</b>		0.00	0.00	0.00	0.00
<b>Annual Nitrate Emissions (kg)</b>		1,664	33,277	1,664	33,277
<b>Annual Emissions Fee (\$/kg nitrate emitted)</b>		\$0.77	\$0.09	\$480.47	\$24.07

**Table C.15. Complete summary of upper and lower limit estimates for nitrate emissions fee (\$/kg nitrate per year) including each combination of technology (NC vs. NCC), energy supply (grid vs. solar), TMNR (1.6% vs. 32%), maintenance frequency (every 5- or 10-year equipment replacement), and finally discount rates of 1.5% (federal and private/farmer), 1.5% (federal) and 7% (private/farmer), and 7% (federal and private/farmer).**

<b>System</b>	<b>NRCS Investment Discount Rate</b>	<b>Farmer Investment Discount Rate</b>	<b>Maintenance Frequency</b>	<b>Grid (32% TMNR)</b>	<b>Grid (1.6% TMNR)</b>	<b>Solar (32% TMNR)</b>	<b>Solar (1.6% TMNR)</b>
NC*	1.50%	1.50%	10 year	\$0.07	\$0.68	\$20.83	\$415.92
NC*	1.50%	1.50%	5 year	\$0.08	\$0.70	\$20.84	\$415.94
NC	1.50%	7.00%	10 year	\$0.07	\$0.75	\$24.06	\$480.45
NC	1.50%	7.00%	5 year	\$0.09	\$0.77	\$24.07	\$480.47
NCC	1.50%	1.50%	10 year	\$0.25	\$2.30	\$28.50	\$424.98
NCC	1.50%	1.50%	5 year	\$0.31	\$2.38	\$28.56	\$425.06
NCC	1.50%	7.00%	10 year	\$0.32	\$2.65	\$32.96	\$490.95
NCC	1.50%	7.00%	5 year	\$0.38	\$2.73	\$33.02	\$491.03
NC	7.00%	7.00%	10 year	\$0.10	\$0.94	\$33.76	\$674.03
NC	7.00%	7.00%	5 year	\$0.11	\$0.96	\$33.77	\$674.05
NCC	7.00%	7.00%	10 year	\$0.53	\$3.70	\$46.34	\$688.86
NCC	7.00%	7.00%	5 year	\$0.59	\$3.78	\$46.40	\$688.94

\*Values discussed in main text